Quantum Space Gravimetry for monitoring Earth's Mass Transport Processes (QSG4EMT)

ESA Contract No. ESA RFP/3-17687/22/NL/SD

Final Report

Issue 1.0

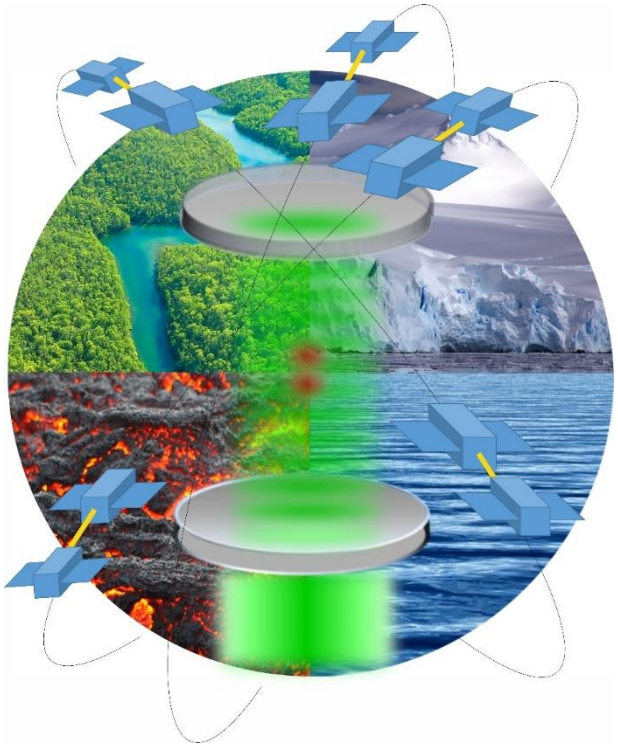

POLITECNICO DI MILANO · TU Delft · hcu HafenCity Universität Hamburg · UNIVERSITÄT BONN · UNIVERSITY OF TRIESTE

ESA STUDY CONTRACT REPORT		
ESA Contract No: 4000138395/22/NL/SD	Subject: Final Report Quantum Space Gravimetry for monitoring Earth's Mass Transport Processes (QSG4EMT)	Contractor: Technische Universität München
*ESA CR( ) No.	No. of Volumes: 1 This is Volume No.: 1	Contractors Reference: Roland Pail

Abstract:

Final Report of ESA study "Quantum Space Gravimetry for monitoring Earth's Mass Transport Processes (QSG4EMT)"

Names of Authors:
Roland Pail, Philipp Zingerle, Thomas Gruber, João Encarnação, Christian Siemes, Federica Migliaccio, Mirko Reguzzoni, Lorenzo Rossi, Öykü Koç, Carla Braitenberg. Annette Eicker, Jürgen Kusche, Christina Strohmenger, Bernd Uebbung, Helena Gerdener, Anne Springer

** NAME OF ESA STUDY MANAGER:	** ESA BUDGET HEADING
Ilias Daras DIV: Mission Science Division DIRECTORATE: Earth Observation Programmes	

Authors

Roland Pail	Technical University Munich (TUM)
Philipp Zingerle	TUM
Thomas Gruber	TUM
João Encarnação	Delft University of Technology (TUD)
Christian Siemes	TUD
Federica Migliaccio	Politecnico di Milano (POLIMI)
Mirko Reguzzoni	POLIMI
Lorenzo Rossi	POLIMI
Öykü Koç	POLIMI
Carla Braitenberg	Trieste University (UNITS)
Annette Eicker	HafenCity University Hamburg (HCU)
Jürgen Kusche	University of Bonn (UNB)
Christina Strohmenger	UNB
Bernd Uebbung	UNB
Helena Gerdener	UNB
Anne Springer	UNB

Document Change Record

ISSUE /REV.	DATE	REASON FOR CHANGE	CHANGED PAGES / PARAGRAPHS
1.0	25.10 2024	Initial Issue	• All

Table of Contents

PREFACE

This Final Report reports on the results of the project "Quantum Space Gravimetry for monitoring Earth's Mass Transport Processes (QSG4EMT)". It addresses all tasks defined in the SoW and the corresponding work packages defined in the WBS:

Part	Title	Task	WP	TN
1	QSG user requirements	1	100	D1
2	Consolidation of QSG user requirements	1	100	D2
3	Gravimetric instrument performances and related noise modelling	2	200	D3
4	Analysis of the added value of quantum sensing to existing and planned missions	3	300	D4
5	Mass change products from QSG mission architectures	4-7	400–700	D5
6	Preliminary QSG mission requirements and their assessment against QSG user requirements	5-7	400–700	D6
7	Applications of QSG mission architectures and related operational services	8-10	800–1000	D7
8	Outreach	12	all	D8-D10-

A summary of the main findings of this project phase and the main conclusions are given in the Executive Summary.

Executive Summary

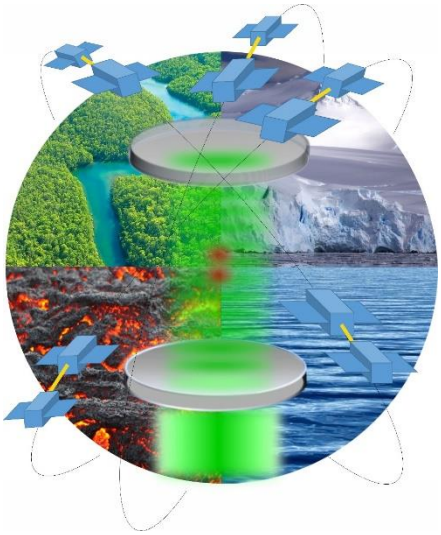

Gravity field observations are a unique measurement technique to observe and monitor mass transport in the Earth's system. Sustained gravity field observation from space contributes significantly to numerous of Essential Climate Variables (ECVs) as defined by Global Climate Observing System (GCOS), and directly measures changes of the recently adopted ECV "Terrestrial water storage".

Next-generation gravity missions are expected to enhance our knowledge of mass transport processes in the Earth system, establishing their products applicable to new scientific fields and serving societal needs. Compared to the current situation (GRACE Follow-On), a significant step forward to increase spatial and temporal resolution can be achieved by new mission concepts such as the joint NASA/ESA mission concept Mass change And Geosciences International Constellation (MAGIC).

Quantum gravity mission constellations are a core component of ESA's Accelerator "Space for a Green Future". The main advantage of quantum instruments such as cold atom interferometers (CAI) is their close to flat error spectrum, thus reducing high-amplitude long-wavelength errors of classical electrostatic accelerometers.

In the frame of the ESA-funded project "Quantum Space Gravimetry for monitoring Earth's Mass Transport Processes (QSG4EMT)", we analyzed the potential of quantum satellite gravity (QSG) missions to improve the monitoring of mass distribution and mass change processes in the Earth system. The error budget of current gravity satellite missions was analyzed, in order to identify the biggest error contributors, and to evaluate potential future improvements regarding instrumentation. Since instrument errors are not the dominant error source, but rather temporal aliasing errors resulting from an under-sampling of high-frequency temporal gravity signals, extended satellite constellations and improved processing techniques have been investigated with the focus on low-low inter-satellite tracking mission constellations, quantum gradiometry and hybrid concepts, with the goal to reduce temporal aliasing errors. In parallel, user requirements have been formulated. The impact of extended constellations in combination with improved sensor technologies have been assessed for the main applications fields, continental hydrology, climate modelling, oceans and solid Earth.

1) Science and user requirements for QSG missions

The goal of this work package (WP100) was the definition of user requirements for future constellations of quantum gravity missions resulting in (1) a list of (new) application fields that can be investigated with such a mission, and (2) performance numbers that would be required from the users' perspective, both leading to an update of the Science and Traceability Matrix (SATM) table. To come up with a consolidated view on user needs and application-dependent science requirements and to identify new users and application fields, we targeted at involving the community as broadly as possible. Therefore, a community online questionnaire was designed and broadly advertised among various potential user groups. Questions targeted the

background of the person, their specific demands regarding the spatial & temporal resolution, latency, and accuracy of mass change products, as well as various topics, e.g. regarding data combination or the assimilation into models. In total, 131 users from 25 different countries spanning all applications fields (hydrology, oceanography, glaciology and ice sheets, solid Earth studies, geodesy, atmosphere & climate modeling) participated.

For the identification of new applications, we added a question to the user questionnaire, that explicitly asked the participants to identify applications that have not been possible with current missions but would be possible with the hypothetical quantum mission scenarios. Answers have been synthesized and new application fields have been extracted from the free-text answers received upon this question and incorporated into the SATM table. When asked about their application driven demands independent of specific mission scenarios („wish list"), users asked for a spatial resolution of 10-100km (40%) to 100-300km (45%) as threshold and <10km (46%) or 10-100km (47%) as desired outcome. For the temporal resolution a peak can be identified for one month (44%), but a considerable number (24%) also prefers one week. For the desired temporal resolution, the majority is interested in a one-day resolution (35%), followed by a weekly resolution (26%). The latency requirements mostly range between one week and three months (threshold) and one day and one month (desired).

While the wish list numbers are partly too optimistic and out of reach for satellite gravimetry, there is still added benefit for the specific application fields, even when the demands cannot be fully satisfied. Therefore, two hypothetical baseline scenarios were defined for a potential future quantum gravity mission with "Baseline 1" referring to a conservative accuracy assumption and "Baseline 2" denoting an optimistic scenario. The table in Figure 0-1 (left) puts the respective (theoretical) performance numbers in perspective to currently achievable accuracies of the GRACE-FO mission and envisaged MAGIC uncertainties. The right side of Figure 0-1 summarizes the assumed benefit of the two baseline scenarios for the applications under question in the survey. Already the less ambitious Baseline 1 is considered to be of at least considerable benefit (40%), large benefit (31%) or major benefit (18%). For the more optimistic Baseline 2 scenario, the largest number of participants (43%) expects a major benefit from such a potential new mission. As this acceptance of the hypothetical performance numbers is very consistent across all application fields, we adopted these numbers as the default values in the SATM table as threshold (Baseline 1) and target (Baseline 2) requirements. It was agreed upon with ESA that these numbers shall only be changed for individual applications where there is strong evidence, e.g., from data bases such as the observation requirements provided by the GCOS for their Essential Climate Variables (ECVs) and OSCAR (Observing Systems Capability Analysis and Review Tool) or from the scientific literature.

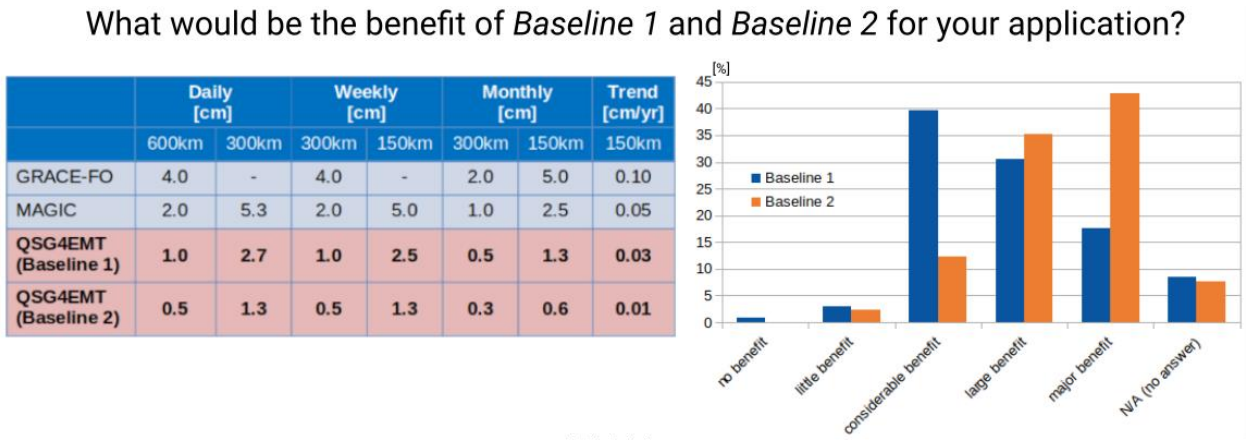

	Daily [cm]		Weekly [cm]		Monthly [cm]		Trend [cm/yr]
	600km	300km	300km	150km	300km	150km	150km
GRACE-FO	4.0	-	4.0	-	2.0	5.0	0.10
MAGIC	2.0	5.3	2.0	5.0	1.0	2.5	0.05
QSG4EMT (Baseline 1)	**1.0**	**2.7**	**1.0**	**2.5**	**0.5**	**1.3**	**0.03**
QSG4EMT (Baseline 2)	**0.5**	**1.3**	**0.5**	**1.3**	**0.3**	**0.6**	**0.01**

Figure 0-1 Accuracies of hypothetical mission scenarios (left) and their benefit for applications as stated by participants of the user questionnaire (right).

2) Sensitivity analysis of scientific instrument performance

In this work package (WP300), two measurement concepts have been considered: low-low satellite-to-satellite tracking (ll-SST), and gravity gradiometry. The most beneficial configurations for temporal gravimetry have been analyzed when using electrostatic and quantum instrumentation for both measurement concepts, except for the combination of gravity gradiometry and electrostatic instruments, since this has been demonstrated unfeasible by GOCE. We assumed an analytical model for the error amplitude of quantum accelerometers that is a function of the laser wavelength, number of atoms, interferometer contrast, degree of entanglement, momentum space separation, interrogation time and measurement cycle period. We consider two operational modes for the CAI (cold atom interferometer) accelerometer/gradiometer: *concurrent* atom cloud preparation and interrogation, where the interferometry takes place at the same time as the Bose-Einstein condensate is being prepared, and *sequential* atom cloud preparation and interrogation, where the processes for cloud preparation and interrogation do not overlap, leading to a more extended measurement cycle period. We derived analytical formulas for the amplitude of the Coriolis and centrifugal accelerations as a function of the thermal velocity of the atom cloud, the initial cloud velocity, the angular velocity of the satellite, and attitude compensation provided by steering mirrors.

One additional error source considered in this study is related to the transformation to the Earth-centered, Earth-fixed (ECEF) reference frame. It requires satellite attitude data and is, therefore, not free of errors. Essentially, this error represents how the measured signal contaminates different axes when misoriented in inertial space, and we refer to it as *attitude uncertainty*.

We show that the advantage of additional measurements provided by the *concurrent* operational mode is insignificant compared to the severe reduction of the amplitude of the errors in reconstructing the Coriolis accelerations (henceforth referred to as *Coriolis errors*) given by the *sequential* operational mode. This is because cloud movement is very limited in the latter. In this case, the state-of-the-art attitude measurement systems (here assumed to be the Astrix 200 laser gyroscope combined with a Star Tracker with similar performance to Swarm) combined with an attitude compensation system allow the full accuracy of the CAI instrument to be exploited. This is shown in Table 0-1 where a simple error propagation considering reasonable values for the input parameters shows no improvement in the Coriolis errors in the *concurrent* mode (second column), even when using attitude compensation (last row).

The attitude compensation system limits the sequential mode, because the Coriolis error is at the level of 10^{-13} m/s^2 as opposed to 10^{-9} m/s^2 in the *concurrent* model.

For quantum accelerometry in ll-SST, we considered CAI parameters that resulted in instrument accuracy of 10^{-13} m/s^2 for the *sequential* mode and ~10^{-14} m/s^2 for the *concurrent* mode, as shown in the solid purple and yellow lines, respectively, in Figure 0-2.

Table-0-1: Standard deviation of the Coriolis term $\boldsymbol{\sigma_{\mathrm{Cor},i}}$, assuming $\boldsymbol{\sigma_{\omega,j} = \sigma_{\omega,j} = 5 \times 10^{-8}}$ rad/s, $\boldsymbol{v_{\mathrm{atom,therm}} = 10^{-6}\,\mathrm{m/s}}$ and $\boldsymbol{\sigma_{v_{\mathrm{cloud,initial}}} = 10^{-7}\,\mathrm{m/s}}$ for several combinations of angular velocity compensation scenarios and operational modes (affecting the cloud velocity), for the case of along-track ll-SST and the *i*-axis aligned with the along-track direction.

Attitude compensation scenario	Residual angular velocity [rad/s]	Concurrent mode [m/s^2]	Sequential mode [m/s^2]
		$v_{\mathrm{cloud,k}} = \sigma_{v_{\mathrm{cloud,therm}}} = 2.3\mathrm{nm/s}$ $v_{\mathrm{cloud,j}} = 2.5\mathrm{cm/s}$	$v_{\mathrm{cloud,k}} = v_{\mathrm{cloud,j}} = \sigma_{v_{\mathrm{cloud,therm}}} = 2.3\mathrm{nm/s}$
No tilting mirror	$\omega_{\mathrm{j}} = 1.1 \times 10^{-3}$ $\omega_{\mathrm{k}} = 10^{-4}$	2.5×10^{-9}	2.2×10^{-10}
Minimum pitch-rate compensation	$\delta\omega_{\mathrm{j}} = \omega_{\mathrm{k}} = 10^{-4}$	2.5×10^{-9}	2.8×10^{-11}
Full attitude compensation	$\delta\omega_{\mathrm{j}} = \delta\omega_{\mathrm{k}} = = 5 \times 10^{-7}$	2.5×10^{-9}	2.0×10^{-13}

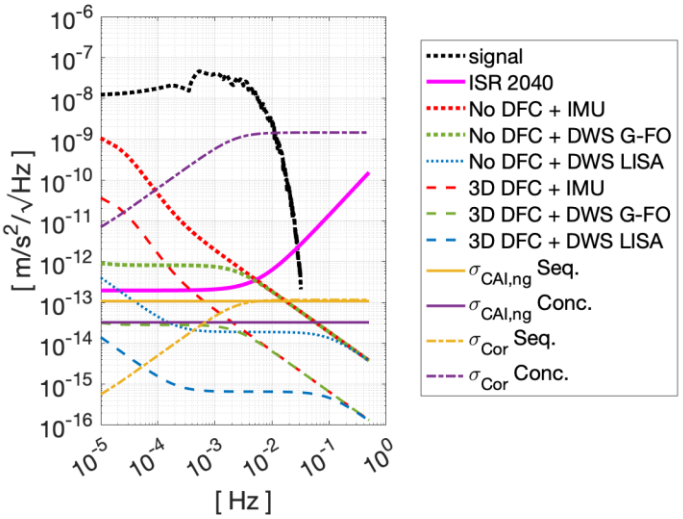

Figure 0-2. Instrument performance of ll-SST concept for various sensor noise assumptions and error sources

The CAI error amplitudes are both well below the expected inter-satellite error amplitude in 2040, shown in the solid pink line. The Coriolis errors for the sequential and concurrent modes are shown in the dash-dotted purple and yellow lines, respectively. While these errors are not problematic in the case of the *sequential* mode, since they are at most of the same amplitude as the CAI errors, they are destructive for the concurrent mode since they are from 3 to 5 orders of magnitude above. Figure 0-2 also shows the errors associated with the attitude uncertainty when Drag-Free Control (DFC) is present or not (long or short dashed lines), in combination

with attitude derived with a star tracker, laser gyroscope and 3 options for a Differential Wavefront Sensor (DWS), in the red, green and blue lines. If there is no DFC, then DWS at the accuracy of the LISA mission must be used with a slight degradation below 0.03 mHz (short-dashed blue line). If 3D DFC is used, then the DWS currently available in GRACE-FO is sufficient (long-dashed green line).

For CAI gradiometry, considering only pairs of CAI accelerometers operating in the *sequential* model, shown in Figure 0-3, its sensitivity (red line) is barely enough to resolve time-variable gravity signal up to 3 mHz, corresponding roughly to SH degree 17. The Coriolis errors (yellow line) make it impossible to observe this signal below 0.4 mHz or SH degree 2. The effects of attitude uncertainty (dashed green line) are at least one order of magnitude below the Coriolis effects, and only surpass the magnitude of the gradiometer CAI sensitivity below 0.02 mHz.

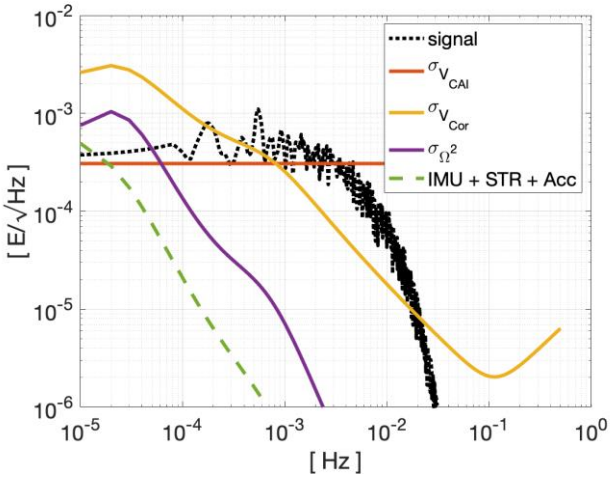

Figure 0-3. Instrument performance of SGG concept

In contrast to the ll-SST case using quantum accelerometers, where the complete signal spectrum is resolved with a high signal-to-noise ratio, the quantum gradiometer with the same CAI parameters is barely able to determine the time variable signal, with an SNR mostly between 1 and 2, peaking at 3 and dipping at 0.5 at some frequencies. This example reinforces that the high accuracy of all instruments is critical to the success of CAI gradiometry. Although quantum technology may allow for extremely high CAI sensitivities, a proportional improvement of the attitude sensors is necessary.

We demonstrated that the effects of inaccurately measured attitude in the Coriolis accelerations are of paramount importance to the success of the CAI satellite gravimetry. Any CAI concept operating in *concurrent* mode is not limited by its sensitivity, but by the Coriolis effects, even in the quiet environment of space. For demonstration purposes of CAI technology to measure the time-variable gravity field, the best option is the ll-SST measurement concepts and a CAI accelerometer operating in *sequential* mode because this requires less demanding CAI parameters. With the progress of laser metrology, this is still the best option to ensure the accuracy of the LTI instrument is fully exploited since the parallel development of CAI technology allows for comparable accuracies. Of note is the low sampling rate inherently associated with the *sequential* mode, which limits the ability to measure high frequencies. The obvious solution is to consider the hybrid use of CAI and classical accelerometers, which would also allow for validation and calibration of both instruments, of special interest during the initial stages of the exploitation of CAI technology.

3) Trade-space and simulation results of current and extended constellations

The benefit of quantum accelerometers on future satellite gravity missions is assessed based on (1) existing/upcoming satellite gravity mission scenarios (WP300, applying the LL-SST resp. gradiometry principle), (2) on future scenarios incorporating larger constellations (WP400 for LL-SST, WP500 for gradiometry), and (3) based on future mission scenarios applying alternative concepts (WP600). Eventually, the different mission performances and benefits have been assessed for all investigated scenarios (WP300-600). Hence, to achieve a better overview, the executive summary for these WPs is merged to provide a better consistency. This is also in line with the project strategy to create and investigate one single trade-space for all investigated constellations.

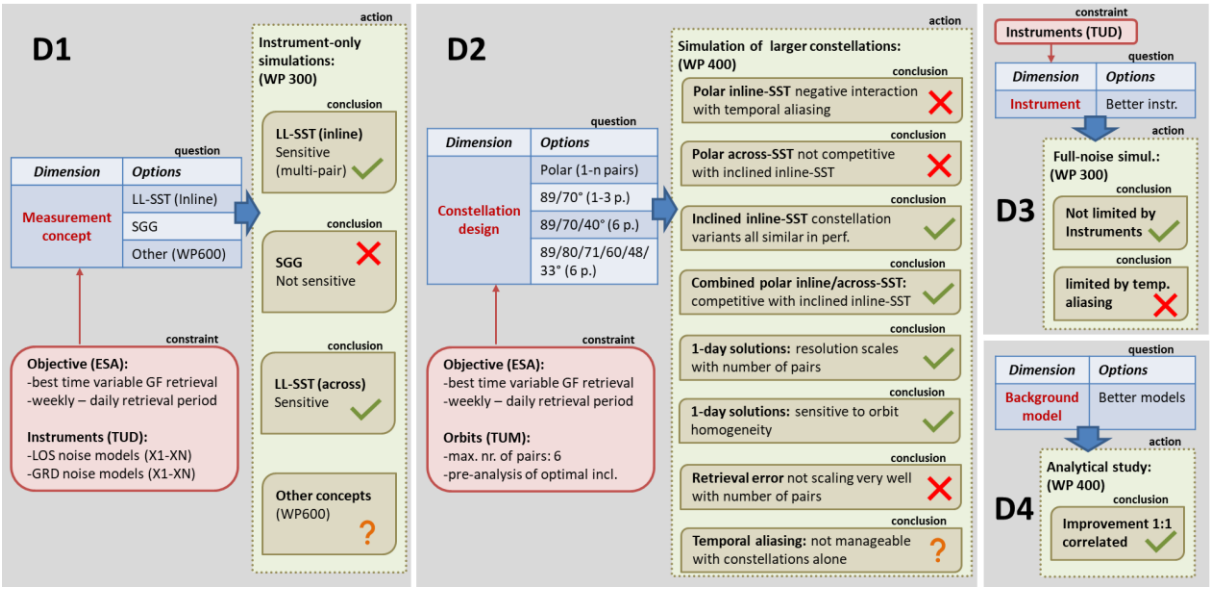

Figure 0-4 Illustration of the final trade-space with important constraints (red boxes), feasible options (blue boxes) and investigative actions with conclusions (green boxes). Green ticks represent positive conclusions, red crosses negative conclusions (regarding a possible future quantum gravity mission) and yellow question marks still open issues.

The investigated trade-space (see Figure 0-4) summarizes well the structure of the work performed within WP300-600. It abstractly describes the most important variables (i.e. dimensions) that may impact future satellite gravity missions. Concretely, three main entities (dimensions) have been identified which govern a satellite gravity mission: (D1) the measurement concept (e.g., LL-SST, gradiometry, HL-SST, etc.), (D2) the constellation design (e.g., 1-, 2-, n-satellite/-pair constellations), and (D3) the instrument performances (e.g., accelerometers, ranging instruments). Also, a fourth dimension (D4), the background model performance, has been defined. However, D4 is not seen as a direct mission variable since the background model performance cannot be influenced by the mission itself directly, but has to be provided from external sources (geophysical models). The impact of all dimensions has been investigated by performing a multitude of simulations with different settings (corresponding to points in the trade-space). The results of simulations are validated by retrieving the gravity field through two different approaches.

Starting with the measurement concept (D1), the established (inline) LL-SST and SGG principle were mainly investigated (WP300-500). In addition (WP600) also possibly feasible alternatives have been analyzed. Concretely, it has been found that the LL-SST concept is likely

the most suited option for future (quantum) gravity missions (see Figure 0-5). The reason for this is that, compared to SGG, the sensitivity to the gravity field is several orders of magnitude better when deploying the same quantum sensors. On the other hand, SGG requires very high sensitivity from the quantum instrument and a like-wise high accuracy in the reconstruction of the satellite's attitude to become sensitive to Earth's time-variable gravity field (see Figure 0-6). At the time of writing, the associated technical hurdles seem still too high to consider SGG as a viable alternative to SST (see WP200). As another alternative LL-SST, also high-low SST (HL-SST) has been taken into consideration (in WP600). While HL-SST shares the same sensitivity property than LL-SST, the inter-satellite distances are much larger in comparison. Unfortunately, the performance of all investigated ranging instruments decays proportional with the distance, which is why a future quantum HL-SST mission will likely be governed by the ranging noise and, hence, would not benefit from the high performance of the quantum accelerometers. Hence, for a future quantum mission, there is currently no better option found than LL-SST. However, for LL-SST there exists theoretically an alternative variant where the satellites of one pair are not orbiting on the same orbital plane following each other (inline SST, I-SST), but on different orbital planes side-by-side (so called across-track SST, A-SST, see Figure 0-7). The advantage of this concept is the perpendicular measurement direction which could complement the inline measurements from an I-SST mission (to form an IA-SST mission) while orbiting on near polar planes (and, thus, retaining global coverage). It is shown that multi-pair IA-SST missions might pose a real alternative to multi-pair inclined I-SST missions (see Figure 0-11a). The downside of A-SST is the strongly changing inter-satellite distance and high relative velocities, which might comprise additional technical challenges.

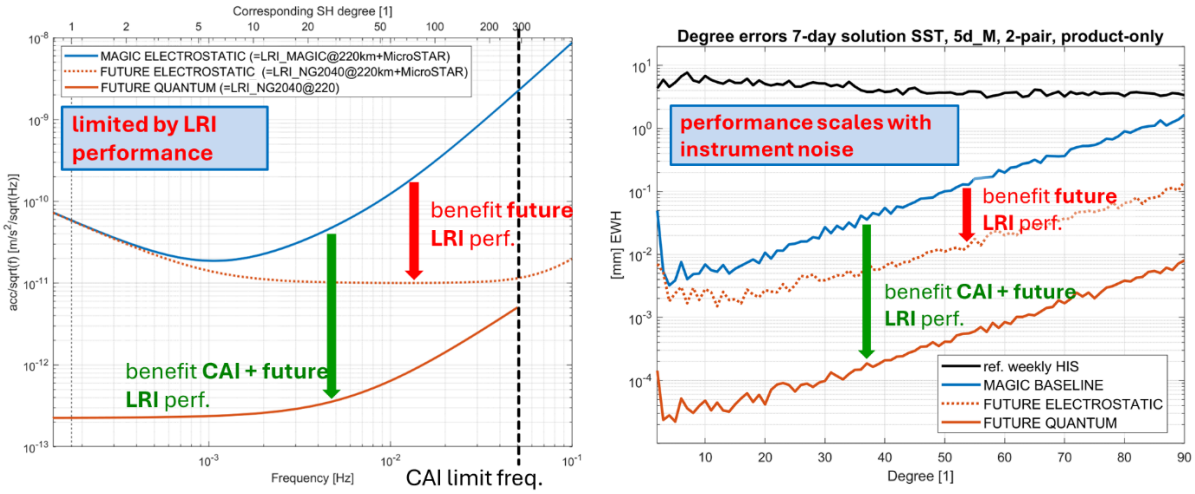

(a) **(b)**

Figure 0-5 Quantum SST mission performance. (a) Comparison of Amplitude Spectral Densities (ASDs) of the SST observation noise for current-gen. electrostatic (blue) and future quantum accelerometers (orange). (b) Simulated static gravity field retrieval performance in terms of error degree amplitudes for an inclined two-pair mission when assuming the instrument performance from Fig. a.

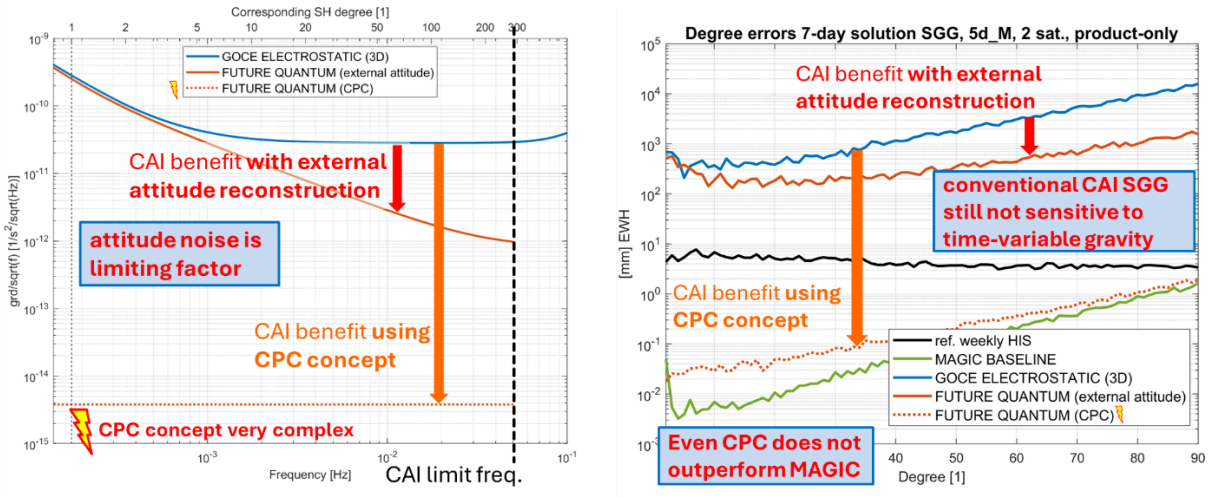

(a) **(b)**

Figure 0-6 Quantum SGG mission performance. (a) Comparison of Amplitude Spectral Densities (ASDs) of the SGG observation noise for current-gen. electrostatic (blue) and future quantum accelerometers (orange). (b) Simulated static gravity field retrieval performance in terms of error degree amplitudes for an inclined two-satellite SGG mission when assuming the instrument performance from Fig. a. The Counter-Propagating-Cloud concept is seen as technically too demanding to be a viable option for the near- and mid-term future (see WP200).

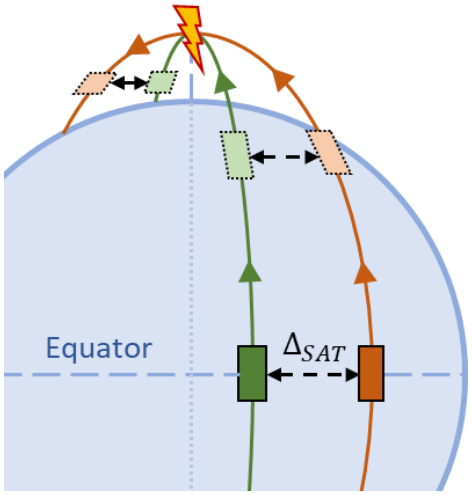

Figure 0-7 Illustration of the across-track SST (A-SST) concept. The satellite orbits are shifted in the right ascension of the ascending arc (RAAN) to have a certain distance at the equator which reduces towards the poles. At the poles, the intersatellite-distance converges towards zero and the satellites switch side on the descending arc.

It could be observed that better instruments (D3) result in a higher sensitivity to the gravity field signal (cf. Figure 0-5 and Figure 0-6). However, under realistic conditions with time-variable gravity signal, all investigated (two-pair/satellite) scenarios are strongly limited by temporal aliasing due to the temporal under-sampling of the gravity field when considering only small constellations (e.g., two pairs, see Figure 0-8). Hence, it is concluded that the instrument noise is currently not the main limiting factor in the time-variable gravity field retrieval. Only when background model errors (D4) would decrease by a factor of >1000, the full potential of future quantum sensors could be exploited (cf., Figure 0-8b). Eventually, it is neither expected that background models improve that much nor that future improvements in these models can be significantly influenced by the designed mission (which is why D4 is not a real trade-space variable).

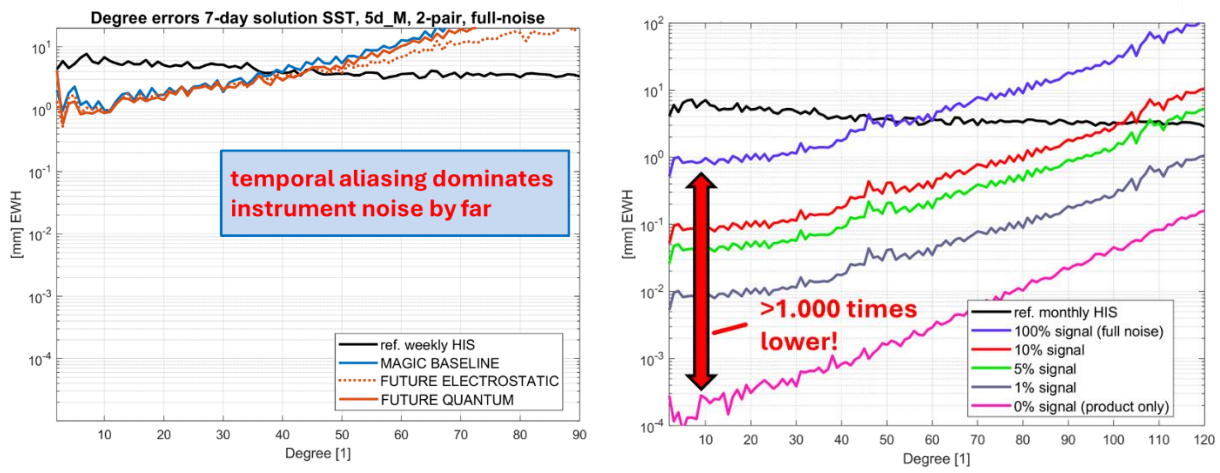

(a) **(b)**

Figure 0-8 (a) Simulated time-variable gravity field retrieval performance in terms of error degree amplitudes for an inclined two-pair SST mission when assuming the instrument performance from **Figure 0-5**a. (b) Impact of the background model errors on the time-variable (quantum) gravity field solution (from Fig. a) when assuming n-times better background model knowledge (see legend).

Since temporal aliasing is dominating, larger constellations (D2) need to be considered to increase the spatial-temporal coverage of the mission. In this project, it has been decided to limit the number of satellites/pairs to six. Hence, several different constellations with up to six satellites/pairs have been investigated. Selected constellations for which later on also the impact was assessed are summarized in Table 0-2, and their ground track distribution is shown in Figure 0-9.

Table 0-2: Selected constellations with 7-day near sub-cycle

Acronym	No. pairs	Inclination [°]
IIC2v1	2 (in-line)	89, 70
IIC3v1	3 (in-line)	89, 70, 40
IIC6v1	6 (in-line)	89, 80, 71, 60, 48, 32
PIAC6v2	6 (3 in-line, 3 across-track)	89, 89, 89, 89, 89, 89

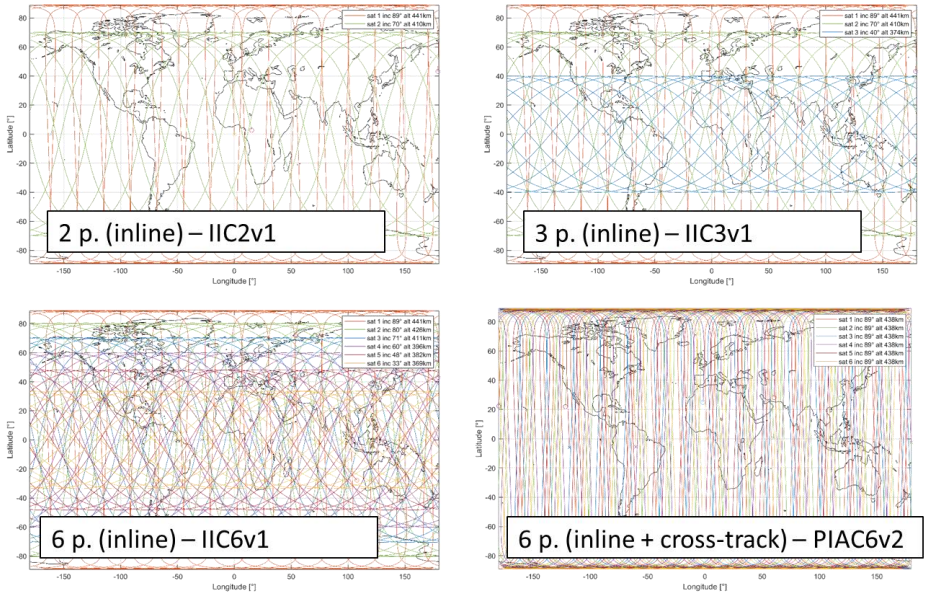

Figure 0-9 Ground track patterns of selected multi-pair constellations.

The resulting gravity field performance of the 2-pair (IIC2v1), 3-pair (IIC3v1) and 6-pair (IIC6v1) constellation is shown in Figure 0-10. It is well seen that larger constellations help indeed to mitigate temporal aliasing to some extent (Figure 0-11a). However, the improvement is far not sufficient to reach the instrument performance level (see Figure 0-11b). A detailed investigation on the constellation design, the benefits and the limitations can be found in Zingerle et al. (2024).

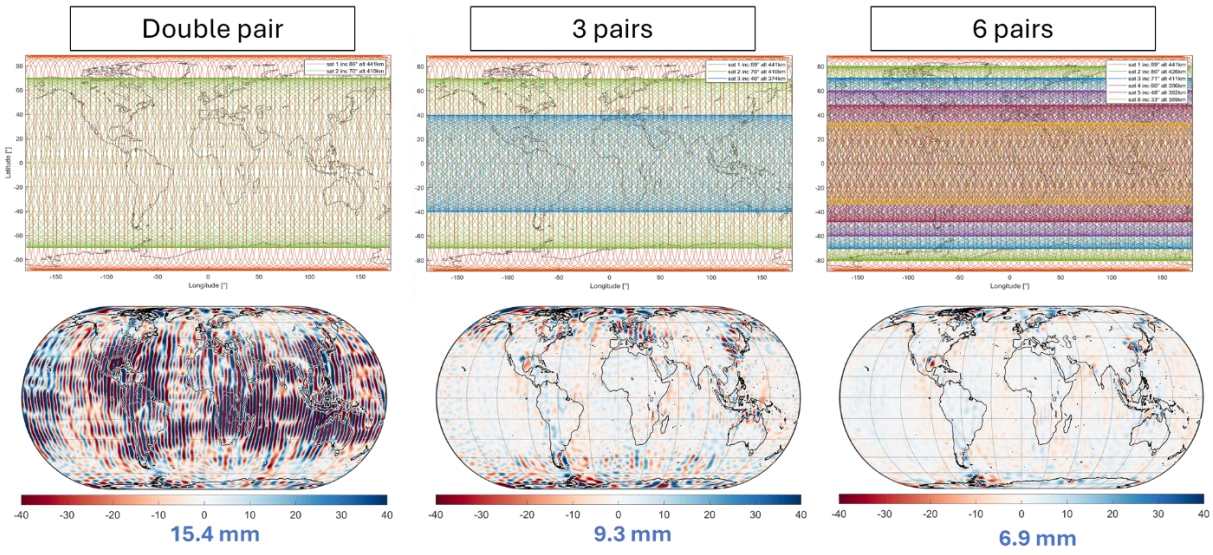

Figure 0-10 Simulation of larger SST constellations (top row, ground-track after 7 days) and retrieved time-variable gravity field solution (bottom row, 7 day mean) with the global RMS at d/o 60 in terms of equivalent water heights [EWH]. Left: inclined double-pair constellation. Center: inclined triple-pair constellation. Right inclined six-pair constellation.

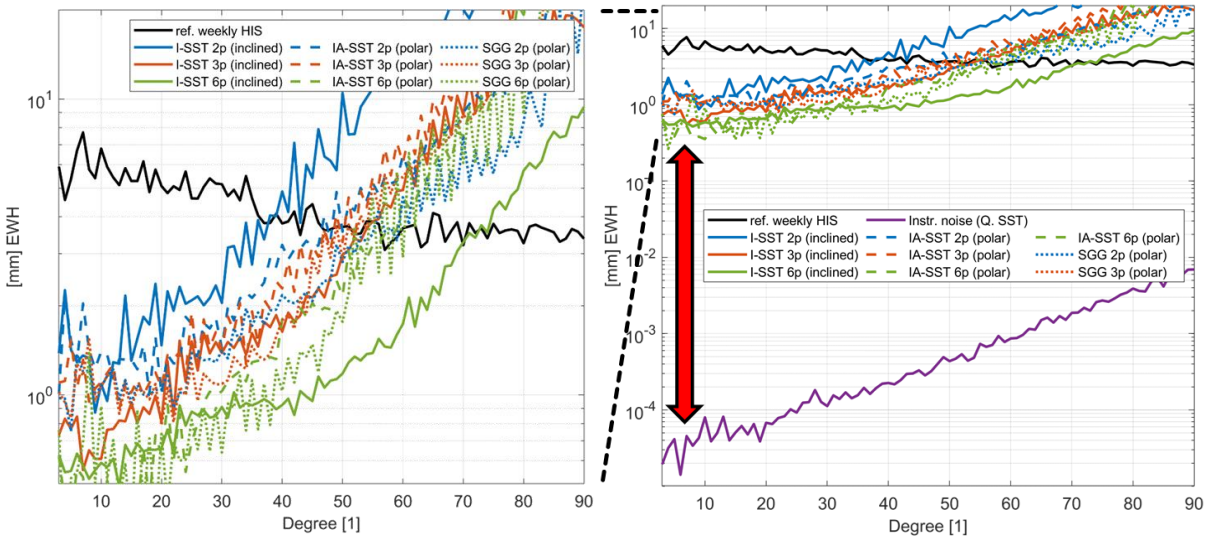

(a) **(b)**

Figure 0-11 Simulated time-variable gravity field retrieval performance for extended constellations (SGG and SST) in terms of error degree amplitudes of a 7 day solution (see legend). (b) Comparisons of the retrieval errors from Fig. a with the quantum instrument sensitivity (purple line, i.e., static gravity field retrieval error).

This leads to the conclusion that the temporal aliasing problem cannot be solved by larger constellations alone, but that also more sophisticated parameterization schemes are needed in the future to account for the steadily changing gravity signal. In the standard processing, the gravity field is usually only modeled to be static within the retrieval period. So, even a linear trend in the signal cannot be represented correctly and introduces instead an aliasing-like error pattern. To overcome this issue, it is proposed to use a time-aware cubic spline parameterization instead. Splines have been chosen, because they can approximate nearly every function, have local support, are easy to construct and to regularize. An exemplary result is shown in Figure 0-12. It is seen that the spline approach performs much better (about one order of magnitude) compared to the static solution. This highlights the importance of not only considering better instruments and larger constellations, but also adapted parameterization schemes. Sufficient benefit, however, can only be achieved with larger constellations to overcome spatial aliasing issues.

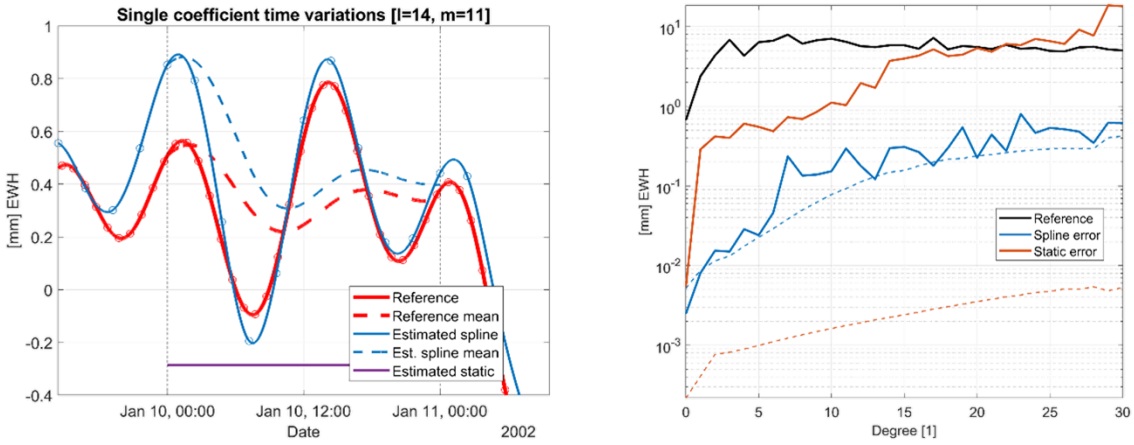

(a) **(b)**

Figure 0-12 Visualization of the spline parameterization on a dedicated 5-pair mission with 1/5th of a day sub-cycle. (a) Time-progression of the reference value of a single coefficient (red) in comparison to the spline solution (blue) and the static solution (violet). Dashed lines depict the cumulative mean. (b) Simulated time-variable gravity field retrieval performance in terms of error degree amplitudes of a daily mean solution when assuming $10^{-12} m/s^2$ white noise instrument behavior. Orange: static solution. Blue: spline solution.

4) Regional solutions

As shown above, satellite constellations for gravity field recovery are promising to provide data allowing for time-variable gravity field investigations with higher accuracy and spatial and temporal resolutions than the current state of the art. In this context, the question arises whether a sequence of global solutions in terms of spherical harmonic coefficients (for example representing Equivalent Water Heights for hydrological applications) is the best option to estimate local signals that may have a stronger amplitude than the global average, and therefore may be inferred with a higher spatial resolution.

The aim of this work package (WP700) was to investigate regional solutions based on collocation by exploiting the space-wise approach. The method basically consists of two steps. Firstly, a global spherical harmonic solution by least-squares adjustment is computed. Then a grid prediction by collocation is performed on the residuals to refine the global solution by exploiting the local characteristics of the gravity field. In this local gridding, modelling signal and noise covariances plays a crucial role. This should be empirically driven by the observations and cannot be done by neglecting the temporal aliasing due to the gravity field variations during the analyzed time span. The method also provides an estimate of the full error covariance matrix of the grid values, which may be useful for subsequent investigations. This matrix is computed by formal error covariance propagation, and it is a-posteriori rescaled based on Monte Carlo simulations.

In order to assess the performance of the space-wise approach in computing regional solutions, some test areas were selected. These are: the East China Sea for ocean applications, some small to large scale river basins (Amazon, Danube, Ganges, Elbe, Rhine, Oder, and Uruguay) for hydrological and climate applications, and the Bengkulu earthquake that occurred in 2007 for solid Earth applications. For each of these regions, a 7-day time-series of local grids was computed, estimating the TWSA in terms of equivalent water height (EWH) for ocean and

hydrological applications and the gravity disturbance at 10 km altitude for geophysical applications.

The solutions were computed considering inline satellite-to-satellite tracking with 2, 3, and 6 pairs of satellites or mixed inline and cross-track satellite-to-satellite tracking with 6 pairs of satellites (for hydrological applications only). Gradiometry was not considered, because its performances are expected to be inferior in a realistic instrumental scenario.

As an example, a comparison between the Amazon total water storage anomaly (TWSA) grid computed from the global least-squares solution and the corresponding local collocation refinement is shown in Figure 0-13 with 3 pairs of satellites over a 7-day retrieval period. The second step of the space-wise approach leads to an improvement in terms of both accuracy and spatial resolution. To give a more comprehensive picture of the results over the test areas selected for hydrological applications, the average RMSE over a time span of 1 year with 7-day solutions is shown in Figure 0-14 for the different mission configurations. Further averaging the root mean square error (RMSE) over all regions, it can be stated that the estimation accuracy is always better than 3 cm (in terms of EWH) independently of the chosen orbit configuration. Increasing the number of satellite pairs, the average estimation accuracy can be improved to 2 cm, with some regions reaching 1 cm level.

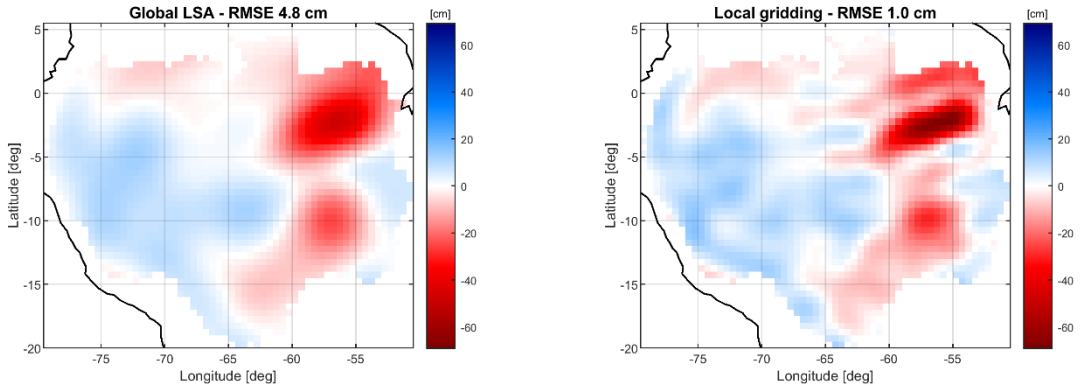

Figure 0-13 TWSA estimate in terms of EWH for the first week of the year 2002, considering quantum instrumentation with 3-pairs of inline satellites. The Least Squares estimate (regularized, up to d/o 120) is reported in the left panel, while the refined gridding estimate is reported in the right panel.

Regarding Solid Earth Applications, the results of the 7-day solutions computed for the Bengkulu Earthquake showed that the time-variable gravity field can be estimated with a spatial resolution between 1.2° (2-pairs) and 1° (6-pairs), corresponding to a spherical harmonic degree between 150 and 180. As for the estimation accuracy, the RMSE is in the range between 10 μGal and 5 μGal, depending on the orbit configuration. Generally, the higher the number of satellite pairs, the better is the accuracy, even if this may depend on the location of the event being studied.

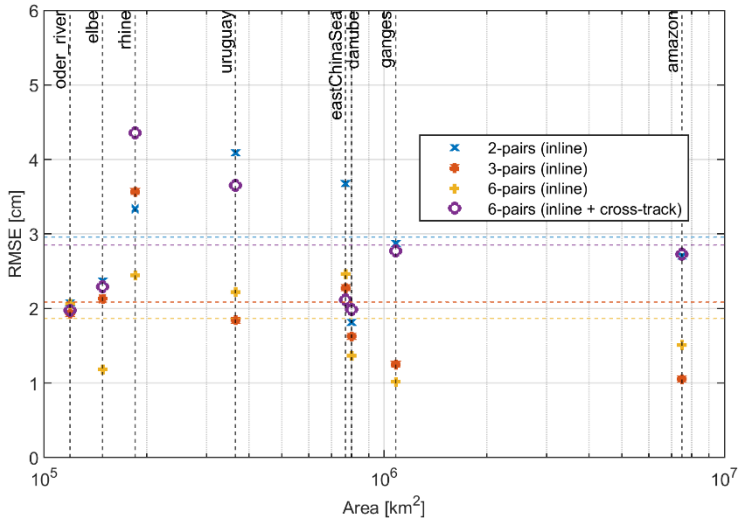

Figure 0-14 Overall empirical estimation error for each selected region as a function of the basin size, considering regional solutions with a 7-day retrieval period for different satellite configurations. The horizontal dashed lines represent the average of this estimation error over all the regions for the corresponding satellite configuration.

Regarding Solid Earth Applications, the results of the 7-day solutions computed for the Bengkulu Earthquake showed that the time-variable gravity field can be estimated with a spatial resolution between 1.2° (2-pairs) and 1° (6-pairs), corresponding to a spherical harmonic degree between 150 and 180. As for the estimation accuracy, the RMSE is in the range between 10 μGal and 5 μGal, depending on the orbit configuration. Generally, the higher the number of satellite pairs, the better is the accuracy, even if this may depend on the location of the event being studied.

5) Impact assessment

The main objective was to assess detectability of various geophysical signals by the different proposed constellations and payload of the quantum technology instrumentation.

5.1 Solid Earth applications

The activities in this work package (WP800) involved the computation of the Solid Earth geophysical signals, and the assessment of their detectability. The computation of the signals was accomplished for tectonic events including earthquakes, unrests at submarine volcanos, uplift and subsidence of the Alpine range, followed by the identification of geologic bodies and fluid incursion into the porous rocks of sediment basin, and at last the signals associated to deep mantle flows were considered. The Earthquake Signal Repository was formed by the computation of the co- and post-seismic signal from synthetic models of real events. The repository allows to isolate the gravity change due to the earthquake rupture and the subsequent viscoelastic relaxation, between any given timeframe from the source time to the subsequent years. At marine volcanoes, or seamounts, the mass change due to sudden submarine eruptions was computed, for a set of documented events, including the Fani Maoré submarine volcano sudden growth (2014-2015) and the Hunga Tonga-Hunga Ha'apai sudden explosion (2022). Onsite surveys and/or remote sensing, in addition to petrologic analogies to other seamount systems, support the mass change estimates. The vertical movements of the Alps and

surrounding regions was computed from a network of GNSS time series, through isolation of the long-term trends in vertical movement, allowing to construct a time-varying surface change model and its gravity effect. Concerning the Lithosphere, using a model of crustal structure in the test area of the Eurasia – Arabia collision (encompassing the Caucasus and Zagros Mountains and the surroundings basins), the spatial distribution of intra-crustal bodies (e.g. different geologic units, volcanic complexes) and sedimentary basins was isolated. It serves as a target signal for the retrieval of large-scale static structures and to analyze mass changing with different porosity scenarios. For the deep Earth signals, Dr. Bernhard Steinberger (GFZ) provided a model of long-term mantle dynamics and their gravity effect. In this case, the signal to be detected consists in the difference between two model snapshots, 1 Myr apart, re-scaled according to the timeframe of the observation (e.g. the 1-year change in gravity is represented by 1 ppm of the snapshot difference).

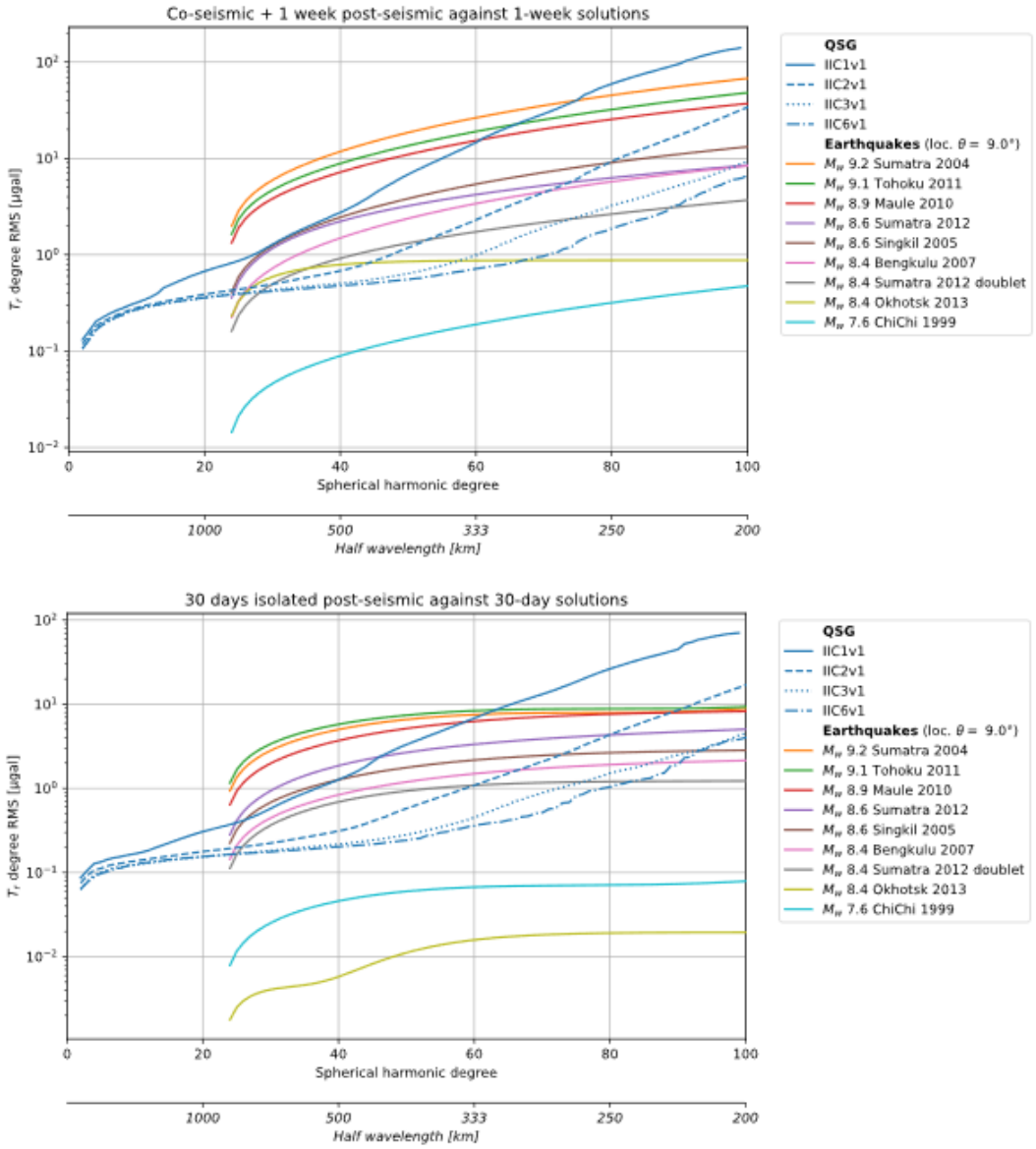

Figure 0-15 Retrieval error spectra of QSG compared to the localized spectra of the collection of earthquake signals. Short-term detectability of co-seismic and post-seismic change in the first 7 days (top) and 30 days (bottom), respectively after an earthquake, compared with the average retrieval errors. Fields calculated at zero height, cumulative spectrum.

The detectability analyses involved two different strategies: a) comparing the signals (as localized spectra) with the spectral retrieval errors, which are computed as residuals between the observed (simulated) signal and the average reference signal in the same time interval. In this strategy, which conforms to the type of detectability analysis made in all of the solid Earth signals, the criterion for positive detectability is a SNR > 1 at each spherical harmonic degree at which both the localized signal spectrum and the error degree spectrum are available (see Figure 0-15).

For the earthquakes we could perform a realistic signal-retrieval analysis of the simulated gravity products, conforming with a workflow that resembles the signal analysis of any real gravity product (e.g., Level-2 global gravity models as available from GRACE). In this strategy (b) the 7-days solutions or averages of more solutions, are compared to the known earthquake signals that are part of the simulations in the updated HIS model. The results show that the two strategies provide consistent results: whenever in strategy a) an earthquake is not visible because the signal spectrum is never above the noise spectrum, in spatial domain (strategy b) the earthquake signal is not above the retrieval error. As an example, the signal of the Maule 2010 is shown in Figure 0-16.

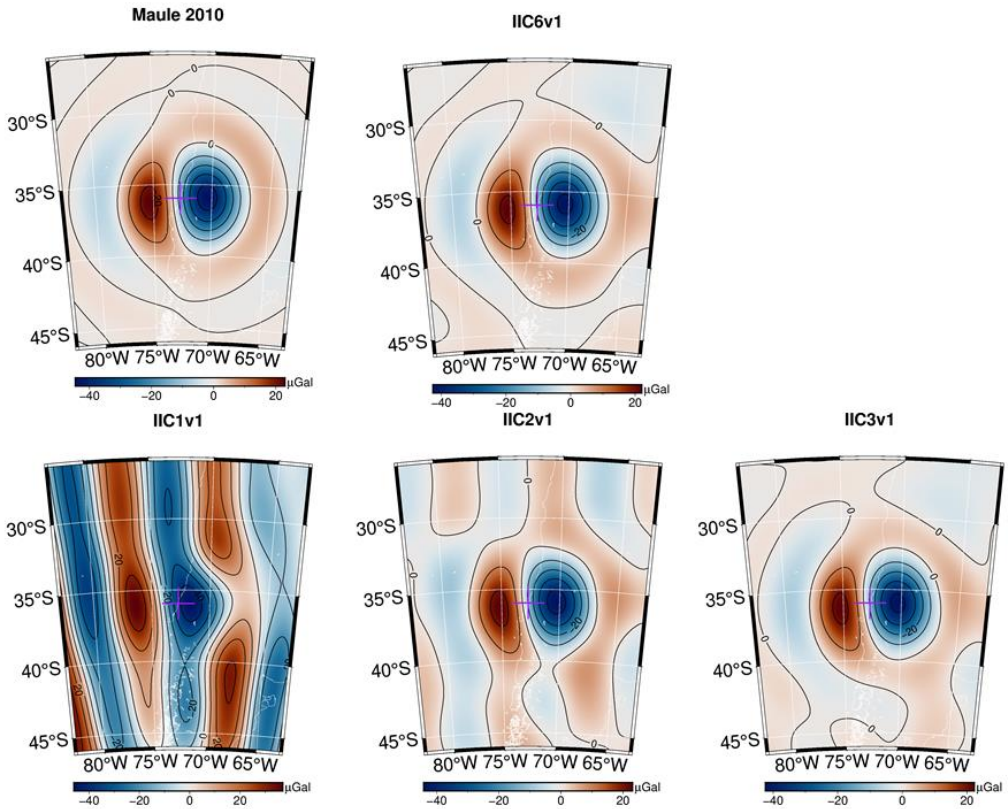

Figure 0-16 Coseismic gravity change for the Maule 2010 earthquake. The sub-figures are identified by their titles: Maule 2010: synthetic coseismic field. IIC1v1 to IIC6v1: retrieved gravity field covering the time of the earthquake, by taking the difference of the field one week after and one week before the The retrieved signal of the constellation includes the HIS variation.

The detectability of the other geophysical signals is summarized in the following. Seamounts: The spectral analysis predicts that the Hunga Tonga volcano 2022 mass change, at weekly sampling, starts to be visible from the double pair constellation upwards. This is confirmed in the space domain, where the retrieval error for a single pair is about ±140 μGal, reducing to a few units of μGal for the six pairs, which compares to the signal reaching values just above 5 μGal. Alps: The Alps show a gravity change rate smaller than 0.5 μGal/yr, positive over the uplifting range, negative in the Po-basin. We compare the localized spectrum of the Alpine gravity change in one year, with the noise curves for 1 year, and the same for 4 years. The signal of one year is too small to be detected, it must be accumulated over four years to achieve detectability with a double couple (or better) constellation. Considering the possibility to detect fluid incursion/extraction in a sedimentary basin, be it natural or anthropogenic, we represented it by the spectral signal curves of air filled against water filled porous rock. For the size of the chosen sediment block (5 km deep, 15 000 km^2 area), with 0.1% and 1% porosity, the water mass is 57 Gt and 570 Gt, respectively. The single couple with weekly sampling could not detect the fluid filling of the 0.1% porosity, whereas the double couple could.

The final topic was concerned with the possibility to detect mass movements in the deep Earth, as the mantle flows induced by the history of slab subduction acting on a inhomogeneous mantle The detection of these small signals is challenging, and would be approached with a several decade long time of acquisition (30 years).

5.2 Ocean applications

The imbalance of water mass fluxes into and out of the global ocean leads to a change in total ocean mass, while at regional scale also barotropic mass rearrangements play a significant role. Ocean mass change (OMC) responds to mass loss of the Greenland and Antarctica ice sheets, land glaciers, river discharge driven by terrestrial hydrology, and changes in the land-ocean precipitation–evapotranspiration balance. In combination with measured or modelled sea level variations, estimates of OMC can be utilized to construct sea level budgets, i.e. partitioning total sea level measured by satellite altimetry, to individual mass and steric contributors in order to better understand contemporary and future sea level drivers. This is in particular relevant for steric sea level changes which are related to ocean warming and salinity change, and which are notoriously difficult to obtain from in-situ measurements for the deep ocean. Approaches exist for retrieving contributions either individually and/or as a residual or jointly in an inverse approach. In WP900, we utilize the inverse approach as it involves an explicit weighting between gravimetric spherical harmonic coefficients and (along-track) altimetric sea surface heights based on a-priori error information, and thus, facilitates error propagation for scenarios. The U Bonn approach works via least-squares fitting of several hundreds of dominating (a-priori) spatial fingerprints of sea level change to monthly gravimetric and altimetric data; these fingerprints include static 'passive' sea level patterns related to ice sheet, glaciers and land hydrological changes derived through the sea level equation. Furthermore, steric patterns that we derive from an EOF decomposition of modelled thermo- and halosteric expansion, and patterns that we interpret as internal mass variability and that are mostly related to barotropic motions in the major ocean basins. We replace the GRACE/-FO error model in our real-data inversion processing by the normal equations from each of the four scenarios introduced above, while keeping the radar altimeter error model (assuming Jason-1 and -2, with errors 5-10 cm derived from binning 20Hz data into 1Hz blocks standard deviation) unmodified. While ocean mass errors are already small with the MAGIC mission concept, we find the benefit of future scenarios mainly in their improved ability to separate different contributions to the sea level

budget. Figure 0-17 shows a map of error level improvement of the ocean mass change component of the 3- and 6-pair quantum simulation scenarios relative to the MAGIC-like simulation scenario.

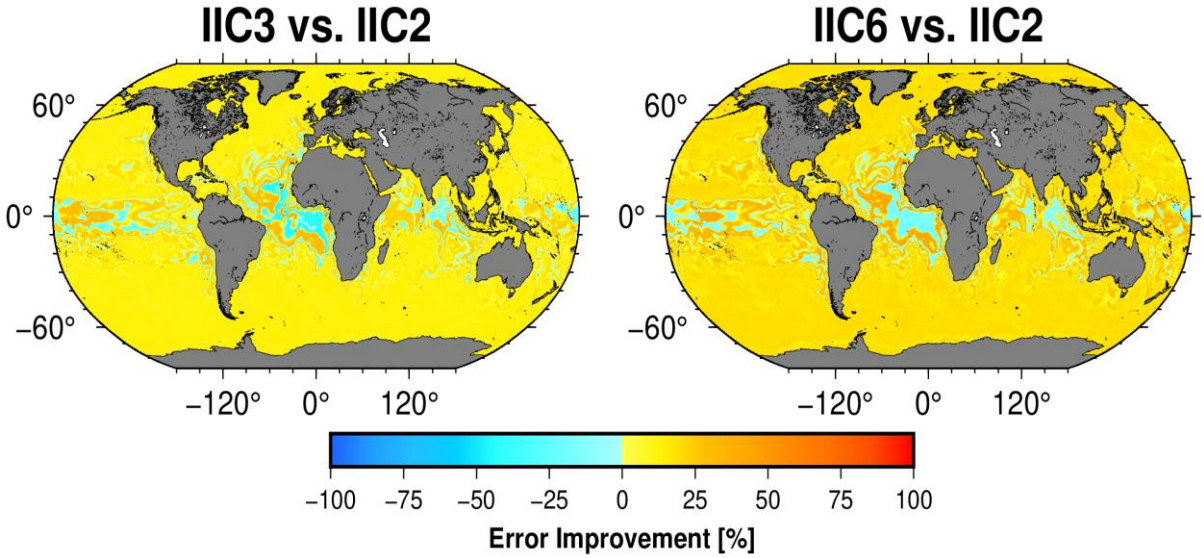

Figure 0-17 Map of error level improvement of the ocean mass change component derived from 3- and 6- pair quantum simulation scenarios IIC3 and IIC6 relative to the MAGIC-like scenario IIC2.

While the global sea level budget is often considered as closed, it is unclear whether this holds true for regional sea level budgets. These budgets are generally more difficult to derive, due to a variety of local physical effects, as, e.g., wind-driven sea level changes or sedimentation, but also retrieval challenges related to satellite gravimetry and altimetry. Earlier studies pointed out problems and demonstrated limited agreement in many areas. The improved spatial resolution associated with future gravity missions is expected to aid in better closing budgets at regional scale. Therefore, we consider also the common "direct" method as this enables to study the impact of spatial resolution for challenging regions in a more straightforward way. To derive regional OMC from the simulated (i.e. ESAESM) gravity fields, we add the GIA correction to the spherical harmonic coefficients, apply DDK3 filtering and restore the de-aliasing product. After converting to water heights and computing the basin average, we apply a leakage correction derived from DDK3-filtering at the LSDM ESAESM hydrology. Basin averages were studied for the East China Sea (ECS), a Western Pacific marginal sea with an area of 770,000 km². What makes the ECS unique and challenging for budget studies is its complex ocean current system, mostly shallow bathymetry and a large amount of sediments transported by rivers or resulting from coastal erosion. In-situ observations, as, e.g., tide gauge data, for external validation are relatively sparse. Simulation results are compared to the truth from the ocean component of the ESAESM; we find consistent improvements with advanced mission concepts as compared to the GRACE/-FO mission. : RMSE values reach from 1.8 cm (GRACE-FO-like scenario) to 1.5 cm (MAGIC-like scenario) and 1.3 cm for IIC3v1 and IIC6v1.

5.3 Short-term hydrology

Data assimilation (DA) provides a way to integrate satellite-derived total TWSA with hydrological model simulations in a statistically optimal manner. It allows to correct model and forcing data deficiencies at scales where gravimetry provides credible information, while

preserving high-resolution information from modelling. DA also enables one to disaggregate TWSA into compartmental storages, and integrate remote sensing data such as snow cover maps in model simulations. In this WP, we investigated the potential benefit of the MAGIC and quantum scenarios compared to the GRACE/-FO mission in an Ensemble Kalman filter (EnKF) assimilation framework, with and without modifying the current DA setup that was developed for integrating GRACE/-FO observations with the WaterGAP model. Different from GRACE/-FO, we find that for MAGIC and quantum scenarios we can assimilate TWSA maps indeed at the native 0,5° resolution of the model, due to improved resolution of these missions over GRACE/-FO. We thus assimilate monthly TWSA simulated with WaterGAP and perturbed with errors that correspond to the four scenarios as discussed above. We implement the DA via the Parallel Data Assimilation Framework (PDAF) framework, which had been coupled with WaterGAP in the online mode for numerical efficiency. Data uncertainty representation in the DA is simplified via a single scaled SHC normal matrix, propagated to the grid while applying the DDK5 filter, while the uncertainty of the hydrological model (i.e. climate forcing and parameter uncertainties) is kept as in our real-data GRACE/-FO analyses. Due to the expensive computational costs we focus exemplary on South America; but results have been found as transferable to other continents. We find that DA clearly benefits from gridded products from advanced mission scenarios, and this is not limited to spatially downscaling TWSA but also to the retrieval of groundwater, surface water and soil moisture anomalies (see Figure 0-17). As groundwater is the largest contributor to TWSA, the strongest improvements are found for groundwater as compared to surface water and soil moisture. However, we caution that these results also depend on assumptions of model errors which we kept conservative here.

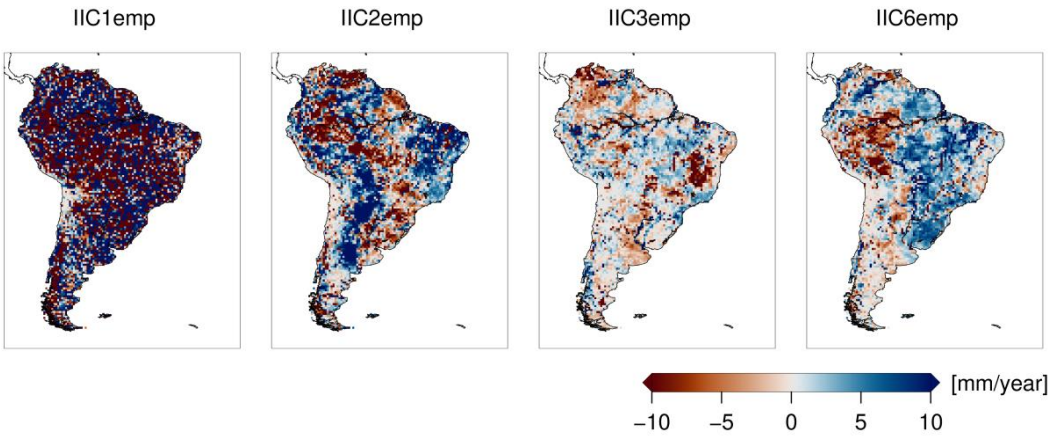

Figure 0-18: Differences of linear TWSA trends [mm/year] for South America derived from the assimilation of WaterGAP TWSA with formal uncertainties of the IIC1, IIC2, IIC3 and IIC6 scenarios towards the WaterGAP model simulations.

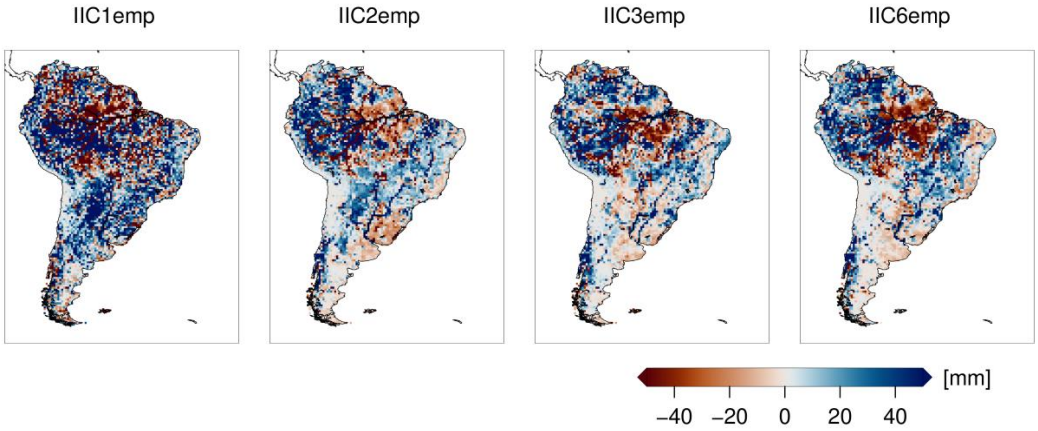

Figure 0-19: Differences of annual TWSA amplitudes [mm] for South America derived from the assimilation of WaterGAP TWSA with formal uncertainties of the IIC1, IIC2, IIC3 and IIC6 scenarios towards the WaterGAP model simulations.

Land surface models (LSMs) represent the coupled cycling of water, energy, and bio-geophysical matter such as carbon within vegetation and soils. They simulate land-atmosphere interactions and provide thus a key component of climate models. In LSMs, assimilation of satellite-derived TWSA enables one to inform the entire vertical profile of soil moisture, in contrast to in-situ and satellite soil moisture (SM) or land surface temperature (LST) assimilation, and, e.g., to identify problems in soil processes representation. Next to the global study mentioned above, in WP900 we investigate the effect of the scenarios for assimilation with the Community Land Model (CLM). We use the TerrSysMP-PDAF assimilation framework, which allows to integrate observations of LST, SM, groundwater head, and others jointly with TWSA. CLM is set up for the Euro-CORDEX region at 12km grid scale and forced by COSMO-REA6 meteorological data. In our experiments, we use the most recent version CLM version 5.0 (CLM5) as the 'truth' and assimilate into CLM3.5; in other words, we seek to correct for random and non-random deficiencies of the model that is implemented in the DA. Results are compared at (aggregated) grid scale for TWSA, and to basin-averages for the major catchments in Europe with area down to about 50,000 km², and for the monthly storage -- discharge budget which corresponds to the precipitation -- evapotranspiration deficit and has been often used for evaluating atmospheric re-analyses. On catchment scale, the extended quantum gravity constellation scenarios indeed perform better than GRACE/-FO in terms of RMSD and correlation with respect to the synthetic truth. Averaged across all catchments, the RMSD relative to the synthetic truth is 8% lower for scenario IIC6 compared to scenario IIC1. The most significant improvements are observed in Eastern Europe. For instance, in the Narva-Jogi catchment, the RMSD decreases from 39.7 mm for scenario IIC1 to 32.5 mm for scenario IIC6, while the correlation coefficient increases from 0.88 to 0.93, respectively. In some regions over Europe also the representation of trends is improved. In this framework, we also developed literature studies of the potential benefit of improving LSMs through integration of space gravimetric data in the context of coupled modelling, and on their use in operational e.g. forecast services.

5.4 Long-term hydrology and climate

One of the most common hydrological applications of satellite gravimetry is the analysis of the time series of water storage variations in hydrological units such as river basins or aquifers. As an estimation of the achievable accuracy of the mission scenarios, temporal root mean square differences (RMSD) were computed between simulation output and reference time series for basin averages of 405 major world-wide river basins. Figure 0-20 shows a scatter plot of the RMSD values vs. the sizes of the river basins. Especially the strong improvement of the future constellations over the current GRACE-FO mission becomes evident by the green dots being one order of magnitude higher than the others. While for MAGIC the RMSD of 70% of the river basins is below a threshold of 2.3 cm, the smaller numbers of 1.5 cm (IIC3v1) and 1.0 cm (IIC6v1) show the improvements achievable by the quantum mission constellations, here shown for a spatial resolution of ~220km corresponding to a spherical harmonic truncation degree of N=90.

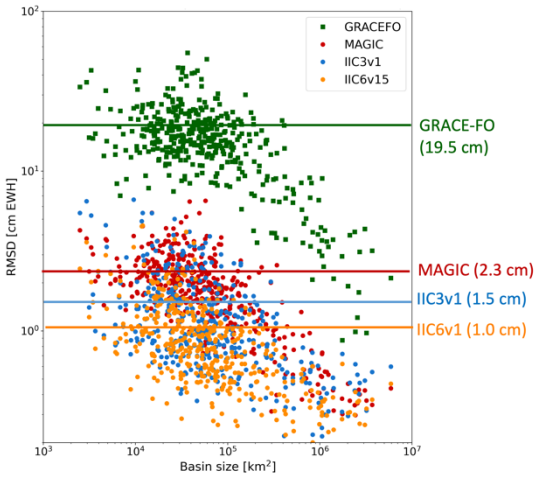

Figure 0-20: Scatter plot of RMSD of basin average time series vs. size of the river basin for different mission scenarios for DDK5 filtered solutions truncated at N=90 (~220 km), including the filter omission error, i.e. compared to the unfiltered reference up to the same degree. The horizontal lines indicate a threshold for which the RMSD of 70% of the rivers basins is smaller.

To assess the impact of the future mission constellations on climate applications, the performance of long-term trend estimates was assessed from the available 12 years of simulation data. While the maps of post-processed (filtered) linear trend estimates are very similar for all mission scenarios, the benefit of the quantum missions is revealed when increasing the spatial resolution, as these missions are expected to provide a reasonable trend estimation even without applying any filtering. In addition to deriving the trend estimate from a time series of short-term simulations (here: 7 days solutions) the benefit of a direct trend parameterization from the full 12 years of satellite data was investigated and a visible improvement discovered for the two quantum scenarios IIC3v1 and IIC6v1. The presence of inter-annual variations was identified as a major challenge for a robust trend estimate from a comparably small time span. To investigate this issue, a model study was set up based on an ensemble of CMIP6 climate models which revealed a considerable better agreement of short-term trends with long-term (200 years) trend estimates when 50 years (e.g. with 10 years of a quantum mission launched in the 2040s) are available instead of the currently available 20 years of data.

Besides linear trends, also the detectability of climate-related changes to the seasonal cycle are of interest to climate scientists, as they might, e.g., be related to an intensification of the global water cycle revealed by an increase of the annual amplitude. The ensemble of CMIP6 climate models was used to estimate expected changes in the annual amplitude. These expected changes were then challenged against accuracy estimates of measured amplitude changes from 30 years of satellite data. The accuracy estimates were derived by error propagation from empirical accuracies (RMSD of reference vs. simulation time series). In Figure 0-21 colored pixels denote regions where the projected amplitude change exceeds the magnitude of the accuracy. In this case we assume the amplitude change to be "detectable". It can be seen, that a GRACE-like mission with the chosen weak DDK5 filtering cannot detect the anticipated amplitude changes

apart from some very few grid cells. The MAGIC mission, however, already performs much better, with amplitude changes being detectable in 57% of the land area after 30 years of observations for the given setting. The quantum constellations show a considerable added benefit with a detectability in 72% (IIC3v1) and 77% (IIC6v1) of the continental area. Particularly the latter leaves only a few desert areas for which the anticipated amplitude changes are not detectable.

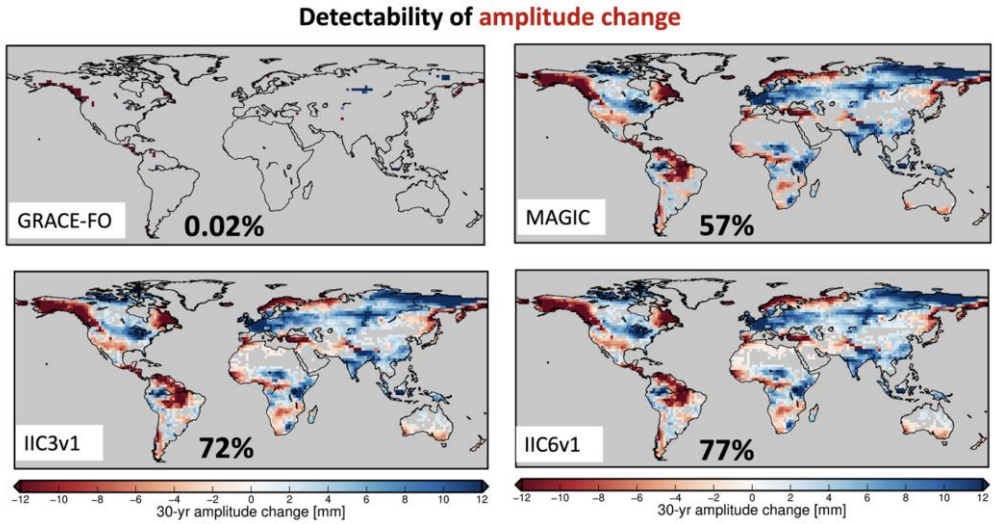

Figure 0-21: Detectability of amplitude change after 30 years based on projected changes from CMIP6 models and error propagation from mission simulations (7-days solutions, truncated at N=90, DDK5 filtered). Colored pixels: amplitude change is regarded as detectable.

6) Outreach

The main results of this project QSG4EMT are summarized in 3 scientific papers, which are either already published or are going to be submitted soon (status: Sept. 2024):

- Encarnação J., Siemes C., Daras I., Carraz O., Strangfeld A., Zingerle P., Pail R. (202x): Towards a realistic noise modelling of quantum sensors for future satellite gravity missions. In preparation for re-submission to Advances of Space Research.
- Zingerle P., Gruber T., Pail R., Daras I. (2024): Constellation design and performance of future quantum satellite gravity missions. Earth Planets Space 76, 101. https://doi.org/10.1186/s40623-024-02034-3
- Kusche J. et al. (202x): Benefit of multi-pair quantum satellite gravity missions in Earth science applications. In preparation for submission to Nature Reviews Physics.

Additionally, further scientific papers on the results of the user survey, the regional solutions and spline parametrization schemes are planned to be written as an offspring of this study.

7) Conclusions

Instrument concepts for satellite-to-satellite tracking (SST) and gradiometry missions and corresponding performance estimates have been established and corresponding sensitivity analysis performed. Under realistic error assumptions, the benefit of quantum/hybrid sensors is higher for inter-satellite ranging concept than for gradiometry. For SST concepts, the LRI performance has to be further improved to match the quantum/hybrid ACC target performance.

For gradiometry, very stringent requirements for the accelerometer and attitude performance apply (accelerometer error level of10^{-15} m/s^2/√Hz, 12 uniaxial gradiometers required for attitude recovery following the counter-propagating cloud concept). Alternatively, the newly developed mission concept of cross-track ranging is an interesting option, but it performs on the same level as in-line constellations.

Compared to the instrument errors, the impact of temporal aliasing is factor of 15 (current instrumentation) to 1000 (QSG instrumentation) higher and thus dominates in all cases the total error budget. Therefore, further improvements in instrument performance have to be complemented by strategies of temporal aliasing reduction, such as extended constellations and improved processing strategies. Therefore, extended constellations of up to 6 pairs have been numerically simulated. They show a gradual performance improvement in terms of temporal aliasing reduction with increasing number of pairs, e.g., a factor of 2.5 from a double-pair to a six-pair constellation, which alone is not sufficient to really make benefit of improved quantum instrumentation.

Improved space-time parametrization strategies such as along-track spline parameterization have been assessed. They show great potential, but they can be applied only for larger constellations to avoid spatial aliasing. Also, a regional gravity retrieval approach has been investigated, which is tailored to regional signal characteristics. It could be demonstrated that regional approaches have the potential to improve global solutions.

In the frame of QSG4EMT, an international user survey with more than 130 participants has been performed. The results of this survey supported the formulation of QSG user requirements. The impact of extended QSG constellations (up to 6 pairs) were evaluated in various applications. In several solid Earth applications, such as big earthquakes, growth of seamounts, tectonic uplift and mantle dynamics, the impact of these different constellations were assessed. The capabilities of extended constellations were also investigated for ocean applications. An inverse approach to separate sea level drivers was applied. Data assimilation (DA) experiments were performed to integrate satellite-derived total water storage anomalies (TWSA) with hydrological and land surface model simulations in a statistically optimal manner. To assess the impact of the future mission constellations on climate applications, the performance of long-term trend estimates was investigated based on the output of a 12 years numerical simulation. Generalizing the results for all investigated application fields, the scientific return increases when extending the constellation. The greatest impact is the step from a polar single to a Bender double pair constellation, and significant further performance improvements can be achieved by adding a third pair in a rather low inclination of 45-55°. Further increasing the constellation (in our study up to 6 pairs) gradually improves the results further. Also from an application point of view, the impact of extending the constellation is much higher than the inclusion of QSG sensors.

To summarize the main conclusions in one sentence:

Quantum/hybrid sensors are a promising technology for future mass change monitoring from space which needs to be embarked at optimized satellite constellations and complemented by processing strategies to fully exploit their metrology advance in scientific applications.

ABBREVIATIONS AND ACRONYMS

AO	Non-tidal Atmosphere and Ocean
AOHIS	Non-tidal Atmosphere and Ocean, Hydrology, Ice, and Solid earth
CAI	Cold Atom Interferometry
D/O	Degree and Order (spherical harmonic)
ESA	European Space Agency
EWH	Equivalent Water Height
FN	Full-Noise (-simulation, with temporal gravity)
GOCE	Gravity field and steady-state Ocean Circulation Explorer
GRACE	Gravity Recovery and Climate Experiment Mission
GRACE-FO	Gravity Recovery and Climate Experiment Mission – Follow On
HIS	Non-tidal Hydrology, Ice and Solid-earth (temporal gravity)
HL-SST	High-Low Satellite-to-Satellite Tracking
IIC	Inclined Inline Constellation
KBR	K-Band Ranging
LL-SST	Low-Low Satellite-to-Satellite Tracking
LRI	Laser Ranging Interferometer
MAGIC	Mass-Change and Geosciences International Constellation
MDT	Mean Dynamic Topography
MS	MicroStar (ONERA accelerometer)
NEQ	Normal EQuation system
NGGM	Next Generation Gravity Mission
NRT	Near Real Time
PAC	Polar Across-track Constellation
PIC	Polar Inline Constellation
PIAC	Polar (combined) Inline and Across-track Constellation
PO	Product-Only (-simulations, w/o temporal gravity)
QSG	Quantum Space Gravimetry
RAAN	Right Ascencion of Ascending Arc
RGT	Repeat Ground Track
RMS	Root Mean Square
SH	Spherical Harmonics
SGG	Satellite Gravity Gradiometry
SLR	Satellite Laser Rangin
SST	Satellite-to-Satellite Tracking
SoW	Statement of Work
TR	Technical Report
TWSA	Total Water Storage Anomaly
VADER	time VAriable DEcoRrelation filter
WBS	Work Breakdown Structure
WP	Work Package

PART 1:

QSG USER REQUIREMENTS

1. INTRODUCTION

This Part 1 refers to Task 1 of the SoW and covers the work performed under WP 100 of the WBS. It refers to the deliverable document D1 "QSG User Requirements".

The main purpose is to define user requirements of QSG missions. In the original version, it is an Excel document. In the following, a copy of this document is provided. For more detailed in formation and better readability, please refer to the original document.

2. QSG USER REQUIREMENTS

Guidelines for experts

Document description:

Within this document multiple tabs are available at the bottom part. The main tabs which need inputs and/or a consolidation of the available values are the ones associated to the main thematic fields: Hydrology, Cryosphere, Oceanography and Solid Earth

Starting from the top table of each thematic field tab, it is possible to find different columns

Thematic field
Time scale: defined in daily to weekly, monthly or long-term trend
State of the art resolutions and accuracies (e.g. GRACE and GRACE-FO)
Thresholds for mid-term mission: taken from the thresholds of the ESA/NASA Joint MAGIC MRD
Targets for mid-term & thresholds for long-term: taken from the targets of the ESA/NASA Joint MAGIC MRD and coinciding with what is planned as threshold for the long-term (Quantum
Target for long-term (Quantum) - Core of the necessary input from experts at this stage

Beyond the first top part which provides the general spatial resolutions and accuracies for the main thematic field, additional inputs are provided for specific thematic sub-fields (e.g. Groundwater storage for Hydrology)

In the bottom table of each thematic field tab, a full view of the services, products and references for the long-term targets are availab

The specific signals (already listed in the top part) are now listed together with other information about services and products. This second table has the following columns

Thematic field
Signals coinciding with the sub-thematic fields provided in the top table
Scientific/societal Questions and objectives identified in the ESA/NASA Joint MAGIC MRD
Services
Products
Copernicus services
References for the long-term targets from the top table. TBD needs to be filled in with the name of experts and sources highlighting such inputs

Input from experts:

Long-term targets need to be confirmed or defined by experts and users.
Please, add relevant services, products and other Copernicus services if there are missing entries in the tables.
If there aren no proposed values for TBDs, ESA suggests to define the long-term targets as a scaled value from the long-term thresholds

Hydrology

Requirements refer to gravimetric data products from gravimetry missions and to the gravimetry contribution in data products resulting from signal separation or data assimilation.

Thematic field	Time scale D: Daily to weekly; M: Monthly; L: Long-term trend	State of the art : Resolution & Accuracy [EWH]	Threshold mid-term* : Resolution & Accuracy [EWH]	Target mid-term (TM)* / Threshold long term (TL): Resolution & Accuracy [EWH]	Target Long-term : Resolution & Accuracy [EWH]
		GRACE-FO	Threshold MAGIC	Threshold QSG Baseline 1	Desired QSG Baseline 2
Hydrology	D	N.A.	Threshold-a: 600 km @ 2.0 cm; Threshold-b: 300 km @ 5.3 cm;	TM/TL-a: 600 km @ 1.0 cm: TM/TL-b: 300 km @ 2.7 cm;	Target-a: 600 km @ 0.5 cm; Target-b: 300 km @ 1.3 cm;
	M	300 km @ 2.0 cm 150 km @ 5.0 cm	Threshold-a: 300 km @ 1.0cm; Threshold-b: 150 km @ 2.5 cm	TM/TL-a: 300 km @ 0.5 cm; TM/TL-b: 150 km @ 1.3 cm	Target-a: 300 km @ 0.3 cm; Target-b: 150 km @ 0.6 cm
	L	150 km @ 0.1 cm/yr	Threshold-a: 150 km @ 0.05 cm/yr	TM/TL-a: 150 km @ 0.03 cm/yr	Target-a: 150km @ 0.01 cm/yr
Applications					
Groundwater monitoring	M	See Hydrology	See Hydrology	See Hydrology	See Hydrology
	L	See Hydrology	See Hydrology	TM/TL: 200-300 km @ 0.1-1 cm/yr (old SATM) TM/TL: 200km @ 1cm/yr (ECV)	Target: ≤100km @ 1.0 mm/yr (old SATM) Target: 100km @ 0.1cm/yr (ECV)
Surface soil moisture monitoring	D, M, L	See Hydrology	See Hydrology	D: 50km @ 0.08 m^3/m^3 (ECV)	D: 10km @ 0.04 m^3/m^3 (ECV)
Agriculatural soil monitoring and forecasting	D, M, L	See Hydrology	See Hydrology	D: 25 km @ 0.04 m^3/m^3 (OSCAR) D: 50km @ 0.08 m^3/m^3 (ECV)	D: 1 km @ 0.4 m^3/m^3 (OSCAR) D: 10 km @ 0.04 m^3/m^3 (ECV)
Drought monitoring and forecasting	M, L	See Hydrology	See Hydrology	See Hydrology	See Hydrology
Flood monitoring	D, M	See Hydrology	See Hydrology	See Hydrology	See Hydrology
Flood potential assessment	D, M	See Hydrology	See Hydrology	See Hydrology	See Hydrology
Global water resources assessment	D, M, L	See Hydrology	See Hydrology	See Hydrology	See Hydrology
Regional water resources assessment	D, M, L	See Hydrology	See Hydrology	See Hydrology	See Hydrology
Snow monitoring (SWE)	M, L	See Hydrology	See Hydrology	D: 25km @ 1cm (ECV)	D: 5km @ 0.5cm (ECV)
Wetland monitoring	M, L	See Hydrology	See Hydrology	See Hydrology	See Hydrology
Permafrost hydrology	M, L	See Hydrology	See Hydrology	See Hydrology	See Hydrology
Monitoring climate change effects on terrestrial water storage	L	See Hydrology	See Hydrology	TM/TL: 200 km @ 0.1 cm/yr (old SATM)	Target: ≤100km @ 1.0 mm/yr (old SATM)
Determination of baseflow dynamics of a river at sub-basin scale	D, M, L	See Hydrology	See Hydrology	See Hydrology	See Hydrology
Quantification of sediment transport	D, M, L	See Hydrology	See Hydrology	L: 100km @ 0.6 cm/yr	L: 100km @ 0.3 cm/yr
Determination of aquifer storativity parameters	L	See Hydrology	See Hydrology	See Hydrology	See Hydrology

* Mid-term reflects to MAGIC MRD

Thematic field	Application	Latency	Scientific/societal Questions & Objectives: See MAGIC MRD	Services	Products	Copernicus Service Reference	Reference traceability for Target Long-Term
Hydrology	Groundwater monitoring	few days	Q: H1, H2, H3, CL1; O: H-1a, H-1c; H2-b, H2-c; H-3a; H4-a; CL-1a	Climate monitoring; Drought and crop assessment; Flood prediction; Estimation of groundwater availability/variability	Groundwater and Terrestrial Water Storage Product; Total Water Storage	Land, Geodesy / time-variable gravity models, Groundwater product (G3P) to be implemented within CSS	GCOS ECV - Groundwater (https://gcos.wmo.int/en/essential-climate-variables/groundwater)
	Surface soil moisture monitoring	few days	Q: H1, H2, H3, CL1; O: H-1a, H1-c; H2-b, H2-c, H2-d; H-3a; H4-a; CL-1a	Climate monitoring; Drought and crop assessment; Flood prediction; Assessment of precipitation on a global scale	Soil moisture Product (ECV_SM); Soil water index	Copernicus Climate Change (lake water level, near-surface soil moisture, glacier mass change)	GCOS ECV - Soil Moisture (https://gcos.wmo.int/en/essential-climate-variables/soil-moisture)
	Agriculatural soil monitoring and forecasting	few days	Q: H1, H2, H3, CL1; O: H-1a, H1-c; H2-b, H2-c, H2-d; H-3a; H4-a; CL-1a	Climate monitoring; Drought and crop assessment; Flood prediction; Assessment of precipitation on a global scale	Soil moisture Product (ECV_SM); Soil water index	Copernicus Climate Change (lake water level, near-surface soil moisture, glacier mass change)	GCOS ECV - Soil Moisture (https://gcos.wmo.int/en/essential-climate-variables/soil-moisture)
	Drought monitoring and forecasting	few days (if operational)	Q: H1, H3, H4; O: H-1a; H-2c; H-3a; H4-a	Agriculture/crop assessment, public water supply, energy production, inland transport, terrestrial & freshwater ecosystems, forestry, tourism, human health, early warning of large scale droughts and floods regional estimates	Drought Severity Index (DSI)	Copernicus Climate Change and Emergency (lake water level, near-surface soil moisture, glacier mass change); Security. Emergency Management	TBD WMO Handbook of Drought Indicators and Indices (https://www.droughtmanagement.info/literature/GWP_Handbook_of_Drought_Indicators_and_Indices_2016.pdf)
	Flood monitoring	few days	Q: H1, H4; O: H1-a, H4-a	Flood monitoring	Terrestrial Water Storage Product	Copernicus Emergency (Global Flood Awareness System (GloFAS)	TBD
	Flood potential assessment	few days	Q: H1, H4; O: H1-a, H4-a	Flood early warning	wetness index, flood potential index	Copernicus Emergency (Global Flood Awareness System (GloFAS)	TBD
	Global water resources assessment	few days	Q: H1, H2, H3, CL1; O: H-1a, H-1c; H-2b, H-2c; H-3a; CL1-a	Climate monitoring; Drought Monitoring, Water Resource Assessment and Global Climate Monitoring	Groundwater and Terrestrial Water Storage Product; Total Water Storage	Copernicus Climate Change (lake water level, near-surface soil moisture, glacier mass change)	CNES, LEGOS (A. Blazquez & B. Meyssignac) - EC/ESA GSG WS Sep 2021
	Regional water resources assessment	few days	Q: H1, H2, H3, CL1; O: H-1a, H-1c; H-2b, H-2c; H-3a; CL1-a	Climate monitoring; Drought Monitoring, Water Resource Assessment and Regional Climate Monitoring	Groundwater and Terrestrial Water Storage Product; Total Water Storage	Copernicus Climate Change	TBD
	Snow monitoring (SWE)	few days	Q: H1, H2, CL1; O: H-1b, H-2a, H-2c; H-3a; CL1-a	Climate monitoring; Water Resource Assessment	Snow water product	Copernicus Climate Change	GCOS ECV - Snow (https://gcos.wmo.int/en/essential-climate-variables/snow)
	Wetland monitoring	few days	Q: H1 O: H-1a	Climate monitoring;	Wetland product	Copernicus Climate Change	TBD
	Permafrost hydrology	few months	Q: H1 O: H-1a, H-1b	Climate monitoring;	Permafrost water storage	Copernicus Climate Change	TBD
	Monitoring climate change effects on terrestrial water storage	few months	Q: H1, H2, H3, CL1; O: H-1a, H-1c; H2-b, H2-c; H-3a; CL-1a	Climate monitoring	Groundwater and Terrestrial Water Storage Product; Total Water Storage	Copernicus Climate Change (lake water level, near-surface soil moisture, glacier mass change)	GCOS user requirements (A. Güntner) - EC/ESA GSG WS Sep 2021
	Determination of baseflow dynamics of a river at sub-basin scale	few months	Q: H1, H3; O: H-1a, H-1c; H-3a	Climate monitoring	Baseflow quantification	Copernicus Climate Change	TBD
	Quantification of sediment transport	few months	Q: H2; O: H-2b	Sediment transport monitoring	Sediment quantification	Copernicus Land	Mouyen et al. (2018), Nature Communications
	Determination of aquifer storativity parameters	---	Q: H2, H3, S4; O: H-2b; H-3a; S-4b, S-4c	Estimation of groundwater availability/variability	Storativity indices	Groundwater product (G3P) to be implemented within CSS	TBD

Scientific/societal Questions & Objectives: See MAGIC MRD			
H1: How is the water cycle changing? How are these changes expressed in frequency and magnitude of extremes events such as droughts and floods? Is it possible to close the water budget on various spatial and temporal scales? • H1-a. Develop and evaluate an integrated Earth system analysis with sufficient observational input to accurately quantify the components of the water and energy cycles and their interactions, and to close the water balance from headwater catchments to continental-scale river basins (confined to scales larger or equal than 150x150 km2). Provide constraints of the net fluxes. • H1-b. Quantify rates of snow accumulation, snowmelt and ice melt at regional scales. • H1-c. Estimate water storage change in small river basins and separate medium-scale drainage basins.	H2: How do anthropogenic changes in climate, land use, water use, and water storage interact and modify the water and energy cycles locally, regionally, and globally, and what are the short- and long-term consequences? Is it possible to identify the climate change signature on the hydrological cycle? • H2-a. Quantify the magnitude of anthropogenic processes that cause changes in snowmelt, and ice melt, as they alter downstream water quantity (See CL2). • H2-b. Quantify how changes in land use, land cover, and water use related to	H3: How do changes in the water cycle impact local and regional freshwater availability and the services these provide? • H-3a. Monitor and understand the coupled natural and anthropogenic processes that change water quality, fluxes, and storages in and between all reservoirs (atmosphere, rivers, lakes, groundwater, and glaciers) and the response to extreme events as a basis for developing sustainable water resource management strategies.	H4: How does the water cycle interact with other Earth system processes to change the predictability and impacts of hazardous events and hazard chains (e.g. floods, wildfires, landslides, coastal loss, subsidence, droughts, human health, and ecosystem health)? E.g. soil moisture affects landslide conditions and improving soil moisture through adding space-geometric and remote sensing data by way of data assimilation has a positive effect on predictability (Felsberg et al., 2021) How do we improve preparedness and mitigation of water-related extreme events? How can we improve seasonal climate forecasts and the predictions of such extreme scenarios? • H4-a. Improve drought and flood monitoring to forecast short-term impacts more accurately and to assess potential mitigations based on near real-time observations. Include gravity data into operational forecasting of drought and flood events (from long- to short-term).

Cryosphere

Requirements refer to gravimetric data products from gravimetry missions and to the gravimetry contribution in data products resulting from signal separation or data assimilation.

Thematic field	Time scale D: Daily to weekly; M: Monthly; L: Long-term trend	State of the art: Resolution & Accuracy [EWH]	Threshold mid-term*: Resolution & Accuracy [EWH]	Target mid-term (TM)* / Threshold long term (TL): Resolution & Accuracy [EWH]	Target Long-term: Resolution & Accuracy [EWH]**
		GRACE-FO	Threshold MAGIC	Threshold QSG Baseline 1	Desired QSG Baseline 2
Cryosphere	D	N.A.	Threshold-a: 600 km @ 2.0 cm; Threshold-b: 300 km @ 5.3 cm;	TM/TL-a: 600 km @ 1.0 cm; TM/TL-b: 300 km @ 2.7 cm;	Target-a: 600 km @ 0.5 cm; Target-b: 300 km @ 1.3 cm;
	M	300 km @ 2.0 cm 150 km @ 5.0 cm	Threshold-a: 300 km @ 1.0cm; Threshold-b: 150 km @ 2.5 cm	TM/TL-a: 300 km @ 0.5 cm; TM/TL-b: 150 km @ 1.3 cm	Target-a: 300 km @ 0.3 cm; Target-b: 150 km @ 0.6 cm
	L	150 km @ 0.1 cm/yr	Threshold-a: 150 km @ 0.05 cm/yr	TM/TL-a: 150 km @ 0.03 cm/yr	Target-a: 150km @ 0.01 cm/yr
Applications					
Identification of sea level fingerprint of ice mass loss	M, L	See Cryosphere	See Cryosphere	See Cryosphere	See Cryosphere
Quantification of freshwater flux from the cryosphere into the ocean and its impact on the ocean	M, L	See Cryosphere	See Cryosphere	See Cryosphere	See Cryosphere
Separation of present-day ice mass change and GIA	M	See Cryosphere	See Cryosphere	TM/TL: 200 km @ 1.0 cm (old SATM)	Target: 100km @ 5.0 cm (old SATM)
	L	See Cryosphere	See Cryosphere	TM/TL: 150 km @ 0.2 cm/yr (old SATM)	Target: 100km @ 1.0 mm/yr (old SATM)
Quantifying mass changes of ice sheet and glaciers	L	See Cryosphere	See Cryosphere	TM/TL: 200 km @ 0.1 cm/yr (old SATM) TM/TL: xx km @ 0.05 cm/yr (ECV) (no resolution provided)	Target: 100km @ 1.0 mm/yr (old SATM) Target: xx km @ 0.2 mm/yr (ECV) (no resolution provided)
Spatial separation of peripheral glaciers	M, L	See Cryosphere	See Cryosphere	See Cryosphere	See Cryosphere
Quantification of firn compaction rates	M, L	See Cryosphere	See Cryosphere	See Cryosphere	See Cryosphere

* Mid-term reflects to MAGIC MRD

** Values are taken from hydrology due to lack of inputs/information

Thematic field	Application	Latency	Scientific/societal Questions & Objectives: See MAGIC MRD	Services	Products	Copernicus Service Reference	Reference traceability for Target Long-Term
Cryosphere	Identification of sea level fingerprint of ice mass loss	---	Q: C1, C2, O2, CL1; O: C-1a, C-1c; C-2a; O-2a, O-2b; CL-1a	Climate Monitoring, Explain causes for sea level rise	"Fingerprinted" regional sea level rise	Copernicus Climate Change	TBD
	Quantification of freshwater flux from the cryosphere into the ocean and its impact on the ocean	---	Q: C1 O: C-1d	Climate Monitoring	Freshwater flux estimates	Copernicus Climate Change	TBD
	Separation of present-day ice mass change and GIA	---	Q: C1, C2, CL1; O: C-1a, C-1c; C-2a; CL-1a, CL-1b	Estimation of ice load history and separation of hydrological effects from long-term climate changes	Global GIA models	Copernicus Climate Change	TBD
	Quantifying mass changes of ice sheet and glaciers	---	Q: C1, C2, CL1; O: C-1b; C-2a, C-2b, C-2c, C-2d, C-2e; CL-1a, CL-1b	Estimation of total freshwater storage on land. Glacier volume estimation by ground measurements of thickness. Glaciers and ice sheet mass change monitoring. Outlet glacier depths needed for use of ice velocities for mass change on ice sheets.	Ice velocity; Surface elevation change; Ice mass change	Copernicus Climate Change	GCOS ECV - Glaciers (https://gcos.wmo.int/en/essential-climate-variables/glaciers/)
	Spatial separation of peripheral glaciers	---	Q: C1, C2, CL1; O: C-1b; C-2a, C-2b, C-2c, C-2d, C-2e; CL-1a, CL-1b	Glaciers and ice sheet mass change monitoring	Ice mass change	Copernicus Climate Change	TBD
	Quantification of firn compaction rates	---	Q: C2; O: C-2b, C-2c	Glaciers and ice sheet mass change monitoring	Ice mass change	Copernicus Climate Change	TBD

Scientific/societal Questions & Objectives: See MAGIC MRD		
C1: How much will ice sheets contribute to sea level change, globally and regionally, over the next decade and beyond? How can we determine the changes of ice shets? How can the impact of freshwater fluxes into the ocean be quantified? • C1-a. Determine the contribution of the ice sheets and mountain glaciers to global mean sealevel change to within 0.1 mm/yr over the course of a decade (assuming 15 Gt/yr [See C2-b]). • C1-b. Improve the knowledge on the dynamic response of ice flow to changing oceanic and atmospheric boundary conditions, including interactions with intra- and sub-glacial hydrology [See C2]. • C1-c. Determine the contribution of ice sheets and mountain glaciers to regional patterns of sea-level change to within 0.05 mm/yr over the course of a decade. • C1-d. Determine freshwater fluxes from the cryosphere into the ocean and determine their impact on the ocean.	C2: What will be the consequences of climate change on mass changes ice sheets and glaciers? • C2-a. Reduce current uncertainties related to mountain glaciers and caps relative to the "eustatic" contribution to sea level rise. • C2-b. Determine the changes in surface mass balance and glacier ice discharge and uncertainties within the 15 Gton/yr accuracy over the entire ice sheets, continuously, for decades to come. Disentangle the superimposed processes from a combination of geodetic observations and modelling approaches (See Solid Earth). • C2-c. Improve modelling capabilities to fully understand ice sheet and glacier changes and provide enhanced robust predictions. Enhance number and accuracy of observations. Validate model developments, provide boundary conditions and allow model initialization. Understand the processes revealed by observations for further developing models with the aim of reaching predicting capabilities for emergency applications like meltwater flooding. • C2-d. Separating ice sheet changes from coastal ocean changes. This task includes the account for the gravitationally consistent ocean changes induced by the ice mass changes themselves, as well as changes due to ocean dynamics. • C2-e. Cryosphere mass balance at monthly to decadal time scales to understand climate forcing on ice sheets and glaciers.	C3: How can we improve the description of geodynamic processes, induced by continental ice mass changes, which act globally? How can we better interpret Glacial Isostatic Adjustment (GIA) and distinct spatial "fingerprints" of global oceanic mass redistributions? • C3-a. Improve the information on glacial history and solid Earth rheology, as well as consistency in the observing systems, and therefore embrace a large range of geoscience disciplines. Gravity has a key role due to its integrative nature and its direct relationship to conditions of mass conservation between changes in the cryosphere, the oceans and continental hydrology.

Oceanography

Requirements refer to gravimetric data products from gravimetry missions and to the gravimetry contribution in data products resulting from signal separation or data assimilation.
Some oceanic applications require the combination with altimetry, e.g. steric sea level, ocean heat content.

Thematic field	Time scale D: Daily to weekly;M: Monthly;L: Long-term trend	State of the art: Resolution & Accuracy [EWH]	Threshold mid-term*: Resolution & Accuracy [EWH]	Target mid-term (TM)* / Threshold long term (TL): Resolution & Accuracy [EWH]	Target Long-term: Resolution & Accuracy [EWH]**
		GRACE-FO	Threshold MAGIC	Threshold QSG Baseline 1	Desired QSG Baseline 2
Oceanography	D	N.A.	Threshold-a: 600 km @ 2.0 cm; Threshold-b: 300 km @ 5.3 cm	TM/TL-a: 600 km @ 1.0 cm; TM/TL-b: 300 km @ 2.7 cm;	Target-a: 600 km @ 0.5 cm; Target-b: 300 km @ 1.3 cm
	M	300 km @ 2.0 cm 150 km @ 5.0 cm	Threshold-a: 300 km @ 1.0cm; Threshold-b: 150 km @ 2.5 cm	TM/TL-a: 300 km @ 0.5 cm; TM/TL-b: 150 km @ 1.3 cm	Target-a: 300 km @ 0.3 cm; Target-b: 150 km @ 0.6 cm
	L	150 km @ 0.1 cm/yr	Threshold-a: 150 km @ 0.05 cm/yr	TM/TL-a: 150 km @ 0.03 cm/yr	Target-a: 150km @ 0.01 cm/yr
Applications					
Quantification of global and regional sea-level change	M	See Oceanography	See Oceanography	M: 100km @ 2-4mm (global, ECV)	See Oceanography
	L	See Oceanography	See Oceanography	L: 100km @ <0.3mm/yr (global, ECV)	L: 10km @ <0.03mm/yr (global, ECV)
Evaluation of and data assimilation into ocean models (based on ocean bottom pressure)	M, L	See Oceanography	See Oceanography	See Oceanography	See Oceanography
Monitoring large scale current variability (e.g. ACC and AMOC)	M	See Oceanography	See Oceanography	M: 200 km @ 1.5 cm (old SATM)	M: 100 km @ 5.0 cm (old SATM)
	L	See Oceanography	See Oceanography	See Oceanography	See Oceanography
Improvement of ocean tidal models	D	See Oceanography	Threshold: 400 km @ 5.0 cm (old SATM)	TM/TL: 400 km @ 0.5 cm (old SATM)	Target: 100 km @ 0.6 cm (old SATM)
Determination of steric sea level (gridded)	M, L	See Oceanography	See Oceanography	See Oceanography	See Oceanography
Quantification of ocean heat content (ocean basin averages)	M	See Oceanography	See Oceanography	TM/TL: 200 km @ 1.0 cm (old SATM)	Target: 100 km @ 5.0 cm (old SATM)
	L	See Oceanography	See Oceanography	See Oceanography	See Oceanography
Investigation of ocean mass as a sea level budget component	M	See Oceanography	See Oceanography	TM/TL: 200 km @ 1.0 cm (old SATM)	Target: 100 km @ 5.0 cm (old SATM)
	L	See Oceanography	See Oceanography	See Oceanography	See Oceanography
Improving ocean circulation models	M	See Oceanography	See Oceanography	See Oceanography	See Oceanography
Determination of stationary ocean transports (from mean dynamic topography)	M	See Oceanography	See Oceanography	100 km @ 0.4 cm (OSCAR)	10 km @ 0.2 cm (OSCAR)

* Mid-term reflects to MAGIC MRD | m hydrology due to

Thematic field	Application	Latency	Scientific/societal Questions & Objectives: See MAGIC MRD	Services	Products	Copernicus Service Reference	Reference traceability for Target Long-Term
Oceanography	Quantification of global and regional sea-level change	---	Q: O1, O2, CL1; O: O-1a, O-1b; O-1c, O-1d; O-2a, O-2b; CL-1a, CL-1b	Climate Monitoring, Explain causes for sea level rise	Sea level estimates	Marine, Geodesy, C3S	GCOS ECV - Sea Level (https://gcos.wmo.int/en/essential-climate-variables/sea-level)
	Evaluation of and data assimilation into ocean models (based on ocean	few days	Q: O1; O: O-1c, O-1e	Climate Monitoring, model improvement	Mass Transport determination,ocean model	Copernicus Climate Change	TBD
	Monitoring large scale current variability (e.g. ACC and AMOC)	---	Q: O1; O: O-1a, O-1c, O-1d	Climate Monitoring	Ocean currents	Marine, C3S	TBD
	Improvement of ocean tidal models	---	Q: O1; O: O-1d	model improvement	Tide model	Marine, Geodesy	TBD
	Determination of steric sea level (gridded)	----	Q: O2, CL1 O: O-2a, O2-b, CL-1a, CL-1b	Climate Monitoring, Explain causes for sea level rise	Steric sea level estimates	C3S	TBD
	Quantification of ocean heat content (ocean basin averages)	----	Q: O2; CL1 O: O-2a, O2-b; CL-1a, CL-1b	Climate Monitoring, Explain causes for sea level rise	Ocean heat content estimates	C3S	TBD
	Investigation of ocean mass as a sea level budget component	---	Q: O1, O2, CL1; O: O-1e; O-2a; CL-1a, CL-1b	Climate Monitoring; Monitor ocean mass changes, Explain causes for sea level rise	Ocean mass estimate	C3S	TBD
	Improving ocean circulation models	---	Q: O1; O: O-1a, O-1b, O-1c, O-1d, O-1e	Climate Monitoring; Monitor ocean circulation	Ocean circulation model	Marine, Geodesy	TBD
	Determination of stationary ocean transports (from mean dynamic	----	Q: O3 O: O-3a	quantify ocean transport	stationary ocean transport estimates	Marine	OSCAR https://space.oscar.wmo.int/variables/view/ocean_dynamic_topography

Scientific/societal Questions & Objectives: See MAGIC MRD		
O1: How are decadal-scale global ocean circulation patterns changing, and what are the effects of these changes on seasonal climate processes, extreme events, and longer term environmental change? • O1-a. Quantify the changes in the oceanic circulation patterns, reducing the uncertainty by a factor of 2. • O1-b. Quantify the linkage between natural and anthropogenic forcing and oscillations in the climate system and the one between the dynamical and thermodynamic state of the ocean on decadal time scales. For both, reduce the uncertainty by a factor of 2. • O1-c. Quantify the linkage between global climate sensitivity and circulation change on regional scales, including the occurrence of extremes and abrupt changes. Quantify the changes in the strength of AMOC to within 5% per decade; changes in ENSO spatial patterns, amplitude, and phase. • O1-d. Provide observational verification of models used for climate projections. Enhanced simulations on evolution of the large-scale patterns in the ocean circulation and tides are necessary. Improving descriptions nearby coasts and current de-aliasing models and methods is crucial. Improved tidal models by co-estimation of ocean tide parameters requires long time series as well as increased accuracy compared to the current state. • O1-e. The ocean bottom pressure variations and the time mean dynamic topography can be provided by satellite	O2: How much will sea level change, globally and regionally, and along coastlines over the next decade and beyond, and what will be the role of ocean heat storage? • O2-a. Quantify the rates of sea-level change and its driving processes at global and regional scales. • O2-b. Determining how and where heat is being taken up by the ocean, stimating how much is being stored in the deep ocean, and understanding the processes that control this are all important to understand sea level rise and improve the predictive skill of	O3: How can the determination of stationary ocean transports be improved? O-3a: Determination of stationary ocean transports (from mean dynamic topography)

Solid Earth

Requirements refer to gravimetric data products from gravimetry missions and to the gravimetry contribution in data products resulting from signal separation or data assimilation.

Geohazard estimate	Time scale D: Daily to weekly, M: Monthly;L: Long-term trend	State of the art: Resolution & Accuracy [EWH]	Threshold mid-term*: Resolution & Accuracy [EWH]	Target mid-term (TM)/ / Threshold long term (TL): Resolution & Accuracy [EWH]	Target Long-term: Resolution & Accuracy [EWH]**
		GRACE-FO	Threshold MAGIC	Threshold QSG Baseline 1	Desired QSG Baseline 2
Solid Earth	D	N.A.	Threshold-a: 600 km @ 2.0 cm; Threshold-b: 300 km @ 5.3 cm;	TM/TL-a: 600 km @ 1.0 cm; TM/TL-b: 300 km @ 2.7 cm;	Target-a: 600 km @ 0.5 cm; Target-b: 300 km @ 1.3 cm;
	M	300 km @ 2.0 cm 150 km @ 5.0 cm	Threshold-a: 300 km @ 1.0cm; Threshold-b: 150 km @ 2.5 cm	TM/TL-a: 300 km @ 0.5 cm; TM/TL-b: 150 km @ 1.3 cm;	Target-a: 300 km @ 0.3 cm; Target-b: 150 km @ 0.6 cm
	L	150 km @ 0.1 cm/yr	Threshold-a: 150 km @ 0.05 cm/yr	TM/TL-a: 150 km @ 0.03 cm/yr	Target-a: 150km @ 0.01 cm/yr
Applications					
Geohazards	D	N.A.	Threshold: 300 km @ <10.0 cm (Mw 8 earthquakes)	TM/TL: <250 km @ 10.0-1.0 cm	Target-a: 300 km @ 1 cm; Target-b: 200 km @ 3 cm;
	M	See Solid Earth	Threshold: 300 km @ 1-2 cm (Mw 8 earthquakes)	TM/TL: 200 km @ 1.0 cm (Mw > 7.6 earthquakes)	Target-a: 300 km @ 0.1 cm; Target-b: 200 km @ 0.3 cm; (M >7.5)
	L	See Solid Earth	Threshold: 200 km @ 1 cm/yr	TM/TL: 100 km @ 1.0 cm/yr	see Solid Earth
Evolution of Earth's crust under external or internal forcing	L	See Solid Earth	See Solid Earth	TM/TL: <100 km @ 10 cm/yr	see Solid Earth
Natural resources exploitation	D	See Solid Earth	See Solid Earth	see Solid Earth	see Solid Earth
	M	See Solid Earth	See Solid Earth	see Solid Earth	see Solid Earth
	L	See Solid Earth	Threshold: 300 km @ 10.0 cm	TM/TL: <250 km @ 10.0-1.0 cm	see Solid Earth
Deep interior properties and dynamics	D	N.A.	See Solid Earth	TM/TL: 6000 km @ 0.15 mm (Body tides)	TM/TL: 6000 km @ 0.15 mm (Body tides)
	L	See Solid Earth	See Solid Earth	TM/TL-a: 2000-6000 km @ 0.05-0.1 mm/10 yr; TM/TL-b: 230-330 km @ 1 mm/10 yr	TM/TL-a: 2000-6000 km @ 0.05-0.1 mm/10 yr; TM/TL-b: 230-330 km @ 1 mm/10 yr

* Mid-term reflects to MAGIC MRD

** Information not available

Thematic field	Application	Latency	Scientific/societal Questions & Objectives: See MAGIC MRD	Services	Products	Copernicus Service Reference	Reference traceability for Target Long-Term
Solid Earth	Monitoring of large-scale land slides; regional estimates to monitor medium-sclae land slides	daily	Q: S1; O: S1-a	Geohazard estimate	Mass changes due to displacements	Emergency, Copernicus Global Land	TBD
	Reliable constraints on slip distribution on off-shore faults	daily-monthly-yearly	Q: S1; O: S1-a	Geohazard estimate	Mass changes at capable off-shore faults	Emergency, Copernicus Global Land, Seismological hazard assessment	see ref to right
	Assessment of earthquake cycle. Long-term strain variations efficiently corrected by hydrological loading.	daily-monthly-yearly	Q: S1; O: S1-a	Geohazard estimate	Mass changes at selected faults	Emergency, Copernicus Global Land, Seismological hazard assessment	see ref to right
	Tsunami risk estimate	daily-monthly-yearly	Q: S1; O: S1-b	Geohazard estimate	Mass changes at tsunami generating faults	Emergency, Tsunami hazard assessment	TBD
	Volcano hazard estimate. Determining the functioning of volcanic plumbing system.	daily-monthly-yearly	Q: S1, O: S1b, S1c	Geohazard estimate	Mass changes at volcanos, on shore and submarine	Emergency, Volcano hazard assessment	see ref. to right
	Detect aseismic creep events at all depths and inter-seismic deformations.	daily-monthly-yearly	Q: S1, S3 O: S1a, S3c, S3d	Geohazard estimate	Mass change due to tectonic deformation	Crustal deformation monitoring; earthquake hazard estimation	see ref. to right
	Detect Land uplift and subsidence due to past and present ice sheet melt. GIA forebulge migration.	yearly	Q: S3, O: S-2a; S-3a, S-3b, S-3c, S-3d; S-4a	Global land uplift from GNSS/Geodesy.	Mass changes in response to glacial load change	Climate change, Glaciers monitoring	see ref. to right
	Detect deep water fluxes originating from geologic process and distinguish from groundwater fluxes; Mass fluxes of fossil waters.	daily-monthly-yearly	Q: S4, O: S4a, S4b, S4c	Surficial mass variations for multidisciplinary applications; Estimation of groundwater availability/variability; Management of energy/water resources; Triggered	Superficial mass changes	Natural resource exploitation	TBD
	Detection of deep precursory signals before a rupture	daily-monthly-yearly	Q: S2, S3: O: S-2a; S-3a, S-3b, S-3c, S-3d	Deep interior properties and dynamics	Deep earth mass changes	Emergency, Security, Land	see ref. to right
	Constrain mantle dynamic models: Monitor mass changes from deep interior of earth.	monthly to decadal	Q: S2, S3: O: S-2a; S-3a, S-3b, S-3c, S-3d	Deep interior properties and dynamics	Deep earth mass changes	Earth Observation	see ref. to right
	Define crust and lithosphere structures relevant for natural resource exploration	static	Q: S4 O: S-4a	Natural resources exploration	Lithosphere structure	Earth Observation	See comment to right

De Viron, O., Panet, I., Mikhailov, V., Van Camp, M., Diament, M., 2008. Retrieving earthquake signature in grace gravity solutions. Geophys. J. Int. 174, 14–20.

Cambiotti, G., Douch, K., Cesare, S., Haagmans, R., Sneeuw, N., Amoruso, A., Marotta, A.M., Sabadini, R., 2020. On Earthquake Detectability by the Next-Generation Gravity Mission. Surv. Geophys. 41, 1049–1074; Chao, B.F., Liau, J.R., 2019. Gravity Changes Due to Large Earthquakes Detected in GRACE Satellite Data via Empirical Orthogonal Function Analysis. J. Geophys. Res. Solid Earth 124, 3024–3035; Vallée, M., Juhel, K., 2015. Multiple Observations of the Prompt Elastogravity Signals Heralding Direct Seismic Waves. J. Geophys. Res. Solid Earth 124, 2970–2989; Tanaka, Y., Hirai, K., 2014. Long- and short-term postseismic gravity changes of megathrust earthquakes from satellite gravimetry. Geophys. Res. Lett. 41, 5451–5456.

Spatiotemporal gravity changes at the Santorini Volcanic complex and their interpretation. Quat. Sci. Adv. 13, 100140; Bielenberg, C., Pesterotti, A., 2024. Detectability of Seamount Eruptions Through a Quantum Technology Gravity Mission MOCASTY: Hunga Tonga, Fani Maoré and Other Smaller Eruptions. Surv. Geophys. 45, 1331–1361;

2022. Deep mass redistribution prior to the 2010 Mw 8.8 Maule (Chile) Earthquake revealed by GRACE satellite gravity. Earth Planet. Sci. Lett. 584, 117465; Crawford, O., Al-Attar, D., Tromp, J., Mitrovica, J.X., 2017. Forward and inverse modelling of post-seismic deformation. Geophys. J. Int. 209, 845–876;

Mikhailov, L., Caron, L., Greff-Lefftz, M., Panet-Mikhailov, G., Fleitout, L., Rouby, H., 2016. Evidence for postglacial signatures in gravity gradients: A clue in lower mantle viscosity. Earth Planet. Sci. Lett. 452, 146–156.

2022. Deep mass redistribution prior to the 2010 Mw 8.8 Maule (Chile) Earthquake revealed by GRACE satellite gravity. Earth Planet. Sci. Lett. 584, 117465.

Chen, J., Cazenave, A., Dahle, C., Llovel, W., Panet, I., Pfeffer, J., Moreira, L., 2022. Applications and Challenges of GRACE and GRACE Follow-On Satellite Gravimetry. Surv. Geophys. 43, 305–345; Marquart, G., Steinberger, B., Nishusa, K., 2005. On the effect of a low viscosity asthenosphere on the temporal change of the geoid—A challenge for future gravity missions. J.

Legeramont of works on gravity inversion for lithosphere structure in areas which host natural resources.

Scientific/societal Questions & Objectives: See MAGIC MRD			
S1. How can large-scale geological hazards be accurately forecast? In a socially relevant time frame? How do geological disasters directly impact the Earth system and society following an event? How can we monitor geohazards associated with earthquakes, tsunamis and volcanoes? • S1-a. Measure and forecast inter-seismic, pre-seismic, co-seismic, and post-seismic activity over tectonically active areas on time scales ranging from hours to decades to distinguish the inter-effects from long-term movements. Detect tectonic, aseismic creep events equivalent to magnitude >7. Rapid capture of the transient processes following disasters is needed for improved predictive modelling, as well as response and mitigation through optimal re-tasking and analysis of space data. A spatial resolution of 200 km with an accuracy of 0.5 μGal is needed. Monthly resolution is required, acquisition of daily to weekly data with low latency is vital for specific short-term monitoring. • S1-b. Forecast, model, and measure tsunami generation, propagation, and run-up for major tsunamigenic events.	S2. How does energy flow from the core to Earth's surface? Can we better quantify the physical properties in the deep interior and their relationship to deep and shallow geodynamic processes? • S2-a. Determine the effects of convection within Earth's interior, specifically the dynamics of Earth's core and its changing magnetic field and the interaction between mantle convection and plate motions. If high accuracy (signals amplitude: 0.5-1 mm EWH in 10 years) can be reached at long wavelengths (thousands km) and decadal timescales, ongoing deep Earth dynamics may become observable: geostrophic flows near the top of the core that change pressures at the CMB [R315], on-going large-scale convective mantle flow [R313]. Time-integrated body tides perturbations from the heterogeneous mantle mass distribution are 10 time larger than the above deep Earth dynamics signals, reaching 0.5-1 mm EWH in one year [R314]. Observe gravimetric perturbations caused by tidal forcing of convection-induced mantle heterogeneity.	S3. How can we jointly quantify and improve separation of the ongoing glacial Earth deformation in response to surface loads, as the last deglaciation (i.e., the post-glacial rebound (GIA) signal), or resulting from the internal dynamics, together with the present-day ice sheet loss and water mass variations [R08][R0267]? • S3-a. Identification of long-term effects and the separation from annual to inter-annual climatic factors which affect surface deformation of the crust. Time series length in combination with past and existing missions of at least 30 years is required. A long time series characterized by a trend accuracy of 0.05 μGal/yr on scales of 200 km will be critical to provide regional scale estimates of ongoing crustal deformation across the tectonically land surface, ocean bottom and lower crustal boundary. • S3-b. Quantify global, decadal landscape change produced by abrupt events and by continuous	S4. How much water is traveling deep underground and how does it affect geological processes over the long term and short term (earthquakes) and water supplies (e.g. water management)? How do we improve discovery and management of energy, mineral, and soil resources? How can we achieve sustainable exploitation of natural resources? • S4-a. Improve spatial resolution for imaging of the 3D structure of the crust and mantle using the static gravity field. This is needed in order to locate and monitor changes in key resources. • S4-b. Monitor underground anthropogenic driven mass variations. Monthly resolution is adequate, weekly resolution is desirable. • S4-c. Measure all significant fluxes in and out of the groundwater system across the recharge zone. Determine the transport and storage properties in situ within a factor of 5 for shallow aquifers and an order of magnitude for deeper systems. Assess the impact of these water redistributions on earthquakes.

Geodesy

Requirements refer to gravimetric data products from gravimetry missions and to the gravimetry contribution in data products resulting from signal separation or data assimilation.

Thematic field	Time scale D: Daily to weekly;M: Monthly;L: Long-term trend	State of the art: Resolution & Accuracy [EWH]	Threshold mid-term*: Resolution & Accuracy [EWH]	Target mid-term (TM)* / Threshold long term (TL): Resolution & Accuracy [EWH	Target Long-term: Resolution & Accuracy [EWH]**
		GRACE-FO	Threshold MAGIC	Threshold QSG Baseline 1	Desired QSG Baseline 2
Geodesy	D	N.A.	Threshold-a: 600 km @ 2.0 cm; Threshold-b: 300 km @ 5.3 cm	TM/TL-a: 600 km @ 1.0 cm; TM/TL-b: 300 km @ 2.7 cm;	Target-a: 600 km @ 0.5 cm Target-b: 300 km @ 1.3 cm
	M	300 km @ 2.0 cm 150 km @ 5.0 cm	Threshold-a: 300 km @ 1.0cm; Threshold-b: 150 km @ 2.5 cm	TM/TL-a: 300 km @ 0.5 cm; TM/TL-b: 150 km @ 1.3 cm	Target-a: 300 km @ 0.3 cm; Target-b: 150 km @ 0.8 cm
	L	150 km @ 0.1 cm/yr	Threshold-a: 150 km @ 0.05 cm/yr	TM/TL-a: 150 km @ 0.03 cm/yr	Target-a: 150km @ 0.01 cm/yr
Applications					
Height system unification	L	See Geodesy	See Geodesy	static: 1' @ 0.1 m^2/s^2	static: 1' @ 0.03 m^2/s^2 trend: 1' @ 0.003 $m^2/s^2/yr$
Satellite orbit determination	M	See Geodesy	See Geodesy	Threshold-a: 300 km @ 1.0cm; Threshold-b: 150 km @ 2.5 cm (same as Thresold mid-term)	Threshold-a: 300 km @ 1.0cm; Threshold-b: 150 km @ 2.5 cm (same as Thresold mid-term)
Time-mean geopotential or gravity anomaly assessment	L	See Geodesy	See Geodesy	See Geodesy	See Geodesy
Determination of time-variability of geoid	L	See Geodesy	See Geodesy	See Geodesy	trend: 1' @ 0.03 cm/yr geoidheight
Determination of time-variable loading corrections for GNSS	D, M, L	See Geodesy	See Geodesy	See Geodesy	See Geodesy
Constructing the ITRF reference frame, deriving EOP parameters	D, M, L	See Geodesy	See Geodesy	See Geodesy	See Geodesy
* Mid-term reflects to MAGIC MRD	* Mid-term reflects to MAGIC MRD	** Information not available			

Thematic field	Application	Latency	Scientific/societal Questions & Objectives: See MAGIC MRD	Services	Products	Copernicus Service Reference	Reference traceability for Target Long-Term
Geodesy	Height system unification	yearly	Q: G1; O: G1-b, G1-c	national geodetic or cartographic agencies	Unified vertical reference frames	---	Sanchez et al. (2021), JoG
	Satellite orbit determination	real-time … 19 days	Q: G1, G2; O: G1-d; G-2a	satellite mission providers	satellite ephemerides, satellite clock solutions, troposphere estimates and global ionosphere maps	Copernicus POD Service	TBD
	Time-mean geopotential or gravity anomaly assessment		Q: G2; O3 O: G-2a; O-3a	TBD	Global gravity models (GGMs), geoid models, geoid anomaly maps	---	Sanchez et al. (2021), JoG
	Determination of time-variability of geoid	yearly	Q: G1; O: G1-b, G1-c	national geodetic or cartographic agencies	time-variable part of GGMs, time-variable regional geoid models, dynamic height reference surfaces	----	
	Determination of time-variable loading corrections for GNSS	few days	Q: G2; O: G-2b	GNSS loading correction services	time-variable surface loading	----	TBD
	Constructing the ITRF reference frame, deriving EOP parameters	near real-time … yearly	Q: G1; O: G1-a, G-1d	International Earth Rotation and Reference systems Service, International DORIS Service, International GNSS Service, International Laser Ranging Service, International VLBI Service	Global reference frames	----	TBD

Scientific/societal Questions & Objectives: See MAGIC MRD	
G1: How can a consistent and stable global reference frames be established, both for 3D coordinates and as unified height reference? How can a consistent height reference be established in regions with temporal changes of the geoid? G-1a: Determine stable global reference frames for precise positioning services, geolocation of Earth observing instruments, timing and navigation services, and the monitoring of variations in Earth rotation G-1b: Create consistent height reference surfaces across borders, for land and marine infrastructure projects, marine charts, etc. G-1c: Create consistent height reference surfaces in regions affected by GIA or land uplift in general G-1d: Enable geolocation of Earth satellite-based observing instruments for precise positioning services, timing and navigation services, vertical land motion and ocean (sea level change) measurements.	G2: Which accuracy and resolution can be achieved for time-mean and temporally varying maps of gravity field functionals? G-2a: Generate high-resolution maps of time-mean geoid and gravity anomalies, e.g. for resource exploration G-2b: Determine precise and high-resolution time-variable loading corrections for GNSS to enable precise positioning services

Climate

Requirements refer to gravimetric data products from gravimetry missions and to the gravimetry contribution in data products resulting from signal separation or data assimilation

Thematic field	Time scale D: Daily to weekly M: Monthly L: Long-term trend	State of the art: Resolution & Accuracy [EWH]	Threshold mid-term*: Resolution & Accuracy [EWH]	Target mid-term (TM)* / Threshold long term (TL): Resolution & Accuracy [EWH]	Target Long-term: Resolution & Accuracy [EWH]**
		GRACE-FO	Threshold MAGIC	Threshold QSG Baseline 1	Desired QSG Baseline 2
Atmosphere and climate modeling	D	N.A.	Threshold-a: 600 km @ 2.0 cm; Threshold-b: 300 km @ 5.3 cm	TM/TL-a: 600 km @ 1.0 cm; TM/TL-b: 300 km @ 2.7 cm	Target-a: 600 km @ 0.5 cm; Target-b: 300 km @ 1.3 cm
	M	300 km @ 2.0 cm 150 km @ 5.0 cm	Threshold-a: 300 km @ 1.0cm Threshold-b: 150 km @ 2.5 cm	TM/TL-a: 300 km @ 0.5 cm TM/TL-b: 150 km @ 1.3 cm	Target-a: 300 km @ 0.3 cm Target-b: 150 km @ 0.6 cm
	L	150 km @ 0.1 cm/y	Threshold-a: 150 km @ 0.05 cm/y	TM/TL-a: 150 km @ 0.03 cm/y	Target-a: 150km @ 0.01 cm/y
Applications					
Quantifying hydro-meteorological fluxes	D, M, L	See Atmosphere and Climate Monitoring	See Atmosphere and Climate Monitoring*	See Atmosphere and Climate Monitoring*	See Atmosphere and Climate Monitoring*
Extreme event forecasting	D, M	See Atmosphere and Climate Monitoring	See Atmosphere and Climate Monitoring	See Atmosphere and Climate Monitoring	See Atmosphere and Climate Monitoring
Quantifying atmospheric state including wate and energy cycle	M, L	See Atmosphere and Climate Monitoring	See Atmosphere and Climate Monitoring	See Atmosphere and Climate Monitoring	See Atmosphere and Climate Monitoring
Monitoring pressure systems	D	See Atmosphere and Climate Monitoring	See Atmosphere and Climate Monitoring	See Atmosphere and Climate Monitoring	See Atmosphere and Climate Monitoring
Precipitation (incl. Snowfall) monitoring	D, M	See Atmosphere and Climate Monitoring	See Atmosphere and Climate Monitoring	M: 125km @ 2mm (ECV)	D: 50 km @ 1mm (ECV)
Soil moisture monitoring	D, M, L	See Atmosphere and Climate Monitoring	See Atmosphere and Climate Monitoring	D: 50km @ 0.08 m^3/m^3 (ECV)	D: 10km @ 0.04 m^3/m^3 (ECV)
Attribution of anthropogenic forcing	M, L	See Atmosphere and Climate Monitoring	See Atmosphere and Climate Monitoring	See Atmosphere and Climate Monitoring	See Atmosphere and Climate Monitoring
* Mid-term reflects to MAGIC MRD	* Mid-term reflects to MAGIC MRD	** Information no available			

*I in a finite differencing approach to retrieve dS/dt, likely more stringent requirement apply

Thematic field	Application	Latency	Scientific/societal Questions & Objectives: See MAGIC MRD	Services	Products	Copernicus Service Reference	Reference traceability for Target Long-
Atmosphere and Climate Monitoring	Quantifying hydro-meteorological fluxes	< 1day … few days	Q: CL1, CL2; H1 O: CL1-a, CL2-a; H1-a	ECMWF, Weather services, GEWEX, …	Reanalyses of atmosphere-land-ocean state	Copernicus Climate Change (lake water level, near-surface soil moisture, glacier mass change)	TBD
	Extreme event forecasting	few days	Q: CL1; H4 O: CL1-a, CL1-c; H4-a	Early warning	Flood and drought risk indicators, warning alerts	Copernicus Emergency Service (e.g. Global Flood Awareness System (GloFAS) and European Drought Observatory – EDO)	TBD
	Quantifying atmospheric state including water and energy cycle	< 1day	Q: CL1, CL2 O: CL1-a, CL2-b, CL2-c	ECMWF, Weather services	Reanalyses and forecasts	Copernicus Climate Change (lake water level, near-surface soil moisture, glacier mass change	TBD
	Monitoring pressure systems	< 1day	Q: CL2 O: CL2-b	ECMWF, Weather services	Reanalyses and forecasts	Copernicus Climate Change (lake water level, near	TBD
	Precipitation (incl. Snowfall) monitoring	< 1day	Q: CL1, CL2; H1 O: CL1-a, CL2-b, H1-b	ECMW, Weather services	Reanalyses and forecasts	Copernicus Climate Change (lake water level, near-surface soil moisture, glacier mass change	GCOS ECV - Precipitation (https://gcos.wmo.int/en/essential-climate-variables/precipitation)
	Soil moisture monitoring	< 1day … few days	Q: CL1, CL2; H2 O: CL1-a; CL2-a, H--2d	ECMWF, Weather services	Reanalyses and forecasts	Copernicus Climate Change (lake water level, near-surface soil moisture, glacier mass change	GCOS ECV - Soil Moisture (https://gcos.wmo.int/en/essential-climate-variables/soil-moisture)
	Attribution of anthropogenic forcing	few months	Q: CL1; O: CL1-c	IPCC, CORDEX	Earth digital twins	Copernicus Climate Change (lake water level, near-surface soil moisture, glacier	TBD

Scientific/societal Questions & Objectives: See MAGIC MRD	
CL1: Is it possible to separate the effects of natural climate variability, long-term climate change and direct anthropogenic impacts on the water cycle? • CL1-a. Evaluate seasonal to decadal climate predictions and assess long-term climate model projections [RD11] [RD10]. • CL1-b. Ensure the continuation of current mass transport observations to provide multidecadal time series [RD21] [RD22]. • CL1-c. Provide observational constraints on anthropogenic changes in the water cycle (attribution)	CL2: How can atmosphere and land surface models be improved? • CL2-a. Provide observational constraints on precipitation minus evapotranspiration budget from storage change minus discharge (at river basin scale), with precipitation minus evaporation equalling to moisture convergence in the models • CL2-b. Improve weather forecasting […] • CL2-c. Observe/separate atmospheric moisture convergence in observations of mass change

Annex 1 – EC input

Domain	Phenomenon	Requirement	Current Spatial resolution	Target Spatial resolution	Current Temporal resolution	Target Temporal resolution	Signal	Services	Products	Copernicus service reference
Cryosphere / ice sheets	Glaciers (static)	60% of existing mountain glacier area					1 µGal @ d/2≥120; ground level	Glaciers volume estimation in support to ground measurements of depth		Copernicus Global Land: (snow water equivalent, river water level, soil water index)
Cryosphere / ice sheets	Seamount growth	10 m thickness eruption → Volume change 1 x 109 m3					0.2 µGal @ d/2≥ 40 @ 250 km height	Global monitoring of underwater mass changes		Copernicus Climate Change (lake water level, near-surface soil moisture, glacier mass change)
Cryosphere / ice sheets	Glaciers mass variations	Detect localized deglaciations: 0.1 m over 2000 km2					0.1 µGal @ d/2≥ 50 @ 250 km height	Glaciers mass variations monitoring, mass tracking between cryosphere/hydrosphere		Copernicus Climate Change (lake water level, near-surface soil moisture, glacier mass change)
Cryosphere / ice sheets	Glaciers mass variations	measurement uncertainty/stability: 0.1 m/year				30 days		climate monitoring and deep soil moisture	Ice velocity	Copernicus Climate Change (lake water level, near-surface soil moisture, glacier mass change)
Cryosphere / ice sheets	Glaciers mass variations	measurement uncertainty/stability: 0.1 m/year		20km, 30-100 km Aim to obtain the secular trend with 2 mm equivalent water height per year accuracy at 150 km resolution. -> enable the separation of ice mass, ocean mass, and glacio-isostatic adjustment signals based on their specific fingerprints in the		1-10 days and longer		climate monitoring and deep soil moisture	Surface Elevation change	Copernicus Climate Change (lake water level, near-surface soil moisture, glacier mass change)
Cryosphere / ice sheets	Glaciers mass variations	measurement uncertainty/stability: 1[illegible]/year						climate monitoring and deep soil moisture	Ice mass change	Copernicus Climate Change (lake water level, near-surface soil moisture, glacier mass change)
Cryosphere / ice sheets	Climate science (Monitor ice sheets and glaciers mass loss.Monitor ocean mass changes. Explain the causes for sea level rise. Estimation the Earth energy imbalance, Estimation the total land water content) has improved significantly over the last 2 decades with the monitoring of mass transports at the Earth surface. Monitoring at mass transports is done with the		300x300 km and 0.8mm/y SLE	< 200x200 km and 1 cm/m and 0.1 mm/y SLE				Estimation of freshwater availability on land (water and ice). Monitoring of large scale land slides Early warning of large scale droughts and floods		Copernicus Climate Change (lake water level, near-surface soil moisture, glacier mass change)
Hydrology	Drought / Flood	vary on spatial (100km for drought and groundwater storage) for and temporal scales (3days for precipitation assessment). TWS (total water storage).	1 degree	≤ 0.25 degrees, 100km	1 month / Delivery Lag: 45 days	Temporal resolution 3 days. Lag in data delivery max 1/2 week (near real-time).		agriculture/crop assessment, public water supply, energy production, inland transport, terrestrial & freshwater ecosystems, forestry, tourism, human health		Copernicus Climate Change and Emergency (lake water level, near-surface soil moisture, glacier mass change)
Hydrology	Groundwater and water balance		220 km at mid-latitudes	100 km at mid-latitudes (all large river basins would be resolved. Impacts of groundwater withdrawals on smaller aquifer systems could be tackled. Direct application of the data to drought and flood mapping and snowpack monitoring would be enabled. Data can be directly ingested by most global models. < 150 km resolution (about 95% of	monthly	10-14 days or better for drought mapping and snowmelt monitoring for runoff prediction. Daily data with at most a few days latency (near real-time) would be required for flood response efforts and forecast model initialization.		climate monitoring and deep soil moisture		Copernicus Climate Change (lake water level, near-surface soil moisture, glacier mass change)
Hydrology		long-term and global coverage of ECV data sets	200-300 km	100km , 0.5° spatial resolution	seasonal	monthly, bi-weekly	required measurement uncertainty: 1mm/yr, current 10 mm/year		Groundwater storage Product	Land, Geodesy / time-variable gravity models
Oceanography	variable earth gravity field	very precise: 200x200 km, monthly	GRACE has been used to observe the AMOC at a single latitude with a favourable bathymetric profile. However it is not possible to estimate the AMOC for all latitudes using GRACE.	1 cm - 0.1 mm/year at global scales; 100 - 200 km -> the transport fluctuations of the Sub-Antarctic Front and Polar Front could be separated from those of the Sub-tropical Front and the Southern Antarctic Circumpolar Current Front.		Monthly, seasonal or even annual averages would be sufficient		altimetry and **marine services**; mean and regional long-term sea level variations, exchanges of mass between ice caps, continents and the ocean, earth energy imbalance, ocean circulation and heat flux, meridional overturning circulation (MOC), bottom		Marine, Geodesy / time-variable gravity models
Oceanography	mean earth gravity field	[illegible] (< 1 cm and < 100 km resolution) is of great interest (in particular for the coastal								Marine, Geodesy / time-variable gravity models
Oceanography	ocean bottom pressure variable earth gravity field, tides, wind-driven circulation, tidal modulations	[illegible] fields thus exhibit higher spatial resolution in North-South direction • For AMOC (Atlantic Meridional Overturning Circulation) monitoring, however, high resolution in		Observing the AMOC across all latitudes is desirable such that transport coherence can be studied. Goal for future gravimetry missions.			Signal (1 – 2 hPa) is spatially coherent all along the North American Shelf, but has a very narrow East-West extension (few hundred km only) cm, in bottom pressure		Mass transport determination	Copernicus Climate Change (lake water level, near-surface soil moisture, glacier mass change)
Solid Earth – Geohazards	Earthquakes	10 fold increase in number of detectable earthquakes					0.001 mE @ d/o 30 @ 360 km height	[illegible] constrains on slip distribution on off-shore faults; assessment of earthquake cycle and		Emergency, Security, Copernicus Global Land
Solid Earth – Geohazards	variable earth gravity field	Higher spherical harmonic coefficients of GGMs [illegible]							Mass transport determination	Land, Geodesy / time-variable gravity models
Solid Earth – Geohazards	Earthquake cycle	High spatial resolution & accuracy High temporal resolution (to test early co-seismic slip models, short term post-seismic processes	GOCI: spatial scale as small as 80 km GRACE sensitivity at Mw 8.6 earthquake magnitude	≤ 250 km @ 10-1.0cm; earthquakes with magnitude as small as Mw 7.0. the so-called silent or slow earthquakes, observable by future missions. It must be recalled that the most devastating earthquakes (causing e.g., tsunamis) are located under the sea, in areas that cannot – or only		Daily to weekly	Co-seismic signal of a Mw 7.0 earthquake: 0.5 mGals@100 km (~ 1.25 cm EWH)			Emergency, Copernicus Global Land
Solid Earth – Geohazards	Deeper Earth structure and dynamics	High accuracy at long wavelengths over short timescale or decadal [illegible]				Daily to weekly				Emergency, Security, Land

PART 2:

CONSOLIDATION OF QSG REQUIREMENTS

3. INTRODUCTION

The purpose of this document is to assess, define and consolidate the user requirements of QSG mission constellations. It refers to Task 1 of the SoW and WP 100 of the WBS.

4. CRITICAL REVIEW OF USER REQUIREMENTS AND UPDATES

The initial user requirements table (QSG_UR_SATM_v2.0.xlsx Excel sheet) that was provided to the study team has been critically discussed across the team and with ESA. On this basis, we provide updated recommendations for the different application fields below.

Before this we suggest the following more general modifications, regarding the logic of the requirements table and independent of the thematic area (Table 4-1).

The recommendations have been implemented in v3 of the SATM table.

Table 4-1: Proposed general modifications to the user requirements table

Topic	Suggestions by project team	Suggestions ESA	Actions (All)
Logic of the tables	In the different areas such as hydrology, ocean, … the table entries should be consistently arranged as per application area, instead of following a mixture of observing storages (e.g. groundwater) and applications (e.g. flood monitoring).	There is no definite application domain for all geophysical signals recovered by satellite gravimetry. This is the reason we keep in the Science and Applications Traceability Matrix both geophysical signals and applications.	As agreed at PM2, the matrix shall list only applications (no signals). The table has been updated accordingly.
	It should be clarified whether threshold and target requirements apply to gravimetric data products only (what can be derived from a mission) or to products derived from other space missions via signal separation or data assimilation (e.g. groundwater, ocean heat)	Requirements refer to gravimetric data products from gravimetry missions and to the gravimetry contribution in data products resulting from signal separation or data assimilation.	Acknowledged. The numbers in the table have been defined accordingly.
	It should be clarified whether applications that require improved knowledge of the mean (static) gravity field should be included.	It has to be assessed to what extent can a time-varying gravity field mission improve the current state-of-the-art knowledge of the static	A "Geodesy" tab has been added to the table. This includes requirements for the static gravity field.

		gravity field. We can also add a "Geodesy" tab. See new MRTD SATM.	
References	Traceable references should be provided. If published papers are not available we should try to add e.g. technical reports references	References are indeed crucial and shall be provided in the lower table (see last column to the right and color to track long term requirements' references with values above). Modifications of the structure of the table are welcome, e.g., we could place this column in the upper table.	References have been added to the last column of the SATM table.

4.1. HYDROLOGY AND CLIMATE

The Table 4-2 provides recommendations in the hydrology and climate applications areas.

Table 4-2: Proposed modifications to the user requirements table in the hydrology and climate application areas

Topic	Suggestions by project team	Suggestions ESA	Actions
Soil moisture	Affects landslide conditions. In recent works (Felsberg et al., 2021) it has been shown that improving soil moisture through adding space-gravimetric and remote sensing data by way of data assimilation (DA) has a positive effect on predictability. This could be mentioned more prominently in H4. Felsberg et al (2021) https://journals.ametsoc.org/view/journals/hydr/22/5/JHM-D-20-0228.1.xml	Are there specific requirements on spatial resolution and uncertainty needed to work on predictions in Felsberg et al. 2021?	Felsberg et al derive topographic shear from assimilating different remote sensing soil moisture products into a model. We think the requirements in resolution and latency to add value would therefore need to match the other RS data sets (40km, daily)
	Space gravimetry cannot observe soil moisture without relying on other data sets. We recommend to solicitate feedback from user communities that are interested in different soil moisture variables	This is a very good example of user requirement for product based on data assimilation. The soil moisture signal user	We agree that users should define the requirement based on the specific DA technique

	(SSM in climate/atmosphere modelling, root-zone SM in agriculture, groundwater) and finally to consolidate threshold/targets for integrative SM.	requirements are traced back in the questions and objectives for hydrology in the MRD/MRTD. It should be gravimetry users that define the user requirement based on the assimilation technique.	(including knowing the other data sets and models with uncertainties, resolution & latent). A general statement has been added at the beginning of each table.
H2-c	H2-c mentions "drive and constrain predictive hydrological models with gravity data". We suggest to explicitly distinguish between retrospective applications (e.g. identifying anthropogenic effects in long timeseries) and predictive applications of hydrological modelling	H2-c to be updated in the MRTD too!	The table has been updated accordingly
	We suggest to restructure the table according to the various applications. This will include monitoring of long-term groundwater, soil moisture, … evolution but also extreme event warning, separately for drought and flood. Specific requirements will be added.	If this helps trace better the gravimetry contribution is very welcome. Please provide a precise proposal.	The table has been updated and now lists the applications.

4.2. OCEANS

The Table 4-3 provides recommendations in the oceans applications area.

Table 4-3: proposed modifications to the user requirements table in the "oceans" application area

Topic	Suggestions by project team	Suggestions ESA	Actions
Mass	"Sea level" and "mass" applications are ambiguous. We suggest to rephrase this as "mass contribution to sea level budget"	Agreed!	We added a field "quantification of sea level change" and another field "investigation of ocean mass as a sea level budget component"
Heat	"Heat" is derived from altimetric sea level and ocean mass. Having a	Shall we include "heat" between	We added a field "quantification of

	separate "heat" application seems ambiguous.	brackets in the ocean mass application? To be discussed.	ocean heat content (ocean basin average)
Currents	Threshold/target for the time-mean field as a reference for dynamic topography should be evaluated. MDT should be an application in the table.	Agreed and shall be included in the MRTD as well.	We added a field "determination of stationary ocean transports (from mean dynamic topography)"
	The combination with altimetry needs to be clarified	This is agreed and possibly this can be done as a note or in the introduction to the table.	A note has been added at the beginning of the ocean table.
	The analysis of time-variable gravity and OBP gradients for inferring current changes should be included as a separate application.	Regarding OBP in Oceanography, in the MRTD this application is now removed from the oceanography thematic field.	We have decided to include "Evaluation of and data assimilation into ocean models (based on ocean bottom pressure)" as ocean application.
OBP O1-e	The relation between OBP and mass-driven applications should be clarified. OBP directly depends on ocean mass. Specific OBP applications like comparison to BP sensors should be included where the daily timescale plays a role.	The comparison to OBP sensors serves mainly validation of performance. I don't think that can be conceived as an application.	Acknowledged.
	For user requirements it must be clarified if threshold/target refers to e.g. ocean mass maps without any, or after data assimilation. Both users and producers of ocean reanalyses should be in the target group for formulating requirements.	It shall refer to user needs assuming data assimilation. Threshold and target user requirements can be associated either to QSG Level-2 raw products or post-processed products.	Threshold and target requirements are based on post-processed products. We know that assimilation systems may not be able to cope with "raw" products. So it would be difficult to define requirements for raw products.
ACC, AMOC	We should specify also smaller current systems.	New SATM field (in MRTD)	Acknowledged.

		specifies: "Ocean circulation variability (incl. ACC and AMOC)".	

4.3. SOLID EARTH

The Table 4-4 provides recommendations in the solid Earth applications area.

Table 4-4: proposed modifications to the user requirements table in the "solid Earth" application area

Topic	Suggestions by project team	Suggestions ESA	Actions
Geohazards	Volcanic hazard should be included. Greatest eruptions could be already seen in mid-term (Magic). Dedicated simulations are required, to compare the expected gravity signal with the spectral error curves of the different mission scenarios.	From the MRTD text, geohazards include earthquakes, tsunamis and volcanoes.	As different hazard have different requirements, we have now listed individual items in the MRTD table.
	The target and threshold values should be given also in terms of mGal and mGal/yr at ground level for specific cases, in addition to the homogeneously used unit EWH. A caveat needs to be added to the table.	mGal can be added (between brackets?) to EWH. To be discussed.	The values in the project have been calculated in EWH as this value seems the one that is required.
Earthquakes	Analyze in greater detail the role of post-seismic viscoelastic contribution, compared to the post-seismic afterslip. The signals in some circumstances add or subtract, depending on the crust and lithosphere rheology. The distinction of afterslip and viscoelastic contribution is relevant to the fault characterization and probably also for the risk estimation of the next earthquakes on a fault.	Agreed!	This has been added to the text on Earthquakes in the table.
Natural resources exploitation	Update: temporal scale should include long term evaluations, since effects as subsidence following fluid extractions cover timescales of years up to a decade.	Agreed! To be included in the MRTD too.	Monthly and long-term time scales have been added for natural resources.

5. IDENTIFICATION OF POTENTIAL NEW USERS AND APPLICATIONS

5.1. PLANNING AND IMPLEMENTATION OF THE USER QUESTIONNAIRE

To come up with a consolidated view on user needs and application-dependent science requirements and to identify new users and application fields, we targeted at involving the community as broadly as possible. This was primarily achieved by designing a tailored online questionnaire. The procedure of designing and distributing the questionnaire is outlined in the following:

Online questionnaire:

- **Target audience:** The questionnaire was distributed to (i) representatives of relevant services, (inter-) governmental and research institutions and (ii) the broad community (i.e. all interested individual scientists). An important goal was to involve new institutions/scientists not yet working with GRACE/-FO data to obtain new ideas and discuss possible new application fields.
- **Questions:** To receive answers that are neither biased by the perceived understanding of current mission capabilities ("in my application, the GRACE resolution is simply insufficient"), nor too unrealistic in terms of the needs for temporal/spatial resolution/accuracy, the questionnaire design was two-fold: (i) open questions allowing users to think freely about possible applications ("in your field, would it help if we could observe TWSA with sufficient resolution") and (ii) dedicated questions asking for the added value of specific resolution/accuracy combinations (derived from simulation results) to provide a detailed view on the benefit of realistically achievable mission results. Additional questions on the background of the person (e.g. scientist or administrative staff, previous experience with satellite gravimetry, etc.) helped contextualizing the answers.
- **Distribution:** The questionnaire was to be distributed, by (i) (email) communication, particularly when contacting relevant institutions and new users, by (ii) community email lists, and (iii) by social media. Additionally, (iv), we wanted to make use of conferences, especially EGU 2023 and IUGG 2023, to advertise the questionnaire broadly. To this end, a dedicated slide deck was prepared that could be shown in various sessions. Additionally, a second slide deck served as a tutorial that could be attached when distributing the questionnaire to provide the necessary background information.
- **Time line:**
    - First announcement of initiative at AGU 2022
    - Preparation of questionnaire until EGU 2023
    - Collection of replies until end of July 2023
    - Evaluation of results until approx. end of August 2023

Implementation and advertisement of the questionnaire

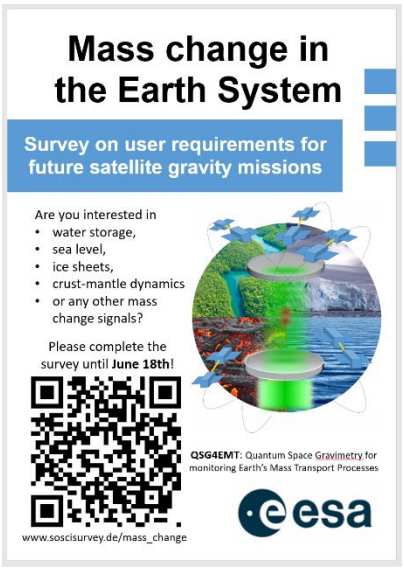

Figure 5-1: Flyer distributed at EGU23

The user requirement survey was implemented via the SoSci Survey portal (www.soscisurvey.de), as this platform follows data protection protocols in accordance with GDPR. The survey has been made available under the URL www.soscisurvey.de/mass_change on April 23th, 2023, i.e. prior to the beginning of the EGU23 General Assembly in Vienna. It was widely advertised during EGU23 by a dedicated slide shown in various gravity application-related oral session in the geodesy programme and in the sessions of neighboring disciplines, such as solid Earth sciences and hydrology. Furthermore, several hundreds of flyer handouts (see Figure 5-1) were distributed during oral and poster sessions. A splinter meeting on the QSG4EMT user requirements and the questionnaire (SPM28 "Quantum Satellite Gravity Mission Requirement Document") was organized and well attended by approximately 20 participants. The project team with support by ESA used the opportunity to introduce the scope of a possible future quantum gravity mission to the community. After EGU23 the advertisement of the questionnaire was continued by distribution via several newsletters (e.g. the GRACE-FO newsletter, the IAG newsletter, the DETECT (coupled climate change modelling project in Bonn/Jülich) newsletter) and email lists (e.g. the EGU Geodesy mailing list, the Cryolist, the OSTST (Ocean Surface Topography Science Team), the IAG Geodynamics and Earth Tides list, and the IAG ICCC list). On social media a tweet was provided to ESA and then re-tweeted by various geodesy-related accounts (IAG, EGU, personal accounts,...). An article was written for the EGU Geodesy blog (https://blogs.egu.eu/divisions/g/2023/05/19/what-would-we-like-to-see-from-future-gravity-missions-help-us-to-define-the-scientific-requirements) to introduce the questionnaire and call for participation. The flyer created for EGU was furthermore used for additional advertisement at several events, such as IUGG23, the General Assembly of the QuantumForntiers cluster of excellence at LUH Hannover and at various smaller project meetings. Besides these more general measures, personally contacting relevant institutions and individual scientists was an important part of advertising the user survey.

5.2. RESULTS OF THE USER QUESTIONNAIRE

General information

After the initial deadline for completing the questionnaire (June 18th, 2023), 107 answers were received. It was decided to extend the initial deadline until July 21st, 2023, such that in total 131 answers could be collected. 115 of the initial replies were submitted by individual scientists, while 16 answered as representatives of institutions (some of them completed the questionnaire more than once for several application fields). The following institutions have so far participated:

- International Groundwater Resources Assessment Center (IGRAC)
- GFZ Potsdam, Dept. 1 Geodesy
- GFZ Potsdam, Section 1.3 (Earth System Modeling)
- Indian Institute of Science Bangalore
- The Australian Centre for Excellence in Antarctic Science
- Alfred-Wegener-Institute Bremerhaven
- SFB 1502 'DETECT'
- Institut Terre et Environnement de Strasbourg, ITES (CNRS, University of Strasbourg)
- Institute of Geodesy, School of Geospatial Engineering and Science, Sun Yat-sen University
- Service Hydrographique et Océanographique de la Marine (Shom)
- Environmental Geodesy Group, Research School of Earth Science, Australian National University
- Department of Geodesy and Surveying, Budapest University of Technology and Economics
- Institute of Planetary Geodesy, Dresden

The individual scientists are from 25 different countries with the largest number of answers coming from Germany (34%), see Figure 5-2 (left). The majority name a university or extra university research institution as their type of affiliation (Figure 5-2, right). But also research and development organizations, government & space agencies, as well as the private sector are among the affiliations listed in the answers to the survey.

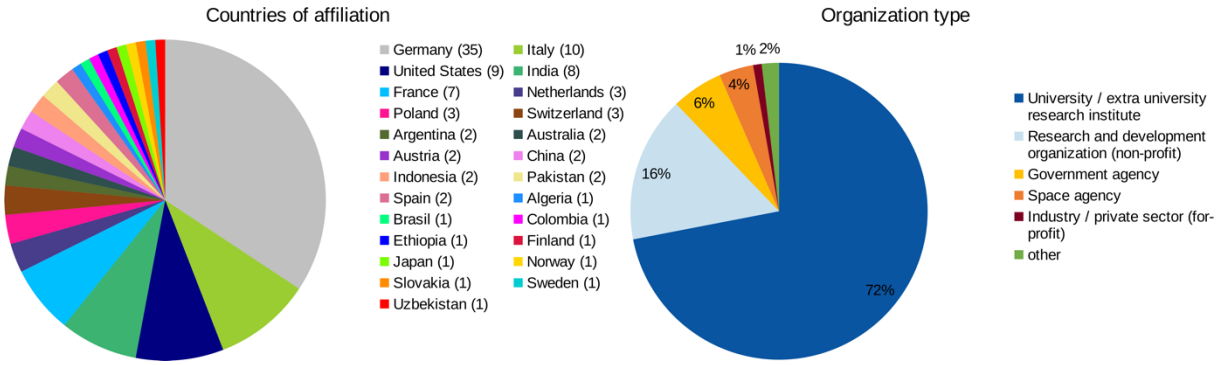

Figure 5-2: Distribution of the answers to the questionnaire regarding country of affiliation (left, 102 answers) and type of affiliation (right, 115 answers).

Among the submitted answers, a large percentage (82%) of the participants has previous experience with GRACE/-FO data, but this means that also 18% of new users took part in the questionnaire. Figure 5-3 illustrates the distribution of the answers among the different scientific disciplines. Hydrologists represent the largest user group (31%) and the other user groups represent between 6% (Atmosphere and Climate Modelling) and 18% (Geodesy) of the participants.

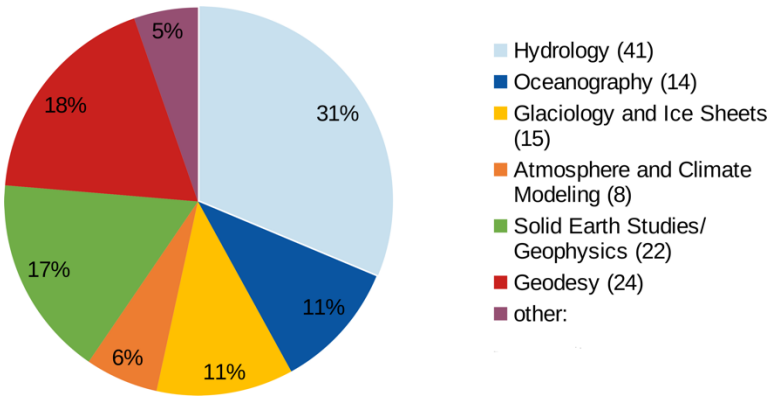

Figure 5-3: Distribution of scientific disciplines among the 107 replies received to the user questionnaire.

Participants are interested in a broad spectrum of purposes for which they intend to use mass change data, see Figure 5-4 (left). A majority of participants is interested in process understanding (66%) and the monitoring of system states (53%). Another major area of interest deals with the validation (47%) or calibration (28%) of models or the assimilation of data into models (30%). Even though only a few participants work on the very local scale (16% state an investigation area smaller than 10km see Figure 5-4 (right)), a considerable portion (37%) are interested in regions of 10-100km, thus below the current GRACE-FO resolution. The other users mainly deal with larger spatial scale of several hundred kilometres up to global. The majority of replies state that they would use mass change data for research applications (92%), and only a small part (6%) of the responses claim the intention of using the data for operational purposes. However, these numbers are most likely strongly biased due to the fact that fellow scientists were much easier approached by the study team. Related the consideration of the research vs. operational purpose is the question, how regularly satellite mission results would need to be accessed. For 62% of the participants, an episodical data access is sufficient, while 37% would require regular access, as it is required for operational use.

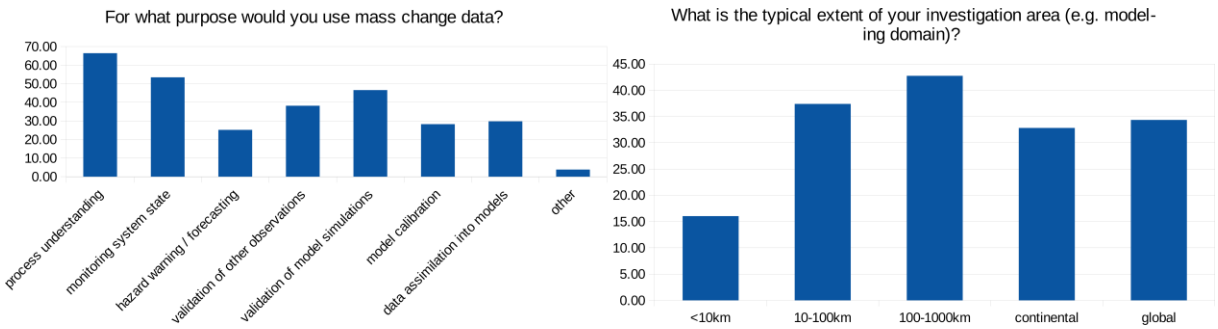

Figure 5-4: Purpose mass change data use (left, 127 answers) and typical extent of investigation area (right, 127 answers). All numbers in percent, multiple answers possible. Questionnaires stating "no answer" have been omitted.

Application-driven demands

An important part of the survey was dedicated to application-driven demands for the quality of mass change data. In this section users were asked to define their threshold/desired demands with respect to spatial/temporal resolution, latency and accuracy independent of specific mission scenarios or achievable performance numbers. The "threshold" numbers relate to

minimum requirements for mass change data to be useful as (new) observable, while data sets with the "desired" quality should enable breakthrough new science. The summary of the answers to the demands in resolution, accuracy, and latency can be found in Figure 5-5. As expected, the demands for the desired quality are in all three cases higher than for the threshold numbers. For the spatial resolution, the majority of answers requires 10-100km (40%) or 100-300km (45%) as threshold, but asks for <10km (46%) or 10-100km (47%) as desired outcome. For the temporal resolution the answers are more diverse. As threshold resolution, a peak can be identified for one month (44%), but a considerable number (24%) also prefers one week. For the desired temporal resolution, the smaller time spans become more important with the majority interested in a one-day resolution (35%), followed by a weekly resolution (26%). The latency requirements mostly range between one week and three months (threshold) and one day and one month (desired).

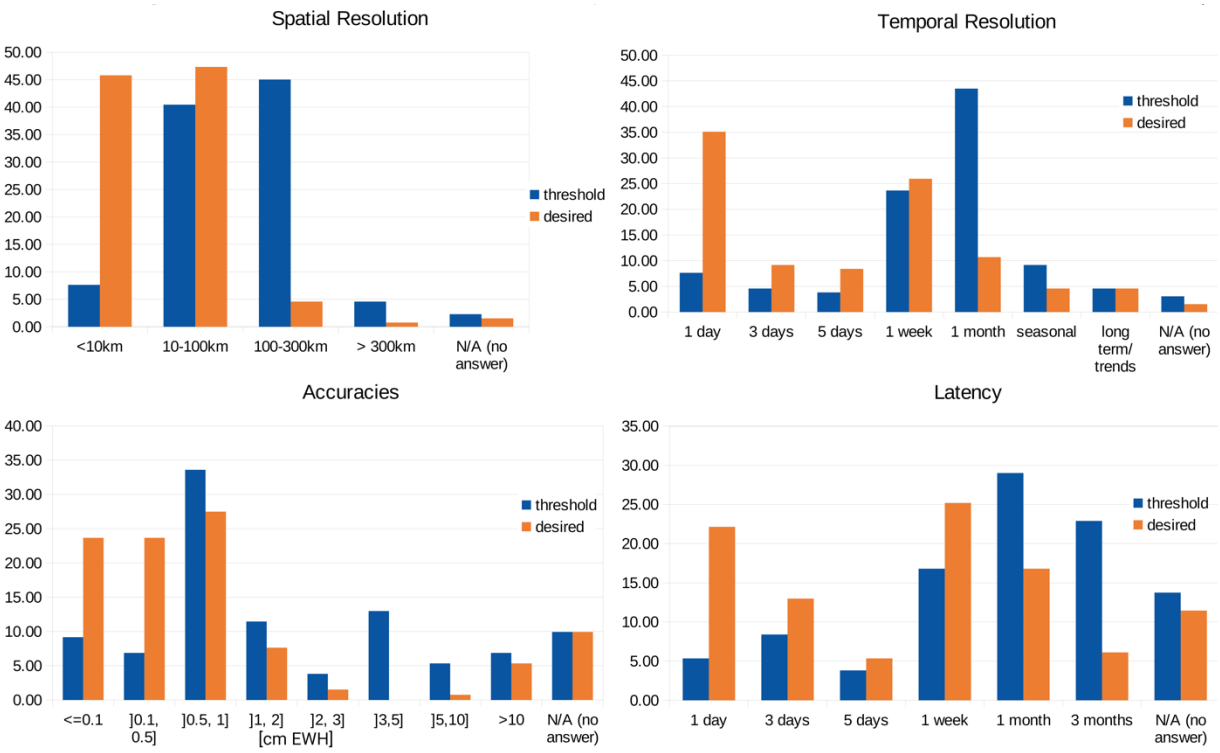

Figure 5-5: Application-driven demands for spatial resolution (top left, 128 answers), temporal resolution (top right, 127 answers), accuracy (bottom left, 118 answers), and latency (bottom right, 113 answers), all numbers in percent, only one answer possible for each category and threshold/desired demands.

Answers on the demands for accuracy peak at 0.5 to 1 cm for the threshold and between 1cm and smaller than 0.1cm for the desired accuracies. However, achievable accuracies depend strongly on the chosen resolution. Therefore, dependencies between the answers on temporal/spatial resolution and accuracies will be discussed further below.

In the following, answers to the application-driven demands are detailed separately for each geoscientific application field in Figure 5-6 (temporal and spatial resolution) and Figure 5-7 (accuracy and latency). While in general the different application fields do not deviate too much in their answers and mostly align with the overall percentages shown in Figure 5-5, a few details can be noted. Regarding the temporal resolution, representatives of oceanography and glaciology and, to a lesser extent of hydrology, are more satisfied with a lower resolution like one month (for threshold) or one week (for desired), while answers from atmosphere, geodesy, solid Earth, or parts of hydrology tend towards higher resolution like one day (for desired).

Similar conclusions can be drawn for the required latency, which is not always but certainly often correlated with the temporal resolution. Again, the high latency demands of down to one day are mainly driven by atmosphere (and climate modelling, even though it might be expected that the atmosphere research is the driving part requesting short latencies as opposed to (long-term) climate modelling), solid earth, geodesy, and hydrology. Representatives of oceanography and glaciology appear to be more satisfied with longer latencies of weeks or months. However, it can be observed that the answers are diverse depending on the specific applications.

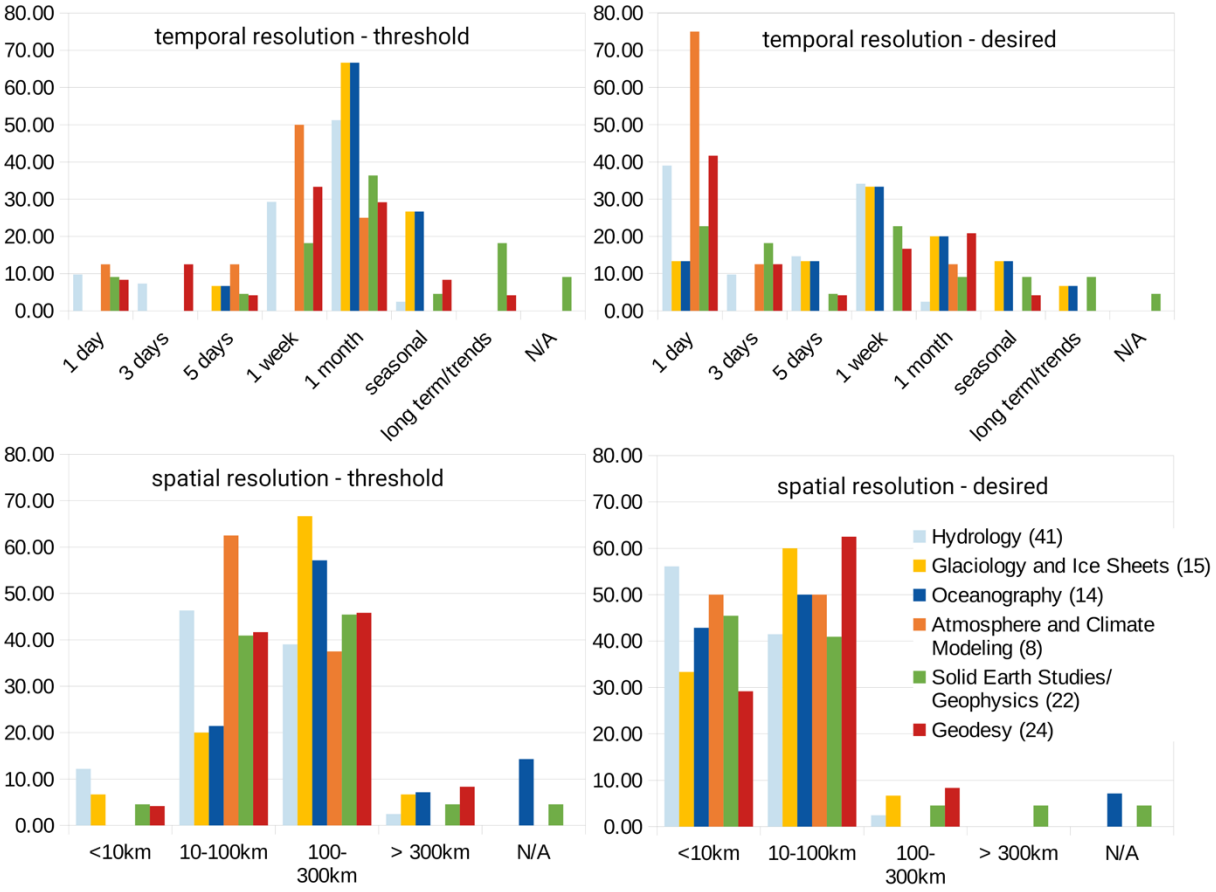

Figure 5-6: Application-driven demands for temporal (top) and spatial (bottom) resolution per application field. Comparison of threshold (left) and desired (right) values. All numbers in percent, only one answer possible for each category and threshold/desired demands.

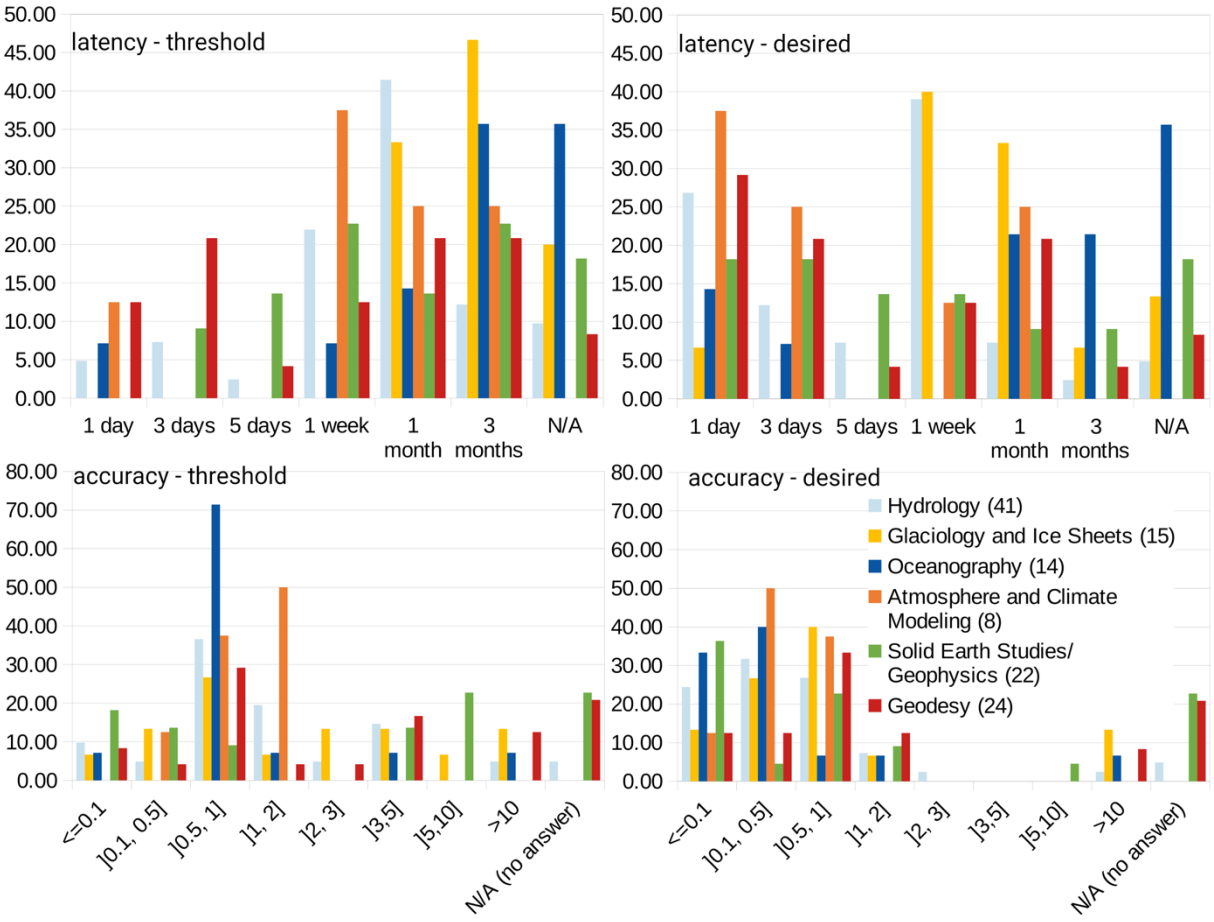

Figure 5-7: Application-driven demands for latency (top) and accuracy (bottom, x-axis in cm EWH) per application field. Comparison of threshold (left) and desired (right) values. All numbers in percent, only one answer possible for each category and threshold/desired demands.

As mentioned above, the achievable accuracy very strongly depends on the targeted temporal/spatial resolution and thus cannot be discussed independently of the resolution. Furthermore, there are similar dependencies and trade-offs between the achievable temporal vs. spatial resolutions. Therefore, a closer look was taken at such dependencies in the answers regarding the application-driven demands, see Figure 5-8 to Figure 5-10. The dependencies between (i) spatial and temporal resolution, (ii) spatial resolution and accuracy, and (iii) temporal resolutions and accuracy are shown in Figure 5-8 for the threshold and in Figure 5-9 for the desired requirements. For threshold, the most relevant combination of temporal/spatial resolution is one month at 100-300km, which is close to what is already achievable by current satellite missions. Other popular answers are different combinations of 1 week to 1 month and 10-100 to 100-300km. For the desired temporal/spatial resolution these combinations go down towards as low as rather unrealistic 1 day at less than 10km as the most popular answer. The accuracy demands range around 0.5-1 cm and up to 3-5cm for 10-100 to 100-300km and for 1 week to 1 month (threshold) and increase dramatically towards less than 1cm to less than 1mm for the desired accuracies. Figure 5-10 is the attempt to display the dependencies between all three aspects (temporal and spatial resolutions and accuracies) in one table. The results mainly confirm what was stated above: For threshold the demands peak for 0.5-1cm accuracy for 1 month temporal and 100-300km spatial resolution. Another cluster of answers is gathered

around 1 week to 1 month and 10-100km with 0.5 to 2 cm accuracy. The desired combinations are rather diverse with the largest peaks for 1 day and <10km with an accuracy of less than 1cm or even <0.1cm.

Spatial vs. temporal: threshold

	<10 km	10-100 km	100-300 km	> 300 km
1 day	4	5	1	0
3 days	2	3	1	0
5 days	0	2	3	0
1 week	2	17	12	0
1 month	1	18	35	3
seasonal	1	7	4	0
long term/trends	0	1	2	3

Spatial vs. accuracy: threshold

	<10 km	10-100 km	100-300 km	> 300 km
<=0.1 cm	2	4	6	0
]0.1, 0.5] cm	1	5	2	1
]0.5, 1] cm	3	16	22	3
]1, 2] cm	1	9	4	1
]2, 3] cm	0	1	3	1
]3,5] cm	0	8	8	0
]5,10] cm	0	3	4	0
>10 cm	2	2	4	0

Temporal vs. accuracy: threshold

	1 day	3 days	5 days	1 week	1 month	seasonal	long term / trends
<=0.1 cm	3	1	0	1	4	1	2
]0.1, 0.5] cm	0	1	1	2	2	2	1
]0.5, 1] cm	3	2	3	9	23	2	2
]1, 2] cm	2	1	0	5	6	1	0
]2, 3] cm	0	0	0	0	5	0	0
]3,5] cm	1	0	0	8	6	1	0
]5,10] cm	0	0	0	2	3	2	0
>10 cm	1	0	1	2	2	2	0

Figure 5-8: Pairwise dependencies between temporal resolution, spatial resolution and accuracy (threshold)

Spatial vs. temporal: desired

	<10 km	10-100 km	100-300 km	> 300 km
1 day	29	16	1	0
3 days	2	9	1	0
5 days	4	7	0	0
1 week	14	19	1	0
1 month	5	8	1	0
seasonal	4	0	2	0
long term/trends	2	3	0	1

Spatial vs. accuracy: desired

	<10 km	10-100 km	100-300 km	> 300 km
<=0.1 cm	16	14	0	1
]0.1, 0.5] cm	12	18	1	0
]0.5, 1] cm	19	14	3	0
]1, 2] cm	3	7	0	0
]2, 3] cm	2	0	0	0
]3,5] cm	0	0	0	0
]5,10] cm	0	1	0	0
>10 cm	3	2	1	0

Temporal vs. accuracy: desired

	1 day	3 days	5 days	1 week	1 month	seasonal	long term / trends
<=0.1 cm	18	1	0	5	4	0	3
]0.1, 0.5] cm	8	2	5	9	2	2	3
]0.5, 1] cm	16	3	4	8	5	0	0
]1, 2] cm	1	4	0	5	0	0	0
]2, 3] cm	0	0	0	2	0	0	0
]3,5] cm	0	0	0	0	0	0	0
]5,10] cm	0	0	0	1	0	0	0
>10 cm	2	0	1	0	1	2	0

Figure 5-9: Pairwise dependencies between temporal resolution, spatial resolution and accuracy (desired)

Spatial vs. temporal vs. accuracy: threshold

temporal resolution	spatial resolution	<10km								10-100km								100-300km								> 300km							
	accuracy	1	2	3	4	5	6	7	8	1	2	3	4	5	6	7	8	1	2	3	4	5	6	7	8	1	2	3	4	5	6	7	8
	1 day	2	0	0	1	0	0	0	1	1	0	3	0	0	1	0	0	0	0	0	1	0	0	0	0	0	0	0	0	0	0	0	0
	3 days	0	1	0	0	0	0	0	0	1	0	1	1	0	0	0	0	0	0	1	0	0	0	0	0	0	0	0	0	0	0	0	0
	5 days	0	0	0	0	0	0	0	0	0	1	1	0	0	0	0	0	0	0	2	0	0	0	0	1	0	0	0	0	0	0	0	0
	1 week	0	0	2	0	0	0	0	0	0	2	5	4	0	4	0	0	1	0	2	1	0	4	2	2	0	0	0	0	0	0	0	0
	1 month	0	0	1	0	0	0	0	0	1	1	5	4	1	2	1	2	3	1	16	1	3	4	2	0	0	0	1	1	1	0	0	0
	seasonal	0	0	0	0	0	0	0	1	1	1	1	0	0	1	2	0	0	1	1	1	0	0	0	1	0	0	0	0	0	0	0	0
	long term/trends	0	0	0	0	0	0	0	0	0	0	0	0	0	0	0	0	2	0	0	0	0	0	0	0	0	1	2	0	0	0	0	0

Spatial vs. temporal vs. accuracy: desired

temporal resolution	spatial resolution	<10km								10-100km								100-300km								> 300km							
	accuracy	1	2	3	4	5	6	7	8	1	2	3	4	5	6	7	8	1	2	3	4	5	6	7	8	1	2	3	4	5	6	7	8
	1 day	12	4	10	1	0	0	0	2	6	4	5	0	0	0	0	0	0	0	1	0	0	0	0	0	0	0	0	0	0	0	0	0
	3 days	0	0	1	0	0	0	0	0	1	2	1	4	0	0	0	0	0	0	1	0	0	0	0	0	0	0	0	0	0	0	0	0
	5 days	0	2	2	0	0	0	0	0	0	3	2	0	0	0	0	1	0	0	0	0	0	0	0	0	0	0	0	0	0	0	0	0
	1 week	2	3	3	2	2	0	0	0	3	6	5	3	0	0	1	0	0	0	0	0	0	0	0	0	0	0	0	0	0	0	0	0
	1 month	2	0	3	0	0	0	0	0	2	2	1	0	0	0	0	1	0	0	1	0	0	0	0	0	0	0	0	0	0	0	0	0
	seasonal	0	1	0	0	0	0	0	1	0	0	0	0	0	0	0	0	0	1	0	0	0	0	0	1	0	0	0	0	0	0	0	0
	long term/trends	0	2	0	0	0	0	0	0	2	1	0	0	0	0	0	0	0	0	0	0	0	0	0	0	1	0	0	0	0	0	0	0

class	1	2	3	4	5	6	7	8
Accuracy [cm]	<=0.1	]0.1,0.5]	]0.5,1]	]1,2]	]2,3]	]3,5]	]5,10	>10

Figure 5-10: All dependencies between temporal resolution, spatial resolution and accuracy for threshold (top) and desired (bottom) demands.

If given the choice between an increase in temporal or spatial resolution, the spatial resolution is the priority for 55% of participants. However, it should be stated that this means that for 45% the temporal resolution is at least as important with 9% declaring that temporal resolution is even more important and 36% finding both equally important for their application field.

Another issue that arises when aiming for short-period signals (e.g. daily) is the question, whether the gravity field models need to be estimated independently from each other, or if they may depend on the previous time step, as it is the case, e.g. in a Kalman filter framework or when estimating sliding window solutions. To this question 50% replied that they prefer independent estimates, while for 50% a dependency on previous time steps is okay.

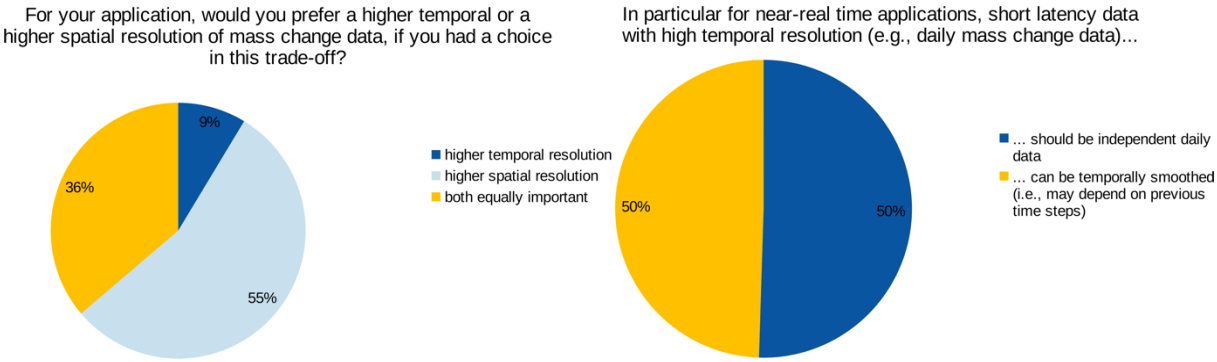

Figure 5-11: Priority of spatial vs. temporal resolution (left, 127 answers) and preference whether short-term data needs to be independent from each other or may depend on previous time steps (right, 101 answers). Questionnaires stating "no answer" have been omitted.

Added benefit of pre-defined mission scenarios

The application-driven demands shown in Figure 5-5 can be regarded as the user "wishlist", which, as expected, contains some very ambitious numbers that cannot necessarily be fulfilled by satellite gravimetry. However, there might still be added benefit for the specific application

fields, even when the demands cannot be fully satisfied. Therefore, two hypothetical baseline scenarios were defined for a potential future quantum gravity mission with "Baseline 1" referring to a conservative accuracy assumption and "Baseline 2" denoting an optimistic scenario. The table in Figure 5-12 (left) puts the respective (theoretical) performance numbers in perspective to currently achievable accuracies of the GRACE-FO mission and envisaged MAGIC uncertainties. Figure 5-12 (right) summarizes the assumed benefit of the two baseline scenarios for the applications under question in the survey. It can be observed that already the less ambitious Baseline 1 is considered to be of at least considerable benefit (40%) with a considerable number even certifying a large benefit (31%) or a major benefit (18%). For the more optimistic Baseline 2 scenario, the largest number of participants (43%) expect a major

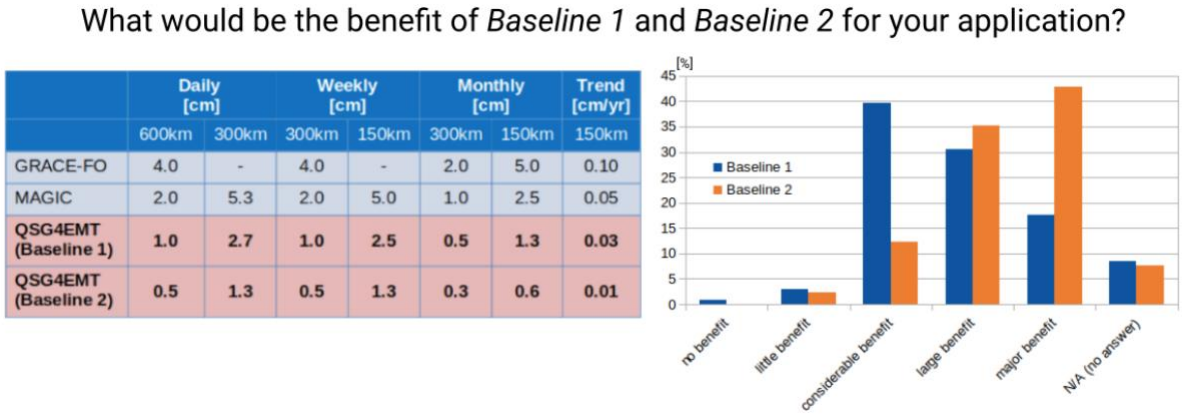

	Daily [cm]		Weekly [cm]		Monthly [cm]		Trend [cm/yr]
	600km	300km	300km	150km	300km	150km	150km
GRACE-FO	4.0	-	4.0	-	2.0	5.0	0.10
MAGIC	2.0	5.3	2.0	5.0	1.0	2.5	0.05
QSG4EMT (Baseline 1)	**1.0**	**2.7**	**1.0**	**2.5**	**0.5**	**1.3**	**0.03**
QSG4EMT (Baseline 2)	**0.5**	**1.3**	**0.5**	**1.3**	**0.3**	**0.6**	**0.01**

benefit from such a potential new mission.

.

Data combination and models

For various application fields, the value of gravity-derived mass change information is not based on the data sets alone but can only be fully explored by combining them with other Earth observation data sets and/or in combination with numerical models, see Figure 5-13. Out of the participants of the survey, 81% stated that they need to combine mass change data with other Earth observation data sets and/or in combination with numerical models (Figure 5-13, left) and 74% of these answers claimed that the accuracy of mass change data is currently the limiting factor in these experiments (Figure 5-13, middle). Numerical models are required for 89% of the applications referred to by the questionnaire (Figure 5-13, right).

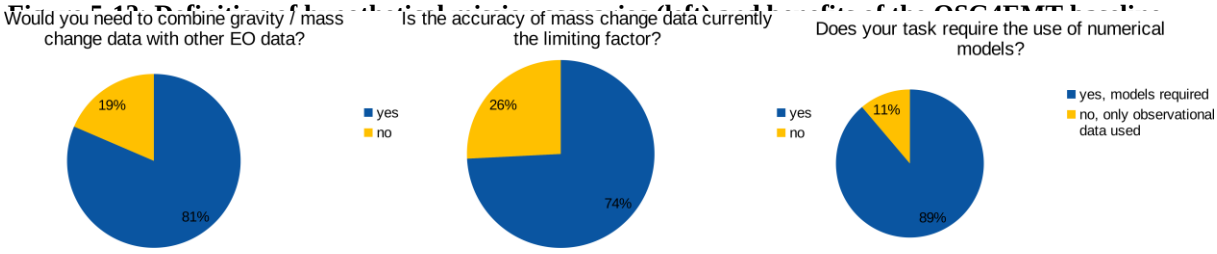

Figure 5-13: Questions related to the combination of mass change data with other Earth observation data and models. Questionnaires stating "no answer" have been omitted. From left to right: 124 answers, 93 answers, 125 answers.

Specific questions per application field

Depending on the chosen geoscientific application field at the beginning of the questionnaire, the participants were asked specific questions relevant for their field. For each application this includes a question of the specific variables or processes that the users are interested in, followed by selected further questions. Figure 5-14 shows the results for the field of hydrology, for which hydrological models, most of them run offline, play a major role. A large majority of 87% of the users state that they use models and 64% would consider using mass change data for model calibration or data assimilation.

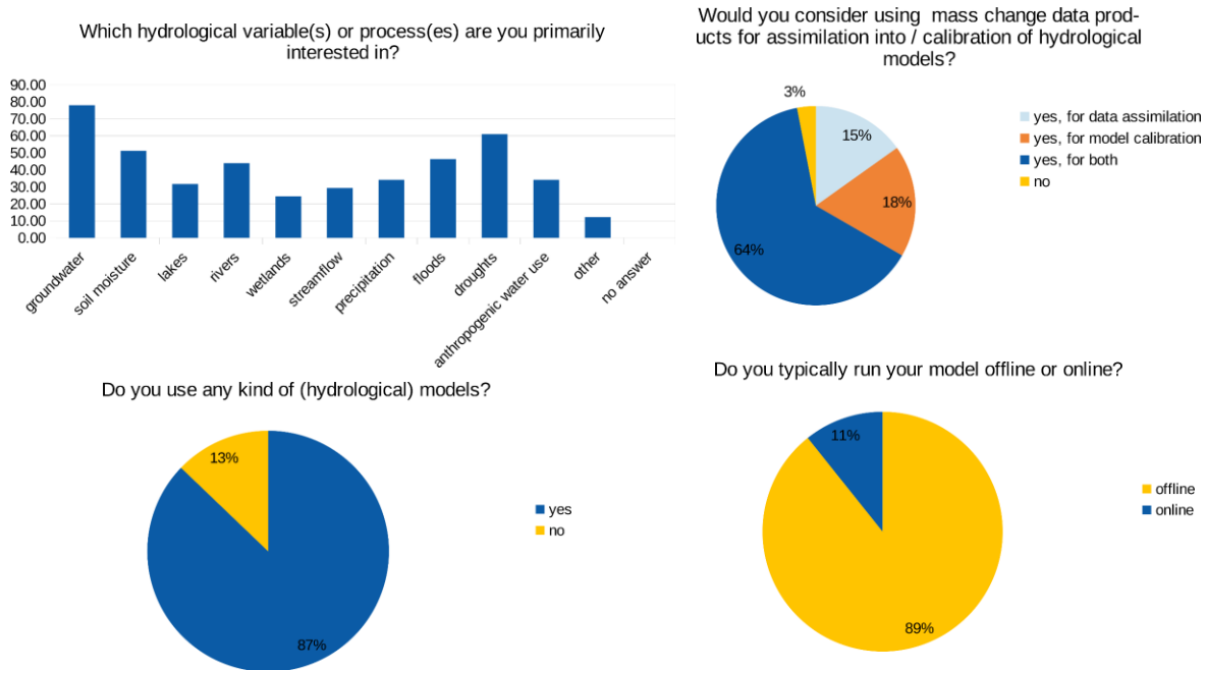

Figure 5-14: Specific questions for hydrology. All numbers in percent, for top left figure multiple answers possible.

Figure 5-15 shows the variables and processes that were chosen by users representing the research field of glaciology and ice sheets and Figure 5-16 indicates the same for oceanography. For the latter not only the temporal gravity field variations, but also the static mean field can be relevant, which was stated by 17% of the users.

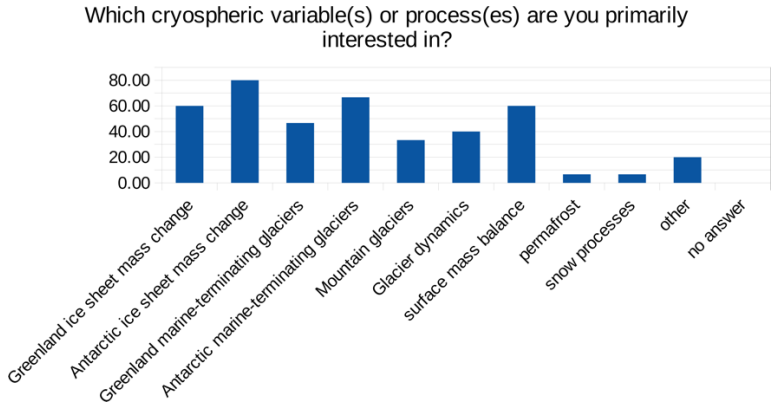

Figure 5-15: Specific question for glaciology and ice sheets, All numbers in percent, multiple answers possible.

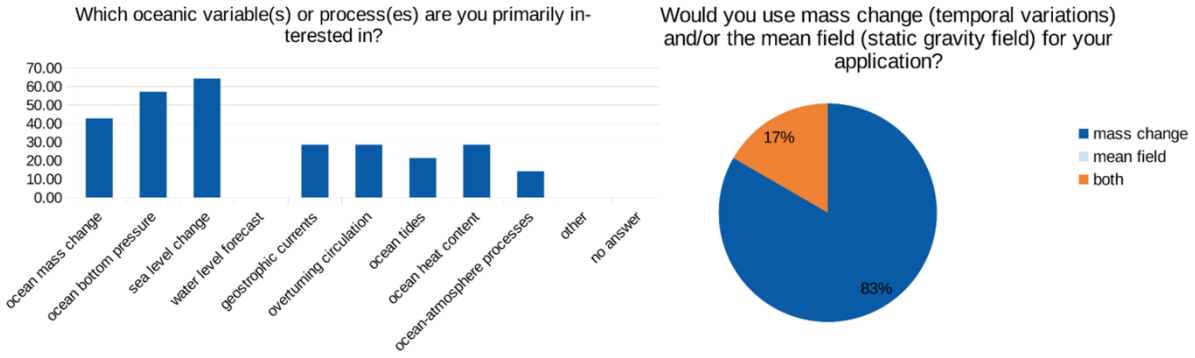

Figure 5-16: Specific questions for oceanograph. All numbers in percent, for left figure multiple answers possible.

For atmosphere and climate modelling (Figure 5-17) the relevant time scales for hindcast modelling or services were asked in addition to the relevant processes. A daily time scale was listed as most popular, but answers range from diurnal to centennial. However, for this application field the limited number of answers (only 8 participants) hampers the robustness of the conclusions and should, therefore, be treated with care. A similar question regarding the relevant time scales was also asked for the thematic field of solid earth studies/geophysics (Figure 5-18), with 80% of users requiring time scales of one month or shorter. Most users working with geophysical models are interested either in simulations (38%) or reanalysis (63%). The process and variable relevant for geodesy are summarized in Figure 5-19 with the most popular answers being orbit determination, height systems unification, and GNSS loading corrections.

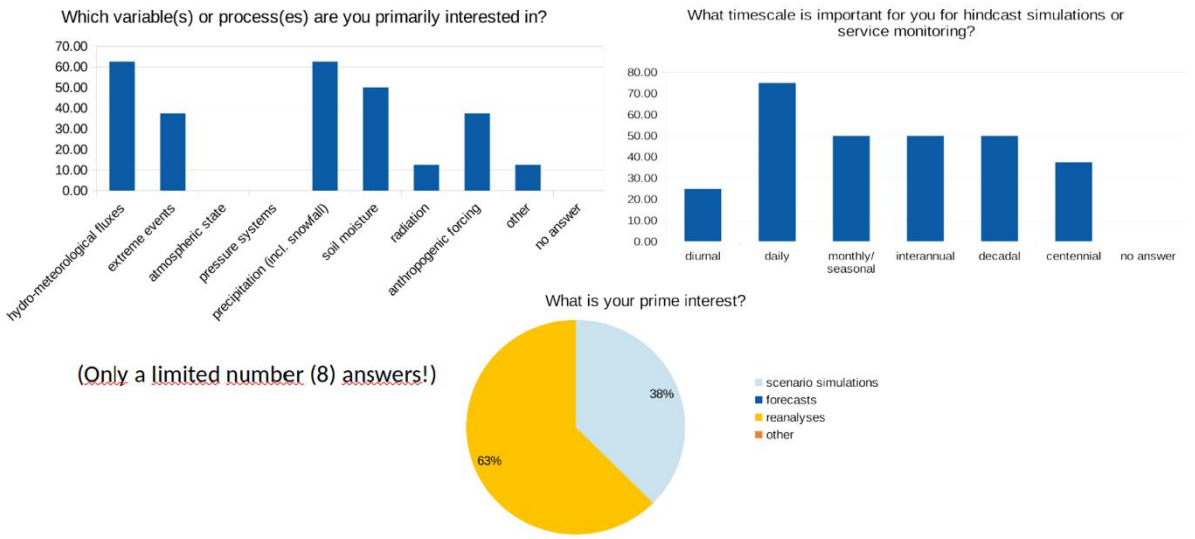

Figure 5-17: Specific questions for atmosphere and climate modeling. All numbers in percent, for top figures multiple answers possible.

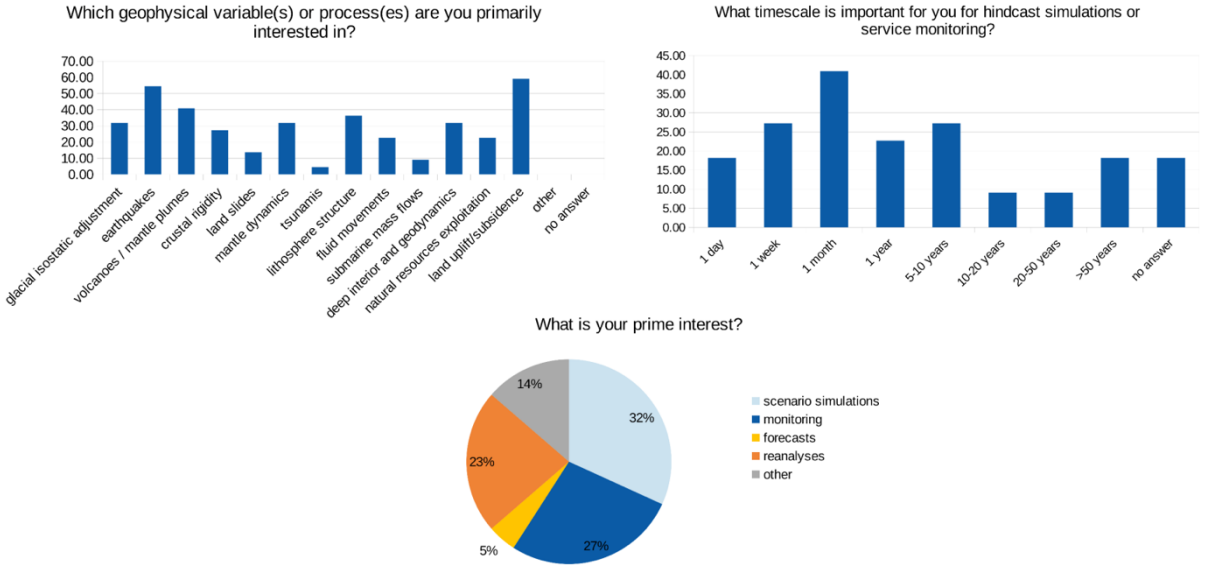

Figure 5-18: Specific questions for solid Earth studies and geophysics. All numbers in percent, for top figures multiple answers possible.

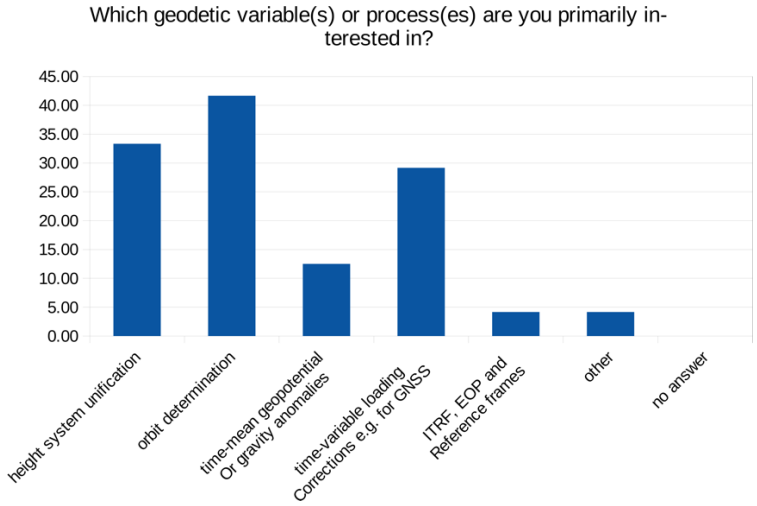

Figure 5-19: Specific question for geodesy. All numbers in percent, multiple answers possible.

Presentation of results

The results of the questionnaire have been presented to the scientific community during the MAGIC Science and Applications Workshop in November 2023 in Assisi, Italy and as a poster (EGU24-14722) at the EGU General Assembly 2024 in Vienna.

5.3. UPDATE OF USER REQUIREMENTS AND IDENTIFICATION OF NEW APPLICATIONS

Conclusions from the questionnaire were used to update the numbers of the user requirements. It was agreed upon with ESA that the numbers are purely from the user perspective and reflect what users want independent of mission simulation results. In the questionnaire we asked users for the benefit of hypothetical mission scenarios (see Figure 5-12). These numbers are not directly based on simulation results, but it was clarified with the TUM group that the accuracies about two times (Baseline 1) and four times (Baseline 2) better than MAGIC are realistic. A big majority of users replied that they see a considerable to large benefit from what we called „Baseline 1", we assumed these numbers as good estimates for the "Target mid-term/Threshold long term" requirements. And as a large majority replied that they would see large to major benefit from the numbers called „Baseline 2" we assumed them as good estimates for user requirements for "Target long-term". Additionally, the MAGIC numbers were agreed upon with ESA to use as "Threshold mid-term" requirements. The answers from the questionnaire were very similar for all application fields. Therefore, we adopted these numbers as the general values in the top part the table of each application field. It was agreed upon with ESA that these numbers shall only be changed for individual applications (lower part of the table) where we have strong evidence to do so. Therefore, we searched data bases such as the observation requirements provided by the Global Climate Observing System (GCOS) for their Essential Climate Variable (ECVs) and OSCAR (Observing Systems Capability Analysis and Review Tool) and the scientific literature. Whenever we found requirement numbers for specific applications that deviate from the general numbers given in the top part of each table, those were indicated in the lower part of the table. We strongly advise that the remaining numbers shall be filled by specific experts on each individual application.

For the identification of new applications, we added a question to the user questionnaire, that explicitly asked the participants to identify applications that have not been possible with current missions but would be possible with the hypothetical quantum mission scenarios: "Which new variable/process one could potentially determine/constrain?" Answers have been synthesized and new application fields have been extracted from the free-text answers received upon this question (see tables below for the different application fields). These suggestions have been incorporated into the SATM table (see second column of tables below).

Table 5-1: Hydrology – New application fields

New applications from questionnaire	Applications in SATM table
Water resources at sub- catchment level	Regional water resources assessment
Drought severity in low storage basins	Drought monitoring and forecasting
Water use at watershed size, irrigation	Regional water resources assessment
Extreme snowfall events	Snow monitoring (SWE)
Baseflow dynamics of a river at a sub-basin scale	Determination of baseflow dynamics of a river at sub-basin scale
Sediment transport	Quantification of sediment transport

Aquifer storativity parameters	Determination of aquifer storativity parameters

Table 5-2: Cryosphere - New application fields

New applications from questionnaire	Applications in SATM table
Ice flow dynamics	Quantifying mass changes of ice sheet and glaciers
Basin-level ice mass change	Quantifying mass changes of ice sheet and glaciers
Constrain mass loss in marine-terminating Greenland outlet glaciers	Quantifying mass changes of ice sheet and glaciers
Daily melt-water runoff estimation	Quantification of freshwater flux from the cryosphere into the ocean and its impact on the ocean
Sub glacial hydrology	Quantifying mass changes of ice sheet and glaciers
Better ability to separate Glacial isostatic adjustment from current ice mass changes	Separation of present-day ice mass change and GIA
(Transient) GIA signals in areas of low mantle viscosity	Separation of present-day ice mass change and GIA
Spatial separation of peripheral glaciers	Spatial separation of peripheral glaciers
Firn compaction rates	Quantification of firn compaction rates

Table 5-3: Oceanography - New application fields

New applications from questionnaire	Applications in SATM table
Bottom pressure variations on continental slope of western Atlantic	Determination of stationary ocean transports (from mean dynamic topography)
Interannual and secular changes in meridional overturning circulation	Monitoring large scale current variability (e.g. ACC and AMOC)
Detection of minor ocean tides signals in different frequency bands	Improvement of ocean tidal models
Antarctic bottom water export better constrained to the point that we could start looking for drivers	Monitoring large scale current variability (e.g. ACC and AMOC)

Table 5-4: Solid Earth - New application fields

New applications from questionnaire	Applications in SATM table
Regional subsidence	Detect Land uplift and subsidence due to past and present ice sheet melt.

Local project planning/ mitigation of landslide	Monitoring of large-scale land slides; regional estimates to monitor medium-scale land slides
Interseismic and postseismic deformation at active plate boundaries	Detect aseismic creep events at all depths and inter-seismic deformations.
Possibly inter-seismic trends	Detect aseismic creep events at all depths and inter-seismic deformations.
Long-term strain variations efficiently corrected by hydrological loading	·Assessment of earthquake cycle. Long-term strain variations efficiently corrected by hydrological loading.
GIA forebulge migration	Detect Land uplift and subsidence due to past and present ice sheet melt. GIA forebulge migration.

Table 5-5: Atmosphere and climate modeling - New application fields

New applications from questionnaire	**Applications in SATM table**
Flux/storage response of watersheds to precipitation inputs	Quantifying hydro-meteorological fluxes
Estimates of evapotranspiration & precipitation, regional precip patterns	• Quantifying hydro-meteorological fluxes • Precipitation monitoring
Targeting individual atmospheric river events	• Extreme events forecasting • Monitoring pressure systems • Quantifying atmospheric state

6. APPLICABLE DOCUMENTS, REFERENCE DOCUMENTS, AND PUBLICATIONS TO PART 2

6.1. APPLICABLE DOCUMENTS

[AD-1] Mission Requirements Document, Next Generation Gravity Mission as a Mass-change And Geosciences International Constellation (MAGIC) - A joint ESA/NASA double-pair mission based on NASA's MCDO and ESA's NGGM studies (2020). ESA-EOPSM-FMCC-MRD-3785

[AD2] Scientific Readiness Levels (SRL) Handbook, Issue 1, Revision 0, 05-08-2015

[AD3] Study of Cold Atom Interferometry (CAI) Gravity Gradiometer Sensor and Mission Concepts - ESA Contract 4000112677, Summary Report "Concept study and preliminary design of a cold atom interferometer for space gravity gradiometry"

[AD4] Cold Atom Inertial Sensors: Mission Applications – ESA Contract 4000117930, Final Report TASI-SD-CAI-FR

[AD5] Hybrid Atom Electrostatic System for Satellite Geodesy – ESA Contract 4000113573, Final Report RF_7-24721_DMPH

[AD6] Hybrid Atom Electrostatic System for Satellite Geodesy Follow-On – ESA Contract 4000112290, Final Report RT 6/27346 DPHY

[AD7] QSG_UR_SATM_v2.0.xlxs – ESA/EC Quantum Space Gravimetry User Requirements Science and Traceability Matrix v2.0 (2022)

[AD8] Quantum Space Gravimetry for monitoring Earth's Mass Transport Processes (QSG4EMT). Project Proposal, Proposal No. TUM/2022-QSG4EMT, Technical University of Munich

6.2. REFERENCE DOCUMENTS

Not applicable.

PART 3:

GRAVIMETRIC INSTRUMENT PERFORMANCES AND RELATED NOISE MODELLING

7. INTRODUCTION

The purpose of this chapter is to describe and motivate the set of error specifications for the relevant gravimetric instruments for QSG, including the supporting attitude, gyroscope, and acceleration sensors.

8. INSTRUMENT SPECIFICATIONS

We present in this section the noise ASD of all sensors we consider in this study, including the star sensors, differential wavefront sensors (DWS), K-band ranging instrument (KBR), laser tracking instrument (LTI), electrostatic accelerometers, laser gyroscopes, and predicted CAI instruments. We subdivide into attitude sensors, ranging instruments, electrostatic and quantum accelerometers.

We provide a non-exhaustive list of sensors that are representative of state-of-the-art technology. In the case of the ll-SST, we also provide the expected performance of the laser ranging instrument in the foreseeable future.

Multiple sensors that measure the same quantity may be installed in future gravimetric missions. In that case, we assume that *m* different instruments with error spectra are combined optimally, similar to the combination of attitude sensors by Stummer, Fecher, and Pail (2011):

$$\sigma^2(f) = \left(\sum_{m=1}^{M} \sigma_m^{-2}(f) \right)^{-1} . \quad (1)$$

Here, $\sigma_m(f)$ is the noise ASD of sensor m, and $\sigma(f)$ is the noise ASD when all sensors are combined optimally. We use the symbol σ to identify the frequency-dependent errors, even if omitting the dependency of frequency, e.g., σ.

Integration or differentiation of the noise ASD of a quantity requires the factor $2\pi f$ or its inverse, respectively. In the general case of the *n*-th derivative ($n > 0$) or n-th integral ($n < 0$), using Lagrange's notation for differentiation and antidifferentiation:

$$\sigma\left(f^{(n)}\right) = (2\pi f)^n \sigma(f). \quad (2)$$

8.1. ATTITUDE SENSORS

This section presents the noise ASD of the attitude instruments considered in the study. We present a wide selection of attitude instruments to assess what is technically feasible in the foreseeable future. Figure 8-1 shows an overview of the attitude noise ASDs, where all quantities have been converted to attitude (left) and angular rates (right) for convenience.

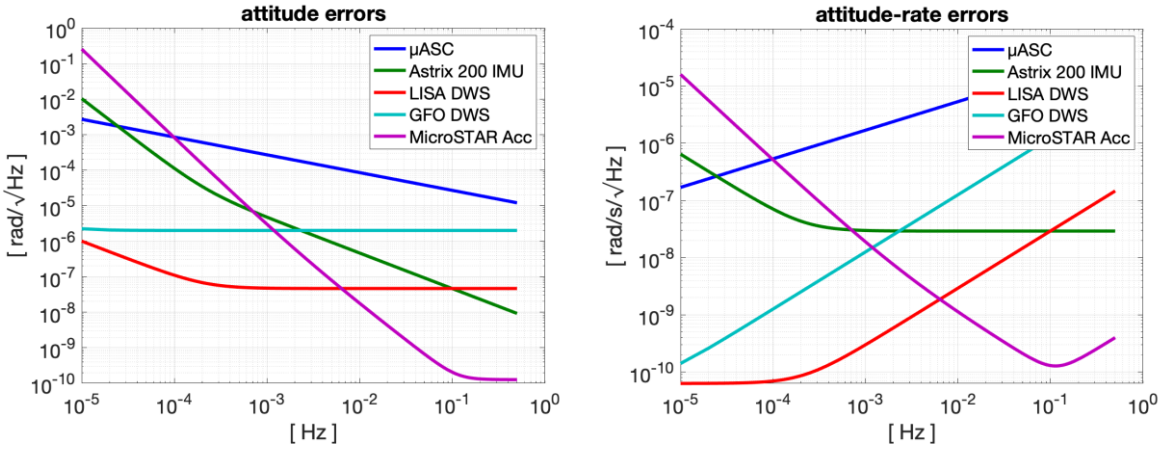

Figure 8-1: Overview of attitude errors in terms of attitude (left) and angular rates (right).

To clarify our notation, the symbols σ_θ, σ_ω and $\sigma_{\dot{\omega}}$ relate to angular, angular rate and angular acceleration errors, respectively.

8.1.1. STAR TRACKER

The star sensor of the Swarm satellites is the Micro Advanced Stellar Compass (μASC) (Herceg, Jørgensen, and Jørgensen 2017). We believe that this instrument is a representative state-of-the-art star sensor. Goswami et al. (2021) analysed its in-flight accuracy and specified that noise ASD as

$$\sigma_{\mu\mathrm{ASC},\theta}(f) = 8.5 \times 10^{-6}\sqrt{f^{-1}} \left[\frac{\mathrm{rad}}{\sqrt{\mathrm{Hz}}}\right]. \quad (3)$$

8.1.2. INERTIAL MEASUREMENT UNIT

One of the most accurate inertial measurement units (IMU) is the Astrix 200 laser gyroscope, the accuracy of which is specified by Airbus (2022). It has a white noise component of 3×10^{-8} rad/s and a f^{-1} component associated with a bias drift, as shown in Figure 8-2. The combined analytical expression is

$$\sigma_{\mathrm{IMU},\omega}(f) = 3 \times 10^{-8}\sqrt{1 + 4.6 \times 10^{-8} f^{-2}} \left[\frac{\mathrm{rad/s}}{\sqrt{\mathrm{Hz}}}\right]. \quad (4)$$

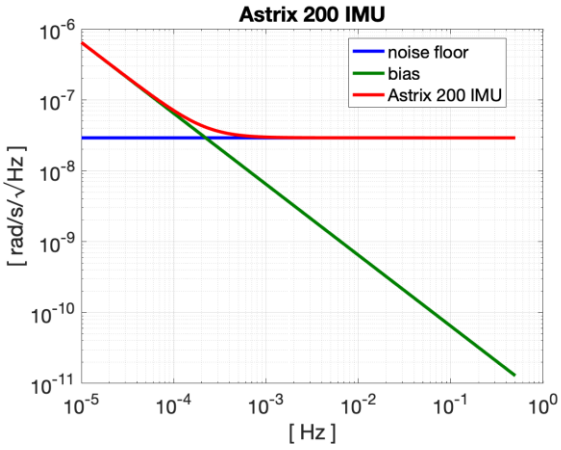

Figure 8-2: ASD of the angular velocity noise of the Astrix 200 IMU as inferred from Airbus (2022).

8.1.3. DIFFERENTIAL WAVE SENSOR

The DWS measures pitch and yaw relative to the inter-satellite laser. In combination with the GNSS-derived positions, it is possible to derive the absolute pitch and yaw attitude of the satellite because the GNSS positions provide the absolute attitude of the vector connecting the two satellites. The DWS noise spectra are provided for two cases in the following sections. As for the errors in GNSS σ_{GNSS} (supposing white noise with an amplitude of 1 cm), they proportionally affect the attitude error in the Line-Of-Sight (LOS) unit vector $\sigma_{\mathrm{LOS},\theta}$. Finally, this effect is dampened proportionally to the inter-satellite distance L_{ISR}, assumed to be 200km:

$$\sigma_{\mathrm{LOS},\theta} = \frac{\sigma_{\mathrm{GNSS}}}{L_{\mathrm{ISR}}} \cong 5 \times 10^{-8} \left[\frac{\mathrm{rad}}{\sqrt{\mathrm{Hz}}}\right]. \qquad (5)$$

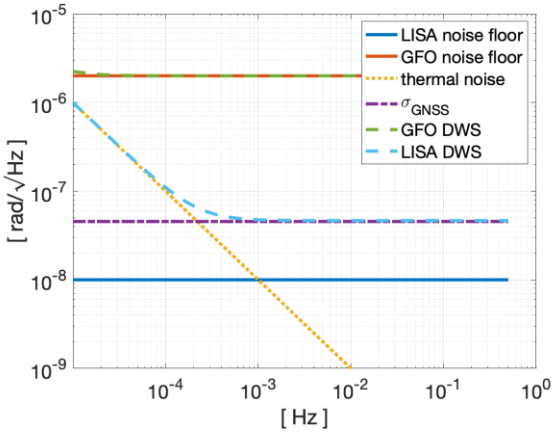

Figure 8-3: ASD of the attitude errors for the DWS of LISA (dashed blue line), based on Schütze et al. (2013) **and for the DWS of GRACE-FO (dashed green line), adapted from** (Goswami et al. 2021).

8.1.3.1. LISA

For LISA, the noise ASD of the DWS is taken from Schütze et al. (2013). As shown in Figure 8-3, it is composed of the white noise floor (solid blue line) at the level of 10 nrad/$\sqrt{Hz}$ between 1mHz and 1 Hz and the thermal noise (dotted yellow line) with a spectrum of 1/f below 1 mHz.

8.1.3.2. GRACE-FO

Referring to Figure 8-3, for GRACE-FO, it is also possible to derive an estimate for the DWS-derived pitch and yaw attitude errors considering the white noise floor (red line) reported by Goswami et al. (2021), which has an amplitude of 2 µrad/$\sqrt{\mathrm{Hz}}$. The thermal noise floor (dotted yellow line) and the attitude error of the LOS unit vector (dot-dashed purple line) are assumed to be equal to the LISA case in Section 8.1.3.1. The noise floor of the DWS sensor is dominant over the GNSS and the thermal components in contrast to the DWS of LISA.

8.1.4. ACCELEROMETER-DERIVED ATTITUDE

Since each facet of the proof-mass cavity contains multiple electrodes, the MicroSTAR accelerometer can measure angular accelerations, with error amplitude reported by Christophe et al. (2018). The associated analytical expression for the ASD is:

$$\sigma_{\mathrm{MicroSTAR},\dot{\omega}}(f) = 1 \times 10^{-10}\sqrt{0.4 + 0.001f^{-1} + 2500f^{4}} \left[\frac{\mathrm{rad}/s^{2}}{\sqrt{\mathrm{Hz}}}\right]. \qquad (6)$$

We assume this noise ASD is the same for all three axes, considering a cubic proof mass, identical gaps between the proof mass and electrodes on all sides, and neglecting the influence of the gold wire connected to the proof mass needed to neutralise the build-up of static charge.

8.2. INTER-SATELLITE RANGING

This section presents the noise ASD of the ISR instruments considered in the study. The overview of the noise ASD is shown in Figure 8-4.

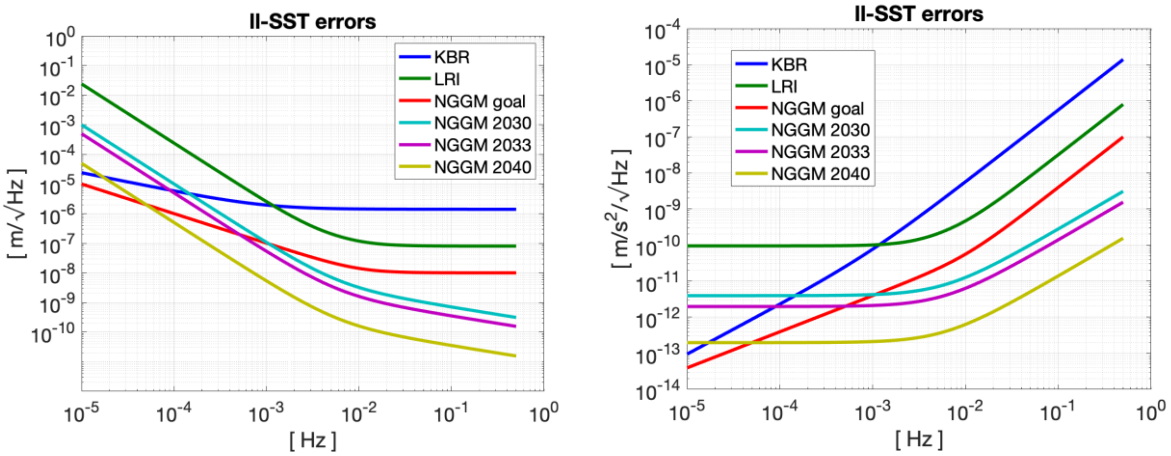

Figure 8-4: Overview of ISR noise ASD at the level of distance (left) and acceleration (right).

As we intend to quantify the errors for quantum gravimetric missions, which are currently in the early stages of development, we will consider the error spectra associated with the *NGGM 2040* scenario. We report numerous other scenarios for the ranging instrument to contextualise our assumptions with existing instruments and assumptions in the literature.

8.2.1. GRACE-FO KBR

Sheard et al. (2012) provides accuracy of the KBR system. It is composed of thermal and Ultra-Stable Oscillator (USO)-related components described by the analytical expression and illustrated in Figure 8-5:

$$\sigma_{\mathrm{KBR},\rho} = \sigma_{\mathrm{KBR,thermal}} + \sigma_{\mathrm{KBR,USO}}(f)$$
$$= 1.4 \times 10^{-6}\left[\frac{m}{\sqrt{Hz}}\right] + 1.8 \times 10^{-8} f^{-\frac{1}{1.6}}\left[\frac{m}{\sqrt{Hz}}\right] \quad (7)$$

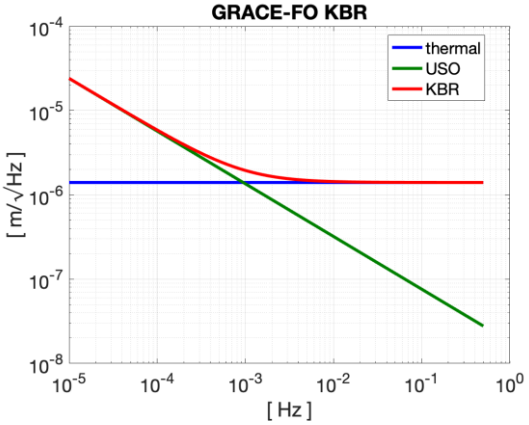

Figure 8-5: Noise ASD of the GRACE-FO KBR, according to Figure 2 of Sheard et al. (2012).

8.2.2. GRACE-FO LRI

For the noise ASD of the Laser Ranging Interferometer (LRI) of the GRACE-FO mission, we refer to Kornfeld et al. (2019), which provides the following analytical expression in terms of range noise:

$$\sigma_{\mathrm{LRI},\rho}(f) = 8 \times 10^{-8}\sqrt{1 + (f/0.003)^{-2}}\sqrt{1 + (f/0.01)^{-2}} \ \left[\frac{m}{\sqrt{Hz}}\right]. \quad (8)$$

Refer to the green line in Figure 8-4.

8.2.3. NGGM "GOAL" LTI

The ISR sensors presented so far are indicative of the existing instruments. A comparison between these and future QSG would not correctly represent the capabilities of the former. For that reason, we include in this study the "goal" performance of the NGGM mission concept proposed by Massotti et al. (2021). The associated analytical expression is a function of the inter-satellite range L_{ISR}:

$$\sigma_{\mathrm{NGGM},\rho}(f) = L_{\mathrm{ISR}} 10^{-13}\sqrt{1 + (0.01/f)^{2}}\sqrt{1 + (0.001/f)^{2}} \ \left[\frac{m}{\sqrt{Hz}}\right]. \quad (9)$$

Refer to the red line in Figure 8-4.

8.2.4. NGGM PREDICTED

For the projected accuracy of future ISR laser instruments, we consider the following spectra, which are predicted to be representative of the errors of these instruments at different years (p.c. Vitali Müller, Albert-Einstein-Institut, Hannover, March 2023):

$$\sigma_{\mathrm{NGGM\ 2030},\rho}(f) = L_{\mathrm{ISR}} \frac{\mathbf{1} \times 10^{-15}}{f} + \frac{\mathbf{1} \times 10^{-13}}{f^{2}} \ \left[\frac{m}{\sqrt{Hz}}\right], \quad (10)$$

$$\sigma_{\mathrm{NGGM\ 2033},\rho}(f) = L_{ISR} \frac{\mathbf{5} \times 10^{-16}}{f} + \frac{\mathbf{5} \times 10^{-14}}{f^{2}} \ \left[\frac{m}{\sqrt{Hz}}\right], \quad (11)$$

$$\sigma_{\mathrm{NGGM\ 2040},\rho}(f) = L_{ISR} \frac{\mathbf{5} \times 10^{-17}}{f} + \frac{\mathbf{5} \times 10^{-15}}{f^{2}} \ \left[\frac{m}{\sqrt{Hz}}\right]. \quad (12)$$

The subscript indicates the year in which the instrument is predicted to be ready for flight. Refer to the teal, purple and yellow lines, respectively, in Figure 8-4. We note that Equation (11) is equivalent to Equation (10), considering only thermal noise at low frequency (<1mHz) and, therefore, no dependency on inter-satellite distance at low frequency. Equation (12) is an improvement of factor 2 over Equation (11), as already shown in GRACE-FO (Abich et al. 2019). Equation (13) is one order of magnitude improvement, as expected by LISA (Dahl et al. 2019).

8.3. ACCELEROMETRY

8.3.1. ELECTROSTATIC ACCELEROMETRY

As electrostatic accelerometers, we consider the goal requirements of the NGGM mission concept and the performance of the MicroSTAR accelerometer for the linear acceleration measurements. Figure 8-6 presents an overview.

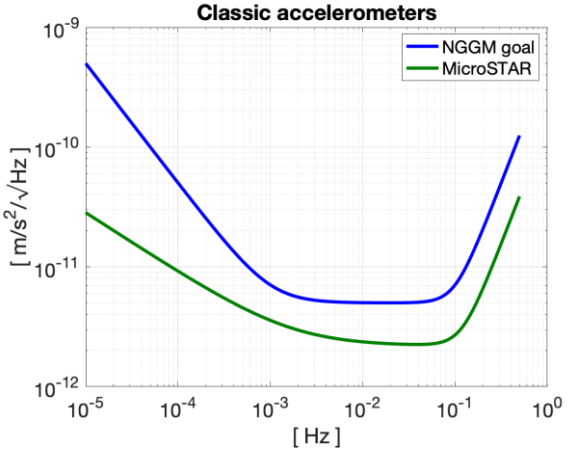

Figure 8-6: Overview of the noise ASD of electrostatic accelerometers.

8.3.1.1. NGGM "GOAL" ACCELEROMETER

Massotti et al. (2021) reports "goal" and "threshold" requirements for the accelerometer performance of the NGGM mission concept. We selected the "goal" scenario with the associated noise ASD is defined by:

$$\sigma_{\mathrm{NGGM,ng}}(f) = 5 \times 10^{-12}\sqrt{1 + (0.001/f)^2 + (100f^2)^2}\ \left[\frac{\mathrm{m}/s^2}{\sqrt{\mathrm{Hz}}}\right] \quad (13)$$

8.3.1.2. MICROSTAR

Christophe et al. (2018) provides the MicroSTAR performance, with the noise ASD given by the expression:

$$\sigma_{\mathrm{MicroSTAR,ng}}(f) = 2 \times 10^{-12}\sqrt{1.2 + 0.002f^{-1} + 6000f^4}\ \left[\frac{\mathrm{m}/s^2}{\sqrt{\mathrm{Hz}}}\right]. \quad (14)$$

8.3.2. QUANTUM ACCELEROMETRY

We assume a CAI scheme similar to Malossi et al. (2010):

i) a Bose-Einstein Condensate (BEC) atomic cloud is produced from a Magneto-Optical Trap (MOT) by laser cooling and magnetic trapping techniques,

ii) a Raman pulse splits the wave-packet in two, kicking them in opposite directions along the axis of the Raman lasers and over the interrogation period T,

iii) a second Raman pulse imparts opposite momentum to the wave-packet, forcing them to converge,

iv) after the same period of interrogation, a third Raman pulse recombines the wave-packet, and

v) the interferometric measurement is conducted on the recombined wave-packet.

We use the term *wave-packet* to recognise the wave-particle duality of the BEC because, formally, there is no physical separation of the atomic clouds. Only the wave function is spread in two directions. Henceforth, the term *(atom) cloud* intends to loosely refer to both the physical cloud (in the case of quantum gradiometry in Sections 8.4 and 8.3.2) and the wave-packet, except when it is essential to make a distinction. The first and third pulses are also called π/2 pulses, and the second pulse is called a π pulse.

A non-zero acceleration $\boldsymbol{a}$ along the axis of the Raman laser will induce phase shift ϕ proportional to the acceleration the atom clouds have experienced during $2T$:

$$\phi = \boldsymbol{k}_{eff} \cdot \boldsymbol{a} T^2. \quad \textbf{(15)}$$

The magnitude of effective wavevector k_{eff} is inversely proportional to the wavelength of the Raman laser λ. In the case of the double-diffraction scheme considered in this study, because of the direct and reflected Raman laser:

$$k_{\text{eff}} = \frac{8\pi}{\lambda}. \quad \textbf{(16)}$$

By introducing the degree of entanglement α (e.g. for α = 0, there is no entanglement and therefore reaching quantum projection noise; for α=1 the Heisenberg limit is attained), with interferometer contrast C and the number of atoms N, the interferometric phase noise is:

$$\sigma_{\Phi} = \frac{1}{\mathrm{C}} N^{-\frac{1+\alpha}{2}}. \quad \textbf{(17)}$$

The interferometer contrast represents the visibility in which the interferometry fringes appear in the detector. The beam splitting efficiency and any external perturbations influence its value because they lead to a loss of atoms in the phase shift, mainly due to non-inertial effects. Experimental values go from 0.6 (Zhu et al. 2022) or 0.65 (Peters et al. 1999) to $\mathrm{C} = 0.8$ (Knabe et al. 2022), while the maximum value is 1 (Douch et al. 2018). The degree of entanglement refers to different quantum enhancement techniques that allow the phase difference after the interrogation time T to be observed more accurately (Szigeti, Hosten, and Haine 2021), with *Spin Squeezing* being the most common (Gross 2012). Parameter α reflects the proportion of atoms in the cloud that are entangled, ranging from 0 to 1, where the value 0 means there is no entanglement.

In the case of concept involving multiple momentum diffraction, the momentum transfer δp is the product of k_{eff} with the Momentum Space Separation β, which has unit value for the baseline double diffraction:

$$\delta p = \hbar \beta k_{\text{eff}} \quad \textbf{(18)}$$

Under these assumptions, with T being the interrogation period, the CAI accelerometer shot-to-shot sensitivity is:

$$\sigma_{\text{CAI,ng}}^{(s2s)} = \frac{\hbar \sigma_{\Phi}}{\delta p T^2} = \frac{1}{C \beta k_{\text{eff}} N^{\frac{1+\alpha}{2}} T^2} \quad \textbf{(19)}$$

We assume that the noise spectra of the CAI accelerometers are flat, corresponding to white noise; for this reason, the standard deviation is sufficient to describe these errors entirely.

8.3.2.1. MODE OF OPERATION

So far, we have restricted our analysis to the shot-to-shot sensitivity CAI sensitivity, which represents the best-case scenario where the measurements are made continuously without any interruptions. In reality, this is impossible because the atom cloud needs time to be prepared, which we assume to be $T_{\text{prep}} = 1s$ (Müntinga et al. 2013). Additionally, we define T_{cycle} as the complete measurement cycle period.

We identify two distinct modes for the design and operation of the CAI:

- *Concurrent* atom cloud preparation and interrogation, where the interferometry takes place at the same time as the BEC is being prepared: $T_{\text{cycle}} = T_{\text{prep}}$
- *Sequential* atom cloud preparation and interrogation, the process for cloud preparation and interrogation do not overlap, leading to a more estended measurement cycle period: $T_{\text{cycle}} = 2T + T_{\text{prep}}$.

In the concurrent case, the next atom cloud can be launched before the cold atom interferometer sequence of the current atom cloud is finished, i.e., the measurement cycle T_{cycle} is only limited by the atom cloud preparation time T_{prep}, and we avoid any dead time between measurement cycles.

For both cases, the standard deviation of the CAI acceleration is:

$$\sigma_{\text{CAI,ng}} = \sqrt{T_{\text{cycle}}}\,\sigma_{\text{CAI,ng}}^{(s2s)}. \qquad \textbf{(20)}$$

Additional considerations regarding how the Coriolis accelerations influence both operation modes are discussed in Section 11.1.

One consequence of the two operational modes is the cloud velocity, which will be analysed in Section 11.1. The sequential mode of operation allows for initial zero-atom cloud velocity since the preparation of the BEC and interferometric chambers are placed at the same location. The BEC is directly prepared at the CoM and the wave packet propagates exclusively along the axis of the Raman laser (left of Figure 8-7), with velocity depicted by the blue arrows, resulting from the momentum transfer imparted by the Raman laser alone. For the concurrent mode of operation, the atom cloud enters one side of the chamber with a non-zero (physical) velocity perpendicular to the Raman laser (green arrow in Figure 8-7), for example, $v_{\text{cloud}} = 2.5\ \text{cm/s}$ (Carraz et al. 2014; Trimeche et al. 2019). An additional recoil laser with an axis perpendicular to the Raman laser imparts the transverse velocity v_{cloud} to the atom cloud. The first π/2 pulse is done on one side of the chamber by the first Raman laser, the π pulse is done by a second Raman laser in the middle of the chamber, and the third Raman laser on the opposite side of the chamber is responsible does the second π/2 pulse.

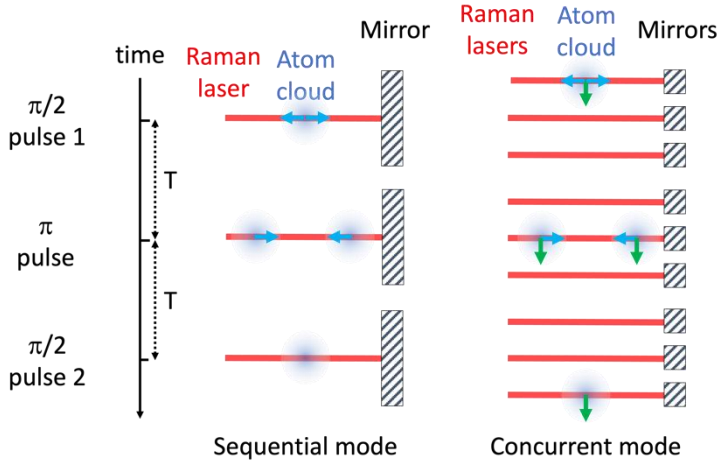

Figure 8-7: Diagram of the interferometry scheme for the sequential (left) and concurrent modes (right), showing the velocity of the wave-packets after the respective Raman laser pulses, which add momentum as represented by the blue arrows. In the case of the concurrent mode (right), the transverse (physical) velocity represented by the green arrow is provided at the start of the measurement sequence by an additional laser (not shown) perpendicular to the Raman lasers.

For both operation models, the mirror(s) tilt to compensate for the satellite rotation, i.e., they rotate between the laser pulses of the cold atom interferometer. The concurrent mode requires three mirrors in different locations along the direction of the atom movement.

8.4. GRADIOMETRY

In both classic and quantum gravity gradiometry, we consider this technique to be implemented by combining pairs of accelerometers. As such, the error spectra of the electrostatic and quantum accelerometers can be directly converted to gradiometer measurements by dividing the former by the length of the gradiometer arm L_{GG}, which is the distance between pairs of accelerometers in the same axis. Therefore, considering the MicroSTAR accelerometer (Section 8.3.1.2), with a noise floor of 2×10^{-12} m/s^2, a gradiometer built with these instruments with $L_{GG} = 0.5$m would have a noise floor of 4×10^{-12} s^{-2} or 4 mE.

The motivation for including a gradiometer in this study is to establish the requirements for a CAI gradiometer, considering that electrostatic accelerometers are unable to attain the necessary accuracy, as depicted in Figure 8-8. In this figure, the gravity gradient signal in the direction due to the time-variable gravity field, i.e. excluding the mean gravity field, at altitudes of 200 km and 300 km is shown in the yellow and red lines, respectively; the noise of GOCE gravity gradients is shown for reference in the blue line. Sub-mE gradiometry is required, which would need an electrostatic instrument that is at least one order of magnitude more accurate than the MicroSTAR accelerometer operating in ideal conditions.

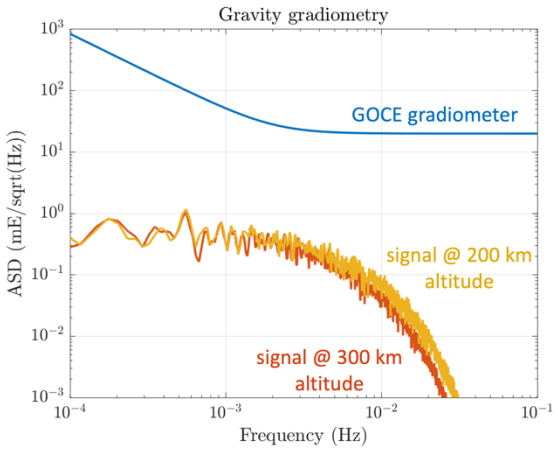

Figure 8-8: Comparison between the GOCE gradiometer errors (blue line) with the time-variable signal in terms of gravity gradient at 200 km (yellow line) and 300 km altitudes (red lines).

For quantum gradiometry, the measurement concept is similar to quantum accelerometry (Section 8.3.2), except that it is doubled along the axis where the gravity gradient is measured. The original atom cloud is physically split in two with a high recoil laser pulse, originating two CAI accelerometers. Differential acceleration is therefore measured between the 2 CAI accelerometers. Common acceleration is then rejected as the 2 CAI share the same Raman laser pulses and the gravity gradient along the Raman axis remains. This scheme applies to both sequential and concurrent modes of operation, with the obvious difference that the atom clouds will not be moving perpendicularly to the Raman laser in the first mode. The amplitude of the gravity gradient as a function of the differential phase measurement and associated errors is closely related to ϕ in Equation (15) and $\sigma_{\mathrm{CAI,ng}}$ in Equation (20), as discussed in Section 9.2.2.

9. MEASUREMENT CONCEPTS AND NOISE MODELLING

We consider two measurement concepts: low-low satellite-to-satellite tracking (ll-SST) and gravity gradiometry. We discuss the most beneficial configurations when using electrostatic and quantum instrumentation for both measurement concepts. For all cases, we derive the product noise spectra as a function of the instrument noise spectra, which were defined in Section 8.

In the following, vector equations are transformed into their components using indexes *i*, *j* and *k* for the coordinate axes x, y and z. Their relation is as arbitrary as the definition of the reference frames. For example, we may define $i, j, k \equiv x, y, z$ for along-track ll-SST and $i, j, k \equiv y, z, x$ for cross-track ll-SST, assuming the traditional axis nomenclature of *x* being aligned with the along-track direction, *y* with the cross-track direction and *z* with the radial direction, in a circular low-Earth orbit (LEO) orbit.

9.1. LL-SST

The ll-SST concept relies on precise ranging between two satellites flying in the same low-altitude orbit, separated by a certain distance along the orbit (220 km in the case of the GRACE and GRACE-FO missions). In a variant of this concept, labelled cross-track ll-SST, the along-

track distance is kept minimal, and the second orbit has a different right ascension of the ascending node than the first orbit to achieve ranging predominantly in the cross-track acceleration, away from the poles. The cross-track ll-SST has to respect a minimum along-track separation for collision avoidance at the poles, where the orbit crosses each other. In all ll-SST cases, the changes in the inter-satellite distance are caused by variations in gravity and non-gravitational forces. Therefore, the concept foresees accelerometers to measure the non-gravitational accelerations so that the signal due to gravity can be extracted from the ranging measurements.

9.1.1. LL-SST WITH ELECTROSTATIC ACCELEROMETERS

The proposed ll-SST concept is illustrated in Figure 9-1. The ISR system is similar to GRACE-FO's LRI, which is implemented in the so-called racetrack configuration with a triple mirror assembly (TMA). This concept has the benefit that the ISR is performed between the satellites' centres of masses without physically occupying those locations while not compromising the ranging performance (Sheard et al. 2012). In the case of electrostatic instrumentation, we foresee two accelerometers, labelled ACC 1 and ACC 2, symmetrically placed around the satellite centre of mass (CoM). This arrangement has the benefit that the accelerometers are sensitive to accelerations due to centrifugal and Euler forces and gravity gradients, which facilitates an accurate calibration of the accelerometers that would not be possible in the case of a single accelerometer placed into the satellite CoM. Although GRACE and GRACE-FO, at least for a part of their missions, operated successfully with only one accelerometer, the calibration process has always been problematic and requires parametrisation strategies that are usually derived empirically (Teixeira da Encarnação et al. 2020). We assume that the two accelerometers are at the nominal distance of L_{acc} = 0.5 m from each other.

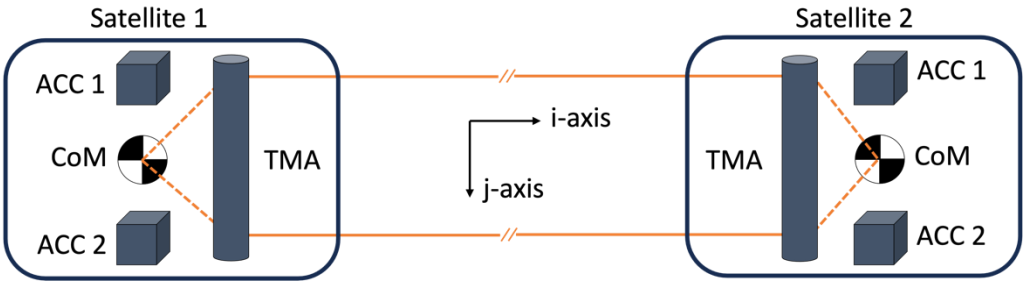

Figure 9-1: Diagram of the assumed concept for ll-SST with electrostatic accelerometers.

The LTI is equipped with a DWS sensor that measures the direction of the incoming laser beam. Combined with accurate knowledge of the positions of the satellites from GNSS, this allows for deriving the attitude of the satellites relative to the Line-of-Sight (LOS) vector (Section 8.1.3.2). Obviously, this provides pitch and yaw, but not the roll about the LOS. The attitude is also observed by star trackers (Section 8.1.1), augmented by the accelerometers (Section 8.1.4), and optionally, a high-performance IMU (Section 8.1.2).

To extract the non-gravitational acceleration from the measurements of the accelerometers, we form the so-called common-mode acceleration (Massotti et al. 2021). The common mode acceleration along the generic axis *i* is:

$$a_{\mathrm{ng},i} = \frac{a_{1i} + a_{2i}}{2}, \qquad (21)$$

where $i \equiv x$ is for the along-track ISR, and $i \equiv y$ is for the cross-track ISR. Through error propagation, we obtain the associated noise spectrum as a function of the linear acceleration error measured by a single accelerometer $\sigma_{\mathrm{acc,ng}}(f)$ (Section 8.3.1):

$$\sigma_{\mathrm{ng}}^2(f) = \frac{1}{2}\sigma_{\mathrm{acc,ng}}^2(f). \quad (22)$$

The inter-satellite range acceleration $\ddot{\rho}$ still contains the effects of non-gravitational accelerations acting on the two satellites, which we remove by subtracting the common-mode accelerations, assuming that the i-axis is aligned with the LTI axis:

$$\ddot{\rho}_{\mathrm{grav}} = \ddot{\rho} - a_{\mathrm{ng},i}^{(1)} + a_{\mathrm{ng},i}^{(2)}. \quad (23)$$

Error propagation gives the noise spectrum of $\ddot{\rho}_{grav}$ as a function of σ_{ng} and the ISR error σ_{ISR} (Section 8.2):

$$\sigma_{\ddot{\rho}}^2(f) = \sigma_{\mathrm{ISR}}^2(f) + 2\sigma_{\mathrm{ng}}^2(f). \quad (24)$$

9.1.2. LL-SST WITH QUANTUM ACCELEROMETERS

The ll-SST concept is limited by the performance of the electrostatic accelerometers at longer wavelengths (frequencies near and below the orbital period), which motivates replacing them with quantum accelerometers to eliminate this limitation (Nicklaus et al. 2019). Contrary to the electrostatic accelerometers, the quantum ones do not need to be calibrated. Therefore, it is sufficient to place one quantum accelerometer into the satellite centre of mass, as shown in Figure 9-2, which has the benefit that the accelerometer directly measures the non-gravitational acceleration and is insensitive to centrifugal and Euler forces and gravity gradients. However, depending on the operational mode (Section 8.3.2.1), the atom cloud may be moving during the interferometric measurement process, and we need to account for the effects of the Coriolis force (Section 9.1.2.2).

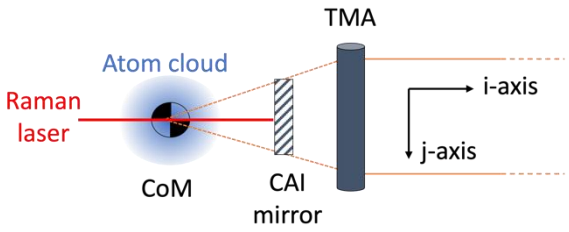

Figure 9-2: Diagram with the assumed concept of ll-SST with quantum accelerometers. Only one satellite is shown.

The quantum accelerometer measures the phase Φ of the CAI, which is proportional to the acceleration of the atom cloud $\boldsymbol{a}_{\mathrm{cloud}}$ relative to the acceleration of the mirror that reflects the laser $\boldsymbol{a}_{\mathrm{mirror}}$ and the square of interrogation time T between laser pulses:

$$\Phi = \boldsymbol{k}_{\mathrm{eff}} \cdot (\boldsymbol{a}_{\mathrm{cloud}} - \boldsymbol{a}_{\mathrm{mirror}})T^2, \quad (25)$$

where $\boldsymbol{k}_{\mathrm{eff}}$ is the effective wavevector that defines the direction in which the acceleration is sensed, and its magnitude is given by Equation (16).

Since the mirror is firmly attached to the satellite, it serves as a reference for the non-gravitational accelerations $\boldsymbol{a}_{\mathrm{ng}}$ experienced by the satellite so that:

$$\boldsymbol{a}_{\mathrm{mirror}} = \boldsymbol{a}_{\mathrm{ng}}. \tag{26}$$

In contrast, the atom cloud freely floated in inertial space during the interrogation time. The acceleration of the atom cloud can be expressed as:

$$\boldsymbol{a}_{\mathrm{cloud}} = -\left(\boldsymbol{V} - \boldsymbol{\Omega}^2 - \dot{\boldsymbol{\Omega}}\right)(\boldsymbol{r}_{\mathrm{cloud}} - \boldsymbol{r}_{\mathrm{CoM}}) + 2\boldsymbol{\omega} \times \boldsymbol{v}_{\mathrm{cloud}}, \tag{27}$$

with the gravity gradient tensor as:

$$\boldsymbol{V} = \begin{bmatrix} V_{ii} & V_{ij} & V_{ik} \\ V_{ij} & V_{jj} & V_{jk} \\ V_{ik} & V_{jk} & V_{kk} \end{bmatrix}, \tag{28}$$

the angular velocity vector as:

$$\boldsymbol{\omega} = \begin{bmatrix} \omega_i \\ \omega_j \\ \omega_k \end{bmatrix},$$

the angular rate tensor as:

$$\boldsymbol{\Omega} = \begin{bmatrix} 0 & -\omega_k & \omega_j \\ \omega_k & 0 & -\omega_i \\ -\omega_j & \omega_i & 0 \end{bmatrix} \text{ and } \boldsymbol{\Omega}^2 = \begin{bmatrix} -\omega_j^2 - \omega_k^2 & \omega_i\omega_j & \omega_i\omega_k \\ \omega_i\omega_j & -\omega_k^2 - \omega_i^2 & \omega_j\omega_k \\ \omega_i\omega_k & \omega_j\omega_k & -\omega_i^2 - \omega_j^2 \end{bmatrix} \tag{29}$$

and the angular acceleration as:

$$\dot{\boldsymbol{\Omega}} = \begin{bmatrix} 0 & -\dot{\omega}_k & \dot{\omega}_j \\ \dot{\omega}_k & 0 & -\dot{\omega}_i \\ -\dot{\omega}_j & \dot{\omega}_i & 0 \end{bmatrix}. \tag{30}$$

The remaining symbols are the position of the atom cloud $\boldsymbol{r}_{\mathrm{cloud}}$, position of the satellite CoM $\boldsymbol{r}_{\mathrm{CoM}}$, and the velocity of the atom cloud $\boldsymbol{v}_{\mathrm{cloud}}$ relative to the satellite centre of mass. The term $\dot{\boldsymbol{\Omega}}$ represents the angular acceleration matrix which causes Euler accelerations, $\boldsymbol{\Omega}^2$ causes the centrifugal accelerations, and $2\boldsymbol{\omega} \times \boldsymbol{v}_{\mathrm{cloud}}$ is the Coriolis acceleration.

It should be noted that $\boldsymbol{\Omega}$ is the angular velocity after any compensation by a tilting mirror, which also minimises the loss of contrast of the cold atom interferometer (Trimeche et al. 2019).

Combining the above, we obtain the measured acceleration along the direction defined by the Raman laser axis, represented by the unit vector $\boldsymbol{e}_i = \boldsymbol{k}_{\mathrm{eff}}/k_{\mathrm{eff}}$, as:

$$\boldsymbol{e}_i \cdot \boldsymbol{a}_{\mathrm{ng}} = \\ = -\frac{\Phi}{k_{\mathrm{eff}}T^2} + \boldsymbol{e}_i \cdot \left(-\left(V - \boldsymbol{\Omega}^2 - \dot{\boldsymbol{\Omega}}\right)(\boldsymbol{r}_{\mathrm{cloud}} - \boldsymbol{r}_{\mathrm{CoM}}) + 2\boldsymbol{\omega} \times \boldsymbol{v}_{\mathrm{cloud}}\right). \tag{31}$$

The derivation of the equation above can be found in Section 14.1.

Since we measure the acceleration in the direction of the wavevector $\boldsymbol{k}_{\mathrm{eff}}$, this vector must be aligned with the laser used for measuring the inter-satellite range. Further, we ignore any effects of magnetic fields and self-gravity on the atom cloud, which might play a role in view of the

extreme sensitivity of the quantum sensor. These considerations are beyond the scope of this study because they heavily depend on the specific instrument and satellite design.

If the atom cloud is in the satellite centre of mass, i.e., $\boldsymbol{r}_{\text{cloud}} - \boldsymbol{r}_{\text{CoM}} = 0$, the equation above simplifies to:

$$\boldsymbol{e}_i \cdot \boldsymbol{a}_{\text{ng}} = -\frac{\Phi}{k_{\text{eff}} T^2} + \boldsymbol{e}_i \cdot (2\boldsymbol{\omega} \times \boldsymbol{v}_{\text{cloud}}), \quad (32)$$

leaving the Coriolis term as the only effect to consider. In this context, we note that $\boldsymbol{r}_{\text{cloud}} - \boldsymbol{r}_{\text{CoM}} = 0$ holds for the initial atom cloud position. The first laser pulse of the cold atom interferometer splits the wave-packet in two that move at a similar speed in opposite directions along the laser axis away from the initial position, indicated as step ii in Section 8.3.2. We assume that the rate of rotation of the Raman laser, i.e., the rotation of the satellite after the compensation by the tilting mirror, does not change significantly during the outward and inward wave-packet drift, indicated as steps ii to iv in Section 8.3.2. Under these conditions, the integrated effect of the rotational and gravity gradient terms cancel out over the outward and inward motion of the two wave-packets and are negligible at their recombination.

Considering axis i, j and k are arbitrary, e.g., $i, j, k \equiv x, y, z$ for along-track ll-SST and $i, j, k \equiv y, z, x$ for cross-track ll-SST, we can express the equation in scalar form as:

$$a_{\text{ng},i} = -\frac{\Phi}{k_{\text{eff}} T^2} + 2\omega_j v_{\text{cloud},k} - 2\omega_k v_{\text{cloud},j}. \quad (33)$$

9.1.2.1. ERROR AMPLITUDE OF QUANTUM ACCELEROMETERS

Considering the error in the atom cloud velocity knowledge $\sigma_{v,\text{cloud}}$, angular rate error σ_ω after compensation by the tilting mirror, and applying error propagation, we obtain:

$$\sigma^2_{a_{\text{ng},i}} = \frac{\sigma^2_\Phi}{k^2_{\text{eff}} T^4} + \\ +4\omega_j^2 \sigma^2_{v,\text{cloud},k} + 4\omega_k^2 \sigma^2_{v,\text{cloud},j} + 4\sigma^2_{\omega,j} v^2_{\text{cloud},k} + 4\sigma^2_{\omega,k} v^2_{\text{cloud},j}. \quad (34)$$

We can group the first term as the CAI acceleration sensitivity error $\sigma_{\text{CAI,ng}}$ (cf. Section 8.3.2) and the last four terms as the errors $\sigma_{\text{Cor},i}$ caused by the Coriolis effect:

$$\sigma^2_{a_{\text{ng},i}} \equiv \sigma^2_{\text{CAI,ng},i} + \sigma^2_{\text{Cor},i}. \quad (35)$$

For the conservative case that errors, cloud velocities and angular rates are homogeneous in any direction, the errors resulting from Coriolis acceleration $\sigma_{Cor,i}$ is:

$$\sigma^2_{\text{Cor},i} = 8\omega^2 \sigma^2_{v,\text{cloud}} + 8\sigma^2_\omega v^2_{\text{cloud}}. \quad (36)$$

9.1.2.2. AMPLITUDE OF THE CORIOLIS TERM

The equation of the variance of the Coriolis term depends on the velocity of the atom cloud and the angular velocity of the Raman laser, cf. Equation (36). In this section, we analyse the individual contributions in more detail and explain the underlying assumptions on signals and errors.

Cloud velocity

The atom cloud velocity components that contribute to the variance of the Coriolis term are perpendicular to the Raman laser axis since we assume that the integrated effects from the outwards and inwards movement of the cloud along the Raman laser axis are negligible.

Since no instrument is perfect, the atom cloud will have a random non-zero velocity when released from the MOT. We assume the worst-case value of the initial cloud velocity to be $\sigma_{v_{\text{cloud,initial}}} = 10^{-7}\text{m/s}$. It should be noted that treating this worst-case value as an error is a conservative estimate.

The thermal velocity (most probable speed) of individual atoms is:

$$v_{\text{atom, therm}} = \sqrt{\frac{2k_B T_{\text{atom}}}{m}}, \quad \textbf{(37)}$$

where k_B is the Stefan Boltzmann constant, T_{atom} is the atom temperature, and m is the atom mass. In practice, $v_{\text{atom,therm}}$ tends to be at the order of 10^{-4} m/s, but a technique called Delta Kick-Collimation (DKC) allows for values at the micrometre per second (Amri, 2022). For this reason, we assume that $v_{\text{atom,therm}} = 10^{-6}$ m/s.

Recalling that the velocity dispersion follows the Maxwell-Boltzmann distribution (Amri, 2022)**,** we are interested in the difference between the most probable speed $v_{\text{atom,therm}}$ and the velocity RMS, which is given by $\sqrt{3/2}v_{\text{atom,therm}}$. Under this assumption, the thermal velocity of the atom cloud is:

$$\sigma_{v_{\text{cloud,therm}}} = \frac{\left(\sqrt{\frac{3}{2}} - 1\right) v_{\text{atom, therm}}}{\sqrt{N}}, \quad \textbf{(38)}$$

due to the averaging over N atoms. Thus, assuming that $\sigma_{v_{\text{cloud,initial}}}$ is uncorrelated to $\sigma_{v_{\text{cloud,therm}}}$, the variability of the atom cloud velocity is:

$$\sigma^2_{v_{\text{cloud}}} = \sigma^2_{v_{\text{cloud,therm}}} + \sigma^2_{v_{\text{cloud,initial}}}. \quad \textbf{(39)}$$

Angular velocity

We remind that the angular velocity ω_i is not necessarily the satellite angular velocity but the residual angular velocity after compensation by the tilting mirror if the mission concepts under analysis assume this capability. To make this distinction, we introduce the symbol $\delta\omega$ when relevant but derive all equations with the original symbol for angular velocity ω.

The mean angular velocity of a nadir-pointing satellite in low-Earth orbit is the pitch rate of about $\omega_y = 1.1 \times 10^{-3}$rad/s, with the *y*-axis aligned with the cross-track direction. The yaw and roll rate are typically at least one order of magnitude smaller, i.e., about $\omega_x = \omega_z = 1 \times 10^{-4}$rad/s, with the *x*-axis aligned with the along-track direction and the *z*-axis right-hand orthogonal (which is parallel to the radial direction in a circular orbit).

The compensation of the angular velocity requires that either the satellite attitude or the tilting mirrors are controlled, taking input from a sensor that provides angular velocity measurements. One of the best-performing angular velocity sensors is the Astrix 200 laser gyroscope, which

has an accuracy of $\sigma_\omega = 5 \times 10^{-8}\text{rad/s}$. We believe that it will not be possible to fully exploit the gyroscope's performance in real-time and assume an accuracy degradation given by the factor f_ω:

$$\delta\omega = f_\omega \sigma_\omega, \quad (40)$$

taken to be one order of magnitude, $f_\omega = 10$, worse than the measurement system, i.e., $\delta\omega = 5 \times 10^{-7}\text{rad/s}$ for the case of the mirror compensating the satellite rotation driven by the Astrix 200 gyroscope. When the satellite rotation is compensated in this way, we assume $\boldsymbol{\omega} = \delta\boldsymbol{\omega}$. In addition to avoiding loss of contrast in the cold atom interferometer, these figures already suggest that the compensation of the satellite rotation is necessary for quantum accelerometers, depending on the sensitivity to the Coriolis effect, to be quantified in Section 11.1.

We only consider attitude compensation for the cases of quantum accelerometry or gradiometry. We do not consider this for electrostatic accelerometers or classic gradiometers, for example, by physically rotating the instrument within the satellite body.

9.2. GRADIOMETRY

The only distinction between classic and quantum gradiometry is that in the case of the former, the accelerometers are sensitive to all directions, which results in the possibility of measuring off-diagonal gravity gradient components, even with a single gradiometer arm. In the case of quantum gravimetry, the CAI instruments we consider are inherently unidirectional and only sensitive to the gravity gradient along the axis connecting the atom clouds. Three CAI gradiometer instruments installed perpendicular to each other in the same satellite are needed to retrieve all diagonal terms of the gravity gradient tensor. For simplicity, we assume this to be the case without going into more detail regarding the engineering aspects of this configuration. For more details of the configuration, the reader is invited to read Trimeche et al. (2019).

9.2.1. GRADIOMETRY WITH ELECTROSTATIC ACCELEROMETERS

The GOCE mission demonstrated gravity gradiometry based on electrostatic accelerometers. The configuration of accelerometers is illustrated in Figure 9-3. Here, we assume the same concept but with more advanced accelerometers and, potentially, a high-performance gyroscope. For reference, we will assume a distance of $L_{GG} = 0.5\,\text{m}$ between the accelerometers located on the same axis.

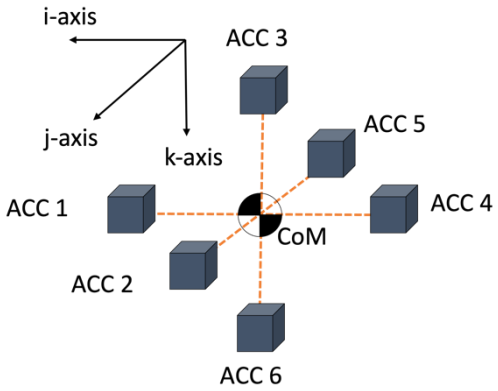

Figure 9-3: Accelerometer configuration in the classic gravity gradiometry concept.

9.2.1.1. ERROR AMPLITUDE OF CLASSIC GRADIOMETERS

The diagonal element V_{ii} of the gravity gradient tensor, measured by the accelerometer pair 1 and 4, is calculated by (Rummel, Yi, and Stummer 2011):

$$V_{ii} = -\frac{a_{1,i} - a_{4,i}}{L_{\mathrm{GG}}} - \omega_j^2 - \omega_k^2. \quad (41)$$

For the remaining diagonal elements V_{jj} and V_{kk}, the expressions are similar with accelerometers pairs 2,5 and 3,6, respectively, and angular velocity components *i,k* and *i,j*, respectively. After error propagation, there will be non-linear terms that result in the product of angular velocity and angular velocity noise components, following approximations such as:

$$(\omega_i + \sigma_{\omega,i})^2 \approx \omega_i^2 + 2\omega_i\sigma_{\omega,i}. \quad (42)$$

This relation illustrates the coupling between the angular velocity signal ω_i and the angular velocity noise $\sigma_{\omega,i}$, along the generic axis *i*.

The errors associated with classic gradiometry are:

$$\sigma_{V_{ii}}^2(f) = \frac{2}{L_{\mathrm{GG}}^2}\sigma_{\mathrm{acc,ng}}^2(f) + 4\left(\left(\mathrm{RMS}(\omega_j)\right)^2 + \left(\mathrm{RMS}(\omega_k)\right)^2\right)\sigma_{\omega}^2(f), \quad (43)$$

where $\mathrm{RMS}(\omega_j)$ and $\mathrm{RMS}(\omega_k)$ are the RMS of the angular velocity signal, which signifies the coupling between signal and noise in the non-linear error propagation. For the pitch rate, we assume $\mathrm{RMS}(\omega_y) \approx 1.1 \times 10^{-3}\ rad/s$ and for the yaw and roll rate, $\mathrm{RMS}(\omega_x) \approx \mathrm{RMS}(\omega_z) \approx 10^{-4}\ rad/s$. The underlying assumptions for deriving these RMS values are explained in Appendix 14. For the remaining diagonal terms, the corresponding expressions are similar to Equation (43), considering the RMS of the orthogonal angular velocity components.

The off-diagonal elements of the gravity gradient tensor are given by:

$$\begin{aligned} V_{ij} &= -\frac{a_{2,i} - a_{5,i}}{2L_{\mathrm{GG}}} - \frac{a_{1,j} - a_{4,j}}{2L_{\mathrm{GG}}} + \omega_i\omega_j \\ V_{ik} &= -\frac{a_{1,k} - a_{4,k}}{2L_{\mathrm{GG}}} - \frac{a_{3,i} - a_{6,i}}{2L_{\mathrm{GG}}} + \omega_i\omega_k \\ V_{jk} &= -\frac{a_{3,j} - a_{6,j}}{2L_{\mathrm{GG}}} - \frac{a_{2,k} - a_{5,k}}{2L_{\mathrm{GG}}} + \omega_j\omega_k \end{aligned} \quad (44)$$

Applying error propagation results in:

$$\sigma_{V_{ij}}^2(f) = \frac{1}{L_{GG}^2}\sigma_{\mathrm{acc,ng}}^2(f) + \left(\left(\mathrm{RMS}(\omega_i)\right)^2 + \left(\mathrm{RMS}(\omega_j)\right)^2\right)\sigma_{\omega}^2(f). \quad (45)$$

The expressions for the remaining off-diagonal components are similar, with the RMS of the angular velocity components ω_i, ω_k and ω_j, ω_k relevant to the tensor component *ik* and *jk*, respectively.

9.2.1.2. ATTITUDE RECONSTRUCTION WITH CLASSIC GRADIOMETERS

We analyse the capability of the classic gradiometer to measure angular acceleration and separate gravity gradients from frame rotations. It is fair to assume that the satellite will be

equipped with star sensors attitude reconstruction, both on board as well as in-ground processing. We assume the errors of this instrument are given by Equation (3).

The gravity gradiometer also functions by design as an accurate angular acceleration sensor, from which the angular velocity can be obtained by numerical integration. The noise ASD of the gradiometer-derived angular accelerations are derived from the accelerometer measurements as follows:

$$\begin{aligned}\dot{\omega}_i &= \frac{a_{2,k} - a_{5,k}}{2L_{\mathrm{GG}}} - \frac{a_{3,j} - a_{6,j}}{2L_{\mathrm{GG}}},\\ \dot{\omega}_j &= \frac{a_{3,i} - a_{6,i}}{2L_{\mathrm{GG}}} - \frac{a_{1,k} - a_{4,k}}{2L_{\mathrm{GG}}},\\ \dot{\omega}_k &= \frac{a_{1,j} - a_{4j}}{2L_{\mathrm{GG}}} - \frac{a_{2,i} - a_{5,i}}{2L_{\mathrm{GG}}}.\end{aligned} \qquad \textbf{(46)}$$

Since all accelerometer axes have the same performance, we find:

$$\sigma_{\dot{\omega},GG}(f) = \frac{1}{L_{\mathrm{GG}}}\sigma_{\mathrm{acc,ng}}(f), \qquad \textbf{(47)}$$

for the noise ASD of the gradiometer-derived angular acceleration measurements, where $\sigma_{\mathrm{acc,ng}}(f)$ is the noise ASD of a linear acceleration measurement of an individual accelerometer. It is worthwhile to note that the angular acceleration measurements derived in this way are more accurate than the angular acceleration measurements of the individual accelerometers as illustrated in Figure 9-4, taking MicroSTAR (Section 8.3.1.2) as an example.

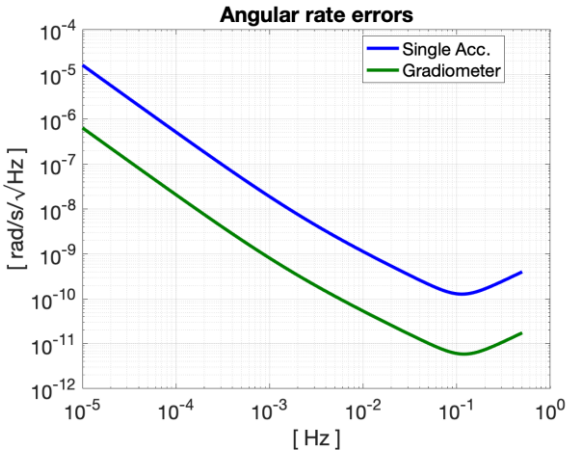

Figure 9-4: Noise spectra of the angular velocity derived from the linear acceleration measurements of two accelerometers installed in a gradiometer arm with length $L_{\mathrm{GG}} = 0.5$ m (green line) and of the angular acceleration measurements of a single accelerometer (blue line).

The discrepancy between the attitude accuracies in Figure 9-4 can be explained by the small distance (a few cm) between the electrodes for the single accelerometer and the larger gradiometer arm (50 cm) separating the accelerometers.

9.2.2. GRADIOMETRY WITH QUANTUM SENSORS

Gravity gradiometry based on quantum sensors relies on generating an initial cloud of atoms that is physically split into two atom clouds, labelled "Cloud 1" and "Cloud 2" in Figure 9-5. The advantage is that the relative cloud positions are well-known because the splitting is performed by a laser pulse that gives an accurately known kick to the initial cloud of atoms. Once the two atom clouds are in position, the cold atom interferometric sequence starts for both atom clouds simultaneously using the same Raman laser. In principle, it is the same sequence of laser pulses as for quantum accelerometers. Thus, the quantum gradiometer is also based on sensing the differential acceleration along the laser axis over the precisely known distance between the atom clouds. Consequently, the equations presented in Section 8.3.2 also apply to quantum gravity gradiometry.

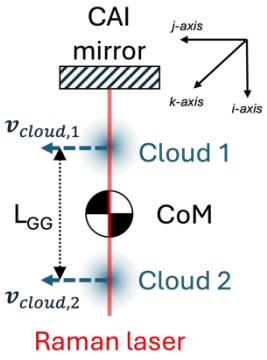

Figure 9-5: Quantum gravity gradiometer concept.

By re-arranging Equation (31), we find:

$$\frac{\Phi_{i,l}}{k_{\text{eff}}T^2} = \boldsymbol{e}_i \cdot \left(-\boldsymbol{a}_{\text{ng,l}} - \left(V - \boldsymbol{\Omega}^2 - \dot{\boldsymbol{\Omega}}\right)\left(\boldsymbol{r}_{\text{cloud,l}} - \boldsymbol{r}_{\text{CoM}}\right) + 2\boldsymbol{\omega} \times \boldsymbol{v}_{\text{cloud,l}}\right), \qquad (48)$$

where $l = 1$ or 2 identifies the atom cloud (cf. Figure 9-5). Setting the origin of the reference axis at the CoM, the atom clouds are at the positions $\boldsymbol{r}_{\text{cloud},1} = -\boldsymbol{r}_{\text{cloud},2} \equiv L_{\text{GG}}/2\boldsymbol{e}_i$ at the time the interferometry is done.

Regarding the cloud velocity, we have $\boldsymbol{v}_{\text{cloud},1} = \boldsymbol{v}_{\text{cloud},2}$ and:

$$\boldsymbol{v}_{\text{cloud},l} = \boldsymbol{v}_{\text{cloud,therm},l} + \boldsymbol{v}_{\text{cloud,initial},l} = \boldsymbol{v}_{\text{cloud,therm},l} + v_{\text{cloud,initial},l}.\boldsymbol{e}_j. \qquad (49)$$

In the case of the concurrent mode of operation (Section 8.3.2.1), $\boldsymbol{v}_{\text{cloud,initial},l}$ reflects the transverse velocity imparted by an additional laser perpendicular to the Raman laser axis. In this case, we note that $v_{\text{cloud,initial},1} = v_{\text{cloud,initial},2}$ because both clouds are accelerated with the same recoil laser (not shown in Figure 9-5). In the case of the sequential mode, $v_{\text{cloud,initial},1} = v_{\text{cloud,initial},2} = 0$. In both cases, $\boldsymbol{a}_{\text{ng},1} = \boldsymbol{a}_{\text{ng},2}$ because the non-gravitational accelerations affect both clouds equally. As a result, these two terms cancel when computing the differential measurement $\delta\Phi_i \equiv \Phi_{i,1} - \Phi_{i,2}$:

$$\frac{\delta\Phi_i}{k_{\text{eff}}T^2} = \boldsymbol{e}_i \cdot \left(-\left(\boldsymbol{V} - \boldsymbol{\Omega}^2 - \dot{\boldsymbol{\Omega}}\right)L_{\text{GG}}\boldsymbol{e}_i + 2\boldsymbol{\omega} \times \boldsymbol{v}_{\text{cloud,therm}}\right), \qquad (50)$$

The term on $\boldsymbol{v}_{\text{cloud,therm},l}$ does not cancel because it is related to the thermal velocity of the cloud, which is akin to a random variable.

Recognising that $\dot{\boldsymbol{\Omega}}\boldsymbol{e}_i = \dot{\boldsymbol{\Omega}}\boldsymbol{e}_j = \dot{\boldsymbol{\Omega}}\boldsymbol{e}_k = 0$ (cf. Equation (30)), isolating the gravity gradient term, and reducing the vector equation to a scalar quantity results in:

$$V_{ii} = -\frac{1}{L_{\text{GG}}}\frac{\delta\Phi_i}{k_{\text{eff}}T^2} - \omega_j^2 - \omega_k^2 + \frac{2}{L_{\text{GG}}}\left(\omega_j v_{\text{cloud,therm},k} - \omega_k v_{\text{cloud,therm},j}\right). \quad \textbf{(51)}$$

The derivation of the equation above and the one for other axes is in Appendix 14.2. As a side note, if we assume a quantum gravity gradiometer concept where the satellite rotation is compensated by a tilting mirror, as described in Section 9.1.2, the symbol ω should be interpreted as the compensated attitude $\delta\omega$, given by Equation (40).

9.2.2.1. ERROR AMPLITUDE OF QUANTUM GRADIOMETERS

Applying error propagating to Equation (50), under the assumption that Raman laser is rotating at the residual angular velocity after compensation by the tilting mirror $\delta\boldsymbol{\omega}$, and considering uncorrelated phase errors, $\sigma^2_{\delta\Phi_{\text{i}}} = \sigma^2_{\Phi_{i,1}} + \sigma^2_{\Phi_{i,2}} = 2\sigma^2_{\Phi}$, results in the errors associated with quantum gradiometry:

$$\begin{aligned}\sigma^2_{V_{ii}} &= \frac{2}{L^2_{\text{GG}}}\frac{\sigma^2_{\Phi_i}}{k^2_{\text{eff}}T^4} + 4\omega_j^2\sigma^2_{\omega_j} + 4\omega_k^2\sigma^2_{\omega_k} \\ &+ \frac{16}{L^2_{\text{GG}}}(\omega_j^2\sigma^2_{v_{\text{cloud,therm}},k} + \omega_k^2\sigma^2_{v_{\text{cloud,therm}},j} + \end{aligned} \quad \textbf{(52)}$$

$$\sigma^2_{\omega,j}v^2_{\text{cloud,therm},k} + \sigma^2_{\omega,k}v^2_{\text{cloud,therm},j}).$$

Under the conservative assumption of homogeneous noise in all components:

$$\begin{aligned}\sigma^2_V &= \frac{2}{L^2_{\text{GG}}}\frac{\sigma^2_{\Phi}}{k^2_{\text{eff}}T^4} + 8\omega^2\sigma^2_{\omega} + \frac{32}{L^2_{\text{GG}}}\left(\omega^2\sigma^2_{v_{\text{cloud,therm}}} + \sigma^2_{\omega}v^2_{\text{cloud,therm}}\right) \\ &\equiv \sigma^2_{V_{\text{CAI}}} + \sigma^2_{\Omega^2} + \sigma^2_{V_{\text{Cor}}} = \frac{2}{L^2_{\text{GG}}}\sigma^2_{\text{CAI,ng}} + \sigma^2_{\Omega^2} + \frac{4}{L^2_{\text{GG}}}\sigma^2_{\text{Cor}},\end{aligned} \quad \textbf{(53)}$$

with expressions for $\sigma_{\text{CAI,ng}}$ and σ^2_{Cor} given in Section 9.1.2.1, and the errors associated with the centrifugal accelerations are $\sigma_{\Omega^2} = \sqrt{8}\omega\sigma_{\omega}$.

9.2.2.2. ATTITUDE RECONSTRUCTION WITH QUANTUM GRADIOMETERS

In the case of classic gradiometry (Section 9.2.1), the 6 capacitive accelerometers that compose the 3D gradiometer make it possible to estimate the rate of change of the attitude (Section 9.2.1.2). For CAI gradiometry, the case is not the same since the "accelerometers" are unidimensional. This section explores how single-axis quantum gradiometers can be arranged so that they also provide complete attitude information.

Consider the *m*-th CAI gradiometer aligned with the *i*-axis (parallel to $\boldsymbol{e}_i$), shown in Figure 9-6.

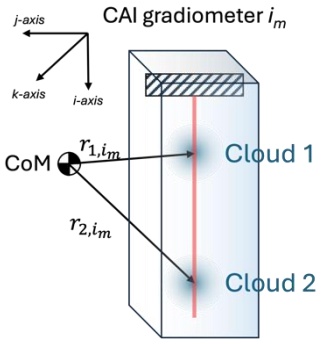

Figure 9-6: CAI gradiometer *m*, aligned with axis *i*, showing the positions of the atom clouds 1 and 2.

From Equation (27), with the reference frame at the CoM, the phase measurement Φ_{l,i_m} of the atom cloud *l* is:

$$\frac{\Phi_{l,i_m}}{k_{\text{eff}}T^2} = \boldsymbol{e}_i \cdot \left(-\left(\boldsymbol{V} - \boldsymbol{\Omega}^2 - \dot{\boldsymbol{\Omega}}\right)\boldsymbol{r}_{l,i_m} + 2\boldsymbol{\omega} \times \boldsymbol{v}_{\text{cloud}}\right) =$$

$$\boldsymbol{e}_i \cdot \begin{bmatrix} -V_{ii} - \omega_j^2 - \omega_k^2 & -V_{ij} + \omega_i\omega_j - \dot{\omega}_k & -V_{ik} + \omega_i\omega_k + \dot{\omega}_j \\ -V_{ij} + \omega_i\omega_j + \dot{\omega}_k & -V_{jj} - \omega_i^2 - \omega_k^2 & -V_{jk} + \omega_j\omega_k - \dot{\omega}_i \\ -V_{ik} + \omega_i\omega_k - \dot{\omega}_j & -V_{jk} + \omega_j\omega_k + \dot{\omega}_i & -V_{kk} - \omega_i^2 - \omega_j^2 \end{bmatrix} \boldsymbol{r}_{l,i_m} + \qquad (54)$$

$$\boldsymbol{e}_i \cdot \begin{bmatrix} \omega_j v_{l,i_m,k} - \omega_k v_{l,i_m,j} \\ \omega_k v_{l,i_m,i} - \omega_i v_{l,i_m,k} \\ \omega_i v_{l,i_m,j} - \omega_j v_{l,i_m,i} \end{bmatrix} + \boldsymbol{e}_i \cdot \boldsymbol{a}_{\text{ng}} .$$

Any linear combination of the two phase measurements Φ_{1,i_m} and Φ_{2,i_m} will unavoidably include off-diagonal terms of $\boldsymbol{V}$, $\boldsymbol{\Omega}^2$ and $\dot{\boldsymbol{\Omega}}$ because $\boldsymbol{r}_{l,i_m}$ is not aligned with $\boldsymbol{e}_i$. Therefore, there will be 15 unknowns:

- 6 gravity gradients $\boldsymbol{V}$,
- 3 angular rates $\boldsymbol{\omega}$ (or accelerations $\dot{\boldsymbol{\Omega}}$),
- 3 non-gravitational accelerations $\boldsymbol{a}_{\text{ng}}$ and
- 3 Coriolis accelerations $\boldsymbol{\omega} \times \boldsymbol{v}_{\text{cloud}}$ (or atom cloud velocities $\boldsymbol{v}_{\text{cloud}}$).

In the case of the common and differential linear combinations, 3 degrees of freedom cancel out: the diagonal of the gravity gradient and the non-gravitational accelerations, respectively. In both cases, we are left with 12 unknowns, which require 12 CAI gradiometers to resolve fully.

One possible arrangement of CAI gradiometers is indicated in Figure 9-7 as a "ring" of 4 gradiometer arms arranged symmetrically around the CoM in the same plane, perpendicular to the *k*-axis and intersecting the CoM.

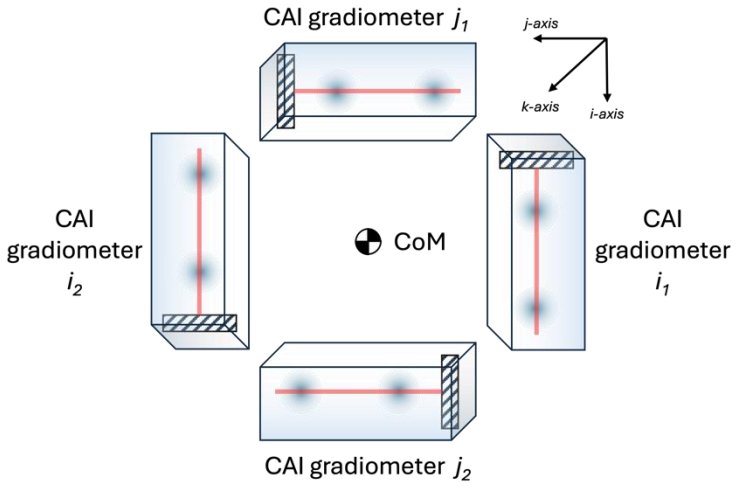

Figure 9-7: Arrangement of 4 CAI gradiometers placed symmetrically around the CoM that are able to measure $a_{ng,i}$, $a_{ng,j}$ and $\dot{\omega}_k$.

The common phase measurement $\sum \Phi_{i1}$ (or $\sum \Phi_{i2}$) and $\sum \Phi_{j1}$ (or $\sum \Phi_{j2}$) of gradiometer *i1* (or *i2*) and *j1* (or *j2*) provides information on the *i*-th and *j*-th component of the non-gravitational accelerations, respectively. The difference between the common phases $\sum \Phi_{i1} - \sum \Phi_{i2}$ or $\sum \Phi_{j1} - \sum \Phi_{j2}$ cancels the Coriolis and non-gravitational accelerations. The sum of the difference of the common phases $\sum \Phi_{i1} - \sum \Phi_{i2} + \sum \Phi_{j1} - \sum \Phi_{j2}$ cancels the gravity gradients and centrifugal accelerations, isolating the $\dot{\omega}_k$ term and, consequently, ω_k by numerical integration. It should be noted that the complete attitude of the satellite could only be determined with the help of an absolute attitude sensor, such as a star tracker, to resolve the attitude bias and bias rate in the case of the proposed CAI gradiometer ring, resulting from the unknown integration constant.

If two orthogonal rings measure the *k* and *j* components of the angular acceleration, that would be sufficient to completely retrieve the measurement of the V_{ii}, which would ideally be aligned with the radial direction. This is because ω_i does not affect the measurement of V_{ii}. If a third orthogonal ring is added, then the complete diagonal of $\boldsymbol{V}$ is available.

10. EFFECTS OF ATTITUDE UNCERTAINTY

So far, we derive the noise spectra for the observations in the satellite reference frame. However, the observations need to be transformed to the Earth-centred, Earth-fixed (ECEF) reference frame. The transformation requires satellite attitude data and is, therefore, not free of errors. In this section, we will analyse the impact of attitude errors.

The effects of attitude uncertainty discussed in this section are conceptually separate from other attitude errors discussed so far. This refers notably to the Coriolis effect on CAI accelerometers or gradiometers (Section 9.1.2.2) and the capability of gradiometers to observe attitude rates, analysed in Section 9.2.1.2 for the classical case, and in Section 9.2.2.2 for a collection of CAI gradiometers.

10.1. LL-SST

Conceptually, we need to subtract the ISR acceleration $\ddot{\rho}_{ng}$ due to non-gravitational accelerations from the measured ISR acceleration $\ddot{\rho}$ to obtain the ISR $\ddot{\rho}_{\text{grav}}$ due to gravitational accelerations:

$$\ddot{\rho}_{\text{grav}} = \ddot{\rho} - \ddot{\rho}_{\text{ng}}. \quad (55)$$

The ISR acceleration $\ddot{\rho}_{ng}$ is the differential non-gravitational acceleration projected onto the line-of-sight connecting the two satellites' centres of mass, i.e.:

$$\ddot{\rho}_{\text{ng}} = \left(\boldsymbol{a}_{\text{ng}}^{(1)} - \boldsymbol{a}_{\text{ng}}^{(2)}\right) \cdot \boldsymbol{e}_{\text{LOS}} = \Delta\boldsymbol{a}_{\text{ng}} \cdot \boldsymbol{e}_{\text{LOS}}, \quad (56)$$

where $\boldsymbol{e}_{LOS}$ is the line-of-sight unit vector and $\boldsymbol{a}_{\text{ng}}^{(1)}$ and $\boldsymbol{a}_{ng}^{(2)}$ are the measured non-gravitational accelerations of satellite 1 and satellite 2, respectively, all defined in the Earth-centred, inertial (ECI) reference. The line-of-sight is defined by the satellite positions, which are naturally provided in the ECI frame.

$$\boldsymbol{e}_{\text{LOS}} = \frac{\boldsymbol{r}^{(1)} - \boldsymbol{r}^{(2)}}{\|\boldsymbol{r}^{(1)} - \boldsymbol{r}^{(2)}\|}. \quad (57)$$

If $\boldsymbol{r}^{(1)}$ or $\boldsymbol{r}^{(2)}$ are provided in the ECEF frame, we assume that the coordinate transformations do not introduce a significant error because the Earth Orientation Parameters are well known. As for the non-gravitational accelerations, they are measured in the Satellite Reference Frame (SRF), which we represent $\boldsymbol{a}_{\text{ng}}^{(\text{SRF},s)}$ for satellite *s*.

We need to perform a coordinate transformation for the accelerations, based on the satellite attitude data, from the Satellite Reference Frame (SRF) to the Earth-centred, inertial frame, which can be represented as

$$\boldsymbol{a}_{\text{ng}}^{(\text{ECI},s)} = \boldsymbol{R}^{(\text{ECI}\leftarrow\text{SRF},s)}\boldsymbol{a}_{\text{ng}}^{(\text{SRF},s)}. \quad (58)$$

The SRF-to-ECI rotation matrix contains errors, here represented by the small angle rotation matrix $\boldsymbol{\Theta}^{(\text{ECI}\leftarrow\text{SRF},s)}$:

$$\boldsymbol{R}^{(\text{ECI}\leftarrow\text{SRF},s)} = \boldsymbol{R}^{(\text{ECI}\leftarrow\text{SRF},s,\text{true})}\boldsymbol{\Theta}^{(\text{ECI}\leftarrow\text{SRF},s)}. \quad (59)$$

We split $\boldsymbol{\Theta}^{(\text{ECI}\leftarrow\text{SRF},s)}$ into the identity matrix and the small angle rotations, given as Euler angles errors $\theta_{\text{roll,s}}$, $\theta_{\text{pitch,s}}$ and $\theta_{\text{yaw,s}}$ for satellite *s*:

$$\boldsymbol{\Theta}^{(\text{ECI}\leftarrow\text{SRF},s)} = \boldsymbol{E}^{(s)} + \boldsymbol{I} = \begin{bmatrix} 0 & -\theta_{\text{yaw,s}} & \theta_{\text{pitch,s}} \\ \theta_{\text{yaw,s}} & 0 & -\theta_{\text{roll,s}} \\ -\theta_{\text{pitch,s}} & \theta_{\text{roll,s}} & 0 \end{bmatrix} + \boldsymbol{I}. \quad (60)$$

With these definitions, we can write:

$$\boldsymbol{a}_{\text{ng}}^{(\text{ECI},s)} = \boldsymbol{a}_{\text{ng}}^{(\text{ECI,true},s)} + \boldsymbol{E}^{(s)}\boldsymbol{a}_{\text{ng}}^{(\text{SRF},s)}, \quad (61)$$

where the only term on the right-hand side that is not perfectly known (for this analysis) is $\boldsymbol{E}^{(s)}\boldsymbol{a}_{\text{ng}}^{(\text{SRF},s)}$. Replacing in Equation (51):

$$\ddot{\rho}_{\text{ng}}^{(ECI)} = \left(\Delta\boldsymbol{a}_{\text{ng}}^{(\text{ECI,true})} + \left(\boldsymbol{E}^{(1)} - \boldsymbol{E}^{(2)}\right)\Delta\boldsymbol{a}_{\text{ng}}^{(\text{SRF})}\right) \cdot \boldsymbol{e}_{\text{LOS}}^{(\text{ECI})}, \quad (62)$$

Assuming the attitude errors of $\boldsymbol{E}^{(s)}$, represented by the vector $\boldsymbol{\sigma}_\theta$, are the same for both satellites, the error propagation of Equation (56), after replacing Equation (61), is

$$\sigma_{\ddot{\rho}_{\mathrm{ng}},\theta}^{(ECI)} = \boldsymbol{\nabla}\ddot{\rho}_{\mathrm{ng}}^{(ECI)}[\sigma_\theta]\boldsymbol{\nabla}\ddot{\rho}_{\mathrm{ng}}^{(ECI)^T}, \tag{63}$$

with the Jacobian $\boldsymbol{\nabla} = \left[\frac{\partial}{\partial\theta_{\mathrm{roll}}}\ \frac{\partial}{\partial\theta_{\mathrm{pitch}}}\ \frac{\partial}{\partial\theta_{\mathrm{yaw}}}\right]$ and $[\sigma_\theta]$ the diagonal matrix with the errors of θ_{roll}, θ_{pitch} and θ_{yaw}, i.e., $\sigma_{\theta_{\mathrm{roll}}}$, $\sigma_{\theta_{\mathrm{pitch}}}$, and $\sigma_{\theta_{\mathrm{yaw}}}$.

Evaluating Equation (63), we arrive at the ranging error due to attitude $\sigma_{\ddot{\rho}_{\mathrm{ng}},\theta}$ as function of $\boldsymbol{\sigma}_\theta = \left[\sigma_{\theta_{\mathrm{roll}}}\ \sigma_{\theta_{\mathrm{pitch}}}\ \sigma_{\theta_{\mathrm{yaw}}}\right]^{\mathrm{T}}$:

$$\sigma_{\ddot{\rho}_{\mathrm{ng}},\theta}^{(ECI)} = \sqrt{2}\begin{bmatrix}\Delta a_{\mathrm{ng,y}}^{(\mathrm{SRF})}e_{\mathrm{LOS,z}}^{(\mathrm{ECI})} - \Delta a_{\mathrm{ng,z}}^{(\mathrm{SRF})}e_{\mathrm{LOS,y}}^{(\mathrm{ECI})} \\ \Delta a_{\mathrm{ng,x}}^{(\mathrm{SRF})}e_{\mathrm{LOS,z}}^{(\mathrm{ECI})} - \Delta a_{\mathrm{ng,z}}^{(\mathrm{SRF})}e_{\mathrm{LOS,x}}^{(\mathrm{ECI})} \\ \Delta a_{\mathrm{ng,x}}^{(\mathrm{SRF})}e_{\mathrm{LOS,y}}^{(\mathrm{ECI})} - \Delta a_{\mathrm{ng,y}}^{(\mathrm{SRF})}e_{\mathrm{LOS,x}}^{(\mathrm{ECI})}\end{bmatrix}^{\mathrm{T}}\boldsymbol{\sigma}_\theta. \tag{64}$$

We make the conservative assumption that the amplitude of $\Delta\boldsymbol{a}_{\mathrm{ng}}^{(\mathrm{SRF})}$ is given by the RMS of the non-gravitation accelerations at orbital altitude and take the component with the largest magnitude in each entry of the row vector in Equation (64). We further assume that the amplitude of $\boldsymbol{e}_{\mathrm{LOS}}^{(\mathrm{ECI})}$ is 1 and drop the superscript of the reference frame because the errors have the same amplitude in any frame. Equation (64) simplifies to

$$\rho_{\ddot{\rho}_{\mathrm{ng}},\theta} = \sqrt{2}\begin{bmatrix}\max\left(\mathrm{RMS}(a_{\mathrm{ng,z}}),\mathrm{RMS}(a_{\mathrm{ng,z}})\right) \\ \max\left(\mathrm{RMS}(a_{\mathrm{ng,x}}),\mathrm{RMS}(a_{\mathrm{ng,z}})\right) \\ \max\left(\mathrm{RMS}(a_{\mathrm{ng,x}}),\mathrm{RMS}(a_{\mathrm{ng,y}})\right)\end{bmatrix}^{\mathrm{T}}\boldsymbol{\sigma}_\theta. \tag{65}$$

In the case of homogenous attitude error, $\sigma_{\theta_{\mathrm{yaw}}} = \sigma_{\theta_{\mathrm{pitch}}} = \sigma_{\theta_{\mathrm{roll}}} \equiv \sigma_\theta$, for example, if there are multiple star tracker cameras and their data is combined optimally with additional attitude sensors, such as an IMU and DWS:

$$\sigma_{\ddot{\rho}_{\mathrm{ng}},\theta} = \sqrt{2}\mathrm{RMS}(a_{\mathrm{ng,x}})\sigma_\theta. \tag{66}$$

The values for $\mathrm{RMS}(a_{\mathrm{ng,x}})$, $\mathrm{RMS}(a_{\mathrm{ng,y}})$ and $\mathrm{RMS}(a_{\mathrm{ng,z}})$ we considered in this study are presented in Appendix 16 and are functions of the DFC system. We quantify the effect of these errors in Section 11.2 for both electrostatic and quantum accelerometry.

10.2. GRADIOMETRY

In the case of gravity gradiometry, the gravity gradients observed in the satellite reference frame $\boldsymbol{V}^{(\mathrm{SRF})}$ are related to the gravity gradients in the ECEF reference frame $\boldsymbol{V}^{(\mathrm{ECEF})}$ by:

$$\boldsymbol{V}^{(\mathrm{ECEF})} = \boldsymbol{R}^{(\mathrm{ECEF}\leftarrow\mathrm{SRF})}\boldsymbol{V}^{(\mathrm{SRF})}\boldsymbol{R}^{(\mathrm{ECEF}\leftarrow\mathrm{SRF})^T}, \tag{67}$$

where $\boldsymbol{R}^{(\mathrm{ECEF}\leftarrow\mathrm{SRF})}$ is the rotation that transforms from the satellite to the ECEF reference frame. The attitude measurements generally relate the ICE frame to the SRF frame, so it makes more sense to split the rotation in these frames:

$$\boldsymbol{V}^{(\mathrm{ECEF})} = \boldsymbol{R}^{(\mathrm{ECEF}\leftarrow\mathrm{ECI})}\boldsymbol{R}^{(\mathrm{ECI}\leftarrow\mathrm{SRF})}\boldsymbol{V}^{(\mathrm{SRF})}\boldsymbol{R}^{(\mathrm{ECI}\leftarrow\mathrm{SRF})^T}\boldsymbol{R}^{(\mathrm{ECEF}\leftarrow\mathrm{ECI})^T}. \quad (68)$$

Assuming the ECI to ECEF frame is known perfectly, we can focus on the gravity gradients in the ECI frame:

$$\boldsymbol{V}^{(\mathrm{ECI})} = \boldsymbol{R}^{(\mathrm{ECI}\leftarrow\mathrm{SRF})}\boldsymbol{V}^{(\mathrm{SRF})}\boldsymbol{R}^{(\mathrm{ECI}\leftarrow\mathrm{SRF})^T}. \quad (69)$$

As for ll-SST, Section 10.1, we model the transformation $\boldsymbol{R}^{(\mathrm{ECI}\leftarrow\mathrm{SRF})}$ as the product of the error-free rotation $\boldsymbol{R}^{(\mathrm{ECI}\leftarrow\mathrm{SRF,true})}$ and a small-angle rotation matrix $\boldsymbol{\Theta}^{(\mathrm{ECEF}\leftarrow\mathrm{SRF})}$:

$$\boldsymbol{R}^{(\mathrm{ECI}\leftarrow\mathrm{SRF})} = \boldsymbol{R}^{(\mathrm{ECI}\leftarrow\mathrm{SRF,true})}\boldsymbol{\Theta}^{(\mathrm{ECI}\leftarrow\mathrm{SRF})}, \quad (70)$$

and Equation (67) becomes:

$$\boldsymbol{V}^{(\mathrm{ECI})} = \boldsymbol{R}^{(\mathrm{ECI}\leftarrow\mathrm{SRF,true})}\boldsymbol{\Theta}^{(\mathrm{ECI}\leftarrow\mathrm{SRF})}\boldsymbol{V}^{(\mathrm{SRF})}\boldsymbol{\Theta}^{(\mathrm{ECI}\leftarrow\mathrm{SRF})^{\mathrm{T}}}\boldsymbol{R}^{(\mathrm{ECI}\leftarrow\mathrm{SRF,true})^{\mathrm{T}}}. \quad (71)$$

If we restrict our analysis to the terms that contain errors, we can safely ignore the error-free transformation $\boldsymbol{R}^{(\mathrm{ECI}\leftarrow\mathrm{SRF,true})}$:

$$\boldsymbol{V}^{(\mathrm{SRF,noisy})} = \boldsymbol{\Theta}^{(\mathrm{ECI}\leftarrow\mathrm{SRF})}\boldsymbol{V}^{(\mathrm{SRF})}\boldsymbol{\Theta}^{(\mathrm{ECI}\leftarrow\mathrm{SRF})^{\mathrm{T}}}, \quad (72)$$

We split $\boldsymbol{\Theta}^{(\mathrm{ECI}\leftarrow\mathrm{SRF})} = \boldsymbol{E} + \boldsymbol{I}$ as before and drop the reference frame superscript:

$$\boldsymbol{V}^{(\mathrm{noisy})} = (\boldsymbol{I} + \boldsymbol{E})\,\boldsymbol{V}(\boldsymbol{I} + \boldsymbol{E})^{\mathrm{T}} \quad (73)$$

As usual, the error propagation of Equation (73) requires the tensor $\boldsymbol{V}^{(\mathrm{noisy})}$ to be collapsed into the vector $\boldsymbol{v}^{(\mathrm{noisy})}$, producing the error 9×9 covariance matrix $\boldsymbol{C_V}$:

$$\boldsymbol{C_V} = \boldsymbol{\nabla v}^{(\mathrm{noisy})}[\sigma_\theta]\boldsymbol{\nabla v}^{(\mathrm{noisy})^{\mathrm{T}}} \quad (74)$$

In evaluating Equation (74), we assume that $\boldsymbol{V}$ is error-free, the small angles are negligible $\theta_{\mathrm{roll,s}} = \theta_{\mathrm{pitch,s}} = \theta_{\mathrm{yaw,s}} \approx 0$, and ignore the cross-correlations such that $[\sigma_{\boldsymbol{V},\theta}] = \mathrm{diag}(\boldsymbol{C_V})$, resulting in

$$\begin{bmatrix}\sigma^2_{\boldsymbol{V}_{xx},\theta}\\ \sigma^2_{\boldsymbol{V}_{yy},\theta}\\ \sigma^2_{\boldsymbol{V}_{zz},\theta}\\ \sigma^2_{\boldsymbol{V}_{xy},\theta}\\ \sigma^2_{\boldsymbol{V}_{xz},\theta}\\ \sigma^2_{\boldsymbol{V}_{yz},\theta}\end{bmatrix} = \begin{bmatrix} 0 & 4V_{xz}^2 & 4V_{xy}^2\\ 4V_{yz}^2 & 0 & 4V_{xy}^2\\ 4V_{yz}^2 & 4V_{xz}^2 & 0\\ V_{xz}^2 & V_{yz}^2 & (V_{xx}-V_{yy})^2\\ V_{xy}^2 & (V_{xx}-V_{zz})^2 & V_{yz}^2\\ (V_{yy}-V_{zz})^2 & V_{xy}^2 & V_{xz}^2\end{bmatrix}\begin{bmatrix}\sigma^2_{\theta_{\mathrm{roll}}}\\ \sigma^2_{\theta_{\mathrm{pitch}}}\\ \sigma^2_{\theta_{\mathrm{yaw}}}\end{bmatrix}. \quad (75)$$

Considering the amplitude of the gravity gradient signal presented in Section 17 and setting the errors $\boldsymbol{\sigma}_\theta$ equal to 1, the scaling of the attitude errors into gravity gradient errors is:

$$[\sigma_{\boldsymbol{V},\theta}] = \begin{bmatrix}0.2 & 5 & 3600\\ & 9.7 & 3603\\ & & 9.7\end{bmatrix} \times 10^{-3}\ E$$

11. RESULTS AND DISCUSSION

We present our results by quantifying the amplitude of frame accelerations, i.e., those related to the effect of the Coriolis accelerations and the centrifugal accelerations in Section 11.1. We quantify the errors for ll-SST in Section 11.2 for both electrostatic (Section 11.2.1) and quantum (Section 11.2.2) accelerometers. Finally, we quantify the errors for quantum gradiometry in Section 11.3 for the gradiometer operating in sequential mode.

11.1. IMPORTANCE OF THE FRAME ACCELERATIONS

In this section, we quantify the amplitude of the Coriolis and centrifugal accelerations. CAI accelerometry is only affected by the former (Section 9.1.2.1), while gradiometry is affected by both (Section 9.2.2.1).

Recall that the variance of the Coriolis term $\sigma^2_{\mathrm{Cor},i}$ in a CAI accelerometer aligned with the *i*-axis, cf. Equations (34) and (35), is :

$$\sigma^2_{\mathrm{Cor},i} = 4\omega_j^2\sigma^2_{v,\mathrm{cloud},k} + 4\omega_k^2\sigma^2_{v,\mathrm{cloud},j} + 4\sigma^2_{\omega,j}v^2_{\mathrm{cloud},k} + 4\sigma^2_{\omega,k}v^2_{\mathrm{cloud},j} \qquad (76)$$

which is valid for both along-track and cross-track ll-SST.

In Section 9.2.2.1, we discussed the variances $\sigma^2_{\omega,j}$ and $\sigma^2_{\omega,k}$ reflect the angular velocity measurement noise, for which we assume $\sigma_{\omega,j} = \sigma_{\omega,k} = 5 \times 10^{-8}$rad/s in the case of using the high-performance Astrix 200 laser gyroscope, here assumed to be white noise for simplicity. For the magnitude of the angular velocity after tilting mirror compensation $\delta\omega$, we proposed one order of magnitude worse performance than the errors, i.e., $\delta\omega = 5 \times 10^{-7}$rad/s, in the *full attitude compensation* scenario. In the *no tilting mirror* scenario, we assume $\omega = 1 \times 10^{-4}$rad/s for yaw and roll and $\omega = 1.1 \times 10^{-3}$rad/s for pitch (cf. Section 9.2.2.1). We also consider the intermediate case of *minimum pitch-rate compensation*, where pitch is compensated to the level of $\delta\omega = 1 \times 10^{-4}$rad/s.

For the atom cloud velocity, we assume that either one component is $v_{\mathrm{cloud,j}} = 2.5$ cm/s and the other components zero in the case of the concurrent operational mode, or all atom cloud velocity components are zero in the case of the sequential mode of operation (cf. Section 8.3.2.1). For the uncertainty of the atom cloud velocity $\sigma_{v_{\mathrm{cloud}}}$, we assume DKC with $v_{\mathrm{atom,therm}} = 10^{-6}$ m/s and $\sigma_{v_{\mathrm{cloud,initial}}} = 10^{-7}$m/s (cf. Equations (38) and (39)), resulting in $\sigma_{v_{\mathrm{cloud,therm}}} = 2.3 \times 10^{-9}$ m/s for $N = 10^4$.

Under these assumptions, we can quantify the effect of the Coriolis term for the concurrent and sequential operational modes combined with different levels of attitude compensation, as summarised in Table 11-1.

Table 11-1: Standard deviation of the Coriolis term $\sigma_{\mathrm{Cor},i}$, assuming $\sigma_{\omega,j} = \sigma_{\omega,j} = 5 \times 10^{-8}$ rad/s, $v_{\mathrm{atom,therm}} = 10^{-6}$ m/s and $\sigma_{v_{\mathrm{cloud,initial}}} = 10^{-7}$m/s for several combinations of angular velocity compensation scenarios and operational modes (affecting the cloud velocity), for the case of along-track ll-SST and the *i*-axis aligned with the along-track direction.

Attitude compensation scenario	Residual angular velocity [rad/s]	Concurrent mode $[\mathrm{m/s^2}]$	Sequential mode $[\mathrm{m/s^2}]$
		$v_{\mathrm{cloud,k}} = \sigma_{v_{\mathrm{cloud,therm}}} = 2.3\mathrm{nm/s}$ $v_{\mathrm{cloud,j}} = 2.5\mathrm{cm/s}$	$v_{\mathrm{cloud,k}} = v_{\mathrm{cloud,j}} = \sigma_{v_{\mathrm{cloud,therm}}} = 2.3\mathrm{nm/s}$
No tilting mirror	$\omega_{\mathrm{j}} = 1.1 \times 10^{-3}$ $\omega_{\mathrm{k}} = 10^{-4}$	2.5×10^{-9}	2.2×10^{-10}
Minimum pitch-rate compensation	$\delta\omega_{\mathrm{j}} = \omega_{\mathrm{k}} = 10^{-4}$	2.5×10^{-9}	2.8×10^{-11}
Full attitude compensation	$\delta\omega_{\mathrm{j}} = \delta\omega_{\mathrm{k}} = = 5 \times 10^{-7}$	2.5×10^{-9}	2.0×10^{-13}

In the concurrent case, the Coriolis effect is dominated by the large cloud velocity and is insensitive to attitude compensation. This means that the only possibility for a CAI accelerometer to outperform the MicroSTAR accelerometer, which has a precision of $2 \times 10^{-12}\mathrm{m/s^2}$ (cf. Section 8.3.1.2), is to consider full attitude compensation and zero atom cloud velocity provided by the sequential mode of operation. This choice limits the measurement cycle to be equal to the interrogation time, as explained in Section 8.3.2.1.

To make the concurrent mode of operation competitive, one would have to reduce the initial cloud velocity to at least 10^{-5} m/s for the Coriolis effects to reduce to the level of 10^{-12} m/s^2. This extremely slow velocity would increase the sampling time prohibitively; one may as well cycle through interferometry and atom production in a sequential way. The only other option is to decrease the attitude uncertainty by 3 orders of magnitude, which is very technically challenging for classic attitude sensors.

For CAI gradiometry, the effect of the Coriolis accelerations in Equation (53) is:

$$\sigma_{V_{\mathrm{Cor}}} = \frac{2}{L_{GG}} \sigma_{\mathrm{Cor}}, \qquad (77)$$

which effectively means that noise in the gravity gradients is a factor of 4 worse compared to CAI accelerometers, assuming $L_{GG} = 0.5\mathrm{m}$. In addition to that, the problem is exacerbated by the small gravity gradient time-variable signal shown in Figure 8-8. A gradiometer operating in sequential mode with full attitude compensation would have $\sigma_{V_{\mathrm{Cor}}} = 0.8\,\mathrm{mE} = 8.0 \times 10^{-13}\mathrm{s^{-2}}$, which is insufficient to sense the time-variable gravity field. We note that this discussion is exclusively based on the effect of the Coriolis force, with no regard to the CAI interferometric sensitivity discussed in Section 8.3.2.

The amplitude of the effect of the centrifugal accelerations is $\sigma_{\Omega^2} = \sqrt{8}\delta\omega\sigma_{\omega}$, which follows from Equation (53). Continuing with the assumption that the angular rate has a noise of $\sigma_{\omega} = 5 \times 10^{-8}\mathrm{rad/s}$ and that ω is related to the tilting mirror compensation $\delta\omega = 5 \times 10^{-7}\mathrm{rad/s}$, we expect $\sigma_{\Omega^2} = 0.071$ mE. Consequently, unlike the Coriolis forces, the centrifugal accelerations do not limit the CAI gradiometer's sensitivity to temporal variations of the gravity field.

11.2. LL-SST

In this analysis, we include the effects of attitude uncertainty presented in Section 10.1, for which the magnitude of non-gravitational accelerations is important. We consider the 3 scenarios motivated in Section 16: the RMS of the non-gravitational accelerations experienced at 230 km, those experienced roughly at the same altitude with a 1D DFC system similar to GOCE, and the residual non-gravitational accelerations with a 3D DFC system.

11.2.1. ELECTROSTATIC ACCELEROMETRY

We start our analysis of ll-SST future gravimetric missions with the case of electrostatic accelerometry. The three DFC scenarios differently amplify the attitude errors σ_ω, for which we assume 3 scenarios: DWS of LISA (Section 8.1.3.1), DWS of GRACE-FO (Section 8.1.3.2), and no DWS. In all scenarios, the measurements of the sensors above are optimally combined with the attitude measurements from the star tracker (Section 8.1.1), Astrix 200 laser gyroscope (Section 8.1.2), and accelerometer (Section 8.1.4). The results are shown in Figure 11-1, along with the errors of the MicroSTAR accelerometer (Section 8.3.1.2) and the predicted performance of the ISR instrument in 2040 (Section 8.2.4).

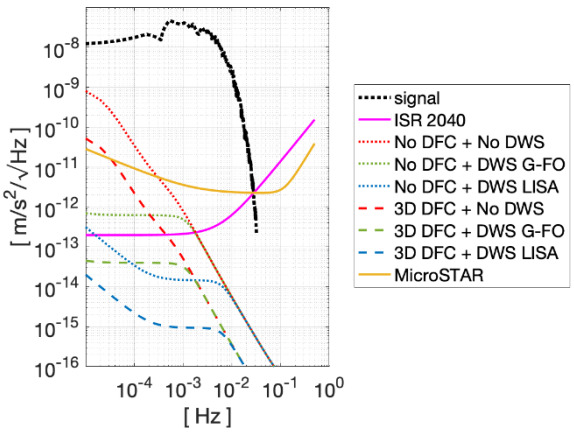

Figure 11-1: Effect of the attitude errors for no (red, blue and green dotted lines) and 3D (red, blue and green dashed lines) drag-free control (DFC) with three different combinations of attitude instruments indicated in the legend plus the attitude derived from the μASC star tracker (Section 8.1.1) and accelerometer (Section 8.1.4), compared to the errors of the accelerometer (Section 8.3.1.2, solid yellow line), ISR errors predicted for 2040 (Section 8.2.4, solid pink line) and the estimated time-variable signal magnitude (dotted black line).

We note that the case of the 1D DFC system has been omitted in Figure 11-1 because they are identical to the *no DFC* scenario since the y and z-axis non-gravitational accelerations are relevant to the case the ISR axis is (roughly) aligned with the x-direction. Those are the same for both DFC scenarios, cf. Equation (65).

The main message of Figure 11-1 is that the signal composed of the Atmosphere, Ocean, Hydrology, Ice and Solid-Earth (AOHIS) components of the time-variable gravity field model proposed by Dobslaw et al. (2016), is fully observed until 30mHz, or roughly spherical harmonic (SH) degree 170, assuming sufficiently high dense ground track coverage in a sufficiently short period. At this frequency, the signal represented by the black dotted line crosses both the errors of the ISR instrument and of the accelerometer. More importantly, the

high accuracy of the ISR instrument is not utilized below this frequency because of the insufficient accelerometer performance.

The attitude errors are insignificant for the majority of the scenarios. We predict that the need for DFC is only necessary if DWS is not available, which is unlikely since that has already been demonstrated for GRACE-FO. More important are the attitude determination errors, particularly at low frequencies. In this respect, the availability of a DWS is of special importance because it actively reduces the amplitude of attitude errors at low frequencies.

11.2.2. QUANTUM ACCELEROMETRY

In order to make complete use of the high accuracy of the ISR instrument predicted for 2040 (Section 8.2.4), we propose the CAI accelerometer indicated in Table 11-2, with one order of magnitude increase in the number of atoms and the doubling of the momentum space separation. We indicate the updated parameters in bold.

Table 11-2: CAI parameters: ll-SST case.

Parameter	Equation	Symbol	Value
Laser wavelength	(16)	λ	780 nm
Number of atoms	(17)	N	10^7
Interferometer contrast	(17)	C	0.8
Degree of entanglement	(17)	α	0.25
Momentum space separation	(18)	β	2
Interrogation time	(19)	T	5 s
Measurement cycle period	(20)	T_{cycle}	1 s
Atom thermal velocity	(37)(38)	$v_{\text{atom, therm}}$	10^{-6} m/s
Initial cloud velocity error	N/A	$\sigma_{v_{\text{cloud,initial}}}$	10^{-7}m/s
Cloud velocity	(39)	v_{cloud}	0 or 2.5 cm/s
Attitude accuracy degradation factor	(40)	f_ω	10

We selected the parameters in Table 11-2 so that the noise amplitude of the CAI accelerometer is below the noise floor of the ISR 2040 instrument, as shown in Figure 11-2. For this analysis, we maintained the DFC and attitude scenarios of Section 11.2.1, with the exception that the accelerometer-derived attitude is not available. For the Coriolis effects, we considered only one scenario: DWS of GRACE-FO (Section 8.1.3.2), tracker (Section 8.1.1), and Astrix 200 laser gyroscope (Section 8.1.2); the case with LISA DWS yields a reduced amplitude of the Coriolis effects (not shown) but with no change to the interpretation of the results.

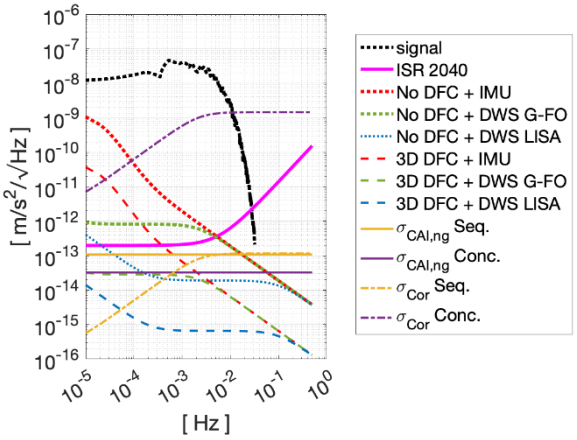

Figure 11-2: Comparison of the effect of attitude errors (dotted and dashed red, blue and green lines, Section 10.1) with the ISR errors predicted for 2040 (Section8.2.4, solid pink line, identical to Figure 11-1) and the estimated time-variable signal magnitude (dotted black line, identical to Figure 11-1), with the errors of the CAI accelerometer operating under the sequential mode (yellow lines) and concurrent mode (purple lines, cf. Section 8.3.2.1), distinguished between the CAI sensitivity (solid purple and yellow lines, Section 8.3.2) and Coriolis effects (dot-dashed purple and yellow lines, Section 9.1.2)

In the case of the CAI accelerometer operating in concurrent mode, the noise amplitude is dominated by the Coriolis (legend "σ_{cor} Conc.") effect due to the non-zero cloud velocity, as explained in Section 11.1, with a noise floor two orders of magnitude above the CAI sensitivity (legend "$\sigma_{\mathrm{CAI,ng}}$ Conc."). With such an instrument, not even GRACE's KBR would operate at full capacity, cf. Figure 8-4. It should be noted that with LISA DWS, it would be possible to use GRACE-FO's LRI with no reduced performance (not shown). In contrast, this instrument operating in sequential mode has a sensitivity (legend "$\sigma_{\mathrm{CAI,ng}}$ Seq.") a factor of 3 worse than in concurrent mode, as a result of the reduced sampling rate, Equation (20), but a much-reduced effect of the Coriolis accelerations (legend "σ_{cor} Seq."), with a noise floor two orders of magnitude below (4 orders of magnitude if compared to the Coriolis effects of the concurrent mode of operation) and reaching the amplitude of the CAI sensitivity at 3 mHz.

As for attitude and DFC options, the situation is much more demanding than electrostatic accelerometry. For quantum accelerometry, there is a need for LISA-level DWS if DFC is unavailable (legend *No DFC + DWS LISA*). If 3D DFC is available, GRACE-FO's DWS is sufficient (legend *3D DFC + DWS G-FO*). This illustrates the strict attitude requirements that the increased sensitivity of quantum accelerometers demands.

The temporal signal is resolved up to 30 mHz, or SH degree 170, as is the case with the electrostatic case (Section 11.2.1) because at those frequencies the LTI is the limiting factor. Unlike the electrostatic case, the quantum accelerometer is more accurate than the LTI at all frequencies, and the time-variable signal is measured with a Signal-to-Noise ratio (SNR) of at least 10^4 up to 10 mHz (SH degree 57).

11.3. GRADIOMETRY

In Section 11.1, we quantify the effect of the Coriolis accelerations $\sigma_{V_{\mathrm{Cor}}}$ under the assumption of white noise for the attitude measured by the Astrix 200 laser gyroscope. In reality, the spectra of the errors of this instrument are far from showing constant amplitude with frequency, cf. Section 8.1.2. Additionally, the combination with other attitude instruments was not quantified.

We do not consider classic gradiometry because electrostatic accelerometers lack the necessary accuracy to observe the time-variable gravity signal, as shown in Figure 8-8.

We compare the error spectra of the Coriolis and centrifugal terms with the CAI sensitivity in Table 11-2, thus making the ll-SST (discussed in Section 11.2.2) and gradiometry cases directly comparable. We only consider the sequential mode of operation (cf. Section 8.3.2.1) because of the destructive effect of the Coriolis accelerations already demonstrated for the ll-SST case. For the effect of attitude uncertainty presented in Section 10.2, we consider the gravity gradient signal amplitudes presented in Section 17. Unlike the ll-SST case, drag compensation is not relevant to the errors we analyse in this section because it only affects the non-gravitational signal amplitude. We consider that attitude is measured with the star tracker (Section 8.1.1), Astrix 200 laser gyroscope (Section 8.1.2), and accelerometer (Section 8.1.4). We include the attitude derived from the accelerometer since the demonstration of an early CAI gradiometer in space would benefit from the validation with proven instruments, such as an electrostatic accelerometer. Additionally, this instrument reduces the amplitude of the attitude errors above 0.7 mHz, cf. Figure 8-1, which is critical for collecting the small time-variable gravity field disturbances. The results of this analysis are presented in Figure 11-3.

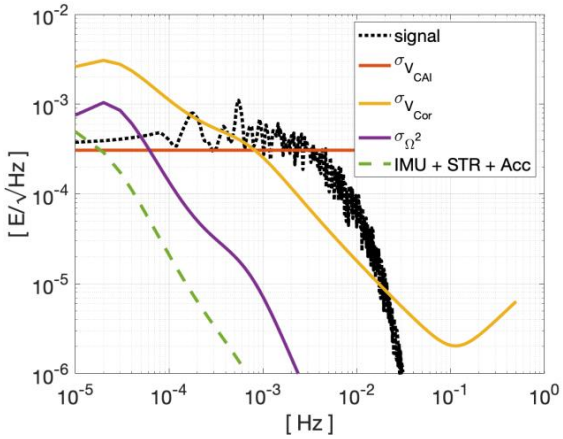

Figure 11-3: Comparison of the effect of attitude errors (dashed green line, Section 10.2) with the time-variable gravity gradient signal (dotted black line, same as Figure 8-8) gradiometer CAI sensitivity (red line, Section 9.2.2), the Coriolis effect (yellow line, Section 9.2.2) and the effects of centrifugal accelerations (purple line, Section 9.2.2), as measured by the IMU (Section 8.1.2), star tracker (Section 8.1.1) and attitude derived from the electrostatic accelerometer (Section 8.1.4).

Although the gradiometer CAI sensitivity is barely enough to resolve time-variable gravity signal up to 3 mHz, corresponding roughly to SH degree 17, the Coriolis effects make it impossible to observe this signal below 0.4 mHz or SH degree 2. The effects of attitude uncertainty are at least an order of magnitude below the Coriolis effects and only surpass the magnitude of the gradiometer CAI sensitivity below 0.02 mHz. Of note is that the Coriolis errors (and those associated with centrifugal and attitude errors) are only a function of the attitude sensors and remain the same even if more accurate CAI gradiometers are considered.

In contrast to the ll-SST case using quantum accelerometers (Section 11.2.2), where the complete signal spectrum is resolved with a high SNR, the quantum gradiometer with the same CAI parameters is barely able to resolve the time variable signal, with an SNR mostly between 1 and 2, peaking at 3 and dipping at 0.5 at some frequencies.

This example reinforces that the high accuracy of all instruments is critical to the success of CAI gradiometry. Although quantum technology may allow for extremely high CAI sensitivities, a proportional improvement of the attitude sensors is necessary.

12. NOISE MODELS AT PRODUCT LEVEL

12.1. NOISE MODEL X1

We combined the most promising and interesting-to-study sensor suites for the X1 noise model. An overview of the sensor suites is presented in Table 12-1. Upon request by ESA, we created three variants of the ll-SST noise model, labelled X1.1, X1.2, and X1.2. They differ only in the assumed ISR performance, as detailed in Table 12-2. The noise ASDs were derived as described in the previous sections and are shown in Figure 12-1 for gravity gradiometry and in Figure 12-2 for ll-SST.

Table 12-1: Overview of sensor suites and assumptions on which the X1 noise models are based.

Observation concept	Gravity gradiometry		ll-SST	
Instrument type	Attitude	Instrument	Attitude	Instrument
Classic	• NGGM accelerometer requirement • IMU • Star sensor	• NGGM accelerometer requirement	Drag compensation • 1D • 3D	• NGGM accelerometer requirement • ISR see Table 12-1
Quantum	• IMU • Star sensor	• CAI accelerometer scenario 127	• LISA DWS • GRACE-FO DWS • IMU • Star sensor	• CAI accelerometer scenario 127 • ISR see Table 12-1

Table 12-2: ISR performance of noise model X1, including variants X1.1, X1.2, and X1.3

Noise model	ISR
X1	NGGM LRI requirement
X1.1	NGGM 2033 performance
X1.2	GRACE KBR
X1.3	GRACE-FO LRI

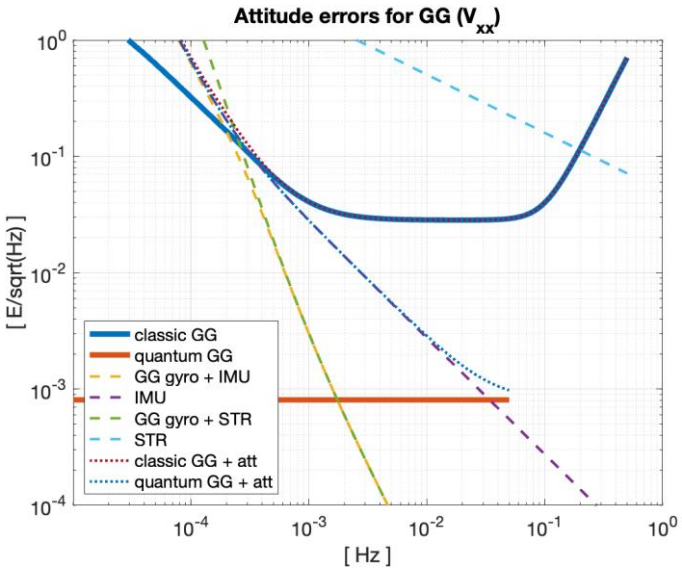

Figure 12-1: X1 noise model for classic and quantum gravity gradiometry

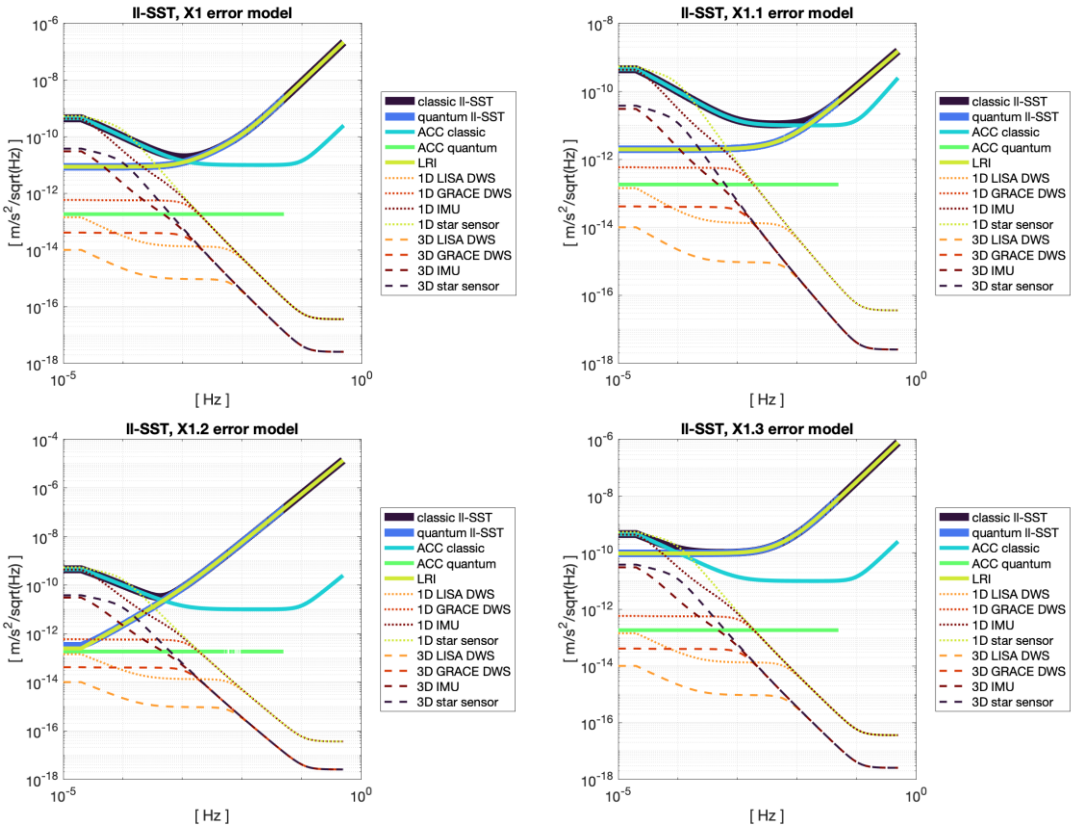

Figure 12-2: X1 noise model for classic and quantum ll-SST (cf. Table 12-2 for the noise model variants)

12.2. NOISE MODEL X2

The noise model X2 intends to explore the possibilities of CAI technology. We propose the instruments shown in Table 12-3, which intend to define the technological requirements of CAI to make it relevant for satellite gravimetry.

Table 12-3: Overview of sensor suites and assumptions on which the X2 noise models are based. The attitude-induced errors (*) are for illustration only and not included in X2 because it is not dominant by design.

Mission type	Gravity Gradiometry		ll-SST	
	attitude-induced (*)	instrument	attitude-induced (*)	instrument
Classic	No reasonable options for time-variable gravity field retrieval		• Drag compensation: 1D • Attitude: IMU+μASC	• acc: NGGM • ISR: NGGM-2040
Quantum	CPC-CAI	GG: Scenario 104	• Drag compensation: 1D • Attitude: LISA DWS+IMU+μASC	• acc: Scenario 95 • ISR: NGGM-2040

The CAI parameters for Scenarios 104 (assumed for gravity gradiometry) and 95 (assumed for ll-SST) are listed in Table 12-4.

Table 12-4: CAI parameters considered in X2

Parameter	Scenario 104 (GG)	Scenario 95 (ll-SST)
N_{atoms}	10^8	10^7
T [s]	5	5
β	4	4
α	0.25	0.25
C	0.8	0.8
Cost	0.26	0.21

12.2.1. CLASSIC LL-SST

As shown in Figure 12-3, the classic accelerometer (yellow solid line) is the bottleneck, making it impossible to take advantage of the highly accurate ll-SST predicted to be available in 2040 (red solid line). As a result of the relatively high errors of the MicroSTAR accelerometer, it is sufficient to have a 1D drag compensation combined with the IMU (dotted red line).

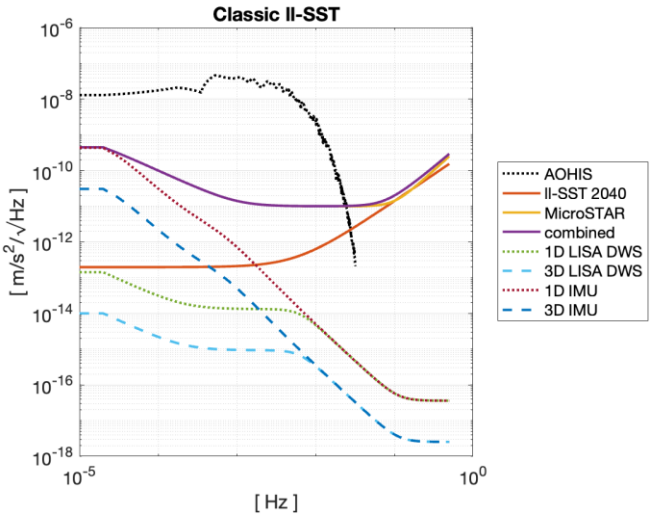

Figure 12-3: Error for classic ll-SST in the X2 noise model.

12.2.2. LL-SST WITH QUANTUM GRADIOMETRY

In contrast with classic accelerometry, quantum accelerometry allows for much more accurate measurements of the non-gravitational accelerations, if the CAI parameters listed in Table 12-4 are implemented. In that case, the only option is to use the sequential mode, which supresses the Coriolis effects substantially (green dash-dotted line), while the concurrent mode amplifies them (light blue dash-dotted line) up to 2 orders of magnitude above the ISR errors (red line).

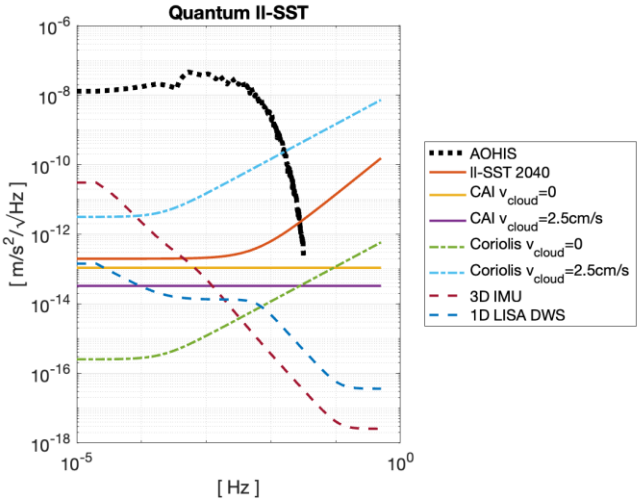

Figure 12-4: Error for ll-SST with quantum accelerometry in the X2 noise model.

We also show that 3D drag compensation combined with the IMU would dominant the errors below 0.5 mHz (red dashed line), which can be avoided by considering 1D drag compensation with a LISA-DWS (blue dashed line). Of note is that in both options, the IMU and μASC star-tracker are considered.

13. SUMMARY

In this study, we model the sensitivity of a CAI accelerometer as a function of interferometry contrast, degree of entanglement, number of atoms, momentum space separation and interrogation period (Section 8.3.2). We assume the CAI gradiometer is composed of two CAI accelerometers in the form of two cloud-pairs in the same interferometric chamber. In this way, we model quantum gradiometry in a similar way as classic gradiometry, i.e., that the latter is composed of two electrostatic accelerometers. One important difference is that a CAI accelerometer is inherently a one-dimensional instrument, unlike the electrostatic accelerometer. However, this is irrelevant for the diagonal components of the gravity gradient tensor. With the assumed model for CAI sensitivity, we predict a noise level of $\sigma_{\mathrm{CAI,ng}} = 3.2 \times 10^{-14}\mathrm{m/s^2}$ with the CAI parameters in Table 11-2, where notably the degree of entanglement is $\alpha = 0.25$, the number of atoms is $N = 10^7$, and the momentum space separation $\beta = 2$ associated with a second atom. This example scenario intends to illustrate a possible path for the development of CAI instruments with increasing accuracy and their capabilities for gradiometry, which are discussed in the following paragraphs.

In order to reduce the effects of inaccurately known attitude rates on Coriolis accelerations in quantum instruments, defined analytically in Section 9.1.2.1 for CAI accelerometers and in Section 9.2.2.1 for CAI gradiometers, we distinguish between concurrent and sequential modes of operation, with the former allowing for a higher sampling rate and accuracy. The latter minimises atom cloud velocity and, consequently, Coriolis accelerations (Section 8.3.2.1). In Section 11.1, we demonstrate that CAI accelerometry operating in the concurrent mode results in prohibitively high effects resulting from the Coriolis accelerations, limiting the sensitivity of any CAI accelerometer to $\sigma_{\mathrm{Cor}} = 2.5 \times 10^{-9}\ \mathrm{m/s^2}$, for which we assume an initial cloud velocity error of $\sigma_{v_{\mathrm{cloud,initial}}} = 10^{-7}\mathrm{m/s}$, a thermal cloud velocity of $v_{\mathrm{atom,therm}} = 10^{-6}\ \mathrm{m/s}$ and transverse cloud velocity of $v_{\mathrm{cloud}} = 2.5\mathrm{cm/s}$. For the sequential mode of operation, the cloud velocity is solely associated with thermal motion, and the Coriolis effects are limited to $\sigma_{\mathrm{Cor}} = 2.0 \times 10^{-13}\mathrm{m/s^2}$, including the effect of a lower sampling rate than the concurrent operational mode. This requires full attitude compensation with tilting mirrors, which reduce the satellite's attitude rates down to $\delta\omega = 5 \times 10^{-7}\mathrm{rad/s}$, assumed to be one order of magnitude worse than what the high-performance Astrix 200 laser gyroscope can measure (Section 8.1.2). Although such a CAI instrument is well suited as an accelerometer for ll-SST, it is unable to measure temporal gravity changes as a gradiometer since the sensitivity would be limited to $\sigma_{V_{\mathrm{Cor}}} = 0.8$ mE for a distance between could-pairs (i.e., the gradiometer arm length) of $L_{GG} = 0.5\mathrm{m}$. In Section 11.2.2, we consider a CAI accelerometer with increased performance operating in sequential mode to have a sensitivity of $\sigma_{\mathrm{CAI,ng}} = 1.1 \times 10^{-13}\mathrm{m/s^2}$ that is not significantly limited by the effects of the Coriolis accelerations, since it they have an amplitude of $\sigma_{Cor} = 1.2 \times 10^{-13}\ \mathrm{m/s^2}$. This means that the LTI predicted for 2040 is not hampered in any way, down to the sub-orbital frequencies. In contrast, in the case of ll-SST with an electrostatic accelerometer, Section 9.1.1, the MicroSTAR electrostatic accelerometer dominates the noise spectrum in all the frequencies below 30 mHz. Of note is that in either case, the signal amplitude is at least two orders of magnitude above the total noise, and the system is sensitive to the temporal gravity field up to SH degree 170.

We presented electrostatic and quantum accelerometers for ll-SST and gradiometer satellite mission concepts, modelling the measurements and their errors analytically (Section 9). The attitude determination was given special attention, particularly the modelling of the accelerometers and gradiometers for this purpose, as well as associated errors. For electrostatic

accelerometers, the instrument provides attitude information directly since there are multiple electrodes in each facet of the proof mass cavity (Section 8.1.4). On the other hand, no attitude data can be measured by a quantum accelerometer. For classic gradiometry, attitude is estimated with one order of magnitude better accuracy than the electrostatic accelerometer (Section 9.2.1.2). For quantum gradiometry, we demonstrate that 12 uniaxial CAI gradiometers are needed to uniquely resolve the attitude of the satellite (Section 9.2.2.2).

We considered the errors related to the rotation of the measurements in the body (for gradiometry) or local (for ll-SST) frames to the Earth corotating frame (Section 10), which are of importance given the high accuracy of the measurements and the potential large acceleration or gravity gradient signal at LEO altitudes. These errors tie the signal amplitude of non-gravitational accelerations (for the case of accelerometers) or gravity gradient amplitudes (for gradiometry) with the attitude accuracy. For those cases when attitude measurements have limited accuracy, e.g., classic attitude sensors, while the signal can be measured with increased accuracy, e.g., quantum sensors, these errors become important. This is the case with ll-SST equipped with a CAI accelerometer, Section 11.2.2, where the need for a 3D DFC system is required in the case the attitude derived with the DWS is retrieved with accuracy comparable to what GRACE-FO is capable; if this can be done with an accuracy predict for LISA, then no DFC is necessary. For quantum gradiometers, the attitude errors are not significant, as shown in Section 11.3. We apply the CAI parameters derived for the case of ll-SST to quantum gradiometry in, using the CAI operating in sequential mode. We demonstrated that, unlike the case for ll-SST, this instrument is barely sensitive enough to resolve temporal changes in Earth's gravity. The maximum SH degree it is sensitive to is 17, and the Coriolis accelerations make it impossible to measure spatial features with length associated with SH degree 2 or longer. This is an illustrative example of the much-reduced gravity gradient signal amplitude, compared to gravitational accelerations, to which ll-SST is sensitive.

We recognise that there are important technological challenges associated with the solutions considered in this study. We have generally neglected such details because we restrict our analysis to the conceptual level. The obvious consequence is the high cost for the necessary technical and engineering developments, most notably those associated with i) the highly accurate rotation compensation provided by the tilting mirrors and ii) the colling of the atom cloud during the BEC preparation that is required to reduce the thermal velocity of the atoms as assumed in this study. We also note that we did not model the loss of interferometric contrast associated with the scenarios without rotation compensation since that parameter is specific to the design of the instrument.

Nevertheless, we have demonstrated that the effects of inaccurately measured attitude in the Coriolis accelerations are of paramount importance to the success of the CAI satellite gravimetry, such that any CAI concept operating in concurrent mode can never have its sensitivity accurately determined, even in the quiet environment of space. For demonstration purposes of CAI technology to measure the time-variable gravity field, the best option is the ll-SST measurement concepts and a CAI accelerometer operating in sequential mode because this requires less demanding CAI parameters. With the progress of laser metrology, this is still the best option to ensure the accuracy of the LTI instrument is fully exploited since the parallel development of CAI technology allows for comparable accuracies.

14. APPENDIX – DERIVATIONS

14.1. CAI ACCELEROMETER OBSERVATION EQUATION

Assume that the axis of the Raman laser is aligned with the i-axis:

$$\frac{\boldsymbol{k}_{\text{eff}}}{k_{\text{eff}}} = \boldsymbol{e}_i.$$

Starting from Equation (25):

$$\Phi = \boldsymbol{k}_{\text{eff}} \cdot (\boldsymbol{a}_{\text{cloud}} - \boldsymbol{a}_{\text{mirror}})T^2$$

The non-gravitation accelerations $\boldsymbol{a}_{\text{ng}} = \boldsymbol{a}_{\text{mirror}}$ project along $\boldsymbol{e}_i$ are given by:

$$\Phi = \boldsymbol{k}_{\text{eff}} \cdot \left(\boldsymbol{a}_{\text{cloud}} - \boldsymbol{a}_{\text{ng}}\right)T^2$$

$$\frac{\Phi}{k_{\text{eff}}} = \frac{\boldsymbol{k}_{\text{eff}}}{k_{\text{eff}}} \cdot \left(\boldsymbol{a}_{\text{cloud}} - \boldsymbol{a}_{\text{ng}}\right)T^2$$

$$\frac{\Phi}{k_{\text{eff}}T^2} = \boldsymbol{e}_i \cdot \left(\boldsymbol{a}_{\text{cloud}} - \boldsymbol{a}_{\text{ng}}\right) = \boldsymbol{e}_i \cdot \boldsymbol{a}_{\text{cloud}} - \boldsymbol{e}_i \cdot \boldsymbol{a}_{\text{ng}}$$

$$\boldsymbol{e}_i \cdot \boldsymbol{a}_{\text{ng}} = -\frac{\Phi}{k_{\text{eff}}T^2} + \boldsymbol{e}_i \cdot \boldsymbol{a}_{\text{cloud}}$$

Replacing the acceleration of the atom cloud is given by Equation (27) in the equation above, which results in Equation (31):

$$\boldsymbol{e}_i \cdot \boldsymbol{a}_{\text{ng}} = -\frac{\Phi}{k_{\text{eff}}T^2} + \boldsymbol{e}_i \cdot \left(-\left(V - \boldsymbol{\Omega}^2 - \dot{\boldsymbol{\Omega}}\right)(\boldsymbol{r}_{\text{cloud}} - \boldsymbol{r}_{\text{CoM}}) + 2\boldsymbol{\omega} \times \boldsymbol{v}_{\text{cloud}}\right)$$

14.2. CAI GRADIOMETER OBSERVATION EQUATION

From Equation (48):

$$\frac{\Phi_{i,l}}{k_{\text{eff}}T^2} = \boldsymbol{e}_i \cdot \left(-\boldsymbol{a}_{\text{ng,l}} - \left(V - \boldsymbol{\Omega}^2 - \dot{\boldsymbol{\Omega}}\right)\left(\boldsymbol{r}_{\text{cloud,l}} - \boldsymbol{r}_{\text{CoM}}\right) + 2\boldsymbol{\omega} \times \boldsymbol{v}_{\text{cloud,l}}\right),$$

the phase measurement of cloud l is:

$$\Phi_{i,l} = k_{\text{eff}}T^2\boldsymbol{e}_i \cdot \left(-\boldsymbol{a}_{\text{ng,l}} - \left(V - \boldsymbol{\Omega}^2 - \dot{\boldsymbol{\Omega}}\right)\left(\boldsymbol{r}_{\text{cloud,l}} - \boldsymbol{r}_{\text{CoM}}\right) + 2\boldsymbol{\omega} \times \boldsymbol{v}_{\text{cloud,l}}\right),$$

and the differential measurement $\delta\Phi_i$ is:

$$\delta\Phi_i \equiv \Phi_{i,1} - \Phi_{i,2} =$$

$$k_{\text{eff}}T^2\boldsymbol{e}_i \cdot \left(-\boldsymbol{a}_{\text{ng,1}} - \left(V - \boldsymbol{\Omega}^2 - \dot{\boldsymbol{\Omega}}\right)\left(\boldsymbol{r}_{\text{cloud,1}} - \boldsymbol{r}_{\text{CoM}}\right) + 2\boldsymbol{\omega} \times \boldsymbol{v}_{\text{cloud,1}}\right) -$$

$$k_{\text{eff}}T^2\boldsymbol{e}_i \cdot \left(-\boldsymbol{a}_{\text{ng,2}} - \left(V - \boldsymbol{\Omega}^2 - \dot{\boldsymbol{\Omega}}\right)\left(\boldsymbol{r}_{\text{cloud,2}} - \boldsymbol{r}_{\text{CoM}}\right) + 2\boldsymbol{\omega} \times \boldsymbol{v}_{\text{cloud,2}}\right)$$

If $\boldsymbol{r}$ is measured from the CoM, $\boldsymbol{v}_{\text{cloud,1}}$ and $\boldsymbol{v}_{\text{cloud,2}}$ are both given by $\boldsymbol{v}_{\text{cloud,therm}}$(assumed to be a random variable):

$$\frac{\delta\Phi_i}{k_{\text{eff}}T^2} = \boldsymbol{e}_i \cdot \left(-\boldsymbol{a}_{\text{ng,1}} + \boldsymbol{a}_{\text{ng,2}} - \left(V - \boldsymbol{\Omega}^2 - \dot{\boldsymbol{\Omega}}\right)\delta\boldsymbol{r}_{\text{cloud}} + 2\boldsymbol{\omega} \times \boldsymbol{v}_{\text{cloud,therm}}\right)$$

Since $\boldsymbol{a}_{\text{ng,1}} = \boldsymbol{a}_{\text{ng,2}}$ and $\delta\boldsymbol{r}_{\text{cloud}} = L_{\text{GG}}\boldsymbol{e}_i$, we arrive at Equation (50):

$$\frac{\delta\Phi_i}{k_{eff}T^2} = \boldsymbol{e}_i \cdot \left(-\left(\boldsymbol{V} - \boldsymbol{\Omega}^2 - \dot{\boldsymbol{\Omega}}\right)L_{\mathrm{GG}}\boldsymbol{e}_i + 2\boldsymbol{\omega} \times \boldsymbol{v}_{\mathrm{cloud,therm}}\right)$$

The scalar evaluation of this expression requires:

$$\boldsymbol{V}\boldsymbol{e}_i = \begin{bmatrix} V_{ii} \\ V_{ij} \\ V_{ik} \end{bmatrix} \text{ and } \boldsymbol{e}_i \cdot (\boldsymbol{V}\boldsymbol{e}_i) = V_{ii},$$

$$\boldsymbol{\Omega}^2\boldsymbol{e}_i = \begin{bmatrix} -\omega_j^2 - \omega_k^2 \\ \omega_i\omega_j \\ \omega_i\omega_k \end{bmatrix} \text{ and } \boldsymbol{e}_i \cdot (\boldsymbol{\Omega}^2\boldsymbol{e}_i) = -\omega_j^2 - \omega_k^2,$$

$$\dot{\boldsymbol{\Omega}}\boldsymbol{e}_i = \begin{bmatrix} 0 \\ \dot{\omega}_k \\ \dot{\omega}_j \end{bmatrix} \text{ and } \boldsymbol{e}_i \cdot \left(\dot{\boldsymbol{\Omega}}\boldsymbol{e}_i\right) = 0,$$

$$\boldsymbol{\omega} \times \boldsymbol{v} = \begin{bmatrix} \omega_j v_k - \omega_k v_j \\ \omega_k v_i - \omega_i v_k \\ \omega_i v_j - \omega_j v_i \end{bmatrix} \text{ and } \boldsymbol{e}_i \cdot (\boldsymbol{\omega} \times \boldsymbol{v}) = \omega_j v_k - \omega_k v_j,$$

resulting in:

$$\frac{\delta\Phi_i}{k_{eff}T^2} = -\left(V_{ii} + \omega_j^2 + \omega_k^2\right)L_{\mathrm{GG}} + 2\omega_j v_{\mathrm{cloud,therm},k} - 2\omega_k v_{\mathrm{cloud,therm},j}$$

$$\frac{\delta\Phi_i}{k_{eff}T^2}\frac{1}{L_{\mathrm{GG}}} = -V_{ii} - \omega_j^2 - \omega_k^2 + \frac{2}{L_{\mathrm{GG}}}\omega_j v_{\mathrm{cloud,therm},k} - \frac{2}{L_{\mathrm{GG}}}\omega_k v_{\mathrm{cloud,therm},j}$$

Rearranging, produces Equation (51):

$$V_{ii} = -\frac{1}{L_{\mathrm{GG}}}\frac{\delta\Phi_i}{k_{eff}T^2} - \omega_j^2 - \omega_k^2 + \frac{2}{L_{\mathrm{GG}}}\left(\omega_j v_{\mathrm{cloud,therm},k} - \omega_k v_{\mathrm{cloud,therm},j}\right)$$

For a CAI gradiometer oriented along the other axes:

$$V_{jj} = -\frac{1}{L_{\mathrm{GG}}}\frac{\delta\Phi_j}{k_{eff}T^2} - \omega_k^2 - \omega_i^2 + \frac{2}{L_{\mathrm{GG}}}\left(\omega_k v_{\mathrm{cloud,therm},i} - \omega_i v_{\mathrm{cloud,therm},k}\right),$$

$$V_{kk} = -\frac{1}{L_{\mathrm{GG}}}\frac{\delta\Phi_k}{k_{eff}T^2} - \omega_i^2 - \omega_j^2 + \frac{2}{L_{\mathrm{GG}}}\left(\omega_i v_{\mathrm{cloud,therm},j} - \omega_j v_{\mathrm{cloud,therm},i}\right),$$

derived considering the following relations:

$\boldsymbol{e}_j \cdot \left(\boldsymbol{V}\boldsymbol{e}_j\right) = V_{jj}$ and $\boldsymbol{e}_k \cdot (\boldsymbol{V}\boldsymbol{e}_k) = V_{kk}$

$\boldsymbol{e}_j \cdot \left(\boldsymbol{\Omega}^2\boldsymbol{e}_j\right) = -\omega_i^2 - \omega_k^2$ and $\boldsymbol{e}_k \cdot (\boldsymbol{\Omega}^2\boldsymbol{e}_k) = -\omega_i^2 - \omega_j^2$

$$\boldsymbol{e}_j \cdot \left(\dot{\boldsymbol{\Omega}}\boldsymbol{e}_j\right) = \boldsymbol{e}_k \cdot \left(\dot{\boldsymbol{\Omega}}\boldsymbol{e}_k\right) = 0$$

$\boldsymbol{e}_j \cdot (\boldsymbol{\omega} \times \boldsymbol{v}) = \omega_k v_i - \omega_i v_k$ and $\boldsymbol{e}_k \cdot (\boldsymbol{\omega} \times \boldsymbol{v}) = \omega_i v_j - \omega_j v_i$

15. ANGULAR VELOCITY SIGNAL MAGNITUDE

To assess the signal size of the angular velocity, we make several assumptions on the orbit and attitude control. First, we assume an orbit at an altitude of 500 km, which gives an orbital period of $T_{orb} = 95\ min$. Next, we assume that the satellite is nadir pointing, which results in a mean pitch rate of:

$$\text{mean}(\omega_y) = 2\pi/T_{orb} = 1.1\ \text{mrad/s}. \tag{78}$$

Further, we assume that the satellite is pointing in the direction of atmospheric flow to minimise the effects of drag. The direction of the flow relative to the satellite is composed of the inertial velocity of 7.6 km/s and the corotation of the atmosphere of 500 m/s at the equator in an eastward direction. The worst case is a polar orbit, in which the inertial velocity is perpendicular to the velocity of the corotating atmosphere. The maximum yaw angle at the equation is $\arcsin(0.5\ km/7.6\ km) = 3.77°$. Since the velocity of the corotating atmosphere is zero at the pole, the yaw angle will also be zero. Thus, the yaw angle changes from 3.77° to 0° during a quarter of an orbit, i.e., by $3.77°/(T_{orb}/4) = 4.6 \times 10^{-5} rad/s$. To calculate the RMS of the angular velocity, we assume that the yaw angle varies like a sine function with an orbital period, i.e.:

$$\psi = 3.77° \sin(2\pi t/T_{orb}). \tag{79}$$

The angular velocity is the time derivative of that function:

$$\omega_z = \frac{\partial \psi}{\partial t} = 3.77°\ 2\pi/T_{orb} \cos(2\pi t/T_{orb}). \tag{80}$$

The integral of the squared function is:

$$\begin{aligned}
\int_0^{T_{orb}} \omega_z\, dt &= (3.77°\ 2\pi/T_{orb})^2 \int_0^{T_{orb}} \cos^2(2\pi t/T_{orb})\, dt \\
&= (3.77°\ 2\pi/T_{orb})^2 \frac{1}{2} \int_0^{T_{orb}} 1 - \sin(4\pi t/T_{orb})\, dt \\
&= (3.77°\ 2\pi/T_{orb})^2 \frac{1}{2} [t - 4\pi/T_{orb} \cos(4\pi t/T_{orb})]_0^{T_{orb}} \\
&= (3.77°\ 2\pi/T_{orb})^2 T_{orb}/2.
\end{aligned} \tag{81}$$

The RMS is then the square root of the integral divided by T_{orb}:

$$\text{RMS}(\omega_z) = \sqrt{\frac{1}{T_{orb}} \int_0^{T_{orb}} \omega_z\, dt} = 3.77° \frac{2\pi}{T_{orb}\sqrt{2}} = 5.1 \times 10^{-5}\ rad/s. \tag{82}$$

When magnetic torquers are the only means for attitude control, there is typically no control of the roll at the equator because the magnetic field lines are parallel to the roll axis. With that in mind, we assume that the RMS of the roll rate is:

$$\text{RMS}(\omega_x) = 0.1\ \text{mrad/s}.$$

16. NON-GRAVITATIONAL ACCELERATION SIGNAL MAGNITUDE

Some of the error propagations require assumptions of the non-gravitational acceleration signal size. Considering that aerodynamic accelerations are large at low altitudes, we use GOCE data as a worst-case scenario. Typical acceleration signal sizes are reported in Table 16-1.

Table 16-1: Non-gravitational signal size in nm/s^2, mean for long-track and standard deviation for cross-track and radial directions, for the case of the GOCE mission, considering 1D and (hypothetical) 3D drag control (Visser and van den IJssel 2016)**.**

[nm/s^2]	GOCE 230km	1D Drag Control	3D Drag Control
Along-track (mean)	10000	10	10
Cross-track (STD)	289	289	10
Radial (STD)	22	22	10

Referring to Christoph Steiger, Mardle, and Emanuelli (2014), the DFC of GOCE was estimated to reduce non-gravitation accelerations down to 1 nm/s^2. As such, the assumptions on 1D and 3D DFC shown in Table 16-1 are conservative.

17. GRAVITY GRADIENT SIGNAL MAGNITUDE

Assuming a LEO orbit, the signal amplitude of the (symmetric) gravity gradient tensor in the LHRF $\boldsymbol{V}^{(\mathrm{LHRF})}$ at 450km altitude is (e.g. Rosen 2021):

$$\mathrm{RMS}\left(\boldsymbol{V}^{(\mathrm{LHRF})}\right) \approx \begin{bmatrix} 1200 & 0 & 0 \\ & 1200 & 0 \\ & & 2400 \end{bmatrix} + \begin{bmatrix} 3.01 & 0.03 & 0.09 \\ & 4.22 & 4.38 \\ & & 7.23 \end{bmatrix} [E].$$

The first term is associated with the signal caused by the central term of the gravity field, and the static gravity field of the Earth causes the second term. We ignored the term caused by the temporal variations of the gravity field.

18. APPLICABLE DOCUMENTS, REFERENCE DOCUMENTS, AND PUBLICATIONS OF PART 3

18.1. APPLICABLE DOCUMENTS

[AD-1] Mission Requirements Document, Next Generation Gravity Mission as a Mass-change And Geosciences International Constellation (MAGIC) - A joint ESA/NASA double-pair mission based on NASA's MCDO and ESA's NGGM studies (2020). ESA-EOPSM-FMCC-MRD-3785

[AD-1] Scientific Readiness Levels (SRL) Handbook, Issue 1, Revision 0, 05-08-2015

[AD-2] Study of Cold Atom Interferometry (CAI) Gravity Gradiometer Sensor and Mission Concepts - ESA Contract 4000112677, Summary Report "Concept study and preliminary design of a cold atom interferometer for space gravity gradiometry"

[AD-3] Cold Atom Inertial Sensors: Mission Applications – ESA Contract 4000117930, Final Report TASI-SD-CAI-FR

[AD-4] Hybrid Atom Electrostatic System for Satellite Geodesy – ESA Contract 4000113573, Final Report RF_7-24721_DMPH

[AD-5] Hybrid Atom Electrostatic System for Satellite Geodesy Follow-On – ESA Contract 4000112290, Final Report RT 6/27346 DPHY

[AD-6] QSG_UR_SATM_v2.0.xlxs – ESA/EC Quantum Space Gravimetry User Requirements Science and Traceability Matrix v2.0 (2022)

[AD-7] Quantum Space Gravimetry for monitoring Earth's Mass Transport Processes (QSG4EMT). Project Proposal, Proposal No. TUM/2022-QSG4EMT, Technical University of Munich

18.2. REFERENCE DOCUMENTS

Abich, Klaus, Alexander Abramovici, Bengie Amparan, Andreas Baatzsch, Brian Bachman Okihiro, David C. Barr, Maxime P. Bize, et al. 2019. "In-Orbit Performance of the GRACE Follow-on Laser Ranging Interferometer." *Physical Review Letters* 123 (3): 031101. https://doi.org/10.1103/PhysRevLett.123.031101.

Airbus. 2022. "ASTRIX® 200 Specification Sheet." https://www.airbus.com/sites/g/files/jlcbta136/files/2022-02/ScE-AVIONICS-ASTRIX200v3_2022.pdf.

Amri, Sirine. 2022. "Optimized Matter-Wave Lensing of Quantum Gases for Precision Atom Sensors." Doctorate dissertation, Université Paris-Saclay. https://theses.hal.science/tel-03852963.

Carraz, Olivier, Christian Siemes, Luca Massotti, Roger Haagmans, and Pierluigi Silvestrin. 2014. "A Spaceborne Gravity Gradiometer Concept Based on Cold Atom Interferometers for Measuring Earth's Gravity Field." Atomic Physics. *Microgravity Science and Technology* 26 (3): 139–45. https://doi.org/10.1007/s12217-014-9385-x.

Christoph Steiger, Nic Mardle, and Pier Paolo Emanuelli. 2014. "GOCE End-of-Mission Operations Report." GO-RP-ESC-FS-6268.

Christophe, B., B. Foulon, F. Liorzou, V. Lebat, D. Boulanger, P.-A. Huynh, N. Zahzam, Y. Bidel, and A. Bresson. 2018. "Status of Development of the Future Accelerometers for Next Generation Gravity Missions." In *International Association of Geodesy Symposia*, 149:85–89. https://doi.org/10.1007/1345_2018_42.

Dahl, Katrin, Pelin Cebeci, Oliver Fitzau, Martin Giesberts, Christian Greve, Markus Krutzik, Achim Peters, et al. 2019. "A New Laser Technology for LISA." In *International Conference on Space Optics — ICSO 2018*, edited by Nikos Karafolas, Zoran Sodnik, and Bruno Cugny, 11180:11. SPIE. https://doi.org/10.1117/12.2535931.

Dobslaw, Henryk, Inga Bergmann-Wolf, Ehsan Forootan, Christoph Dahle, Torsten Mayer-Gürr, Jürgen Kusche, and Frank Flechtner. 2016. "Modeling of Present-Day Atmosphere

and Ocean Non-Tidal de-Aliasing Errors for Future Gravity Mission Simulations." *Journal of Geodesy* 90 (5): 423–36. https://doi.org/10.1007/s00190-015-0884-3.

Douch, Karim, Hu Wu, Christian Schubert, Jürgen Müller, and Franck Pereira dos Santos. 2018. "Simulation-Based Evaluation of a Cold Atom Interferometry Gradiometer Concept for Gravity Field Recovery." *Advances in Space Research* 61 (5): 1307–23. https://doi.org/10.1016/j.asr.2017.12.005.

Goswami, Sujata, Samuel P. Francis, Tamara Bandikova, and Robert E. Spero. 2021. "Analysis of GRACE Follow-On Laser Ranging Interferometer Derived Inter-Satellite Pointing Angles." *IEEE Sensors Journal* 21 (17): 19209–21. https://doi.org/10.1109/JSEN.2021.3090790.

Gross, Christian. 2012. "Spin Squeezing, Entanglement and Quantum Metrology with Bose–Einstein Condensates." *Journal of Physics B: Atomic, Molecular and Optical Physics* 45 (10): 103001. https://doi.org/10.1088/0953-4075/45/10/103001.

Herceg, M., P. S. Jørgensen, and J. L. Jørgensen. 2017. "Characterization and Compensation of Thermo-Elastic Instability of SWARM Optical Bench on Micro Advanced Stellar Compass Attitude Observations." *Acta Astronautica* 137 (April): 205–13. https://doi.org/10.1016/j.actaastro.2017.04.018.

Knabe, Annike, Manuel Schilling, Hu Wu, Alireza HosseiniArani, Jürgen Müller, Quentin Beaufils, and Franck Pereira dos Santos. 2022. "The Benefit of Accelerometers Based on Cold Atom Interferometry for Future Satellite Gravity Missions." In *International Association of Geodesy Symposia*, 213–20. https://doi.org/10.1007/1345_2022_151.

Kornfeld, Richard P., Bradford W. Arnold, Michael A. Gross, Neil T. Dahya, William M. Klipstein, Peter F. Gath, and Srinivas Bettadpur. 2019. "GRACE-FO: The Gravity Recovery and Climate Experiment Follow-On Mission." *Journal of Spacecraft and Rockets* 56 (3): 931–51. https://doi.org/10.2514/1.A34326.

Malossi, N., Q. Bodart, S. Merlet, T. Lévèque, A. Landragin, and F. Pereira Dos Santos. 2010. "Double Diffraction in an Atomic Gravimeter." *Physical Review A* 81 (1): 013617. https://doi.org/10.1103/PhysRevA.81.013617.

Massotti, Luca, Christian Siemes, Günther March, Roger Haagmans, and Pierluigi Silvestrin. 2021. "Next Generation Gravity Mission Elements of the Mass Change and Geoscience International Constellation: From Orbit Selection to Instrument and Mission Design." *Remote Sensing* 13 (19): 3935. https://doi.org/10.3390/rs13193935.

Müntinga, H., H. Ahlers, M. Krutzik, A. Wenzlawski, S. Arnold, D. Becker, K. Bongs, et al. 2013. "Interferometry with Bose-Einstein Condensates in Microgravity." *Physical Review Letters* 110 (9): 093602. https://doi.org/10.1103/PhysRevLett.110.093602.

Nicklaus, K., S. Cesare, L. Massotti, L. Bonino, S. Mottini, M. Pisani, and P. Silvestrin. 2019. "Laser Metrology Concept Consolidation for NGGM." In *International Conference on Space Optics — ICSO 2018*, edited by Nikos Karafolas, Zoran Sodnik, and Bruno Cugny, 11180:151. SPIE. https://doi.org/10.1117/12.2536071.

Peters, Achim, KY Chung, Steven Chu, and San Francisco. 1999. "Measurement of Gravitational Acceleration by Dropping Atoms." *Nature* 400: 849–52. https://doi.org/10.1038/23655.

Rosen, Mitchell David. 2021. "Analysis of Hybrid Satellite-to-Satellite Tracking and Quantum Gravity Gradiometry Architecture for Time-Variable Gravity Sensing Missions." Master Thesis, University of Texas at Austin.

Rummel, Reiner, Weiyong Yi, and Claudia Stummer. 2011. "GOCE Gravitational Gradiometry." *Journal of Geodesy* 85 (11): 777–90. https://doi.org/10.1007/s00190-011-0500-0.

Schütze, D., G. Stede, V. Müller, O. Gerberding, C. Mahrdt, B. Sheard, G. Heinzel, and K. Danzmann. 2013. "LISA-like Laser Ranging for GRACE Follow-On." *Astronomical Society of the Pacific Conference Proceedings* 467 (2003): 285–90. http://www.apc.univ-paris7.fr/~beckmann/Proceedings/Schutze.pdf.

Sheard, B. S., G. Heinzel, K. Danzmann, D. A. Shaddock, W. M. Klipstein, and W. M. Folkner. 2012. "Intersatellite Laser Ranging Instrument for the GRACE Follow-on Mission." *Journal of Geodesy* 86 (12): 1083–95. https://doi.org/10.1007/s00190-012-0566-3.

Stummer, C., T. Fecher, and R. Pail. 2011. "Alternative Method for Angular Rate Determination within the GOCE Gradiometer Processing." *Journal of Geodesy* 85 (9): 585–96. https://doi.org/10.1007/s00190-011-0461-3.

Szigeti, Stuart S., Onur Hosten, and Simon A. Haine. 2021. "Improving Cold-Atom Sensors with Quantum Entanglement: Prospects and Challenges." *Applied Physics Letters* 118 (14): 1–18. https://doi.org/10.1063/5.0050235.

Teixeira da Encarnação, João, Himanshu Save, Byron Tapley, and Hyung-Jin Rim. 2020. "Accelerometer Parameterization and the Quality of Gravity Recovery and Climate Experiment Solutions." *Journal of Spacecraft and Rockets* 57 (4): 740–52. https://doi.org/10.2514/1.A34639.

Trimeche, A., B. Battelier, D. Becker, A. Bertoldi, P. Bouyer, C. Braxmaier, E. Charron, et al. 2019. "Concept Study and Preliminary Design of a Cold Atom Interferometer for Space Gravity Gradiometry." *Classical and Quantum Gravity* 36 (21): 215004. https://doi.org/10.1088/1361-6382/ab4548.

Visser, P.N.A.M, and J.A. van den IJssel. 2016. "Orbit Determination and Estimation of Non-Gravitational Accelerations for the GOCE Reentry Phase." *Advances in Space Research* 58 (9): 1840–53. https://doi.org/10.1016/j.asr.2016.07.013.

Zhu, Zhu, He Liao, Haibo Tu, Xiaochun Duan, and Yanbin Zhao. 2022. "Spaceborne Atom-Interferometry Gravity Gradiometry Design towards Future Satellite Gradiometric Missions." *Aerospace* 9 (5): 253. https://doi.org/10.3390/aerospace9050253.

PART 4:

ANALYSIS OF THE ADDED VALUE OF QUANTUM SENSING TO EXISTING AND PLANNED MISSIONS

19. INTRODUCTION

The purpose of this document is to investigate the added value of quantum sensing to existing and planned gravity field satellite mission. For this, the applied methodologies with the made assumptions and the selected scenarios are described and the simulation results are shown, and an interpretation is provided. It refers to Task 3 of the SoW and WP 300 of the WBS. As input, it relies strongly on the outcome of Task 2 (for the instrument noise specification X1) and the MAGIC phase A science study [RD-1] (for reference noise specifications, basic constellations and background models).

This document is structured as followed: In section 2, all simulation-defining input items to all investigated simulations (i.e., orbit definitions, instrument noise models, background models and parametrizations) are characterized and structured with a logical naming scheme. Additionally, a list of simulated scenarios is appended. Section 2 is relevant for the complete WP 300. In section 3, the results of the investigated scenarios are depicted and interpreted, including results from postprocessing approaches (WPs 310, 321, 322). Section 4 provides background knowledge to the methodology used for the simulation of ll-SST and SGG and contains a validation and cross-validation of the simulation software of POLIMI and TUM is performed (WPs 331, 332).

20. SIMULATOR SETUP AND SCENARIO DEFINITIONS

In this section, the simulator setup is explained by defining all necessary input quantities for all simulated scenarios (SST & SGG) presented in this TN. This should provide the reader with a non-methodological overview of how the simulators work and what they expect as input. For a methodological overview on the simulators, the reader is referred to section 4 (providing more insights which are not necessarily needed to understand the results shown in section 3).
The simulator setup can be subdivided in four principal components: (1) orbit/constellation configuration, (2) instrument (noise) definition, (3) background model setup and (4) simulation settings/solution type. For each component variant used, acronyms are introduced which are used to form a unique scenario identifier. At the end of this section, all scenarios simulated in the different stages of this project will be listed, using the introduced naming convention. Since the presented simulator setup and naming scheme is used for all simulations, this section is relevant for all sub-WP of WP300.

20.1. ORBIT/CONSTELLATION CONFIGURATIONS

For simulation, orbits are defined as osculating Keplerian elements for a given moment in time. In the course of the simulation, these orbits are integrated using the force model resulting from the application of the appropriate background models (see 2.3). Orbit/constellation acronym prefix: ***o?***

20.1.1. MAGIC 3D_H

The baseline simulations in phase A are performed by using the 3d_H orbits from the MAGIC study [RD-1]. 3d_H defines a polar pair (PP) of satellites and inclined pair (IP) with 3- and 7-

day sub-cycles and a 31 day repeat cycle. The osculating Keplerian elements for 3d_H are (for PP sat. A, B and IP sat. A, B):

```
PLEASE NOTE THAT TIME SYSTEM IS UTC, NOT GPS (USED FOR SP3 FILES)

  DATE  GREENWICH TIME         A              E              I           RA ASC NODE      ARC PERIGEE      MEAN ANOMALY
 YYMMDD HHMM  SECONDS       (METERS)                     (DEGREES)       (DEGREES)        (DEGREES)        (DEGREES)
 020101 0000  0.000000     6846058.138  0.00165585454    88.997236132    359.981873073    28.199409842    331.085529881
 020101 0000  0.000000     6846061.861  0.00166631056    88.997236202    359.981889635    28.818288775    331.305620485
 020101 0000  0.000000     6815259.195  0.00086208786    70.016625375      3.971420249     4.992907115    354.288098763
 020101 0000  0.000000     6815262.582  0.00086477282    70.016622926      3.971830396     6.359334258    353.764506377
```

For more details on 3d_H, see [RD-1]. The constellation variants used for simulations are:
o3DH1: single polar pair scenario (for ll-SST)
o3DH2: double pair scenario (for ll-SST)
o3DH1A: single polar satellite A (for SGG)
o3DH2A: polar and inclined satellite A (for SGG)

20.1.2. MAGIC 5D_397_70 (5D_M)

By a request of ESA, the orbits for the baseline simulations in phase B are changed to the orbits of the 5d_397_70 scenario from the MAGIC study [RD-1]. This constellation is abbreviated in the following as 5d_M. 5d_M consists of the PP from the 5d_H constellation and the IP from the 5d_Mb constellation. 5d_M has a common 5 day sub-cycle and no common repeat cycle. The osculating Keplerian elements for 5d_M are (for PP sat. A, B and IP sat. A, B):

```
PLEASE NOTE THAT TIME SYSTEM IS UTC, NOT GPS (USED FOR SP3 FILES)

  DATE  GREENWICH TIME         A              E              I           RA ASC NODE      ARC PERIGEE      MEAN ANOMALY
 YYMMDD HHMM  SECONDS       (METERS)                     (DEGREES)       (DEGREES)        (DEGREES)        (DEGREES)
 020101 0000  0.000000     6871210.979  0.00163140827    88.997295029    359.981763638    27.778751589    331.509706265
 020101 0000  0.000000     6871208.124  0.00165231157    88.997295361    359.981802570    29.173743787    331.953783404
 020101 0000  0.000000     6780418.955  0.00087314057    70.016384998      2.339767172     5.455366210    353.820999362
 020101 0000  0.000000     6780416.219  0.00087823303    70.016370784      2.340690512     8.464575569    352.675180273
```

For more details on 5d_H, see [RD-1]. The constellation variants used for simulations are:
o5DM1: single polar pair scenario (for ll-SST)
o5DM2: double pair scenario (for ll-SST)
o5DM1A: single polar satellite A (for SGG)
o5DM2A: polar and inclined satellite A (for SGG)

20.1.3. GOCE G61D

GOCE real data (kinematic) orbit for validation purpose only, covering a 61 day cycle from 05.03.2010 to 06.05.2010. Data taken from ESA's official L1B data repository. Acronym: ***oG61D***

20.1.4. INCLINED INLINE CONSTELLATIONS V0 (IICXV0)

For WP400, larger inclined constellations are investigated. IICXv0 constellations represent a compromise between the number of inclinations and the number of pairs per constellation. For more information see TR D5. The orbits (in terms of initial state vectors) can be found in the projects data repository Data2. The constellation variants used for simulations are:
oIIC2V0: double pair scenario (1x 89°, 1x 70° incl.)
oIIC3V0: triple pair scenario (1x 89°, 2x 70° incl.)
oIIC6V0: 6 pair scenario (1x 89°, 2x 70°, 3x 40° incl.)

20.1.5. INCLINED INLINE CONSTELLATIONS V1 (IICXV1)

In contrast to IICXv0, IICXv1 constellations try to maximize the number of inclinations (having only one pair per inclination). For more information see TR D5. The orbits (in terms of initial state vectors) can be found in the projects data repository Data2. The constellation variants used for simulations are:
oIIC2V1: double pair scenario (89°, 70° incl.)
oIIC3V1: triple pair scenario (89°, 70°, 40° incl.)
oIIC6V1: 6 pair scenario (89°, 80°, 71°, 60°, 48°, 33° incl.)

20.1.6. POLAR ACROSS-TRACK CONSTELLATIONS V1 (PACXV1)

For WP400, also polar across-track SST constellations are investigated (PACXv1). For more information see TR D5. The orbits (in terms of initial state vectors) can be found in the projects data repository Data2. The constellation variants used for simulations are:
oPAC2V1: double pair scenario (2x 89°, 2x across-track)
oPAC3V1: triple pair scenario (3x 89°, 3x across-track)
oPAC6V1: 6 pair scenario (6x 89°, 6x across-track)

20.1.7. POLAR INLINE/ACROSS-TRACK CONSTELLATIONS V1 (PIACXV1)

In addition to across-track-only polar constellations, also combined polar inline/across-track SST constellations are investigated (PIACXv1). For more information see TR D5. The orbits (in terms of initial state vectors) can be found in the projects data repository Data2. The constellation variants used for simulations are:
oPIAC2V1: double pair scenario (2x 89°, 1x inline, 1x across-track)
oPIAC3V1: triple pair scenario (3x 89°, 1x inline, 2x across-track)
oPIAC6V1: 6 pair scenario (6x 89°, 3x inline, 3x across-track)

20.2. INSTRUMENT DEFINITIONS

The instrument noise for simulation purpose is defined by means of amplitude spectral densities. In a first stage of this project, a set of simplified noise models is introduced (see below, e.g. flat ASD curve for simplified CAI). These noise models are denoted as X0 models. These assumptions are then refined by the noise models denoted with X1 (as outcome from Task 2). The combination of all acronyms of the individual instruments (see below) used by a scenario forms the final combined instrument acronym (e.g., ***tGFOaMSaC11***).

20.2.1. LL-TRACKING

The following ll-tracking variants are considered. ll-tracking noise always refers to the measured distance between a pair of satellites. Note, the X[1-n] noise models are designed as combined product noise models containing already all relevant error sources (ll-tracking, acc., attitude, etc.). Thus, X[1-n] is introduced as ll-tracking noise. Tracking instrument acronym prefix: ***t?***

tGFO: (baseline, as within GRACE-FO, communicated by Vitali Müller, Oct., 2022)

$$lri_{GFO} = 2.2 \cdot 10^{-10} \frac{1}{\sqrt{f}} + 1 \cdot 10^{-12} \frac{1}{f^2} \quad \frac{m}{\sqrt{Hz}}. \tag{1}$$

tNG30: (next generation, ready by 2030, communicated by Vitali Müller, Oct., 2022)

$$lri_{NG30} = L \cdot 10^{-15} \frac{1}{\sqrt{f}} + 1 \cdot 10^{-13} \frac{1}{f^2} \quad \frac{m}{\sqrt{Hz}}. \tag{2}$$

tNG33: (next generation, ready by 2033, communicated by Vitali Müller, Oct., 2022)

$$lri_{NG33} = \frac{1}{2}\left(L \cdot 10^{-15} \frac{1}{\sqrt{f}} + 1 \cdot 10^{-13} \frac{1}{f^2}\right) \quad \frac{m}{\sqrt{Hz}}. \tag{3}$$

tMAGIC: (MAGIC GOAL performance, see [RD-1])

$$lri_{NG33} = L \cdot 10^{-13} \sqrt{\left(1 + \frac{10^{-4}}{f^2}\right)\left(1 + \frac{10^{-6}}{f^2}\right)} \quad \frac{m}{\sqrt{Hz}}. \tag{4}$$

tXn: product noise models ***Xn*** delivered by TUD (see WP200).

tM: product noise model for MAGIC by TUD (see WP200). Identical to ***tMAGICaMS.***

tX0: initial product noise model X0 used by TUM in phase A. Identical to ***tGFOaMSaC11.***

t0: error/noise free ll-tracking

20.2.2. ACCELEROMETERS

If applied, accelerometers are modelled at per-satellite level. Models which are meant as product noise (e.g. ***aMS***) are divided by a factor of $\sqrt{2}$ in the formulas given below to transform them into per-satellite models. Accelerometer instrument acronym prefix: ***a?***

aSS: "SuperStar" - Three equally good accelerometer axes with a noise ASD of: (baseline, as within GRACE, GRACE-FO, see [RD-1])

$$acc_{x,y,z} = 1 \cdot 10^{-10} \sqrt{1 + \frac{0.005\ Hz}{f}} \quad \frac{m}{s^2/\sqrt{Hz}}. \tag{5}$$

aMS: "MicroStar" – Product noise along the line of sight (LOS) between the two satellites of a pair: (baseline, NGGM performance within MAGIC, see [RD-1])

$$acc_{los} = 1 \cdot 10^{-11} \sqrt{\frac{\left(\frac{10^{-3}Hz}{f}\right)^2 \Big/ \left(\left(\frac{10^{-5}Hz}{f}\right)^2 + 1\right) + 1 + \left(\frac{f}{10^{-1}Hz}\right)^4}{2}} \ \frac{m}{s^2/\sqrt{Hz}} \tag{6}$$

aCx: simplified cold atom interferometer with white noise acc. behaviour at level x: (X0 model, max. assumed sampling rate 0.05Hz, all components identical)

$$acc_x = 10^{-x} \ \frac{m}{s^2/\sqrt{Hz}} \tag{7}$$

For X0, hybrid CAI/electrostatic instruments are investigated. E.g., ***aMSaC11*** denotes an optimally combined MicroStar/CAI11 instrument.

a0: error/noise free accelerometer

20.2.3. ABSOLUTE POSITIONING

Kinematic orbits/positions are always assumed to be available for ll-SST simulation. Positioning instrument acronym prefix: ***p?***
If not otherwise stated, positions are assumed to be known with an accuracy of 1cm (for all axis):

$$pos = 1 \cdot 10^{-2} \ \frac{m}{\sqrt{Hz}}. \quad \textbf{(8)}$$

Special case:

p0: error/noise free positioning

20.2.4. GRADIOMETERS

Gradient noise is simulated with 6 uncorrelated, possibly different noise ASDs of the components. Gradients are always assumed as "product-noise" models, containing all error components introduced by the complete measurement system. Gradiometer instrument acronym prefix: ***g?***

gGO: GOCE gradients, empirically derived from GOCE real data pre-fit residuals for a 61-day cycle (same as orbit ***oG61d***, individual ASD for each component)

gCx: simplified cold atom interferometer with white noise gradient behaviour at level x: (X0 model, max. assumed sampling rate 0.2Hz, all components identical)

$$grd_x = 10^{-x} \ \frac{1}{s^2/\sqrt{Hz}} \quad \textbf{(9)}$$

gCx[y]: as above, but just for specified component y. y might be XX, YY, ZZ, XY, XZ, YZ

gXn: (product noise models delivered by TUD, three main diagonals)

g0: error/noise free gradiometer (all components identical)

g0[y]: as above, but just for specified component y. y might be XX, YY, ZZ, XY, XZ, YZ

20.3. BACKGROUND MODELS AND ERROR ASSUMPTIONS

The background models and their errors are chosen to be in line with the models used within the MAGIC phase A science study. The simulated max. d/o of the spherical harmonic models is chosen to be identical with the max. d/o of the (static) parametrization (see 20.4). Background models acronym prefix: ***m?***

In the simulations the following variants are considered:
mPO: product-only, consisting only of static gravity field (no BGMEs, no time-variable field)
mFN: full-noise, consisting of all BGMs and BGMEs (see below)

20.3.1. BACKGROUND MODELS (BGM)

(Identical with MAGIC phase A science study, see [RD-1] for details)

1. Static gravity: GOCO05s
2. Time-variable gravity field: ESA-ESM (AOHIS)

20.3.2. BACKGROUND MODEL ERRORS (BGME)

(Identical with MAGIC phase A science study, see [RD-1] for details)

1. Ocean tides: OT differences: GOT4.7 & EOT11a
2. Non-tidal: ESA-ESM DEAL + AOerr

20.3.3. ADDITIONAL ERRORS

In this study, additional errors (e.g., attitude, angular velocities) are not considered as separate error sources but are modelled through the instrument noise specifications (within X1 noise, as part of Task 2).

20.4. SIMULATION SETTINGS AND SOLUTION TYPES

20.4.1. TIME REFERENCE

If not denoted otherwise, all scenarios are simulated starting with the reference epoch defined by the used orbits (e.g., ***3d_H, 5d_M*** start at 01.01.2002). The data accumulation for a certain solution is then described by the acronym ***dx***, where x is the number of accumulated days (e.g., ***d31*** for a monthly solution). If needed, sub-daily periods are denoted by ***hx***, where x is the number of hours of accumulation. Accumulation time acronyms are just valid in combination with solution type acronyms (see below)

20.4.2. SOLUTION TYPES

For the type of the solution, the following variants are used:
(solution type acronym prefix: ***s?***)

sx[dy]: static parametrization up to d/o x (e.g., ***s120d31***, for a monthly, static solution up to d/o 120).

cx[dy]: co-parametrization up to d/o x for a shorter accumulation time (e.g., ***c20d1***, for daily co-parametrization up to d/o 20). Just valid in combination with static parametrization (e.g., ***s120d31c20d1***).

20.5. LIST OF SIMULATED SCENARIOS

20.5.1. UNIQUE SCENARIO IDENTIFIER

Using the acronyms (IDs) of the configuration variants presented in the last subsections, the unique identifier is constructed by the individual constituents:

[orbit ID _ BGM ID _ solution type ID _ instrument ID]

Where ***orbit ID*** refers to one of the orbit acronyms ***o?***, ***BGM ID*** to one of the background model acronyms ***m?***, ***solution type ID*** to one of the solution type acronyms ***s?*** and ***instrument ID*** to the combined instrument acronym ***t?*** and/or ***a?*** and/or ***p?*** and/or ***g?***.

As an example, to simulate a monthly GRACE-FO-like solution, one would construct the scenario ***o3DH1_mFN_s120d31_tGFOaSS***: here, the polar pair of constellation 3d_H is used (***o3DH1***), assuming full noise in the background model (***mFN***), a static 31-day solution up to d/o 120 (***s120d31***) and instrument noise consisting of the GRACE-FO LRI and the SuperStar accelerometer (***tGFOaSS***). Consequently, a GOCE-like 2-month solution would be, e.g., ***oG61D_mFN_s180d61_gGO***: using a 61-day cycle of the GOCE orbit (***oG61D***), assuming again the full noise background model (***mFN***), a static 61-day solution up to d/o 180 (***s180d61***) and instrument noise consisting of a GOCE-like gradiometer (***gGO***).

20.5.2. PHASE A SIMULATIONS [NOISE MODEL X0]

In the first phase of this project, scenarios using existing noise models (in line with the MAGIC study/GOCE mission) are simulated along with a set of simplified noise assumptions for CAI instruments (white noise models X0):

Sim. #	Simulation identifier	Remarks
1	***o3DH1_mPO_s120d31_tGFOaSS***	Phase A comparison, single-pair, product-only
2	***o3DH1_mPO_s120d31_tGFOaMS***	
3	***o3DH1_mPO_s120d31_tGFOaMSaC11***	
4	***o3DH1A_mPO_s120d31_gGO***	
5	***o3DH1A_mPO_s120d31_gC13***	
6	***o3DH1A_mPO_s120d31_gC14***	
7	***o3DH2_mPO_s120d31_tGFOaSS***	Phase A comparison, double-pair, product-only
8	***o3DH2_mPO_s120d31_tGFOaMS***	
9	***o3DH2_mPO_s120d31_tGFOaMSaC11***	
10	***o3DH2A_mPO_s120d31_gGO***	
11	***o3DH2A_mPO_s120d31_gC13***	
12	***o3DH2A_mPO_s120d31_gC14***	
13	***o3DH1_mFN_s120d31_tGFOaSS***	Phase A comparison, single-pair, full-noise
14	***o3DH1_mFN_s120d31_tGFOaMS***	
15	***o3DH1_mFN_s120d31_tGFOaMSaC11 (X0)***	
16	***o3DH1_mFN_s120d31_t0a0***	
17	***o3DH1A_mFN_s120d31_gC13***	
18	***o3DH1A_mFN_s120d31_gC14***	

19	***o3DH1A_mFN_s120d31_g0***	
20	***o3DH1A_mFN_s120d31_p0***	
21	***o3DH2_mFN_s120d31_tGFOaSS***	Phase A comparison, double-pair, full-noise
22	***o3DH2_mFN_s120d31_tGFOaMS***	
23	***o3DH2_mFN_s120d31_tGFOaMSaC11***	
24	***o3DH2_mFN_s120d31_t0a0***	
25	***o3DH2A_mFN_s120d31_gC13***	
26	***o3DH2A_mFN_s120d31_gC14***	
27	***o3DH2A_mFN_s120d31_g0***	
28	***o3DH2A_mFN_s120d31_p0***	
29	***o3DH1A_mFN_s120d31_g0XX***	SGG component comparison, single-pair, full-noise
30	***o3DH1A_mFN_s120d31_g0YY***	
31	***o3DH1A_mFN_s120d31_g0ZZ***	
32	***o3DH1A_mFN_s120d31_g0XXg0YY***	
33	***o3DH1A_mFN_s120d31_g0YYg0ZZ***	
34	***o3DH1A_mFN_s120d31_g0XXg0YYg0ZZ***	
35	***oG61D_mPO_s180d61_gGO***	for SGG sim. validation *using real data gradients
36	***oG61D_mPO_s180d61_gGO****	

Table 20-1 List of phase A simulations using baseline (MAGIC) scenarios and X0 noise models. Includes GOCE scenarios for SGG simulator validation with real data.

20.5.3. PHASE B SIMULATIONS [NOISE MODEL X1/X1.1]

In the second phase of the project, more realistic noise assumptions for CAI instruments (as output from WP200) are used (X1/X1.1 models) for comparison to the baseline scenario. In agreement with ESA, the baseline scenario (to 5_dM) and retrieval period has been changed for phase B (to 5_dM and 7 days):

Sim. #	Simulation identifier	Remarks
1	***o5DM1_mPO_s90d7_tGFOaSS***	Phase B SST comparison, single-pair, product-only
2	***o5DM1_mPO_s90d7_tMAGIC***	
3	***o5DM1_mPO_s90d7_tX1***	
4	***o5DM1_mPO_s90d7_tX11***	
5	***o5DM1_mPO_s90d7_tX0***	
6	***o5DM1_mPO_s90d7_tNG30***	
7	***o5DM2_mPO_s90d7_tGFOaSS***	Phase B SST comparison, double-pair, product-only
8	***o5DM2_mPO_s90d7_tMAGIC***	
9	***o5DM2_mPO_s90d7_tX1***	
10	***o5DM2_mPO_s90d7_tX11***	
11	***o5DM2_mPO_s90d7_tX0***	
12	***o5DM2_mPO_s90d7_tNG30***	
13	***o5DM1_mFN_s90d7_tGFOaSS***	

14	***o5DM1_mFN_s90d7_tMAGIC***	Phase B SST comparison, single-pair, full-noise
15	***o5DM1_mFN_s90d7_tX1***	
16	***o5DM1_mFN_s90d7_tX11***	
17	***o5DM1_mFN_s90d7_tX0***	
18	***o5DM1_mFN_s90d7_tNG30***	
19	***o5DM2_mFN_s90d7_tGFOaSS***	Phase B SST comparison, double-pair, full-noise
20	***o5DM2_mFN_s90d7_tMAGIC***	
21	***o5DM2_mFN_s90d7_tX1***	
22	***o5DM2_mFN_s90d7_tX11***	
23	***o5DM2_mFN_s90d7_tX0***	
24	***o5DM2_mFN_s90d7_tNG30***	
25	***otDM1A_mPO_s90d7_gGO***	Phase B SGG comparison, polar-satellite, product-only
26	***otDM1A_mPO_s90d7_gX1***	
27	***otDM1A_mPO_s90d7_gX1NA***	
28	***otDM1A_mPO_s90d7_gC13***	
29	***otDM1A_mPO_s90d7_gC14***	
30	***otDM2A_mPO_s90d7_gGO***	Phase B SGG comparison, 2 satellites, product-only
31	***otDM2A_mPO_s90d7_gX1***	
32	***otDM2A_mPO_s90d7_gX1NA***	
33	***otDM2A_mPO_s90d7_gC13***	
34	***otDM2A_mPO_s90d7_gC14***	
35	***otDM1A_mFN_s90d7_gGO***	Phase B SGG comparison, polar-satellite, full-noise
36	***otDM1A_mFN_s90d7_gX1***	
37	***otDM1A_mFN_s90d7_gX1NA***	
38	***otDM1A_mFN_s90d7_gC13***	
39	***otDM1A_mFN_s90d7_gC14***	
40	***otDM2A_mFN_s90d7_gGO***	Phase B SGG comparison, 2 satellites, full-noise
41	***otDM2A_mFN_s90d7_gX1***	
42	***otDM2A_mFN_s90d7_gX1NA***	
43	***otDM2A_mFN_s90d7_gC13***	
44	***otDM2A_mFN_s90d7_gC14***	

Table 20-2 List of phase B simulations using baseline (MAGIC) scenarios and X1/X1.1 noise models. SGG and SST simulation have been separated.

21. SIMULATION RESULTS AND INTERPRETATION

In this section the most important results are shown and interpreted (WPs 310, 321, 322). All results can be found within the Data-1 data repository. This section is structured according to the different simulation phases (with the different noise models, trade-space assumptions). In the last part the benefit of using post-processing methods will be assessed and appropriate results are shown.

21.1. RESULTS OF PHASE A

21.1.1. INSTRUMENT AND CONCEPT COMPARISON

Phase A aims to shrink the trade space to be investigated by analysing the influence of limit cases of instrument noise assumptions when using existing constellations concepts (3d_H polar pair, double pair) and parametrization types (static). Eventually, statements will be made whether and when improved instrument performances can contribute to the overall gravity field retrieval performance in the conservative constellation/parametrization setup. The benefit is measured with respect to the GRACE-FO mission performance (*tGFOaSS*) and the (old) baseline performance from the MAGIC study (*tGFOaMS*). As a second objective, the SST concept is compared against the SGG concept performance-wise.

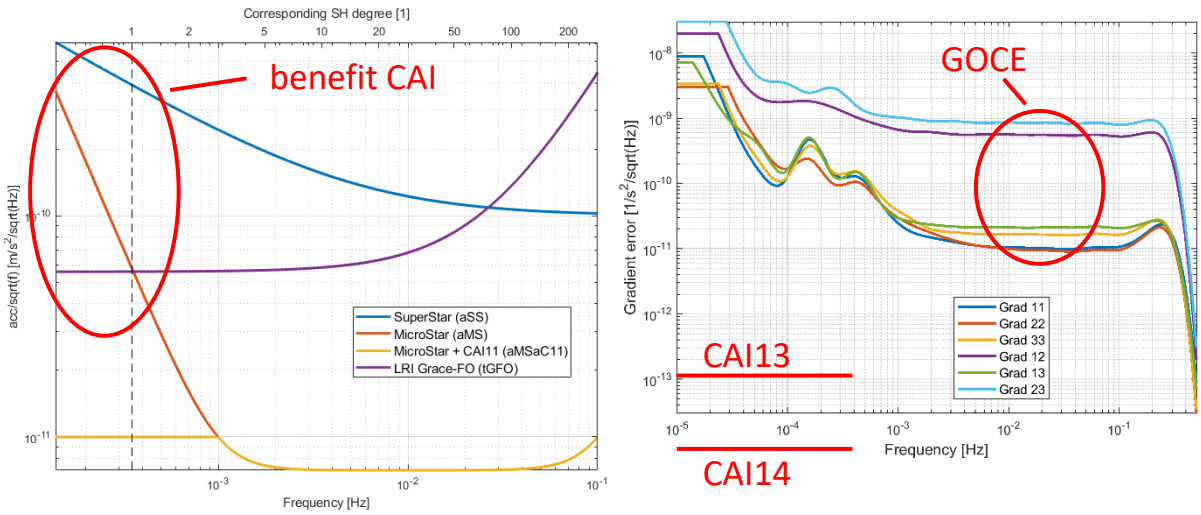

(a) **(b)**

Figure 21-1 ASDs of the different instrument performances regarded in phase A (cf., Sec. 20.2). (a) ASDs of SST related instruments. (b) ASDs of SGG gradiometers.

In Figure 21-1 the ASDs of the different instrument noise assumptions are depicted for SST (Figure 21-1a) and SGG (Figure 21-1b). For SST, one can see that using the current assumption of a GRACE-FO-like LRI, the overall performance is mainly limited by this instrument (the LRI) when assuming better accelerometers (like MicroSTAR or X0). Hence, in the scenarios which are using the GRACE-FO LRI performance it can be assumed that the difference between X0 and MicroSTAR is small in the final gravity field retrieval (since the noise is dominated by the LRI). In case of SGG, a better product-noise for the gradiometer can be directly translated to a better (product-only) gravity field retrieval (even if the assumed product-noise might currently not be achievable technically).

For a first overview, degree variance plots are provided, where all different investigated scenarios are compared against each other. For better comparability, these plots are grouped

regarding full-noise/product-only and single-pair/double pair (resulting in 2 plots in Figure 21-2 and Figure 21-3.

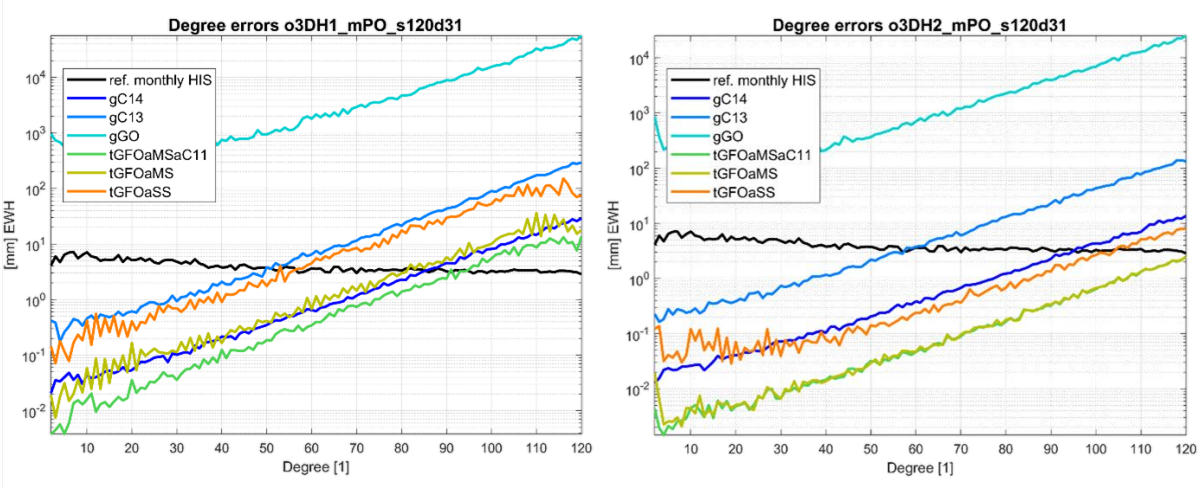

(a) **(b)**

Figure 21-2 Degree errors for different instruments in terms of EWH in case of product-only noise (static gravity field only). (a) For single pair *o3DH1_mPO_s120d31* (i.e., monthly, static single-pair solutions, product-only, corresponding to sim. #1-6). (b) For double-pair *o3DH2_mPO_s120d31* (i.e., monthly, static double-pair solution, product-only, corresponding to sim. #7-12).

The product-only comparisons (Figure 21-2) show the sensitivity of the different instruments regarding time-variable gravity (for monthly solutions, disregarding temporal aliasing). It can be seen that:

- The retrieval performance scales (as expected) with the instrument performance.
- For the single-pair scenario, a $10^{-14}[1/s^2]$ white noise gradiometer (SGG) is needed to be competitive with the NGGM SST performance (assuming a MicroStar accelerometer)
- Vice versa (for the single-pair scenario), a $10^{-13}[1/s^2]$ white noise gradiometer (SGG) is needed to be competitive with current Grace-FO SST performance (assuming a Superstar accelerometer)
- In case of the double-pair scenario, SGG does not scale as well as SST, and, hence, a $10^{-14}[1/s^2]$ gradiometer would be needed to even match GRACE-FO SST performance.
- A GOCE-like gradiometer (*gGO*) is far from being able to recover time-variable gravity (at least for monthly and shorter scales).
- The overall benefit of a quantum accelerometer (X0) for SST is limited since the performance of current ranging instruments (GRACE-FO LRI) limits the overall system performance.
- For the double-pair scenario, the benefit of a quantum instrument is nearly not visible and limited at d/o below 10.

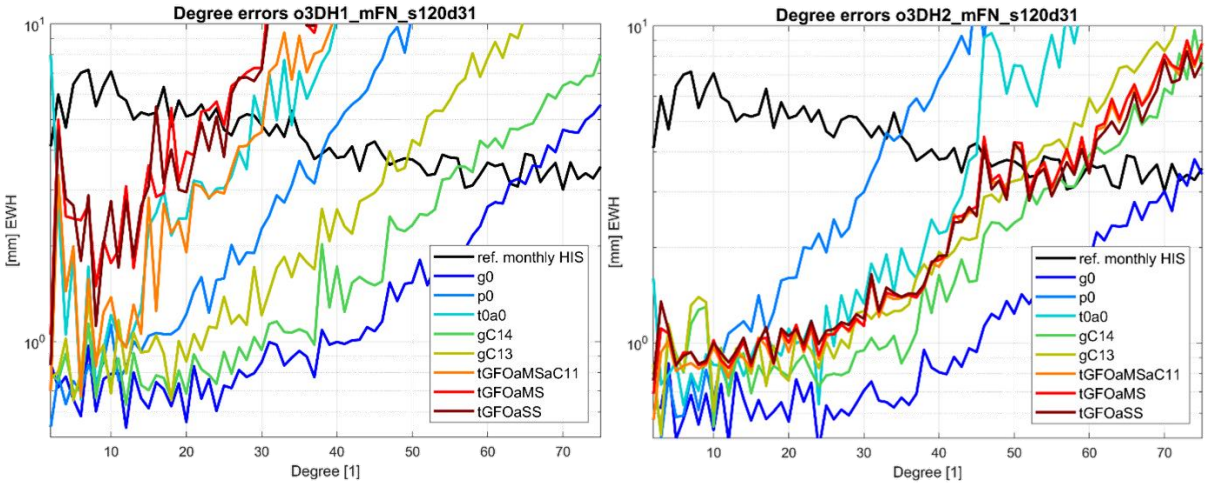

(a) **(b)**

Figure 21-3 Degree errors for different instruments in terms of EWH in case of full-noise (time variable gravity field). (a) For single pair *o3DH1_mFN_s120d31* (i.e., monthly, static single-pair solutions, full-noise, corresponding to sim. #13-20). (b) For double-pair *o3DH2_mFN_s120d31* (i.e., monthly, static double-pair solution, full-noise, corresponding to sim. #21-28).

When comparing the full-noise scenarios (Figure 21-3) the overall retrieval performance including the effect of temporal aliasing can be assessed. Under the influence of temporal aliasing, the following can be noted:

- Temporal aliasing limits the overall retrieval performance by about 3 orders of magnitude (depending on instrument).
- Thus, noise magnitudes of investigated instruments has no impact for the result (for SST, if better than GRACE-FO).
- (SST) retrieval performance is solely driven by the shape of the ASD and its interaction with the time-variable gravity
- A flat ASD shape (in the acc. domain) seems to be favourable for reducing the effect of temporal aliasing (to some extend) in the case of a single-pair mission. Hence, for single pair a CAI acc. is advantageous in this scenario.
- For the double-pair scenario, the shape seems to be less important since all (SST) instruments perform nearly identical
- Multidirectional observations from the gradiometer seem to be important for reducing temporal aliasing. SGG (with 6 components) delivers the best results in presence of time-variable gravity. Additional item to investigate: Which SGG component has the most influence on the retrieval performance? (see next section)

21.1.2. CASE STUDY: INFLUENCE OF DIFFERENT SGG TENSOR COMPONENTS

In this special side-study it is briefly investigated how different SGG gradient tensor components influence the full-noise gravity field retrieval performance. For this, several gravity field solutions for different combination of tensor components are investigated for a polar orbit (see Figure 21-4). The XX-component points in flight direction (along-track), YY-component in the across-track direction and ZZ points in the radial direction.

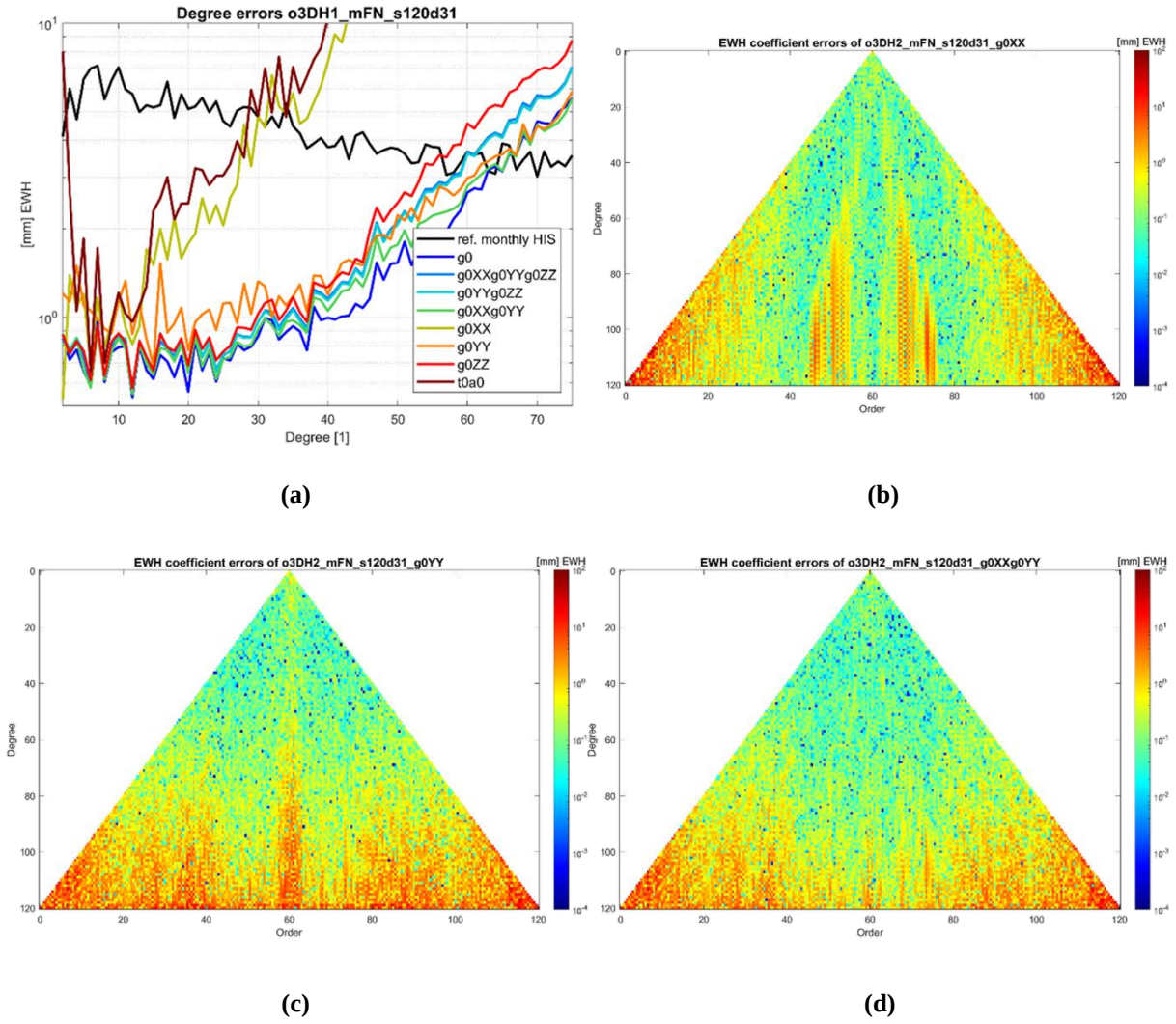

(a) **(b)**

(c) **(d)**

Figure 21-4 Degree errors for different tensor components of SGG scenario *o3DH1A_mFN_s120d31* in terms of EWH (i.e., monthly, static single polar satellite solutions, full-noise, corresponding to sim. #29-34). (a) Degree errors. (b) Coefficient errors of XX-component. (c) Coefficient errors of YY-component. (d) Coefficient errors of XX+YY component.

Inspecting Figure 21-4, one can see, that the XX-only solution shows the worst performance which is comparable to an SST solution. This is reasonable, since (inline-)SST also measures in the along-track direction (through the ranging instrument) similarly to SGG XX. It is further visible that all other components perform much better (and quite similar) in presence of time-variable gravity. The best performing single tensor component is YY and a combination of XX and YY shows a homogeneous error pattern in the coefficient triangle (Figure 21-4d). The finding that the YY direction is favourable and the XX direction complements YY motivates the investigation of across-track SST (in combination with along-track SST) in WP400.

21.1.3. CASE STUDY: IMPACT OF GRADIOMETER TRANSFER FUNCTION

Differently form electrostatic gradiometers, CAI instruments needs an integration time to proper observe accelerations or gradients. This translates into applying an instrument transfer function to the observable quantities. To verify the impact of including a gradiometer transfer function in the data processing, we used the 61-day cycle of the GOCE orbit (*oG61D*), assuming the product-only background model (*mPO*) and instrument noise consisting of a GOCE-like gradiometer (*gGO*). Here, we consider that the gradiometer observations are affected by the transfer function $h(t)$ presented in Figure 21-5, used in the MOCASS and MOCAST+ previous studies [Migliaccio et al., 2019, Migliaccio et al., 2023] where the integration time was of 5 s. Moreover, to better understand the impact of such a transfer function the integration time has been extended to 10 s and 20 s (see Figure 21-6 for the Fourier transform $H(f)$ of the transfer function in the three cases).

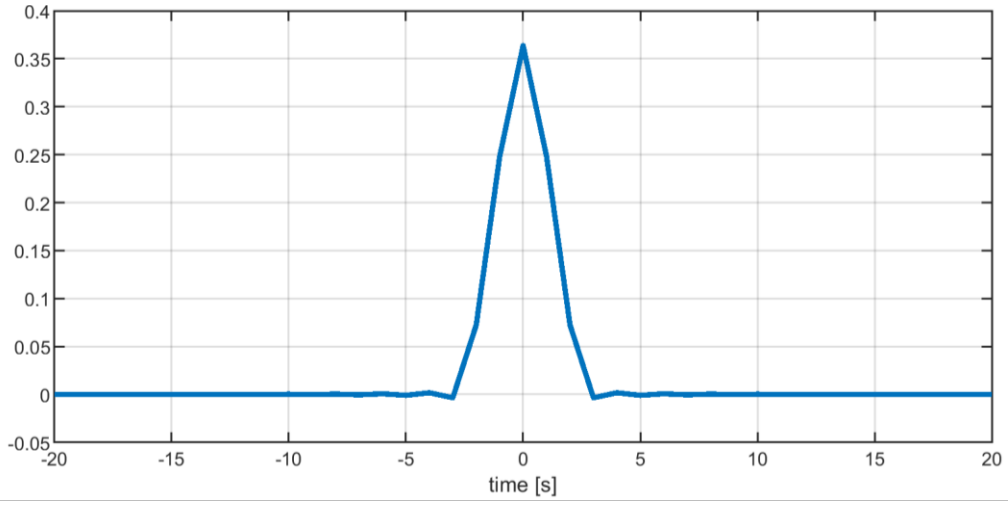

Figure 21-5 Transfer function with integration time of 5 s.

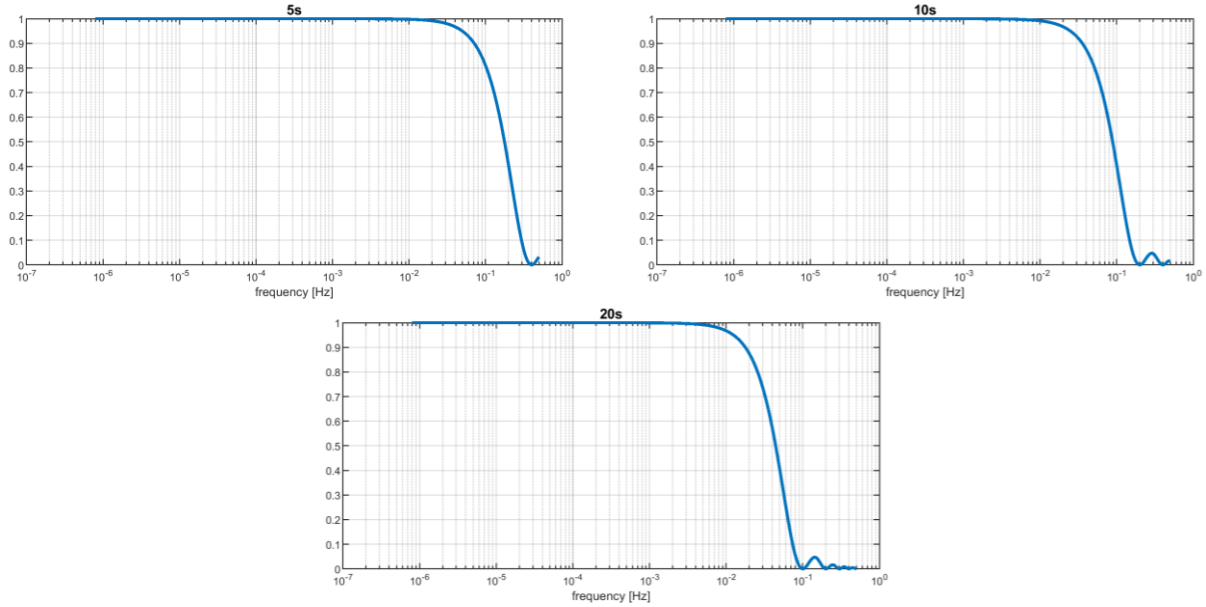

Figure 21-6 Transfer function in frequency domain, considering 5 s, 10 s, and 20 s integration time.

The transfer function enters into the simulation as:

$$y_o(t) = h(t) * y(t) + v(t) \quad \textbf{(10)}$$

where $y_o(t)$ is the vector containing the observed second derivatives, $y(t)$ is the noiseless gravity gradient signal, the $*$ operator stands for the time convolution, and $v(t)$ is the gradiometer measurement noise. To properly consider the effect of the transfer function $h(t)$, the Wiener filtering has been replaced by a deconvolution in the space-wise solver, leading to solutions that are only affected by a slight degradation at the highest degrees (> 140, compare yellow and blue solid lines in Figure 21-7). On the other hand, if the simulated observations $y_o(t)$ of Eq. (10) are processed without introducing the deconvolution step, namely ignoring the presence of an instrumental transfer function, a general degradation arises (compare yellow and dark red solid lines in Figure 21-7). The magnitude of this degradation is strictly related to the ratio between observation sampling rate and instrumental integration time, noting that with a sampling rate of 1 s, only 10 s and 20 s have a significant impact on the solution. Note that in Figure 21-7 the blue line represents the solution accuracy when transfer function is not affecting the observations obtained by the TUM simulator, representing the optimal solution for the considered scenario.

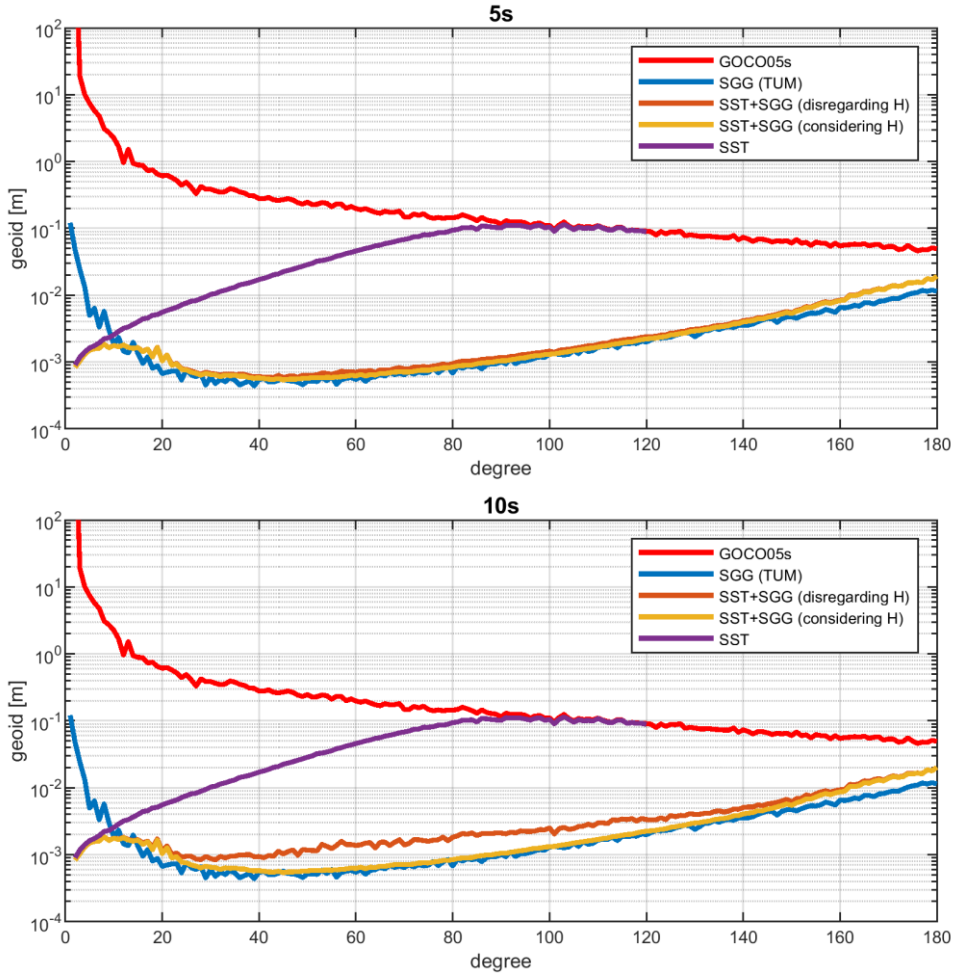

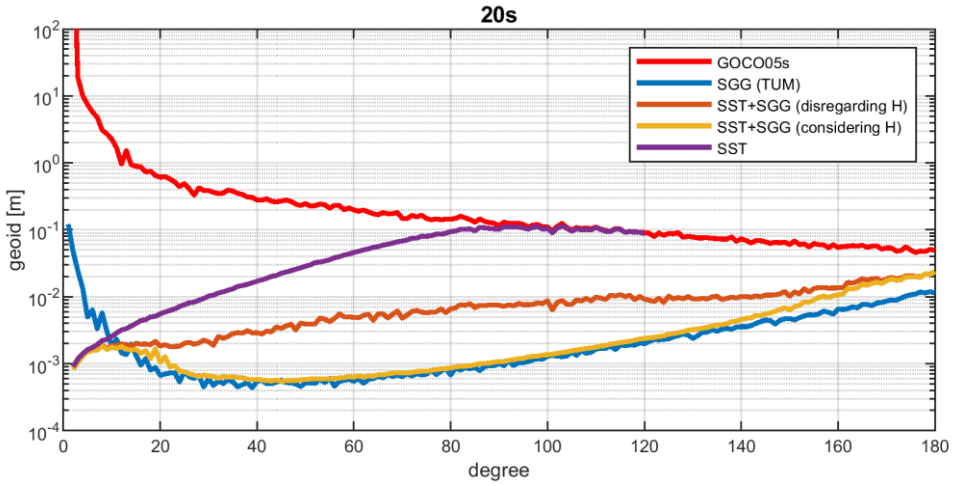

Figure 21-7 Effect of neglecting CAI gradiometer transfer function $\boldsymbol{h(t)}$, considering 5 s, 10 s, and 20 s instrumental integration time, in terms of degree error. Blue lines represent the accuracy of the reference solution obtained without transfer function in the observation, yellow lines represent the accuracy of solution with transfer function in the observation properly treated also into the solver (with a Wiener deconvolution), while dark red lines represent the accuracy of solution with transfer function in the observation treated with the same solver of the reference solution (i.e. with a Wiener filtering instead of a deconvolution).

Before going inside simulations considering different accuracy of the CAI gradiometer, the impact of the accuracy of the attitude control sensor on the gravity gradient measurement in the orbital plane (thus involving gradiometers mounted in the along-track x-axis and in the radial z-axis directions) has been investigated. In fact, angular rotations, through the centrifugal term, put a serious limitation to these measurements. For this reason, compensation of the residual angular rotations around the out-of-orbital-plane y-axis direction is usually needed; the accuracy of this compensation highly influences the gradiometer accuracy on the along-track x-axis and radial direction z-axis. To understand the impact of changing the gradiometer arm direction (x, y, z), the solutions of a series of scenarios considering observations from a single gradiometer mounted onboard a single satellite on polar *o3DH1* orbit were computed. In this framework, a perfect attitude compensation (*gM0*) as ideal scenario as well as a compensation at the level of 1 nrad/s (*gM1*) has been considered, taking as a preliminary input the gradiometer error PSDs used for the MOCAST+ project [Rossi et al., 2023] reported in Figure 21-8. Note that, the noise PSD of the y-axis gradiometer is not affected by compensation of the residual angular rotations, therefore the T_{yy} gradiometer always act as in scenario *gM0*.

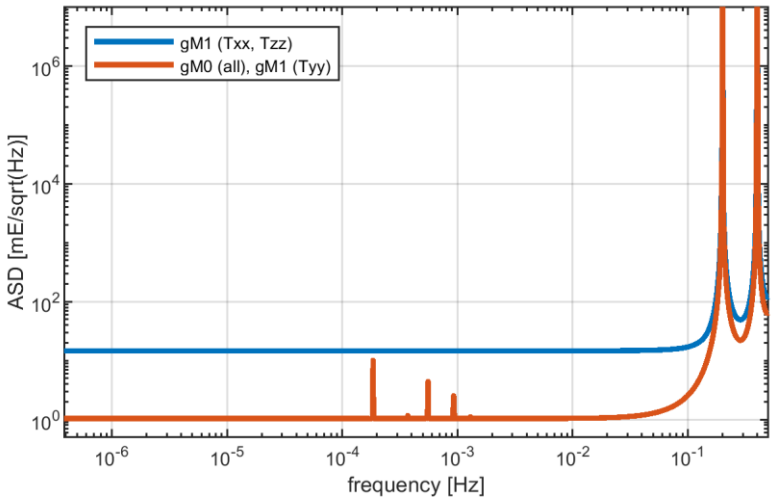

Figure 21-8 Gradiometer noise ASD from Rossi et al. (2023) for the *gM0* and *gM1* scenarios. Note that, the noise ASD of the y-axis gradiometer is not affected by compensation of the residual angular rotations, therefore the T_{yy} gradiometer always act as in scenario *gM0*.

The results of this set of simulations are shown in Figure 21-9. Here, the solutions computed by combining three gradiometers (along-track x-axis, out-of-orbital-plane y-axis, and radial z-axis) are compared with respect to single gradiometer solutions. It can be noticed that the main contribution to the combined solution in the *gM0* scenario (ideal) is carried by the z-axis gradiometer (compare blue and yellow dashed lines in Figure 21-9). On the other hand, considering the *gM1* scenario (namely introducing errors related to attitude compensation error), the main contribution to to the combined solution has been carried by the y-axis gradiometer (compare solid red and blue lines in Figure 21-9). The x-axis gradiometers performances are not reported on the graphs since this is the gradiometer with less contribution to the final combined solution.

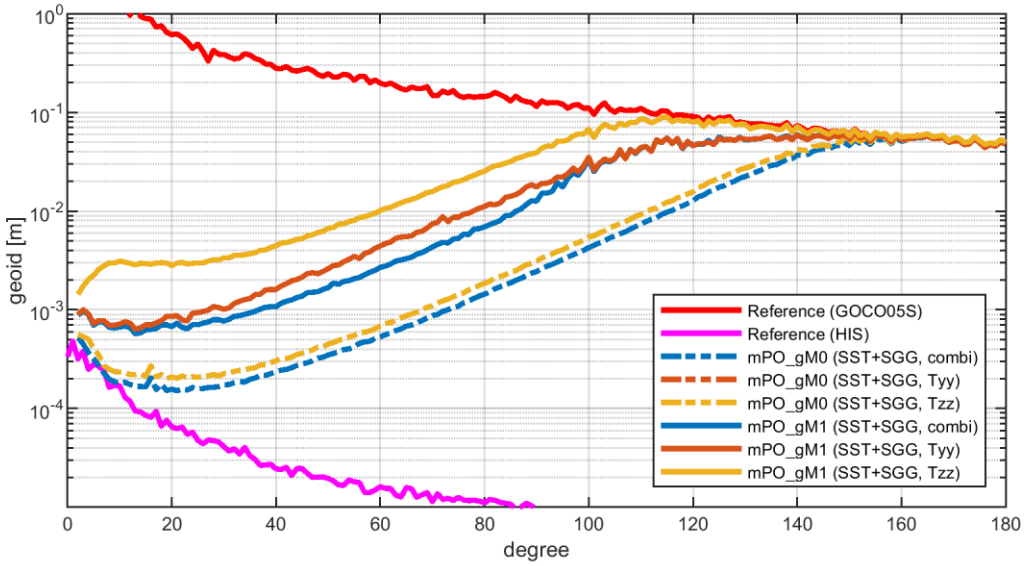

Figure 21-9 Comparison of the estimated degree error in terms of geoid height for gM0 and gM1 scenarios

Focusing on the *gM1* scenario, investigating the impact of attitude compensation errors, a further comparison of the impact of different gradiometer axis orientations was performed at the level of the single spherical harmonic coefficient. The results of this comparison are shown in Figure 21-10. Here, the gradiometer arm direction providing the best estimate, i.e., providing the smallest error variance, is shown for each harmonic degree and order. According to the results shown in Figure 21-9 the main contributions to the coefficient estimation comes from the gradiometer oriented along the y-axis direction. This finding is in agreement with previous works on quantum gradiometry, see e.g. Douch et al. (2018). Nevertheless, a contribution coming from T_{zz} at low orders can be seen.

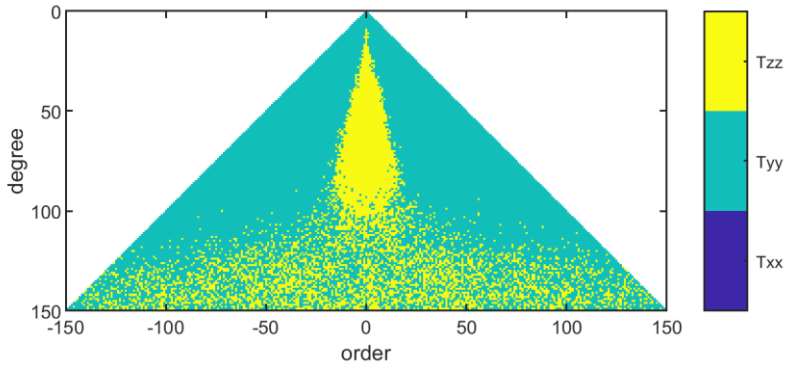

Figure 21-10 Comparison between error variances of spherical harmonic coefficients estimated by observing the gravity gradients in different directions (x, y, z), considering attitude control at the level of 1 nrad/s (scenario gM1); the gradients leading to the smallest error variance are shown for each degree and order.

Finally, solutions with different gradiometer noise levels are computed, considering a single satellite on the *o3DH1* orbit with three CAI gradiometer onboard (x, y, and z axis) or with a triaxial electrostatic gradiometer (*gGO* noise level). As for the latter, a further comparison has been performed by considering the GOCE orbit (*oG61d*). Figure 21-11 shows the results of the comparison, from which the improvement carried by CAI gradiometer is clearly visible, especially at the lower degrees, showing capabilities of this kind of instrument of detecting non-tidal time-variable gravity field effects up to degree 50. To properly check the capability of retrieving the non-tidal time-variable gravity field, solutions considering both the *mPO* (static field only) and *mFN* (static and non-tidal time-variable gravity field) were computed.

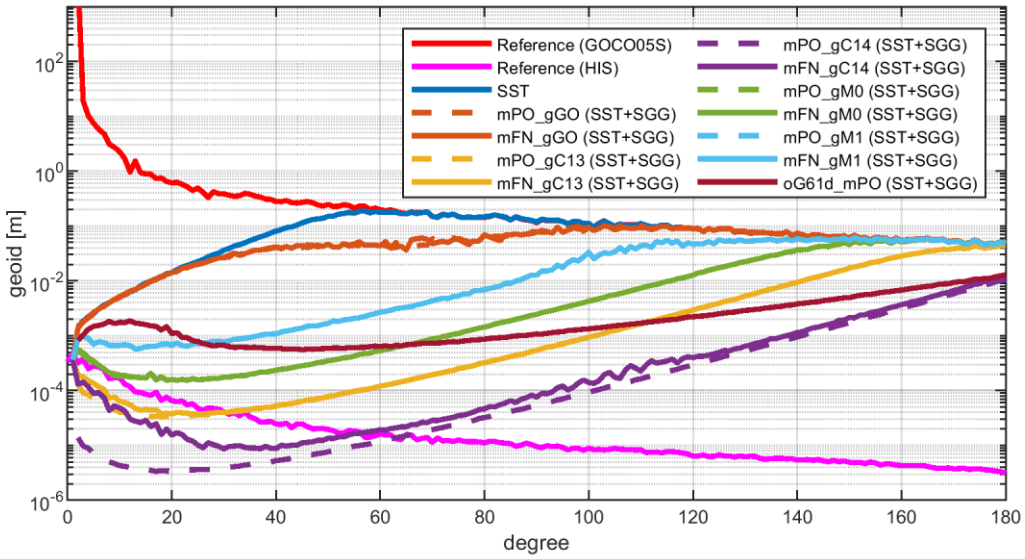

Figure 21-11 Estimated degree error in terms of geoid height comparing electrostatic gradiometers (*gGO* on *o3DH1* or *oG61d* orbits) with CAI gradiometers (*gM0, gM1, gC13, gC14* on *o3DH1* orbit). Dashed and solid lines represent solution with *mPO* and *mFN* background models, respectively. Solid magenta line represents the power of the non-tidal time variable gravity field.

21.2. RESULTS OF PHASE B

21.2.1. INSTRUMENT COMPARISON

Phase B of WP300 complements phase A by adding more realistic noise assumptions for future CAI instruments as a result from WP200. In phase B, the noise models X1 and X11 are added to the comparison (including AI#5). By a request of ESA, the MAGIC baseline scenario has been updated from the 3d_H orbits to 5d_M and the ranging instrument has been changed from GRACE-FO (*tGFO*) to MAGIC (*tMAGIC*) performance. Additionally, the retrieval period has been modified to 7 days and the max. d/o to 90 for the retrieved gravity fields.

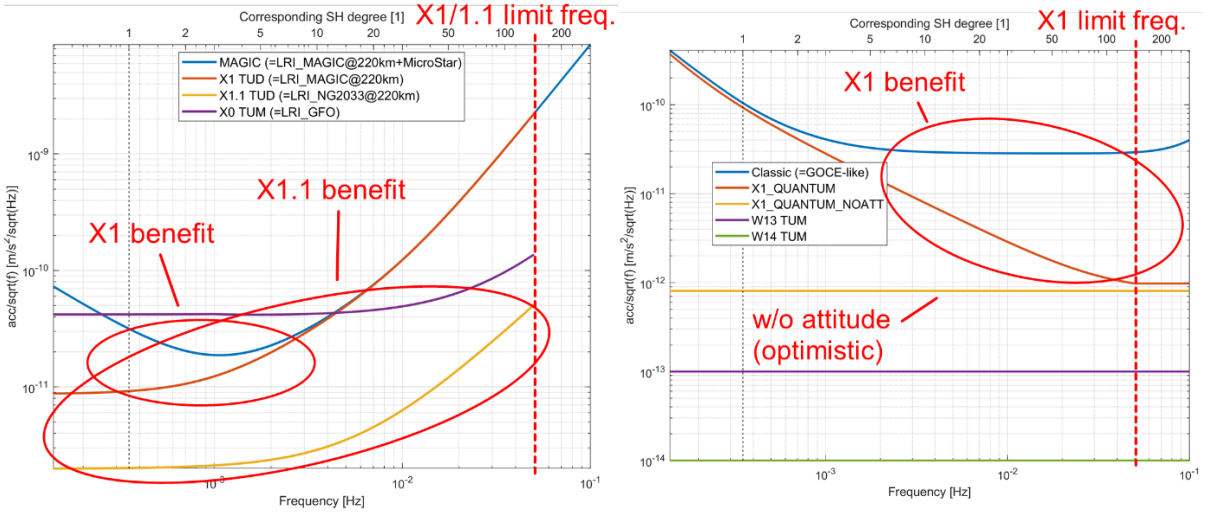

(a) **(b)**

Figure 21-12 ASDs of the different instrument performances regarded in phase B (cf., Sec. 20.2). (a) ASDs of SST related instruments. (b) ASDs of SGG gradiometers. All ASDs refer to product-noise (combining ranging, acc. and other noise sources)

You can find the updated ASD curves in Figure 21-12: Investigating these curves, it is already visible that the improvement of the SST X1 model is relatively moderate since the ranging instrument (*tMAGIC*) is limiting the overall retrieval performance. However, when assuming an improved ranging instrument (*tNG33*) the improvements become more prominent (noise model X1.1). Also for SGG, the benefit of X1 is limited due to technical hurdles in the acquisition of the attitude (when comparing to a GOCE-like performance). Only when neglecting these attitude errors, the product-noise becomes significantly better.
The results for the SST scenarios are shown in Figure 21-13. Comparing these results with the findings in phase A, one can see that all main conclusions remain unchanged. Especially the fact that full-noise retrieval performance cannot be fundamentally improved by improved instruments is still valid. Only things noteworthy in addition:

- For a weekly retrieval period the effect of temporal aliasing is generally more prominent than for a monthly period.
- As expected, X1.1 (SST) has a much better product-only performance than X1 (SST). The benefit of X1 (SST) with respect to MAGIC is marginally.

The SGG scenarios are depicted in Figure 26-17. Also for SGG, the conclusions drawn in phase A remain unimpaired: gradiometer performance needs to be at least at the level of *gC13* to be competitive (with classical) SST. Statements regarding X1 (SGG):

- X1 with attitude noise can only slightly improve with respect to GOCE performance
- X1 without attitude noise shows about two orders of magnitude better performance than GOCE. However, even then X1 remains insensitive to time-variable gravity (at a weekly scale)

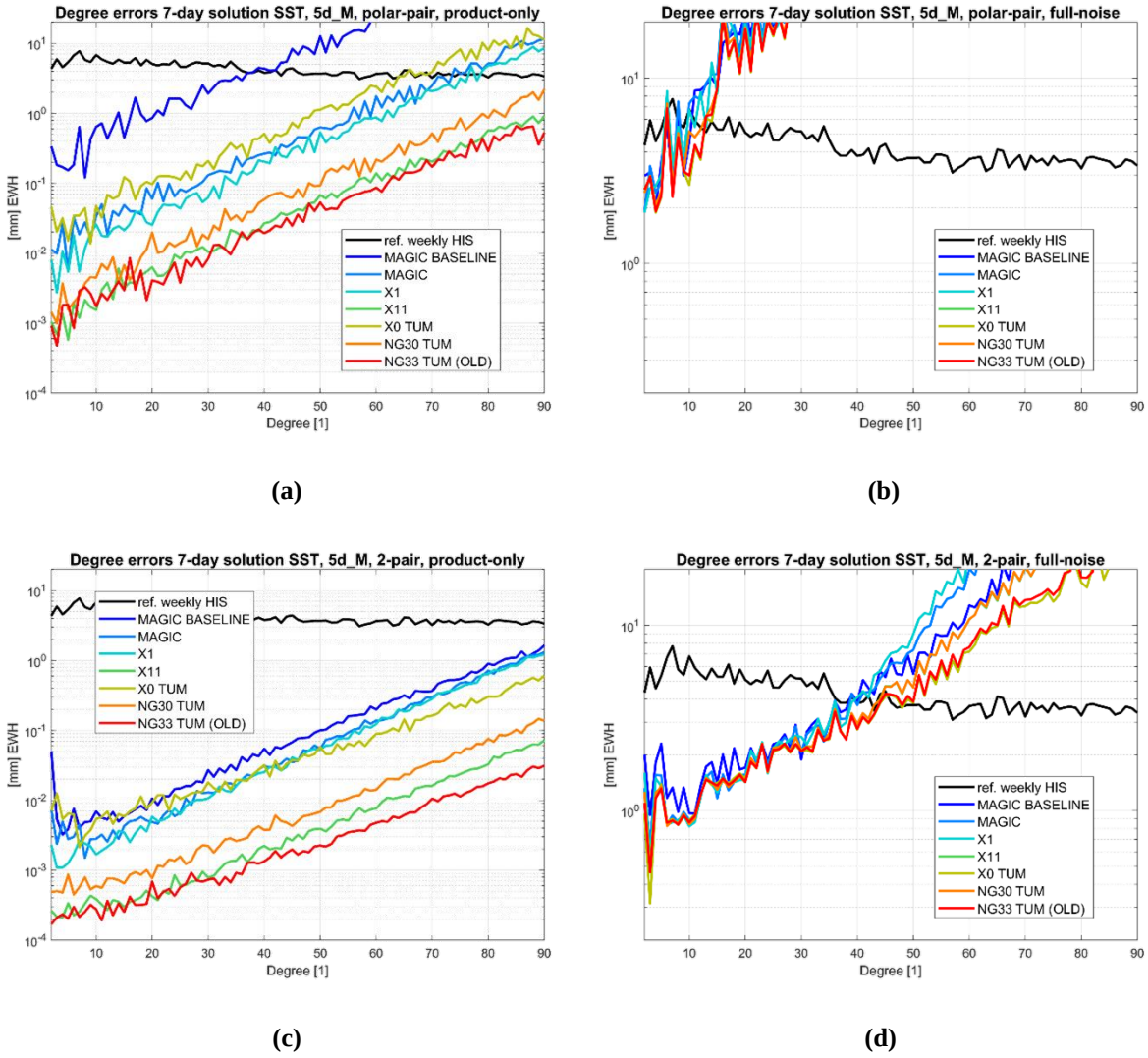

Figure 21-13 Degree errors for X1/X1.1 related instruments for different product-noises of SST scenarios (legend names denote ranging product-noises *t?*). MAGIC BASELINE refers to the special case where the polar pair uses *tGFOaSS* and the inclined pair uses *tMAGICaMS* (=new MAGIC baseline scenario). (a) Product-only, single-pair *o5DM1_mPO_s90d7* (sim. B#1-6). (b) Full-noise, single-pair *o5DM1_mFN_s90d7* (sim. B#7-12). (c) Product-only, double-pair *o5DM2_mPO_s90d7* (sim. B#13-18). (d) Full-noise, double-pair *o5DM2_mFN_s90d7* (sim. B#19-24).

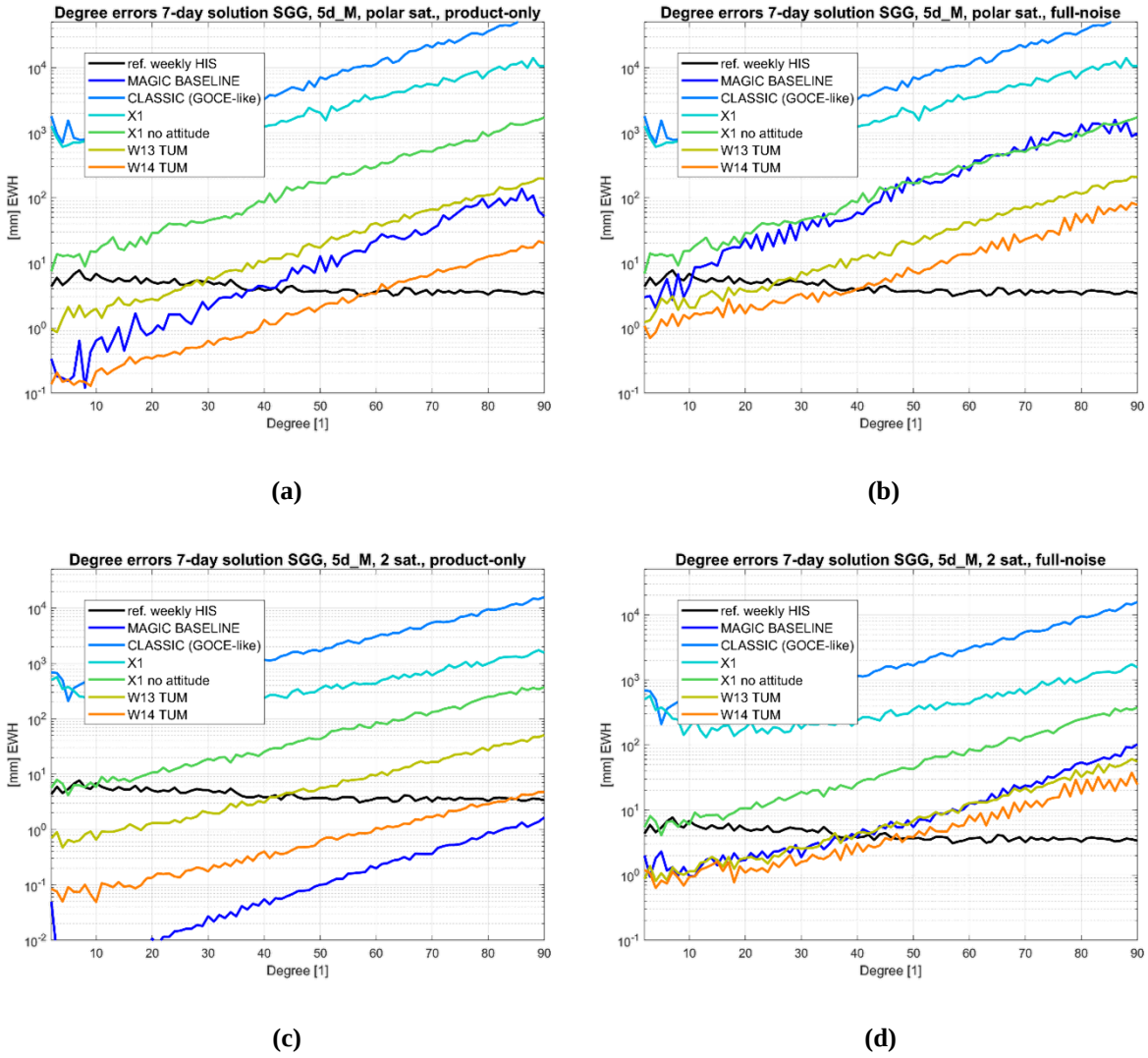

Figure 21-14 Degree errors for X1 related instruments for different product-noises of SGG scenarios (legend names denote gradiometer product-noises *g?*, see simulation list B). (a) Product-only, single-pair/-satellite *o5DM1A_mPO_s90d7* (sim. B#25-29). (b) Full-noise, single-pair/-satellite *o5DM1A_mFN_s90d7* (sim. B#30-34). (c) Product-only, double-pair/-satellite *o5DM2A_mPO_s90d7* (sim. B#35-39). (d) Full-noise, double-pair/-satellite *o5DM2A_mFN_s90d7* (sim. B#40-44).

21.3. POSTPROCESSED RESULTS

Postprocessed results have not been investigated so far since the main focus of WP300 is to primary assess relative improvements in the retrieval performance of future CAI instruments regarding MAGIC. Since it has been shown that the full-noise retrieval performance cannot be fundamentally improved by instruments alone, filtering these models will also not result in further improvements with respect to MAGIC. However, if explicitly requested, (e.g. VADER-) filtered solution can be included in a second moment.

22. METHODOLOGY AND SIMULATOR VALIDATION

In the following, the satellite gravity field mission simulation software for the SST and SGG approach (of POLIMI and TUM) used in this project is examined in more detail. For this, the applied methodologies (for SST and SGG processing) will be explained first. Then, a validation of the simulators is performed where the software shall be validated internally as well as through cross-comparison of simulation results between POLIMI and TUM (individually for SST and SGG, covering WPs 331, 332).

22.1. METHODOLOGY OF THE POLIMI SIMULATOR

The space-wise approach is based on the idea of exploiting the spatial correlation of the Earth gravity field to estimate the spherical harmonic coefficients [Migliaccio et al., 2004]. Thereby, it is possible to obtain a solution by collocation in which the covariance of the signal is modelled as a function of the spatial distance, while the covariance of the instrumental noise is typically correlated in time. The approach gives the possibility to combine observations which are close to one another in space but distant in time, thus overcoming possible problems related to the noise temporal correlation. Nevertheless, a unique collocation procedure is not computationally feasible, mostly due to the amount of the observations to be processed. For this reason and due to the fact that a local covariance modelling is not easily achievable with a unique global covariance matrix, the space-wise approach is implemented as a multi-step procedure as shown in Figure 22-1 The space-wise approach scheme [Reguzzoni and Tselfes, 2009]. The first step of this procedure is to estimate a set of harmonic coefficients by Least Squares adjustment considering low degree and order (e.g. exploiting low-low satellite tracking by GPS). This low-degree least squares solution is later used only to remove the long wavelength part of the gravity field from the gradient observations, thus reducing the signal correlation length. Nevertheless, before the reduction, the gravity gradient observations must be filtered to mitigate the impact of the instrumental noise. This filtering is performed in the frequency domain by Wiener filter or deconvolution. The introduction of a deconvolution is required only in presence of an instrumental transfer function, typical of CAI. The filtering/deconvolution procedure is followed by the gridding on a regular grid of residual gravity gradients in terms of different functionals of the gravity field, by means of a local collocation approach. As a final step, the gridded data are used to estimate the spherical harmonic coefficients of the gravity field by numerical integration and the clock-only solution is restored.

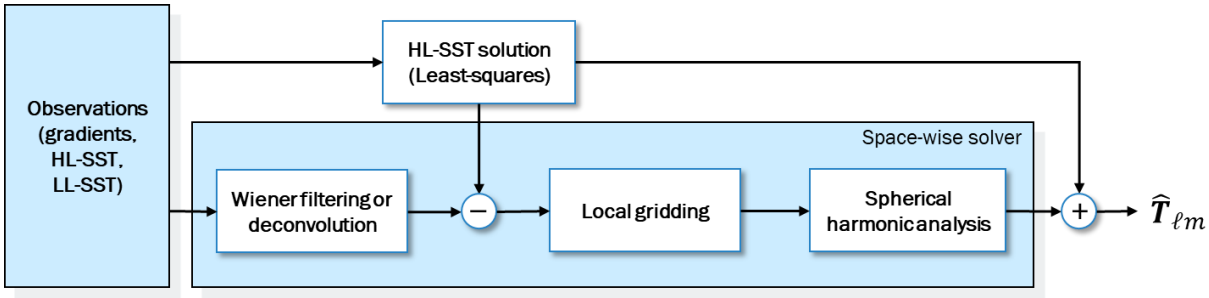

Figure 22-1 The space-wise approach scheme.

The overall solution scheme is applied to a set of Monte Carlo samples considering different realization of the Earth gravity field as well as of the instrumental noise to empirically evaluate

the overall simulation accuracy. In fact, due to the complexity of the solution scheme, especially related to the local gridding, a formal covariance propagation is not feasible.

22.2. METHODOLOGY OF THE TUM SIMULATOR

The TUM full-scale simulator is based on the so-called time-wise short-arc approach (for SST and SGG simulations). In this approach, consecutive short orbit arcs (>2h) are modelled rigorously through dense covariance matrices and are subsequently combined on normal equation level in a least squares adjustment approach.

In the short arc approach, the function model of the gradiometer tensor for SGG simulation can be modelled directly and linearly. For SST, the so-called integral-equation approach [Mayer-Gürr, 2006] is used to model the range-rate observations. In the original TUM full-scale SST simulator, this integral equation approach caused some numerical problems when dealing with very low instrument noise, since it required a distinct orbit integration in the forward- and backward-model. Due to its nature, numerical orbit integration always shows a limited numerical accuracy, and, thus introduces an artificial noise into the system (see Figure 22-2a). This artificial noise is of no relevance if the instrument noise has a significant higher magnitude. However, upcoming instruments (such as CAI accelerometers) show already a noise performance in the level and below the orbit integration noise, and, hence, cannot be simulated accurately with the original approach.

To circumvent this problem, the so-called differential simulation approach has been introduced in the full-scale simulator (see Figure 22-2b). In this new approach, the forward- and backward-modelling is unified by using an identical methodology for orbit integration (i.e., the integral equation approach). In this way, the whole SST simulation becomes linear and instead of working with whole quantities with full magnitude, one can now use differential quantities right from the beginning. Using differential quantities, the problem of cancellation is fundamentally avoided (which has been an additional problem of the original approach).

It should be noted, that the integral equation approach just becomes linear if the a-priori positions of the satellites are known sufficiently well (e.g., through adequate GNSS observations). Additionally, while being mathematically identical to the original approach, the differential approach can obviously just be applied for simulation purpose; in case of real data processing, one needs to explicitly formulate the backward module, reintroducing the original problematic (at least the cancellation error). In real data case, one needs a different solution for the problem by trying to make the orbit integration more accurate. This could be achieved, e.g., by using quadruple-precision arithmetic. Yet, such a solution would introduce a major increase of computation time (factor n). Hence, for simulation purpose, this solution is not really applicable since many scenarios need to be simulated in short periods of time with limited numerical effort.

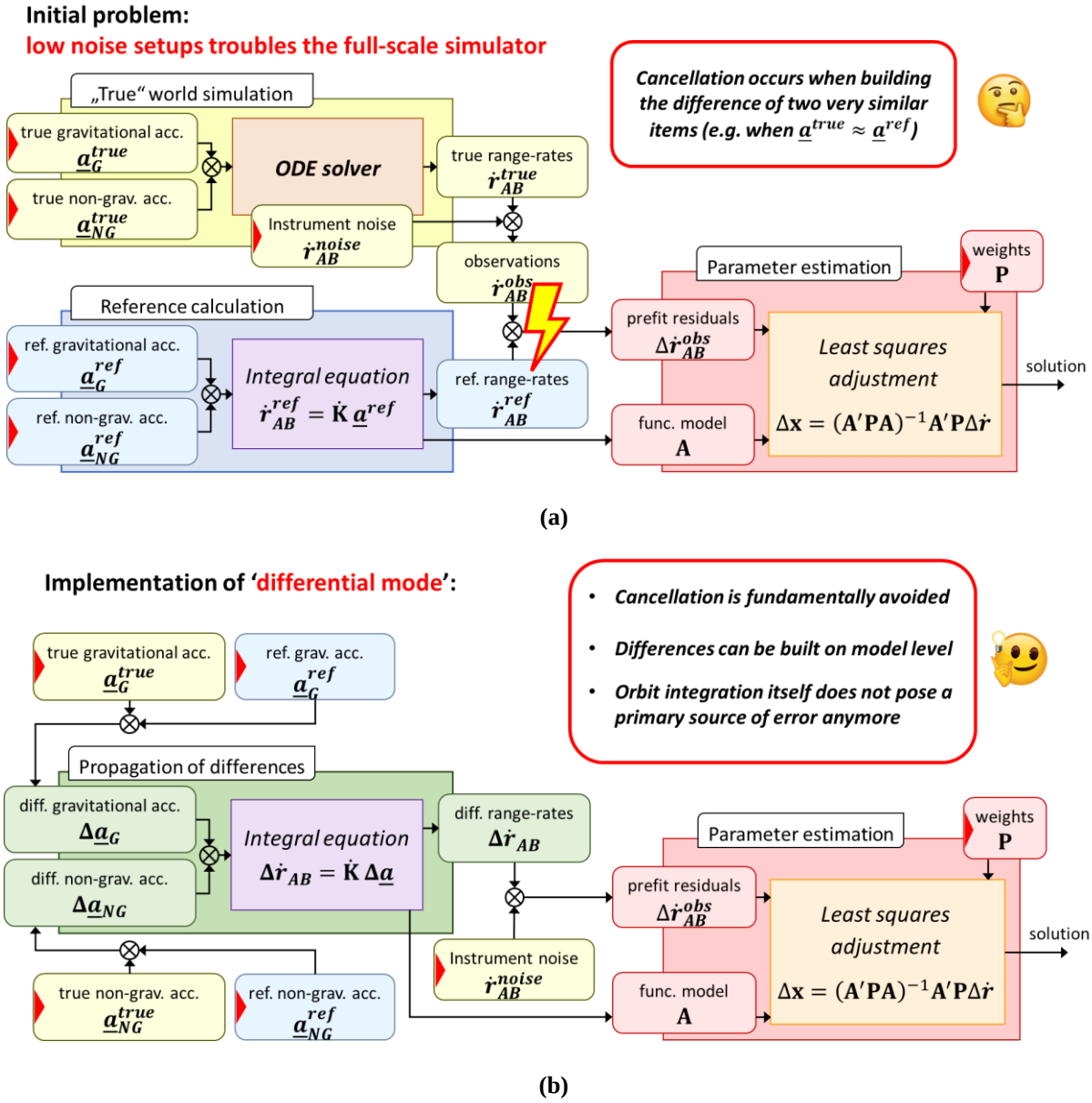

Figure 22-2 Schematic overview of the TUM full-scale SST simulator. (a) original simulation approach with separate forward- and backward module, having the numerical problem of cancellation. (b) differential simulation approach with unified forward- and backward model working with differential items.

22.3. INTERNAL VALIDATION OF THE POLIMI SIMULATOR

A set of simulations using a 61-day cycle of the GOCE orbit (*oG61D*), assuming the product-only background model (*mPO*) and instrument noise consisting of a GOCE-like gradiometer (*gGO*).

These simulations were used to test the impact on the solution of the patch size, number and density of observation points included in each patch. The set of tested parameters can be seen

in Table 22-1. As it can be noticed form Figure 22-3 the main impact of changing these parameters especially influence the lowest degrees.

Table 22-1: List of tested scenarios considering different patch size and point numbers.

Simulation name	Radius	N. of points
MediumPatch	10°	10000
LargePatch	20°	17500
LargeLargePatch	30°	17500
LargePatchDouble	20°	17500
LargeLargeMorePatch	30°	20000
LargeCore	35°	20000

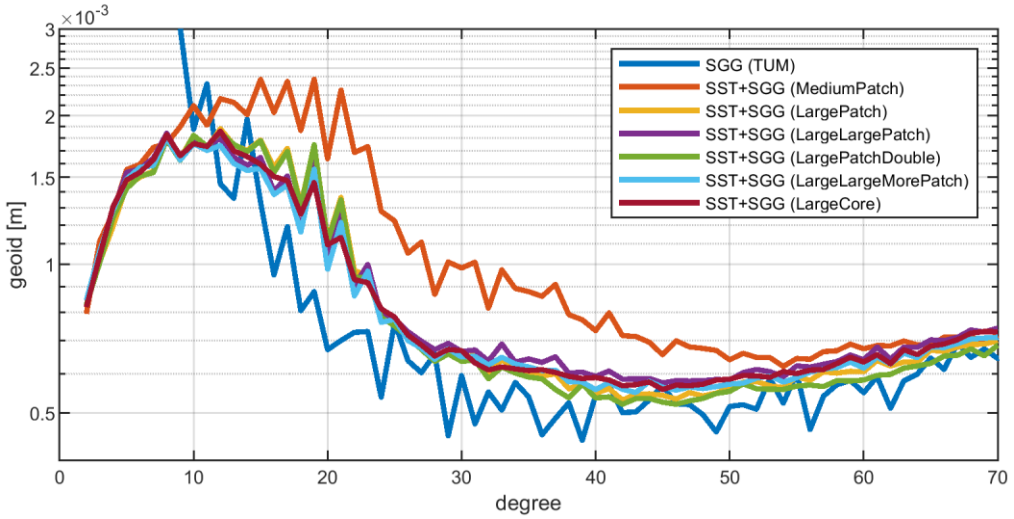

Figure 22-3 Degree errors in terms of geoid heigh for the *oG61D_mPO_gGO* (SST+SGG) computed considering different patch size and point numbers. The results are compared with the error estimate of the same simulation computed by TUM simulator.

According to the presented results all the further simulations will be performed by exploiting the parameter set used for the LargeCore solution.

22.4. INTERNAL VALIDATION OF THE TUM SIMULATOR

22.4.1. INTERNAL VALIDATION OF THE SST SIMULATOR

The TUM SST full-scale simulation software has already been validated several times (see, e.g., [RD-1]). For completeness, also the newly introduced differential mode is briefly validated (even though all core parts are identical to the original software). Figure 22-4 shows a comparison of the results from the original and differential mode of the SST simulator. Since the prefit-residuals match each other as long as a certain noise level is not undershot, it can be assessed the differential mode is working correctly. As expected, for better instruments, the differential mode also delivers better solutions than the original mode (since the original approach is corrupted by orbit integration noise).

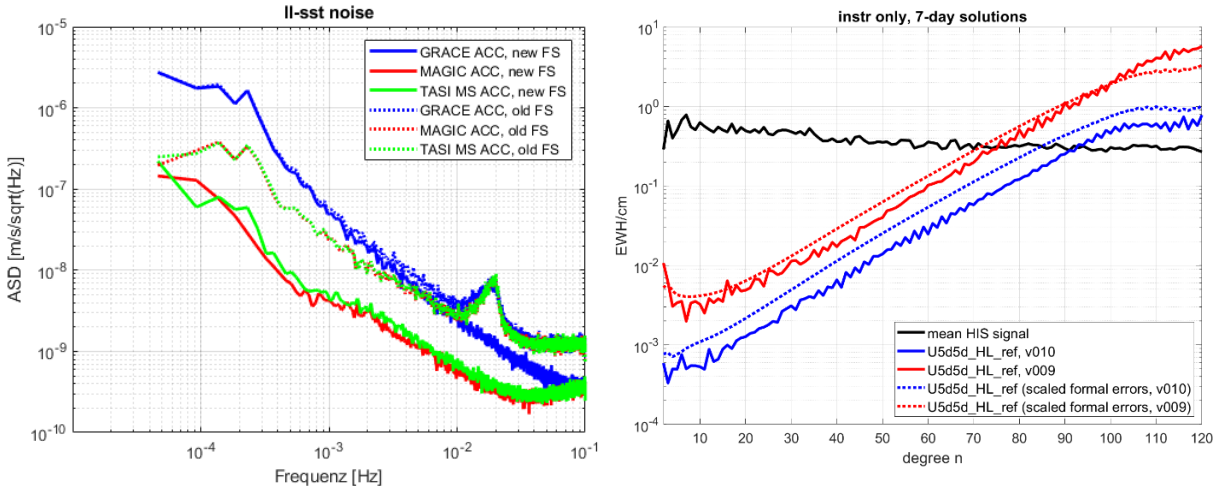

(a) **(b)**

Figure 22-4 (a) Prefit-residuals in comparison between original and differential approach for different accelerometers. Dotted lines depict the original approach, solid lines the differential. It can be seen that the artificial structures can be effectively avoided in differential mode and that lower noise models can be simulated smoothly. (b) Simulation results for a MAGIC baseline product-only scenario using the original mode (red lines) and the differential mode (blue lines). The smaller pre-fits lead to smaller retrieval errors in the final model.

22.4.2. INTERNAL VALIDATION OF THE SGG SIMULATOR

The TUM SGG simulation module has been constructed based on the official TUM GOCE real data processor. Some modifications and simplifications have been applied to be in line with the conventions of the existing SST simulator (e.g., the short-arc approach, outlier-detection). To check if the final SGG simulator is working correctly, a test using real GOCE data from a 61-day period has been performed (see Figure 25-1). It is shown that the differences to the GOCO05s reference model are small and correspond to the estimated formal errors. Additionally, the solution using simulated data comes very close to the real data solution. As to expect, the simulated data solution shows a little bit better performance since the real data includes some data gaps in the 61-day period.

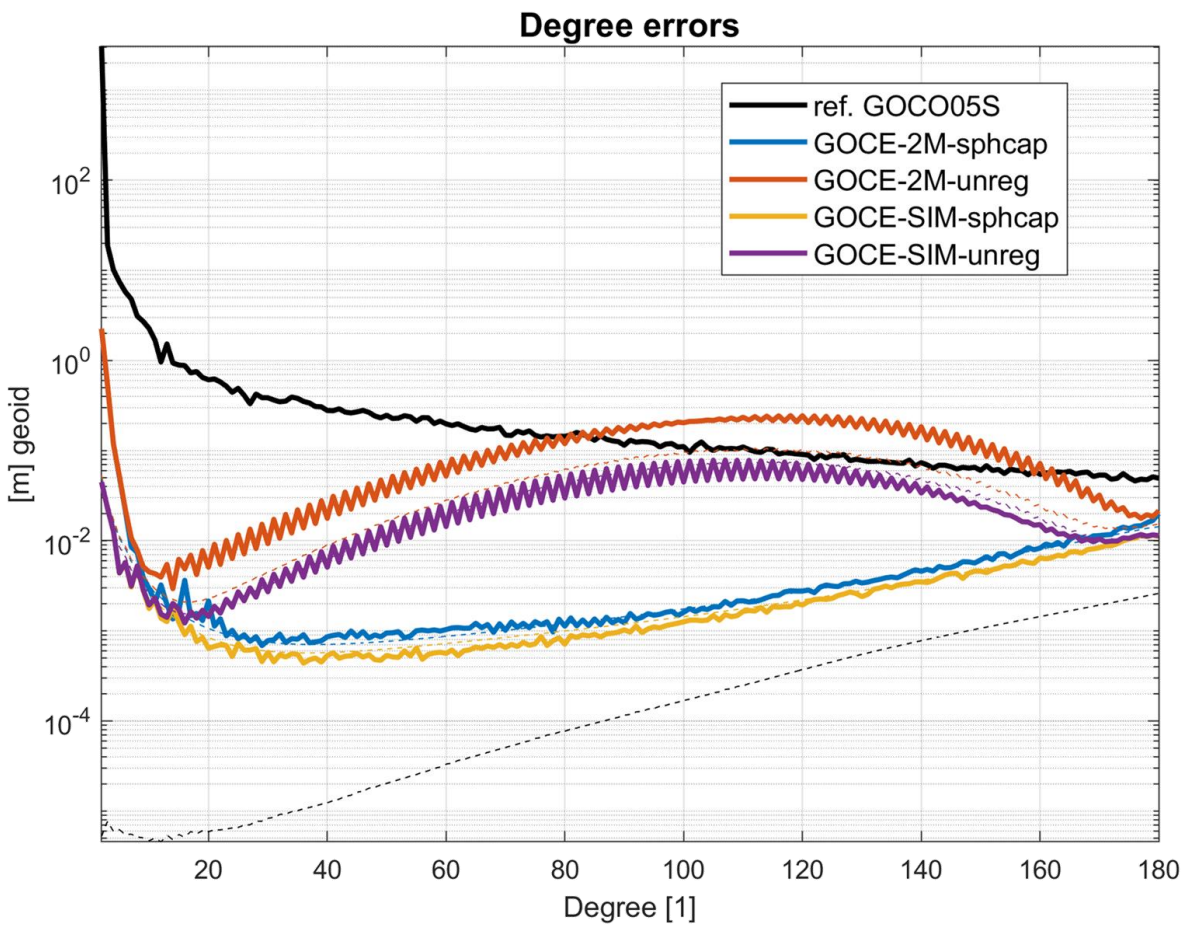

Figure 22-5 Degree errors of GOCE-only solutions for a retrieval period of a 61-day cycle (year 2010) in comparison to the static gravity field (black line, GOCO05s). Blue line: solution difference to GOCO05s from real level 1b data (spherical cap regularized, red line: unregularized). Yellow line: solution difference to GOCO05s from simulated GOCE gradients (spherical cap regularized, violet line: unregularized). Dashed lines show the formal errors.

22.5. CROSS-VALIDATION OF THE POLIMI/TUM SIMULATOR

The TUM and POLIMI simulators are cross-validated by using both the ll-SST and gradiometry cases.

As for the ll-SST case, the chosen scenario exploits the 3D_H orbit, considering a mission with a couple of satellites on the polar orbit (*o3DH1* scenario) or with two couples of satellites in a Bender configuration (*o3DH2* scenario). In both cases the considered on-board accelerometers are the "MicroStar" (*aMS*) while the LRI is the GRACE-FO one (*tGFO*). Each of the solution is computed considering both the product-only (PO) and full-noise (FN) background models. The comparison between TUM and POLIMI simulators is presented in terms of EWH degree error in Figure 22-6 and Figure 22-7, respectively.

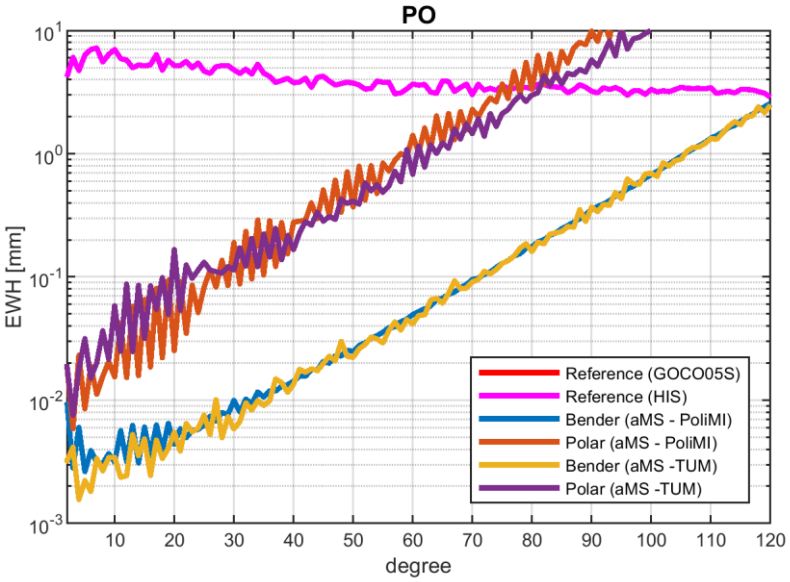

Figure 22-6 EWH degree errors for the ll-SST solutions computed by TUM and POLIMI on the 3D_H scenario considering the Polar (*o3DH1*) and Bender (*o3DH2*) configurations, with the "MicroStar" (*aMS*) accelerometers for the PO background model.

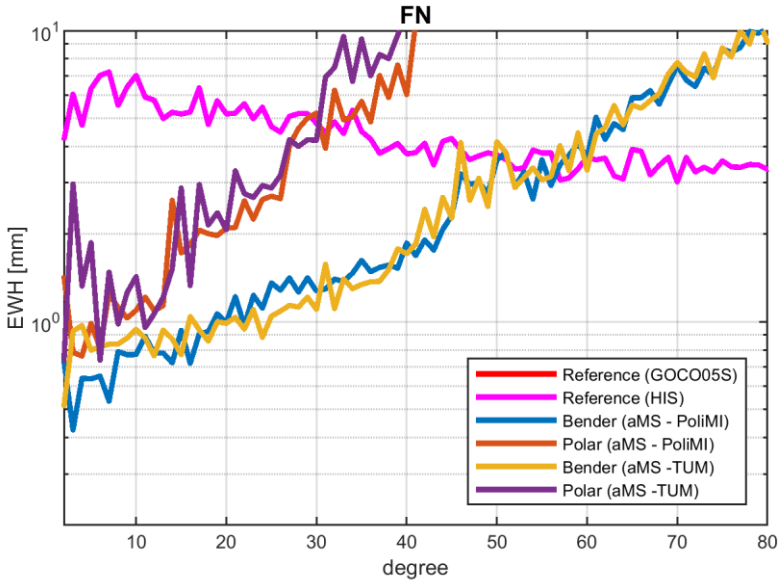

Figure 22-7 EWH degree errors for the ll-SST solutions computed by TUM and POLIMI on the 3D_H scenario considering the Polar (*o3DH1*) and Bender (*o3DH2*) configurations, with the "MicroStar" (*aMS*) accelerometers for the FN background model.

To deeper investigate the differences between the two solutions, spatial estimation error has been also taken into account. This error has been computed as the difference between the spherical harmonic synthesis of the reference background model (i.e., GOCO_05S in the PO case, and GOCO05S + the month average of HIS in the FN case) and the synthesis of the estimated solution. To avoid introducing effects related to the power of the highest degrees and biases depending on very low degrees, the synthesis is performed in the range between degree 3 and 60. The latter is chosen according to the intersection between the estimation error and the

power of the non-tidal time variable signal for the Bender scenario in Figure 22-7. All the comparisons are presented in Figure 22-8, Figure 22-9, Figure 22-10, and Figure 22-11.

The two simulators show a good agreement both in terms of degree error and spatial distribution of the residuals, thus demonstrating similar capacity in processing the data.

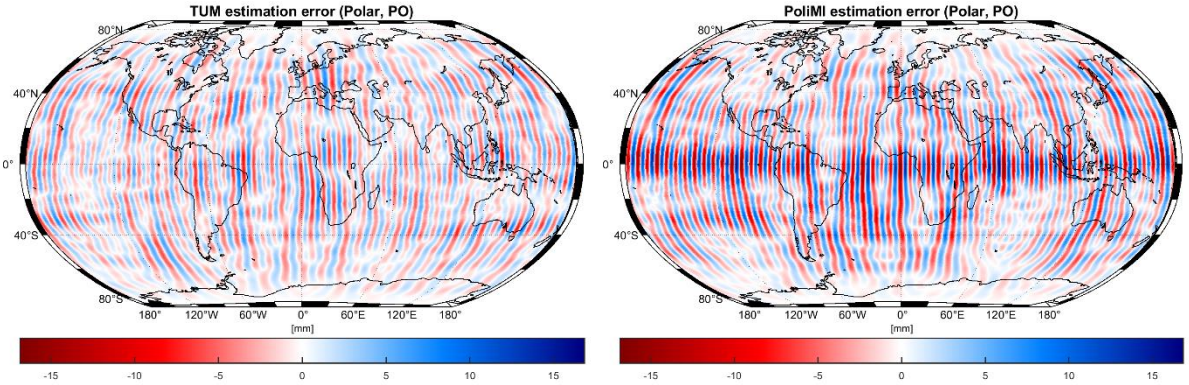

Figure 22-8 Spatial distribution of the EWH error for the solutions computed with a couple of satellites on the polar orbit and PO background model. TUM results on the left, POLIMI results on the right.

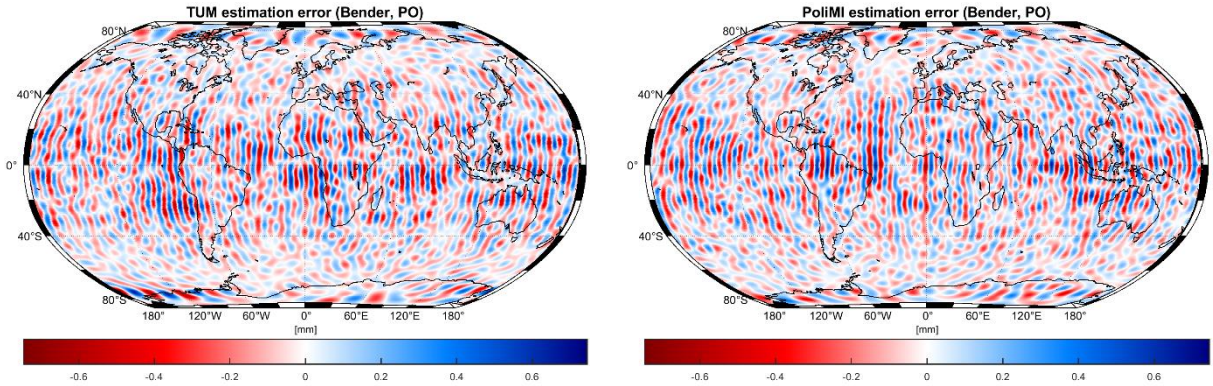

Figure 22-9 Spatial distribution of the EWH error for the solutions computed with two couples of satellites in a Bender configuration and PO background model. TUM results on the left, POLIMI results on the right.

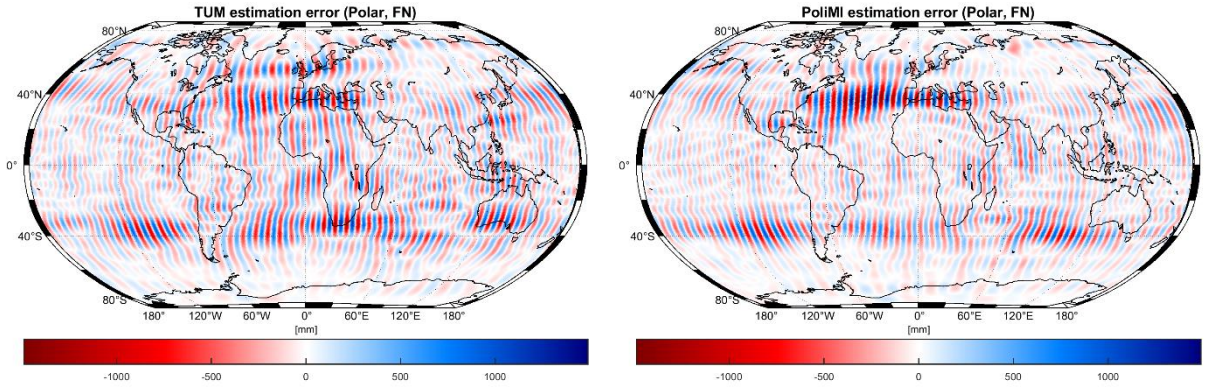

Figure 22-10 Spatial distribution of the EWH error for the solutions computed with a couple of satellites on the polar orbit and FN background model. TUM results on the left, POLIMI results on the right.

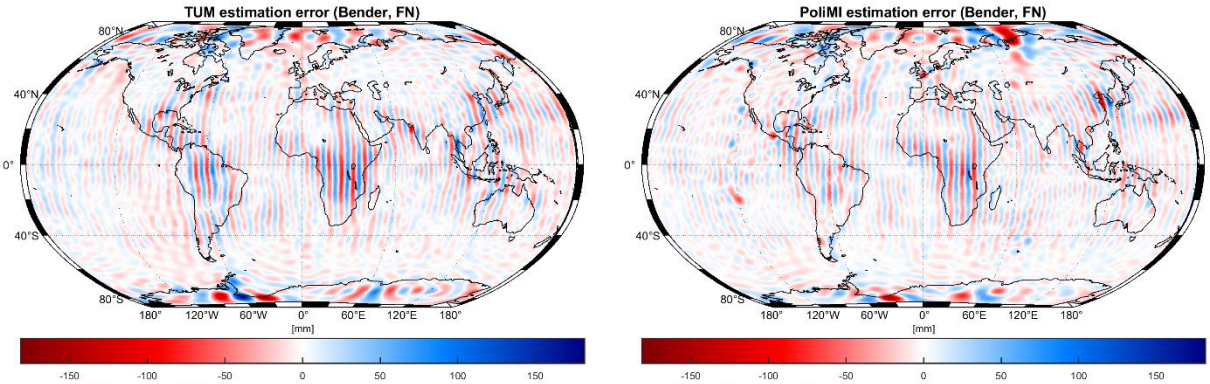

Figure 22-11 Spatial distribution of the EWH error for the solutions computed with a couple of satellites on a Bender orbit and FN background model. TUM results on the left, POLIMI results on the right

Finally, also the empirical estimation error of the single coefficients has been considered for all the cases, comparing the results of the two simulators. The results are reported in Figure 22-12, Figure 22-13, Figure 22-14, and Figure 22-15, considering Polar and Bender configurations and PO and FN background models.

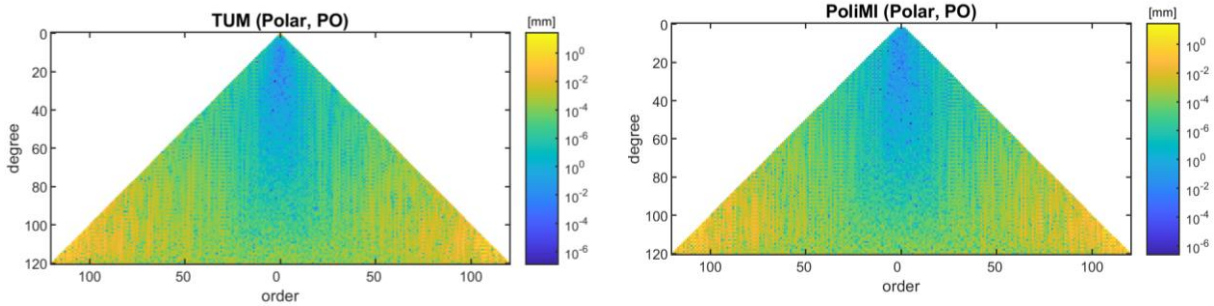

Figure 22-12 Empirical estimation error of spherical harmonic coefficients in terms of EWH for the solutions computed with a couple of satellites on a polar orbit and PO background models. TUM results on the left, POLIMI results on the right.

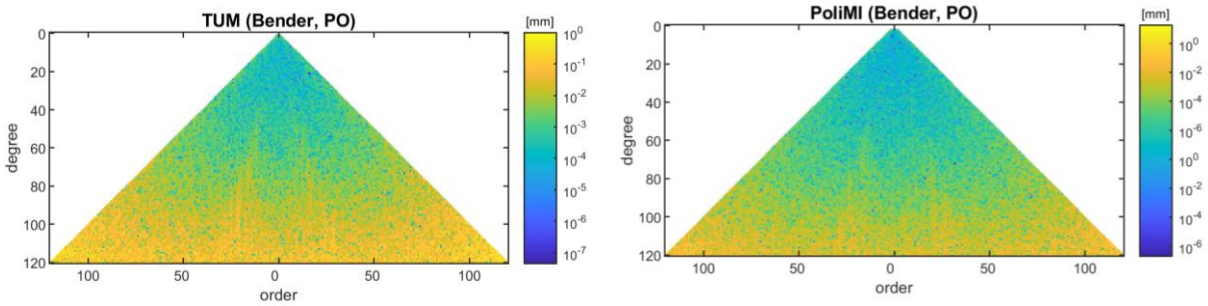

Figure 22-13 Empirical estimation error of spherical harmonic coefficients in terms of EWH for the solutions computed with a couple of satellites on a Bender orbit and PO background models. TUM results on the left, POLIMI results on the right.

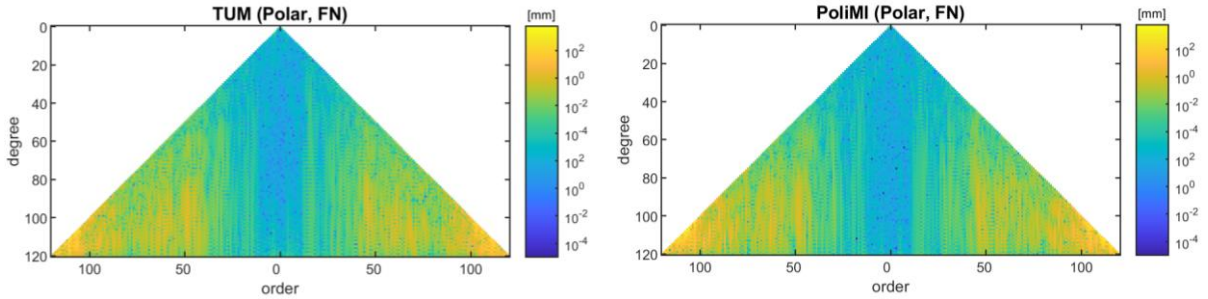

Figure 22-14 Empirical estimation error of spherical harmonic coefficients in terms of EWH for the solutions computed with a couple of satellites on a polar orbit and FN background models. TUM results on the left, POLIMI results on the right.

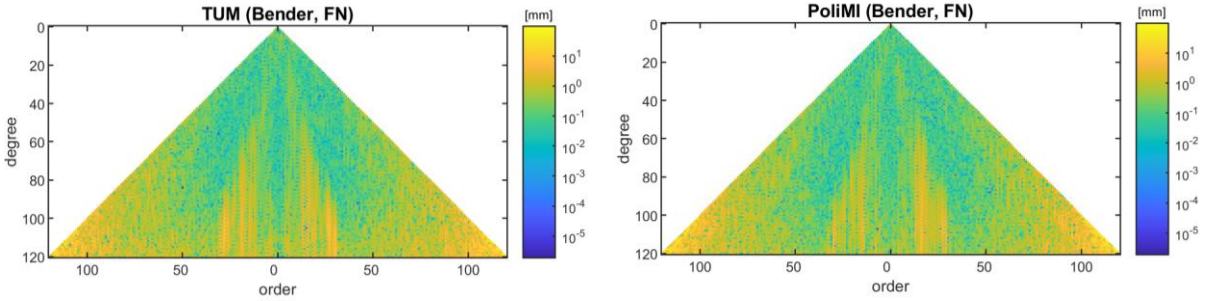

Figure 22-15 Empirical estimation error of spherical harmonic coefficients in terms of EWH for the solutions computed with a couple of satellites on a Bender orbit and FN background models. TUM results on the left, POLIMI results on the right.

As for the gradiometry POLIMI-TUM comparison, the tests have been performed by exploiting the 61-day cycle of the GOCE orbit (*oG61D*), assuming the product-only background model (*mPO*) and instrument noise consisting of a GOCE-like gradiometer (*gGO*).

The results from the two simulators are shown in terms of geoid height degree error in Figure 22-16. In general, the two simulators have a comparable performance at a global level. As for the POLIMI simulator, a proper patch size and point density calibration have been required, following the steps explained in Section 22.3.

Comparing the two error curves of Figure 22-16, the main remarkable difference is at low degrees, i.e. lower than 20. In fact, the POLIMI simulator exploits the combination of gradients with a hl-SST solution that is necessary to perform the remove-restore process for the local

collocation gridding. However, differences at this level are not so relevant, since the main target of gradiometric missions is in the medium-high degree range.

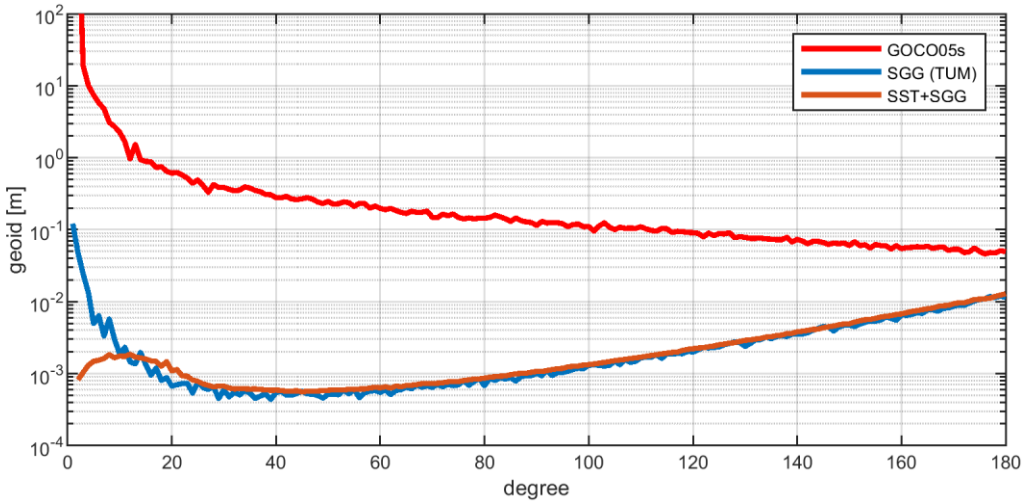

Figure 22-16 Geoid height degree errors for the *oG61D_mPO_gGO* solutions computed by TUM (SGG) and POLIMI (SST+SGG), showing the good consistency of the two simulators.

23. APPLICABLE DOCUMENTS, REFERENCE DOCUMENTS, AND PUBLICATIONS OF PART 4

23.1. APPLICABLE DOCUMENTS

[AD-1] Mission Requirements Document, Next Generation Gravity Mission as a Mass-change And Geosciences International Constellation (MAGIC) - A joint ESA/NASA double-pair mission based on NASA's MCDO and ESA's NGGM studies (2020). ESA-EOPSM-FMCC-MRD-3785

[AD2] Scientific Readiness Levels (SRL) Handbook, Issue 1, Revision 0, 05-08-2015

[AD3] Study of Cold Atom Interferometry (CAI) Gravity Gradiometer Sensor and Mission Concepts - ESA Contract 4000112677, Summary Report "Concept study and preliminary design of a cold atom interferometer for space gravity gradiometry"

[AD4] Cold Atom Inertial Sensors: Mission Applications – ESA Contract 4000117930, Final Report TASI-SD-CAI-FR

[AD5] Hybrid Atom Electrostatic System for Satellite Geodesy – ESA Contract 4000113573, Final Report RF_7-24721_DMPH

[AD6] Hybrid Atom Electrostatic System for Satellite Geodesy Follow-On – ESA Contract 4000112290, Final Report RT 6/27346 DPHY

[AD7] QSG_UR_SATM_v2.0.xlxs – ESA/EC Quantum Space Gravimetry User Requirements Science and Traceability Matrix v2.0 (2022)

[AD8] Quantum Space Gravimetry for monitoring Earth's Mass Transport Processes (QSG4EMT). Project Proposal, Proposal No. TUM/2022-QSG4EMT, Technical University of Munich

23.2. REFERENCE DOCUMENTS

[RD-1] NGGM/MAGIC – Science Support Study During Phase A "MAGIC". ESA Contract No. RFP/3-17035/20/NL/FF/tfd. Final Report. Issue 1.0 (15.11.2022)

23.3. REFERENCES

Douch, K., Wu, H., Schubert, C., Muüller, J. and dos Santos, F. P. (2018). Simulation-based evaluation of a cold atom interferometry gradiometer concept for gravity field recovery, *Advances in Space Research* **61**(5): 1307–1323.

F. Migliaccio, M. Reguzzoni, G. Rosi, C. Braitenberg, G. M. Tino, F. Sorrentino, S. Mottini, L. Rossi, Ö. Koç, K. Batsukh, T. Pivetta, A. Pastorutti, and S. Zoffoli (2023) The MOCAST+ Study on a Quantum Gradiometry Satellite Mission with Atomic Clocks. *Surveys in Geophysics*. DOI: 10.1007/s10712-022-09760-x

Federica Migliaccio, Mirko Reguzzoni, Khulan Batsukh, Guglielmo Maria Tino, Gabriele Rosi, Fiodor Sorrentino, Carla Braitenberg, Tommaso Pivetta, Dora Francesca Barbolla, and Simona Zoffoli (2019) MOCASS: A Satellite Mission Concept Using Cold Atom Interferometry for Measuring the Earth Gravity Field. *Surveys in Geophysics*, **40**, 1029–1053. DOI 10.1007/s10712-019-09566-4

Mayer-Gürr, Torsten (2006): Gravitationsfeldbestimmung aus der Analyse kurzer Bahnbögen am Beispiel der Satellitenmissionen CHAMP und GRACE. Dissertation, Rheinische Friedrich-Wilhelms-Universität Bonn. https://nbn-resolving.org/urn:nbn:de:hbz:5N-09047

Migliaccio, F., Reguzzoni, M. and Sansò, F. (2004). Space-wise approach to satellite gravity field determination in the presence of coloured noise, *Journal of Geodesy* **78**(4): 304–313.

Mirko Reguzzoni and Nikolaos Tslefes (2009) Optimal multi-step collocation: Application to the space-wise approach for GOCE data analysis. *Journal of Geodesy*, **83**(1), 13–29. DOI 10.1007/s00190-008-0225-x

Lorenzo Rossi, Mirko Reguzzoni, Öykü Koç, Gabriele Rosi, and Federica Migliaccio (2023) Assessment of gravity field recovery from a quantum satellite mission with atomic clocks and cold atom gradiometers. *Quantum Science and Technology*, **8**, 014009. DOI: 10.1088/2058-9565/aca8cc

PART 5:

MASS CHANGE PRODUCTS FROM QSG MISSION ARCHITECTURES

24. INTRODUCTION

The purpose of this paart is to describe the mass change products derived from various QSG architectures, such as LL-SST and gradiometry. It refers to Task 4, 5, 6 and 7 of the SoW and WPs 400 to 700 of the WBS.

25. THE TRADE SPACE FOR QUANTUM SPACE GRAVIMETRY

In the context of this project, the trade space consists of all mission variables which influence the target object (i.e., the retrieval of the time-variable gravity field). Since, principally, many different factors (variables) influence the retrieval performance, the focus will be laid on those which can be improved/altered in the scope of this project. This leads in a first phase to a 4 dimensional trade space:

1. Measurement concept
2. Constellation design
3. Instruments
4. [Background models]

Each dimension has its own constraints based on the target objective and predefined boundary conditions. Based on these constraints, feasible discrete options are derived for each variable. Then, investigative actions are carried out to determine the influence of the specific options on the final target objective (i.e., the gravity field retrieval performance). Eventually, assessments will be made whether the investigated option is suitable/beneficial or not. An overview of the initial (phase A) trade-space with first results is given in Figure 25-1. In the following, each dimension, its constraints and derived options will be explained in more detail.

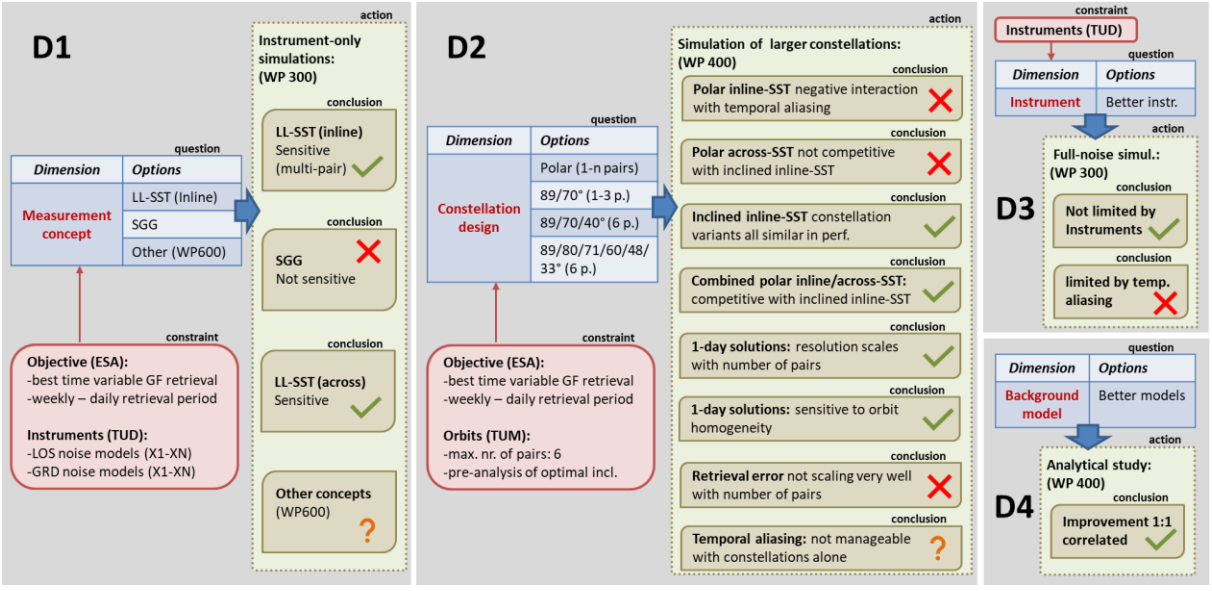

Figure 25-1 Illustration of the final trade-space with important constraints (red boxes), feasible options (blue boxes) and investigative actions with conclusions (green boxes).

25.1. MEASUREMENT CONCEPT

For satellite gravity field missions, different measurement concepts are feasible. The most promising ones in terms of gravity field retrieval performance is low-low satellite to satellite tracking (LL-SST) and satellite gravity gradiometry (SGG). Both concepts have already proven to work in space through the successful completion of the GRACE (LL-SST) and GOCE (SGG) satellite gravity field mission. As constraints for the implementation of these concepts, future instrument noise models (X1-Xn, see WP200, TR D3) are assumed. Having these instrument noise models, the sensitivity of the concepts regarding time-variable gravity can be assessed through instrument-only simulations. These simulations are performed in the scope of WP300 (see TR D4) for GRACE-like and GOCE-like missions with replaced future instrument noise models. As a result of these simulations, it has been shown that the SGG concept is still not sensitive to time-variable gravity (at least for monthly and shorter scales) even when assuming a most optimistic future instrumentation. Thus, a future SGG mission might still be beneficial for retrieving the static gravity field but cannot compete with the LL-SST principle regarding the sensitivity to time-variable gravity. On the other hand, LL-SST shows good sensitivity for the time-variable gravity field signal and improved future instruments allow to increase this sensitivity even further.

Next to LL-SST and SGG, also other concepts exists. On the one hand, there are physically related concepts such as classical HL-SST or SLR. But there exist also novel approaches such as time-measurement/-transfer concepts probing the laws of general relativity. While all of these methods are theoretically able to detect time-variable gravity, it is assumed that they are not (yet) competitive to SST/SGG due to the principle itself or technical hurdles which have not yet been overcome. However, there exist also some further variations of the LL-SST principle which might be worth investigating. For instance, one idea is to pursue the so-called across-track LL-SST approach, where the satellites are tracking each other more or less perpendicular to their flight direction. This is investigated in the scope of WP600. It is shown that this is a promising approach for polar-only constellations in conjunction with regular inline LL-SST pairs (see chapter 28). There, it is also explained why some other concepts (HL-SST, combined SGG+SST) do not really fit for a quantum mission. However, since there is always the possibility of the existence of a not yet invented concept, we left a question mark in the corresponding trade-space branch (even if very unlikely).

The findings from the investigations for D1 are to a large extend independent from all other dimensions: while the constellation design (D2) and the chosen instruments (D3) are impacting the absolute retrieval performance, the relative retrieval performance between LL-SST and SGG will remain widely unchanged (meaning that LL-SST will always be several magnitudes more sensitive than SGG when assuming similar accelerometers/gradiometers). Due to this finding, it has been decided (in agreement with ESA) to not further pursue the SGG principle regarding time-variable gravity field recovery within this project. Improving SGG might still be relevant for static gravity field retrieval which, however, is not in the scope of this project. Instead of investigating SGG, the focus will be shifted more towards improving the parameterization (see section 26.4).

25.2. CONSTELLATION DESIGN

Simulation results from WP300 indicate that the gravity field retrieval performance is strongly limited by temporal aliasing for single and double-pair constellations. Temporal aliasing is caused to a large extend by the temporal (and spatial) under-sampling of the time-variable gravity field. Thus, increasing the spatio-temporal coverage with observations is one of the main drivers when trying to mitigate temporal aliasing. The only way to increase the observation coverage is to add additional pairs to the constellation. As a rule of thumb, to fulfill the Nyquist sampling theorem up to d/o l_{max} and up to a maximum temporal frequency f_{max} (in days), a number of n_{sat} satellites are needed (with n_{rpd} being the number of revolution per day of each satellite, assuming an optimized constellation):

$$n_{sat} = 2\,\frac{f_{max}\,l_{max}}{n_{rpd}}.$$

When choosing $f_{max} = 2$ (covering the fastest tidal constituent), $l_{max} = 90$ (about 200km spatial resolution) a number of $n_{sat} \approx 23$ satellite pairs would be needed (assuming GRACE-like orbits with an orbital period of about 90min). Note that this is only an approximation to satisfy the Nyquist theorem spatially in the one-dimensional case at the equator (accounting for equator crossings). Since the actual two-dimensional distribution is not regular (mostly over-sampled, in some places under-sampled), it is known that the Nyquist rule can be violated to some extent (towards a sparser coverage). Thus, even about 20 pairs may be sufficient for such a scenario without getting significant numerical instabilities. Having such a constellation, it is assumed that temporal aliasing could be widely avoided since the signal energy above half-daily frequencies is assumed to be low (see Zingerle et al., 2024, for a more elaborate discussion).

However, realizing a constellation with about 20 satellite pairs in the midterm future seems to be too unrealistic at the time of writing. Hence, as a compromise, only smaller constellations up to 6 pairs will be investigated in the scope of this project. Even if the problem of temporal aliasing is not (fully) controllable with this smaller constellations, it is presumed that the influence can be at least weakened to a certain extent. The possible influence of such constellations is investigated in chapter 26: in 26.1, the impact of different orbit configurations is evaluated by a kind of brute force approach using the simplified reduced-scale simulator. In 3.2, based on the findings in 26.1, a set of constellations is selected and further refined for an in-depth evaluation. Finally, in 26.3, full-scale simulations are performed using the optimized orbits from 3.2.

It is shown (in sec. 26.1, 26.2, 26.3) that adding pairs to the constellation helps to mitigate temporal aliasing, at least somewhat. Constellation with a maximized number of inclinations seem to perform slightly better than constellations with fewer distinct inclinations even when having the same overall number of pairs. However, at large, there is no game-changing difference between a wide range of different inclined constellations in terms of retrieval performance and in all cases temporal aliasing still poses the overwhelmingly dominant error source: concerning 7-day solutions, a good performing 6-pair constellations reduces the retrieval error by a factor of 2-3 compared to a double-pair constellation. Even though this error reduction is significant, one would need an improvement by a at least a factor of about 1000 to reach the error level where the instruments become relevant again (assuming the X1 model from WP 200). This highlights that, currently, temporal aliasing is by far the most limiting

element regarding the retrieval performance. Consequently, further steps for reducing temporal aliasing must be taken to see any further improvement in the time-variable gravity field retrieval.

Next to increasing the constellation size, the only other (influenceable) element which might help decrease temporal aliasing is an improved parameterization of the time-variable gravity field. Hence, as already mentioned in 25.1, adjusting the parameterization is one central item that is additionally investigated in this project. This is done by introducing and testing the spline parametrization (section 26.4). Since investigating new parametrization schemes is a complex and time-consuming endeavor, only the foundation can be laid within this project. Due to time constraints and the still experimental character, the primary simulation results will not be recomputed with the spline parameterization. Therefore, one shall keep in mind that the results shown in section 26.3 can probably still be improved when adjusting the parametrization and/or stochastic modelling. Thus, the results in section 26.3 might be interpreted as the worst-case performance which can just improve with enhanced future parametrization/modelling techniques.

25.3. INSTRUMENTS

As demonstrated in the previous section, the instruments are currently not the limiting factor. Thus, improving the instruments will not lead to a significant improvement of the time-variable gravity field retrieval. It shall be noted that, with the current static parameterization, there is a relation between the weighting of the instrument and the temporal aliasing. This means that an instrument with an overall better noise behavior might deliver a larger time-variable gravity field retrieval error than an instrument with a worse noise behavior but a different shape in terms of its ASD curve. While this seems counterintuitive at a first glance, it is quite obvious that a different weighting of the observations might interact either in a positive or negative way with the (not parameterized) time-variable gravity field signal (assuming that all considered noise levels are low enough to not play a role). It is assumed that this interaction becomes smaller once more of the temporal aliasing is explained through the functional model (e.g., through a time-aware parameterization).

25.4. BACKGROUND MODELS

The temporal aliasing error scales linearly with the magnitude of the time-variable signal. This is obvious, since the functional model is in a (very) good approximation linear and temporal aliasing is purely caused by the time-variable signal component. Thus, reducing the background model errors to x % of the original errors would directly translate to a reduction of the final gravity field retrieval error to the same x % (of the original error). Referring to sec. 25.2, a reduction to about 0.1% (i.e., about 1000 times better) would be necessary to reach the level of the instrument sensitivity again. Such an improvement is beyond the bounds of possibility, considering a reduction to 50% already as an optimistic improvement within the next 10 years. On the other hand, if background models with errors of 0.1% would be available, the additional benefit of a satellite gravity field mission must be questioned (since the background model would then already explain the gravity field to an overwhelming part). Thus, despite the fact that the performance of the background models cannot be directly influenced by the mission design, solving the temporal aliasing problem by means of an improved background modelling

is not possible: neither realistically (due to limited improvement potential) nor theoretically (due to rendering the mission itself unnecessary if realistically possible).

Additionally, it shall be noted that in a common processing scenario not all time-variable signal components are reduced through background models. Usually, only the non-tidal atmosphere and ocean component (AO) and the ocean-tide component are reduced. The non-tidal hydrology, ice and surface signal component (HIS) is normally not reduced. This means that the actual benefit from improving the background models would be smaller than stated above. This is readily discernible since, even without background model errors, one would still have the full aliasing from the HIS component. Nevertheless, in the scope of this project, improvements in the background models can always be interpreted as an additional benefit which comes on top of all the other improvements. Due to the linear behavior, these improvements are not directly correlated with the other dimension and can therefore be seen as mainly independent from the trade space (as long as not reaching 0.1%). Eventually, since one can not have a direct influence on these improvements, this dimension contributes only marginally to the trade space (since it is not even a real variable as such).

26. MASS CHANGE PRODUCTS FROM MISSION ARCHITECTURES LL-SST WITH 3D HYBRID ACCELEROMETER

26.1. NUMERICAL SIMULATION STUDIES OF DIFFERENT LL-SST ARCHITECTURES AND SELECTION OF SCENARIOS (WP410)

Based on the trade space definition as discussed in chapter 25, extensive simulations studies with the reduced-scale simulator were performed to condense the trade space of LL-SST mission architectures and to identify the key parameters of extended satellite constellations driving the achievable gravity field performance.

The main purpose of extended constellations is their potential to reduce temporal aliasing errors (in comparison to instrument/product errors). Therefore, the idea of this study is to keep the instrument noise fixed, to investigate on this common basis a wide trade space of constellations, and to assess them, e.g., against the expected performance of a MAGIC double pair.

The assumptions for the product-noise were related to the MAGIC baseline. For the accelerometer, we assume a line-of-sight acceleration difference error:

$$acc_{los} = 1 \cdot 10^{-11} \sqrt{\left(\frac{10^{-3}Hz}{f}\right)^2 \Big/ \left(\left(\frac{10^{-5}Hz}{f}\right)^2 + 1\right) + 1 + \left(\frac{f}{10^{-1}Hz}\right)^4} \; \frac{m}{s^2/\sqrt{Hz}}$$

and for the intersatellite ranging:

$$lri = 2 \cdot 10^{-8} \cdot (2\pi f)^2 \cdot \sqrt{\left(\frac{10^{-2}Hz}{f}\right)^2 + 1} \, \frac{m}{s^2\sqrt{Hz}}$$

Regarding background models, ocean tide model differences GOT4.7 – EOT11a were assumed, and for non-tidal BM errors, we assumed either ESA-ESM AOHIS signal (January 2002) as a worst case, or HIS + AOerr, which is in-line with the current MAGIC simulations.

In a first pre-study, we used a wide trade-space in order to identify the main drivers of the performance of multi-satellite LL-SST constellations. For this, we defined physically meaningful orbits with similar altitudes and repeat periods, see Table 26-1. In a kind of brute-force approach, reduced-scale simulations of each combination of these satellite pairs were performed. The only constraint was that at least 1 polar pair has to be part of the constellation. Based on the orbits given in Table 26-1, this results in 112 combinations. In order to reduce the computational load, the max. degree was limited to d/o 50, because we assume that generalized conclusions can be derived already from this set-up. The quality criterion for the evaluation are global EWH differences w.r.t. the ("true") mean temporal signal.

Table 26-1: Orbit parameters for orbits used in the pre-study with a wide trade-space.

Orbit Name	i [°]	N_{days}	N_{revs}	h [km]	M_i [°]	Ω [°]
A	89	13	203	362.58	1	0
B	89	13	203	362.58	1	120
C	89	13	203	362.58	1	240
D	60	15	232	363.09	1	0
E	65	15	232	369.19	1	0
F	70	15	233	356.15	1	0
G	45	18	277	371.70	180	0

Figure 26-1 shows the results of all 112 combinations, for the worst-case of aliasing of the full AOHIS signal, in terms of cumulative global EWH rms errors up to d/o 50. Very obvious is the worse performance of all constellations that are only composed of polar pairs (first line). Therefore, for further analysis they were excluded. Figure 26-2 show the same results, but now excluding the first line, i.e. no inclined pairs involved.

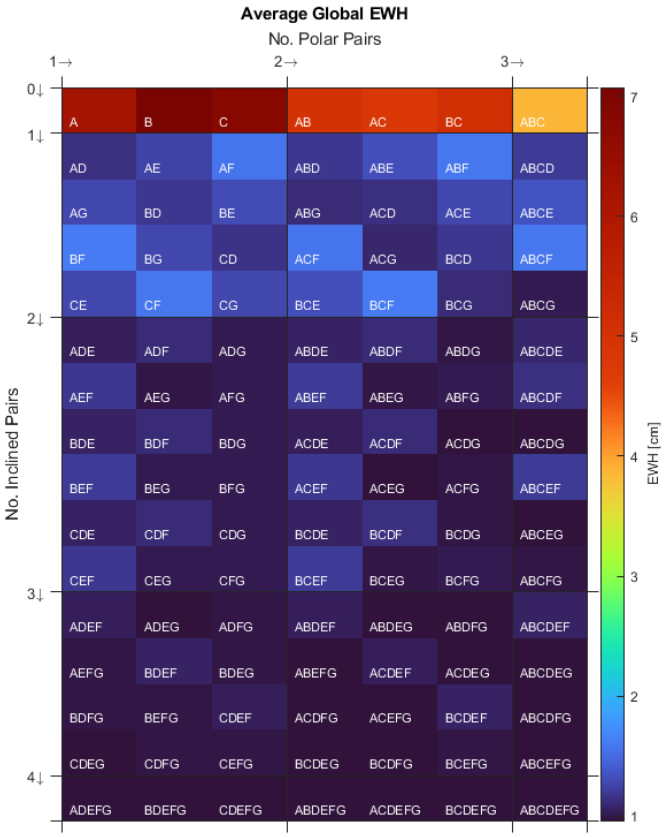

Figure 26-1: Global EWH rms [cm] of 112 satellite constellations. Input signal: full AOHIS, max. d/o 50. Annotation in accordance with the orbits in Table 26-1.

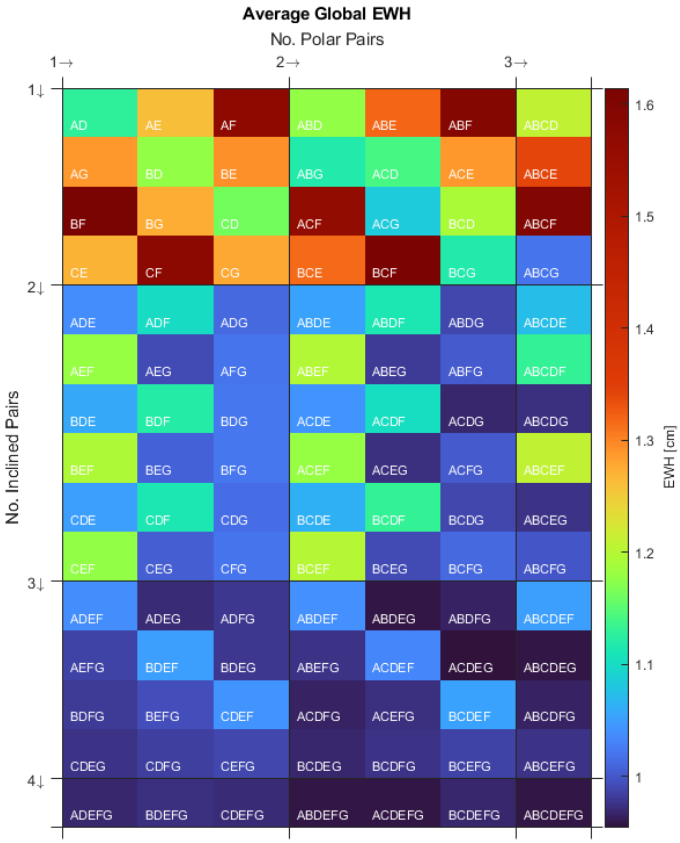

Figure 26-2: Same as Figure 26-1, but first line (polar pair constellations) excluded.

Analyzing Figure 26-2 in detail, the following main conclusions can be drawn:

- There is no systematic improvement when adding polar pairs, i.e. increasing redundancy does not help.
- There is a systematic improvement when adding inclined pairs.
- Adding a low inclined pair (G; i = 45°) delivers the best results.
- As an example, the 2 polar + 1 incl. 45° (ACG) shows an improvement of about 32% compared to 2 polar + 1 incl. 70° (ABF). This is also shown by the EWH error structure in Figure 26-3, which reveals a significant reduction of stripes in the equatorial regions, while the striping is larger for latitudes > |45°|. In total the EWH rms of the ABF constellation is 1.59 cm, and of the ACG constellation 1.08 cm.
- However, the relative gain when adding further pairs is decreasing.

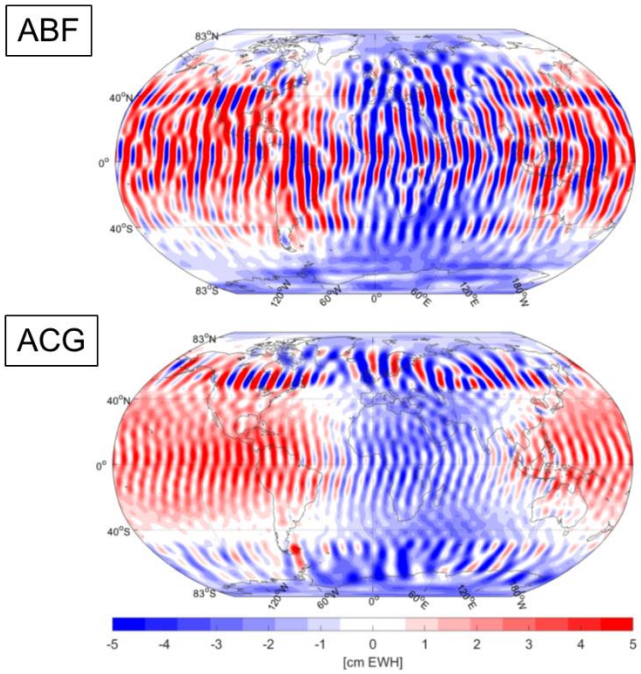

Figure 26-3: Global EHW errors [cm] for constellations ABF and ACG. Input signal: full AOHIS, max. d/o 50.

The second scenarios, where only AO errors instead of the full AOHIS signal are involved, show generally lower amplitudes, but a very similar relative behaviour as the AOHIS case (Figure 26-4).

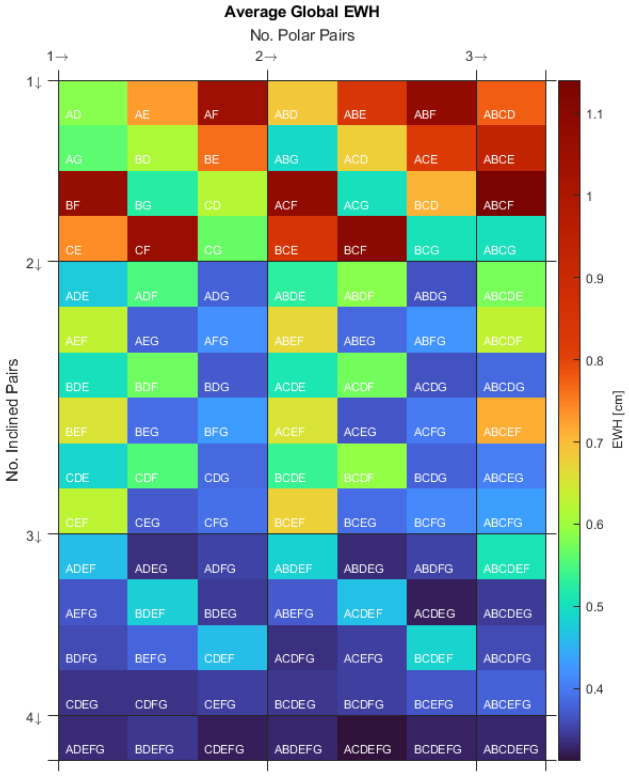

Figure 26-4: Global EWH rms [cm] of multi-pair constellations. Input signal: HIS + AO error, max. d/o 50. Annotation in accordance with the orbits in Table 26-1.

As a sanity check, all these constellations were also computed including only the product-noise. The results are shown in Figure 26-5. As expected, there are much lower error amplitudes, and the performance gradually improves with the number of satellites.

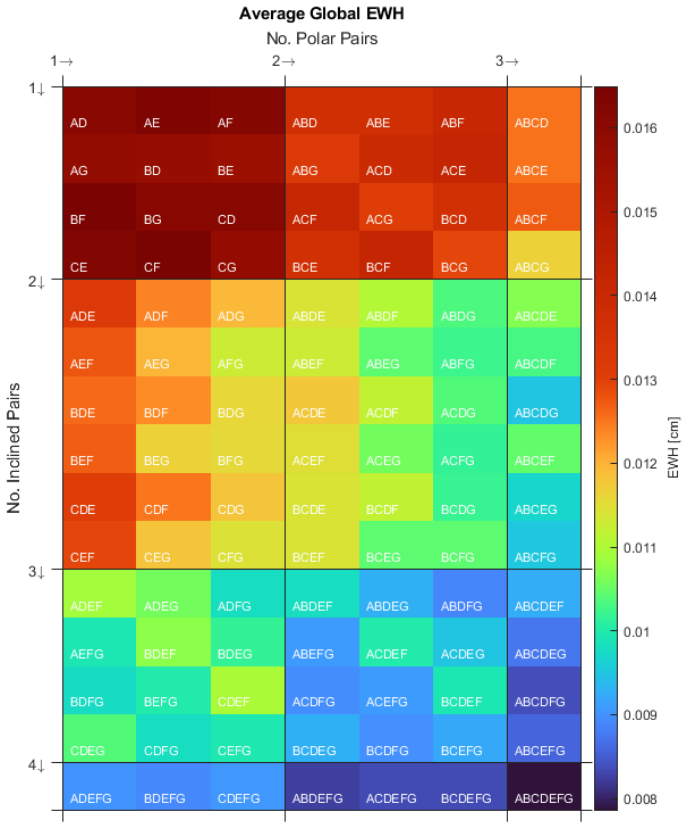

Figure 26-5: Global EWH rms [cm] of multi-pair constellations. Product-only noise, max. d/o 50. Annotation in accordance with the orbits in Table 26-1.

The main lesson learnt from these pre-studies is that the inclination is the main driver of the de-aliasing capabilities of a constellation. In contrast, decreasing the orbit altitude generally improves the performance due to an improved sensitivity (signal-to-noise ratio), but is not directly linked to the de-aliasing behaviour of a constellation.

Therefore, we can reduce the trade-space by mainly concentrating on variations of the inclination when designing multi-pair constellations. In the next step, the dependence of constellations on the involvement of pairs with varying inclination shall be investigated. For this purpose, a new set of satellite orbits were designed, see Table 26-2.

Table 26-2: Orbits (3 polar, 26 inclined) used for the study on the variation of inclinations.

i [°]	N_{days}	N_{revs}	h [km]	M_{i1}/M_{i2} [°]	Ω [°]
89 (A)	13	202	385	0	0
89 (B)	13	202	385	180	0
89 (C)	13	202	385	0	180
20	13	199	383	0/180	0
25	13	199	385	0/180	0
30	13	199	387	0/180	0
35	13	199	389	0/180	0
40	13	199	393	0/180	0
45	13	199	396	0/180	0
50	13	200	377	0/180	0
55	13	200	382	0/180	0
60	13	200	388	0/180	0
65	13	200	393	0/180	0
70	13	201	377	0/180	0
75	13	201	385	0/180	0
80	13	201	392	0/180	0

It involves two groups of satellite pairs with different mean anomaly in order to avoid pairs being in the same location for identical inclinations, resulting in 3 polar and 26 inclined pairs with the same repeat period (13d) and similar altitude. Input to the simulations was the full AOHIS signals, but in the gravity retrieval process daily (Wiese) fields were co-estimated (up to d/o 20 or 30).

At first, we tried to find optimized 3-pair solutions, being composed of 1 polar and 2 inclined pairs. Figure 26-6 shows the performance results in terms of EWH rms up to d/o 50 when varying the inclination of the two inclined pairs. Here, daily fields up to d/o 20 were co-estimated. Evidently, a good global performance can be achieved for the inclinations i_1 = [60°, 65°], i_2 = [30°, 45°], with the best performance for : i_1 = 60°, i_2 = 35°. For comparison, the best double pair in this analysis would have the second pair in an inclination of : i_1 = 55°. The corresponding EWH rms grids are displayed in Figure 26-7, and the related performance numbers are given in Table 26-3.

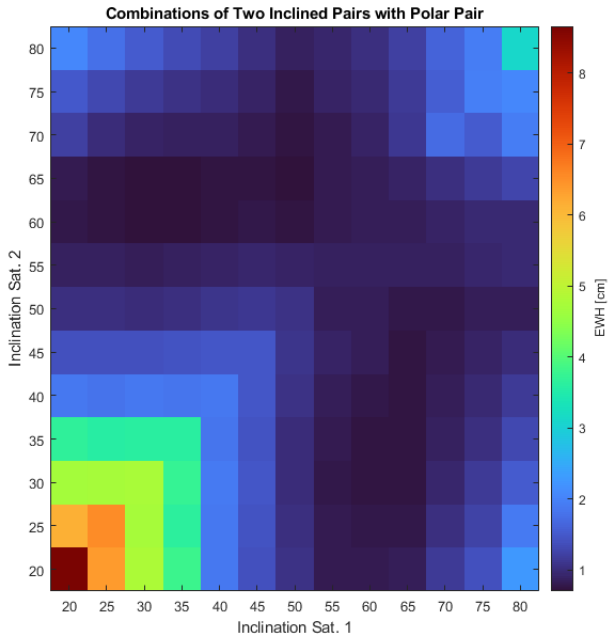

Figure 26-6: Global EWH rms [cm] of 3-pair constellations including 1 polar and 2 inclined pairs. Input signal: full AOHIS, max. d/o 50, daily co-estimation up to d/o 20. Annotation in accordance with the orbits in Table 26-2.

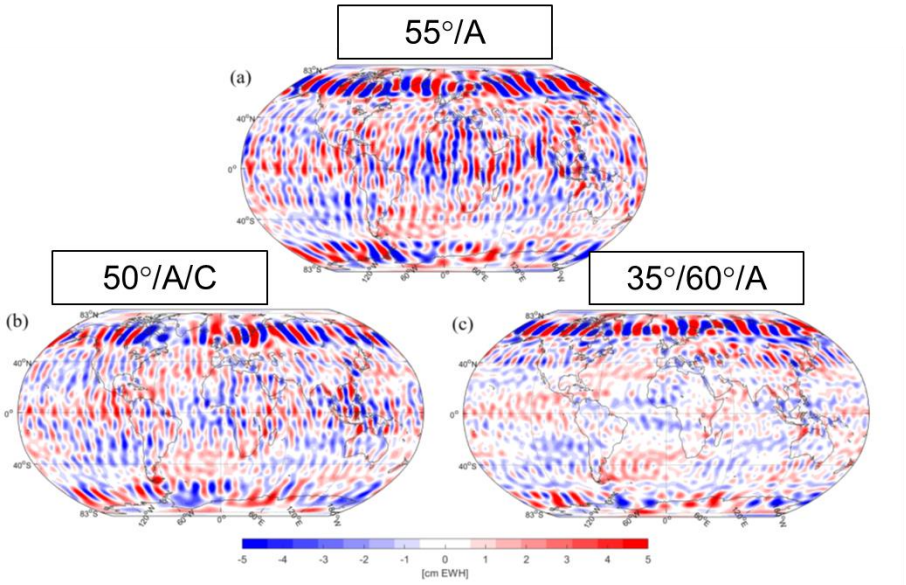

Figure 26-7: Global EHW errors (d/o 50) of the constellations 55°/A, 50°/A/C, 35°60°/A.

Table 26-3: Cumulative EHW errors at d/o 50 of the constellations shown in Figure 26-7.

Constellation	EWH rms [cm]
35°/60°/A	0.71
55°/A	1.10
50°/A/C	0.87

Regarding the performance of the daily co-estimates (d/o 20), the best performance can be achieved for the constellation $i_1 = 55°$, $i_2 = 30°$, see Figure 26-8.

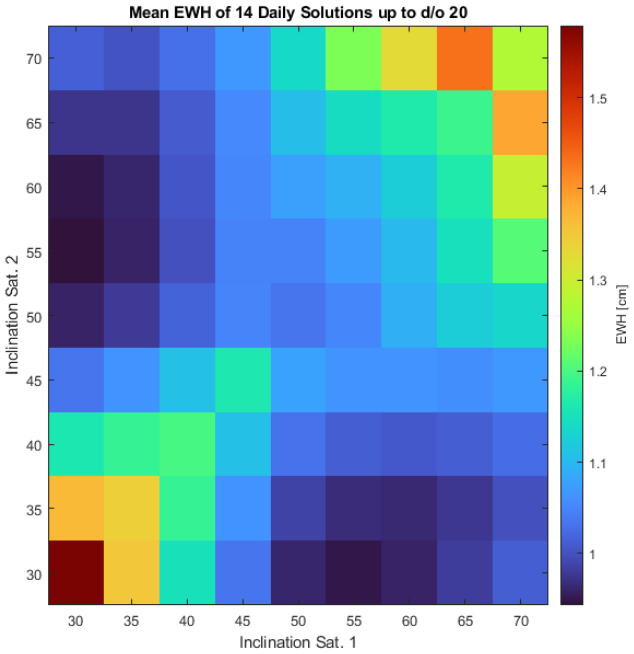

Figure 26-8: Global EWH rms [cm] of daily co-estimates up to d/o 30 for 3-pair constellations including 1 polar and 2 inclined pairs. Input signal: full AOHIS, max. d/o 50, daily co-estimation up to d/o 20. Annotation in accordance with the orbits in Table 26-2.

The performance of the best identified 3-pair constellations involving one or two inclined pairs is compared in terms of SH degree rms curves in Figure 26-9, and global EWH errors in Figure 26-10.

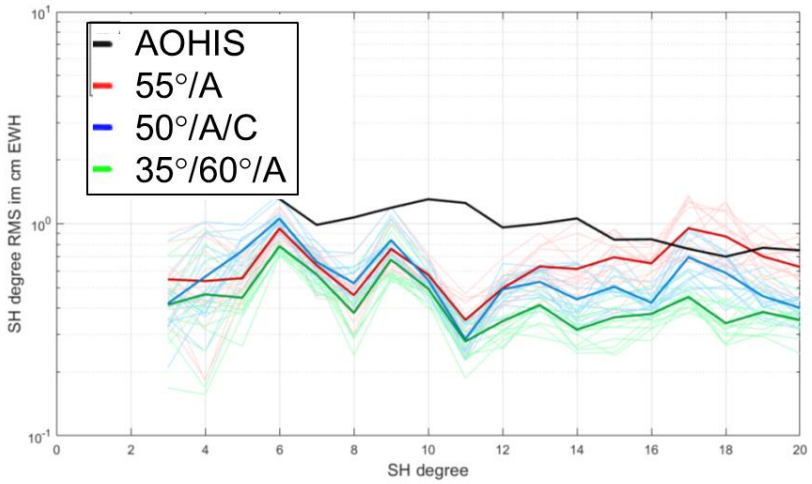

Figure 26-9 SH degree standard deviations of daily co-estimates (d/o 20) for three constellations.

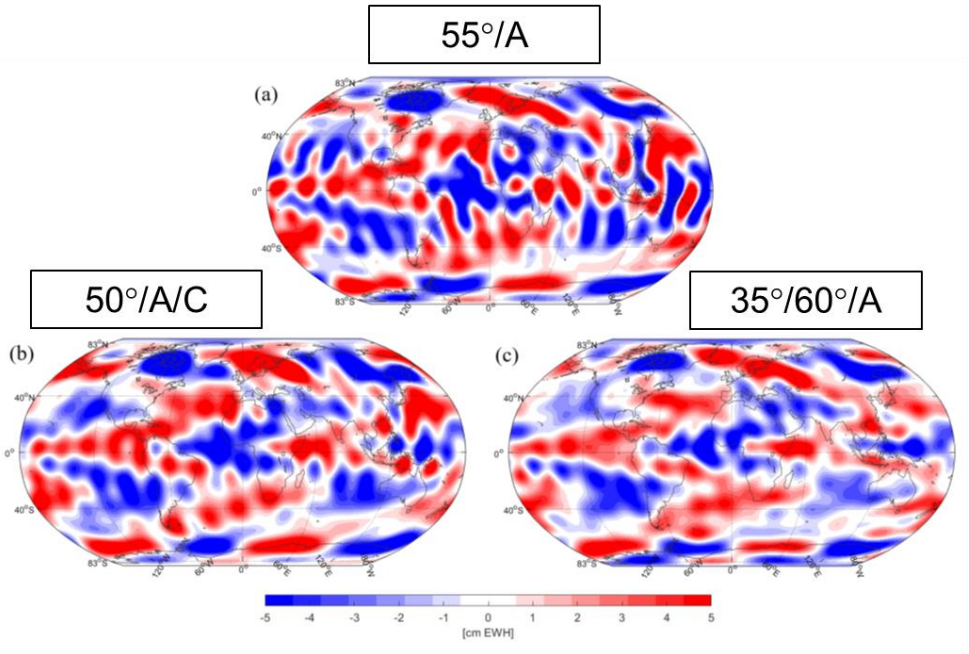

Figure 26-10: EWH errors [cm] of daily co-estimates (d/o 20) for three constellations.

This exercise was repeated for 1 polar and 2 inclined pairs with daily co-estimates up to d/o 30. The best performance is achieved for the constellation $i_1 = 65°$, $i_2 = 40°$ (in comparison of $i_1 = 60°$, $i_2 = 35°$ for the d/o 20 case). Table 26-4 summarizes the mean global EWH for all investigated triple-pair constellations.

Table 26-4: Mean global EWH errors [cm] for triple-pair constellations with varying inclination; input signal: AOHIS d/o 50, daily co-estimation up to d/o 30.

	-	50°	55°	60°	65°	70°
-	-	2.24	2.72	3.74	5.03	15.1
30°	17.7	1.28	.940	.888	.861	1.25
35°	6.49	1.24	.915	.825	.789	1.05
40°	3.63	1.28	.957	.857	.759	.966
45°	2.47	1.33	.980	.890	.783	.857

With this study, the optimum triple-pair constellation was identified. The next step was to investigate larger constellations of up to 6 pairs. The involved orbits are the same as given in Table 26-2. A brute-force approach to evaluate all possible 6-pair constellations would result in the order of ~342,000,000 combinations, which is not manageable from a computational point of view. Therefore, our strategy was to start with the best-performing 1/2/3-pair constellations, and to add consecutively the fourth, fifth, and sixth satellite pair (out of Table 26-2) based on the best performing at each increment. For this study we used a daily co-estimates up to d/o 20. Since the results of the d/o 30 case were quite close, we would not expect significantly different conclusions.

Table 26-5 shows the achieved optimum results for up to 6-pair constellations.

Table 26-5: Global EHW errors [cm] for best-performing 1- to 6-pair constellations; input signal AOHIS d/o 50, daily co-estimation up to d/o 20 (with the exception of single-pair). Subscript refers to group (cf. Table 26-2). Change [%] gives the improvement w.r.t. the previous constellation.

No. Sats	Constellation	EWH [cm]	Change [%]
1	A	2.91×10^4	-
2	$A/55^\circ_1$	1.10	99.9
3	$A/35^\circ_1/60^\circ_2$	.705	35.9
4	$A/35^\circ_1/60^\circ_2/70^\circ_2$	.632	10.3
5	$A/35^\circ_1/60^\circ_2/70^\circ_2/50^\circ_1$	.576	8.96
6	$A/35^\circ_1/60^\circ_2/70^\circ_2/50^\circ_1/35^\circ_2$	.555	3.52

From Table 26-5 it can be included, that although adding pairs improves the performance, the relative benefit of adding pairs (for "long-term" 14-day solution) decreases. The relative improvement from a 2-pair to a 6-pair constellation is about a factor of 2 (at d/o 50). A higher benefit for daily co-estimates is not yet considered here, but is expected to be larger, simply due to the fact that a higher max. d/o for daily solutions will be achievable.

In order to evaluate the impact of daily co-estimation on the de-aliasing capabilities, instead of using the full AOHIS signal plus daily co-estimating, we repeated the above study based in HIS signals and AO errors, using the same pool of orbits (Table 26-2).

Table 26-6 shows the resulting best-performing 3-pair to 6-pair constellations.

Table 26-6: Global EHW errors [cm] for best-performing 1- to 6-pair constellations; input signal AOHIS d/o 50, no daily co-estimation. Subscript refers to group (cf. Table 26-2). Change [%] gives the improvement w.r.t. the previous constellation.

No. Sats	Constellation	EWH [cm]	Change [%]
1	A	18.9	-
2	$A/50^\circ_2$	.921	95.1
3	$A/45^\circ_2/60^\circ_1$	.552	40.1
4	$A/45^\circ_2/60^\circ_1/C$	.436	20.9
5	$A/45^\circ_2/60^\circ_1/C/65^\circ_1$	.367	16.0
6	$A/45^\circ_2/60^\circ_1/C/65^\circ_1/25^\circ_1$	.317	13.6

Evidently, compared to the results for daily co-estimation, a larger gain for the long-term solution can be achieved when adding pairs, because in this case the de-aliasing is not already

(partly) done by the co-parameterization. As an example, the relative improvement from 2 to 6 pairs is about a factor of 3 (at d/o 50), compared to only a factor of 2 when using daily co-estimation. Figure 26-11 shows the EWH error grids for the 6 constellations listed in Table 26-6, demonstrating the continuous reduction of striping by adding pairs.

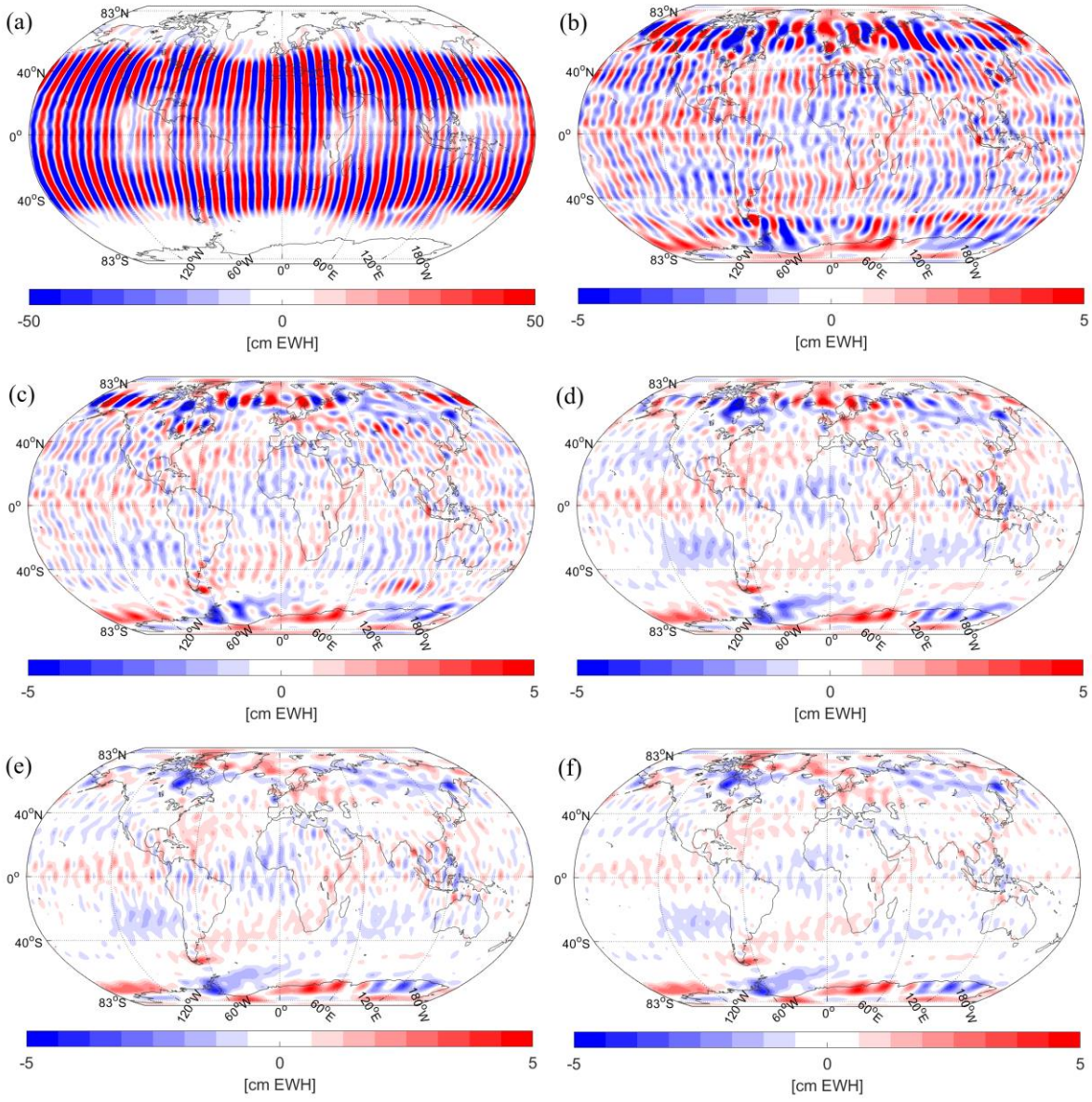

Figure 26-11: Global EWH error [cm] related to constellations given in Table 26-6.

At this point, it should be mentioned that an alternative approach for identifying multi-satellite constellations based on a Multiobjective Genetic Algorithm was proposed by Deccia et al. (2022) [RD-1]. It is based on the definition of a spatial and temporal objective function (representing spatial and temporal "resolution"), and several model assumptions. The performance is evaluated for 29-day repeat orbits at about 500 km altitude, and the study is restricted to 6-pair constellations. The search space is not focussed mainly on the inclination, but is also extended to the RAAN and the mean anomaly. The assembling of daily NEQs is done up to d/o 60, resulting in stand-alone daily solutions plus a "combined" monthly solution,

which is a combination of the daily solutions. They could identify 6-pair constellations that better fit the space and/or time objective function, or fulfil a global optimum. One of the main findings is that there is a huge number of constellations showing very similar performance.

Conclusions

The study clearly demonstrated that there is a "saturation" effect in gaining performance when adding additional satellite pairs (for the full-noise case). This means that the aliasing problem cannot be solved by simply increasing the number of pairs to a big number. It could be shown that 6-pair constellations improve the de-aliasing capabilities of 2-pair constellations by a factor of 2 to 3 (at d/o 50). The performance gain is mainly related to the parameterization. Since a daily co-parameterization of long-wavelength fields already reduces temporal aliasing by itself, the relative gain of adding satellite pairs is lower in this case. Therefore, it will be difficult to gain the factor of 1000 needed to see the gain by improved sensors by enhanced constellations alone. However, adding pairs will be highly beneficial for the quality and achievable max. resolution of daily (or even sub-daily) estimates.

26.2. FULL-SCALE NUMERICAL SIMULATIONS OF LL-SST CONCEPTS AND ASSESSMENT OF RESULTS – TUM (WP421)

In this section, comparable to section 26.1, the impact of larger constellations will be investigated for time-variable gravity field retrieval. While section 26.1 can be considered as a pre-study with a very broad trade-space, this section focuses more on an optimal subset of this initial space to conduct more detailed studies on pre-selected cases. The optimal subset is selected based on the results of the previous section 26.1. For the detailed studies in this section, the TUM full-scale simulator will be used. In 26.2.1, the applied orbits are presented and in 26.2.2 the simulation results will be shown.

26.2.1. ORBIT/CONSTELLATION DESIGN FOR FULL-SCALE SIMULATIONS

In the pre-study in section 26.1, only Keplerian orbits where needed since the reduced-scale simulator has been used. However, for the full-scale simulator, propagated (simulated) orbits are needed since the observations are basically derived from them. This propagated orbits need to satisfy certain requirements in order to be applicable for LL-SST.

The most important requirement is that the satellites of a satellite pair must not drift relative to each other in order to keep the inter-satellite distance within a certain range. To guarantee this without active orbit control, the orbits must be so-called repeat-ground-track (RGT) orbits. RGT orbits have the property that they exactly repeat their ground track (in an Earth-fixed frame) after a certain period. RGT-orbits can just be found if some simplifications are assumed:

1. Non-conservative forces must be neglected
2. Third-body accelerations must be neglected
3. Variations in the rotation of the Earth must be neglected
4. Time-variabilities in the Earth's gravity field must be neglected

In other words, for finding RGT-orbits, only the static gravity field and a constant Earth rotation is regarded. However, all but the non-conservative forces are small and a propagated orbit (which considers all other effects) is still nearly RGT (meaning that the satellites show no significant systematic drift between each other). For the purpose of simulation, the non-conservative forces (atmosphere drag an solar pressure) are not considered within the propagation. In other words it is assumed that they are already somehow compensated by the satellite (e.g., through active orbit control as it would be the case for a real mission to keep the orbital altitude). Eventually, this means that initial state vectors of RGT-orbits can be used for LL-SST simulations. With such orbits, the inter-satellite distance of the propagated orbits can be kept within a range of about 10km even after a propagation time of 3 months. Methodically, RGT-orbits can be found by implementing an iterative variational approach which is numerically demanding (particularly for longer repeat cycles) since many orbits need to be propagated. Noteworthy, RGT-orbits do not exist for every sought combination of orbit parameters; for the iterative approach, an initial guess which approximates an RGT-orbit is needed. To obtain this initial guess, the desired orbit is approximated through a Keplerian orbit considering refinements for the Earth's oblateness.

An optimized orbit has also addition characteristics as, e.g., a certain repeat cycle and related sub-cycles (i.e., periods where each, the number of Earth rotations and number of satellite revolutions is nearly integer). The sub-cycles are usually chosen according to the desired retrieval periods of the gravity field since after each sub-cycle the ground-track pattern is mostly homogeneous. In agreement with ESA, the target retrieval periods to prioritize shall be 7 days and one day. Accordingly, also the target sub-cycles are chosen to have the same periods. It shall be noted, that orbits with sufficiently good sub-cycles at specific periods do not always exist, since the number and quality of the sub-cycles is primarily a function of the orbital altitude and inclination. Both elements are usually crucial mission parameters which cannot be chosen freely and need to be within a narrow range. Hence, to suffice all requirements, actual sub-cycles need sometimes to be chosen slightly smaller than the target sub-cycle to allow a solution (e.g., 5 days instead of 7 days). Without going into detail, the problem of finding common sub-cycles gets even more complicated when having larger satellite constellations (especially when having multiple satellite-pairs at the same inclination and when more than one sub-cycle is needed).

For the actual constellations which are used for the full-scale simulations, several additional constraints apply:

1. Altitude shall be in a range of 370-440 km
2. Orbits shall be nearly circular (eccentricity almost 0)
3. Multiple satellite-pairs on one inclination shall be distributed in that way to optimally speed up the individual sub-cycle completion
4. Optimal inclinations are chosen in agreement with the results shown in section 26.1
5. Constellations with a maximum number of 6 satellite-pairs shall be investigated

Using these constraints (and all additional requirements), the resulting constellations are almost determined. What is still missing is the distribution of the satellite-pairs among the inclinations: firstly, it is already known that distributing more than one pair on a polar inclination is not beneficial regarding the interaction with temporal aliasing (since all measurements are still in north-south direction in this case). Thus, the only question remaining is how to distribute the satellite-pairs among the used inclinations. Here, two main strategies are possible: (1) either

distribute several pairs on several inclinations (limit the number of used inclinations) or (2) distribute all pairs on distinct inclinations (maximizing the number of used inclination). Both distribution strategies will be investigated in the following by denoting these kind of constellations either as IICXv0 (for case 1, the limited number of inclinations) or IICXv1 (for case 2, the maximized number of inclinations). IIC is the abbreviation for (I)nclined (I)nline (C)onstellation, and the X is a placeholder for the number of pairs for an actual constellation. An overview of all constellation considered for the full-scale simulation study is given in Table 26-7. For IICXv0, a maximum of 3 inclinations is considered (for 6 pairs) and the inclinations are chosen according to the optimum found in section 26.1. The number of pairs per inclination is chosen in order to equilibrate observation density w.r.t. the Earth's surface (i.e., more pairs for lower inclinations). For IICXv1, the inclinations are also chosen in order to equilibrate the number of observations per surface area (cosine-distribution, i.e., one additional pair each time the latitude dependent diameter doubles). The overall number of satellite pairs is chosen to be either 2, 3 or 6. This leads to a total number of 5 constellations to investigate (the 2-pair constellations IIC2v0 and IIC2v1 are identical).

Table 26-7: Overview of the constellations considered for full scale simulation

Constellation types →

Number of pairs ↓

Type / N° pairs	Inclined constellations (inline)	
	IICXv0	IICXv1
2-pair	**IIC2v1** (1x89°,1x70°)	
3-pair	**IIC3v0** (1x89°, 2x70°)	**IIC3v1** (89°/70°/40°)
6-pair	**IIC6v0** (1x89°, 2x70°, 3x40°)	**IIC6v1** (89°/80°/71°/60°/48°/33°)

In the following (Figure 26-12 - Figure 26-16), the ground track pattern for each constellation and the target retrieval periods (1 and 7 days) are shown. In addition, the stability of the normal equation matrix (of a reduced scale simulation) in dependency of the max. retrieval d/o is shown to illustrate up to which resolution a gravity field can be retrieved without suffering from major numerical problems (one for each retrieval period/sub-cycle). Each constellation is hand-crafted regarding sub-cycles and, as already mentioned, for some constellations it is not possible to find a good sub-cycle for the target periods which is why a shorter sub-cycle has to be chosen in this cases. From the condition numbers, it can already be seen that denser pattern (i.e., longer retrieval periods and/or more satellite pairs) allow for a higher-resolution gravity field retrieval. This is in agreement with what has been stated in section 25.2 regarding the rule of thumb and the circumstance that this rule can be violated to some extend at the cost of increased numerical instability. Generally, it can be assumed that the (erroneous) interaction with the temporal-aliasing increases with higher instabilities of the system (since then, observations are weighted more individually which disturbs the convergency towards a homogeneous average).

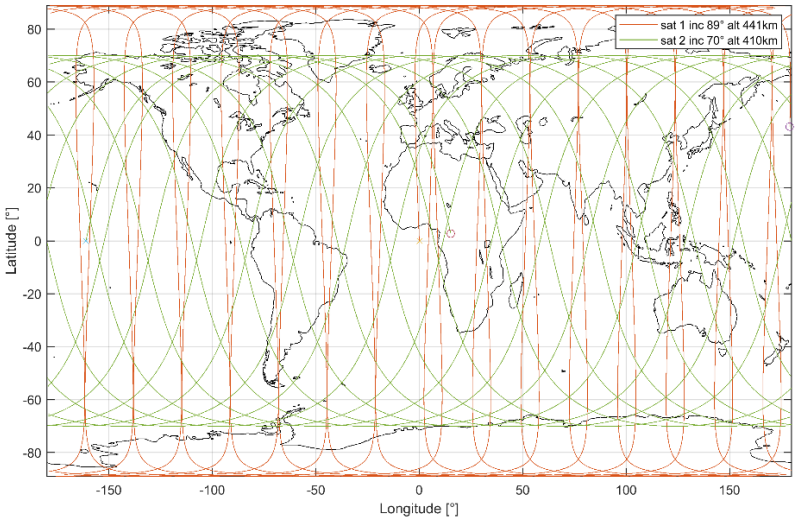

(a)

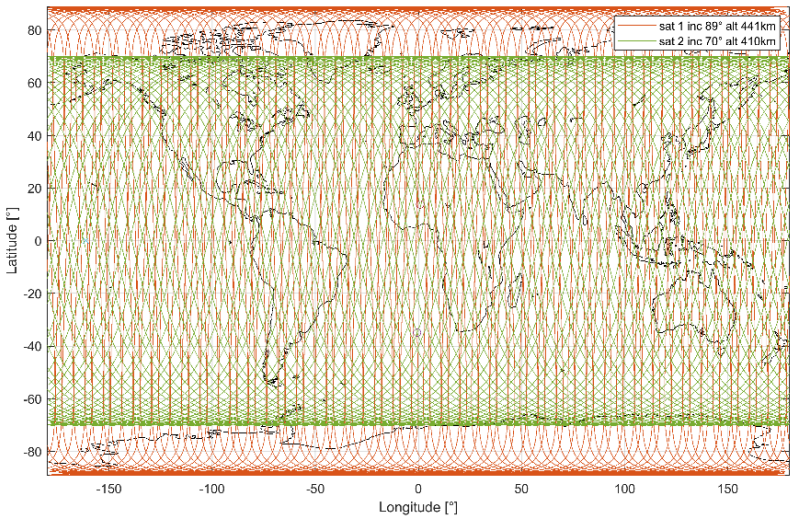

(b)

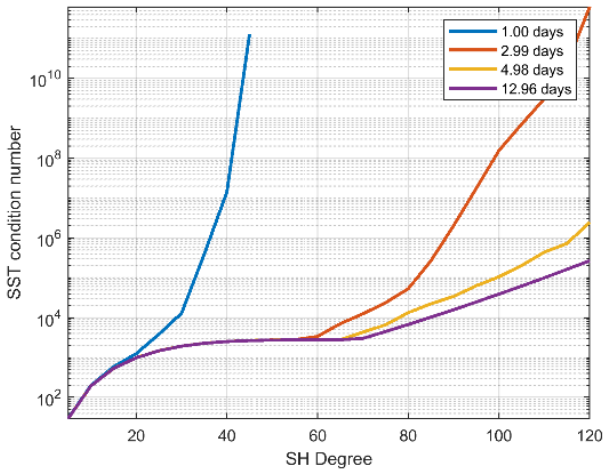

(c)

Figure 26-12 Illustration of constellation IIC2v1 (=IIC2v0). (a) Ground-track pattern for a retrieval period of 1 day. (b) Ground-track pattern for a retrieval period of 5 days. (c) Condition number (L^2-norm) of a normal equation matrix from a reduced scale simulation (assuming white-noise observations) for different max. d/o (see x-axis) and retrieval periods (i.e., sub-cycles, see legend).

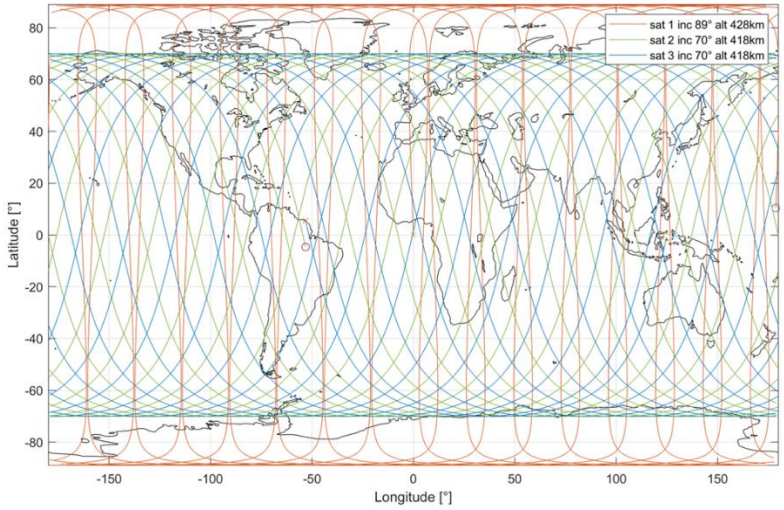

(a)

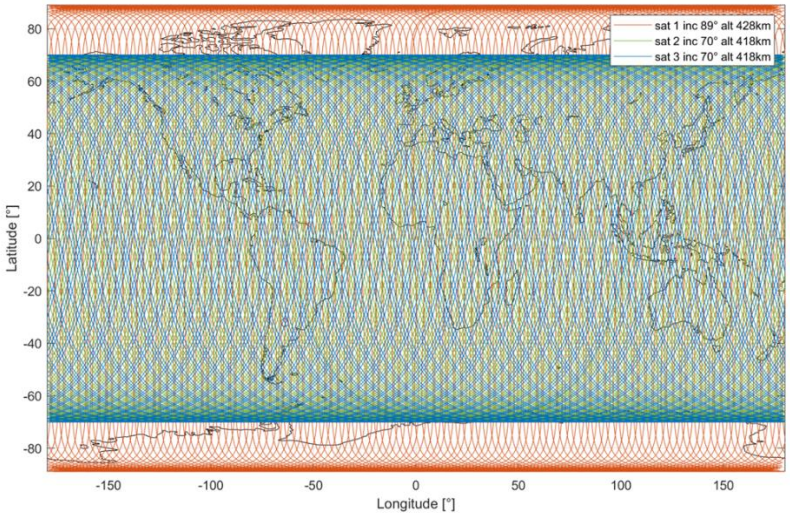

(b)

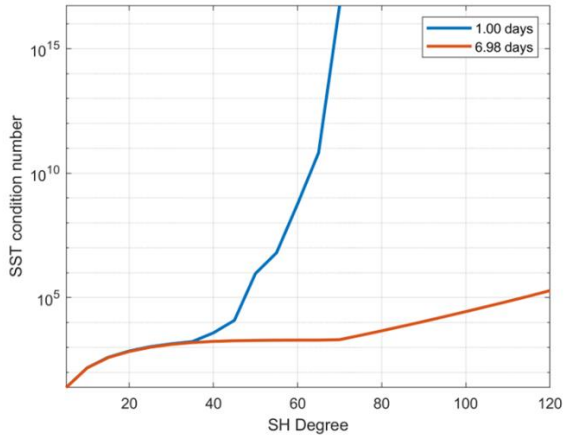

(c)

Figure 26-13 Illustration of constellation IIC3v0. (a) Ground-track pattern for a retrieval period of 1 day. (b) Ground-track pattern for a retrieval period of 7 days. (c) Condition number (L^2-norm) of a normal equation matrix from a reduced scale simulation (assuming white-noise observations) for different max. d/o (see x-axis) and retrieval periods (i.e., sub-cycles, see legend).

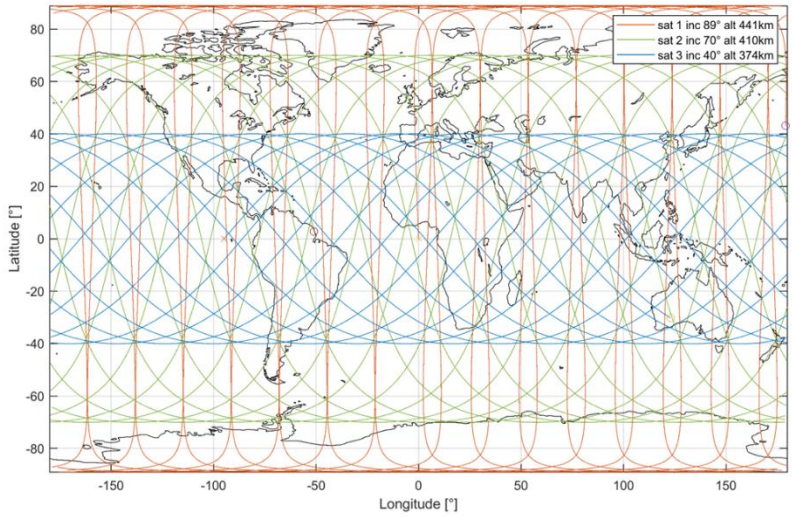

(a)

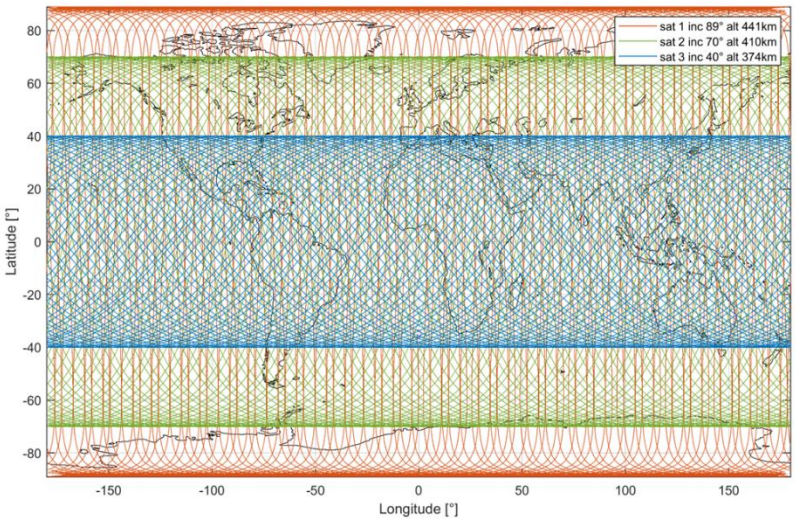

(b)

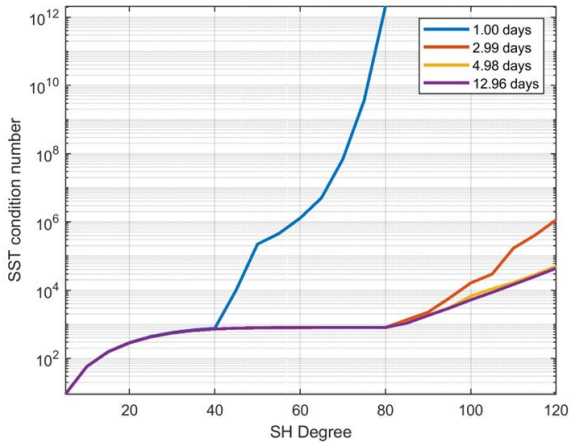

(c)

Figure 26-14 Illustration of constellation IIC3v1. (a) Ground-track pattern for a retrieval period of 1 day. (b) Ground-track pattern for a retrieval period of 5 days. (c) Condition number (L^2-norm) of a normal equation matrix from a reduced scale simulation (assuming white-noise observations) for different max. d/o (see x-axis) and retrieval periods (i.e., sub-cycles, see legend).

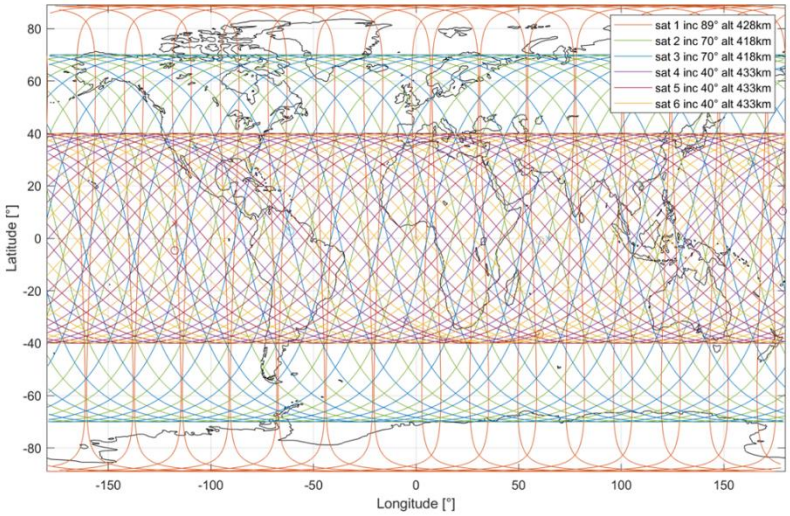

(a)

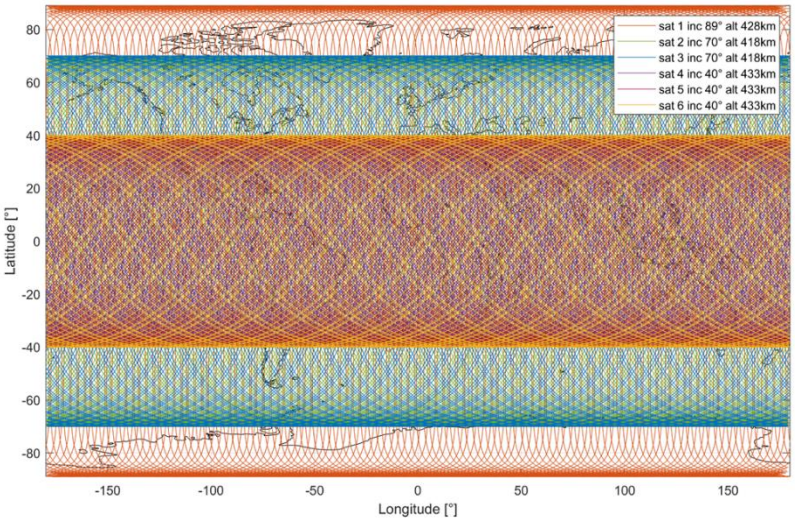

(b)

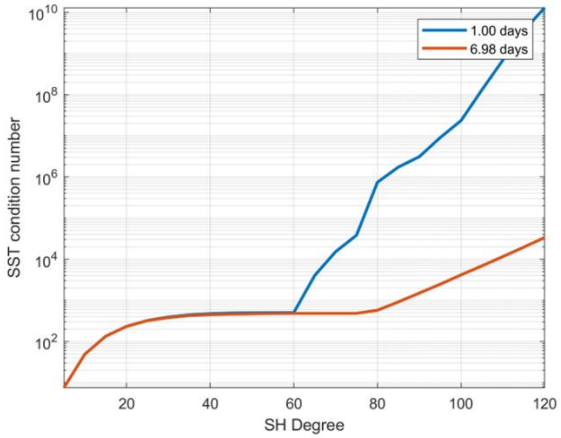

(c)

Figure 26-15 Illustration of constellation IIC6v0. (a) Ground-track pattern for a retrieval period of 1 day. (b) Ground-track pattern for a retrieval period of 7 days. (c) Condition number (L^2-norm) of a normal equation matrix from a reduced scale simulation (assuming white-noise observations) for different max. d/o (see x-axis) and retrieval periods (i.e., sub-cycles, see legend).

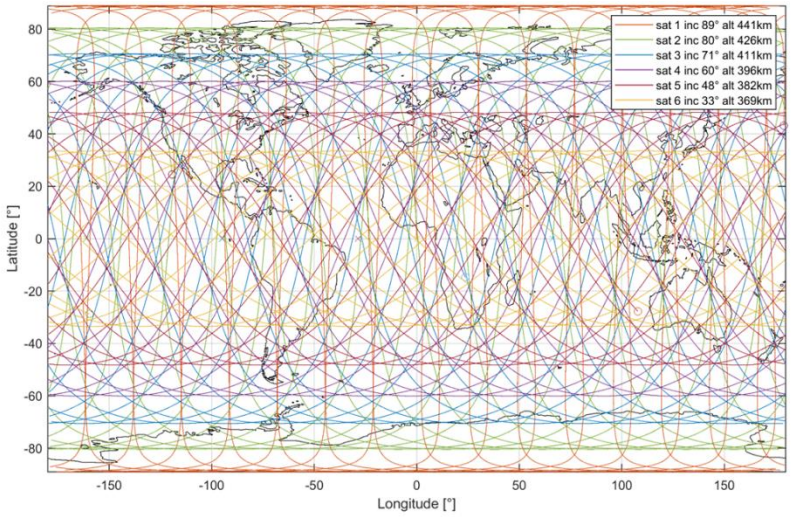

(a)

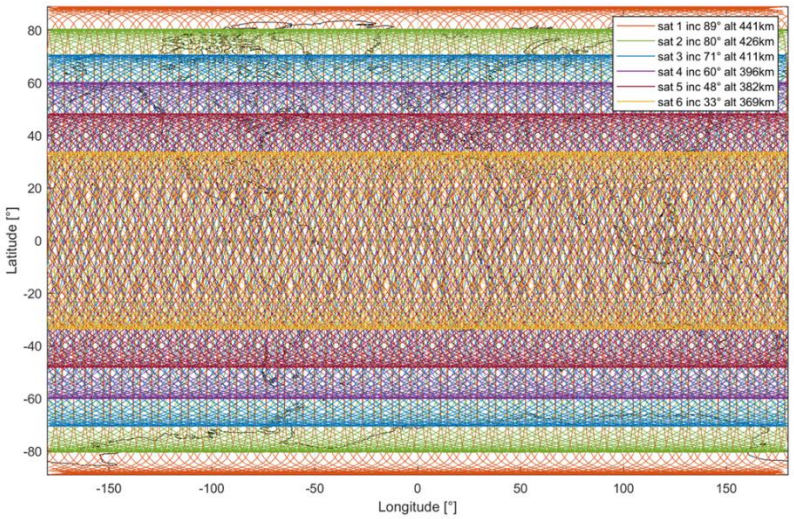

(b)

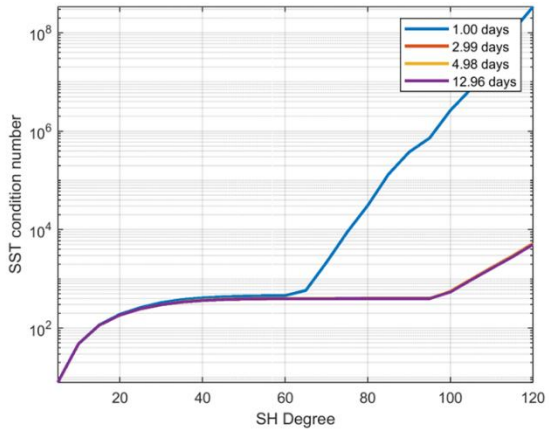

(c)

Figure 26-16 Illustration of constellation IIC6v1. (a) Ground-track pattern for a retrieval period of 1 day. (b) Ground-track pattern for a retrieval period of 5 days. (c) Condition number (L^2-norm) of a normal equation matrix from a reduced scale simulation (assuming white-noise observations) for different max. d/o (see x-axis) and retrieval periods (i.e., sub-cycles, see legend).

26.2.2. FULL-SCALE SIMULATION RESULTS

For each constellation shown in the previous section (26.2.1) and each target retrieval period (1 day and 7 days), one full-scale simulation with time variable gravity signal (full-noise) and one without time variable gravity signal (product-only) is performed. To make the comparison fair, the solutions are grouped into plots of same number of pairs and same time variable gravity signal handling (i.e., distinct plots for full-noise and instrument-only cases).

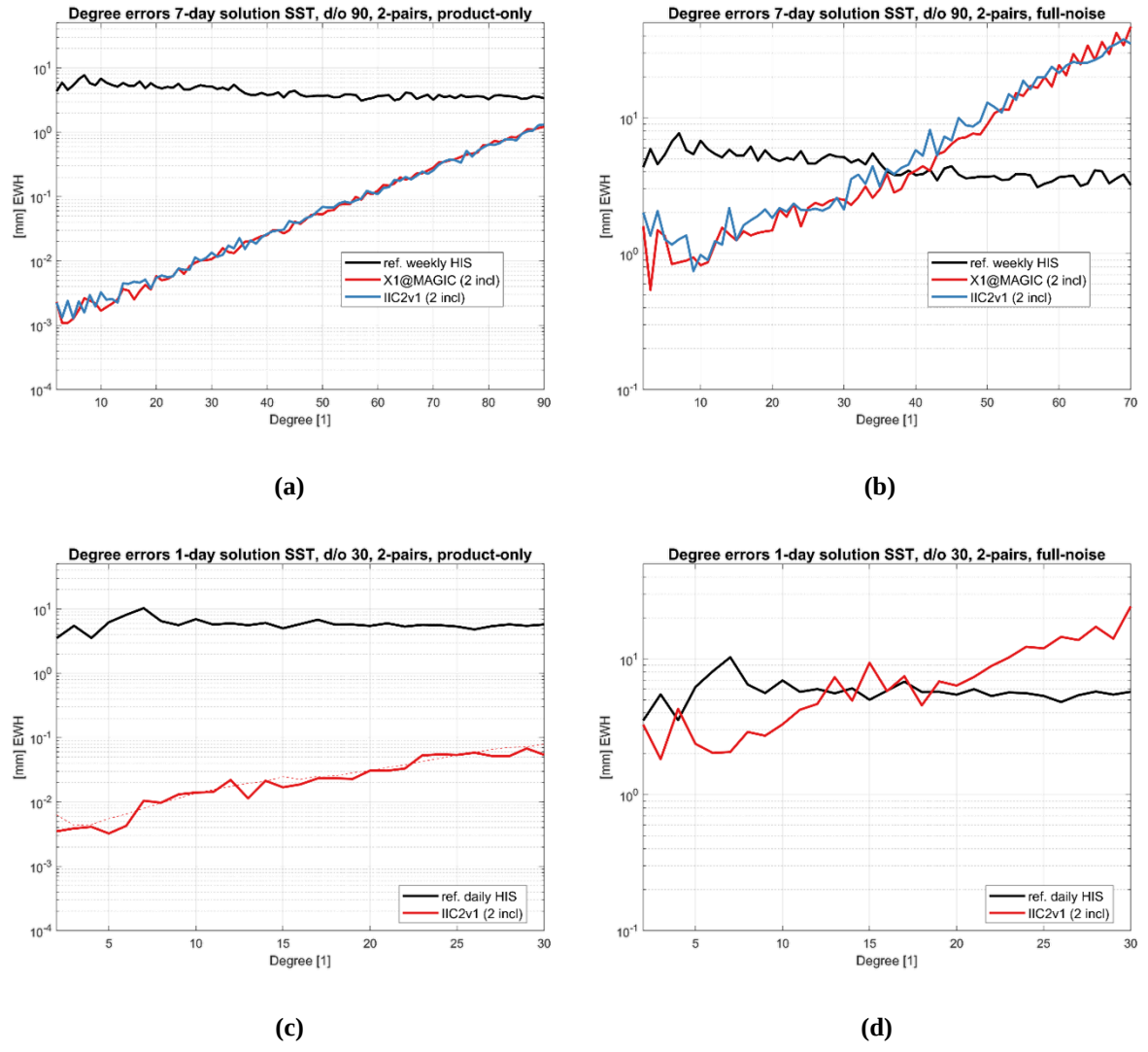

Figure 26-17 Degree errors for 2-pair scenario IIC2v1 (=IIC2v0) assuming the X1 instrument noise model. (a) Product-only, 7-days, *oIIC2v1_mPO_s90d7_tX1*. (b) Full-noise, 7-days *oIIC2v1_mFN_s90d7_tX1*. (c) Product-only, 1-day, *oIIC2v1_mPO_s30d1_tX1*. (d) Full-noise, 1-day, *oIIC2v1_mFN_s30d1_tX1*.

Except the constellation, all simulation settings are identical to the added-value simulations presented in TR D4. For the instrument noise, the X1 model is assumed. In agreement with the statements in 25.3 (and the simulations performed in TR D4) it is not assumed that other (better) instrument performances would lead to significantly different (better) retrieval performances in the full-noise case since there, the error is practically solely caused by temporal aliasing.

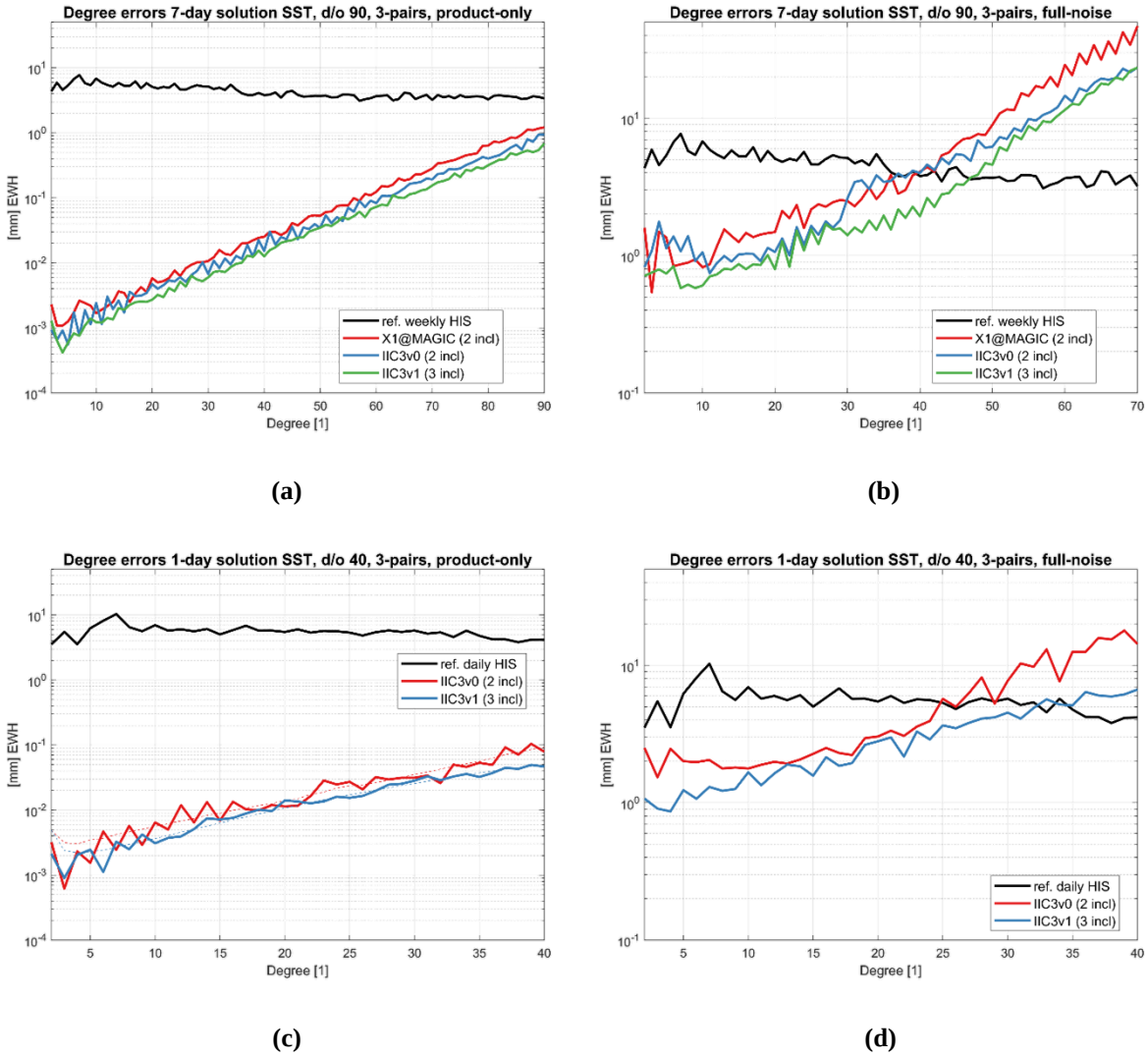

Figure 26-18 Degree errors for 3-pair scenarios IIC3v0 and IIC3v1 assuming the X1 instrument noise model. (a) Product-only, 7-days, *oIIC2vX_mPO_s90d7_tX1*. (b) Full-noise, 7-days *oIIC2vX_mFN_s90d7_tX1*. (c) Product-only, 1-day, *oIIC2vX_mPO_s30d1_tX1*. (d) Full-noise, 1-day, *oIIC2vX_mFN_s30d1_tX1*.

Comparing the degree variances (Figure 26-17-Figure 26-19), the following assessments can be made:

- Additional pairs do not significantly improve the product-only retrieval performance. The improvements are in the range of added redundancy ($\sim\sqrt{n}$).
- IIC2v1 performs nearly identical to MAGIC. This is also to expect since both constellations are very similar
- Full-noise performance improves in the same magnitude as the product-only performance ($\sim\sqrt{n}$). Thus, adding pairs helps to reduce temporal-aliasing ("self-deailiasing") but only in a limited fashion (cf. section 25.2).
- Maximizing the number of inclinations (IICXv1) is slightly more favourable than limiting the number of inclinations (IICXv0) in case of full-scale and product-only.
- Daily solutions benefit more than weekly solutions (from adding pairs).

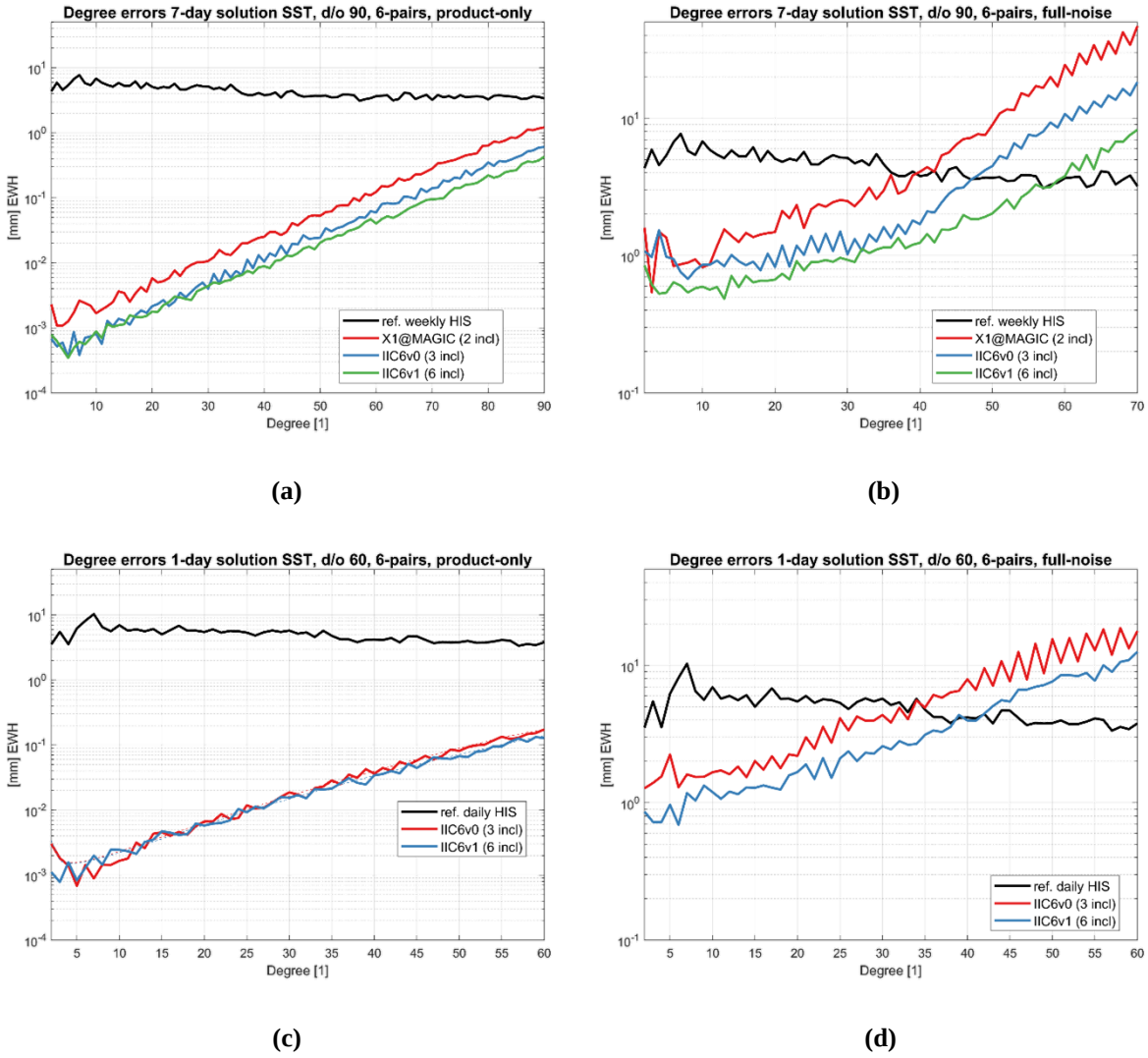

Figure 26-19 Degree errors for 6-pair scenarios IIC6v0 and IIC6v1 assuming the X1 instrument noise model. (a) Product-only, 7-days, *oIIC2vX_mPO_s90d7_tX1*. (b) Full-noise, 7-days *oIIC2vX_mFN_s90d7_tX1*. (c) Product-only, 1-day, *oIIC2vX_mPO_s30d1_tX1*. (d) Full-noise, 1-day, *oIIC2vX_mFN_s30d1_tX1*.

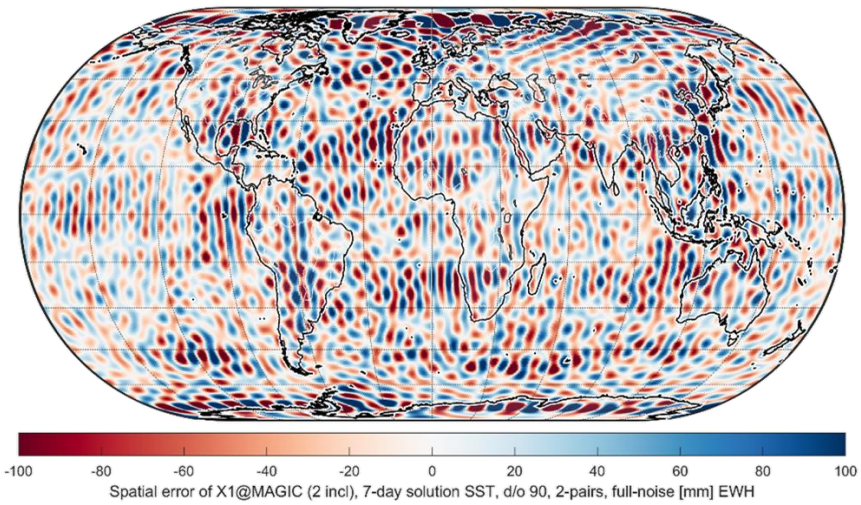

(a)

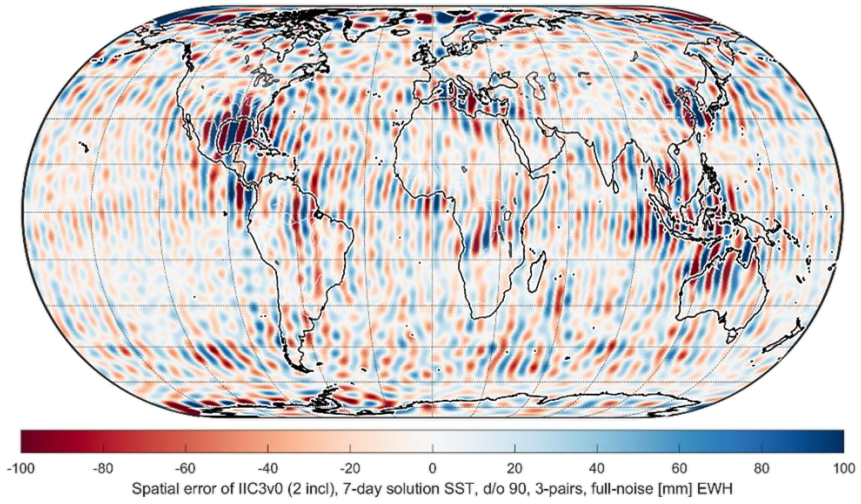

(b)

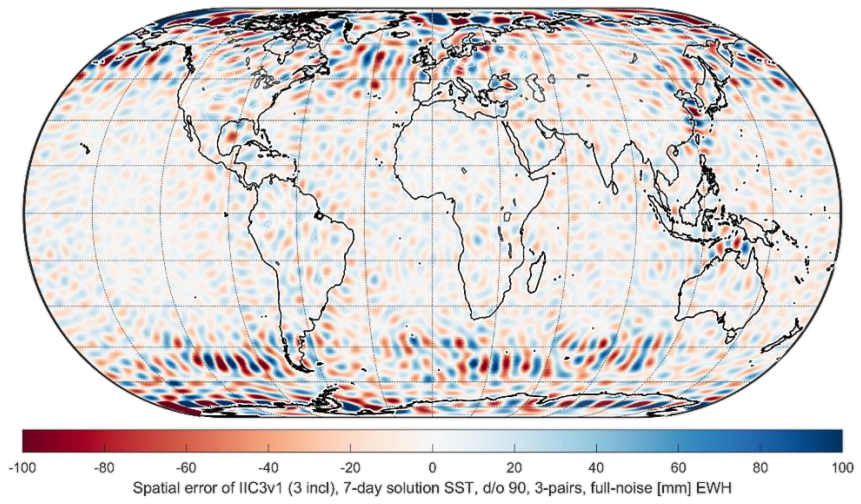

(c)

Figure 26-20 Spatial errors regarding HIS of 7-day full-scale solutions up to d/o 60 of 3-pair constellations in comparison to MAGIC. (a) MAGIC baseline with X1 noise (b) IIC3v0 constellation (c) IIC3v1 constellation.

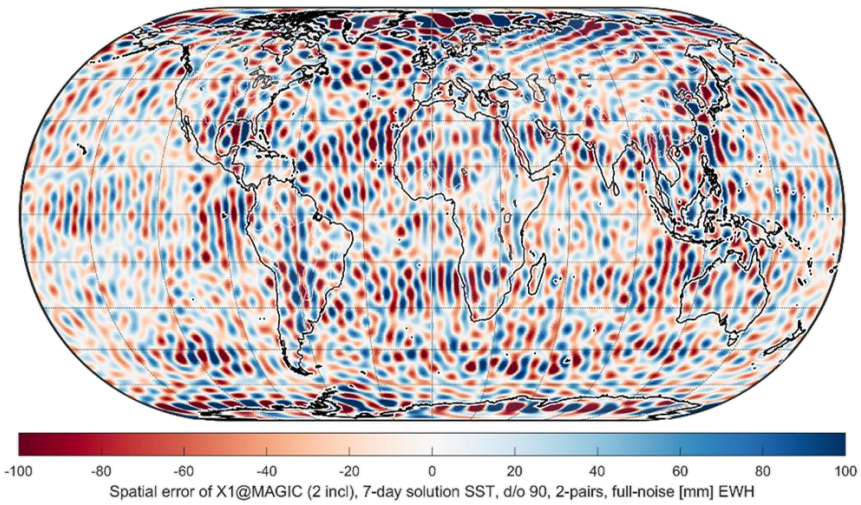

(a)

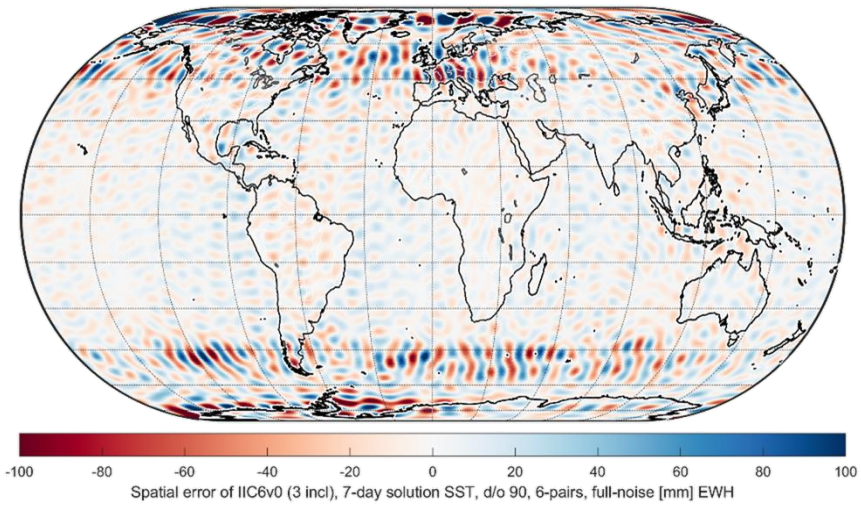

(b)

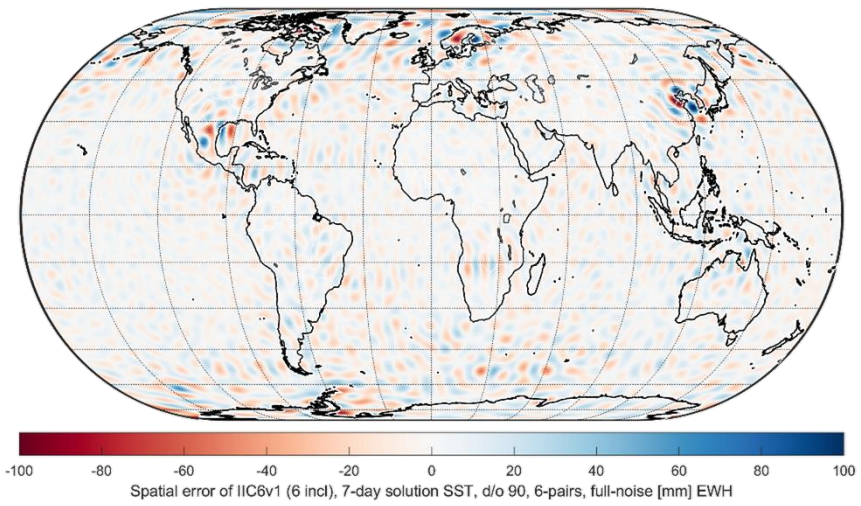

(c)

Figure 26-21 Spatial errors regarding HIS of 7-day full-scale solutions up to d/o 60 of 6-pair constellations in comparison to MAGIC. (a) MAGIC baseline with X1 noise (b) IIC6v0 constellation. (c) IIC6v1 constellation.

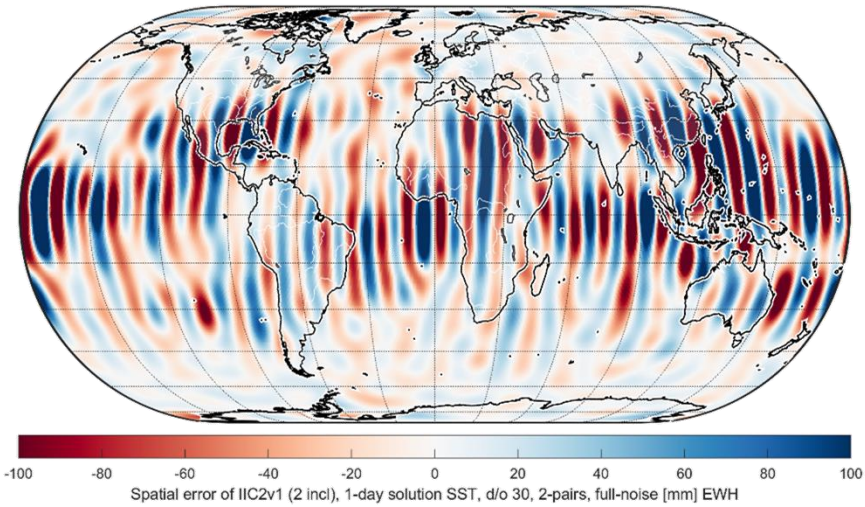

(a)

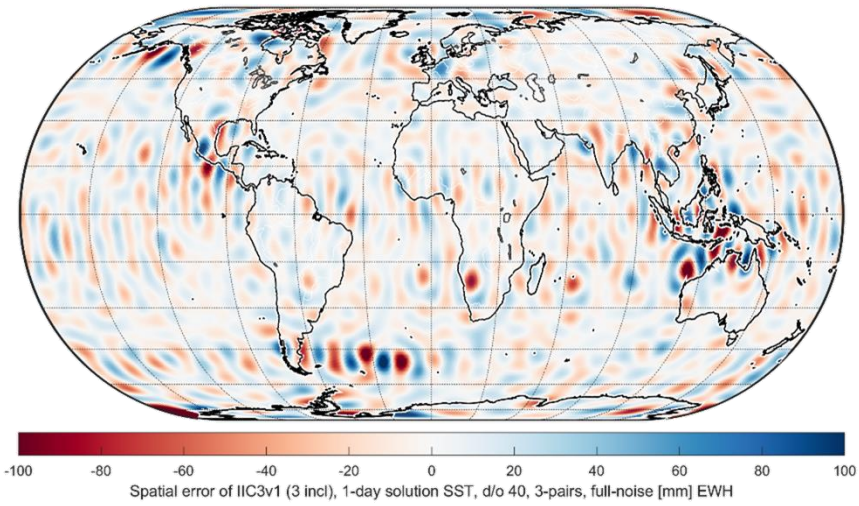

(b)

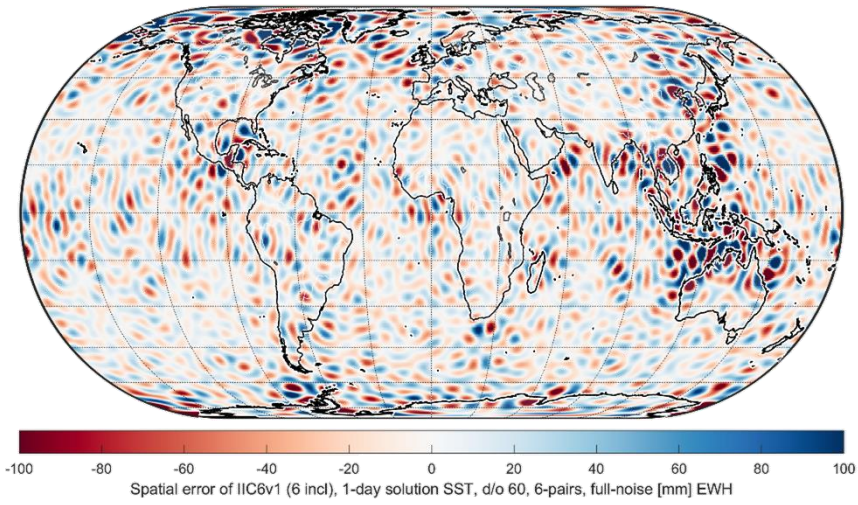

(c)

Figure 26-22 Spatial errors regarding HIS of 1-day full-scale solutions for IICXv1 constellations and varying max d/o. (a) IIC2v1 constellation up to d/o 30. (b) IIC3v1 constellation up to d/o 40. (c) IIC6v1 constellation up to d/o 60.

Investigating the spatial error patterns of the full-noise simulations (Figure 26-20-Figure 26-22) one can discern:

- Adding a third inclination reduces striping significantly in the area covered by all 3 pairs (especially in case of 3-pair constellations).
- Adding more inclinations makes the global error pattern more homogeneous in case of 6-pair constellations; IIC6v0 shows a significant reduction in performance in the higher latitudes
- One-day solutions improve significantly with added pairs. A one-day 6-pair IIC6v1 solution shows smaller errors than a 2-pair constellation.
- More inclinations reduce the striping pattern resulting in a more homogeneous chess-board pattern.
- Even if the improvements are visible and also significant (factor 2-3), the product-only level is still nearly 3 orders of magnitude lower (cf. sections 25.2, 25.3).

An integration of the shown results into the trade space is provided in section 25.2. In agreement with this results the best-performing variants IIC3v1 and IIC6v1 are selected for further investigation in the subsequent sections.

Simulations with further improved noise models (X2.1) and a different stochastic modelling

The aforementioned simulations have also been repeated for an updated noise model with even more optimistic assumptions (X2.1 noise model, see WP200, TR D3). However, since even the inferior X1 noise model has been strongly dominated by temporal aliasing, the obtainable full-noise solutions do not alter significantly when applying the X2.1 model. Therefore, the figures of these solutions are not included at this point but can be found in Zingerle et al, 2024. The observable difference to X2.1 are small and caused by the different shapes of the ASDs of the noise models (and not the overall amplitudes) which introduces a different weighting of the observations and, hence, affects the temporal aliasing influence in the estimation process. In fact, choosing a certain shape of ASD (just for the stochastic modelling) may have a favorable effect on the temporal aliasing error. The POLIMI solutions for instance apply white-noise in the stochastic modelling in terms of range-accelerations (instead of using the actual instrument noise, see section 26.3) and can obtain thereby partially improved results (compare, e.g., Figure 26-30 to Figure 26-19).

Long-term simulations for user work packages

The user work packages required the simulations of longer-term solutions. Hence, simulations of the whole ESM period (1995-2006, i.e., 12 years) have been performed in addition for the scenarios IICv1 (GRACE-like), IIC2v1 (MAGIC-like), IIC3v1 (baseline 1) and IIC6v1 (baseline 2). Detailed analyses of these simulations are shown in the user work packages (WP800-1000). Here, only the empirical derived spatial variances are plotted to provide a first insight into the performance of the different scenarios (see Figure 26-23). It is well recognized that that the empirical error decreases with the number of pairs with the largest improvements seen when transiting from the GRACE-like to the MAGIC-like scenario. This is in line with has been shown/discussed previously in this sections.

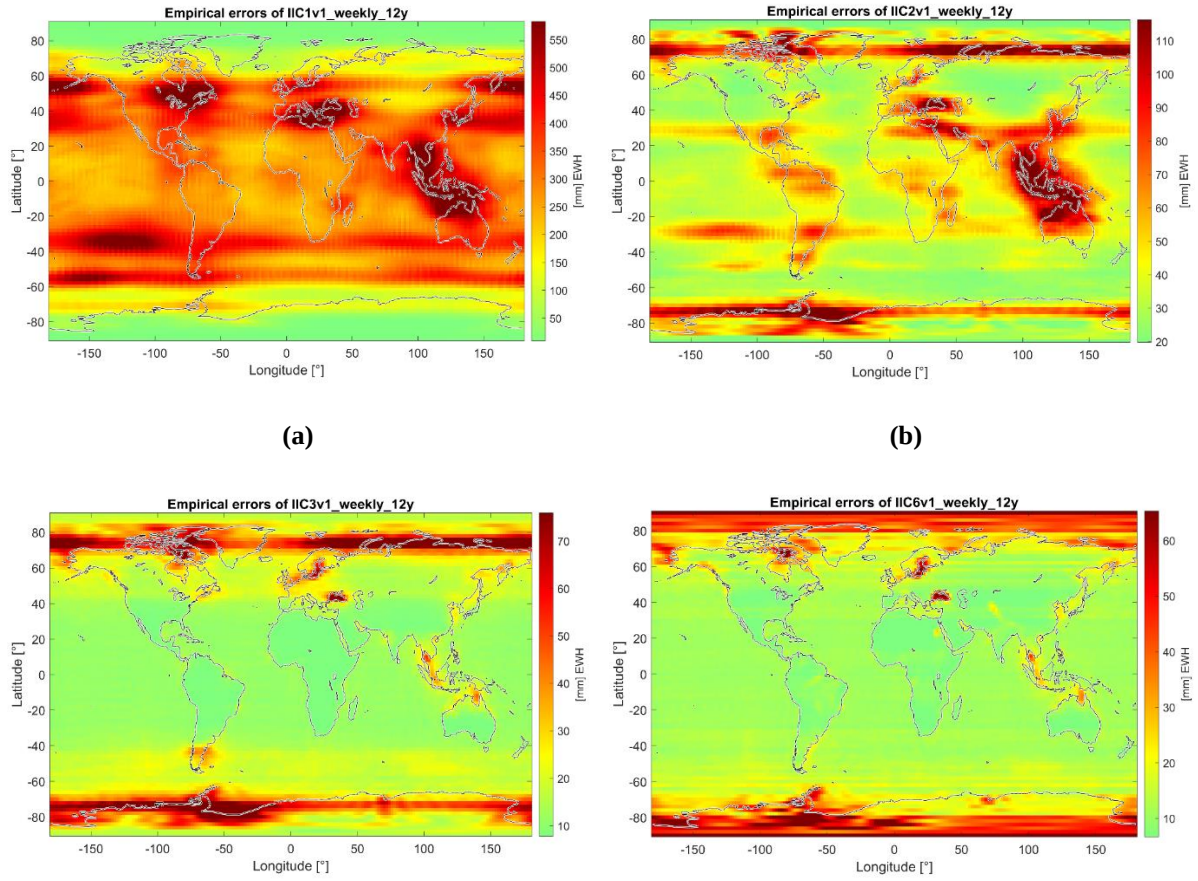

(a) **(b)**

(c) **(d)**

Figure 26-23 Empirical standard deviations derived from 12 years of simulations of weekly solutions up to d/o 60 for the different baseline scenarios in terms of EWH. (a) IIC1v1 scenario (GRACE-like). (b) IIC2v1 scenario (MAGIC-like). (c) IIC3v1 scenario (QSG baseline 1). (d) IIC6v1 scenario (QSG baseline 2).

26.3. FULL-SCALE NUMERICAL SIMULATIONS OF LL-SST CONCEPTS AND ASSESSMENT OF RESULTS – POLIMI (WP422)

For each constellation shown in section 26.2.1 and each target retrieval period (1 day and 7 days), one full-scale simulation with time variable gravity signal (full-noise) and one without time variable gravity signal (product-only) are performed, considering a target retrieval period of 1 day. In all the simulations MicroStar accelerometers are compared to CAI (with X1 noise assumption), while the considered LRI instrument is the GFO one.

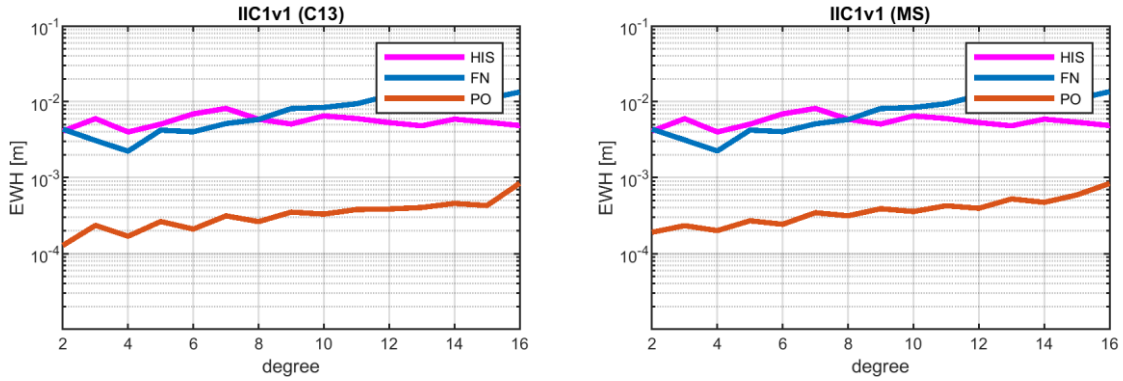

Figure 26-24 Degree errors regarding HIS of 1-day full-scale solutions up to d/o 16 of 1-pair (IIC1v1) constellations comparing CAI (left panel) with electrostatic (right panel) assuming X1 noise.

In case of a single orbit configuration, there are no significant differences in using MicroStar or CAI accelerometers when processing 1 day only (see Figure 26-24), in both PO and FN solutions. Considering the detectability of the non-tidal time-variable signal, it is very limited, up to d/o 8. Moreover, this limit is mainly due to the impact of temporal aliasing and other background model errors. In fact, the PO solution is about two orders of magnitude better in terms of standard deviation.

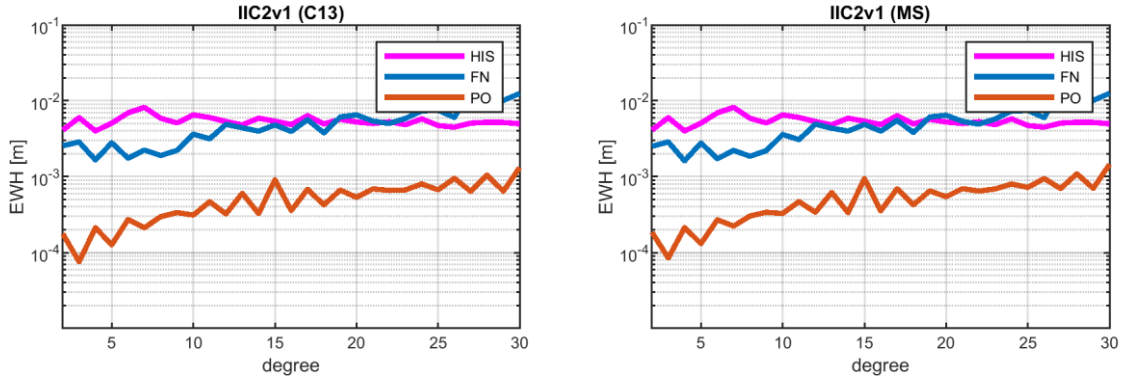

Figure 26-25 Degree errors regarding HIS of 1-day full-scale solutions up to d/o 30 of 2-pair (IIC2v1) constellations comparing CAI (left panel) with electrostatic (right panel) assuming X1 noise.

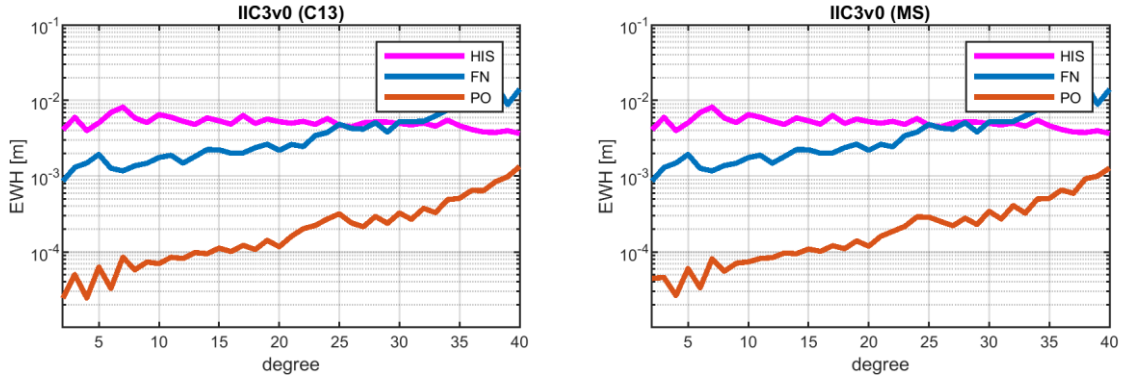

Figure 26-26 Degree errors regarding HIS of 1-day full-scale solutions up to d/o 40 of 3-pair (IIC3v0) constellations comparing CAI (left panel) with electrostatic (right panel) assuming X1 noise.

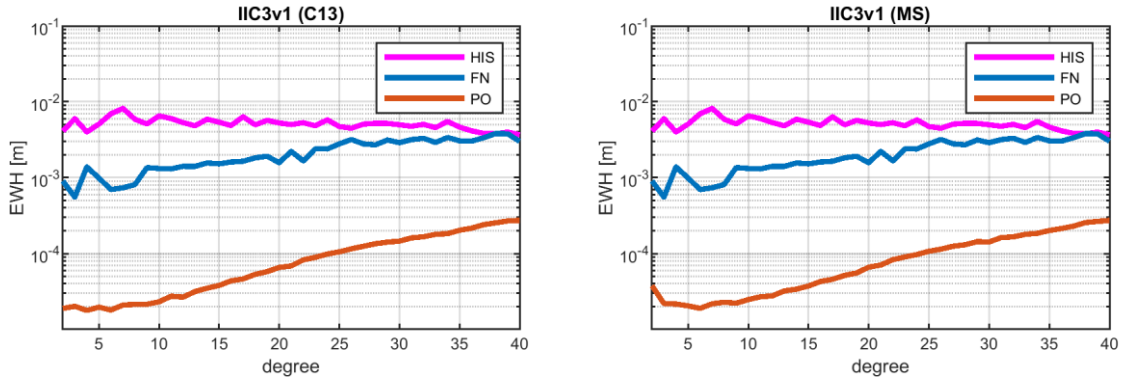

Figure 26-27 Degree errors regarding HIS of 1-day full-scale solutions up to d/o 40 of 3-pair (IIC3v1) constellations comparing CAI (left panel) with electrostatic (right panel) assuming X1 noise.

When introducing a double pair of satellites, the detectability of the time-variable signal is improved (compare blue lines of Figure 26-24 and Figure 26-25, showing the results of the FN simulations) and the maximum detectable degree increases up to about 20.

Considering three pairs of satellites, the time-variable signal detectability could be increased up to about degree 40 (see Figure 26-27, showing the results for the IIC3v1 configuration) in the FN scenario. However, the maximum achievable degree in detecting the non-tidal time variations of the gravity field mainly depends on the orbital inclination chosen for the third pair of satellites. In fact, comparing the results from the IIC2v1 (Figure 26-25) and IIC3v0 (Figure 26-26) configurations, namely introducing a third couple of satellites on the same orbit of the second couple (inclination of 70° degree), the maximum detectable degree is only slightly increased (from 20 to 25, in the FN scenario) with a slight overall improvement of the error curve at all the degrees, mainly due to the increased number of observations.

On the other hand, if the third couple of satellites is added with a different inclination with respect to the first and second couples (like happened in the IIC3v1 scenario, where the third orbit has a 40° inclination) the maximum detectable time-variable degree improves up to about 40 considering the FN scenario (see blue line in Figure 26-27), showing that increasing the ground coverage in the equatorial belt can improve the self-dealiasing capability of the satellite constellation.

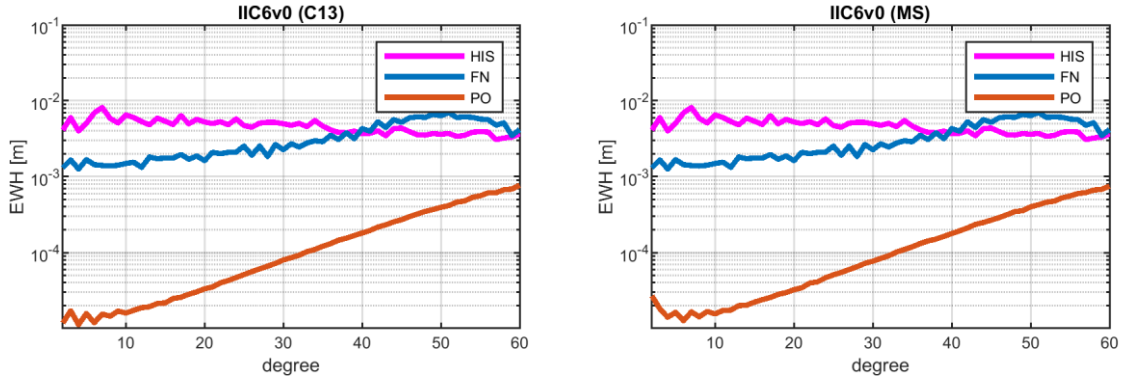

Figure 26-28 Degree errors regarding HIS of 1-day full-scale solutions up to d/o 60 of 6-pair (IIC6v0) constellations comparing CAI (left panel) with electrostatic (right panel) assuming X1 noise.

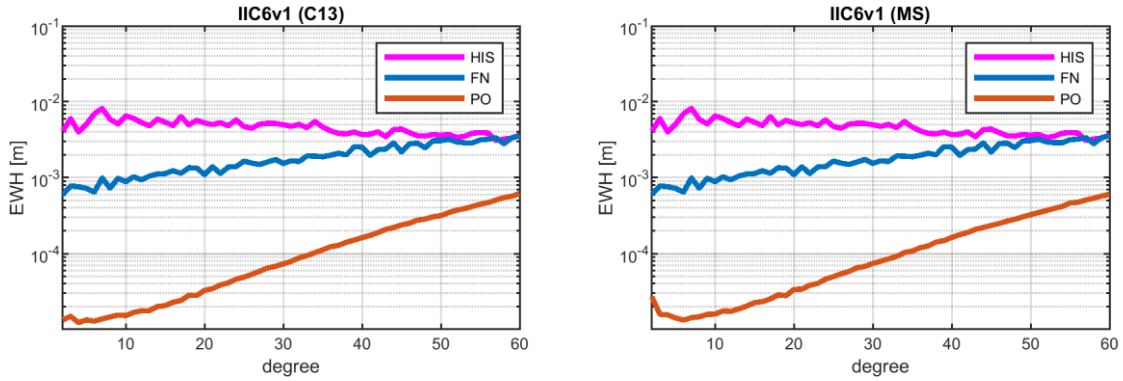

Figure 26-29 Degree errors regarding HIS of 1-day full-scale solutions up to d/o 60 of 6-pair (IIC6v1) constellations comparing CAI (left panel) with electrostatic (right panel) assuming X1 noise.

This outcome can be confirmed also by the simulations performed considering mission configurations including six couples of satellites. In fact, comparing Figure 26-27 and Figure 26-28, it can be noticed that the IIC6v0 configuration, in which only redundant orbits are added with respect to the IIC3v1 case, is not able to significantly increase the maximum time-variable detectability with respect to the case with three couples of satellites (IIC3v1 scenario). On the other hand, increasing the coverage of the equatorial belt (i.e. exploiting IIC6v1 configuration, see Figure 26-29) improves the self-dealiasing capability of the constellation, thus allowing a maximum degree up to about 60 in the FN case.

The results of the simulations presented in Figure 26-24, Figure 26-25, Figure 26-26, Figure 26-27, Figure 26-28 and Figure 26-29 show also that the kind of accelerometer (namely electrostatic or CAI) is not the main limitation in the accuracy of the solution, that is mainly related to the temporal aliasing effect. As for the instrument benefits coming from CAI instruments can be evaluated by looking at the results of PO solutions. In principle, CAI instruments could carry benefits at very low degrees thanks to an almost flat error PSD.

Introducing the X2.1 noise scenario only some constellation setups are chosen, according to the output of the simulations performed with the X1 noise realization. In particular, IIC2v1 (2 pairs of satellites), IIC3v1 (3 pairs of satellites), and IIC6v1 (6 pairs of satellites) have been selected, because these configurations have better performances in terms of de-aliasing capability due to a greater ground-coverage (and consequently resolution) in the equatorial belt. For each orbital configuration both the product only and the full-noise background models have been considered. The results are shown in Figure 26-30, where comparison between the presence of electrostatic accelerometer and the quantum accelerometer is performed.
Considering this product only background model, the impact of adding CAI accelerometers is significative in all the three orbital configurations. In fact, quantum accelerometers show improvements all over the harmonic spectrum (compare solid and dashed lines in the left panel of Figure 26-30). On the other hand, when considering the full noise scenario, no clear improvement is visible switching from electrostatic to CAI accelerometers, since the performances are limited by the temporal aliasing in both cases (see right panel of Figure 26-30).
The results from the three constellations, considering 7-day retrieval time and FN background model, show a capability of retrieving the gravity field up to a maximum degree of about 40, 60, 90, for IIC2v1, IIC3v1, and IIC6v1, respectively. However, these numbers do not benefit from the X2.1 noise model, and are similar to the outcome of the X1 noise scenario.

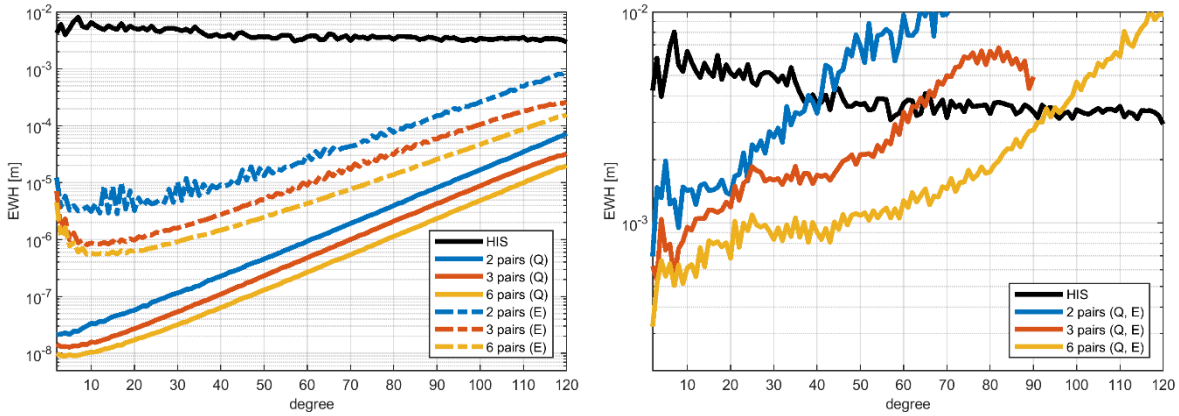

Figure 26-30 Degree errors regarding HIS of 7-day full-scale solutions up to d/o 120 summarizing the three possible constellations of satellites (2, 3, and 6 pair) assuming X2.1 noise scenario and comparing the PO (left panel) and FN (right panel) background models. Inside each panel a comparison between the electrostatic (E) and quantum (Q) instrumentation is reported.

For the sake of completeness, the geographical distribution of the estimation error considering the FN background model over a 7-day solution is reported in Figure 26-31, Figure 26-32, and Figure 26-33. Increasing the number of satellites improves the estimation accuracy especially towards the equator, where the redundancy carried by multiple pair of satellites is playing a crucial role.

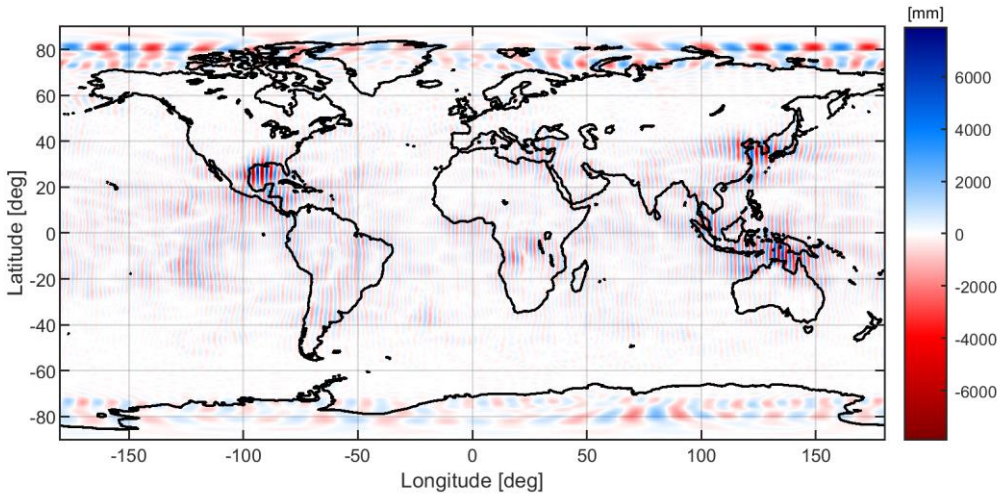

Figure 26-31 Spatial errors regarding HIS of 7-day full-scale solutions up to d/o 120 of 2-pair IIC2v1 constellations considering FN background model.

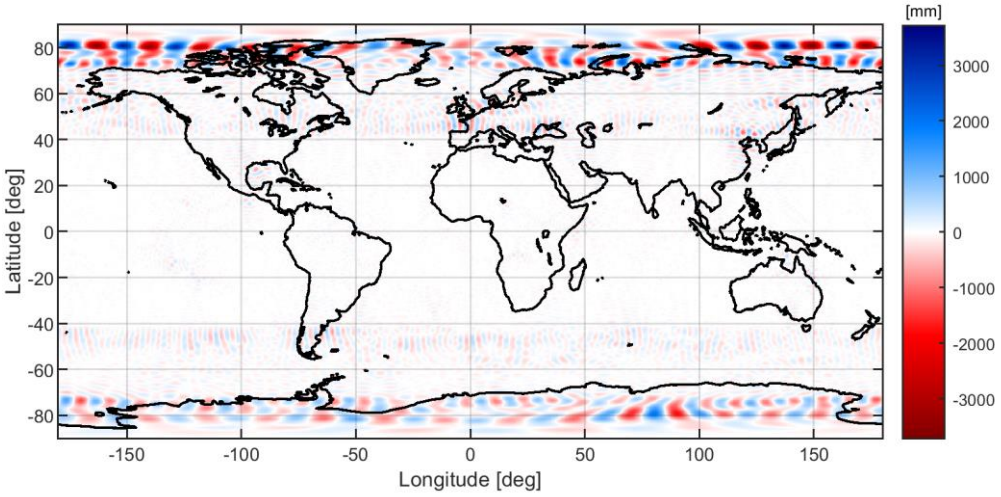

Figure 26-32 Spatial errors regarding HIS of 7-day full-scale solutions up to d/o 120 of 3-pair IIC3v1 constellations considering FN background model.

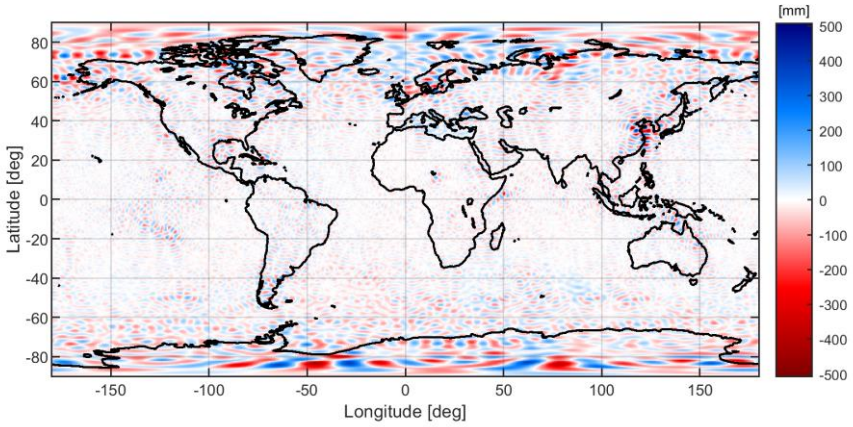

Figure 26-33 Spatial errors regarding HIS of 7-day full-scale solutions up to d/o 120 of 6-pair IIC6v1 constellations considering FN background model.

Finally, full noise simulations considering 2, 3, and 6 pairs constellations (IIC2v1, IIC3v1, IIC6v1) have been performed also on 1-day and 30-day time-span considering the more realistic full-noise background model case and the X2.1 noise scenario. The results are summarized in the following Figure 26-34. The three constellations, IIC2v1, IIC3v1, and IIC6v1 show a capability of retrieving the gravity field up to a maximum degree of about 20, 35, 55, respectively, considering 1-day solutions and of about 50, 70, 110, respectively, considering 30-day solutions.

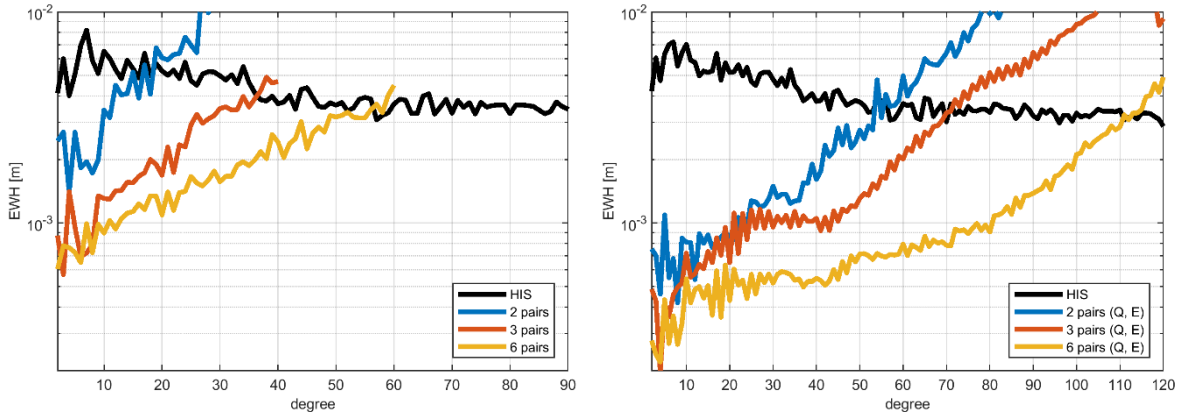

Figure 26-34 Degree errors regarding HIS of 1-day (left) and 30-day (right) full-scale solutions up to d/o 120 considering 2, 3, and 6-pair (IIC2v1, IIC3v1, IIC6v1, respectively) constellations considering quantum accelerometer, under the X2.1 noise assumption.

As a further step, regularization has been applied to the 7-day solutions, to improve the accuracy in the medium and higher part of the spherical harmonic spectrum. The regularization is applied according to the empirical degree variances of an a-priori model (of the HIS). The results are reported in the following Figure 26-35, showing for all three constellations the capability to increase the accuracy above harmonic degree 30. However, despite this improvement, the performances are still far from the PO results even if the difference has been reduced.

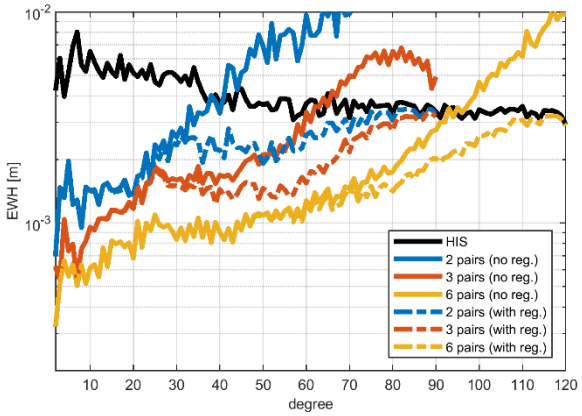

Figure 26-35 Degree errors regarding HIS of 7-day full-scale solutions up to d/o 120 considering 2, 3, and 6-pair (IIC2v1, IIC3v1, IIC6v1, respectively) constellations, quantum accelerometer, under the X2.1 noise assumption, and comparing regularized solutions (dashed lines) with unregularized ones (solid lines).

26.4. NRT ESTIMATES FOR LL-SST CONCEPTS (WP430)

For future missions, it is not expected that estimating a gravity field product with short delay is an essential problem. I.e., existing processing chains can be initiated and quickly finalized on future hardware ($\lesssim$1h) as soon as new data is available. Hence, the delay will primarily be defined by the delay of the needed input products (e.g., the l1b data products when referring to the standard GRACE/-FO processing scheme). There exist several feasible concepts for NRT-estimates such as direct daily solutions, windowed solutions, Kalman-filtered solutions or

along-track products. Hence, one is free to choose among different approaches depending on the individual needs. Since none of these approaches are really innovative there is limited benefit to investigate one individual at this point. Instead, it is proposed to also interpret the presented spline approach as a suited option for NRT solutions since sub-daily gravity field signal can be expressed and theoretically even extrapolated with it (see section 26.5).
The assessments in this section are not peculiar to LL-SST but also apply identically to all other conceivable gravity field mission concepts (i.e. WP530, WP630).

26.5. ENHANCED PARAMETERIZATION STRATEGIES FOR LL-SST CONCEPTS (WP440)

One of the main outcomes of the previous sections (26.1-26.3) is that the gravity field retrieval performance cannot be dramatically improved by either the instruments nor the constellation design when applying the standard time-static parametrization scheme. One reason for this is that the time-static parametrization cannot account for any time variations which means that even a linearly changing gravity signal would introduce major modelling errors. In case of a more or less arbitrarily changing signal as gravity, the mis-modelling errors are, hence, even more pronounced.

The logical consequence of this insight is that the time-variations must not be neglected in the modelling/processing of future satellite gravity missions. In general, there might be many feasible parametrization schemes which enable the consideration of time-variations. One straight-forward way is to use B-splines (basis splines) to model the time-domain since they can (1) approximate nearly any continuous shape, are (2) linear with local support, are (3) fast and stable to calculated, and are (4) easy to regularize. Mathematically, a time-variable spherical-harmonic gravity field coefficient $c_{nm}(t)$ can be expressed through i support point values/coefficients c_{nmi} by

$$c_{nm}(t) = \sum_{i=k-p}^{k} B_{i,p}(t)\, c_{nmi} \tag{1}$$

where $B_{i,p}(t)$ are the B-spline basis functions for support point t_i (knot) and B-spline degree p. The B-spline basis functions $B_{i,p}(t)$ can be calculated efficiently and stably by the well-known Cox-de Boor recursion formula (de Boor, 2003):

$$\begin{aligned} B_{i,0}(t) &:= \begin{cases} 1 & \text{if } \; t_i \le t < t_{i+1} \\ 0 & \text{otherwise} \end{cases} \\ B_{i,p}(t) &= \frac{t - t_i}{t_{i+p} - t_i} B_{i,p-1}(t) + \frac{t_{i+p+1} - t}{t_{i+p+1} - t_{i+1}} B_{i+1,p-1}(t). \end{aligned} \tag{2}$$

In the practical application, to evaluate the spline recursion formula within the defined limits $t_1 \le t < t_{max}$, the knot vector is padded by replicating the first and last element p times. Hence, defining a spline with n support points and a degree of p requires $n + 2p$ B-spline coefficients c_{nmi}. E.g., having a timeframe of a week with daily sample points ($n = 7$) and cubic B-spline ($p = 3$) requires already $7 + 2 \cdot 3 = 13$ B-spline coefficients. For the gravity field retrieval, this means that the number of unknown coefficients to estimate strongly increases with the number of support points and the degree of the spline.

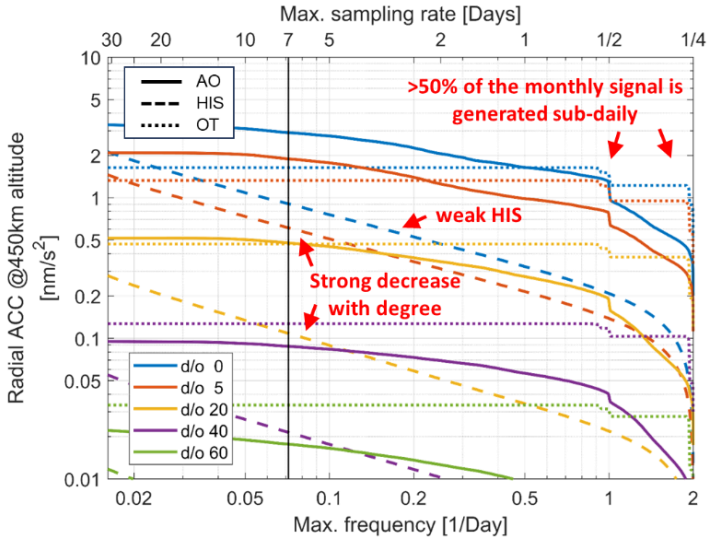

Figure 26-36 Non-recoverable signal energy on satellite altitude of the most important time-variable gravity field components (ESM HIS, residual ESM AO, and residual ocean tides) in dependencies of the retrieval period (i.e., sampling rate) and spatial resolution (i.e., maximum recovered d/o). Signal energy of non-tidal atmosphere and ocean (AO) and ocean tides (OT) refers to residuals after applying de-aliasing products.

As a compromise between smoothness and complexity, cubic splines ($p = 3$) are usually preferred in technical applications which is why this degree is also chosen in the following as the default, when applying splines in the estimation. Once p is defined, one still needs to determine the knot vector (support points). The choice of an appropriate timeframe (i.e. $t_{max} - t_1$) and sampling interval (i.e., $t_{i+1} - t_i$) is crucial for a proper time-variable gravity field solution and must be adjusted to the actual mission: E.g., having chosen a sampling interval which is too short (i.e., short periods in which the constellation cannot reach a full global coverage) will probably result in an unstable (normal equation) system. On the other hand, choosing the interval too long will increase the (residual) temporal aliasing as the corresponding Nyquist frequency is then decreased in comparison to the occurring (high) frequencies in the Earth's gravity field (compare Figure 26-36). The estimation (spline) timeframe is of importance because a warm-up time of several samples (before and after) is usually required to obtain solution in the central region with a proper (not further significantly improving) quality.

In the following, the spline approach will be applied on different gravity field retrieval scenarios, starting with a fictive closed-loop case to have a proof of concept that time-variable gravity field retrieval with B-splines is possible/stable. This closed-loop case will then be expanded step-by-step to eventually reach a realistic scenario. The spline approach will also be extended/modified in this process to solve/mitigate different problems that will occur within these more realistic cases.

Proof of concept

To prove that B-splines are suitable for time-variable gravity field recovery, a closed-loop scenario is set up in a first step. In contrast to the previously shown full-scale full-noise scenarios (sections 26.1-26.3) the forward modelled gravity is herein limited in the time domain to be representable through a spline with daily support. The applied constellation is IIC6v1 which enables a stable recovery of daily fields up to d/o 60 (see Figure 26-16c). Hence, for the closed-loop scenario, the forward modelled gravity signal is also limited to d/o 60. Additionally,

the reduced-scale simulator (acceleration approach) is used, white-noise is assumed for the observation noise ($10^{-11}\ m/s^2$), and tidal signals are omitted (only ESM is used). In the parametrization, the exact same spline with daily support is then estimated again (up to d/o 60). The timeframe is chosen to be a week with two days warm-up before and after.

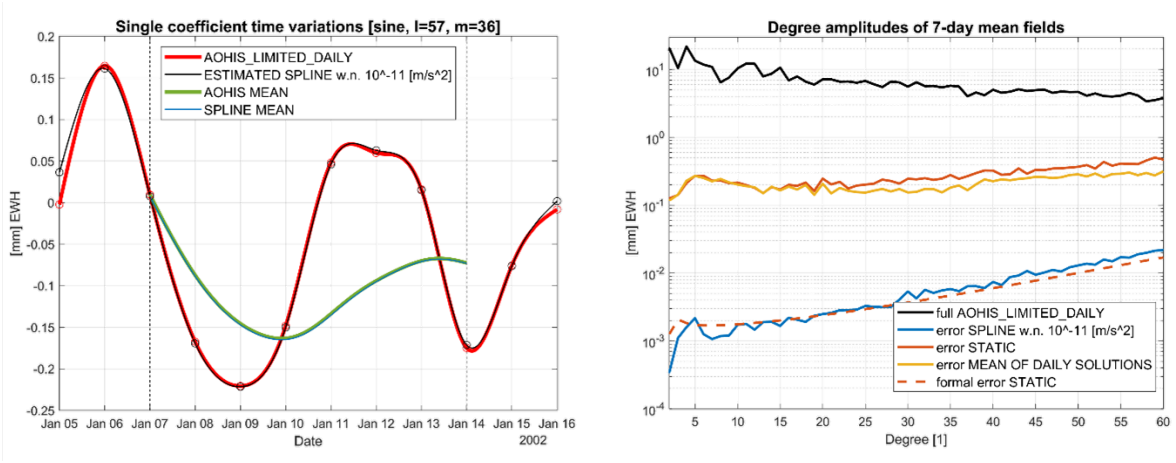

(a) **(b)**

Figure 26-37 Results of the closed-loop test. (a) The temporal evolution of a single coefficient ($c_{57,36}$). Red: reference from ESM data. Black: estimated through spline approach. Green: cumulative time-mean of reference. Blue: cumulative time-mean of the estimated coefficient. (b) Degree-errors of different parametrization strategies in comparison. Red: default static parametrization. Yellow: mean of daily static solution. Blue: Spline parametrization.

The results of the closed loop test are shown in Figure 26-37. As can be seen, in this case, the spline parametrization can stably recover the time-variable gravity field and the empirical errors are on the level of the formal errors of the static parametrization. It is also shown, that it widely outperforms the commonly used static and piece-wise static parametrization schemes. This is a first positive hint that the spline approach is suitable for time-variable gravity field recovery.

Residual temporal aliasing

In a more realistic scenario, the forward modelled gravity is not limited to daily support points but is given through a 6-hourly sampling. The rest of the setup is left identical. This change obviously introduces (residual) temporal aliasing, since the 6-hourly sampling cannot be represented by the daily support points of the estimated signal.

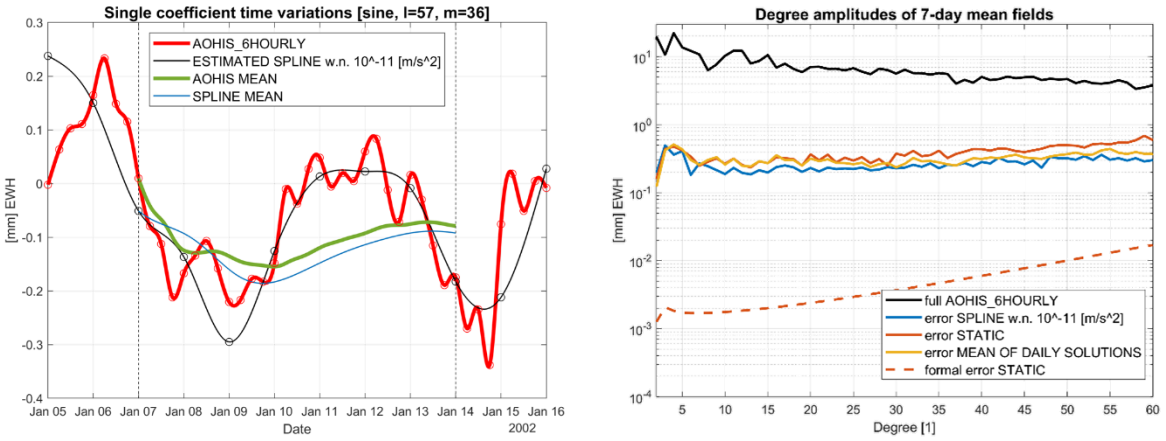

(a) **(b)**

Figure 26-38 Results of the test with temporally unrestricted forward modelled gravity. See Figure 26-37 for a more detailed explanation.

In case of residual temporal aliasing (see Figure 26-38), it is observed that the huge performance advantage of the spline approach shrinks from a factor of two magnitudes down to a factor of about two or less. The reason for this is found in the fact that more than 50% of the weekly (and even monthly) gravity signal is generated in daily and sub-daily wavelengths (see Figure 26-36). Hence, omitting these frequencies, also introduces a similar amount of temporal aliasing (i.e., >50%). The only way to further reduce this error (without improving the de-aliasing models) is to also recover daily and sub-daily frequencies. However, all investigated constellations (such as IIC6v1) are only optimized for daily and longer sampling periods. Half and quarter-daily sampling periods can thus not be recovered stably with these constellations since no global coverage can be obtained in these short periods with them. As a logical consequence, other constellations which achieve sub-daily global coverage need to be investigated in the next step.

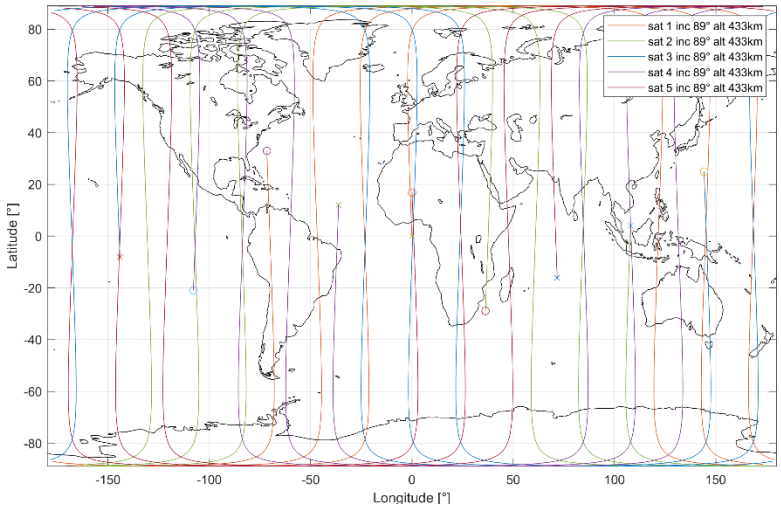

(a)

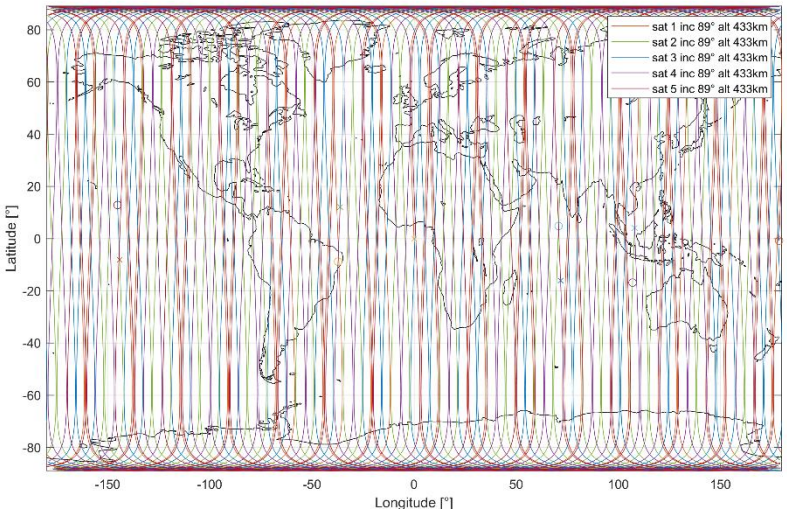

(b)

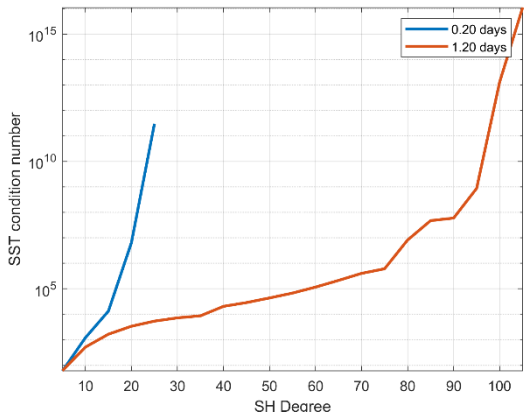

(c)

Figure 26-39 Illustration of constellation PIC5_5h. (a) Ground-track pattern for a retrieval period of 1/5 day (4.8 hours). (b) Ground-track pattern for a retrieval period of 1.2 days (28.8 hours). (c) Condition number (L^2-norm) of a normal equation matrix from a reduced scale simulation (assuming white-noise observations) for different max. d/o (see x-axis) and retrieval periods (i.e., sub-cycles, see legend).

Dedicated constellation with sub-daily global coverage

The only known way to stably achieve sub-daily repeat-cycles (and, thus, global coverage) is to distribute satellites in the time domain on the same ground-track (see Zingerle et al., 2024). The shortest repeat-cycle that is achievable with a single satellite (pair) is obviously one day. With n satellites/pairs distributed on the same ground track this repeat-cycle can effectively be divided by n. Hence, to achieve a quarter-daily repeat cycle (which is about the required minimum regarding the main occurring frequencies, see Figure 26-36), at least 4 satellites/pairs are required. To safely stay below the required Nyquist frequency (some main tidal contributors are slightly shorter than half-daily) it is suggested to use at least 5 satellites/pairs. Since global coverage is desired, these satellites/pairs need to be located on a near polar inclination. Therefore, when only considering smaller constellations (≤ 6 satellites/pairs), a polar constellation is the only feasible option for sub-daily gravity field retrieval.

A realization of this smallest feasible 5-satellites/pairs constellation is given with the *PIC5_5h* constellation (see Figure 26-39a). It is seen that the constellation achieves global coverage in less than 5 hours which means that it is able to cover the most important temporal frequencies of the Earth's gravity field (compare Figure 26-36). However, as shown in Figure 26-39c, the achievable spatial resolution in this period is still very coarse (about d/o 15) which means that spatial aliasing will pose a problem here (see later). In addition to this 5 hourly cycle also a longer 1.2 daily cycle is implemented (Figure 26-39b). This means that lower temporal frequencies can be estimated with higher spatial resolution. It shall be noted that it is straightforward to extent this kind of constellation by a integer factor of n (i.e., 10, 15, 20, … satellites/pairs) which also increases the achievable spatial resolution after 5h by a factor of n (i.e., d/o 30, 45, 60, …). This would then obviously help mitigating spatial aliasing. However, such larger constellation sizes will not be investigated in the scope of this project (since too unrealistic/expensive).

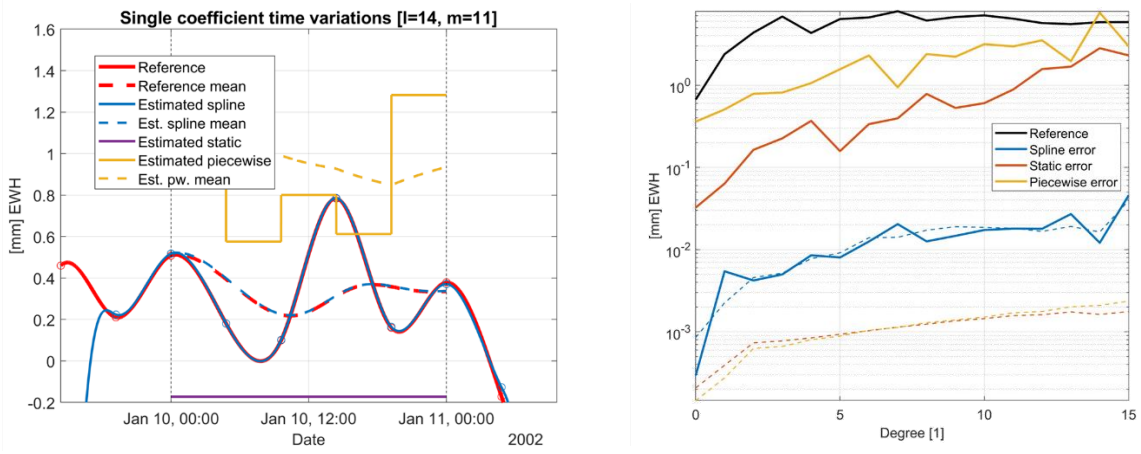

(a) **(b)**

Figure 26-40 Results of the closed-loop test with sub-daily temporal signal. (a) The temporal evolution of a single coefficient ($c_{14,11}$). Red: reference from ESM data. Blue: estimated through spline approach. Yellow: estimated through piece-wise static approach. Violett: estimated through static approach. Dashed lines: corresponding cumulative mean. (b) Degree-errors of different parametrization strategies in comparison. Red: default static parametrization. Yellow: mean of daily static solution. Blue: Spline parametrization. Dashed lines: corresponding formal errors.

Closed-loop with higher temporal resolution

The shown PIC5_5h constellation can now be used to retrieve the sub-daily frequencies which has not been possible beforehand with the IIC6_v1 constellation. To test if this is possible, the initial closed loop is therefore extended to a 6 hourly support point sampling in the parametrization and the forward modelling. On the other hand, to retain the closed-loop case, the spatial resolution has to be adjusted to d/o 15 in the forward model and the parametrization (see previous discussion). In addition to the initial test, also residual tidal signals are now considered. The forward model signal content is hence identical (and, therefore, realistic) to the full-noise solutions in the previous sections. Figure 26-40 shows the result of this test. It is seen that the spline approach achieves again to deliver much better results than the piecewise and the static solution. Also, the formal and empirical error curves overlap which is an indication that the parametrization is able to fully describe the problem (which is expected from a closed loop). As a difference to the original closed loop, the formal error of the spline approach is increased compared to the piecewise and static solutions (but still much better than the empirical static error). This indicates that it is numerically more complex to estimate the sub-daily spline with the PIC5_5h constellation (than the daily splines with the IIC6_v1 constellation).

Dependency on support point location

In the previous (closed-loop) tests, the locations of the support points of the forward model and the parameterization are chosen to match each other. In a realistic scenario, it cannot be assumed that the forward modelled gravity follows exactly a certain spline. Hence, it must be tested if a proper solution can still be obtained when they do not match. To check this, the previous test is modified by simply shifting the support point location by 1/3 of the sampling distance.

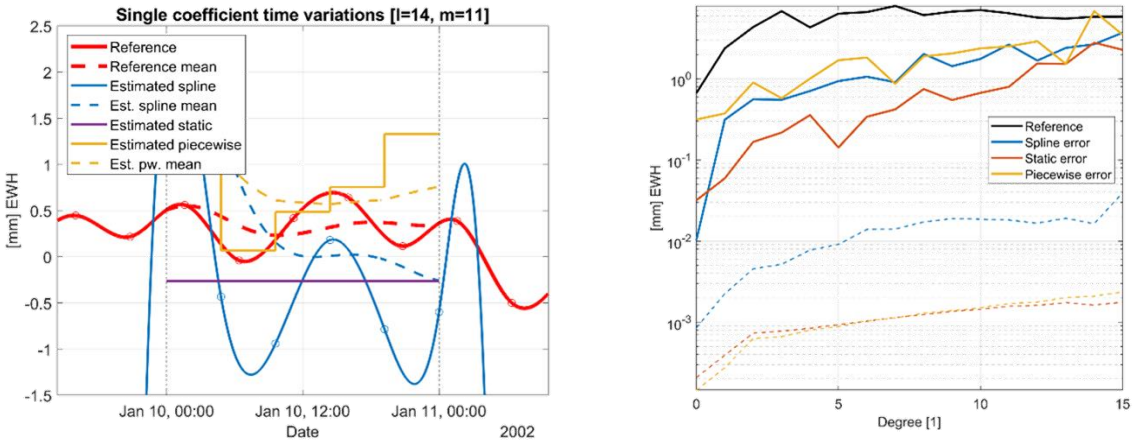

(a) **(b)**

Figure 26-41 Results of the spline scenario with shifted support point location See Figure 26-40 for a more detailed explanation.

The results with shifted support point location are shown in Figure 26-41. Interestingly, the introduced shift completely destroys the initial advantage of the spline parameterization and even deteriorates the mean solution in comparison to the static solution (see Figure 26-41b). This highlights that the spline parameterization is strongly dependent on the support point location which means that the system anticipates the exact same spline in the real data as used

in the backward model. This is obviously not the case if working with real data. Hence, a solution for this problem needs to be found.

Oversampling of the forward modelled spline

A still remaining limitation regarding realism of the simulation is the sampling of the forward modelled spline. While a sampling of 1/5 days is theoretically enough to cover all occurring frequencies in the forward models (ESM and tidal), B-splines are not able to precisely resemble harmonic oscillations (i.e., trigonometric functions). Hence, to reconstruct the signal more precisely, it is suggested to simply oversample the forward modelled signal. Hence, in a next test, forward modelled support points are not only shifted (by 1/3) but also sampled with higher frequency (1 hour).

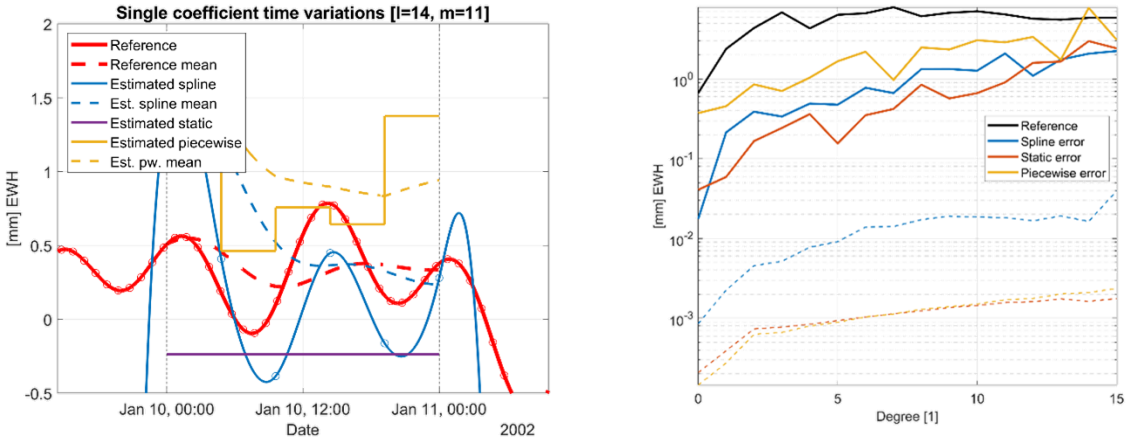

(a) **(b)**

Figure 26-42 Results of the spline scenario with shifted and oversampled support point location. See Figure 26-40 for a more detailed explanation.

When additionally introducing oversampling, the performance of the spline parameterization is not getting any worse in comparison with the shift-only scenario (see Figure 26-42). Instead, the results are again slightly better which implies that the shift-only case is some kind of worst-case scenario for the parametrization. This test again shows that, in a temporally realistically modelled environment, the spline parametrization in its current form has no fundamental benefit over the static parametrization. Also the formal and empirical errors don't agree anymore which is a good indication that the spline parametrization does rely too strongly on the alleged support point location.

Introducing unstable and regularized solutions

As a workaround for the support point dependency, it is proposed to modify the parameterization in a way that it becomes unstable. When unstable and no solution is obtainable, the system cannot draw any benefit anymore from the knowledge of the support point location. Hence, all initially present dependencies vanish automatically. Obviously, an unstable system is of no use in the first place (since no solution is obtainable then). However, such a system might serve as a dependency-free basis for other stabilized system. One way to stabilize unstable systems is to introduce regularization constraints. Fortunately, splines are straight-forward to stabilize by introducing knowledge about their presumed shape (e.g.,

amplitudes, slopes, smoothness, etc.). Therefore, it is proposed to introduce an oversampling (by a factor of 2, i.e., a 1/10 days sampling) to de-stabilize the initial system. By introducing an empirical derived smoothness-constrained (from the forward modelled signal), the system is then stabilized again. Calculating the smoothness constraint involves taking the second derivative which can be easily done analytically in case the (forward modelled) signal is represented as spline.

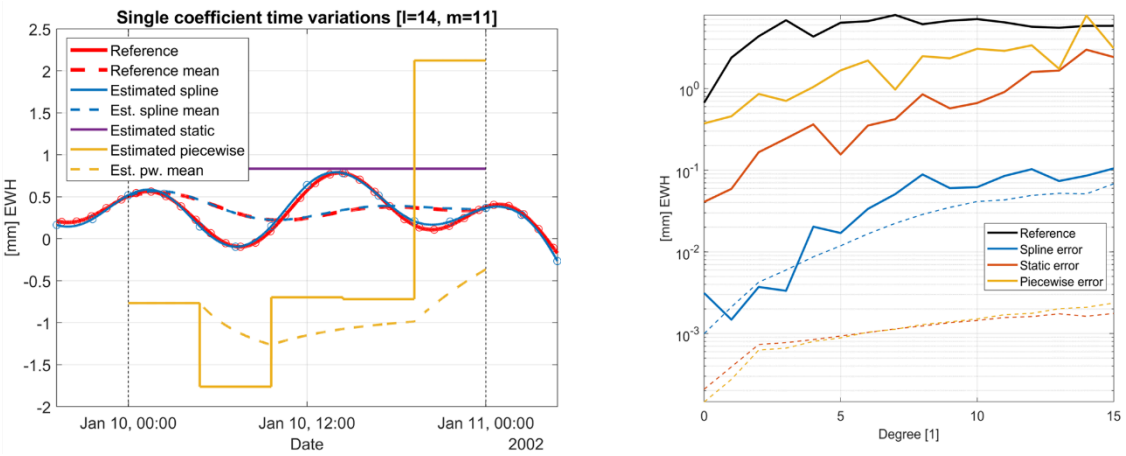

(a) **(b)**

Figure 26-43 Results of the spline scenario with smoothness constraint. See Figure 26-40 for a more detailed explanation.

The results of this modified test scenario are depicted in Figure 26-43. Obviously, this strategy strongly helps to reduce the support point dependency and allows a good approximation of the non-spline forward modelled signal. However, this approach comes with the cost of estimating more parameters than essentially necessary (roughly double the amount).

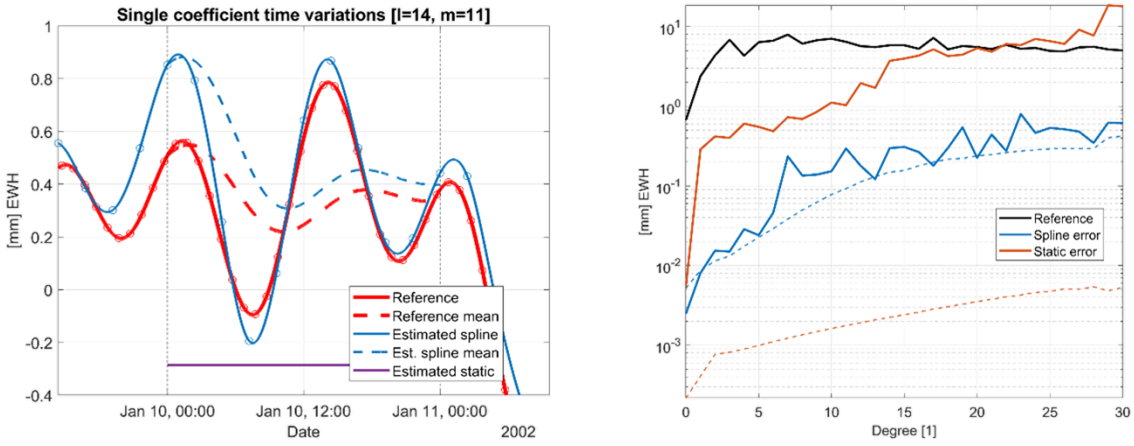

(a) **(b)**

Figure 26-44 Results of the spline scenario with smoothness constraint and extended signal content up to d/o 30. See Figure 26-40 for a more detailed explanation.

Extending the spatial resolution

Since one relies on regularization when introducing the smoothness constraint, it is possible to extend the spatial resolution even beyond the d/o that would be usually solvable. E.g., in the current test case, the spatial resolution can be extended to d/o 30 in the forward modelled signal and in the parameterization and the obtainable result is still considerable better than the static solution. This is shown in Figure 26-44 where the spline approach still provides one order magnitude better results than the static (even if the performance is slightly worse than when just solving up to d/o 15).

Spatial aliasing

The spline test case scenario has been made step-by-step more realistic within the previous discussion in this section. However, to obtain a fully realistic scenario, higher spatial resolutions need to be regarded in the forward modelled signal (which, until now, has still retained the same resolution than the estimated signal). Therefore, two test with spatial aliasing are made which retain the general setup of the previously shown scenarios (i.e., the smoothness-constrained spline scenario) and just increase the maximum d/o of the forward modelled signal.

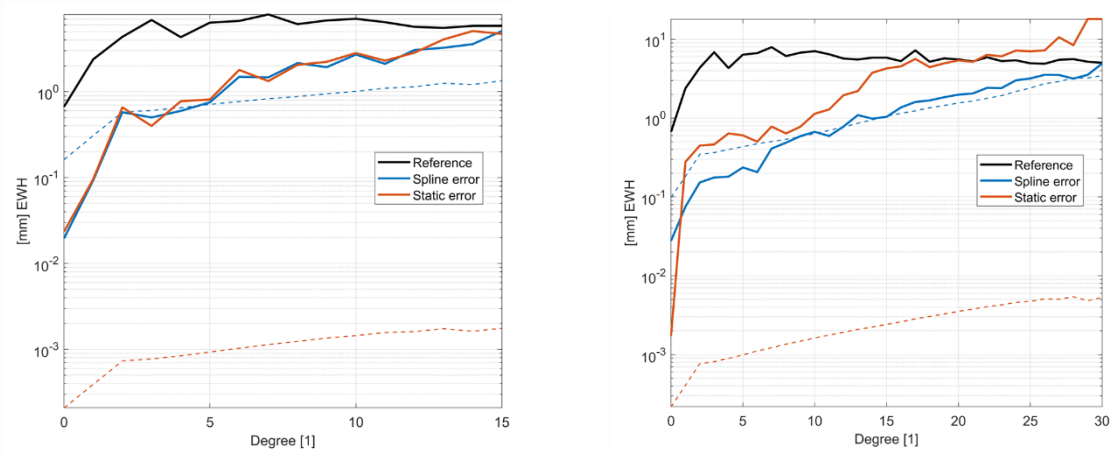

(a) **(b)**

Figure 26-45 Degree errors in case of spatial aliasing for different smoothness-constrained spline scenarios (a) Scenario with parameterization up to d/o 15 and forward modelled signal content up to d/o 30. (b) Scenario with parameterization up to d/o 30 and forward modelled signal content up to d/o 60.

The first spatial aliasing test estimates the signal just up to d/o 15 while the forward modelled signal is given up to d/o 30 (see Figure 26-45a). The second test estimates the signal up to d/o 30 and introduces the forward modelled signal up to d/o 60 (see Figure 26-45b). What is seen is that when retrieving the signal only up to a lower d/o, the spatial aliasing effect is generally stronger. This is to expect since more spatial content is neglected (which then, conversely, causes spatial aliasing). Also, the benefit of the spline approach seems to be smaller (not present) for the lower resolution solution (Figure 26-45a). This indicates that in this case spatial aliasing dominates the temporal aliasing. In contrast, when estimating up to higher d/o (e.g., d/o 30, see Figure 26-45b), the spline approach delivers again significantly better results than the static one. This suggests that, in such cases temporal aliasing dominates again the spatial aliasing. Eventually, this means that spatial aliasing is treated best by estimating the gravity field to a sufficiently high resolution. Hence, mitigating not only the temporal resolution but

also the spatial resolution is of primary importance for a high-quality gravity field retrieval. For the mission design this implies that even more satellites/pairs are needed to enable a sufficiently high spatial and temporal resolution.

Along-track filtering to mitigate spatial aliasing

Since further increasing the spatial resolution by introducing more satellite is very costly, alternative approaches to mitigate spatial aliasing are desirable. As alternative to estimating higher spatial frequencies there is the possibility to filter the temporal high-frequency content out on observation level. The rational behind this is that spatial distances map to temporal distances/periods when the satellites orbit with approximately constant speed (which is the case for near-circular orbits). Consequently, a (spatially) low resolution gravity field can be forward modelled to smooth observations which do not contain temporal high-frequency content. Hence, vice versa, smooth observations shall theoretically lead to an, at least reduced, signal content in the thereof estimated gravity field. Eliminating high-frequencies in the observation can theoretically be done by applying a low pass filter to the initial observation. However, then, the stochastic model does not fit to the observations anymore (which means that the formal errors will be off). As alternative, it is hence suggested to simply specify an artificially high noise level in the higher-frequencies in the stochastic modelling of the observations (and by leaving the observations themselves unchanged). Then, the high-frequency content of the observations will be down-weighted intrinsically within the estimation process which shall eventually reduce spatial aliasing. As a sidenote is shall be mentioned that this only works because the temporal changes in the gravity field map to much longer wavelengths in the along-track observations and do interfere with the spatial wavelengths that one wants to avoid. Otherwise one would also smooth out temporal changes which is obviously not desired.

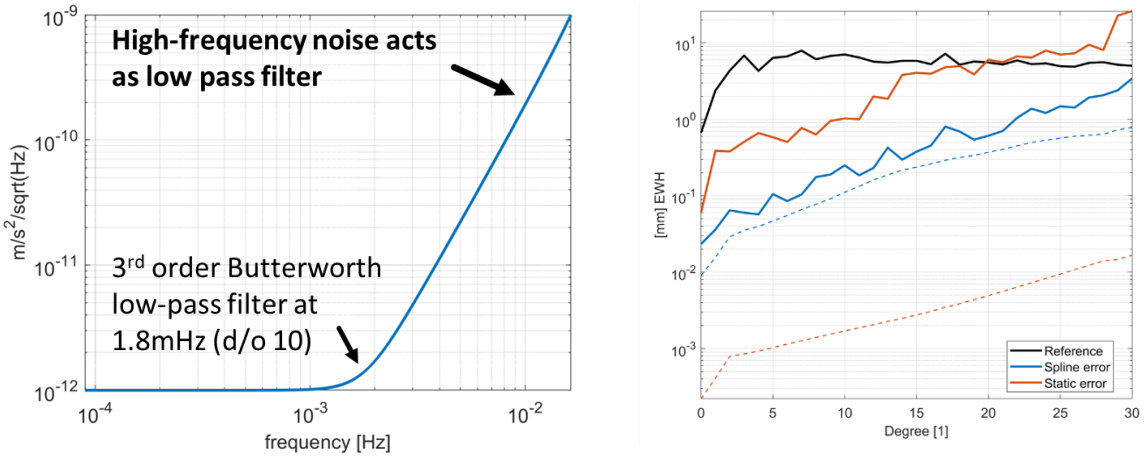

(a) **(b)**

Figure 26-46 Mitigating spatial aliasing by introducing artificial high-frequency noise in the stochastic modelling of the observation noise (a) Amplitude spectral density (ASD) of the along-track observations with artificially increased high-frequency noise (b) Degree errors of the appropriate spline solution with smoothness constraint.

A first test of this approach is shown in Figure 26-46. In this concrete example, a simple inverse 3rd order low-pass Butterworth filter is used to model the artificial increase of the high-frequency observation noise (with a cut-off frequency of 1.8mHz, roughly corresponding to d/o 10, see Figure 26-46a). It is seen that this modification helps to reduce spatial aliasing

significantly (compare Figure 26-46b and Figure 26-45b) which proves that the proposed method works as expected.

These results conclude the initial investigation of the spline approach within this project: it could be shown that

(1) the spline approach is suitable for representing time-variable gravity,

(2) it is able to significantly outperform static approaches,

(3) methods exist to solve the initial limitations,

(4) it is even applicable within a realistic environment.

However, it needs to be highlighted that all shown solutions just represent a first attempt and that probably an even better individual setup for the spline parameterization can be found (e.g., better regularization, choice of support points, warmup period, low-pass filtering, etc.). Such more elaborate investigations cannot to be addressed in the limited scope/timeframe of this project but might be subject for future work.

The assessments in this section are not peculiar to LL-SST but also apply identically to all other conceivable gravity field mission concepts (i.e. WP540, WP640).

26.6. POST-PROCESSING FOR LL-SST CONCEPTS (WP450)

With standard parameterization

For post-processing the selected results of section 26.2, the so-called VADER-filter (see Horvath et al., 2018) is applied. The VADER-filter is a filter which uses the empirical variances of the SH-coefficients of the background models as a-priori information to filter/regularize the original normal equation matrix of the solution. For the post-processing, 1-day and 7-day solutions are investigated over a time span of 3 months. For the VADER-filter, a degree-dependent regularization-parameter (i.e., scaling) is automatically derived through the ratio of the degree-variances of product-only solutions and full-noise solutions.
A comparison between the degree-variances (mean of three months) of original and filtered solutions is given in Figure 26-47:

- Generally, as expected, filtering significantly improves the solution/signal-to-noise ratio in the upper part of the spectra
- All investigated constellations react in a similar way to the filtering, improving the (7-day) solutions by a factor of maximal about 1.5 (at d/o 60)
- An exception to this is the 7-day MAGIC solution up to d/o 120 which apparently cannot be improved through the VADER-filter. A possible explanation for this is that a 7-day 2-pair solution might be less stable than the others (cf. 26.2.1) which, eventually, might negatively bias the filtered result.
- Considering this improvement-factor of about 1.5, the gap to the product-only performance decreases accordingly.

Thus, after filtering, the product-only error level is "just" about 500-750 times smaller than the filtered full-noise error. This shows, that such kind of filters can decrease the temporal-aliasing error but are unable to reduce the error to an extend which would be necessary to benefit from the assumed instruments.

In addition, it must be noted that these filters use actual signal variances which might bias the retrieved result to some extent. In a real-life scenario, it can be assumed that the filter work not that well as in simulations since in the simulated environment the signal coefficient-variance fit perfectly to the filter which cannot be assured in a real application. Though, since the variances are a statistical measure and since it is assumed that the models are somewhat close to reality, it can also be presumed that the real-life filter performance is not degraded significantly.

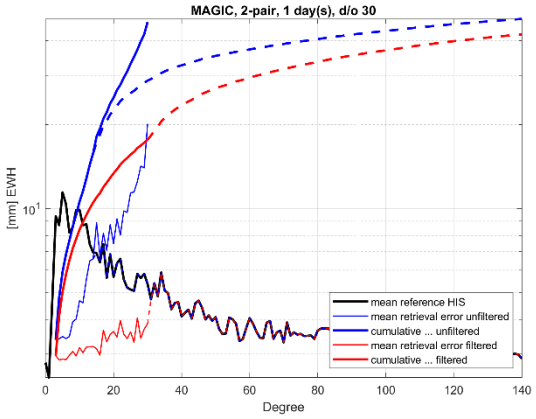

(a)

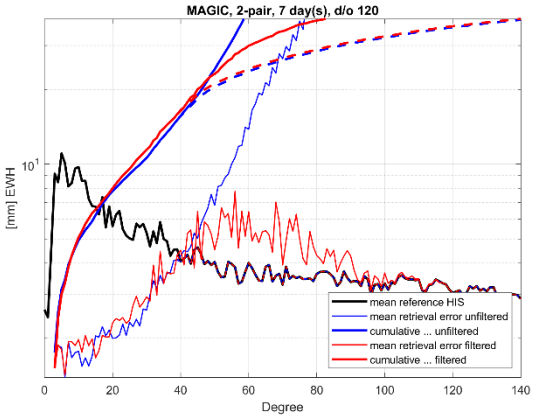

(b)

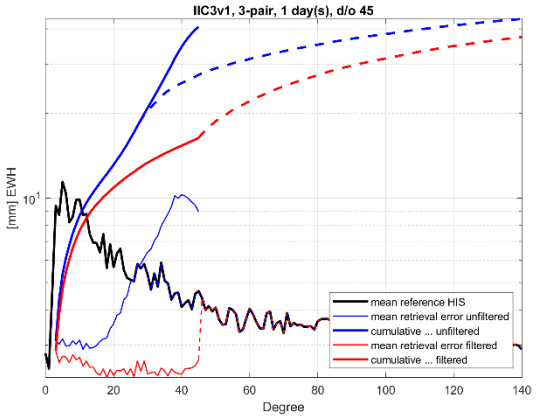

(c)

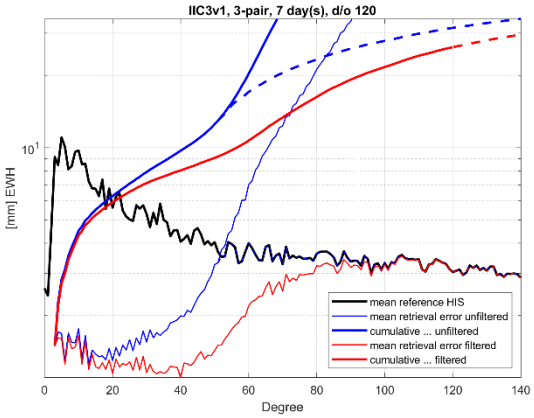

(d)

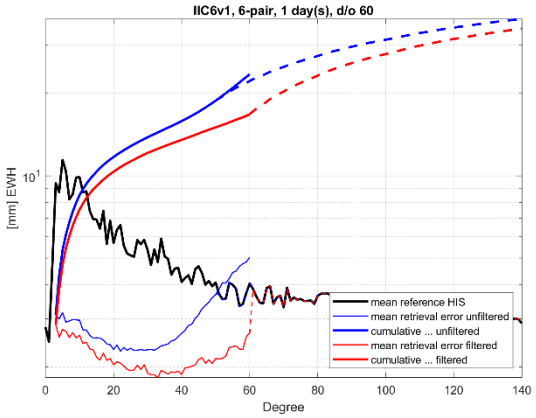

(e)

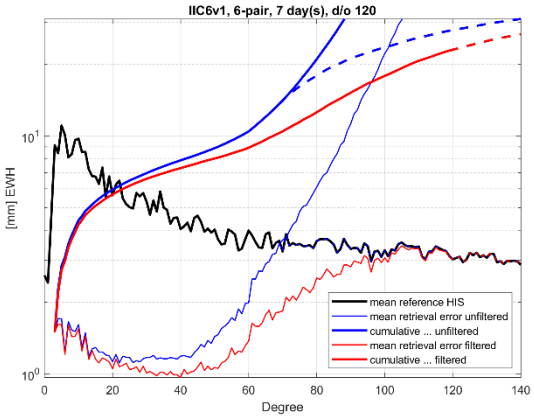

(f)

Figure 26-47 Mean degree errors over a time span of 3 months of full-scale simulations (blue lines) for different constellations (see section 26.2) in comparison to filtered VADER-solutions (red lines). (a) 1-day solution of MAGIC-constellation. (b) 7-day solution of MAGIC-constellation. (c) 1-day solution of IIC3v1-constellation. (d) 7-day solution of IIC3v1-constellation. (e) 1-day solution of IIC6v1-constellation. (f) 7-day solution of IIC6v1-constellation.

With spline parameterization

When applying the presented spline parametrization method (see section 26.4), no post-processing is usually required, since the temporal variations are already considered in the model which means that the solution is already nearly optimal regarding the given observations/mission. This assessment is not peculiar to LL-SST but also applies identically to all other conceivable gravity field mission concepts (i.e. WP540, WP640).

26.7. EVALUATION OF ADDED VALUE W.R.T. ES ACCELEROMETER (WP460)

To evaluate the added value with respect to electrostatic accelerometers, a monthly solution for the MAGIC baseline configuration 3DH with different onboard instrumentation is considered, namely the X1.1, X1.2, and X1.3 noise scenario. In all three scenarios, MicroStar (MS) or CAI accelerometers are considered, as well as different inter satellite range instruments, namely the GRACE KBR (X1.1), the GRACE-FO LRI (X1.2) and the NGGM LRI (X1.3). The instrumentation noise levels, used as inputs for the following simulations, are summarized in Figure 26-48 in terms of ASD. In the following, for each of the possible noise scenario both PO and FN solutions are computed and compared.

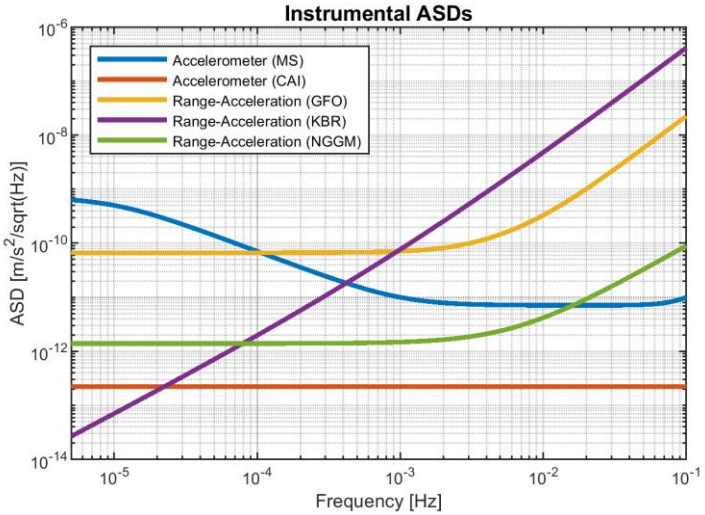

Figure 26-48 Instrumental noise error in terms of ASDs, considering the X1.1 (CAI or MS, KBR), X1.2 (CAI or MS, GFO), and X1.3 (CAI or MS, NGGM) noise scenarios.

Figure 26-49, Figure 26-50, and Figure 26-51 show the results of the performed simulations. Looking at the FN degree error curves it can be noticed that considering the same satellite mission configuration, but different onboard instrumentation (namely, different accelerometers or satellite tracking system), the maximum detectable degree of the non-tidal time-variable signal remains in the range between 50 and 60. In particular, it is slightly worse only in the case of the GRACE KBR instrument (Figure 26-49) due to the lower accuracy of the tracking instrument. Moreover, comparing the estimation accuracy obtained considering MS or CAI accelerometers in the FN scenario (dashed lines in Figure 26-49, Figure 26-50, and Figure 26-51) they are practically independent from the type of accelerometer, showing that one of the main limitation is related to the effects of temporal aliasing.

As for the PO solutions, the limiting factor is represented by the tracking instruments rather than the accelerometer when considering the KBR or GRACE-FO LRI tracking instrument. In fact, in these two cases (see Figure 26-49 and Figure 26-50) the estimation error curves considering MS or CAI accelerometer with the same tracking instrument are practically equivalent (compare solid yellow and blue curve in both Figure 26-49 and Figure 26-50). Of course, comparing the achievable accuracy level of the GRACE KBR case (Figure 26-49) with respect to the one of the GRACE-FO LRI case (Figure 26-50), an overall accuracy improvement of about one order of magnitude in terms of standard deviation happened, thanks to the better tracking instrument.

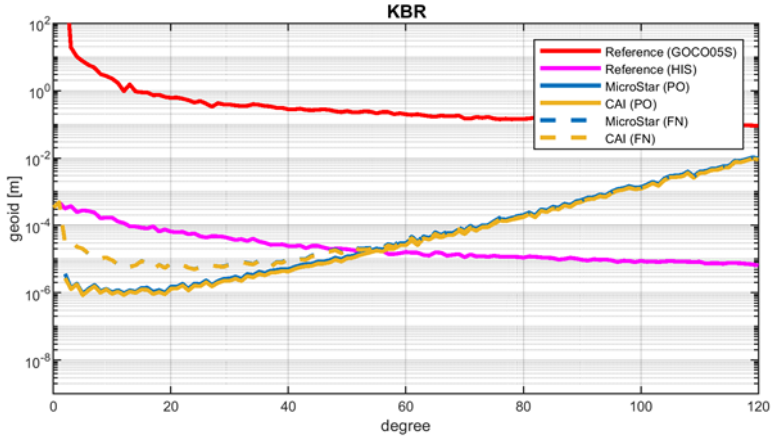

Figure 26-49 Degree error in terms of geoid for the simulations performed under the X1.1 noise assumptions.

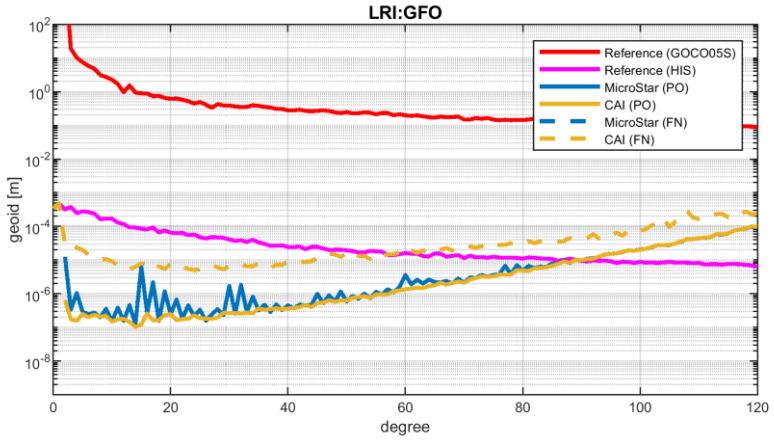

Figure 26-50 Degree error in terms of geoid for the simulations performed under the X1.2 noise assumptions.

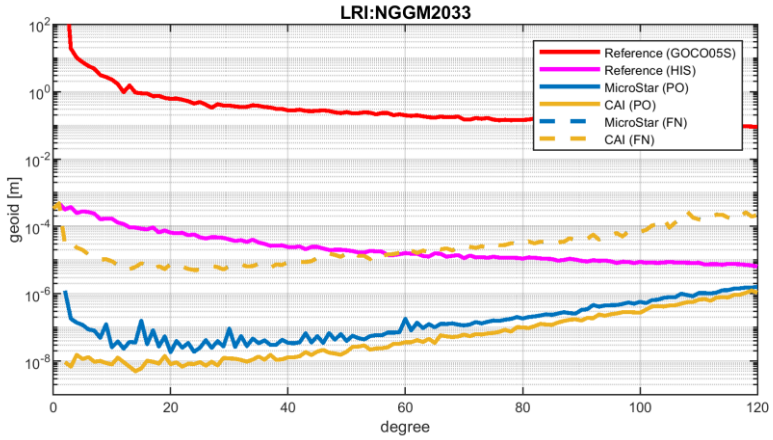

Figure 26-51 Degree error in terms of geoid for the simulations performed under the X1.3 noise assumptions.

To see a possible impact coming from the accelerometer it is necessary to improve the accuracy of the tracking instrument. Therefore, considering the accuracy level of NGGM (Figure 26-51), the resulting error curves (PO scenario, solid yellow and blue lines) show that CAI has a potential improvement with respect to MS, mainly related to the flat shape of CAI error PSD at low frequencies.

These results are confirmed by the simulations performed considering the X2.1 instrumental noise scenario considering different constellations with 2, 3, and 6 pairs of satellites, as shown in Section 26.3. These figures show that improvements related to quantum instrumentation are possible in the product-only case, because the temporal aliasing is still the main limiting factor of the solution retrieval.

However, comparing the results of TUM and Polimi simulations for the FN scenario (see Figure 26-52 including results from Figure 26-17, Figure 26-18, Figure 26-19 and Figure 26-30) some differences are visible in the medium harmonic degrees, especially for the scenario with 6 pairs of satellites (IIC6v1). In fact, the intersection between the error curve and the reference signal curve is around degree 70 for the TUM solution and around degree 90 for the POLIMI solution.

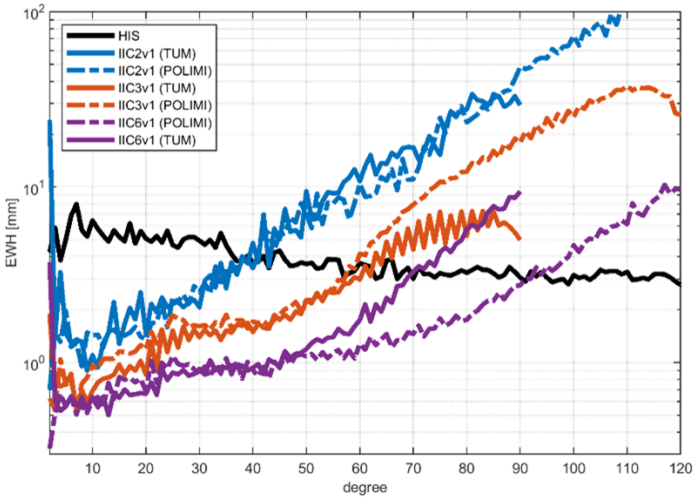

Figure 26-52 Comparison of TUM and POLIMI solutions for the X2 noise scenario considering 2, 3 and 6 pairs of satellites constellation (IIC2v1, IIC3v1, and IIC6vq, respectively), FN background model, and a 7-day time span. Black solid line represents the power of the reference HIS signal.

This discrepancy has been analysed and the outcome is that this is an effect related to the choice of the stochastic modelling in the Least Squares Adjustment. In fact, POLIMI approach used a white noise model with range-acceleration observation, while TUM used the actual instrumental noise PSD considering the range-rate observation.
We checked that if the TUM solution, using the range-rate observations, is computed introducing a $1/f$ noise PSD (that is equivalent to white noise in range-acceleration), it leads to a solution that is fully consistent with the POLIMI results (compare solid and dashed yellow lines in Figure 26-53). On the other hand, if we introduce the actual noise PSD of the range-acceleration as stochastic model in the POLIMI solution, this lead to a (degraded) solution equivalent to the original TUM one results (compare solid and dashed purple lines in Figure 26-53). Note that, in both the POLIMI and TUM simulators, introducing the actual instrumental PSD requires to split the dataset in subsets (arcs) independent from one another for computational reasons.

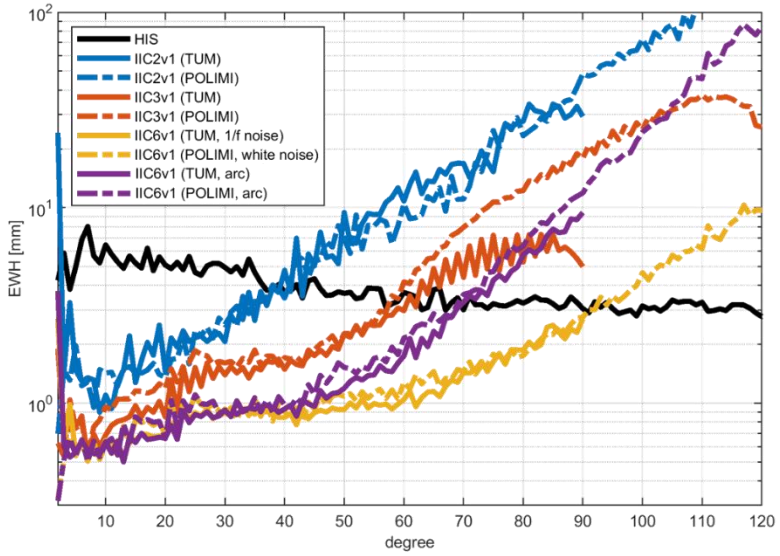

Figure 26-53 Comparison of TUM and POLIMI solutions for the X2 noise scenario considering 2, 3 and 6 pairs of satellites constellation (IIC2v1, IIC3v1, and IIC6vq, respectively), FN background model, and a 7-day time span. The solution with 6 pairs of couples has been computed with two stochastic models with both the TUM and POLIMI approach. Black solid line represents the power of the reference HIS signal.

The conclusion is that the choice of the stochastic model could be a tool to mitigate the degradation carried by the temporal aliasing and that choosing a white-noise stochastic model is much better than the actual instrumental noise PSD in that case. Moreover, this choice has a larger impact when increasing the number of satellite pairs and is mainly visible in the 6-pairs constellation for which the investigation was performed.

27. MASS CHANGE PRODUCTS FROM MISSION ARCHITECTURES FOR QUANTUM/HYBRID GRADIOMETRY

27.1. FULL-SCALE NUMERICAL SIMULATIONS OF GRADIOMETRY CONCEPTS AND ASSESSMENT OF RESULTS – TUM (WP521)

As shown in TR D4 and discussed in section 25.1, applying X1 (and even more optimistic noise models, see TR D3) does not improve gradiometer observations to an extend where they become sensitive to time-variable gravity. Hence, it has been decided (in agreement with ESA) to not pursue the gradiometer principle further. However, for the sake of completeness we will briefly investigate in this section, how SGG would compete against SST if we assume to have sufficiently good gradiometer observations. This is done by assuming the noise model X2.1 which assumes to solve the attitude problem (which, however, seems not to be a viable option for the near-/-midterm future, see TR D3). Figure 27-1 shows a comparison of the SST and SGG concept. It is seen that, with X21, SGG is sensitive enough to retrieve time-variable gravity but is still significantly less sensitive than a comparable SST mission (see Figure 27-1a). However, when introducing time-variable gravity, both concepts are strongly limited by temporal aliasing and show therefore similar performance, independently of the constellation. Only the one-pair SST mission performs significantly worse than the one-satellite SGG mission. This, however, is to expect due to the missing additional observation directions in case of polar inline SST and poses the only case where SGG would have a significant advantage over SST. For larger (inclined) constellations the differences between SGG and SST are more marginal and highlight that there is no fundamental advantage of SGG over SST (when having multiple measurement directions).

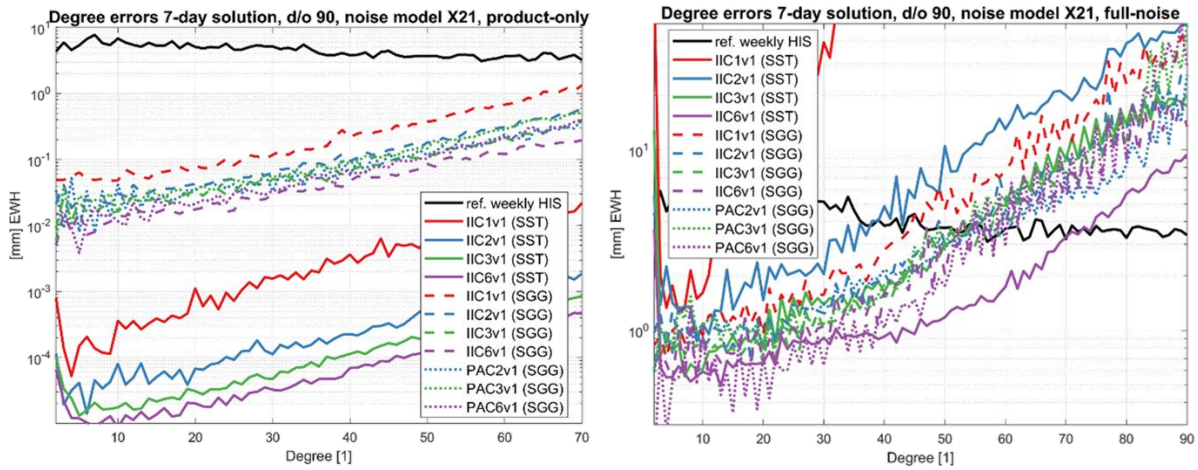

(a) **(b)**

Figure 27-1 Comparison of SST and SGG missions on identical constellations based on a weekly gravity field retrieval performance when applying the overly optimistic noise model X2.1 (same setup as in section 26.2). (a) Performance in terms of static gravity field retrieval (product-only simulation). (b) Performance in terms of temporal gravity field retrieval (full-noise simulations).

27.2. FULL-SCALE NUMERICAL SIMULATIONS OF GRADIOMETRY CONCEPTS AND ASSESSMENT OF RESULTS – POLIMI (WP522)

The same considerations of Section 27.1 hold here. Therefore, for the sake of completeness we will briefly investigate in this section, how SGG would compete against SST if we assume to have sufficiently good gradiometer observations. This is done by assuming the noise model X2.1 which assumes to solve the attitude problem (which, however, seems not to be a viable option for the near/midterm future, see TR D3).

The results are reported in Figure 27-2, and even considering the X2.1 three-axis gradiometer, gradiometry generally remains a weaker solution than ll-SST for investigating time variable field.

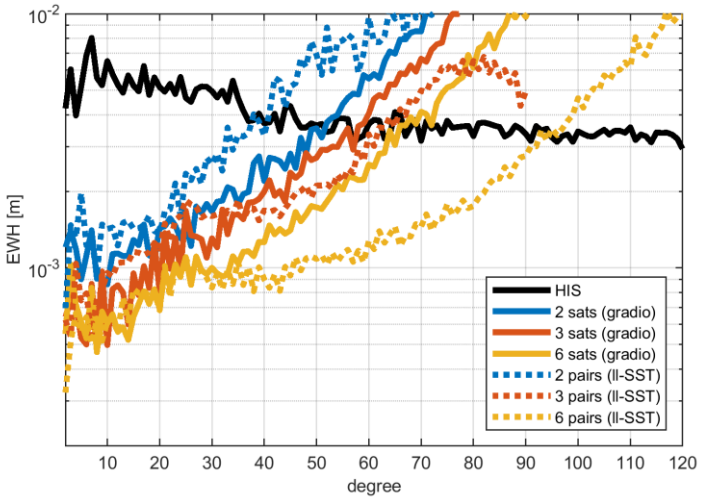

Figure 27-2 Comparison of SST (dashed lines) and SGG (solid lines) missions on identical constellations based on a weekly gravity field retrieval performance when applying the overly optimistic noise model X2.1. Performance in terms of temporal gravity field retrieval (full-noise simulations).

Considering the same orbit configuration and a 7-day solution we can conclude that gradiometry is:

- weaker than ll-SST when 6 orbital planes are considered (IIC6v1)
- slightly worse than ll-SST when 3 orbital planes are considered (IIC3v1)
- better when Bender configuration is considered (IIC2v1)

27.3. IMPACT OF ATTITUDE ERRORS (WP523)

WP skipped.

27.4. NRT ESTIMATES FOR GRADIOMETRY CONCEPTS (WP530)

See section 26.4.

27.5. ENHANCED PARAMETERIZATION STRATEGIES FOR GRADIOMETRY CONCEPTS (WP540)

See section 26.5.

27.6. POST-PROCESSING FOR GRADIOMETRY CONCEPTS (WP550)

Because of the previous results, this WP has been skipped in agreement with ESA.

27.7. EVALUATION OF ADDED VALUE W.R.T. ES ACCELEROMETER (WP560)

Because of the previous results, this WP has been skipped in agreement with ESA.

28. MASS CHANGE PRODUCTS FROM ALTERNATIVE QSG MISSION ARCHITECTURES (WP600)

Combined across-track and inline SST architectures

Through the added-value simulations (see TR D4) it became obvious that the gradiometry concept cannot compete with LL-SST. However, within the gradiometry simulations it has been found, that gradiometry measurements in the across-track direction (perpendicular to velocity and geocentric position vector) show a significantly better behaviour regarding temporal-aliasing than measurements in the along-track direction (parallel to velocity vector). Since the LL-SST principle can be considered as some sort of long-arm gradiometry, it can be assumed that these findings can be transferred to LL-SST as-well. This gives rise to the idea of investigating across-track LL-SST constellations, where satellites of the same pair fly "parallel" to each other (and not behind each other as it is the case for convention inline LL-SST). In the following sections different scenarios (with different combinations of inline and across-track pairs) will be studied.

HL-SST architectures

High-low SST (HL-SST) poses another alternative to the common inline-SST principle. For HL-SST, similar to across-track SST, obtaining high-accuracy ranging observations is more complex due to strongly altering angles and multiple targets. However, in contrast to LL-SST, there is the additional difficulty of the very large distances between the low-flying satellites and

the high-flying ones of several 10.000 km. Unfortunately, the performance of current laser ranging instruments degrades proportionally to the measurement distance (see TR D3). Since in almost all investigated noise scenarios (e.g., X1, X2.1) the ranging instrument is already the limiting factor, an increase of the distance of a factor of about 100 would just further increase the impact of the ranging instrument (see Figure 28-1). Hence, in case of HL-SST, the ranging noise would completely superimpose a supposedly high-accuracy quantum accelerometers. Therefore this concept is not suited to highlight the impact/benefit of quantum sensors and will, thus, not be further investigated in this project (in agreement with ESA).

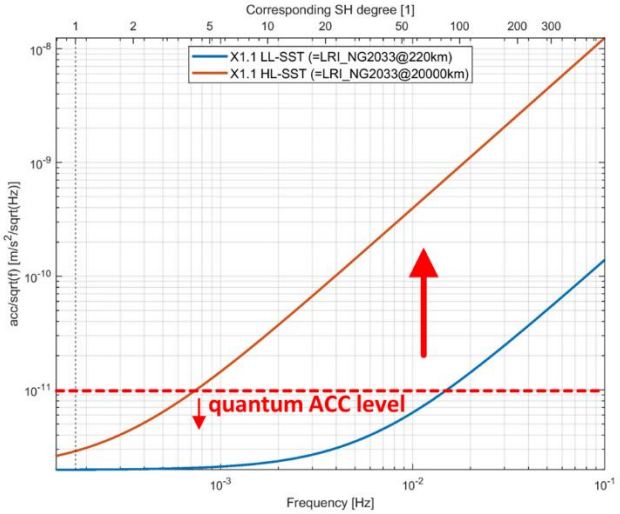

Figure 28-1 Comparison of future ranging noise models (projected to the year 2033, see TR D3) in dependency of the inter-satellite distance. Blue: 220km distance. Orange: 20000km distance.

Combined SGG/SST architectures

Since the near-/mid-future SGG performance is supposedly not sufficient to be competitive with SST (see TR D3 and TR D4), a combination of the SST concept with the SGG concept is obviously not reasonable since the performance would be solely driven by the SST observations. And, on the other hand, even if a sufficient SGG performance would be feasible, the strength of SGG lays in its capability to achieve already a good gravity field retrieval performance with only one polar satellite (without the need of additional SST observations).

28.1. FULL-SCALE NUMERICAL SIMULATIONS OF ALTERNATIVE MISSION CONCEPTS AND ASSESSMENT OF RESULTS – TUM (WP621)

This section investigates (as a mirror of section 26.2) the impact of larger constellations including across-track LL-SST pairs on the time-variable gravity field retrieval performance. The results are then compared to conventional constellations (using inline LL-SST only, section 26.2). For this study, the TUM full-scale simulator is used (to be comparable section 26.2). In 28.1.1, the applied orbits are presented and in 0 the simulation results will be shown.

28.1.1. ORBIT/CONSTELLATION DESIGN FOR ACROSS-TRACK LL-SST

As in section 26.2, also for across-track constellations, a maximum number of 6 satellite pairs will be investigated. For the across-track principle, only polar constellations will be investigated since it is not assumed to benefit from inclined orbits (since one can achieve then already two measurement directions with polar orbits). This simplifies the constellation design since then the search space is reduced by one variable. Applying the same constraints as in section 26.2.1 (i.e., RGT-orbits, retrieval periods, sub-cycle fill-up strategy, altitude, eccentricity) and having fixed the inclination, the only remaining variable/question is if and how to mix up inline pairs with across-track pairs. To study possible different behaviours for different combinations (of inline and across-track pairs), several possible constellation variants are created.

An overview is given in Table 28-1: Identically to section 26.2, also 2-, 3- and 6-pair constellations are be considered. Additionally, either polar across-track-only constellations (PACXv1) or polar mixed across-track/inline constellations (PIACxv1) are studied. For the mixed constellations, it is assumed that across-track and inline pairs are interleaved (temporally). This leads to a total number of 6 constellations.

Table 28-1: Overview of the investigated polar constellations containing across-track LL-SST satellite pairs

Constellation types →

Number of pairs ↓ / Type →	Polar constellations (89°)	
N° pairs	PACXv1	PIACXv1
2-pair	**PAC2v1** (2x ac)	**PIAC2v1** (1x ac, 1x il)
3-pair	**PAC3v1** (3x ac)	**PIAC3v1** (2x ac, 1x il)
6-pair	**PAC6v1** (6x ac)	**PIAC6v1** (3x ac, 3x il)

In the following (Figure 28-2-Figure 28-4), the ground track pattern for each constellation and the target retrieval periods (1 and 7 days) are shown (one combined for each PACXv1+PIACXv1 since the ground track pattern do not change for across-track pairs). In addition, the stability of the normal equation matrix (of a reduced scale simulation) in dependency of the max. retrieval d/o is shown (identical to section 26.2.1).

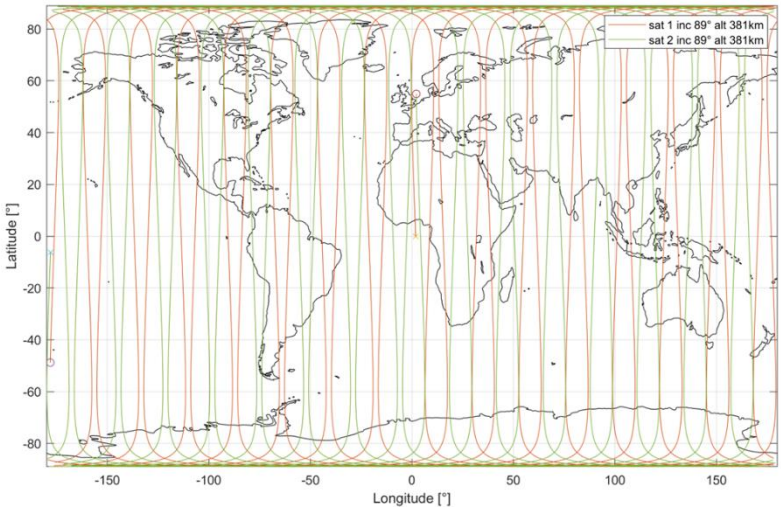

(a)

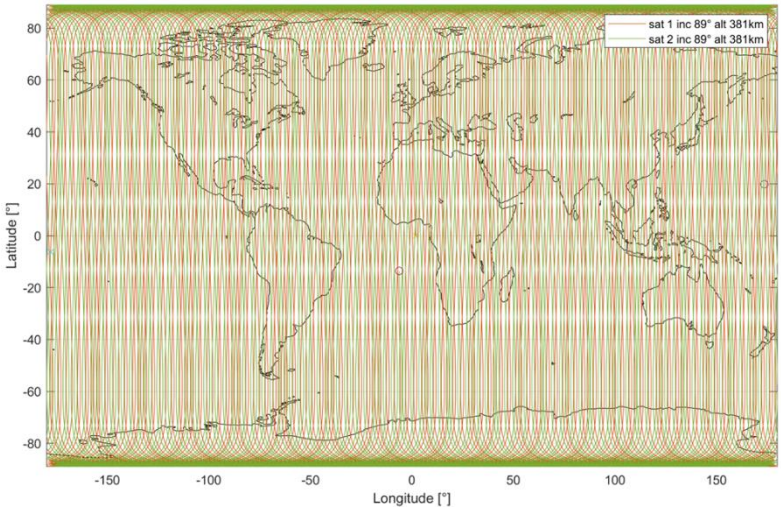

(b)

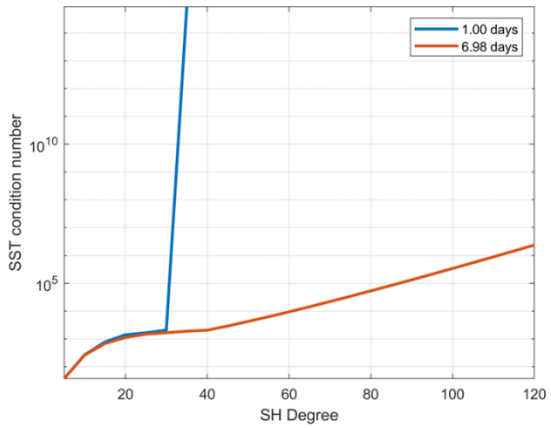

(c)

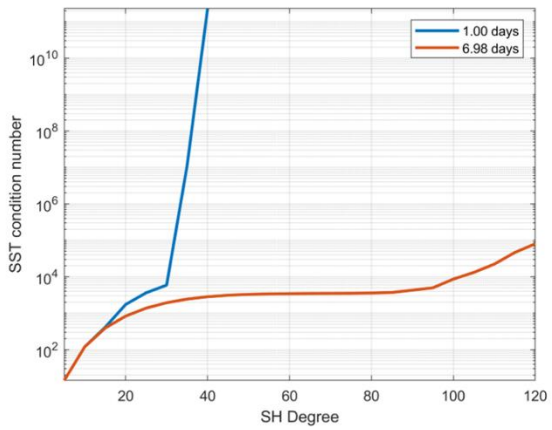

(d)

Figure 28-2 Illustration of constellations PAC2v1/PIAC2v1. (a) Ground-track pattern for a retrieval period of 1 day. (b) Ground-track pattern for a retrieval period of 7 days. (c) Reduced-scale NEQ condition numbers (L^2-norm) for PAC2v1. (d) Same for PIAC2v1.

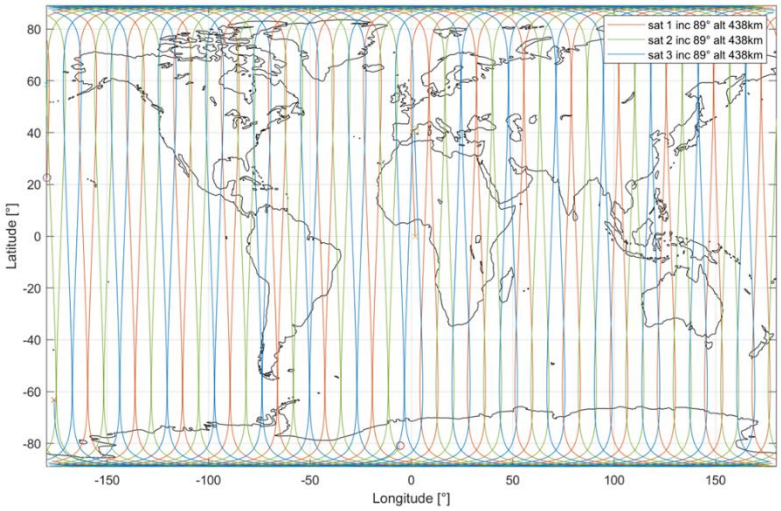

(a)

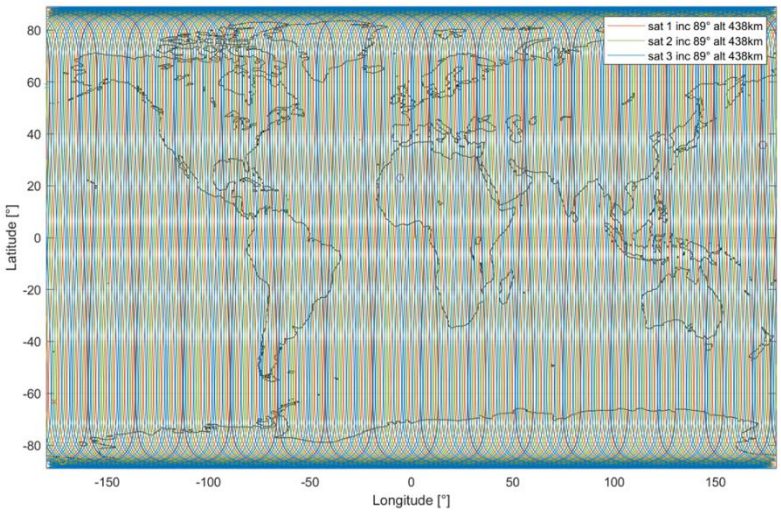

(b)

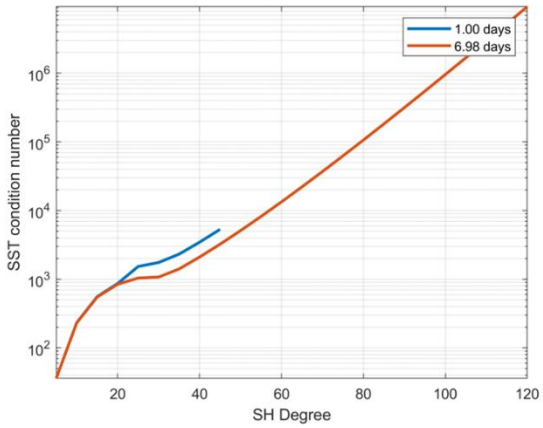

(c)

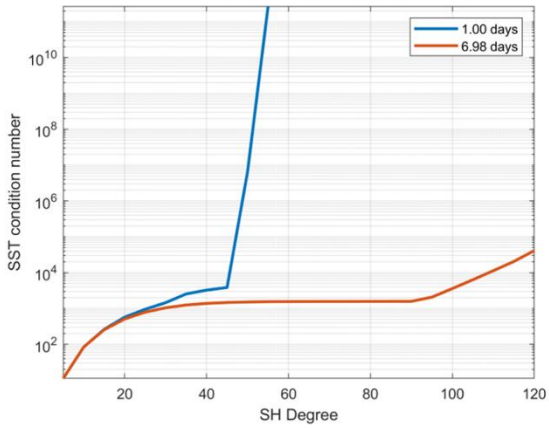

(d)

Figure 28-3 Illustration of constellations PAC3v1/PIAC3v1. (a) Ground-track pattern for a retrieval period of 1 day. (b) Ground-track pattern for a retrieval period of 7 days. (c) Reduced-scale NEQ condition numbers (L^2-norm) for PAC3v1. (d) Same for PIAC3v1.

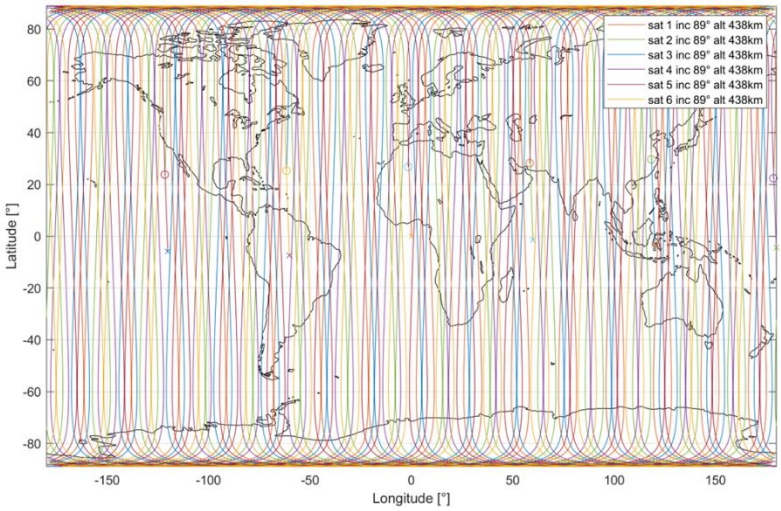

(a)

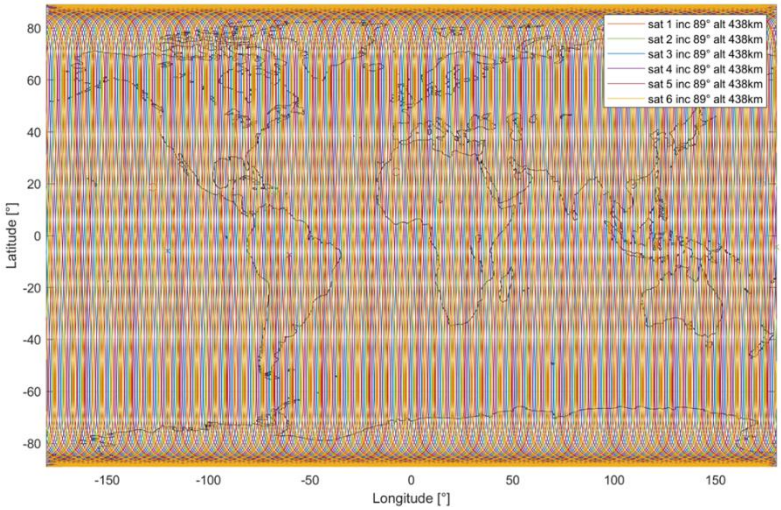

(b)

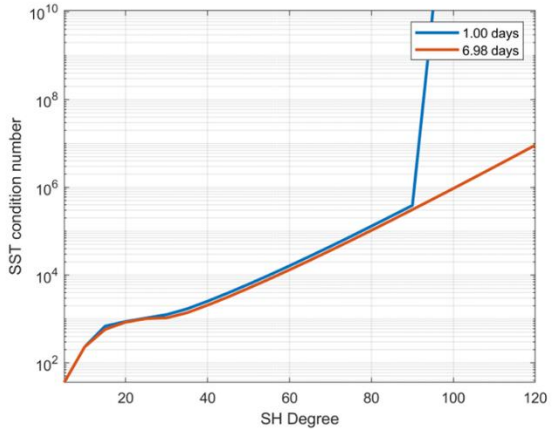

(c)

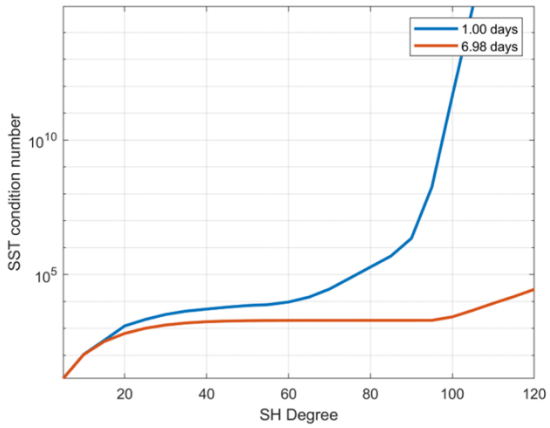

(d)

Figure 28-4 Illustration of constellations PAC6v1/PIAC6v1. (a) Ground-track pattern for a retrieval period of 1 day. (b) Ground-track pattern for a retrieval period of 7 days. (c) Reduced-scale NEQ condition numbers (L^2-norm) for PAC6v1. (d) Same for PIAC6v1.

Looking at the condition numbers, it can already be seen that the across-track only PACXv1 constellations degrade significantly stronger with higher d/o than the combined PIACXv1 constellations. This is an indication, that also the retrieval performance of these PACXv1 constellations might be reduced compared to the PIACXv1 constellations (cf. section28.1.2).

28.1.2. FULL-SCALE SIMULATION RESULTS OF THE ACROSS-TRACK CONCEPT

For each constellation shown in the previous section (28.1.1) and each target retrieval period (1 day and 7 days), one full-scale simulation with time variable gravity signal (full-noise) and one without time variable gravity signal (product-only) is performed. The solutions are again grouped into plots of same number of pairs and same time variable gravity signal handling (i.e., distinct plots for full-noise and instrument-only cases). The proceeding (and setup) is identical to section 26.2.2 and the results presented there will be added for comparison (in the degree-amplitude plots).

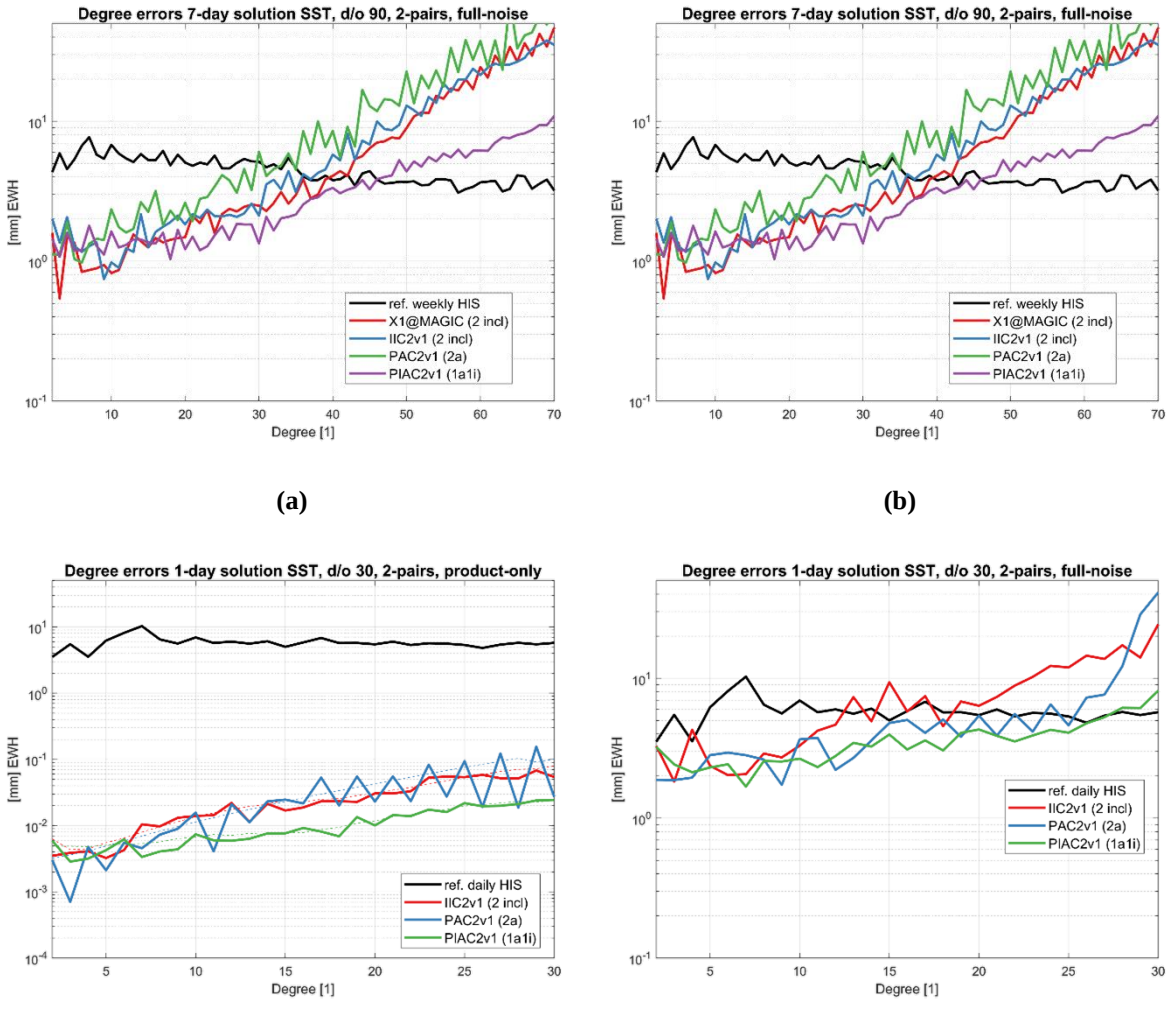

Figure 28-5 Degree errors for 2-pair scenarios PAC2v1/PIAC2v1 assuming the X1 instrument noise model. (a) Product-only, 7-day solution. (b) Full-noise, 7-day solution. (c) Product-only, 1-day solution. (d) Full-noise, 1-day solution.

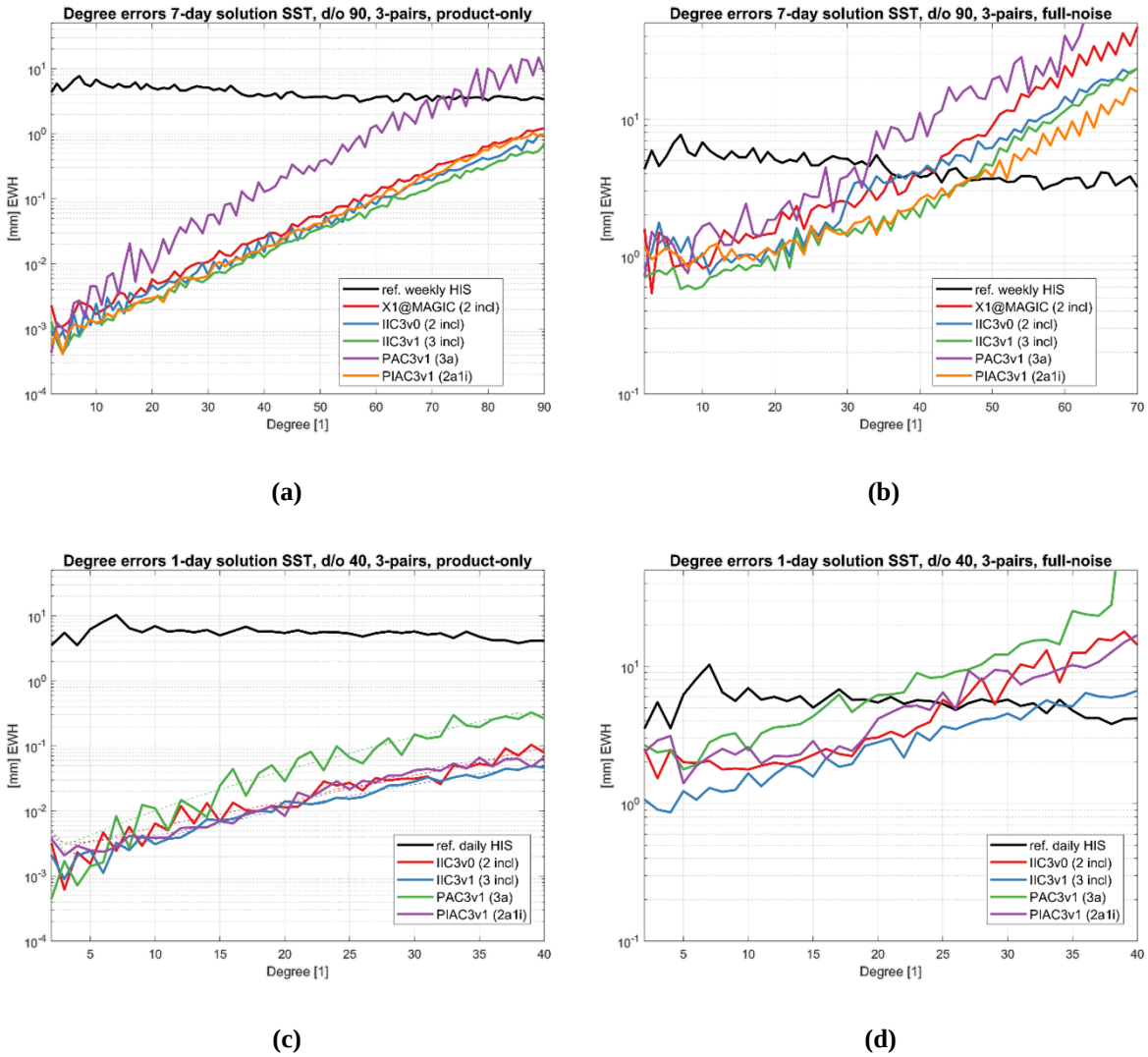

Figure 28-6 Degree errors for 3-pair scenarios PAC3v1/PIAC3v1 assuming the X1 instrument noise model. (a) Product-only, 7-day solution. (b) Full-noise, 7-day solution. (c) Product-only, 1-day solution. (d) Full-noise, 1-day solution.

Inspecting the degree errors (Figure 28-5 to Figure 28-7), the following can be assessed:

- Across-track-only constellations (PACXv1) perform constantly worse than any other constellation investigated. This could already be predicted by looking at the condition numbers in section 28.1.1. This is due to the higher uncertainty of the zonal coefficients when having only across-track observations (cf. gradiometry results in TR D4).
- 7-day combined PIACXv1 constellations perform very similar (sometimes better) than the best-performing conventional constellations IICXv1.
- 1-day combined PIACXv1 constellations (except PIAC2v1) perform worse than the best-performing IICXv1. This is also already indicated by the condition numbers (in section 28.1.1). The most reasonable explanation for this is that the combined one day sub-cycles for PIAC3v1 and PIAC6v1 are not that good (some larger

gaps/inhomogeneities) which negatively influences the geometry and, thus, the numerical stability.

- Again (as already seen in section 26.2.2), the product-only retrieval performance (i.e., the numerical stability) is an indicator for the full-noise retrieval performance.

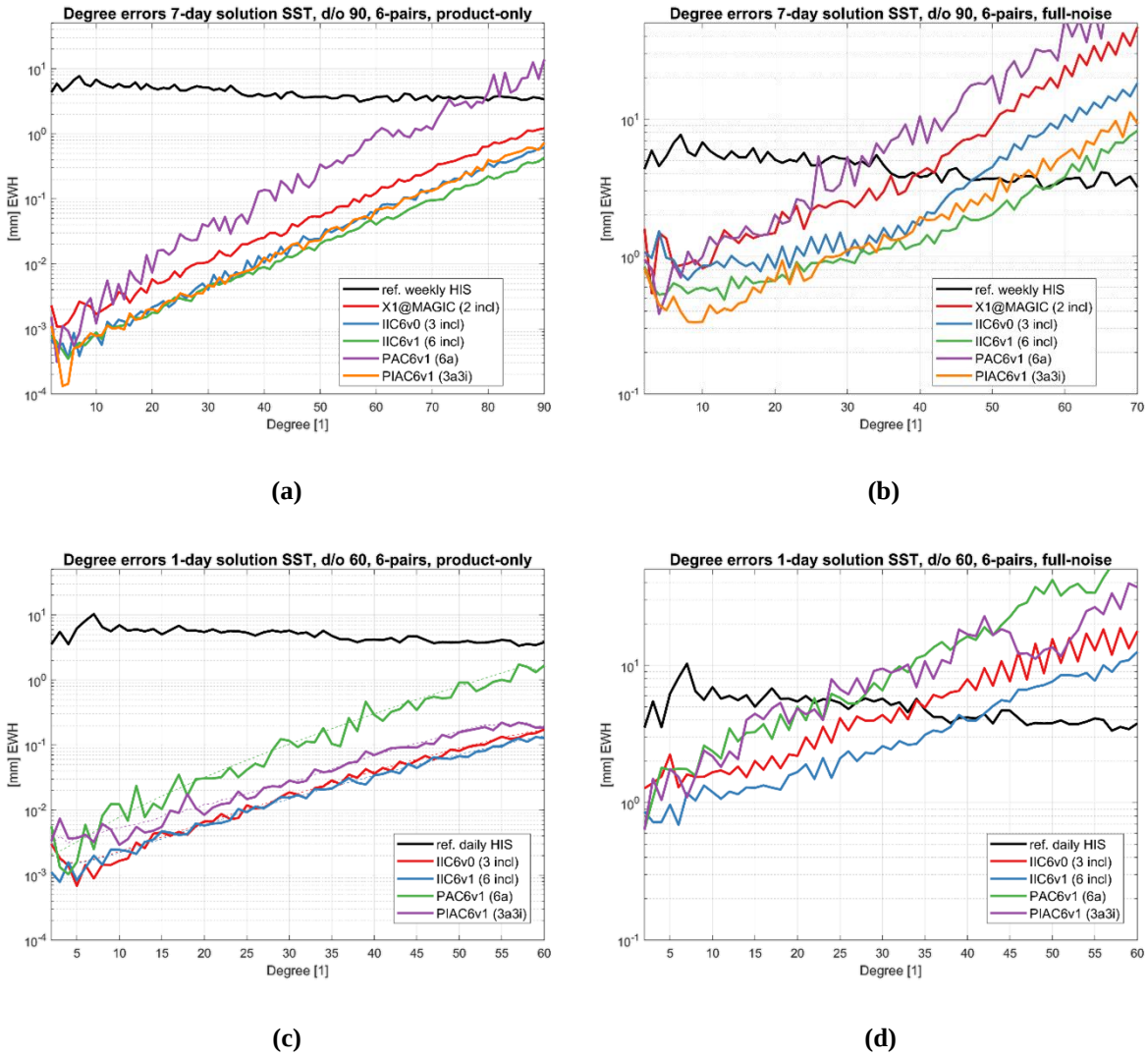

Figure 28-7 Degree errors for 3-pair scenarios PAC3v1/PIAC3v1 assuming the X1 instrument noise model. (a) Product-only, 7-day solution. (b) Full-noise, 7-day solution. (c) Product-only, 1-day solution. (d) Full-noise, 1-day solution.

The spatial plots (Figure 28-8 - Figure 28-10) confirm the conclusions drawn from the degree-error plots: combined PIACXv1 constellations can hold up against the best performing IICXv1 constellations (at least for 7-day solutions). Global patterns a generally more homogeneous than the patterns from IICXv1 constellation (which slightly degrade towards the poles). Across-track-only constellations (PACXv1) show the aforementioned strong zonal error patterns and are therefore less suited for temporal self-dealiasing then PIACv1/IICv1. The spatially heterogeneous error patterns in the 1-day solutions (for PIAC3v1 and PIAC6v1, Figure 28-11) further indicate that the sub-optimal one day sub-cycle of PIAC3v1 and PIAC6v1 might be the

cause for decreased performance (which might be solved through a dedicated 1 day constellation).

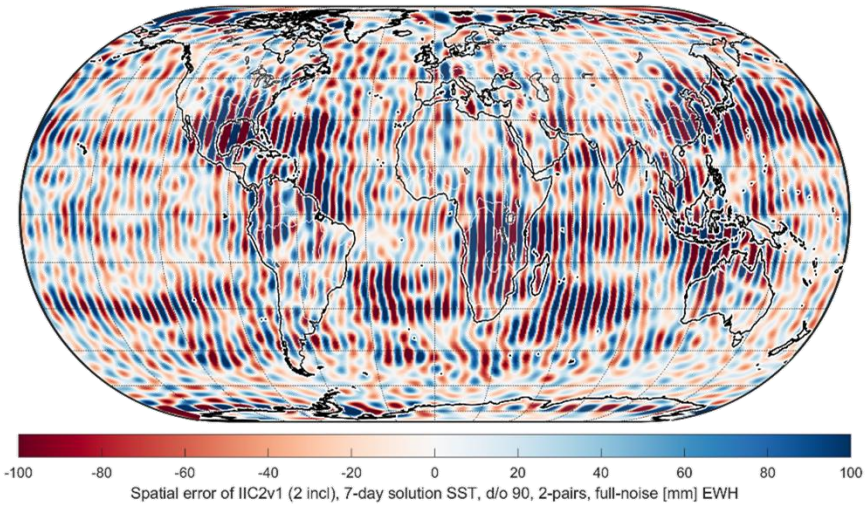

(a)

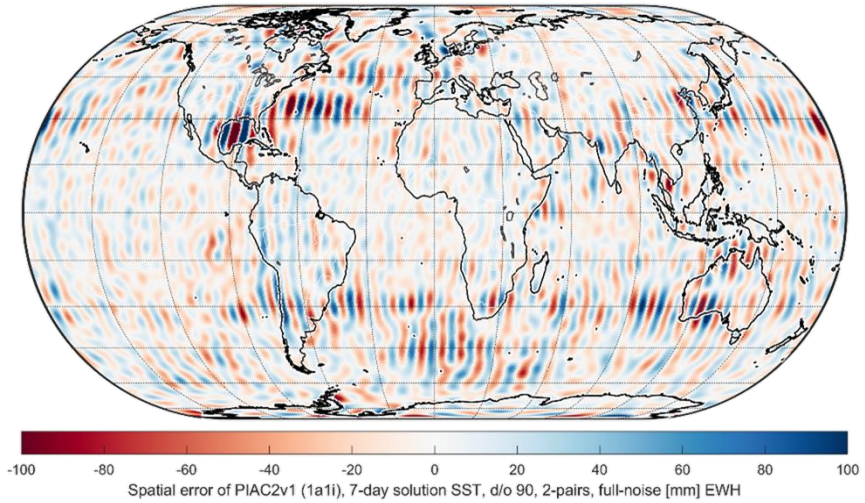

(b)

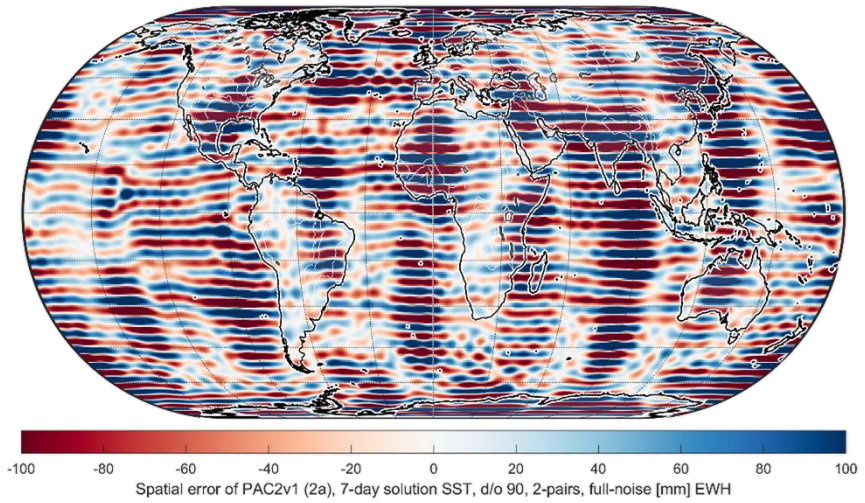

©

Figure 28-8 Spatial errors regarding HIS of 7-day full-scale solutions for 2-pair PAC2v1/PIAC2v1 constellations in comparison to IIC2v1 up to d/o 60. (a) IIC2v1. (b) PIAC2v1. (c) PAC2v1.

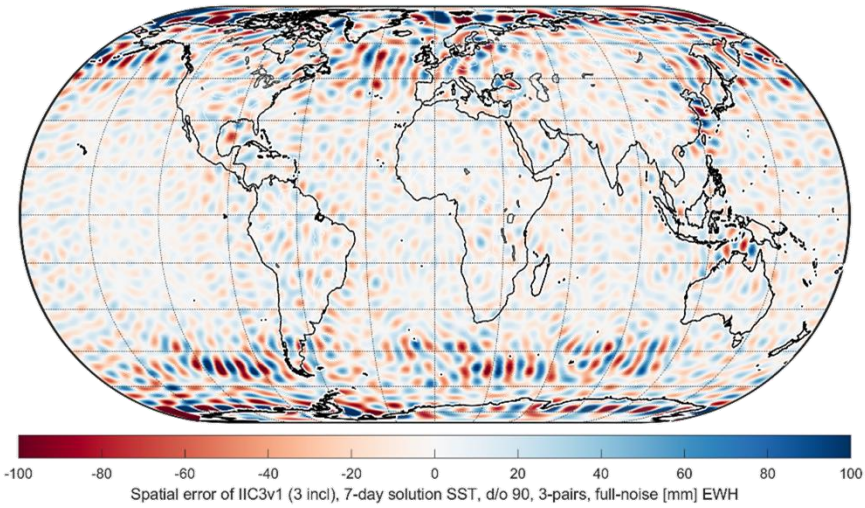

(a)

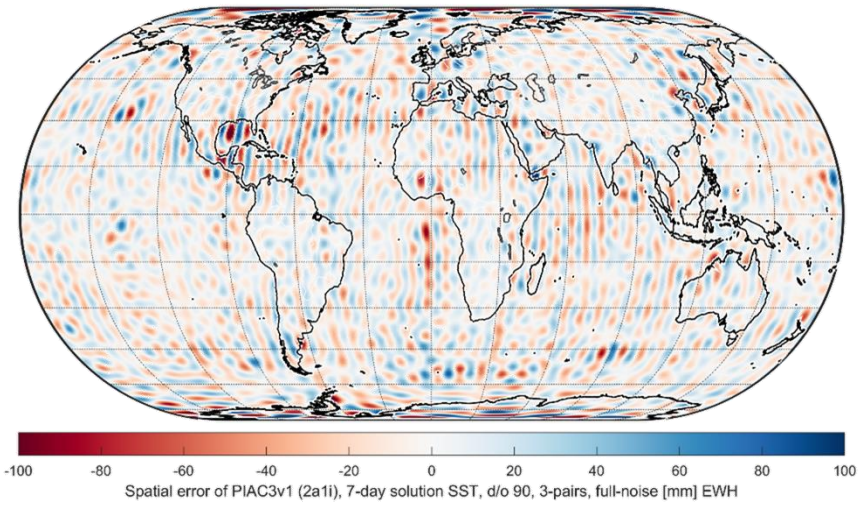

(b)

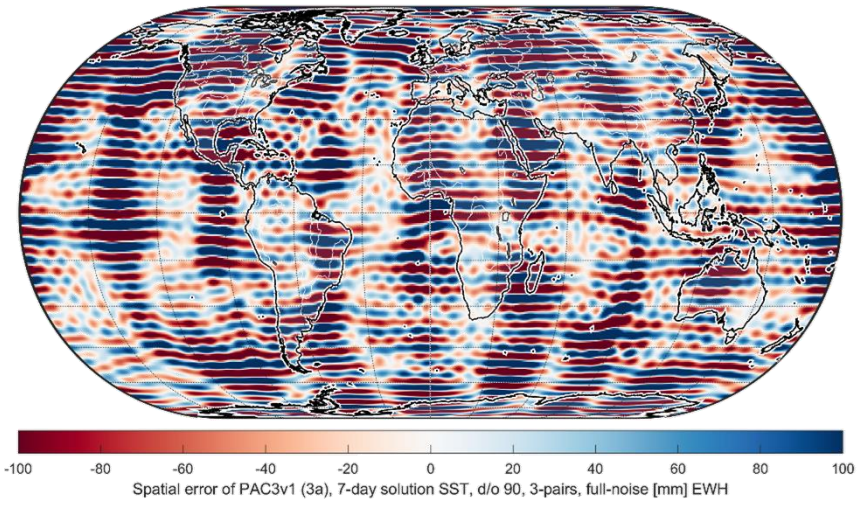

(c)

Figure 28-9 Spatial errors regarding HIS of 7-day full-scale solutions for 3-pair PAC3v1/PIAC3v1 constellations in comparison to IIC3v1 up to d/o 60. (a) IIC3v1. (b) PIAC3v1. (c) PAC3v1.

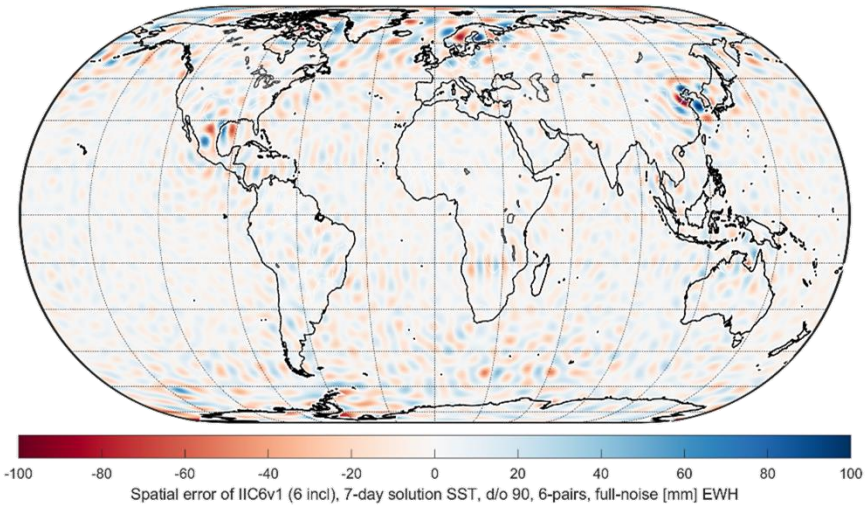

(a)

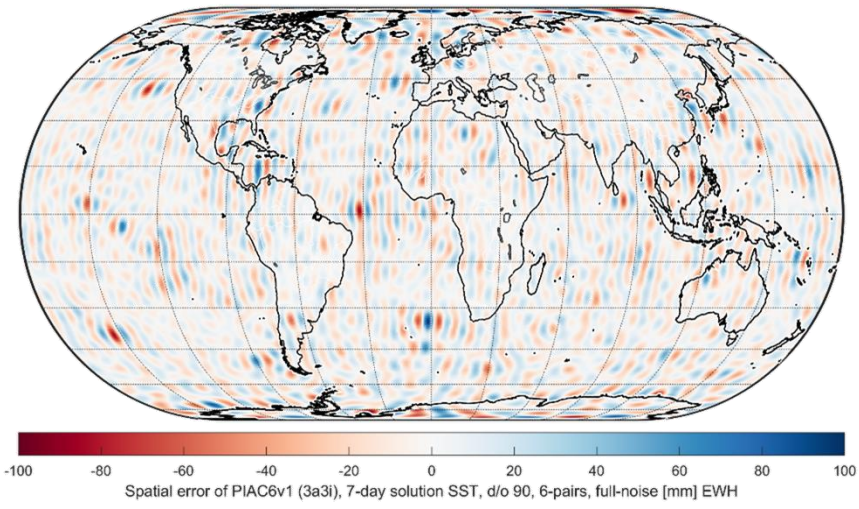

(b)

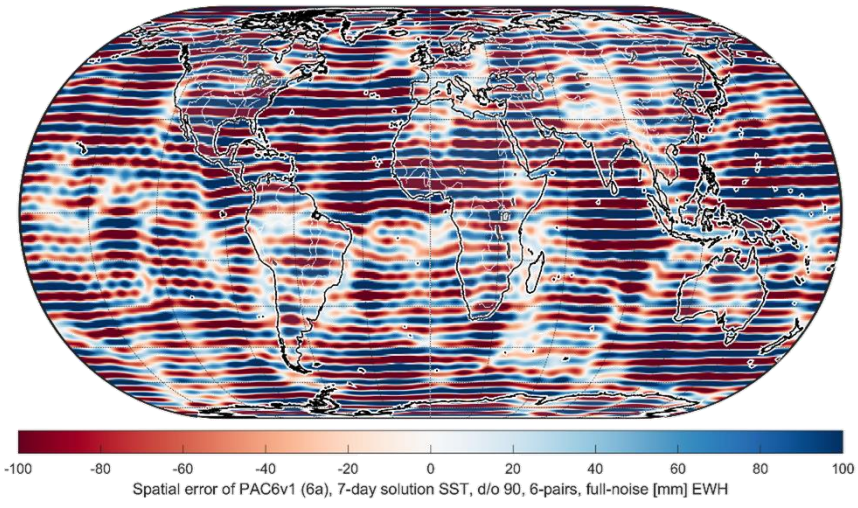

(c)

Figure 28-10 Spatial errors regarding HIS of 7-day full-scale solutions for 6-pair PAC6v1/PIAC6v1 constellations in comparison to IIC6v1 up to d/o 60. (a) IIC6v1. (b) PIAC6v1. (c) PAC6v1.

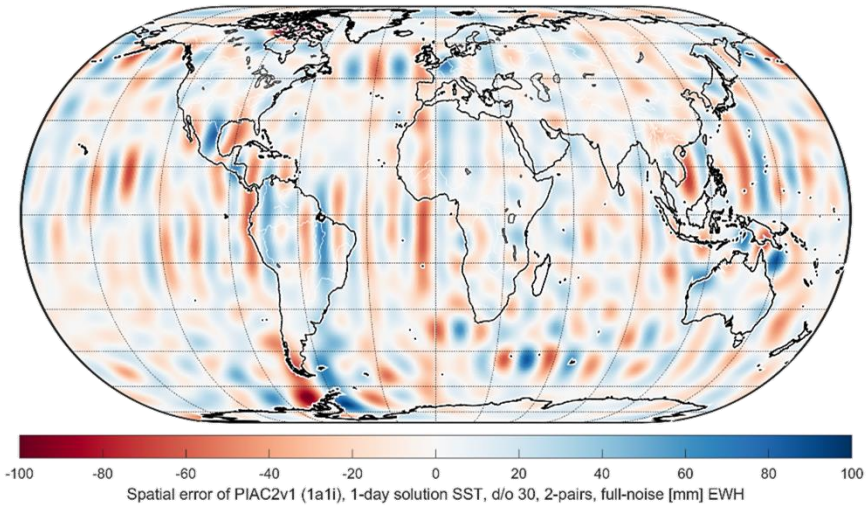

(a)

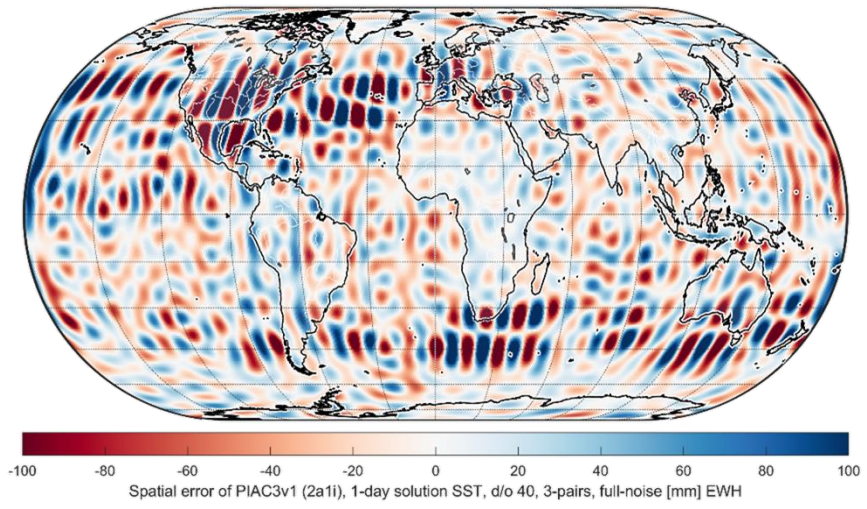

(b)

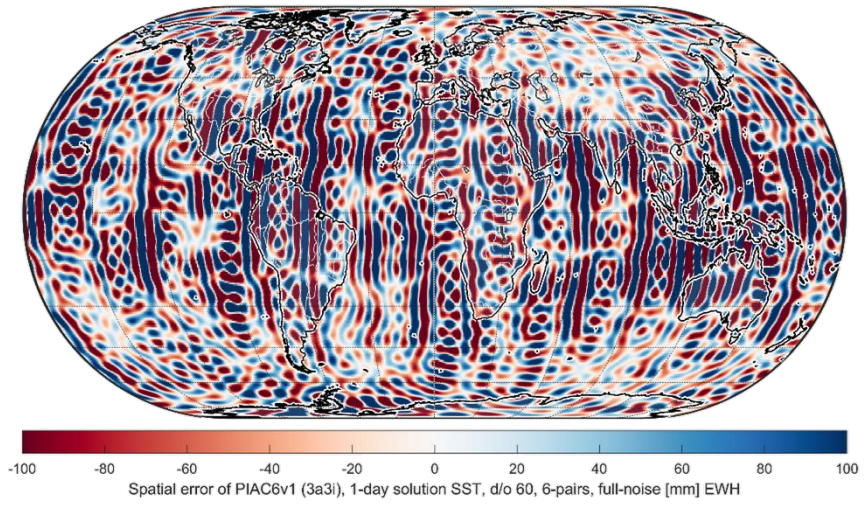

(c)

Figure 28-11 Spatial errors regarding HIS of 1-day full-scale solutions for PIACXv1 constellations and varying max d/o. (a) PIAC2v1 constellation up to d/o 30. (b) PIAC3v1 constellation up to d/o 40. (c) PIACv1 constellation up to d/o 60.

Eventually, PIACXv1 constellations might be seen as a possible alternative for IICXv1, having similar performance but the advantage of just polar flying pairs. The disadvantage may be the higher complexity of the realization of the across-track measurement concept compared to the conventional inline concept which would need further investigation. According to the findings in this section, the best-performing PIACXv1 constellations are selected for further investigations in section 28.5.

28.2. FULL-SCALE NUMERICAL SIMULATIONS OF ALTERNATIVE MISSION CONCEPTS AND ASSESSMENT OF RESULTS – POLIMI (WP622)

For each constellation shown in section 28.1.1 and considering a 7-day retrieval period, full-scale simulations considering the FN background model are performed considering both the PACXv2 (cross-track ll-SST) and PIACXv2 (mixed across-track and inline ll-SST) constellations. The following plots show the degree retrieval errors of the time-variable signal considering the non-regularized (see Figure 28-12) or regularized (see Figure 28-13) solutions. Three and six pairs of satellites give the possibility of estimating the time-variable gravity field up to a maximum degree of about 60 and 70, respectively. Combination of cross-track and inline ll-SST seems to bring a slight improvement.

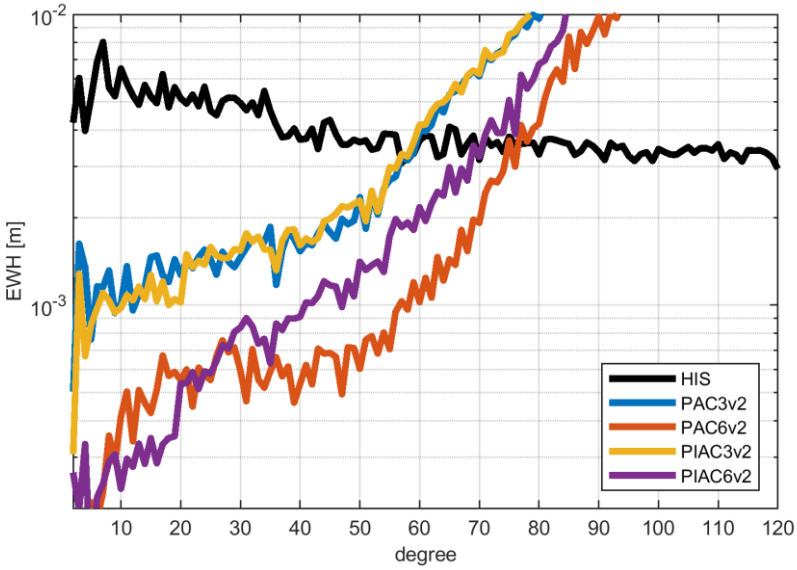

Figure 28-12 Degree errors for 3 and 6 pair scenarios PAC3v2, PIAC3v2, PAC6v2, PIAC6v2 assuming the X2.1 instrument noise model, over a retrieval time span of 7 days, without applying regularization.

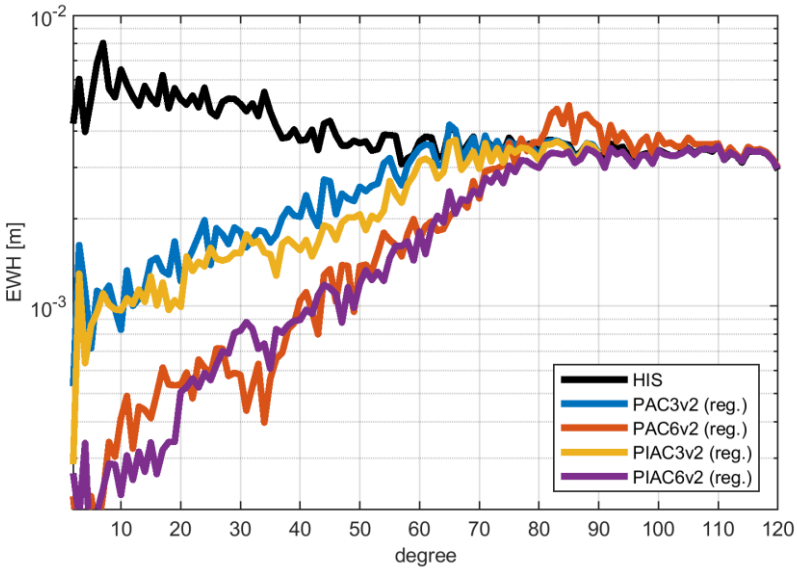

Figure 28-13 Degree errors for 3 and 6 pair scenarios PAC3v2, PIAC3v2, PAC6v2, PIAC6v2 assuming the X2 instrument noise model, over a retrieval time span of 7 days, applying the regularization.

The difference in the maximum achievable harmonic degree with respect to the one obtainable from TUM solutions (see Figure 28-6 and Figure 28-7) is probably due to the use of white noise in the Least Squares stochastic modelling, as it happened for the inline 6-pair IIC6v1 configuration (see the comments in section 26.7).

Looking at the spatial distribution of the error (see Figure 28-14) we can notice that north-south strips are more visible in the error distribution without the inline ll-SST as observation in the satellite constellation (i.e., considering the PACXv2 configurations). These errors appear to be different from the TUM solution, again due to the different adopted stochastic modelling in the Least Squares adjustment (see the comments in section 26.7), leading to a different de-aliasing capability of the constellations.

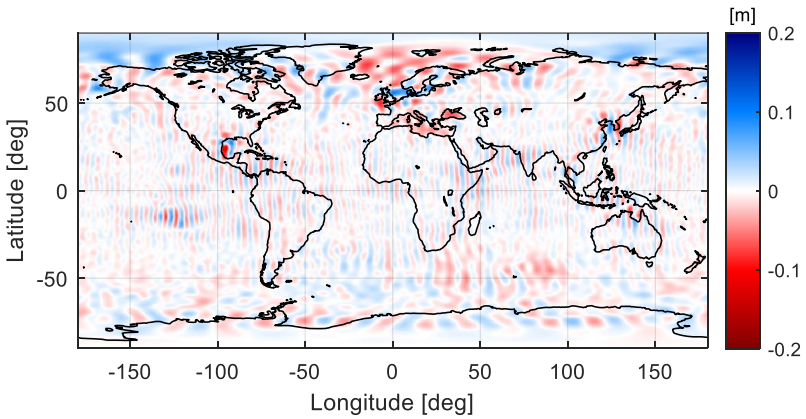

Spatial error of 6 pairs inline + across track (PIAC6v2)

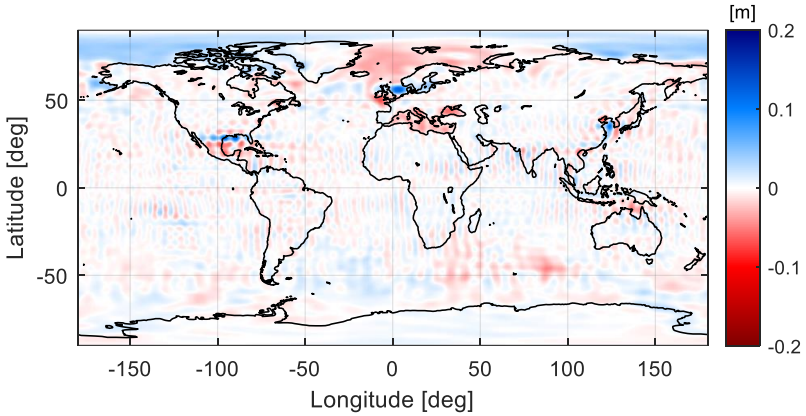

Spatial error of 6 pairs across track (PAC6v2)

Figure 28-14 Spatial errors regarding HIS of 7-day full-scale solutions for 6-pair PAC6v2 and PIAC6v2 constellations for un-regularized solution up to d/o 80. (a) PIAC6v2. (b) PAC6v2.

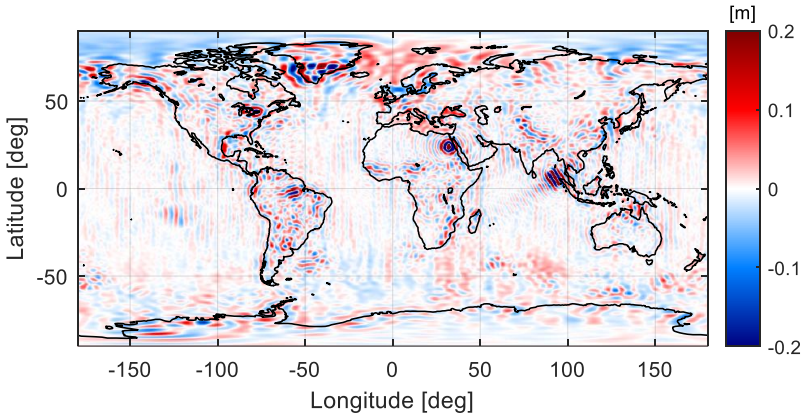

Spatial error of 6 pairs inline + across track (PIAC6v2)

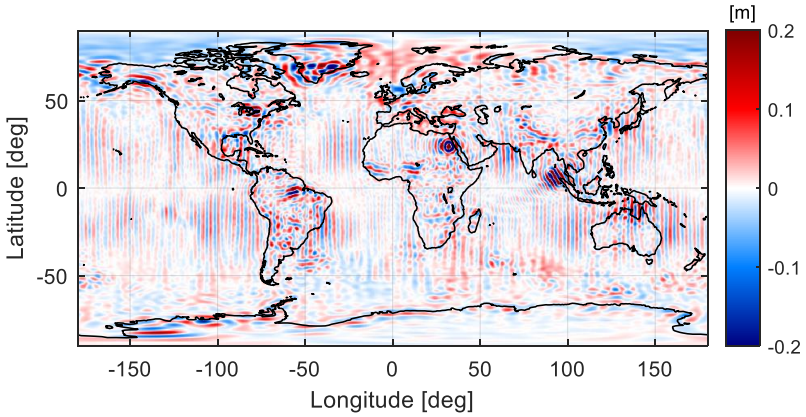

Spatial error of 6 pairs across track (PAC6v2)

Figure 28-15 Spatial errors regarding HIS of 7-day full-scale solutions for 6-pair PAC6v2 and PIAC6v2 constellations for regularized solution up to d/o 120. (a) PIAC6v2. (b) PAC6v2.

Considering the non-regularized solutions (see Figure 28-15), PAC6v2 (across-track) works better than PIAC6v2 (combination of across-track and inline observations), probably due to the

use of white noise in the Least Squares stochastic modelling. The regularization cancels these differences and introduces artefacts in the PAC6v2 (across-track only configuration).

As a further alternative mission concept, another simulation has been considered introducing the potential difference observed by atomic clocks between a pair of satellites tracking one another and a gradiometer on board each satellite. For this test the 2-pair IIC2v1 orbit configuration has been considered.
This mission principle has been devised according to the one proposed during the MOCAST+ project (Migliaccio et al., 2023; Rossi et al., 2023), thus introducing the following instrumental accuracies:

- potential difference by atomic clocks: white noise with 0.2 m^2/s^2 standard deviation;
- single-arm gradiometers: white noise with ~2×10^{-15} $1/s^2$ standard deviation (X2.1 gradiometer noise), oriented in x and z directions of the two satellites of the polar orbit, and in y and z directions on the two satellites of the inclined orbit.

The simulation was performed considering the full-noise scenario over a 7-day time span. The results are reported in Figure 28-16, where it can be noticed that the most significant contribution to the accuracy of the solution is brought by the gradiometers rather than the atomic clocks. In fact, the clock-only solution, shown in red in Figure 28-16, is quite far from estimating the time-variable component of the gravity field with enough accuracy.

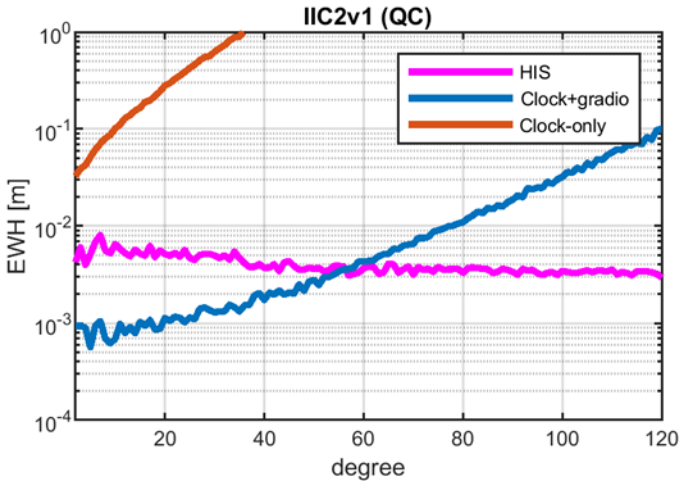

Figure 28-16 Degree error of 7-day solution considering the combination of atomic clocks and gradiometers on the IIC2v1 orbit configuration. Red line refers to the clock-only solution and, while blue one shows the combined clock and gradiometer solution.

28.3. NRT ESTIMATES FOR ALTERNATIVE MISSION CONCEPTS (WP630)

See section 26.4.

28.4. ENHANCED PARAMETERIZATION STRATEGIES FOR ALTERNATIVE MISSION CONCEPTS (WP640)

See section 26.5.

28.5. POST-PROCESSING FOR ALTERNATIVE MISSION CONCEPTS (WP650)

With standard parameterization

Identical to section 28.4, the VADER-filter can also be applied in the same manner to the PIACXv1 constellations. To limit the effort, the VADER-filtered solutions will only be calculated for PIAC3v1. It is not assumed that VADER-filtering PIAC2v1 and PIAC6v1 as well will bring additional insights.

Figure 28-17 shows the results for PIAC3v1 in comparison to IIC3v1 (cf. section 28.4). One can discern that the filtered results for PIAC3v1 are slightly worse (w.r.t. IIC3v1) in case of the 1-day solution and that the filter does not work properly for the 7-day solution (while it works for IIC3v1). The reason why the filter fails for the 7-day solution is not completely understood. The only difference between IIC3v1 and PIAC3v1 regarding the filter is the shape of the respective normal equation system (NEQ). Due to the omission of a time-variable parameterization, both NEQs are generally erroneous regarding the underlying function model. Hence, also the interaction with the filter cannot be predicted and it is not guaranteed that its application results in an improvement of the final solution.

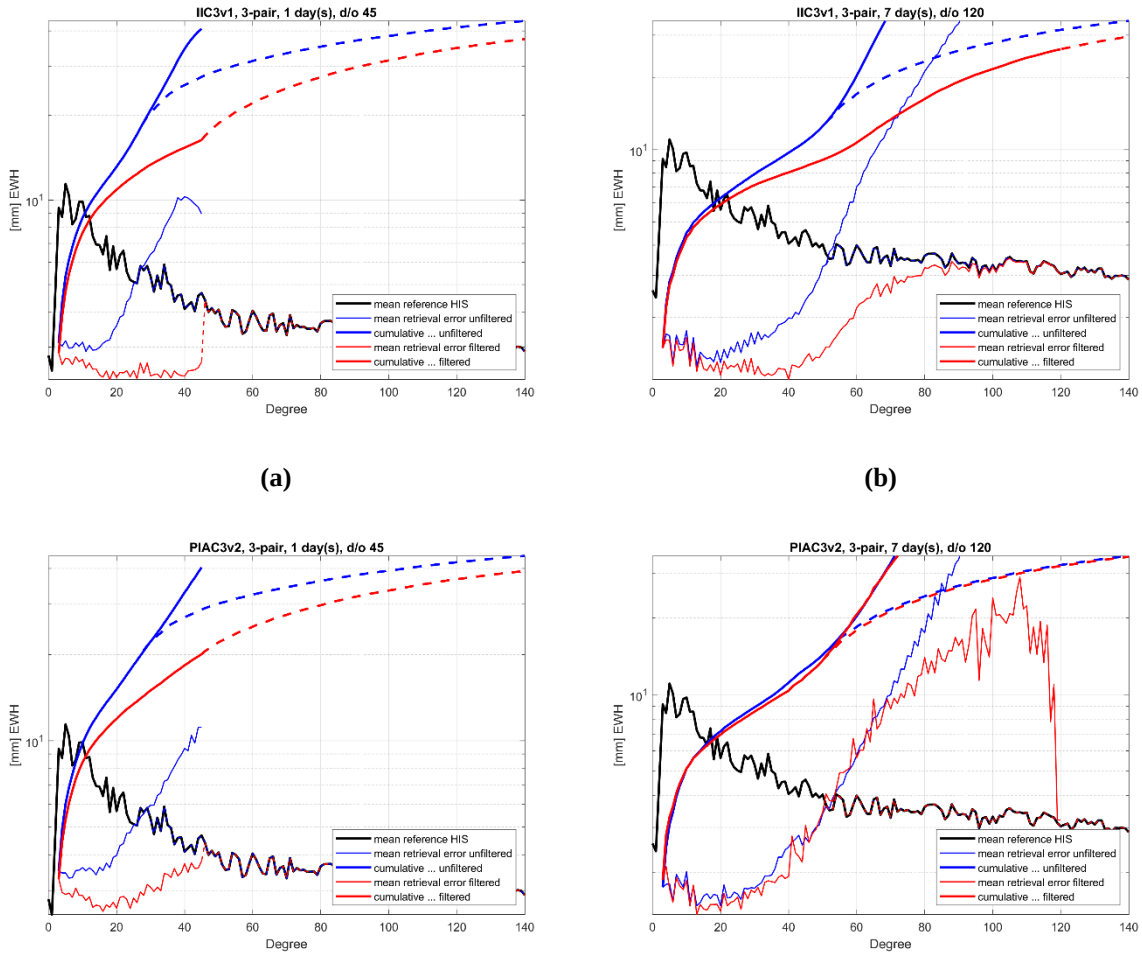

(a) **(b)**

(c) **(d)**

Figure 28-17 Mean degree errors over a time span of 3 months of full-scale simulations (blue lines) for PIAC3v1 constellation (see section 28.2) in comparison to filtered VADER-solutions (red lines). (a) 1-day solution of IIC3v1-constellation. (b) 7-day solution of IIC3v1-constellation. (c) 1-day solution of PIAC3v1-constellation. (d) 7-day solution of PIACv1-constellation.

With standard parameterization

See section 26.6.

29. OPTIMIZED REGIONAL SOLUTIONS AND THEIR GEOPHYSICAL PRODUCTS (WP700)

29.1. SPECIFICATION OF CRITERIA (WP710)

Regarding Solid Earth applications of QSG mission architectures (WP 800):

- Relevant functionals: gridded values of geoid undulations, gravity anomaly, potential field with variances or VCMs.
- Requested time resolution: daily, monthly.
- Requested space resolution: 0.1° to 1.0° depending on area specification and resolution of simulated data

Regarding Hydrological (short-term) and ocean applications (WP 900) and Hydrological (medium to long-term) and climate applications (WP 1000):

- Relevant functionals: gridded TWSA (total water storage anomaly) maps with VCMs plus assessment of systematic errors. Time series will also be important (e.g. one year of monthly/weekly data)
- Requested time resolution: the priority would be on weekly resolution to show improvement in spatial resolution and/or accuracy
- Requested space resolution: 0.1° to 1.0° depending on area specification and resolution of simulated data

29.2. SELECTION OF MISSION ARCHITECTURES AND OPTIMIZED REGIONAL SOLUTIONS (WP720)

Regarding the Solid Earth applications of QSG mission, namely WP800, relevant regions have been selected for earthquakes, volcanos, and lithosphere:

- For earthquakes, one region at low latitudes, and one at high (negative) latitudes, at 5-10 km grid resolution. The analyses are focused on the 2007 Bengkulu Earthquake.
- For volcanos, area of radius 8° centred on the Mayotte volcano (Lat 12.83°S, Lon 45.17°E), resulting in Lat min: 4.83° S, Lat Max: 20.83° S, Lon min: 37.00° E, Lon Max=53.00° E.

Regarding Hydrological (short-term) and ocean applications (WP 900), East China Sea has been chosen as the area of interest by HCU and UNB. For Hydrological (medium to long-term) and climate applications (WP 1000), some small to large scale river basins have been chosen. Smaller river basins are included to investigate the gain in spatial resolution.

- Relevant region for WP900: East China Sea.
- Relevant region for WP1000: Amazon, Danube, Ganges, Elbe, Rhine, Oder, and Uruguay river basins.

The optimized regional solutions are computed by applying a collocation gridding at local level, after reducing the signal by a de-aliasing model and by a global model (e.g. a model of the static gravity field or a Least Squares solution).

In the following, the structure of the proposed remove-compute-restore Least Squares Collocation algorithm to properly include the modelling of the time-variable signal is presented. Starting from the description of the observed signal as:

$$y_o(\underline{x},t) = s(\underline{x}) + v(\underline{x},t) + \varepsilon(t) \quad \textbf{(11)}$$

where $y_o(\underline{x},t)$ is the observation that is dependent on position $\underline{x}$ and time t, $s(\underline{x})$ refers to the static signal of the gravity field, which is assumed to be isotropic in space and invariant in time, whereas $v(\underline{x},t)$ is the time variable signal that is non-stationary, and finally $\varepsilon(t)$ is the random observation noise, that is assumed to be stationary in time and therefore can be described by a PSD.

To mitigate the impact of the temporal aliasing, the first step is to remove the unwanted high (temporal) frequency signals $\tilde{v}(\underline{x},t)$ such as non-tidal atmosphere and ocean, and ocean tides. The reduced observation $y_o^r(\underline{x},t)$ can be written as

$$y_o^r(\underline{x},t) = s(\underline{x}) + v(\underline{x},t) - \tilde{v}(\underline{x},t) + \varepsilon(t) = s(\underline{x}) + u(\underline{x},t) + \varepsilon(t) \quad \textbf{(12)}$$

where $u(\underline{x},t) = v(\underline{x},t) - \tilde{v}(\underline{x},t)$ is the residual time-variable signal after applying the de-aliasing model. Then $y_o^r(\underline{x},t)$ is used as observation in a Least Squares Adjustment (LSA) in which a set of spherical harmonic coefficients $\{\hat{\mathcal{T}}_{lm}\}$ describing the global behaviour of the model are estimated, focusing on the description of the low harmonic degrees

$$\mathbb{L}_s\left(y_o^r(\underline{x},t)\right) \xrightarrow{yields} \{\hat{\mathcal{T}}_{\ell m}\} \quad \textbf{(13)}$$

This estimation could be considered as the sum of the static model plus the average time variable gravity field over the observation period, namely

$$\bar{u}(\underline{x}) = \mathbb{E}_t[u(\underline{x},t)] \quad \textbf{(14)}$$

In the next step, the estimated spherical harmonic coefficients $\{\hat{\mathcal{T}}_{lm}\}$ are used to synthetize the signal $\tilde{s}(\underline{x}) + \tilde{\bar{u}}(\underline{x})$ to reduce the observation to be gridded, thus shortening the signal spatial correlation by removing the estimated long wavelengths. Therefore, starting from Equation (12) and removing the long-wavelength signal we obtain:

$$\begin{aligned} \delta y_o^r(\underline{x},t) &= s(\underline{x}) - \tilde{s}(\underline{x}) + u(\underline{x},t) - \tilde{\bar{u}}(\underline{x}) + \varepsilon(t) = \\ &= \delta s(\underline{x}) + u(\underline{x},t) - \tilde{\bar{u}}(\underline{x}) + \varepsilon(t) \end{aligned} \quad \textbf{(15)}$$

Now, defining

$$u(\underline{x},t) = q(\underline{x},t) + \bar{u}(\underline{x}) \quad \textbf{(16)}$$

where the term $q(\underline{x},t)$ contains the variations with respect to the time average signal $\bar{u}(\underline{x})$ over the considered period (see Equation (14)), Equation (15) can be written as

$$\delta y_o^r(\underline{x},t) = \delta s(\underline{x}) + q(\underline{x},t) + \bar{u}(\underline{x}) - \tilde{\bar{u}}(\underline{x}) + \varepsilon(t) = \\ = \delta s(\underline{x}) + \delta\bar{u}(\underline{x}) + q(\underline{x},t) + \varepsilon(t) \quad \textbf{(17)}$$

As the end product of gridding, we would like to estimate a (linear) functional of the gravity field $z(\underline{x}')$ which is

$$z(\underline{x}') = F[s(\underline{x}') - \tilde{s}(\underline{x}') + \bar{u}(\underline{x}') - \tilde{\bar{u}}(\underline{x}')] = F[\delta s(\underline{x}') + \delta\bar{u}(\underline{x}')] \quad \textbf{(18)}$$

where $\underline{x}'$ is the estimation position (usually a set of points on a regular grid), $\delta s(\underline{x}')$ is the residual stationary signal and $\delta\bar{u}(\underline{x}')$ is the residual average of the time-variable gravity field over the observation period. In order to capture the spatio-temporal details over the selected area / local grid, the covariance modelling is redesigned to compute the covariance matrix of the static part of the model separately from the time-variable part. Therefore, $\hat{z}$ is now represented as

$$\hat{z}(\underline{x}') = \left[\mathcal{C}_{z\delta s}(\underline{x}',\underline{x}) + \mathcal{C}_{z\delta\bar{u}}(\underline{x}',\underline{x})\right] \\ \left[\mathcal{C}_{\delta s\delta s}(\underline{x},\underline{x}) + \mathcal{C}_{\delta\bar{u}\delta\bar{u}}(\underline{x},\underline{x}) + \mathcal{C}_{qq}(\underline{x},t,\underline{x},t) + \mathcal{C}_{\varepsilon\varepsilon}(t,t)\right]^{-1}\delta y_o^r(\underline{x},t) \quad \textbf{(19)}$$

where $\mathcal{C}_{\delta s\delta s}(\underline{x},\underline{x})$ is the covariance of the static gravity field, $\mathcal{C}_{\delta\bar{u}\delta\bar{u}}(\underline{x},\underline{x})$ is the covariance of the average time-variable signal of the gravity field over the observation period, $\mathcal{C}_{qq}(\underline{x},t,\underline{x},t)$ is the covariance of the zero-mean time-variable gravity field in the observation period and $\mathcal{C}_{\varepsilon\varepsilon}(t,t)$ is noise covariance matrix. $\mathcal{C}_{z\delta s}(\underline{x}',\underline{x})$ and $\mathcal{C}_{z\delta\bar{u}}(\underline{x}',\underline{x})$ are the cross-covariance matrixes between the observed and estimation functional.

Note that $\mathcal{C}_{\delta s\delta s}(\underline{x},\underline{x})$ and $\mathcal{C}_{\delta\bar{u}\delta\bar{u}}(\underline{x},\underline{x})$, as well as $\mathcal{C}_{z\delta s}(\underline{x}',\underline{x})$ and $\mathcal{C}_{z\delta\bar{u}}(\underline{x}',\underline{x})$ are isotropic in space and can be modelled starting from the knowledge of the signal degree variances $\sigma^2_{\delta s}(\ell)$ and $\sigma^2_{\delta\bar{u}}(\ell)$. As for the noise covariance matrix $\mathcal{C}_{\varepsilon\varepsilon}(t,t)$ it is generally assumed that to be stationary in time and can be modelled according to the noise PSD, while the covariance matrix of the time-variable part of the gravity field $\mathcal{C}_{qq}(\underline{x},t,\underline{x},t)$ can be assumed to be isotropic in space but non-stationary in time. Therefore, modelling $\mathcal{C}_{qq}$ is not straightforward. A possible solution is to create a block-covariance matrix, considering some sub-periods as stationary, therefore making it possible to create the overall covariance matrix starting from a set of time-variable degree variances $\sigma^2_q(\ell,t_i)$, where t_i identifies the considered sub-period. The whole procedure is summarized by the scheme shown in Figure 29-1.

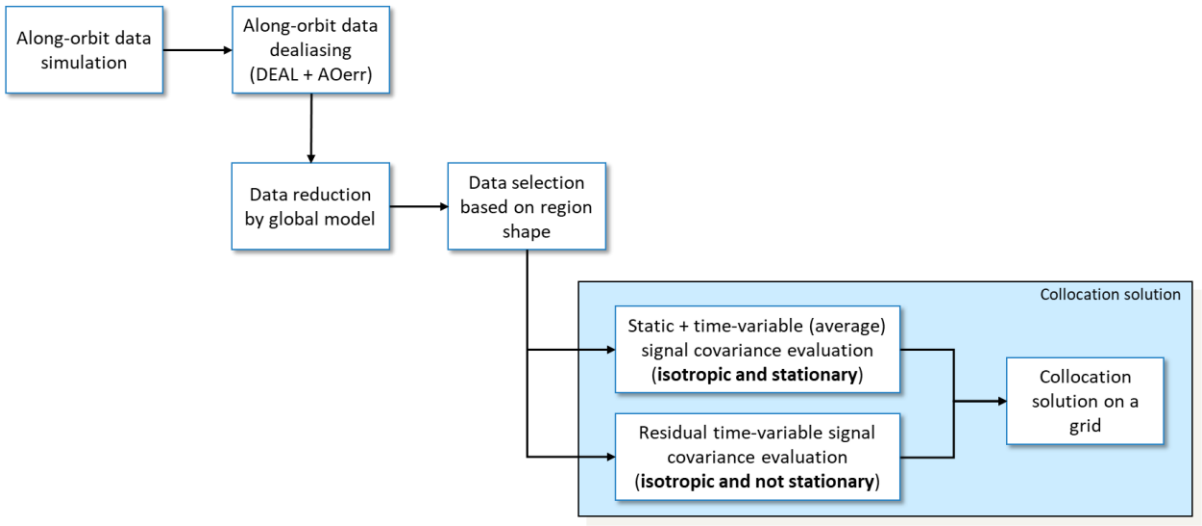

Figure 29-1 Local collocation gridding procedure applied to compute optimized regional solutions.

29.3. HIGH-RESOLUTION REGIONAL VARIANCE-COVARIANCE INFORMATION (WP730)

Together with the grid estimation, the collocation approach gives the possibility of computing the corresponding (full) covariance matrix of the estimation error *e*, namely of the difference between the estimated quantities and their unknown true values. The estimate of this covariance matrix $\mathcal{C}_{ee}(\underline{x}', \underline{x}')$ can be written as

$$\mathcal{C}_{ee}(\underline{x}', \underline{x}') = \mathcal{C}_{zz}(\underline{x}', \underline{x}') - \left[\mathcal{C}_{z\delta s}(\underline{x}', \underline{x}) + \mathcal{C}_{z\delta\bar{u}}(\underline{x}', \underline{x})\right] \left[\mathcal{C}_{\delta s\delta s}(\underline{x}, \underline{x}) + \mathcal{C}_{\delta\bar{u}\delta\bar{u}}(\underline{x}, \underline{x}) + \mathcal{C}_{qq}(\underline{x}, t, \underline{x}, t) + \mathcal{C}_{\varepsilon\varepsilon}(t, t)\right]^{-1} \left[\mathcal{C}_{z\delta s}(\underline{x}', \underline{x}) + \mathcal{C}_{z\delta\bar{u}}(\underline{x}', \underline{x})\right]^{T} \quad \textbf{(20)}$$

Note that the error $e = z(\underline{x}') - \hat{z}(\underline{x}')$ is no longer isotropic, therefore the error covariance matrix is not a function of the spherical distances, but it must be evaluated for any couple of points on the grid.
Also note that the original observations can be initially reduced by subtracting the contribution of an a-priori static global model with the aim of concentrating on the time-variable part only. In this case, the reduction is performed at the beginning of the procedure, i.e. before applying the least-squares adjustment to compute the long wavelength solution. In the simulations, the background static model was subtracted, thus leaving the signal with the time-variable part only with any additional residual of the static one. This means that the term δs is no longer included into the observation equation for the gridding and all covariances related to δs must be deleted from the collocation formulas:

$$\hat{z}(\underline{x}') = \mathcal{C}_{z\delta\bar{u}}(\underline{x}', \underline{x})\left[\mathcal{C}_{\delta\bar{u}\delta\bar{u}}(\underline{x}, \underline{x}) + \mathcal{C}_{qq}(\underline{x}, t, \underline{x}, t) + \mathcal{C}_{\varepsilon\varepsilon}(t, t)\right]^{-1} \delta y_o^r(\underline{x}, t) \quad \textbf{(21)}$$

$$\mathcal{C}_{ee}(\underline{x}', \underline{x}') = \mathcal{C}_{zz}(\underline{x}', \underline{x}') - \mathcal{C}_{z\delta\bar{u}}(\underline{x}', \underline{x})\left[\mathcal{C}_{\delta\bar{u}\delta\bar{u}}(\underline{x}, \underline{x}) + \mathcal{C}_{qq}(\underline{x}, t, \underline{x}, t) + \mathcal{C}_{\varepsilon\varepsilon}(t, t)\right]^{-1} \quad \textbf{(22)}$$

$$\mathcal{C}_{z\delta\bar{u}}(\underline{x}', \underline{x})^T$$

In other words, we directly estimate the time-variable information, which is regularized according to its own degree variances, namely applying what is known as VADER filter. Attention should be paid to the fact that in the real world the subtracted a-priori model inevitably contains some errors, and therefore a residual static signal δr will remain in the data. However, in this case, this residual is not a quantity that we want to estimate but rather an additional noise to filter out. Therefore, assuming that the error degree variances of the subtracted global model and the degree variances of the time-variable gravity signal are uncorrelated, the collocation estimates become:

$$\hat{z}(\underline{x}') = \mathcal{C}_{z\delta\bar{u}}(\underline{x}', \underline{x})\big[\mathcal{C}_{\delta\bar{u}\delta\bar{u}}(\underline{x}, \underline{x}) + \mathcal{C}_{\delta r\delta r}(\underline{x}, \underline{x}) + \mathcal{C}_{qq}(\underline{x}, t, \underline{x}, t) + \mathcal{C}_{\varepsilon\varepsilon}(t, t)\big]^{-1} \delta y_o^r(\underline{x}, t) \quad \textbf{(23)}$$

$$\mathcal{C}_{ee}(\underline{x}', \underline{x}') = \mathcal{C}_{zz}(\underline{x}', \underline{x}') - \mathcal{C}_{z\delta\bar{u}}(\underline{x}', \underline{x})\big[\mathcal{C}_{\delta\bar{u}\delta\bar{u}}(\underline{x}, \underline{x}) + \mathcal{C}_{\delta r\delta r}(\underline{x}, \underline{x}) + \mathcal{C}_{qq}(\underline{x}, t, \underline{x}, t) + \mathcal{C}_{\varepsilon\varepsilon}(t, t)\big]^{-1} \mathcal{C}_{z\delta\bar{u}}(\underline{x}', \underline{x})^T \quad \textbf{(24)}$$

To validate the formal covariance matrix a test in ideal conditions was performed. In particular, a 7-day solution over the Amazon region was computed, considering the ll-SST mission principle and the IIC2v1 orbit configuration. The instrumental noise was assumed (and simulated) to be white for the sake of simplicity and only a static gravity field model was considered as a background model, to avoid effects related to the temporal-aliasing (to be investigated later).

The estimated formal covariance matrix for the TWSA grid in terms of EWH is shown in Figure 29-2.

The comparison between the formal and empirical standard deviation has been performed by comparing the square root of the diagonal of the covariance matrix with the empirical RMSE of the solution computed over 50 Monte Carlo Samples. This comparison is shown in Figure 29-3 in terms of EWH evaluating the TWSA functional. The same comparison was performed for the estimated second radial derivative (T_{rr}) at mean satellite altitude and is shown in Figure 29-4.

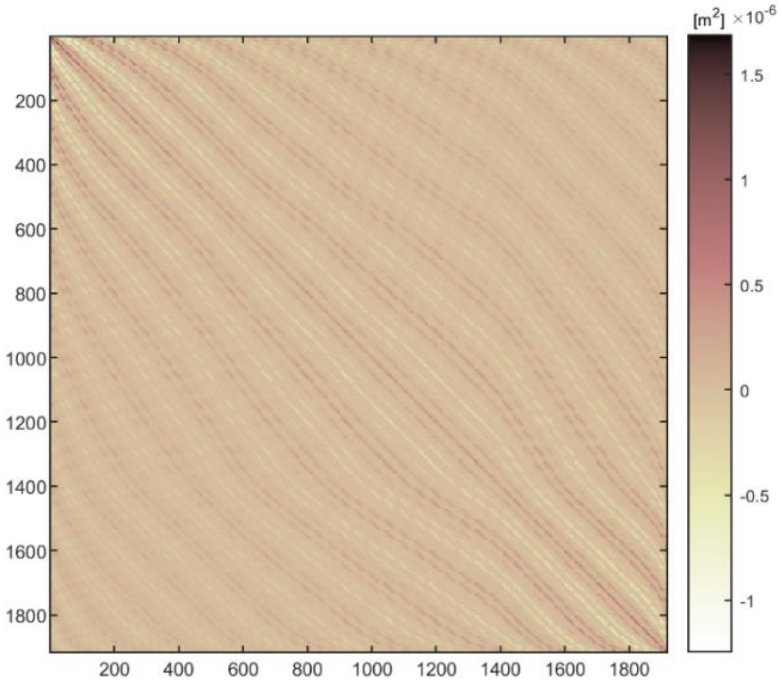

Figure 29-2 Estimated covariance matrix for the TWSA over the Amazon region. The numbers on the x and y axes refer to the grid point index. Data are provided in m^2.

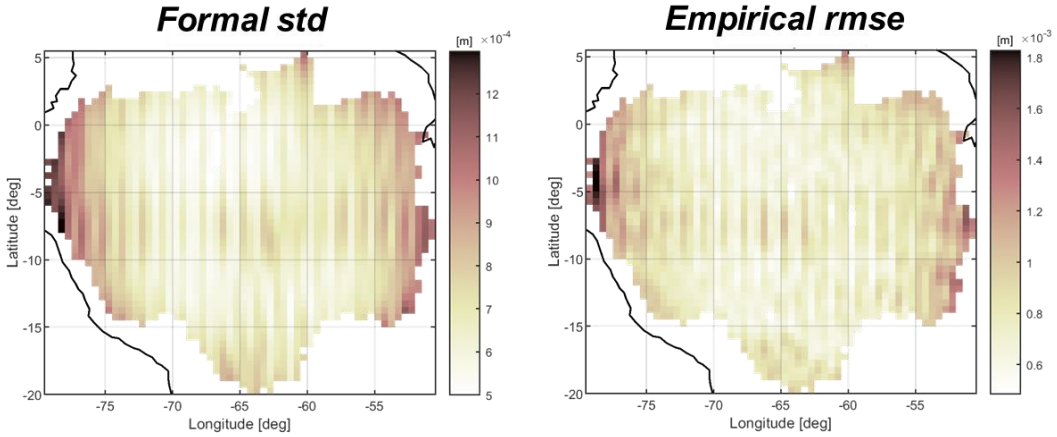

Figure 29-3 Comparison between the estimated TWSA in terms of EWH formal standard deviation (i.e., the square root of the diagonal of the covariance matrix shown in Figure 29-2) and the empirical estimation of RMSE over 50 Monte Carlo Sample. Values are expressed in terms of EWH [m].

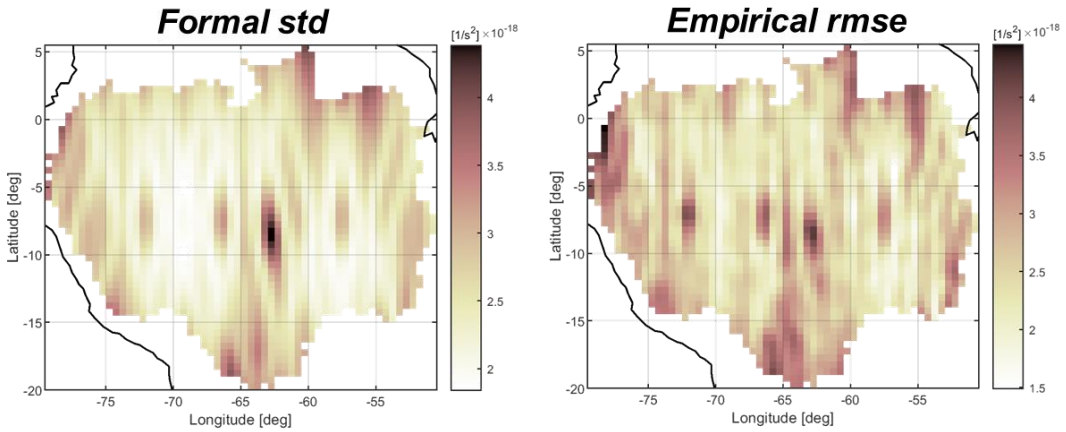

Figure 29-4 Comparison between the estimated second radial derivative (T_{rr}) formal standard deviation (i.e., the square root of the diagonal of the covariance matrix shown in Figure 29-2) and the empirical estimation of RMSE over 50 Monte Carlo Sample. Values are expressed in terms of 1/s2.

Comparisons between formal and empirical error show a good agreement, as highlighted by the maps of empirical to formal error ratio reported in Figure 29-5. This Figure shows that the ratio is close to one in both cases, demonstrating the compliancy of the formal error propagation with its empirical determination.

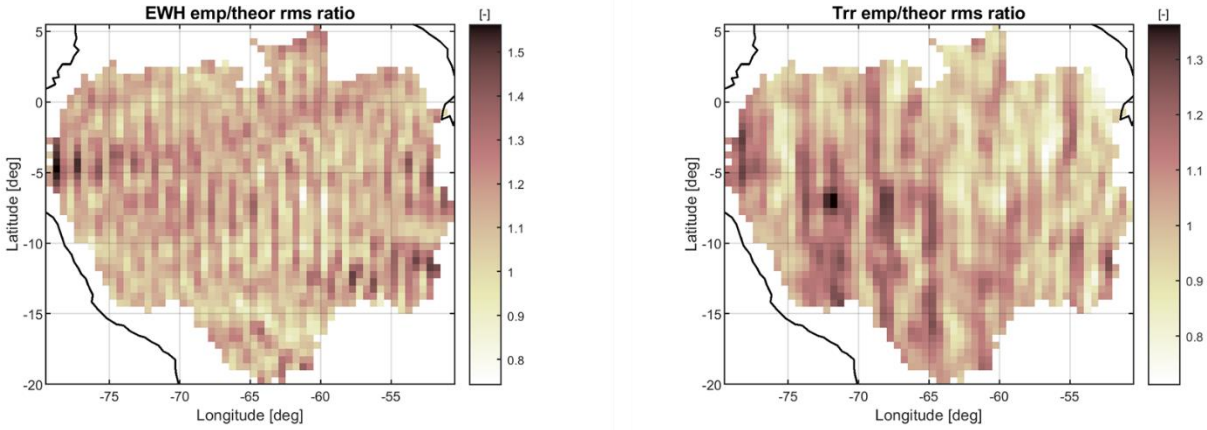

Figure 29-5 Ratio between the empirical and formal error standard deviation considering the estimated TWSA and the estimated second radial derivative (T_{rr}) at mean satellite altitude.

29.4. SPECIFIC REGIONAL PARAMETERIZATION (WP740)

As we discussed in the previous sections, regional "parametrization" in the case of collocation gridding mainly means definition of the signal and noise covariance functions. Concerning the noise, this information comes from the instrumental knowledge, in case propagated through previous data processing (e.g., Wiener filtering). Therefore, this noise modelling has a global characteristic depending on the time correlation and, generally, it is independent from the specific region under study. This is not true for the gravitational signal which of course has a spatial signature and, therefore, a spatial correlation to be locally modelled. The focus here is on the modelling of the time-variable signal and in particular on the EWH that can be expressed as a functional of the anomalous potential. Therefore, taking into account the regions selected in Section 29.2, we computed the empirical covariance functions (under the assumption of an isotropic random field) of regional EWH grids with a spatial resolution of 0.5°×0.5° and a

sampling rate of 1 month. In other words, we took the ESA ESM spherical harmonic coefficients, we averaged them over a time span of 1 month (starting from 1st January 2002), we synthesized a grid of EWH values on the selected region using the averaged coefficients, we computed the corresponding empirical covariance function and finally we interpolated it with a powered exponential covariance function, namely:

$$C(\psi) = Ae^{-(a\psi)^b} \text{ with } A, a, b > 0 \quad \textbf{(25)}$$

This was done for a sequence of 8 months and for all the regions. The results are reported in Figure 29-6, emphasizing how the EWH signal variance changes in time. The corresponding degree variance models, computed by exploiting the orthogonality of the Legendre polynomials, are reported in Figure 29-7, showing that also the correlation (and not only the variance) is changing in time. Finally, the same analysis was performed for weekly sub-periods (see Figure 29-8), considering 26 consecutive weeks, again starting from 1st January 2002.

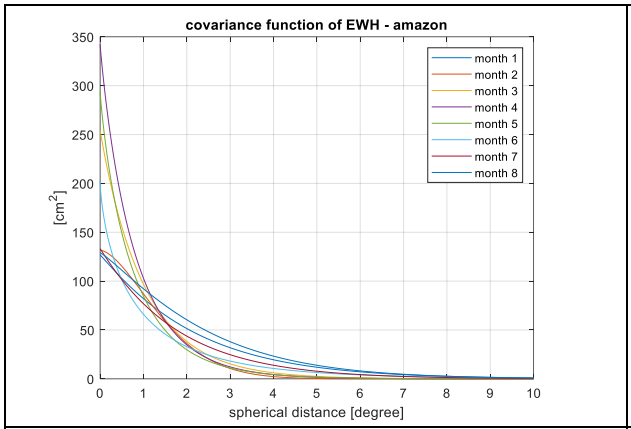
covariance function of EWH - amazon
month 1
month 2
month 3
month 4
month 5
month 6
month 7
month 8
[cm^2]
spherical distance [degree]

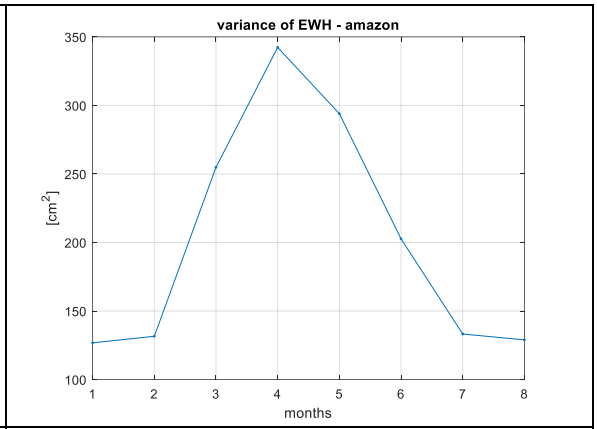
variance of EWH - amazon
[cm^2]
months

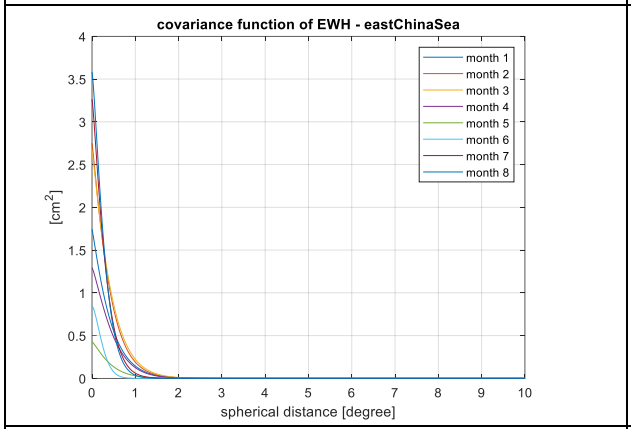
covariance function of EWH - eastChinaSea
month 1
month 2
month 3
month 4
month 5
month 6
month 7
month 8
[cm^2]
spherical distance [degree]

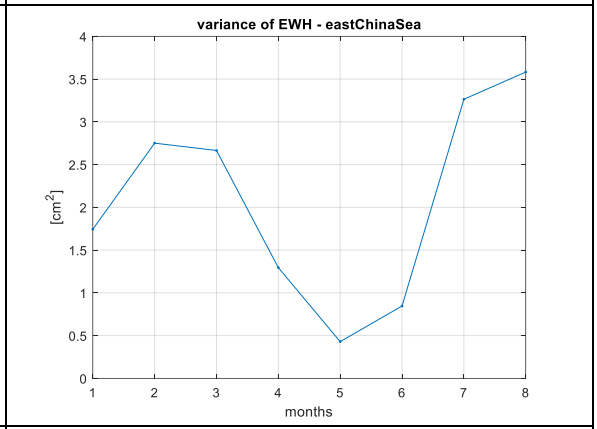
variance of EWH - eastChinaSea
[cm^2]
months

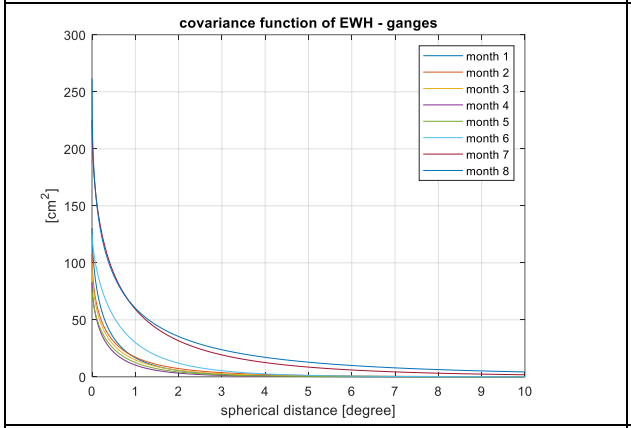
covariance function of EWH - ganges
month 1
month 2
month 3
month 4
month 5
month 6
month 7
month 8
[cm^2]
spherical distance [degree]

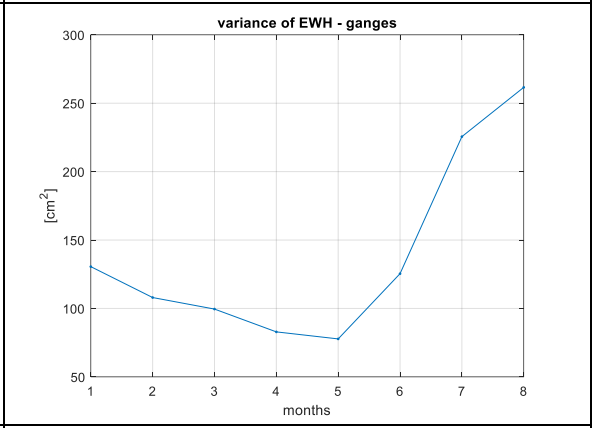
variance of EWH - ganges
[cm^2]
months

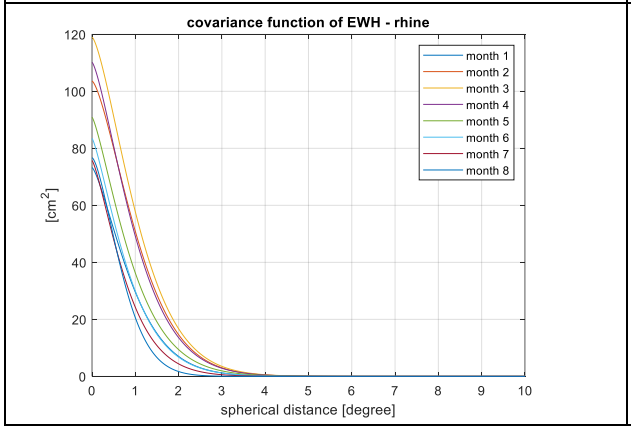
covariance function of EWH - rhine
month 1
month 2
month 3
month 4
month 5
month 6
month 7
month 8
[cm^2]
spherical distance [degree]

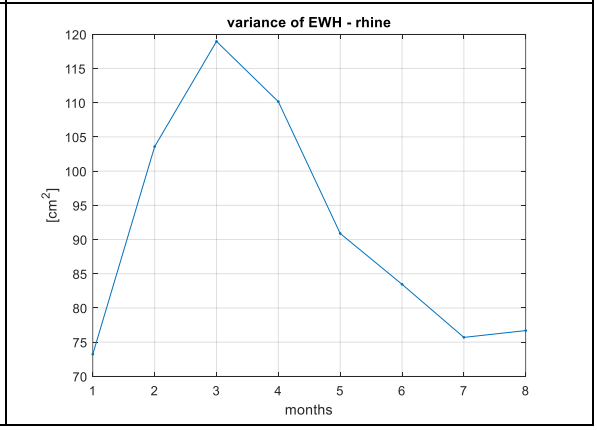
variance of EWH - rhine
[cm^2]
months

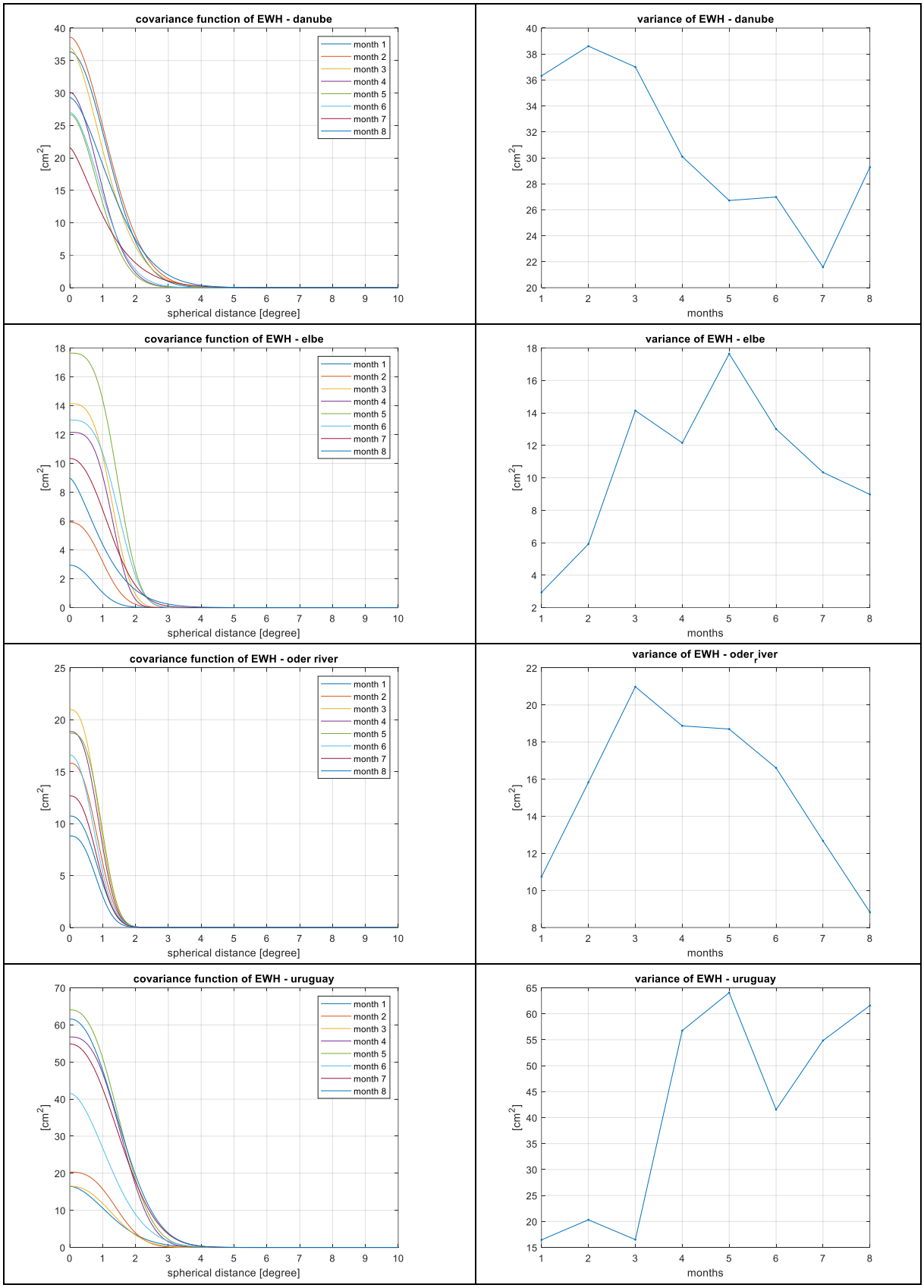

Figure 29-6 Covariance function models for each selected region and for 8 consecutive months (left panels) with the corresponding variance time series (right panels).

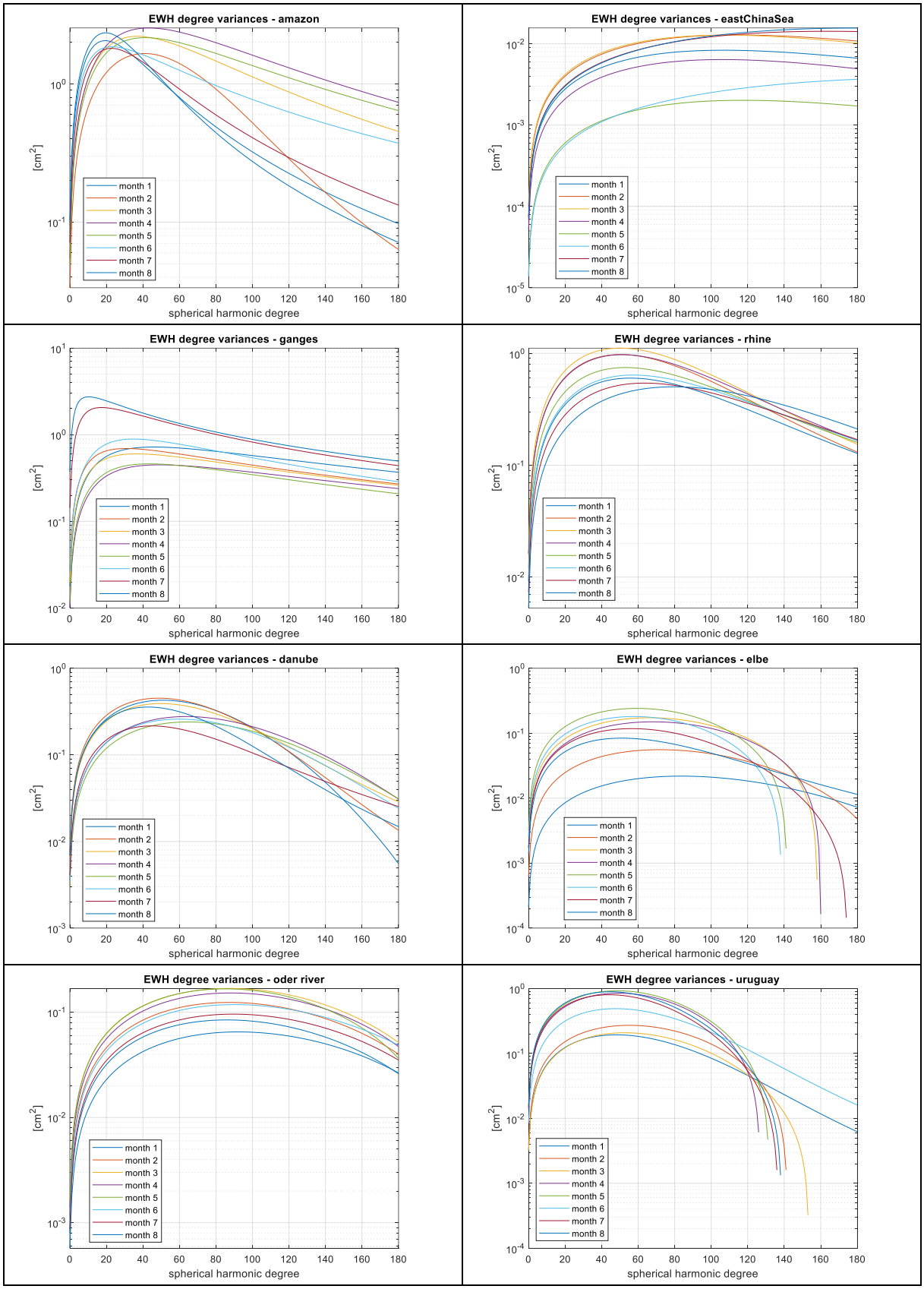

Figure 29-7 Degree variance models for each selected region and for 8 consecutive months.

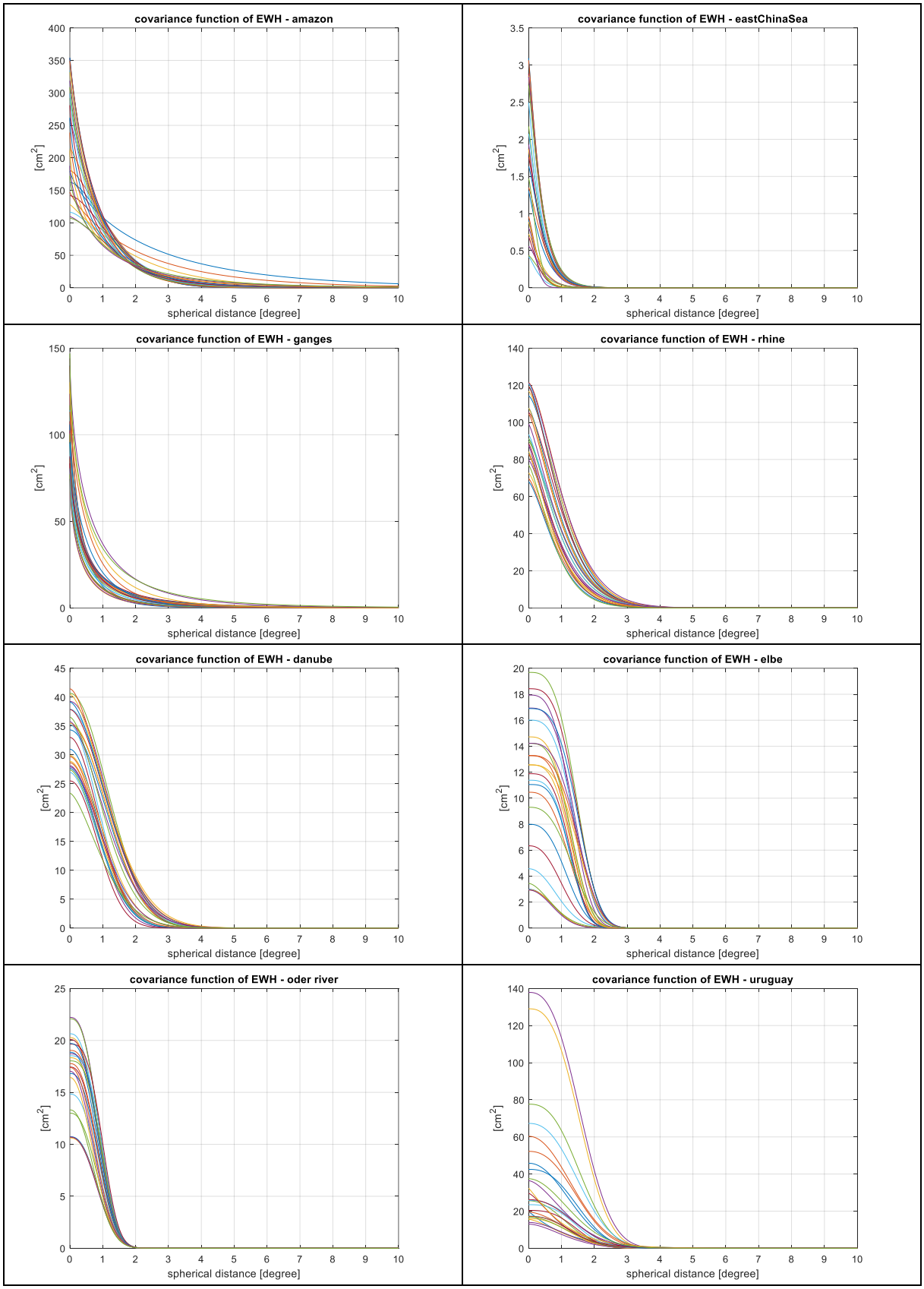

Figure 29-8 Covariance function models for each selected region and for 26 consecutive weeks.

29.5. ASSESSMENT OF MISSION PERFORMANCE AND MATCH AGAINST USER REQUIREMENTS (WP750)

To perform the assessment of the mission performance, weekly and monthly solutions were computed over the first week or month of the time series of solutions considered for the aims of WP800, WP900, and WP1000, with 2-pair, 3-pair, or 6-pair in-line constellations (IIC2v1, IIC3v1, and IIC6v1) and 6-pair mixed in-line and cross-track constellation (PIAC6v2).
As explained in the previous sections, local solutions are provided as gridded values over the selected area or region with the corresponding covariance matrix. The computed functionals are the TWSA in terms of EWH or T_r at 10 km altitude, for hydrological and solid Earth applications, respectively.
Moreover, we considered different background models depending on the applications. For hydrological applications the background model was chosen according to the FN case, while for the solid Earth case, the signal generated from the Bengkulu earthquake only has been considered, assuming that it is possible to isolate it from all the rest.

In the following, we will compare the local collocation solution with the global Least Squares solutions (used as input to the gridding for the data reduction in the remove-restore workflow) to show the improvements obtained by using tailored parameters in the local processing. In fact, thanks to the locally calibrated covariance function, the resolution of local features could be improved by the collocation approach.

Hydrological and climate changes applications

First, we focus on the solutions computed for hydrological applications in which the output is provided at 0.5° resolution. For each of the considered regions the Least Square global solutions are compared to the local gridding solution, as well as their empirical errors. A summary of the retrieval performances is presented in the following figures.

Amazon

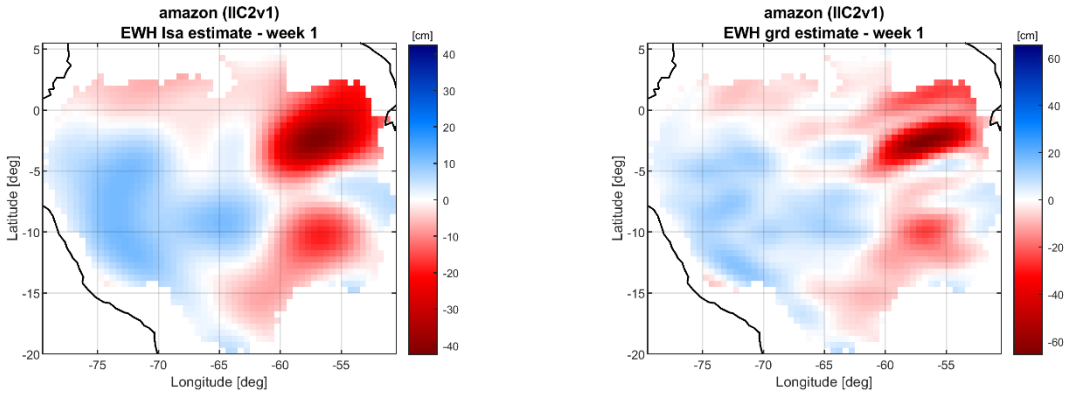

Figure 29-9 TWSA estimate in terms of EWH for the first week of the year 2002, considering quantum instrumentation (X2.1 noise level) with 2-pairs of inline satellites (IIC2v1 constellation). Least Squares estimate (regularized up to d/o 120) is reported in the left panel, while the refined gridding estimate is reported in the right panel.

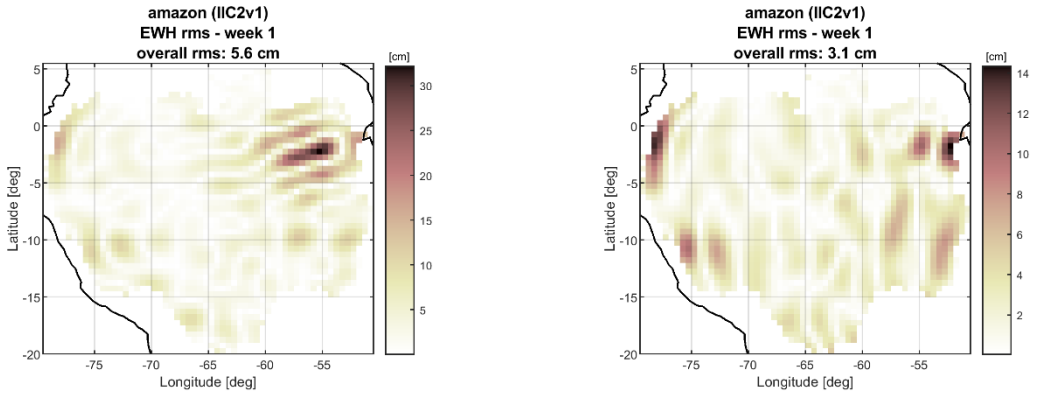

Figure 29-10 Estimation error of TWSA in terms of EWH for the first week of the year 2002, considering quantum instrumentation (X2.1 noise level) with 2-pairs of inline satellites (IIC2v1 constellation). The error of the Least Squares estimate (regularized up to d/o 120) is reported in the left panel, while error of the refined gridding estimate is reported in the right panel.

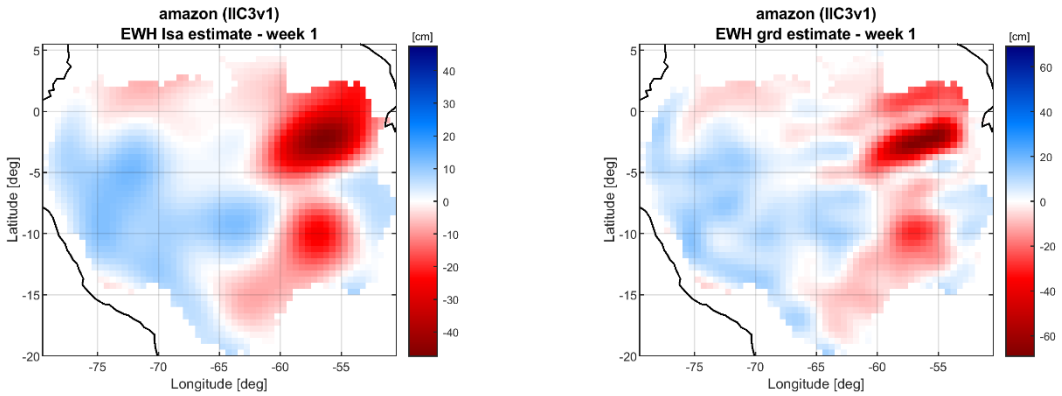

Figure 29-11 TWSA estimate in terms of EWH for the first week of the year 2002, considering quantum instrumentation (X2.1 noise level) with 3-pairs of inline satellites (IIC3v1 constellation). The Least Squares estimate (regularized up to d/o 120) is reported in the left panel, while the refined gridding estimate is reported in the right panel.

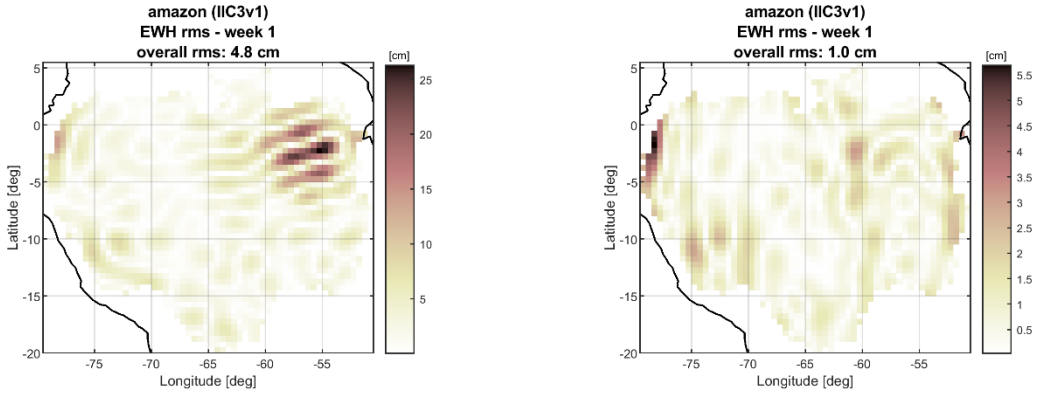

Figure 29-12 Estimation error of TWSA in terms of EWH for the first week of the year 2002, considering quantum instrumentation (X2.1 noise level) with 3-pairs of inline satellites (IIC3v1 constellation). The error of the Least Squares estimate (regularized up to d/o 120) is reported in the left panel, while the error of the refined gridding estimate is reported in the right panel.

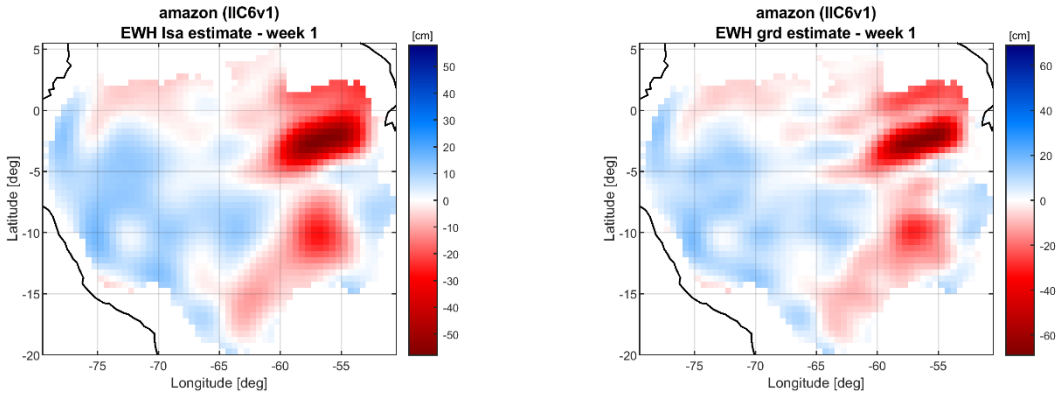

Figure 29-13 TWSA estimate in terms of EWH for the first week of the year 2002, considering quantum instrumentation (X2.1 noise level) with 6-pairs of inline satellites (IIC6v1 constellation). The Least Squares estimate (regularized up to d/o 120) is reported in the left panel, while the refined gridding estimate is reported in the right panel.

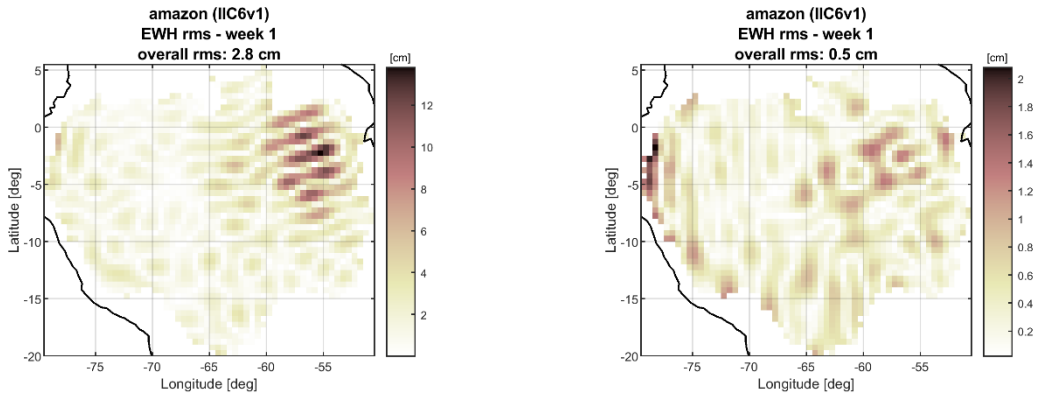

Figure 29-14 Estimation error of TWSA in terms of EWH for the first week of the year 2002, considering quantum instrumentation (X2.1 noise level) with 6-pairs of inline satellites (IIC6v1 constellation). The error of the Least Squares estimate (regularized up to d/o 120) is reported in the left panel, while the error of the refined gridding estimate is reported in the right panel.

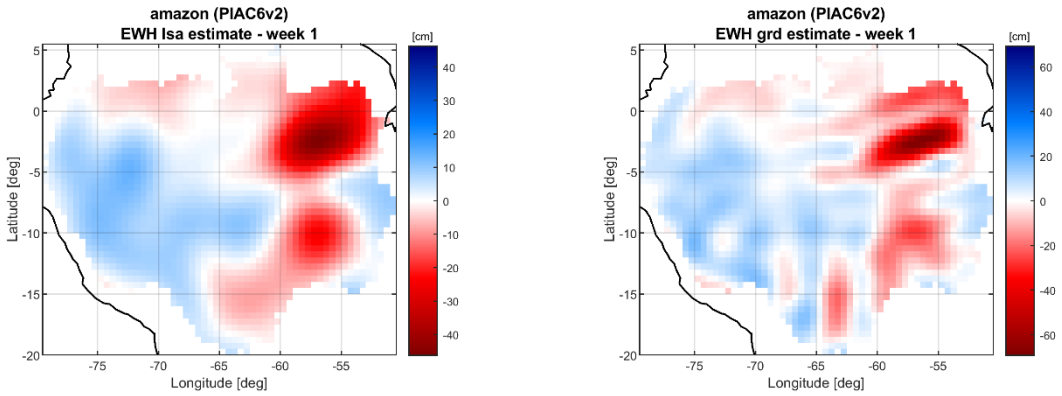

Figure 29-15 TWSA estimate in terms of EWH for the first week of the year 2002, considering quantum instrumentation (X2.1 noise level) with 6-pairs of mixed inline and cross-track satellites (PIAC6v2 constellation). The Least Squares estimate (regularized up to d/o 120) is reported in the left panel, while the refined gridding estimate is reported in the right panel.

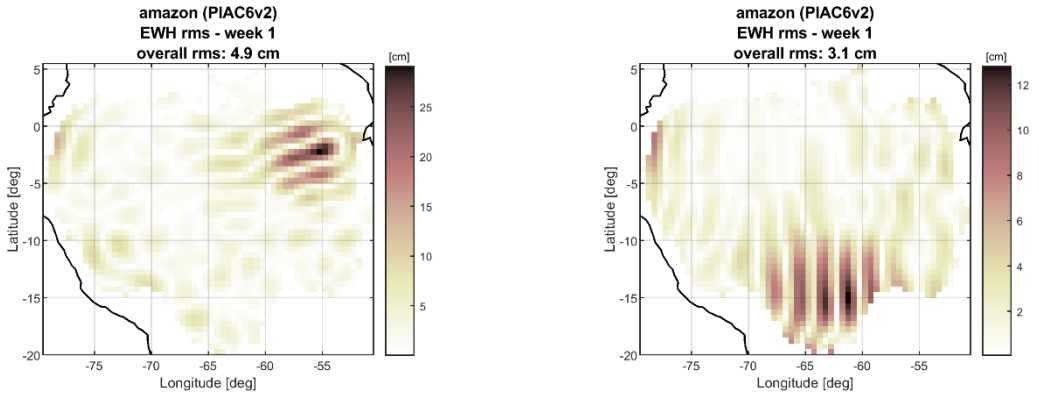

Figure 29-16 Estimation error of TWSA in terms of EWH for the first week of the year 2002, considering quantum instrumentation (X2.1 noise level) with 6-pairs of mixed inline and cross-track satellites (PIAC6v2 constellation). The error of the Least Squares estimate (regularized up to d/o 120) is reported in the left panel, while the error of the refined gridding estimate is reported in the right panel.

Danube

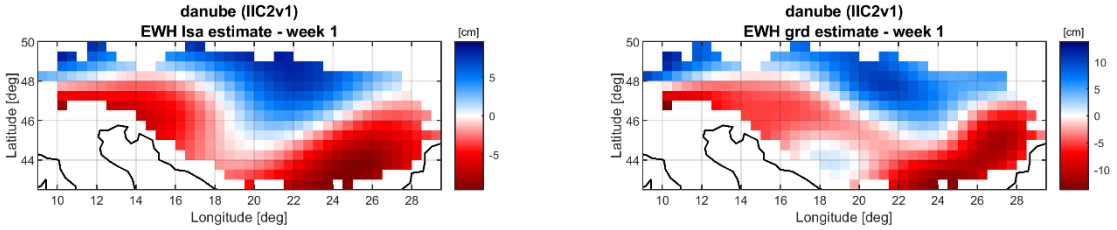

Figure 29-17 TWSA estimate in terms of EWH for the first week of the year 2002, considering quantum instrumentation (X2.1 noise level) with 2-pairs of inline satellites (IIC2v1 constellation). The Least Squares estimate (regularized up to d/o 120) is reported in the left panel, while the refined gridding estimate is reported in the right panel.

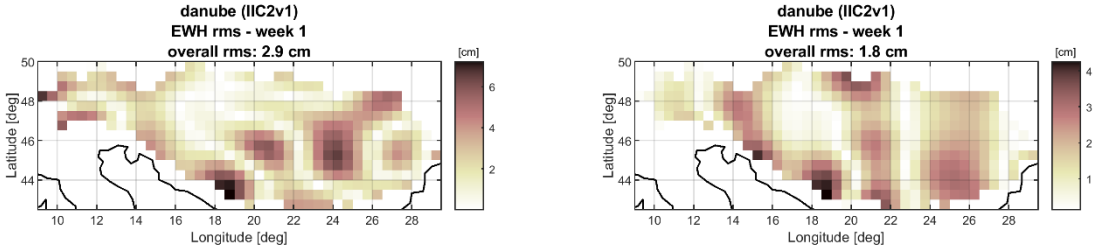

Figure 29-18 Estimation error of TWSA in terms of EWH for the first week of the year 2002, considering quantum instrumentation (X2.1 noise level) with 2-pairs of inline satellites (IIC2v1 constellation). The error of the Least Squares estimate (regularized up to d/o 120) is reported in the left panel, while the error of the refined gridding estimate is reported in the right panel.

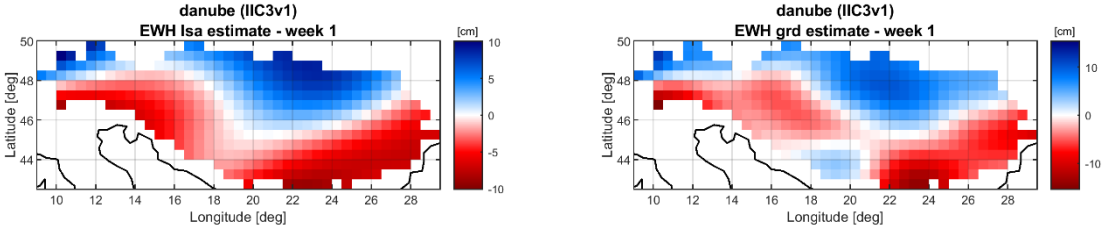

Figure 29-19 TWSA estimate in terms of EWH for the first week of year 2002, considering quantum instrumentation (X2.1 noise level) with 3-pairs of inline satellites (IIC3v1 constellation). The Least Squares estimate (regularized up to d/o 120) is reported in the left panel, while the refined gridding estimate is reported in the right panel.

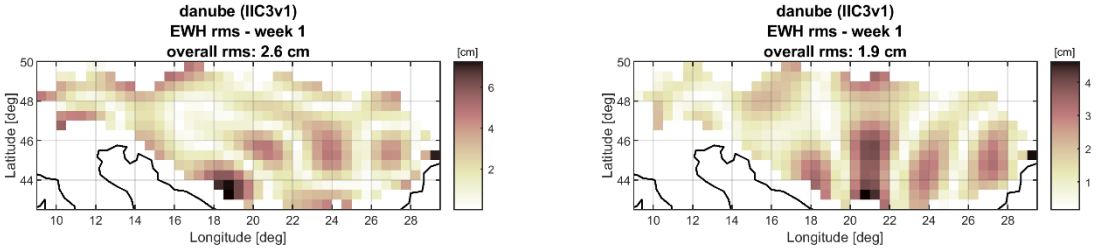

Figure 29-20 Estimation error of TWSA in terms of EWH for the first week of year 2002, considering quantum instrumentation (X2.1 noise level) with 3-pairs of inline satellites (IIC3v1 constellation). The error of the Least Squares estimate (regularized up to d/o 120) is reported in the left panel, while the error of the refined gridding estimate is reported in the right panel.

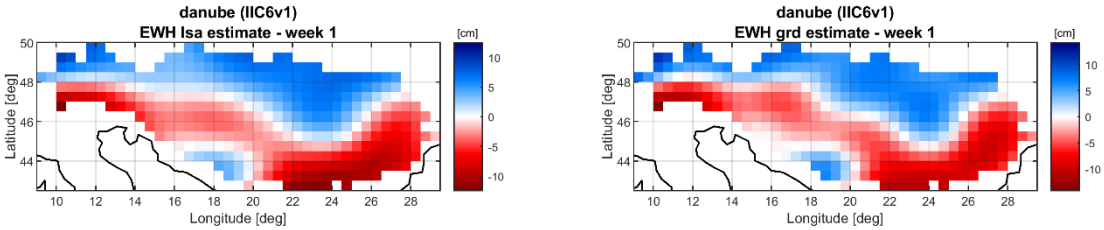

Figure 29-21 TWSA estimate in terms of EWH for the first week of year 2002, considering quantum instrumentation (X2.1 noise level) with 6-pairs of inline satellites (IIC6v1 constellation). The Least Squares estimate (regularized up to d/o 120) is reported in the left panel, while the refined gridding estimate is reported in the right panel.

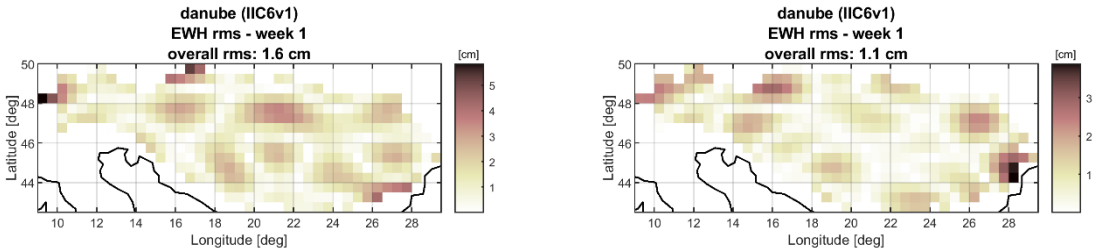

Figure 29-22 Estimation error of TWSA in terms of EWH for the first week of year 2002, considering quantum instrumentation (X2.1 noise level) with 6-pairs of inline satellites (IIC6v1 constellation). The error of the Least Squares estimate (regularized up to d/o 120) is reported in the left panel, while the error of the refined gridding estimate is reported in the right panel.

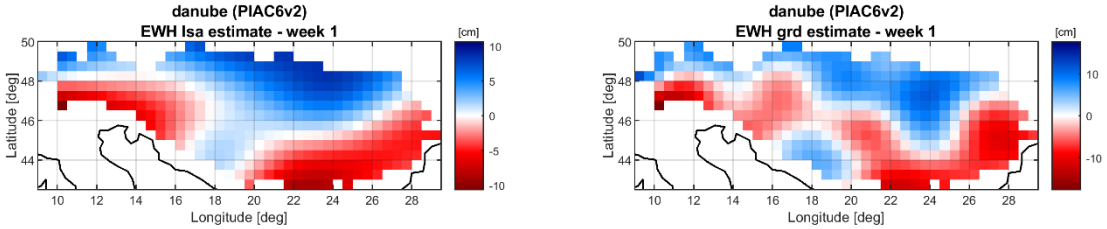

Figure 29-23 TWSA estimate in terms of EWH for the first week of year 2002, considering quantum instrumentation (X2.1 noise level) with 6-pairs of mixed inline and cross-track satellites (PIAC6v2 constellation). The Least Squares estimate (regularized up to d/o 120) is reported in the left panel, while the refined gridding estimate is reported in the right panel.

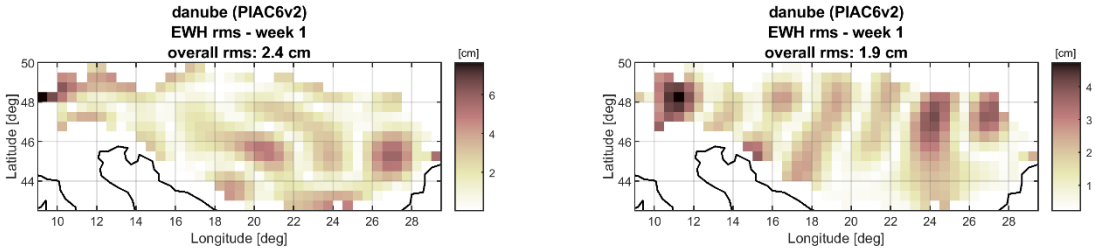

Figure 29-24 Estimation error of TWSA in terms of EWH for the first week of year 2002, considering quantum instrumentation (X2.1 noise level) with 6-pairs of mixed inline and cross-track satellites (PIAC6v2 constellation). The error of the Least Squares estimate (regularized up to d/o 120) is reported in the left panel, while the error of the refined gridding estimate is reported in the right panel.

East China Sea

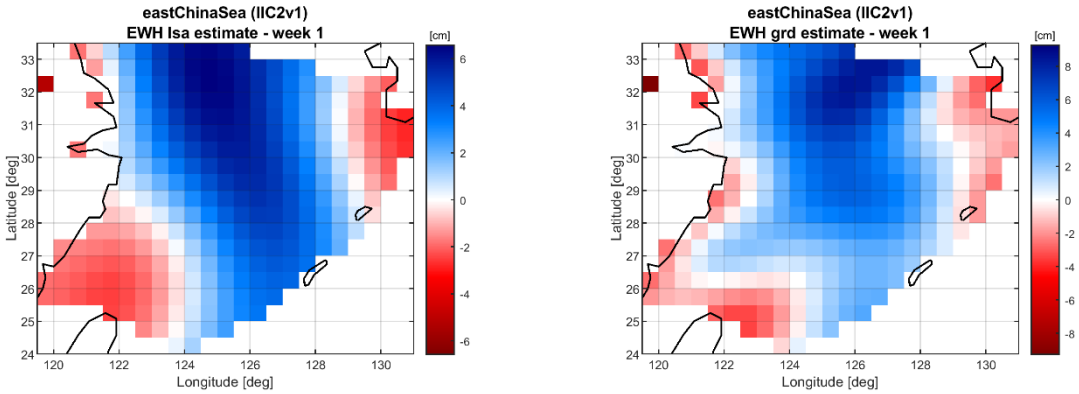

Figure 29-25 TWSA estimate in terms of EWH for the first week of year 2002, considering quantum instrumentation (X2.1 noise level) with 2-pairs of inline satellites (IIC2v1 constellation). The Least Squares estimate (regularized up to d/o 120) is reported in the left panel, while the refined gridding estimate is reported in the right panel.

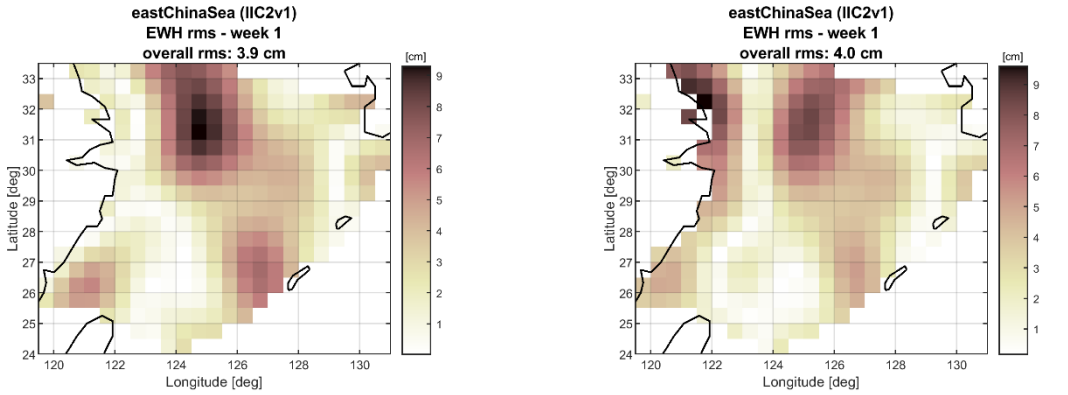

Figure 29-26 Estimation error of TWSA in terms of EWH for the first week of year 2002, considering quantum instrumentation (X2.1 noise level) with 2-pairs of inline satellites (IIC2v1 constellation). The error of the Least Squares estimate (regularized up to d/o 120) is reported in the left panel, while the error of the refined gridding estimate is reported in the right panel.

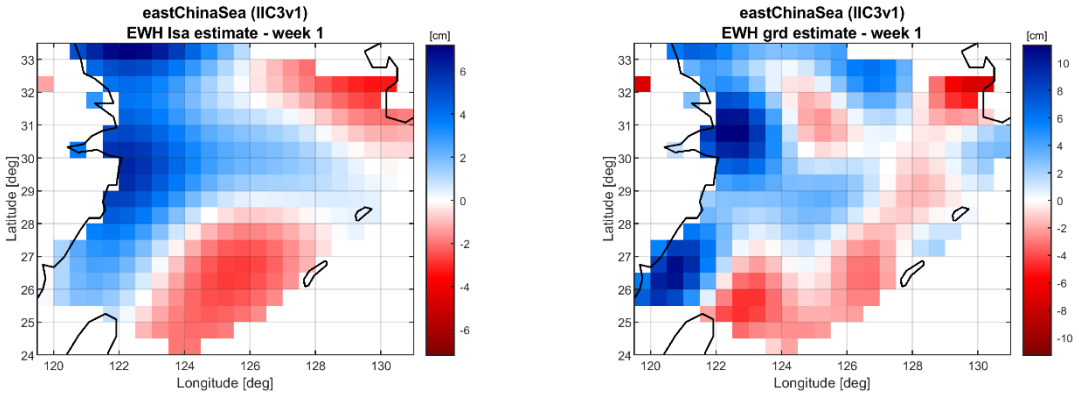

Figure 29-27 TWSA estimate in terms of EWH for the first week of year 2002, considering quantum instrumentation (X2.1 noise level) with 3-pairs of inline satellites (IIC3v1 constellation). The Least Squares estimate (regularized up to d/o 120) is reported in the left panel, while the refined gridding estimate is reported in the right panel.

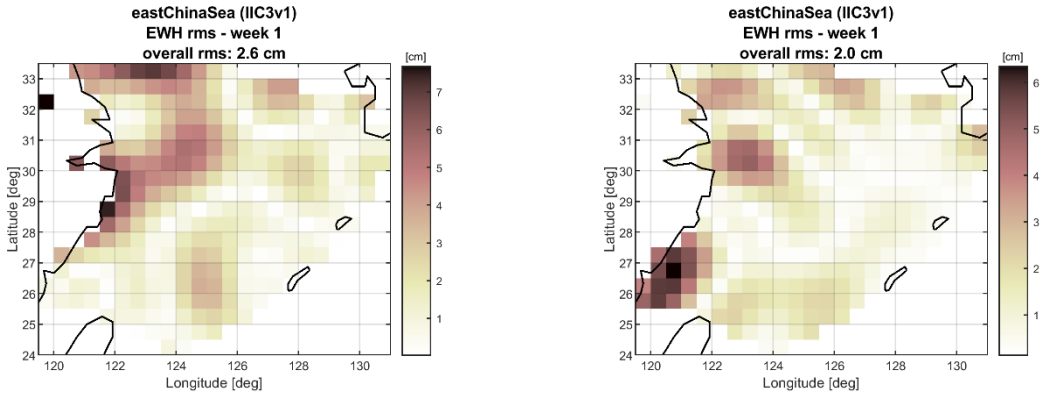

Figure 29-28 Estimation error of TWSA in terms of EWH for the first week of year 2002, considering quantum instrumentation (X2.1 noise level) with 3-pairs of inline satellites (IIC3v1 constellation). The error of the Least Squares estimate (regularized up to d/o 120) is reported in the left panel, while the error of the refined gridding estimate is reported in the right panel.

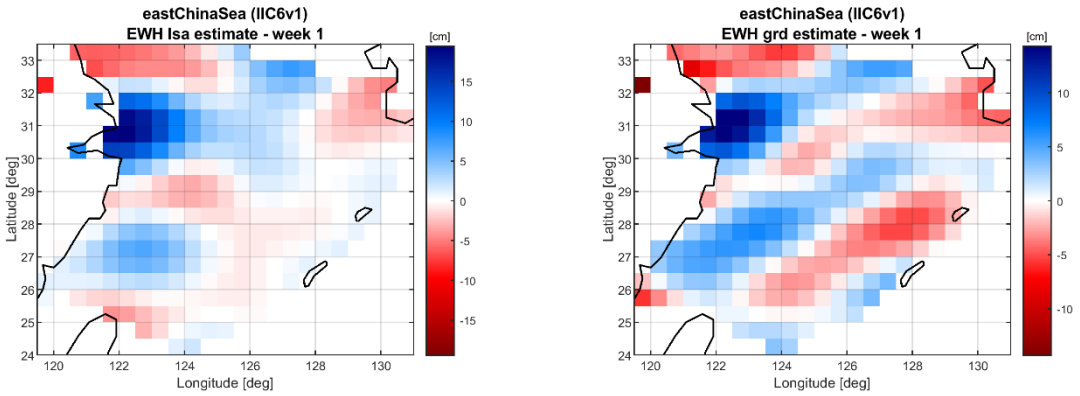

Figure 29-29 TWSA estimate in terms of EWH for the first week of year 2002, considering quantum instrumentation (X2.1 noise level) with 6-pairs of inline satellites (IIC6v1 constellation). The Least Squares estimate (regularized up to d/o 120) is reported in the left panel, while the refined gridding estimate is reported in the right panel.

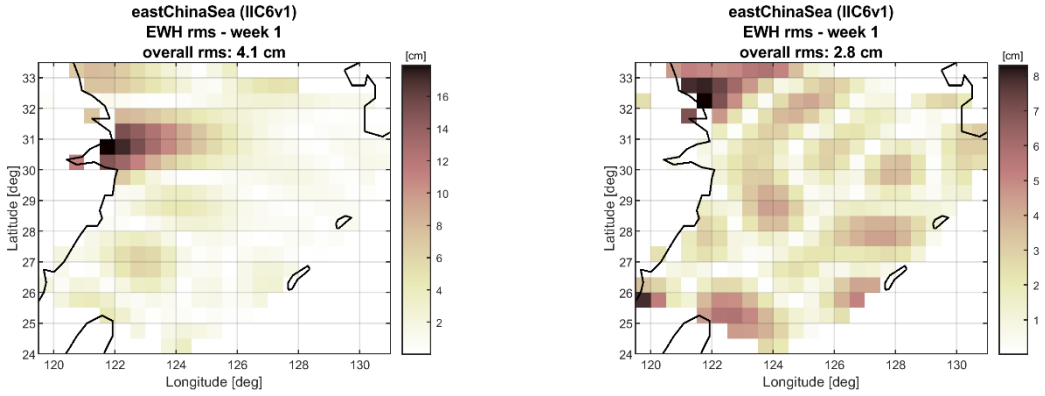

Figure 29-30 Estimation error of TWSA in terms of EWH for the first week of year 2002, considering quantum instrumentation (X2.1 noise level) with 6-pairs of inline satellites (IIC6v1 constellation). The error of the Least Squares estimate (regularized up to d/o 120) is reported in the left panel, while the error of the refined gridding estimate is reported in the right panel.

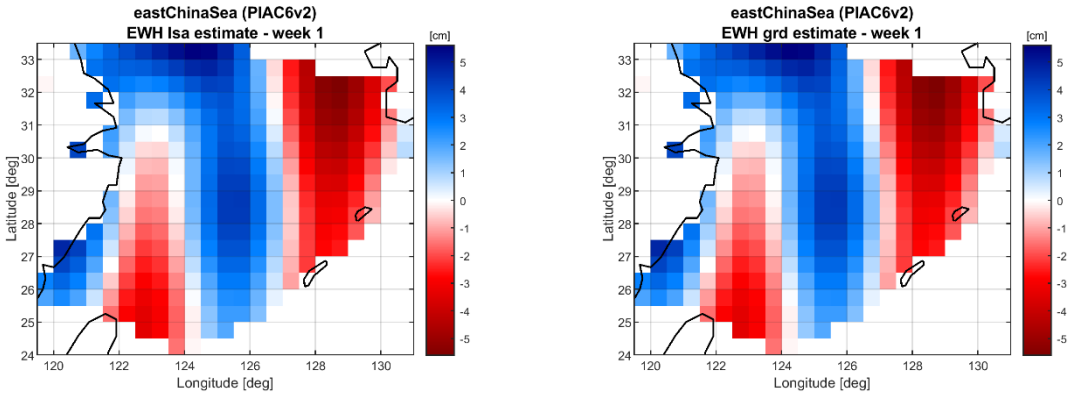

Figure 29-31 TWSA estimate in terms of EWH for the first week of year 2002, considering quantum instrumentation (X2.1 noise level) with 6-pairs of mixed inline and cross-track satellites (PIAC6v2 constellation). The Least Squares estimate (regularized up to d/o 120) is reported in the left panel, while the refined gridding estimate is reported in the right panel.

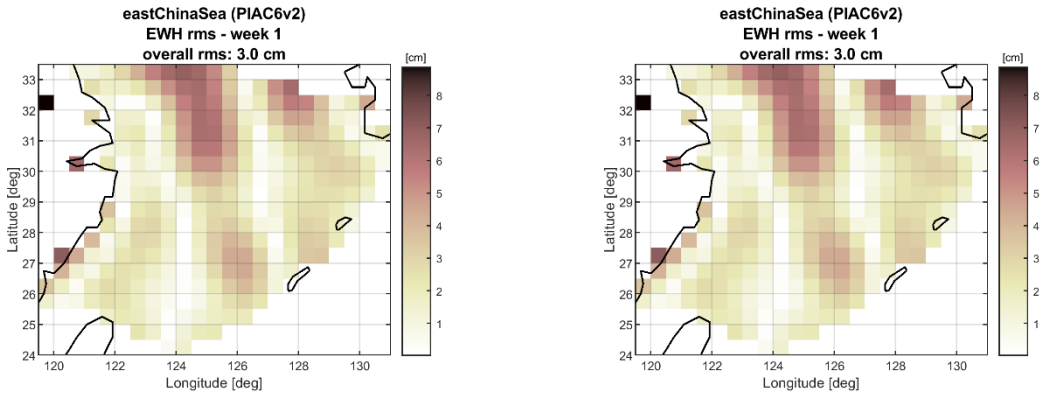

Figure 29-32 Estimation error of TWSA in terms of EWH for the first week of year 2002, considering quantum instrumentation (X2.1 noise level) with 6-pairs of mixed inline and cross-track satellites (PIAC6v2 constellation). The error of the Least Squares estimate (regularized up to d/o 120) is reported in the left panel, while the error of the refined gridding estimate is reported in the right panel.

Elbe

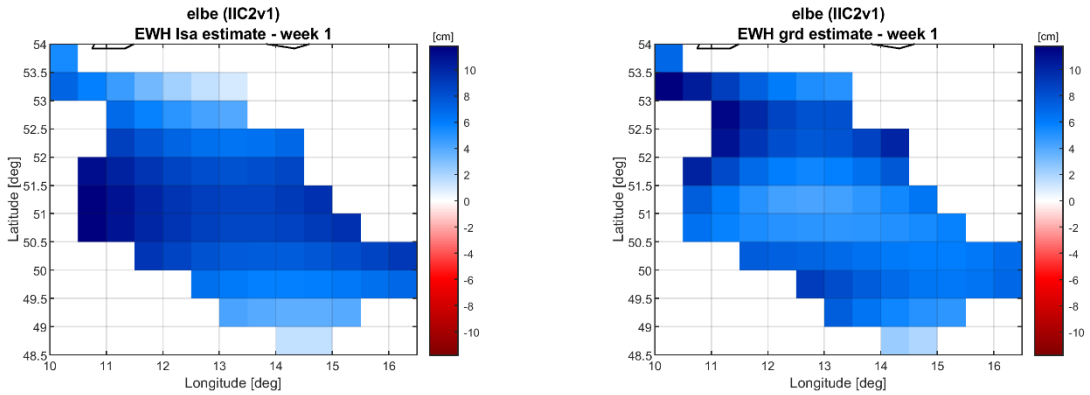

Figure 29-33 TWSA estimate in terms of EWH for the first week of year 2002, considering quantum instrumentation (X2.1 noise level) with 2-pairs of inline satellites (IIC2v1 constellation). The Least Squares estimate (regularized up to d/o 120) is reported in the left panel, while the refined gridding estimate is reported in the right panel.

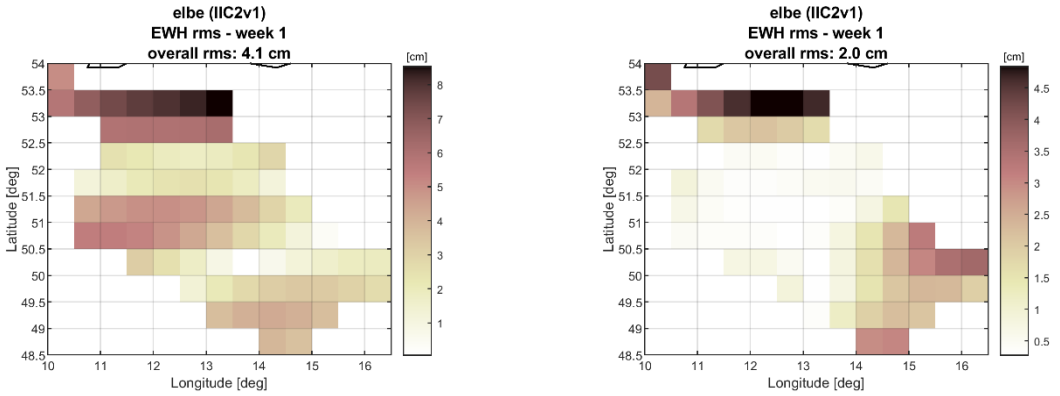

Figure 29-34 Estimation error of TWSA in terms of EWH for the first week of year 2002, considering quantum instrumentation (X2.1 noise level) with 2-pairs of inline satellites (IIC2v1 constellation). The error of the Least Squares estimate (regularized up to d/o 120) is reported in the left panel, while the error of the refined gridding estimate is reported in the right panel.

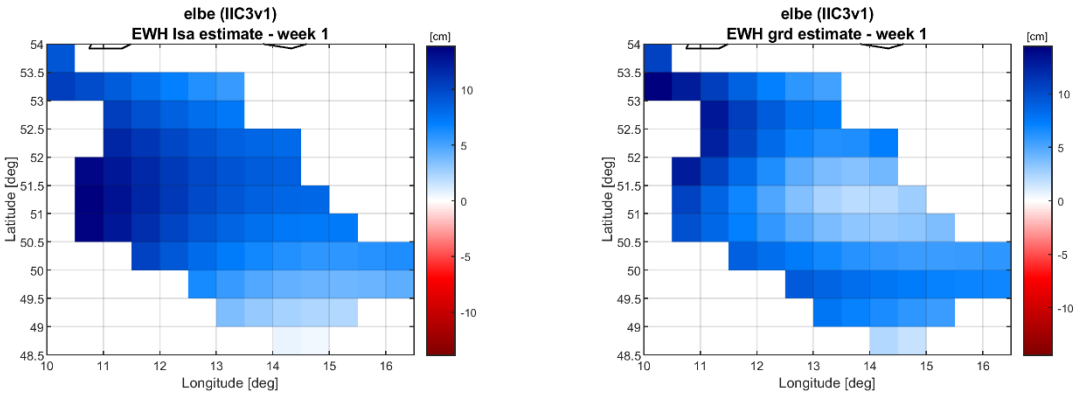

Figure 29-35 TWSA estimate in terms of EWH for the first week of year 2002, considering quantum instrumentation (X2.1 noise level) with 3-pairs of inline satellites (IIC3v1 constellation). The Least Squares estimate (regularized up to d/o 120) is reported in the left panel, while the refined gridding estimate is reported in the right panel.

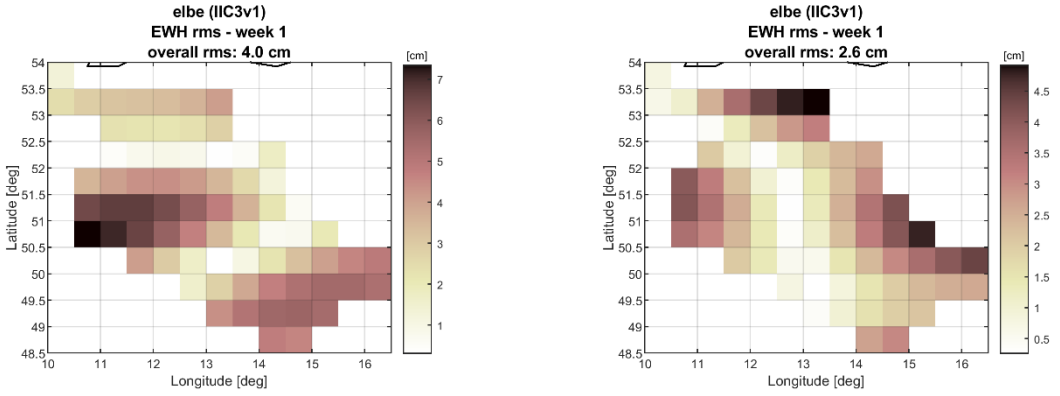

Figure 29-36 Estimation error of TWSA in terms of EWH for the first week of year 2002, considering quantum instrumentation (X2.1 noise level) with 3-pairs of inline satellites (IIC3v1 constellation). The error of the Least Squares estimate (regularized up to d/o 120) is reported in the left panel, while the error of the refined gridding estimate is reported in the right panel.

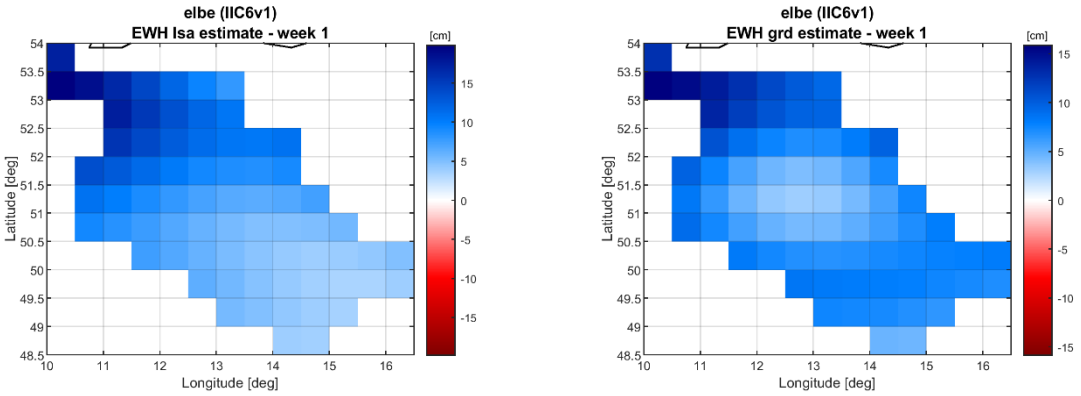

Figure 29-37 TWSA estimate in terms of EWH for the first week of year 2002, considering quantum instrumentation (X2.1 noise level) with 6-pairs of inline satellites (IIC6v1 constellation). The Least Squares estimate (regularized up to d/o 120) is reported in the left panel, while the refined gridding estimate is reported in the right panel.

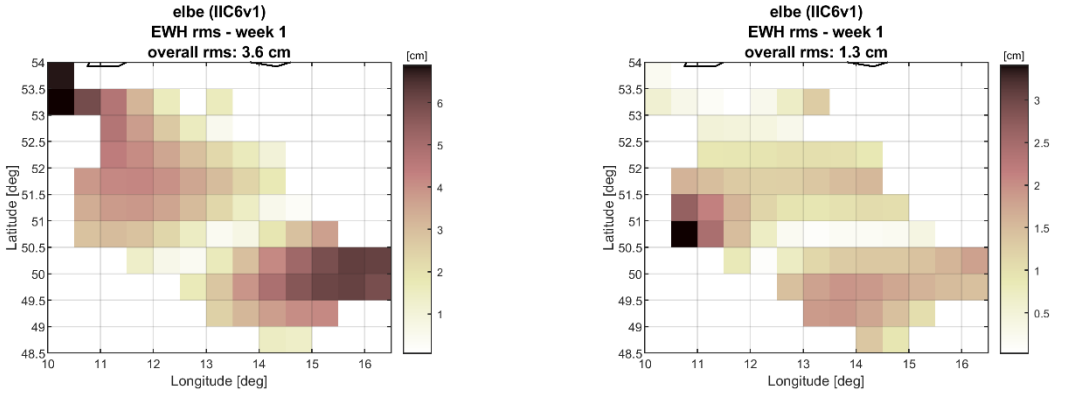

Figure 29-38 Estimation error of TWSA in terms of EWH for the first week of year 2002, considering quantum instrumentation (X2.1 noise level) with 6-pairs of inline satellites (IIC6v1 constellation). The error of the Least Squares estimate (regularized up to d/o 120) is reported in the left panel, while the error of the refined gridding estimate is reported in the right panel.

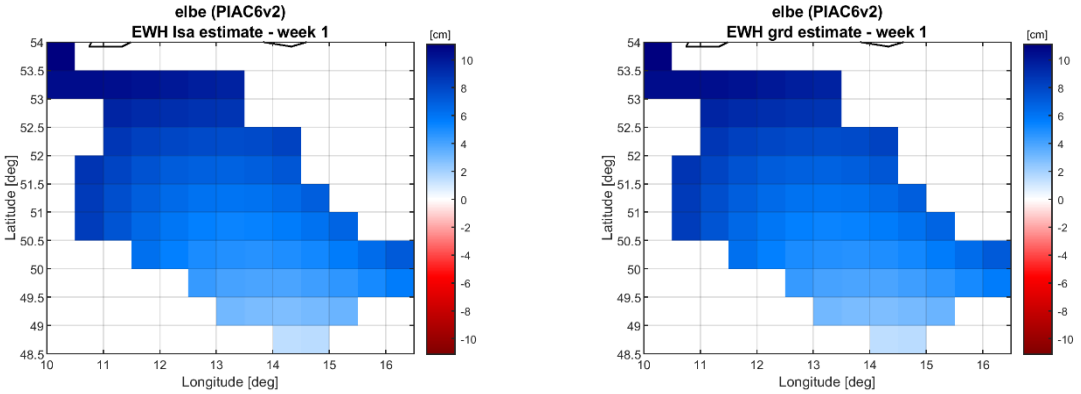

Figure 29-39 TWSA estimate in terms of EWH for the first week of year 2002, considering quantum instrumentation (X2.1 noise level) with 6-pairs of mixed inline and cross-track satellites (PIAC6v2 constellation). The Least Squares estimate (regularized up to d/o 120) is reported in the left panel, while the refined gridding estimate is reported in the right panel.

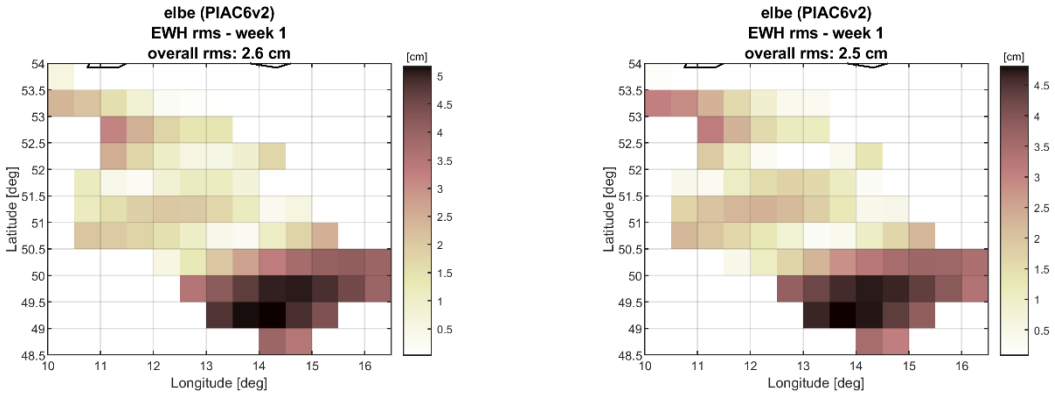

Figure 29-40 Estimation error of TWSA in terms of EWH for the first week of year 2002, considering quantum instrumentation (X2.1 noise level) with 6-pairs of mixed inline and cross-track satellites (PIAC6v2 constellation). The error of the Least Squares estimate (regularized up to d/o 120) is reported in the left panel, while the error of the refined gridding estimate is reported in the right panel.

Ganges

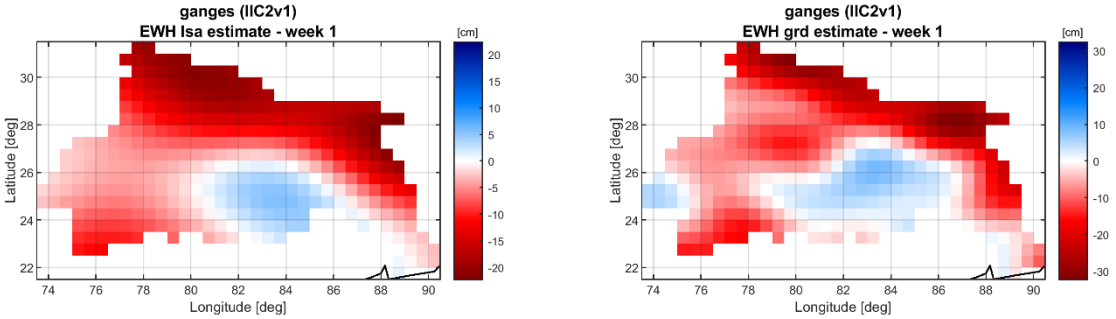

Figure 29-41 TWSA estimate in terms of EWH for the first week of year 2002, considering quantum instrumentation (X2.1 noise level) with 2-pairs of inline satellites (IIC2v1 constellation). The Least Squares estimate (regularized up to d/o 120) is reported in the left panel, while the refined gridding estimate is reported in the right panel.

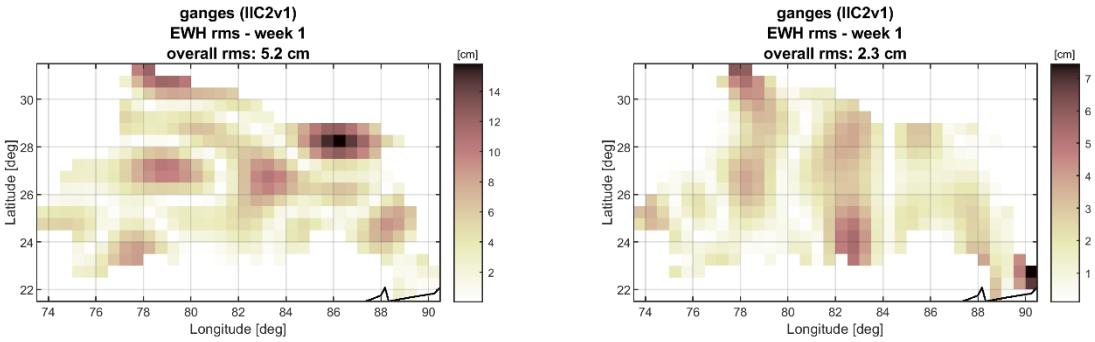

Figure 29-42 Estimation error of TWSA in terms of EWH for the first week of year 2002, considering quantum instrumentation (X2.1 noise level) with 2-pairs of inline satellites (IIC2v1 constellation). The error of the Least Squares estimate (regularized up to d/o 120) is reported in the left panel, while the error of the refined gridding estimate is reported in the right panel.

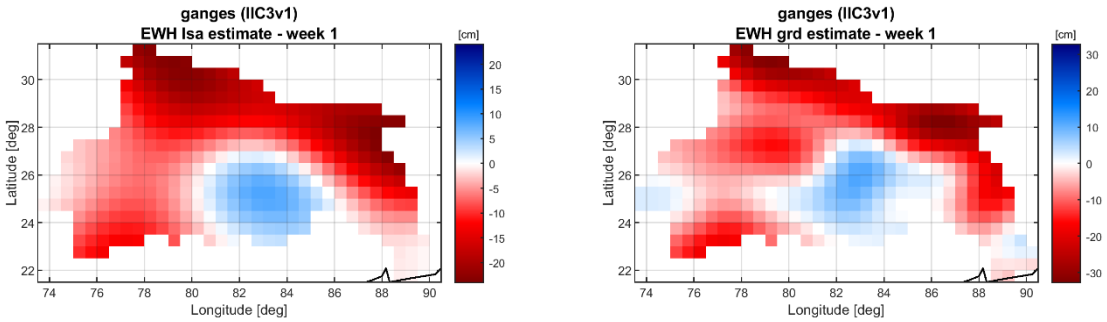

Figure 29-43 TWSA estimate in terms of EWH for the first week of year 2002, considering quantum instrumentation (X2.1 noise level) with 3-pairs of inline satellites (IIC3v1 constellation). The Least Squares estimate (regularized up to d/o 120) is reported in the left panel, while the refined gridding estimate is reported in the right panel.

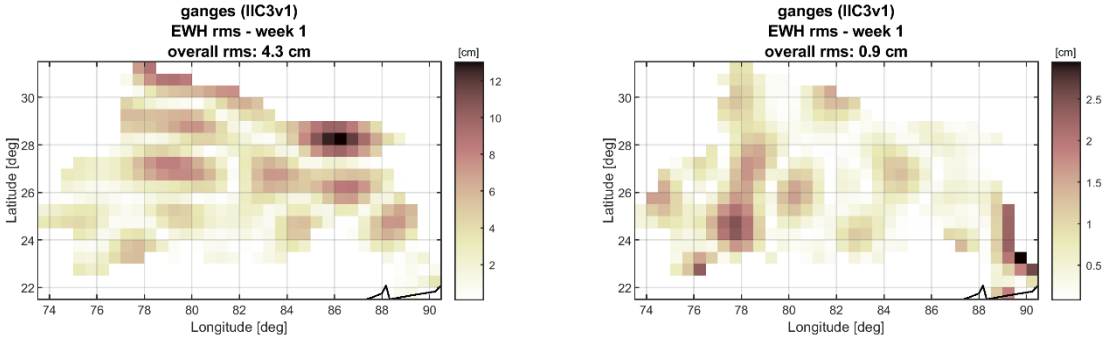

Figure 29-44 Estimation error of TWSA in terms of EWH for the first week of year 2002, considering quantum instrumentation (X2.1 noise level) with 3-pairs of inline satellites (IIC3v1 constellation). The error of the Least Squares estimate (regularized up to d/o 120) is reported in the left panel, while the error of the refined gridding estimate is reported in the right panel.

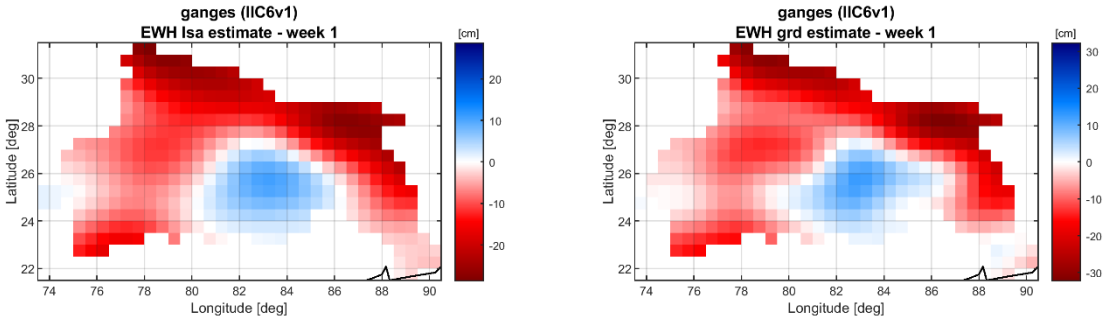

Figure 29-45 TWSA estimate in terms of EWH for the first week of year 2002, considering quantum instrumentation (X2.1 noise level) with 6-pairs of inline satellites (IIC6v1 constellation). The Least Squares estimate (regularized up to d/o 120) is reported in the left panel, while the refined gridding estimate is reported in the right panel.

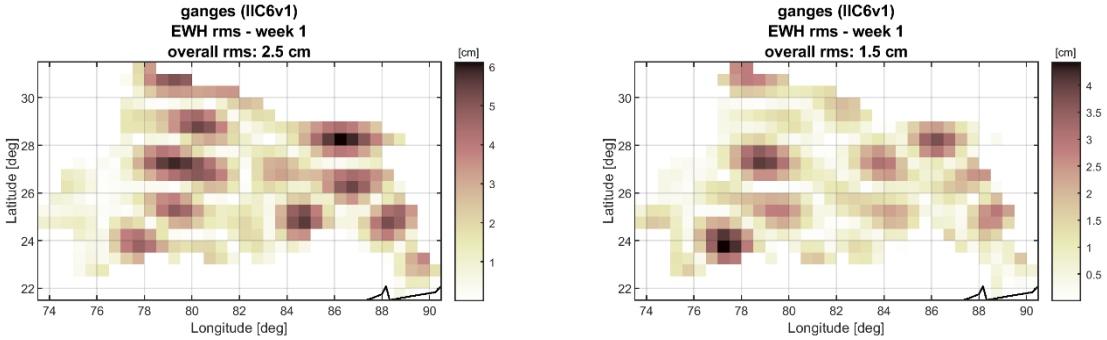

Figure 29-46 Estimation error of TWSA in terms of EWH for the first week of year 2002, considering quantum instrumentation (X2.1 noise level) with 6-pairs of inline satellites (IIC6v1 constellation). The error of the Least Squares estimate (regularized up to d/o 120) is reported in the left panel, while the error of the refined gridding estimate is reported in the right panel.

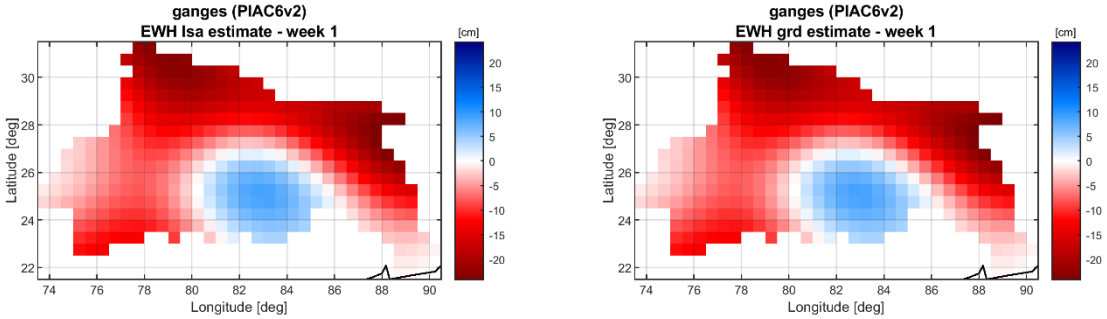

Figure 29-47 TWSA estimate in terms of EWH for the first week of year 2002, considering quantum instrumentation (X2.1 noise level) with 6-pairs of mixed inline and cross-track satellites (PIAC6v2 constellation). The Least Squares estimate (regularized up to d/o 120) is reported in the left panel, while the refined gridding estimate is reported in the right panel.

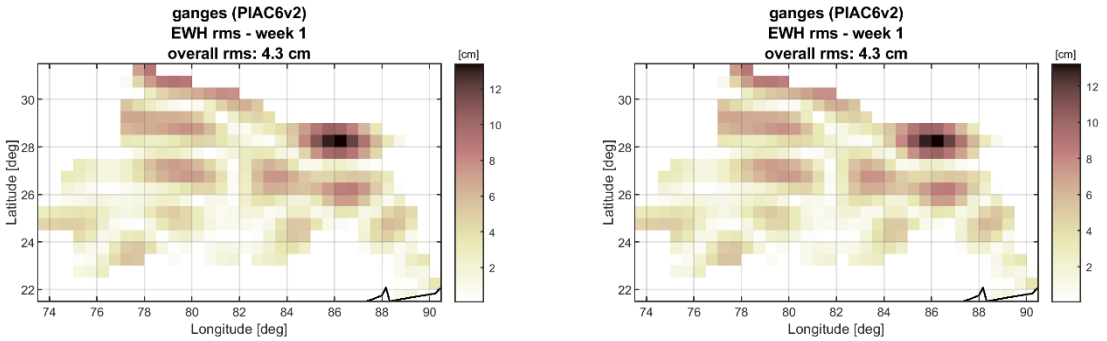

Figure 29-48 Estimation error of TWSA in terms of EWH for the first week of year 2002, considering quantum instrumentation (X2.1 noise level) with 6-pairs of mixed inline and cross-track satellites (PIAC6v2 constellation). The error of the Least Squares estimate (regularized up to d/o 120) is reported in the left panel, while the error of the refined gridding estimate is reported in the right panel.

Oder

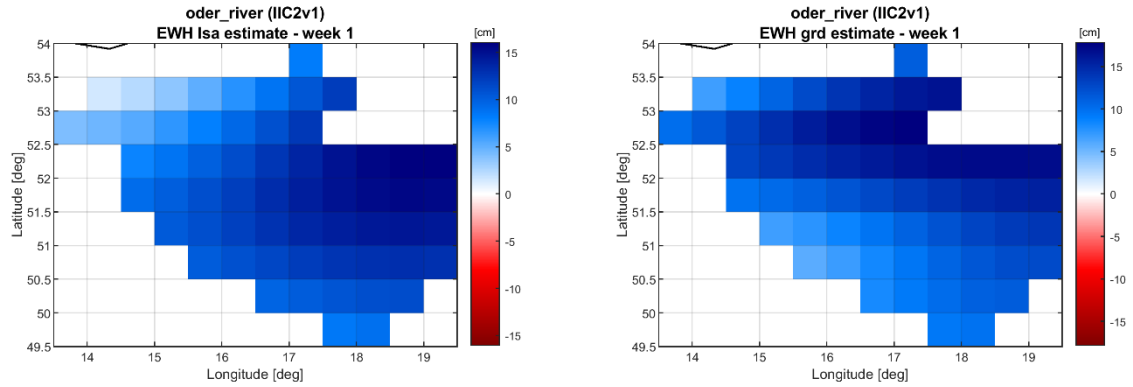

Figure 29-49 TWSA estimate in terms of EWH for the first week of year 2002, considering quantum instrumentation (X2.1 noise level) with 2-pairs of inline satellites (IIC2v1 constellation). The Least Squares estimate (regularized up to d/o 120) is reported in the left panel, while the refined gridding estimate is reported in the right panel.

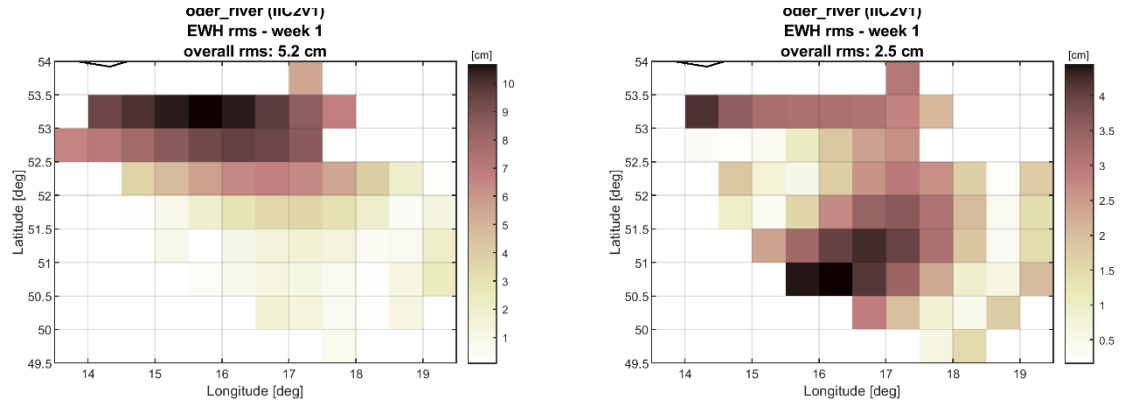

Figure 29-50 Estimation error of TWSA in terms of EWH for the first week of year 2002, considering quantum instrumentation (X2.1 noise level) with 2-pairs of inline satellites (IIC2v1 constellation). The error of the Least Squares estimate (regularized up to d/o 120) is reported in the left panel, while the error of the refined gridding estimate is reported in the right panel.

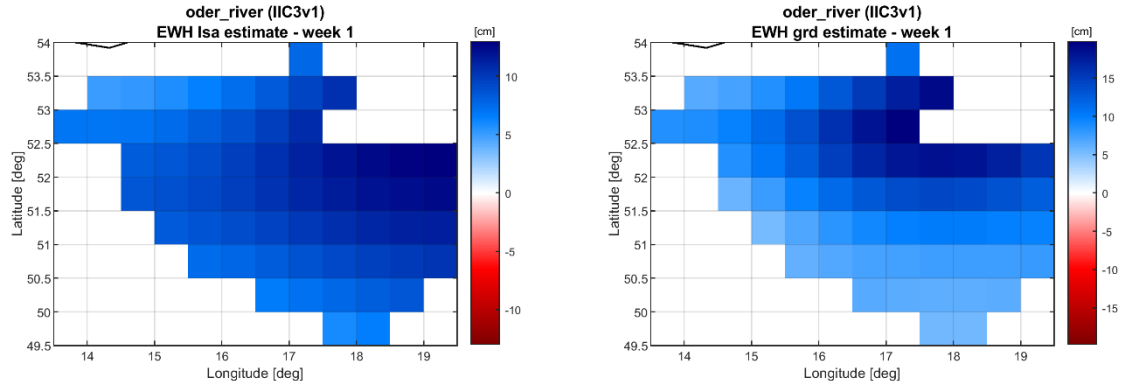

Figure 29-51 TWSA estimate in terms of EWH for the first week of year 2002, considering quantum instrumentation (X2.1 noise level) with 3-pairs of inline satellites (IIC3v1 constellation). The Least Squares estimate (regularized up to d/o 120) is reported in the left panel, while the refined gridding estimate is reported in the right panel.

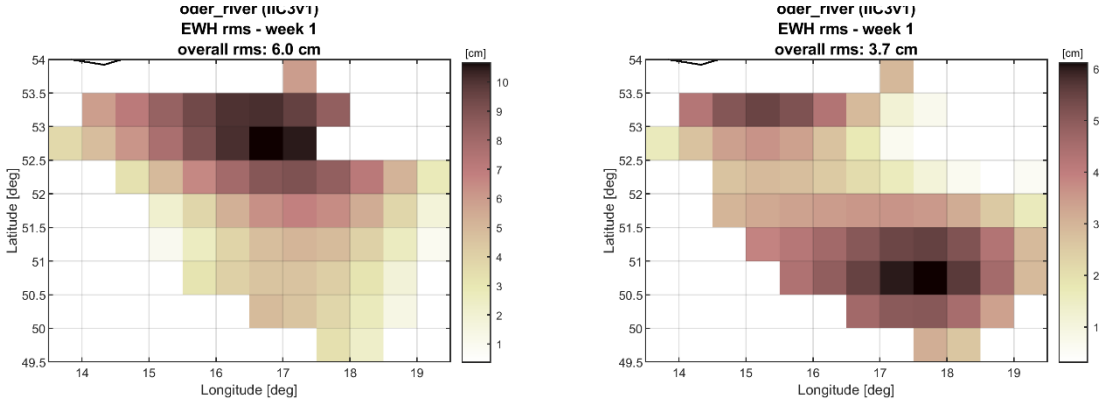

Figure 29-52 Estimation error of TWSA in terms of EWH for the first week of year 2002, considering quantum instrumentation (X2.1 noise level) with 3-pairs of inline satellites (IIC3v1 constellation). The error of the Least Squares estimate (regularized up to d/o 120) is reported in the left panel, while the error of the refined gridding estimate is reported in the right panel.

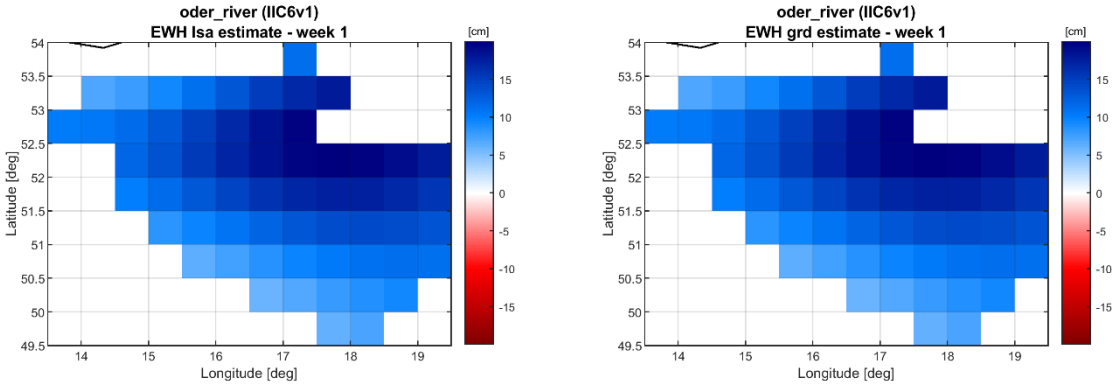

Figure 29-53 TWSA estimate in terms of EWH for the first week of year 2002, considering quantum instrumentation (X2.1 noise level) with 6-pairs of inline satellites (IIC6v1 constellation). The Least Squares estimate (regularized up to d/o 120) is reported in the left panel, while the refined gridding estimate is reported in the right panel.

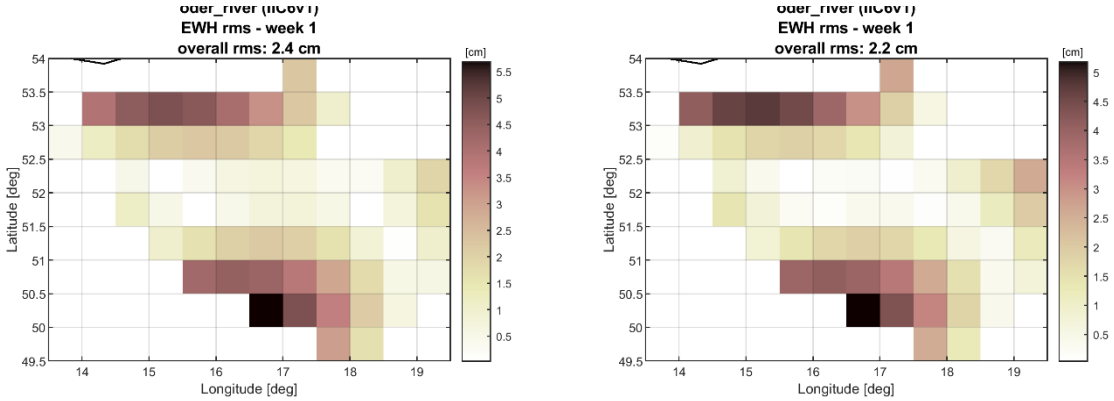

Figure 29-54 Estimation error of TWSA in terms of EWH for the first week of year 2002, considering quantum instrumentation (X2.1 noise level) with 6-pairs of inline satellites (IIC6v1 constellation). The error of the Least Squares estimate (regularized up to d/o 120) is reported in the left panel, while the error of the refined gridding estimate is reported in the right panel.

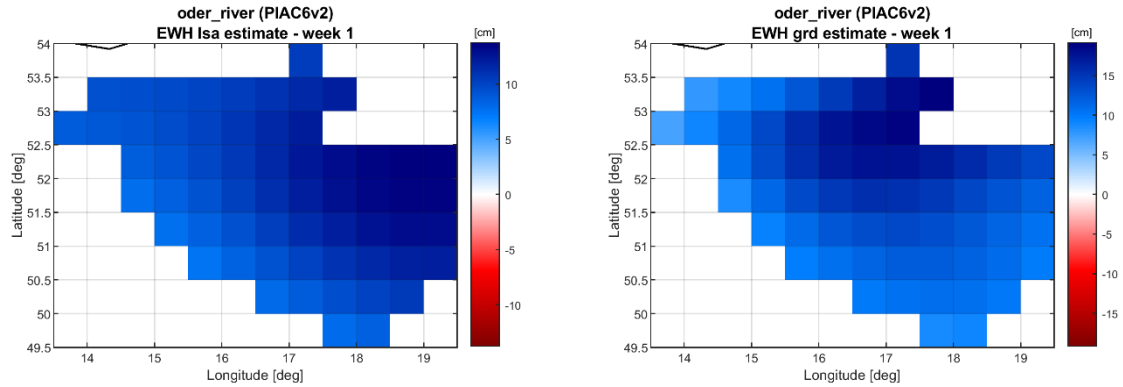

Figure 29-55 TWSA estimate in terms of EWH for the first week of year 2002, considering quantum instrumentation (X2.1 noise level) with 6-pairs of mixed inline and cross-track satellites (PIAC6v2 constellation). The Least Squares estimate (regularized up to d/o 120) is reported in the left panel, while the refined gridding estimate is reported in the right panel.

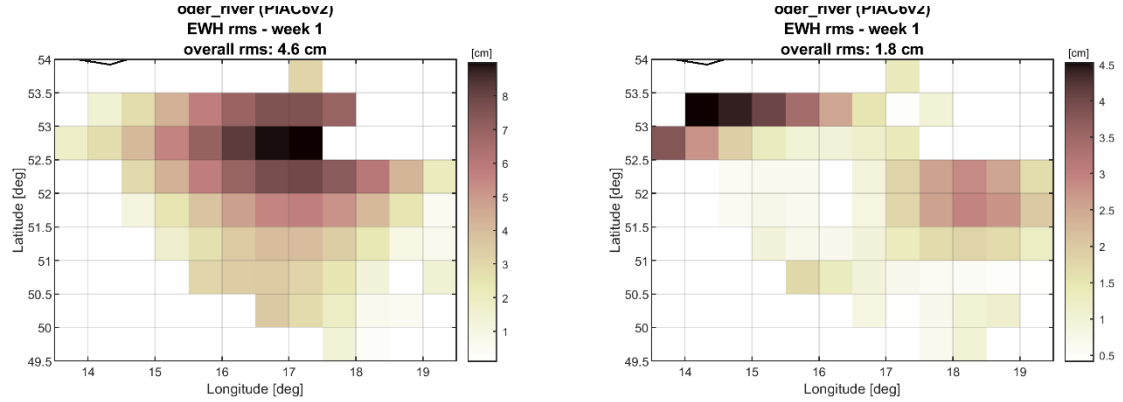

Figure 29-56 Estimation error of TWSA in terms of EWH for the first week of year 2002, considering quantum instrumentation (X2.1 noise level) with 6-pairs of mixed inline and cross-track satellites (PIAC6v2 constellation). The error of the Least Squares estimate (regularized up to d/o 120) is reported in the left panel, while the error of the refined gridding estimate is reported in the right panel.

Rhine

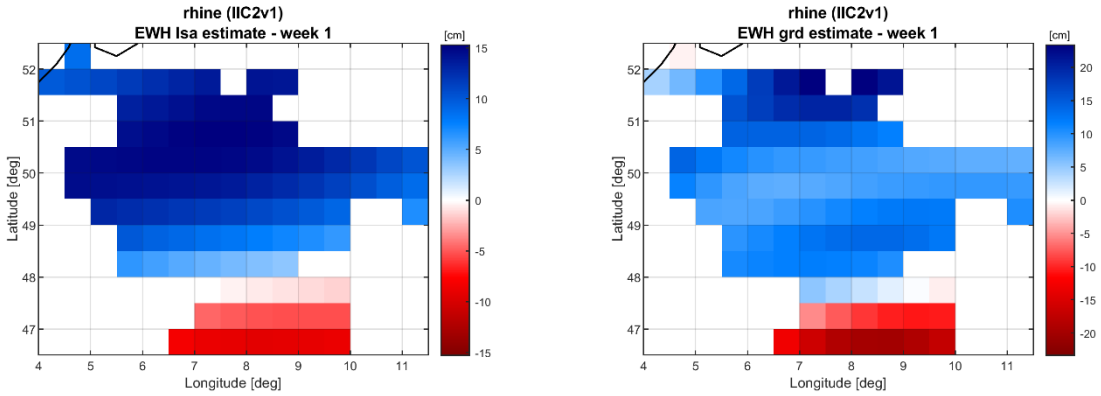

Figure 29-57 TWSA estimate in terms of EWH for the first week of year 2002, considering quantum instrumentation (X2.1 noise level) with 2-pairs of inline satellites (IIC2v1 constellation). The Least Squares estimate (regularized up to d/o 120) is reported in the left panel, while the refined gridding estimate is reported in the right panel.

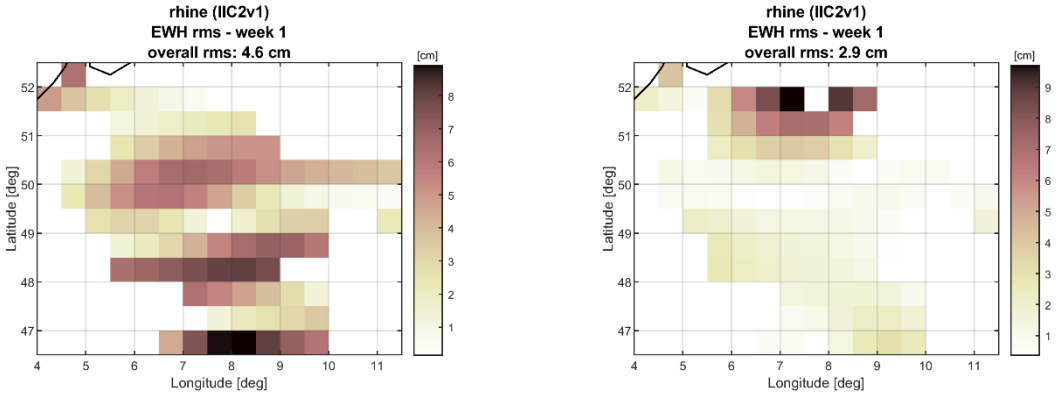

Figure 29-58 Estimation error of TWSA in terms of EWH for the first week of year 2002, considering quantum instrumentation (X2.1 noise level) with 2-pairs of inline satellites (IIC2v1 constellation). The error of the Least Squares estimate (regularized up to d/o 120) is reported in the left panel, while the error of the refined gridding estimate is reported in the right panel.

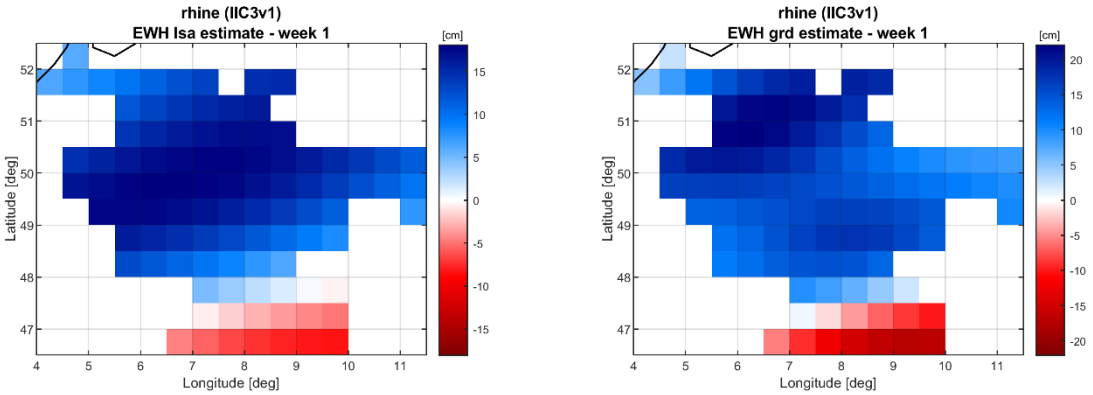

Figure 29-59 TWSA estimate in terms of EWH for the first week of year 2002, considering quantum instrumentation (X2.1 noise level) with 3-pairs of inline satellites (IIC3v1 constellation). The Least Squares estimate (regularized up to d/o 120) is reported in the left panel, while the refined gridding estimate is reported in the right panel.

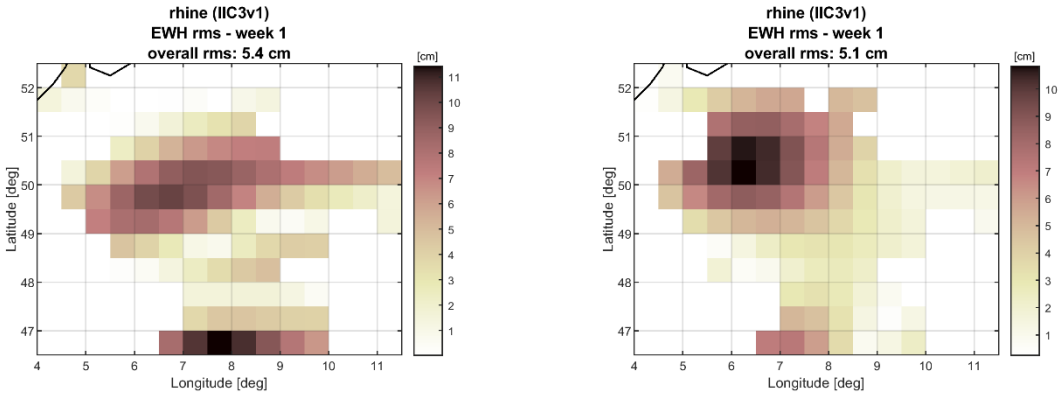

Figure 29-60 Estimation error of TWSA in terms of EWH for the first week of year 2002, considering quantum instrumentation (X2.1 noise level) with 3-pairs of inline satellites (IIC3v1 constellation). The error of the Least Squares estimate (regularized up to d/o 120) is reported in the left panel, while the error of the refined gridding estimate is reported in the right panel.

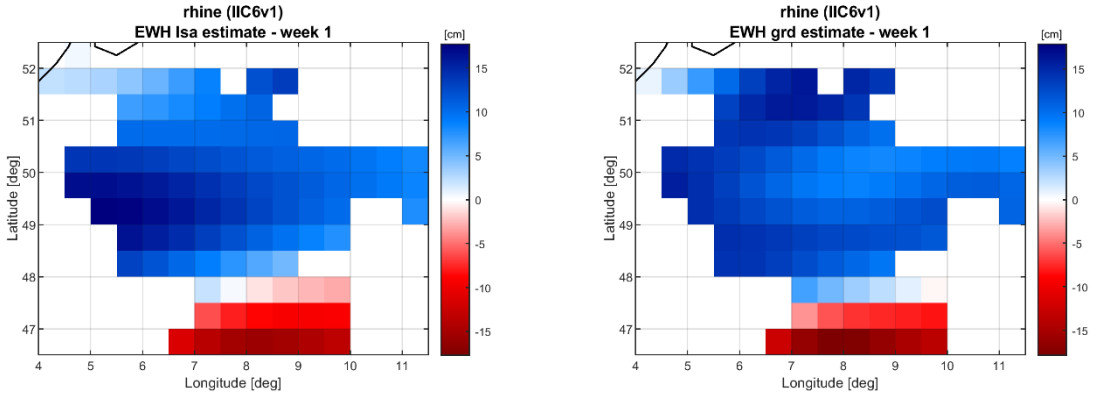

Figure 29-61 TWSA estimate in terms of EWH for the first week of year 2002, considering quantum instrumentation (X2.1 noise level) with 6-pairs of inline satellites (IIC6v1 constellation). The Least Squares estimate (regularized up to d/o 120) is reported in the left panel, while the refined gridding estimate is reported in the right panel.

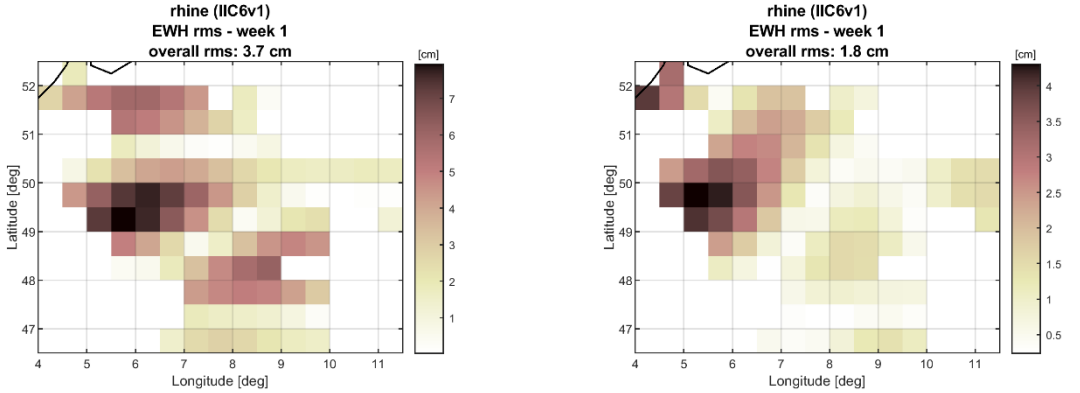

Figure 29-62 Estimation error of TWSA in terms of EWH for the first week of year 2002, considering quantum instrumentation (X2.1 noise level) with 6-pairs of inline satellites (IIC6v1 constellation). The error of the Least Squares estimate (regularized up to d/o 120) is reported in the left panel, while the error of the refined gridding estimate is reported in the right panel.

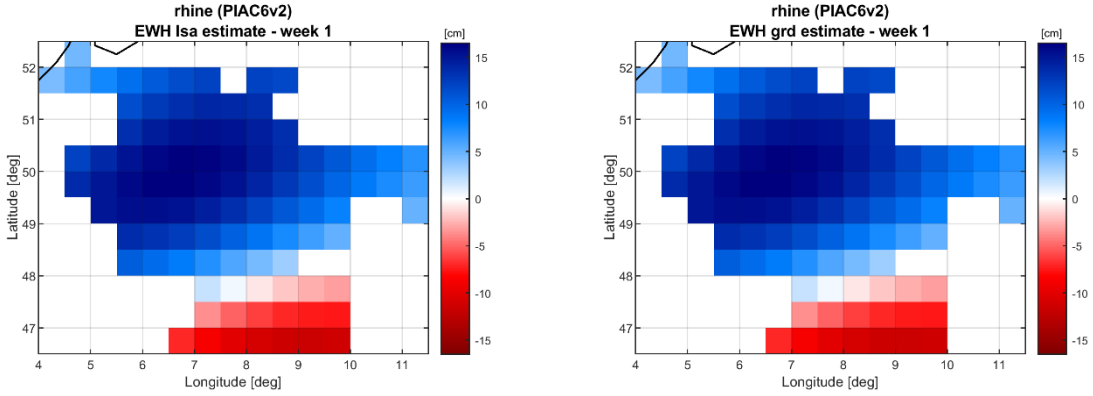

Figure 29-63 TWSA estimate in terms of EWH for the first week of year 2002, considering quantum instrumentation (X2.1 noise level) with 6-pairs of mixed inline and cross-track satellites (PIAC6v2 constellation). The Least Squares estimate (regularized up to d/o 120) is reported in the left panel, while the refined gridding estimate is reported in the right panel.

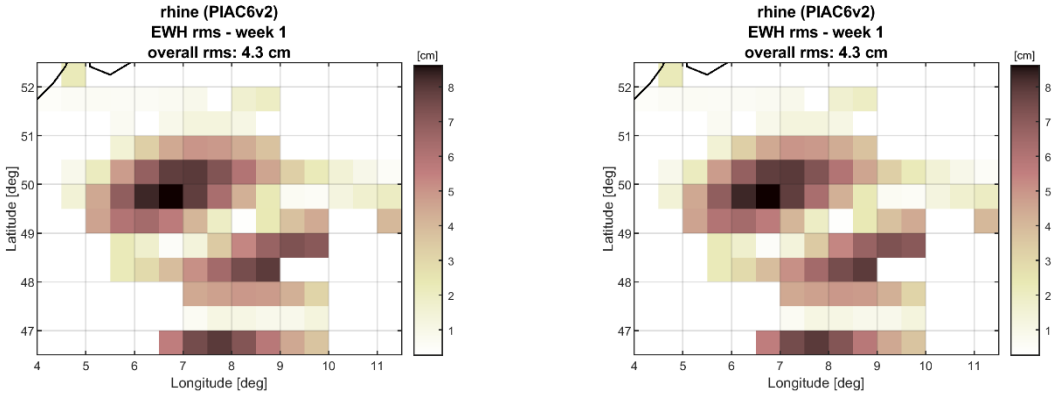

Figure 29-64 Estimation error of TWSA in terms of EWH for the first week of year 2002, considering quantum instrumentation (X2.1 noise level) with 6-pairs of mixed inline and cross-track satellites (PIAC6v2 constellation). The error of the Least Squares estimate (regularized up to d/o 120) is reported in the left panel, while the error of the refined gridding estimate is reported in the right panel.

Uruguay

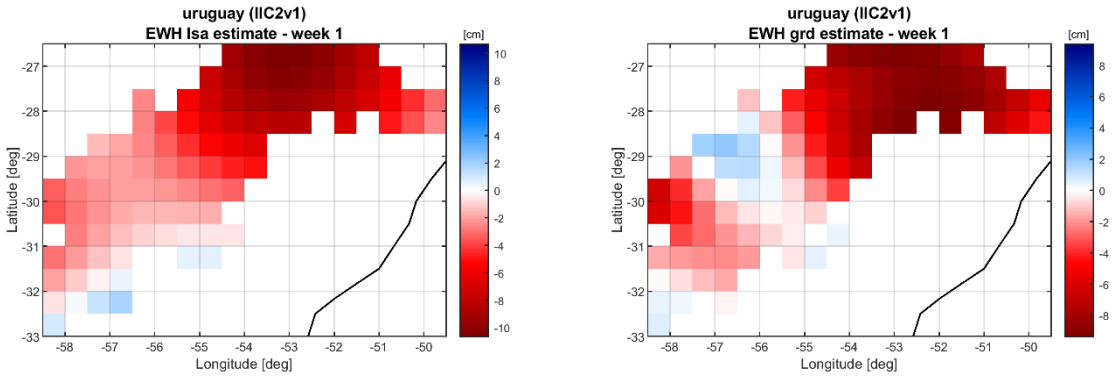

Figure 29-65 TWSA estimate in terms of EWH for the first week of year 2002, considering quantum instrumentation (X2.1 noise level) with 2-pairs of inline satellites (IIC2v1 constellation). The Least Squares estimate (regularized up to d/o 120) is reported in the left panel, while the refined gridding estimate is reported in the right panel.

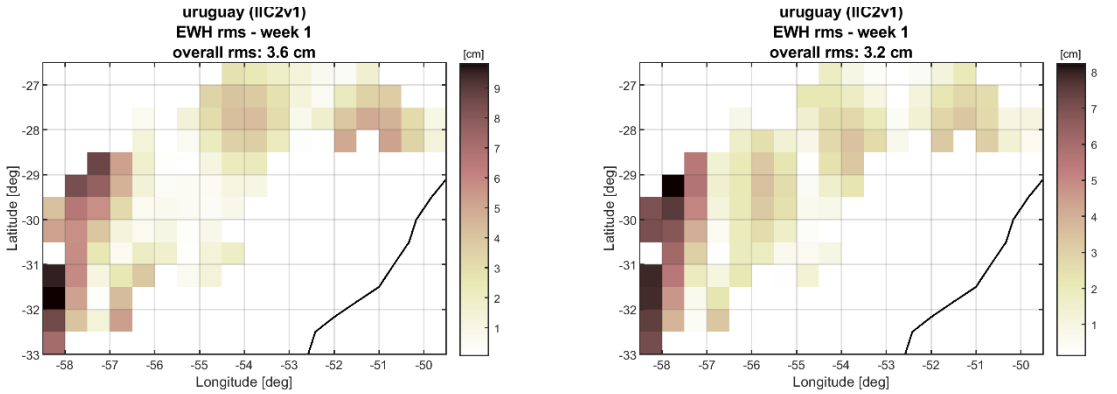

Figure 29-66 Estimation error of TWSA in terms of EWH for the first week of year 2002, considering quantum instrumentation (X2.1 noise level) with 2-pairs of inline satellites (IIC2v1 constellation). The error of the Least Squares estimate (regularized up to d/o 120) is reported in the left panel, while the error of the refined gridding estimate is reported in the right panel.

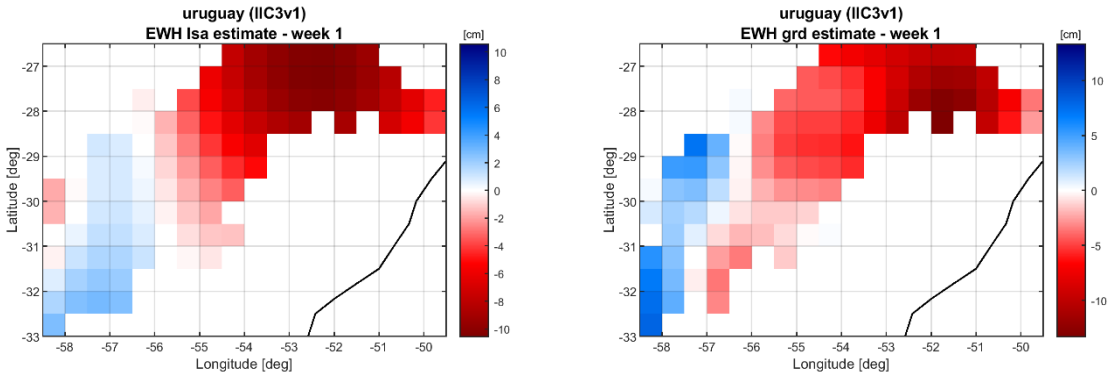

Figure 29-67 TWSA estimate in terms of EWH for the first week of year 2002, considering quantum instrumentation (X2.1 noise level) with 3-pairs of inline satellites (IIC3v1 constellation). The Least Squares estimate (regularized up to d/o 120) is reported in the left panel, while the refined gridding estimate is reported in the right panel.

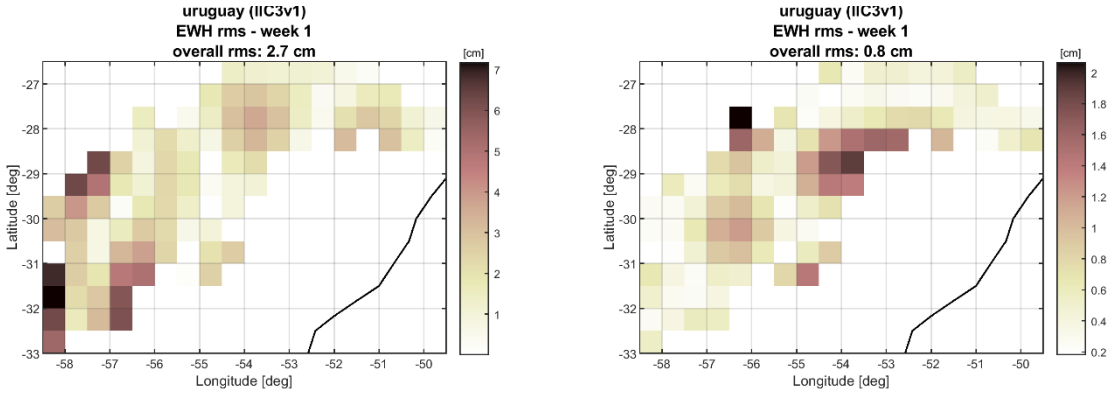

Figure 29-68 Estimation error of TWSA in terms of EWH for the first week of year 2002, considering quantum instrumentation (X2.1 noise level) with 3-pairs of inline satellites (IIC3v1 constellation). The error of the Least Squares estimate (regularized up to d/o 120) is reported in the left panel, while the error of the refined gridding estimate is reported in the right panel.

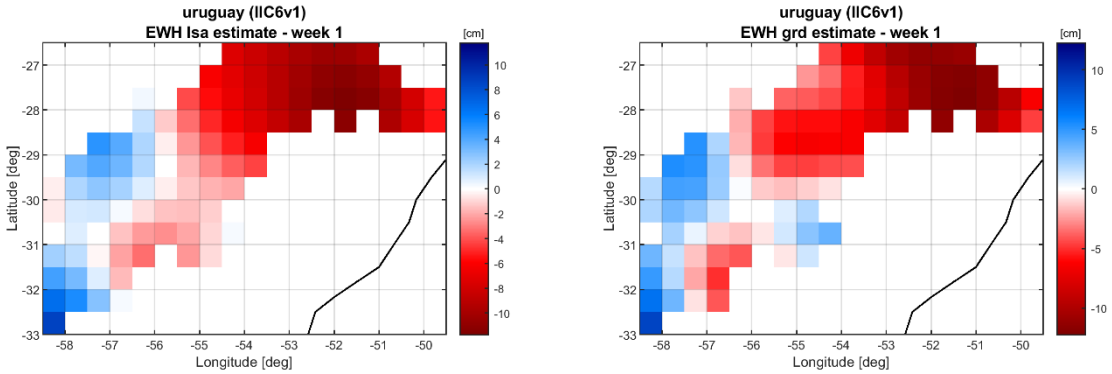

Figure 29-69 TWSA estimate in terms of EWH for the first week of year 2002, considering quantum instrumentation (X2.1 noise level) with 6-pairs of inline satellites (IIC6v1 constellation). The Least Squares estimate (regularized up to d/o 120) is reported in the left panel, while the refined gridding estimate is reported in the right panel.

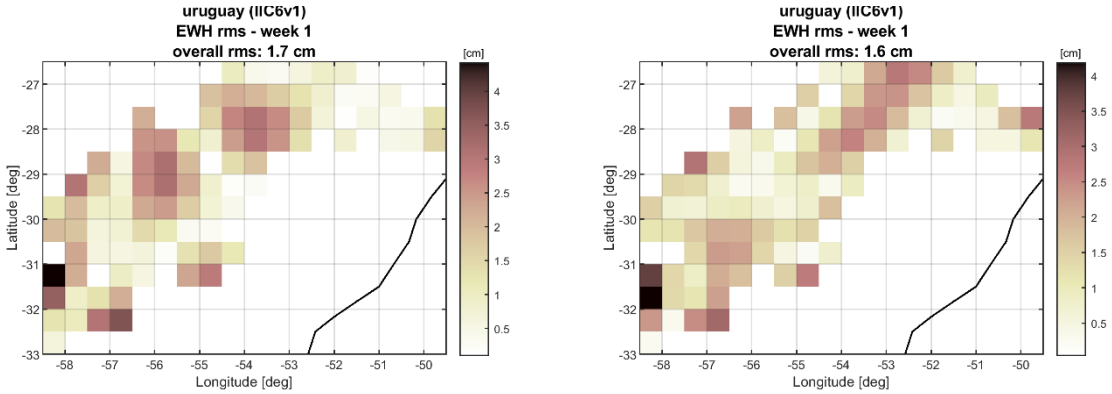

Figure 29-70 Estimation error of TWSA in terms of EWH for the first week of year 2002, considering quantum instrumentation (X2.1 noise level) with 6-pairs of inline satellites (IIC6v1 constellation). The error of the Least Squares estimate (regularized up to d/o 120) is reported in the left panel, while the error of the refined gridding estimate is reported in the right panel.

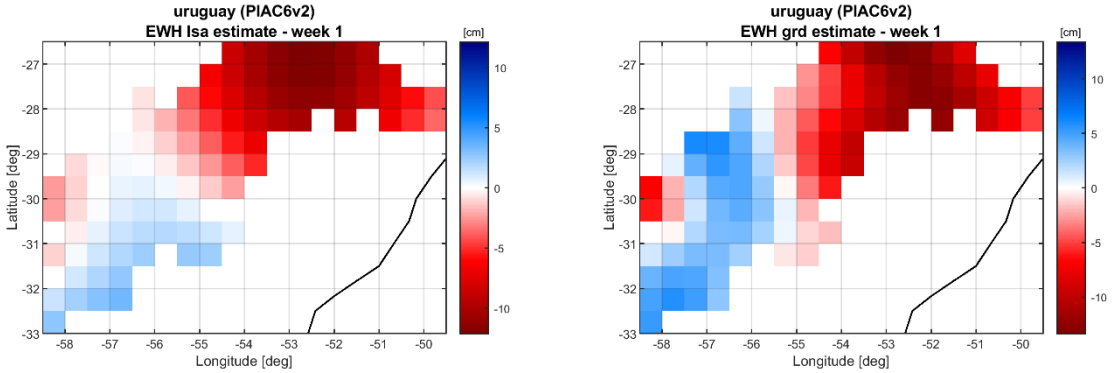

Figure 29-71 TWSA estimate in terms of EWH for the first week of year 2002, considering quantum instrumentation (X2.1 noise level) with 6-pairs of mixed inline and cross-track satellites (PIAC6v2 constellation). The Least Squares estimate (regularized up to d/o 120) is reported in the left panel, while the refined gridding estimate is reported in the right panel.

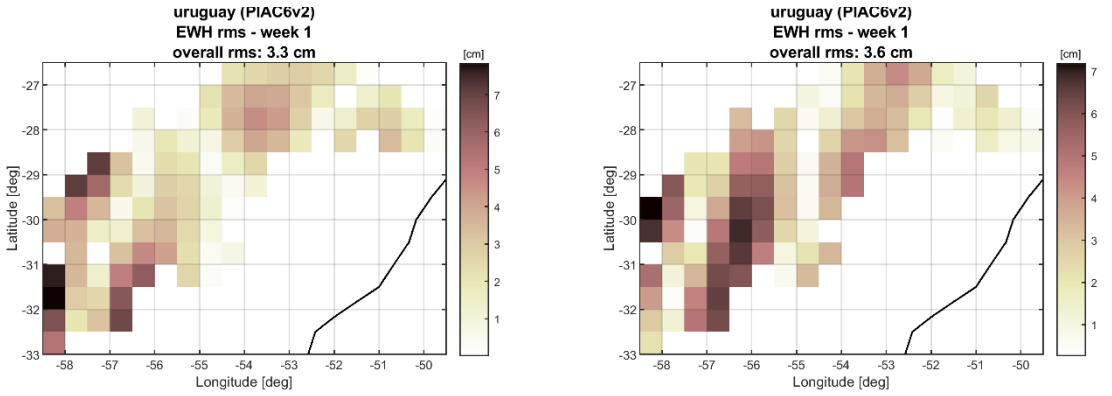

Figure 29-72 Estimation error of TWSA in terms of EWH for the first week of year 2002, considering quantum instrumentation (X2.1 noise level) with 6-pairs of mixed inline and cross-track satellites (PIAC6v2 constellation). The error of the Least Squares estimate (regularized up to d/o 120) is reported in the left panel, while the error of the refined gridding estimate is reported in the right panel.

The previous figures clearly show that the local solutions can generally increase the retrieval accuracy of the time-variable gravity field, as well as the spatial resolution with respect to the

global Least Squares adjustment. The average retrieval error for each region and each constellation is reported in Table 29-1 and Table 29-2 for the global and local solutions, respectively. The improvement carried by local solutions is presented in Table 29-3, where it can be seen that the average improvement obtained by local solutions is about 30%.

Table 29-1: Average estimation error of least squares global solution for each of the considered region and constellation.

	IIC2v1	IIC3v1	IIC6v1	PIAC6v2
Amazon	5.6 cm	4.8 cm	2.8 cm	4.9 cm
Danube	2.9 cm	2.6 cm	1.6 cm	2.4 cm
East China Sea	3.9 cm	2.6 cm	4.1 cm	3.0 cm
Elbe	4.1 cm	4.0 cm	3.6 cm	2.6 cm
Ganges	5.2 cm	4.3 cm	2.5 cm	4.3 cm
Oder	5.2 cm	6.0 cm	2.4 cm	4.6 cm
Rhine	4.6 cm	5.4 cm	3.7 cm	4.3 cm
Uruguay	3.6 cm	2.7 cm	1.7 cm	3.3 cm

Table 29-2: Average estimation error of local gridding solution for each of the considered region and constellation.

	IIC2v1	IIC3v1	IIC6v1	PIAC6v2
Amazon	3.1 cm	1.0 cm	0.5 cm	3.1 cm
Danube	1.8 cm	1.9 cm	1.1 cm	1.9 cm
East China Sea	4.0 cm	2.0 cm	2.8 cm	3.0 cm
Elbe	2.0 cm	2.6 cm	1.3 cm	2.5 cm
Ganges	2.3 cm	0.9 cm	2.5 cm	4.3 cm
Oder	2.5 cm	3.7 cm	2.2 cm	1.8 cm
Rhine	2.9 cm	5.1 cm	1.8 cm	4.3 cm
Uruguay	3.2 cm	0.8 cm	1.6 cm	3.6 cm

Table 29-3: Average improvement of the local gridding solution with respect to the global least squares solution for each of the considered region and constellation.

	IIC2v1	IIC3v1	IIC6v1	PIAC6v2
Amazon	45%	79%	82%	37%
Danube	38%	27%	31%	21%
East China Sea	-3%	23%	32%	0%
Elbe	51%	35%	64%	4%
Ganges	56%	79%	0%	0%
Oder	52%	38%	8%	61%
Rhine	37%	6%	51%	0%
Uruguay	11%	70%	6%	-9%

Moreover, a general improvement can be seen when more satellite pairs are introduced into the constellation. However, in agreement with the outcomes of WP422 and WP622, using cross-

track observations is not beneficial. In fact, comparing the statistics for the PIAC6v2 and for the IIC6v1 orbit configurations, the former is always worse than the latter.

Solid Earth applications

For solid Earth applications we focused on the Bengkulu Earthquake. As for the background model, only the signal of the earthquake is introduced. Ideally, the capability of retrieving this kind of signal rather than isolating is tested at this level. Due to the different resolution of the considered phenomena, the output resolution of the grid is 0.1°. For each of the considered orbit configurations the Least Square global solutions are compared to the local gridding solutions, as well as their empirical errors. This comparison is performed on the signal of the first week after the Earthquake. The reference signal (expressed in terms of first radial derivative at 10 km altitude) is shown in Figure 29-73 and is computed from a model provided in terms of spherical harmonic coefficients up to degree 1439. The computed solutions (both by a global and local approach) are shown in Figure 29-74, Figure 29-75, and Figure 29-76.

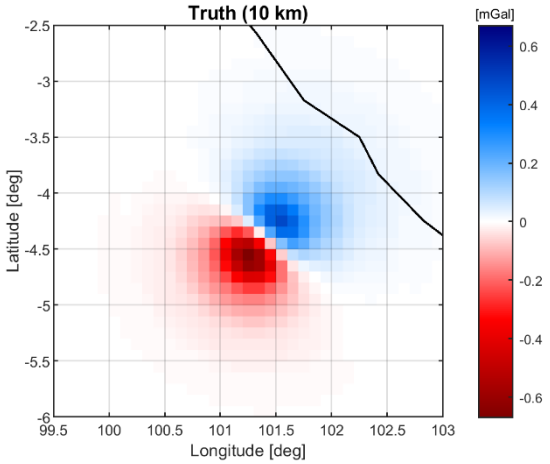

Figure 29-73 Gravitational signal of Bengkulu earthquake, expressed as first radial derivative computed at 10 km altitude for the first week after the event.

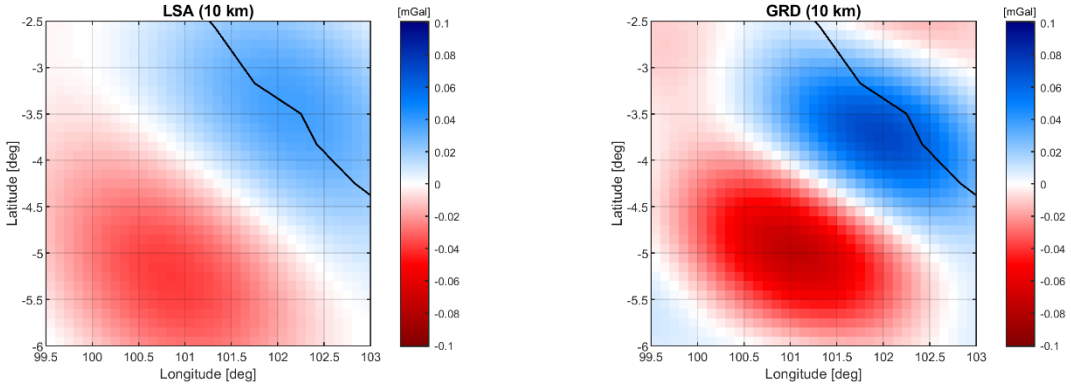

Figure 29-74 Estimated first radial derivative in the region of the Bengkulu earthquake for the first week after the event, considering the 2-pair orbit constellation (IIC2v1). In the left column the Least Squares global solution, in right column the local gridding solutions.

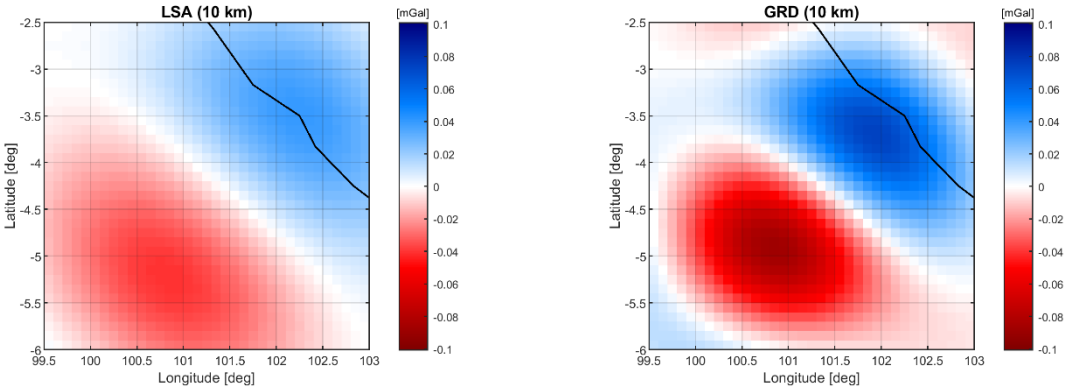

Figure 29-75 Estimated first radial derivative in the region of the Bengkulu earthquake for the first week after the event, considering the 3-pair orbit constellation (IIC3v1). In the left column the least squares global solution, in right column the local gridding solutions.

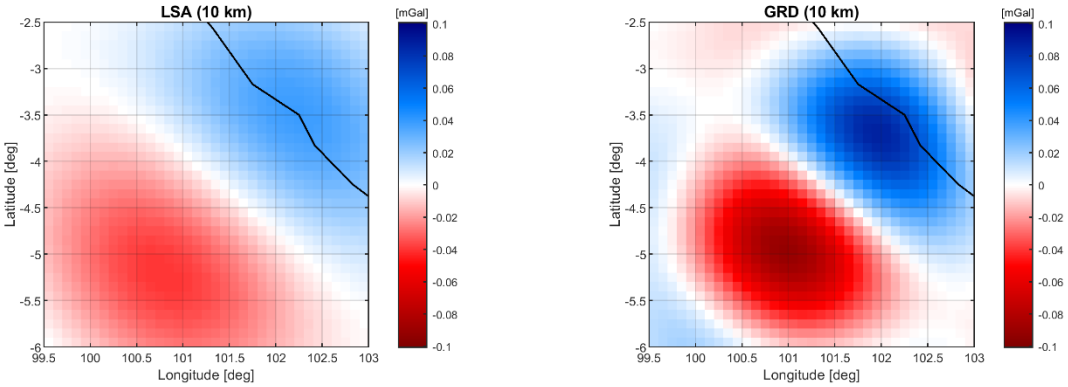

Figure 29-76 Estimated first radial derivative in the region of the Bengkulu earthquake for the first week after the event, considering the 6-pair orbit constellation (IIC6v1). In the left column the least squares global solution, in right column the local gridding solutions.

The empirical RMS error of the estimated solutions can be evaluated (by a Monte Carlo procedure) by comparing the results of Figure 29-74, Figure 29-75, and Figure 29-76, with the true signal of Figure 29-73. The spatial distribution of the computed RMSE is shown in Figure 29-77, Figure 29-78, and Figure 29-79.

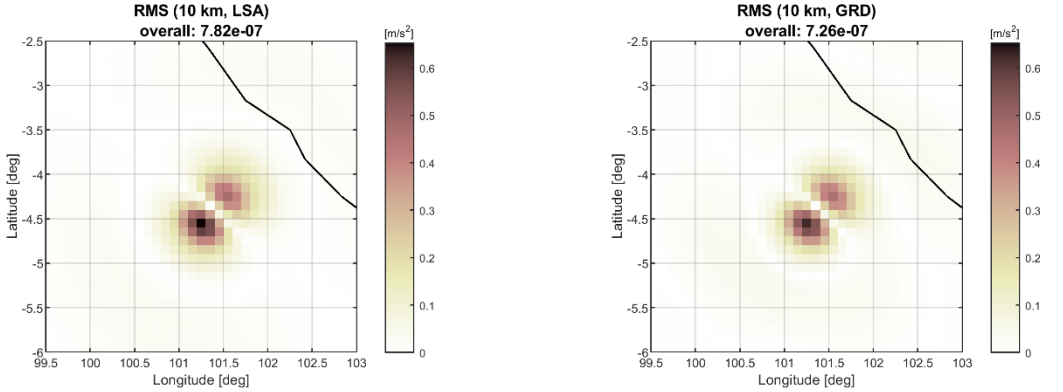

Figure 29-77 RMSE of the estimated first radial derivative in the region of the Bengkulu earthquake for the first week after the event, considering the 2-pair orbit constellation (IIC2v1). In the left column the least squares global solution, in right column the local gridding solutions.

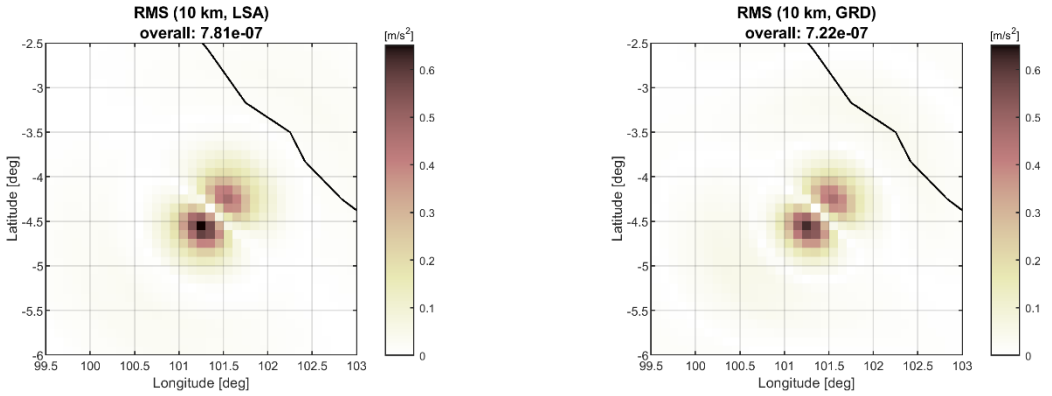

Figure 29-78 RMSE of the estimated first radial derivative in the region of the Bengkulu earthquake for the first week after the event, considering the 3-pair orbit constellation (IIC3v1). In the left column the least squares global solution, in right column the local gridding solutions.

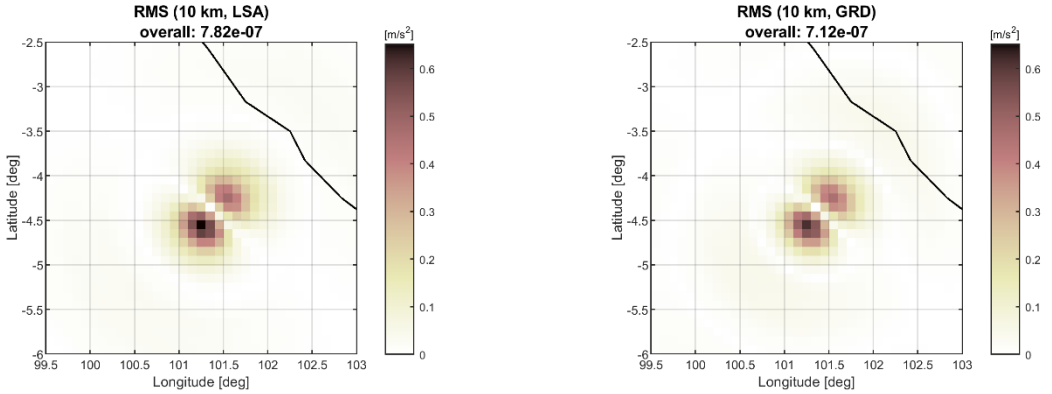

Figure 29-79 RMSE of the estimated first radial derivative in the region of the Bengkulu earthquake for the first week after the event, considering the 6-pair orbit constellation (IIC6v1). In the left column the least squares global solution, in right column the local gridding solutions.

Comparing Figure 29-73 with Figure 29-77, Figure 29-78, and Figure 29-79 it is clear that the main contributor to the estimation error is the omitted high frequency signal that is not retrievable due to the satellite altitude and the instrumental accuracy. To empirically evaluate the intrinsic spatial resolution (in terms of spherical harmonic degree) of the estimated signal, a comparison of the estimated signal with the reference signal computed up to an increasing spherical harmonic degree was performed. The results of this comparison are reported in Figure 29-80. Here, we can see the harmonic degree for which the estimation error is minimum, representing the intrinsic spatial resolution of the solution. Above this optimal harmonic degree, the omission error due to the higher spatial resolution of the reference starts dominating the overall error. This minimum point is always around 120 considering the global solutions. This happens because 120 is the maximum harmonic degree of the computed Least Squares solutions, chosen for computational reasons. Moreover, it is not guaranteed that the earthquake signal is globally strong enough to allow a Least Squares estimation up to a much higher harmonic degree. As for the local solutions, the minimum point is in the range 150-180, depending on the number of satellite pairs. This means that the local solutions can increase the spatial resolution from about 1.5° to 1°. In general, one can see that increasing the number of satellite pairs there is an improvement in the estimation accuracy, as well as a slight improvement in the spatial resolution at which the phenomenon can be seen.

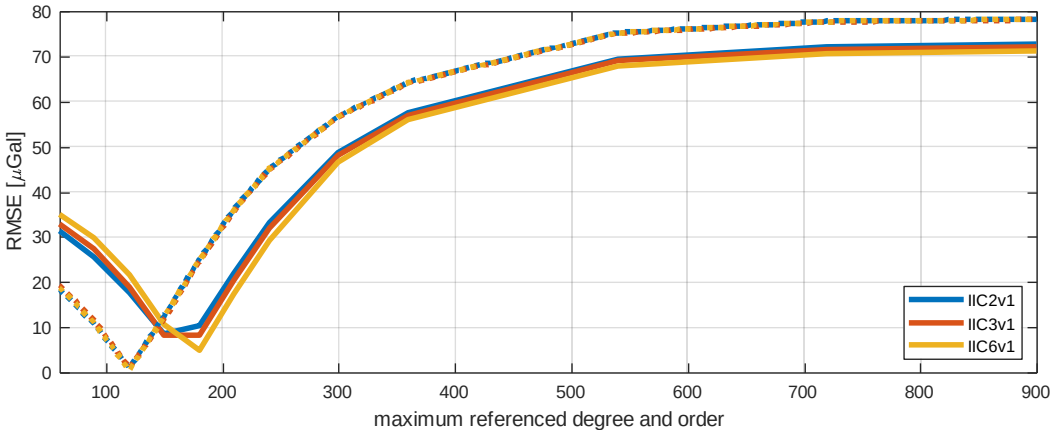

Figure 29-80 Overall RMSE of the estimated first radial derivative grid at 10 km altitude for the first week after the earthquake, considering the global solution. The empirical RMSE is represented as a function of the maximum degree used to synthetise the true reference signal. Dotted lines represent the global Least Squares solution, solid lines represent the local collocation solution. Colours represent different orbit configurations according to the legend.

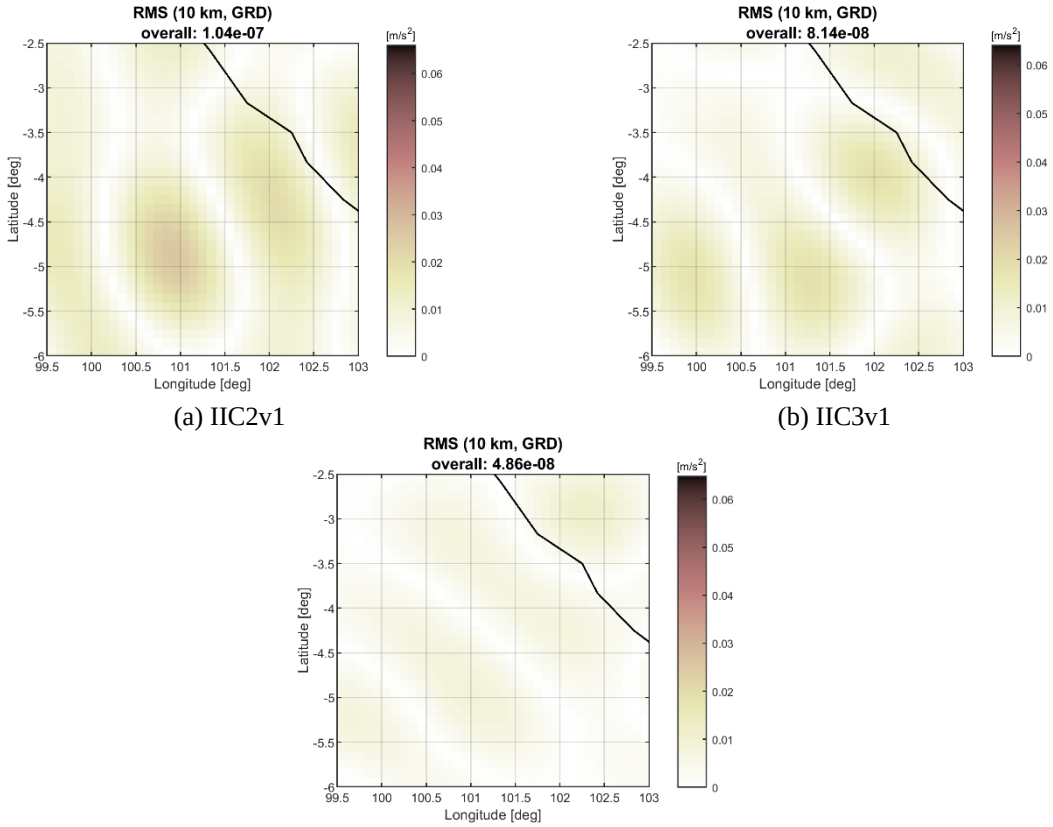

(a) IIC2v1

(b) IIC3v1

(c) IIC6v1

Figure 29-81 RMS error spatial distribution of the local solutions for the first week after the Bengkulu earthquake for (a) IIC2v1, (b) IIC3v1, and (c) IIC6v1 constellations. The reference signal to evaluate the error is synthetised up to harmonic d/o 180, to limit as much as possible the impact of the omitted signal. Units of the plots is m/s2.

30. APPLICABLE DOCUMENTS, REFERENCE DOCUMENTS, AND PUBLICATIONS TO PART 5

30.1. APPLICABLE DOCUMENTS

[AD-1] Mission Requirements Document, Next Generation Gravity Mission as a Mass-change And Geosciences International Constellation (MAGIC) - A joint ESA/NASA double-pair mission based on NASA's MCDO and ESA's NGGM studies (2020). ESA-EOPSM-FMCC-MRD-3785

[AD2] Scientific Readiness Levels (SRL) Handbook, Issue 1, Revision 0, 05-08-2015

[AD3] Study of Cold Atom Interferometry (CAI) Gravity Gradiometer Sensor and Mission Concepts - ESA Contract 4000112677, Summary Report "Concept study and preliminary design of a cold atom interferometer for space gravity gradiometry"

[AD4] Cold Atom Inertial Sensors: Mission Applications – ESA Contract 4000117930, Final Report TASI-SD-CAI-FR

[AD5] Hybrid Atom Electrostatic System for Satellite Geodesy – ESA Contract 4000113573, Final Report RF_7-24721_DMPH

[AD6] Hybrid Atom Electrostatic System for Satellite Geodesy Follow-On – ESA Contract 4000112290, Final Report RT 6/27346 DPHY

[AD7] QSG_UR_SATM_v2.0.xlsx – ESA/EC Quantum Space Gravimetry User Requirements Science and Traceability Matrix v2.0 (2022)

[AD8] Quantum Space Gravimetry for monitoring Earth's Mass Transport Processes (QSG4EMT). Project Proposal, Proposal No. TUM/2022-QSG4EMT, Technical University of Munich

30.2. REFERENCE DOCUMENTS

[RD-1] Deccia, C.M.A.; Wiese, D.N.; Nerem, R.S. Using a Multiobjective Genetic Algorithm to Design Satellite Constellations for Recovering Earth System Mass Change. Remote Sens. 2022, 14, 3340. https://doi.org/10.3390/rs14143340

[RD-2] Horvath, A., Murböck, M., Pail, R., Horwath, M. (2018): Decorrelation of GRACE Time Variable Gravity Field Solutions Using Full Covariance Information. - Geosciences, 8, 9, 323. https://doi.org/10.3390/geosciences8090323

[RD-3] Zingerle, P.; Gruber, T.; Pail, R.; Daras, I. Constellation design and performance of future quantum satellite gravity missions. Earth Planets Space 76, 101 (2024). https://doi.org/10.1186/s40623-024-02034-3

PART 6:

PRELIMINARY QSG MISSION REQUIREMENTS AND THEIR ASSESSMENT AGAINST QSG USER REQUIREMENTS

31. INTRODUCTION

The original purpose of this part as foreseen in the SoW and the project proposal was to describe in this document the QSG mission requirements and their assessment against QSG user requirements from various QSG architectures, such as LL-SST and gradiometry, referring to Task 4, 5, 6 and 7 of the SoW and WPs 400 to 700 of the WBS. However, at the MS2 it was decided that the formulation of mission requirements and thus the corresponding WPs 480, 580 and 670 (mission requirements for various scenarios) can be skipped, because of the results obtained in this project. Consequently, also the main motivation for and the main contents of this document have become obsolete. Instead of deriving the mission requirements directly from the simulations, the assumed requirements are taken directly from WP100 (TR D2) where fictive, but supposedly realistic, performance numbers were estimated for the user questionnaire.

	Daily [cm]		Weekly [cm]		Monthly [cm]		Trend [cm/yr]
	600km	300km	300km	150km	300km	150km	150km
GRACE-FO	4.0	-	4.0	-	2.0	5.0	0.10
MAGIC	2.0	5.3	2.0	5.0	1.0	2.5	0.05
QSG4EMT (Baseline 1)	**1.0**	**2.7**	**1.0**	**2.5**	**0.5**	**1.3**	**0.03**
QSG4EMT (Baseline 2)	**0.5**	**1.3**	**0.5**	**1.3**	**0.3**	**0.6**	**0.01**

Figure 31-1: Accuracies of hypothetical mission scenarios as basis for the fictive mission requirements in terms of global RMS of EWH for different resolutions (taken from WP100).

The performance numbers (i.e., mission requirements) from WP100 of two (fictive) QSG baseline scenarios are provided in Figure 31-1. Even though these numbers are estimates, they seem very much in reach for the two actually investigated baseline scenarios IIC3v1 and IIC6v1. Using the conventional (static) gravity processing strategy, these numbers are slightly missed (see D5). However, it can be assumed that with an improved processing (stochastic modelling and a time-aware parameterization) these requirements can be met for both scenarios.

Results of work packages that are not directly related to the mission requirements are still reported in this document.

32. QSG MISSION REQUIREMENTS FOR LL-SST WITH 3D HYBRID ACCELEROMETER

32.1. TRADE-SPACE DEFINITION OF DIFFERENT LL-SST ARCHITECTURES & SELECTION OF SCENARIOS (WP410)

The tradespace for quantum space gravimetry is defined in discussed in very much detail in D5. This includes also the trade-space definition of different ll-SST architectures.

For ll-SST, we investigated constellations of 3 to 6 pairs. We found out that the inclination is the driving factor for the de-aliasing capabilities of the constellation. Based on a MAGIC-type Bender constellation, a third pair should be injected in an inclination of 40-45° for the best global performance of a triple-pair constellation.

Additionally, we investigated the potential of a new observation concept, which is across-track ranging. The underlying idea is that the cross-track component is much less affected by temporal aliasing than the along-track one. An additional advantage is that the amplitude of non-conservative acceleration is much less in the across-track component.

We investigated also several instrument noise models in association with these constellations. The main conclusion is that the temporal aliasing error is and remains the dominant error contributor.

At PM1, based on a wide trade-space analysis (cf. D5) we identified the following scenarios to be investigated in more detail
:

- Reference: MAGIC (2-pairs: polar + 70°)
- Triple-pair: polar + 70° + 45°
- 6-pairs: polar + 351 + 602 + 702 + 501 + 352

The instrument noise model X1 were used to investigate their performance in the product-only and full-noise case. In addition, the cross-track tracking concepts should be evaluated in detail for single and multiple pairs. The results of these simulations are presented in detail in D5.

In conclusion, polar across-SST constellations cannot compete with the other investigated ones. All inclined inline-SST constellations (with varying inclination) show a similar performance. Polar combined across-/inline-SST constellations can compete against constellations including inclined pairs. The constellations IICv1 and PIAC produce the globally most homogeneous error distributions. The resulting constellation performance rating is IICv1 ≥ PIAC > IICv0 > PAC.

The full noise retrieval error does not scale linearly with the number of pairs. This means, that there is a certain kind of saturation with increasing number of pairs, i.e. the addition of pairs beyond a number of 6 does not improve the de-aliasing capabilities of the constellation significantly. Temporal aliasing cannot be reduced sufficiently by larger constellations alone.

32.2. CRITICAL ASSESSMENT OF SRL (WP470)

The processing algorithms for ll-SST and associated data, in spite of continuous development, are established and well-documented. The following sections assess the readiness level according to [AD2].
For a quantum-equipped ll-SST satellite pair, the existing algorithms are applicable after the point where the CAI accelerometer data have been processed into physically relevant accelerations. The processing of raw cold-atom interferometric data into accelerations is beyond the scope of this assessment.

ATTITUDE

The attitude data processing is deemed to be at SRL 9 because:

- The star-tracker instruments have been developed for decades and flown in numerous satellite missions;
- For gravimetric missions, the impact of attitude errors is well understood [RD-1];
- The combination of data from multiple star trackers is proven [RD-2];
- The attitude data from star trackers can be augmented with the attitude rate collected by capacitive accelerometers [RD-3] [RD-4], and conceptually with any instruments that provide attitude-rate data;
- Systematic effects in attitude data have been identified [RD-5], explained and corrected [RD-6];
- Novel attitude determination techniques, such as the Differential Wavefront Sensor, have been characterized [RD-7].

INTER-SATELLITE RANGING

The laser inter-satellite ranging data processing is assigned the SRL 7 because:

- Space operations has been demonstrated [RD-8]
- Validation of GRACE's LRI and the characterization of errors has been conducted [RD-9]
- Effects external to the instrument that influence the quality of its measurements, such as the Tilt-to-Length coupling, has been identified and characterized [RD-10]

Higher SRL is not adequate because it is not yet fully understood why the gravity field models derived solely from LRI data are slightly noisier than those derived from KBR data. As such, it is difficult to argue that the processing of LRI data has reached the level of *Operational / nominal processing of measurements and observations*, indicative of SRL 8.

NON-GRAVITATIONAL ACCELERATIONS

The processing of non-gravitational accelerations has been developed over 2 decades and has reached SRL 9 because:

- Improved parameterization schemes have led to higher-quality scientific results in GRACE [RD-11] [RD-23], GOCE [RD-17] [RD-20], GRACE-FO and Swarm [RD-22]
- Swarm accelerometer data has been validated [RD-12]
- Methodologies have been developed [RD-21] to derive neutral thermospheric densities from accelerometer data in Swarm [RD-13] [RD-14], GRACE [RD-15], CHAMP [RD-16]
- Spurious, platform and environmental effects have been identified and corrected [RD-24]

ORBIT POSITIONS

The processing of orbit positions has been developed in parallel to the numerous GNSSs. While new processing techniques continue to be developed and the necessary models are constantly improving, the SRL is deemed to be 9. This is because the characteristics of the signals are well understood, as well as the source of errors [RD-25].

32.3. PRELIMINARY MISSION REQUIREMENTS AND MATCH AGAINST USER REQUIREMENTS (WP480)

According to the MoM of MS2, the formulation of concrete mission requirements can be skipped due to the obtained results. Instead, the estimated requirements from WP100 are assumed (cf. chapter 31).

33. QSG MISSION REQUIREMENTS FOR QUANTUM/HYBRID GRADIOMETRY

33.1. TRADE-SPACE DEFINITION, GRADIOMETER INSTRUMENT OPTIONS & SELECTION OF SCENARIOS (WP510)

Numerical studies, which are presented in detail in D5, revealed that with current QSG noise assumptions (X1, X1.1), gradiometry is not sensitive to temporal gravity signals. At least a 10^{-14} $1/s^2$ assumption for ACC is necessary to be competitive with low-low ranging concepts. The CPC-concept as presented in D3 (noise model X2.1) might solve the attitude problem, however, due to technical hurdles, its realization is not deemed realistic within the near and mid-term future. Therefore, together with ESA, the decision has been made to not further pursue the gradiometry concept as long as no fundamentally better and realistic noise model can be assumed.

Also, basic simulations show that, even if the noise model X2.1 (CPC-concept) would be applicable, the obtained solutions would not be fundamentally different better than those of multi-pair inclined ll-SST missions (see D5).

33.2. CRITICAL ASSESSMENT OF SRL (WP570)

As mentioned in Section 33.1, the quantum gradiometer concept requires a high sensitivity (down to 10^{-5} E) and attitude accuracy that is not expected to be available in the near future. The gradiometry requirements on sensitivity result from the low amplitude of the temporal gravity gradient signal, and the requirements on attitude accuracy result from the effect of the Coriolis and centrifugal accelerations, which is destructive at such small signal amplitudes (see D6). For this reason, the analysis of this measurement concept did not develop further than the initial assessment.

As for the processing of these data, except for concerns about the numerical representation of small numbers, we do not foresee significant deviations from what is motivated for the ll-SSH case (Section 32.2) in what concerns attitude, non-gravitational accelerations and orbits. The only new aspect left to be discussed concerns the processing of gravity gradient observations.

GRAVITY GRADIENTS

The processing of gravity gradients is judged to be at SRL 9 because:

- Space operation has been demonstrated (GOCE)
- The data has been validated [RD-26][RD-27] and re-processed [RD-18].
- Advanced data combination strategies has been successfully demonstrated: The processing of gravity gradient data relies on the differential measurements between pairs of accelerometers after reducing the effect of frame rotations, notably Euler and centrifugal accelerations. This means that the processing of gravity gradient data benefits from the most accurate attitude data possible, which means combining all measurements that contain attitude data. In the case of GOCE, this was demonstrated for the angular accelerations retrieved with the accelerometer and start tracker 283[RD-18].

33.3. PRELIMINARY MISSION REQUIREMENTS AND MATCH AGAINST USER REQUIREMENTS (WP580)

According to the MoM of MS2, the formulation of concrete mission requirements can be skipped due to the obtained results. Instead, the estimated requirements from WP100 are assumed (cf. chapter 31).

34. QSG MISSION REQUIREMENTS FOR ALTERNATIVE QSG MISSION ARCHITECTURES (WP600)

34.1. SPECIFICATION OF COMBINED SCENARIOS OF LL-SST, GRADIOMETRY AND MOBILE CONCEPT (WP610)

In D5 it is demonstrated that neither a combined ll-SST/gradiometry mission nor a hl-SST scenario (MOBILE concept) is suited for a future QSG mission. The former is not reasonable due to the lacking sensitivity of realistic QSG gradiometers in comparison to ll-SST. The latter is not appropriate because of the large inter-satellite distances causing increased ranging noise which superimposes the quantum accelerometer noise.

Even though these initially proposed alternative/combined concepts proved to be ineligible for future QSG missions, the alternative across-track SST (A-SST) concept might pose a viable option instead. Especially when combined with conventional (inline) ll-SST pairs on polar orbits a similar performance can be achieved than with incline ll-SST constellation. The main advantage over inclined ll-SST constellations is that all pairs can be placed on (near) polar orbits. The disadvantage is the more complex ranging due to the strongly varying inter-satellite distances of A-SST pairs. See D5 for the specification of the across-track scenarios and the combined trade-space analysis (and also section 32.1).

34.2. CRITICAL ASSESSMENT OF SRL (WP660)

The SLR of the data processing infrastructure for the alternative mission, assumed to be the A-SST, does not deviate from the traditional along-track ll-SST in terms of attitude, accelerometer, and orbit data.

INTER-SATELLITE RANGING (A-SST)

The laser inter-satellite ranging data processing is assigned the SRL 6 because it is expected to have to handle data issues not yet demonstrated, notably data continuity. The ranging system concept has operated for decades onboard the GRACE and GRACE-FO satellites, but only in the relatively favourable configuration that the line-of-sight vector is generally aligned with the orbital plane of both satellites. This leads to infrequent data breaks at a rate dictated by onboard, instrument and operational events. Even if we assume the ideal case is that a feasible engineering solution is found to track both satellites with large angular deviations from the orbital plane, unavoidable data breaks will occur at the poles. The handling of the ll-SST data with gaps is well understood, but dealing with a gap at a systematic geographical location has not been demonstrated.

34.3. PRELIMINARY MISSION REQUIREMENTS AND MATCH AGAINST USER REQUIREMENTS (WP670)

According to the MoM of MS2, the formulation of concrete mission requirements can be skipped due to the obtained results. Instead, the estimated requirements from WP100 are assumed (cf. chapter 31).

35. QSG MISSION REQUIREMENTS FOR OPTIMIZED REGIONAL SOLUTIONS(WP700)

35.1. SPECIFICATION OF CRITERIA (WP710)

Regarding Solid Earth applications of QSG mission architectures (WP 800):

- Relevant functionals: gridded values of geoid undulations, gravity anomaly, potential field with variances or VCMs.
- Requested time resolution: daily, monthly.
- Requested space resolution: 0.1° to 1.0° depending on area specification and resolution of simulated data

Regarding Hydrological (short-term) and Ocean applications (WP 900) and Hydrological (medium to long-term) and climate applications (WP 1000):

- Relevant functionals: gridded TWSA (total water storage anomaly) maps with VCMs plus assessment of systematic errors. Time series will also be important (e.g. one year of monthly/weekly data)
- Requested time resolution: the priority would be on weekly resolution to show improvement in spatial resolution and/or accuracy
- Requested space resolution: 0.1° to 1.0° depending on area specification and resolution of simulated data

35.2. SELECTION OF MISSION ARCHITECTURES AND OPTIMIZED REGIONAL SOLUTIONS (WP720)

Regarding the Solid Earth applications of QSG mission, namely WP800, relevant regions have been selected for earthquakes, volcanos, and lithosphere:

- For earthquakes, one region at low latitudes, and one at high (negative) latitudes, at 5-10 km grid resolution. The analyses are focused on the 2007 Bengkulu Earthquake.
- For volcanos, area of radius 8° centred on the Mayotte volcano (Lat 12.83°S, Lon 45.17°E), resulting in Lat min: 4.83° S, Lat Max: 20.83° S, Lon min: 37.00° E, Lon Max=53.00° E.

Regarding Hydrological (short-term) and Ocean applications (WP 900), East China Sea has been chosen as the area of interest by HCU and UNB. For Hydrological (medium to long-term) and climate applications (WP 1000), some small to large scale river basins have been chosen. Smaller river basins are included to investigate the gain in spatial resolution.

- Relevant region for WP900: East China Sea.
- Relevant region for WP1000: Amazon, Danube, Ganges, Elbe, Rhine, Oder, and Uruguay river basins.

The methodology used for computing the regional solution is described in document D5. As shown in document D7, regional solutions were computed considering inline satellite-to-satellite tracking with 2, 3, and 6 pairs of satellites (IIC2v1, IIC3v1, IIC6v1, respectively) or mixed inline and cross-track satellite-to-satellite tracking with 6 pairs of satellites (PIAC6v2).

Gradiometry was not considered due to not comparable performances with a not too optimistic scenario, as shown in document D5.

35.3. ASSESSMENT OF MISSION PERFORMANCE AND MATCH AGAINST USER REQUIREMENTS (WP750)

According to the MoM of MS2, the formulation of mission requirements can be skipped due to the obtained results.

In the following a summary of the obtained results from the simulations considering different scenarios.
For the hydrological applications the results are presented in Figure 35-1, Figure 35-2, Figure 35-3, and Figure 35-4, considering a 7-day retrieval period. In these figures the overall estimation error over the considered region is shown with respect to the basin area exploiting the different mission configurations (IIC2v1, IIC3v1, IIC6v1, PIAC6v2, respectively).

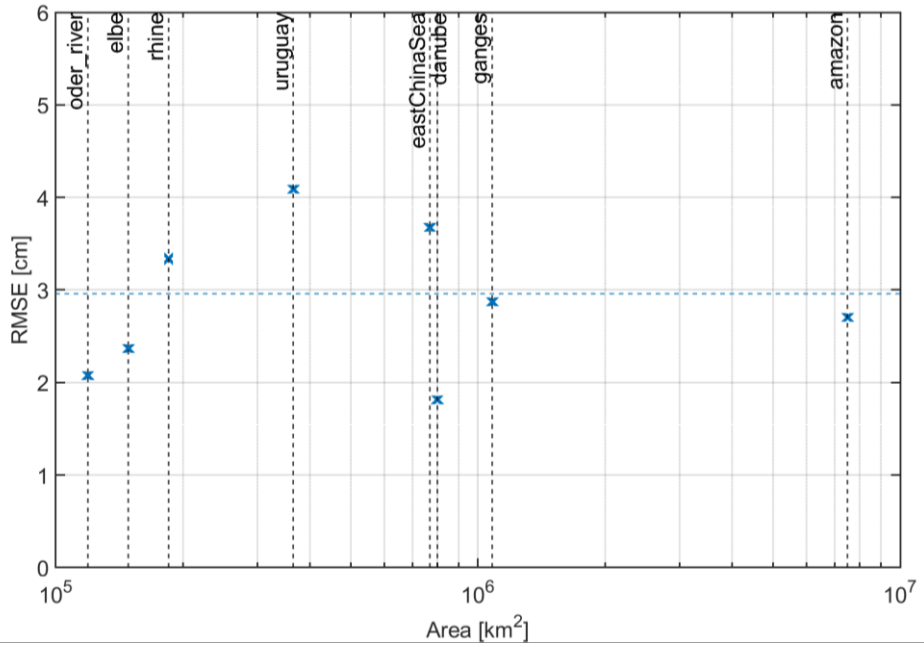

Figure 35-1 Overall estimation error in each selected region with respect to the basin size, considering the 2-pair satellite configuration (IIC2v1) and a 7-day retrieval period. The blue dashed line represents the overall average for the selected mission profile.

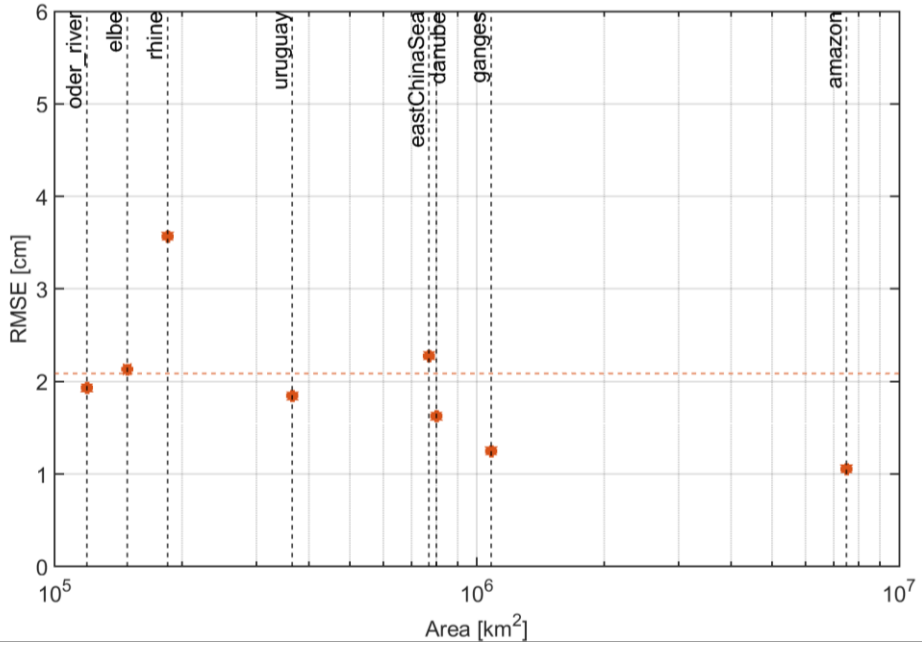

Figure 35-2 Overall estimation error in each selected region with respect to the basin size, considering the 3-pair satellite configuration (IIC3v1) and a 7-day retrieval period. The red dashed line represents the overall average for the selected mission profile.

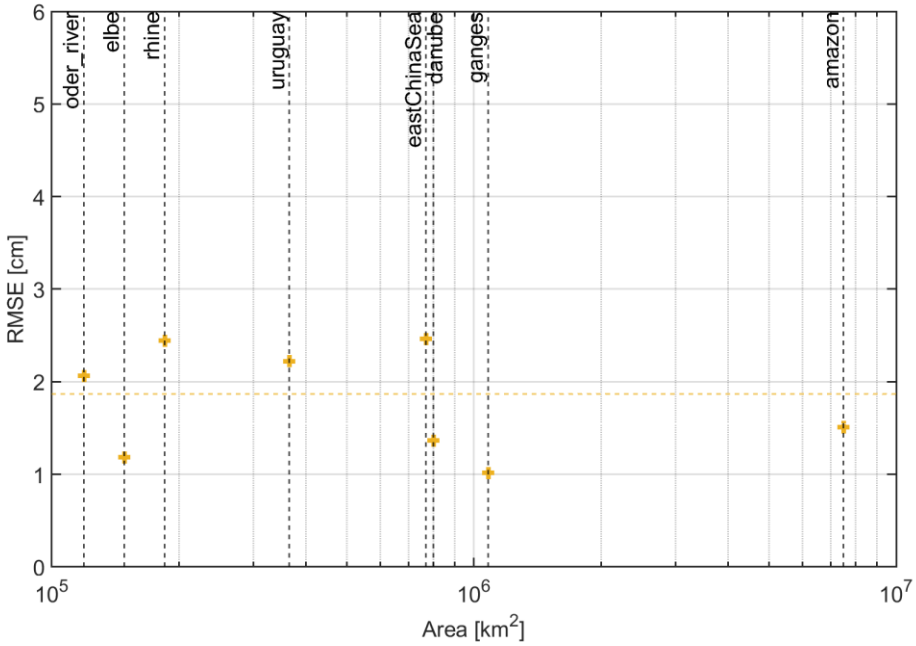

Figure 35-3 Overall estimation error in each selected region with respect to the basin size, considering the 6-pair satellite configuration (IIC6v1) and a 7-day retrieval period. The yellow dashed line represents the overall average for the selected mission profile.

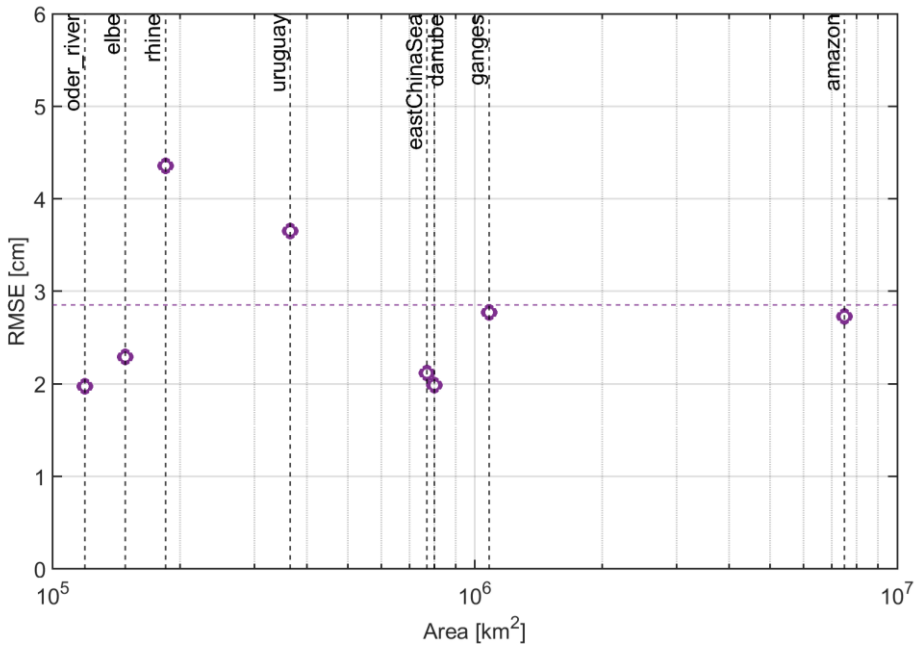

Figure 35-4 Overall estimation error in each selected region with respect to the basin size, considering the 6-pair mixed inline and cross-track satellite configuration (PIAC6v2) and a 7-day retrieval period. The purple dashed line represents the overall average for the selected mission profile.

Finally, Figure 35-5 shows a summary of all the results. The average accuracy for the considered regions is always better than 3 cm (in terms of EWH) independently from the chosen orbit configuration. Increasing the pairs of satellites the estimation accuracy can be improved at a level better than 2 cm.

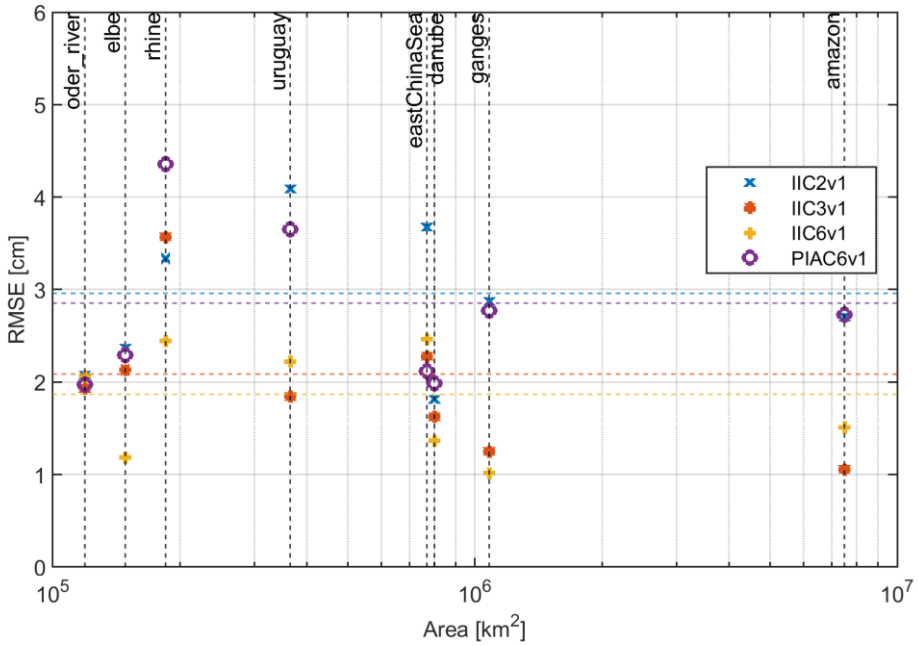

Figure 35-5 Summary of the overall estimation error in the selected regions with respect to the basin size, considering all the satellite configurations with a 7-day retrieval period. The horizontal dashed line represents the overall average for the corresponding mission profile.

As for the solid Earth application the focus was on the Bengkulu Earthquake. The results showed that it is possible to retrieve a solution with a spatial resolution between 1.2° and 1°, which improves with a higher number of satellite pairs. As for the accuracy, the RMSE is in the range between 10 μGal and 5 μGal, depending on the orbit configuration. The higher the number of satellite pairs, the better is the accuracy.

The user requirements in case of weekly solutions are 2.5 cm @ 150 km (Baseline 1) and 1.5 cm @ 150 km (Baseline 2), see Figure 5-12. Comparing these numbers with the results reported in Figure 29-1, the Baseline 1 requirement is always satisfied with 6 inline pairs and almost always satisfied with 3 inline pairs. As for Baseline 2, this requirement can be reached with 3 and 6 inline pairs, but this result cannot be generalized to all the investigated regions.

36. APPLICABLE DOCUMENTS, REFERENCE DOCUMENTS, AND PUBLICATIONS

36.1. APPLICABLE DOCUMENTS

[AD-1] Mission Requirements Document, Next Generation Gravity Mission as a Mass-change And Geosciences International Constellation (MAGIC) - A joint ESA/NASA double-pair mission based on NASA's MCDO and ESA's NGGM studies (2020). ESA-EOPSM-FMCC-MRD-3785

[AD2] Scientific Readiness Levels (SRL) Handbook, Issue 1, Revision 0, 05-08-2015

[AD3] Study of Cold Atom Interferometry (CAI) Gravity Gradiometer Sensor and Mission Concepts - ESA Contract 4000112677, Summary Report "Concept study and preliminary design of a cold atom interferometer for space gravity gradiometry"

[AD4] Cold Atom Inertial Sensors: Mission Applications – ESA Contract 4000117930, Final Report TASI-SD-CAI-FR

[AD5] Hybrid Atom Electrostatic System for Satellite Geodesy – ESA Contract 4000113573, Final Report RF_7-24721_DMPH

[AD6] Hybrid Atom Electrostatic System for Satellite Geodesy Follow-On – ESA Contract 4000112290, Final Report RT 6/27346 DPHY

[AD7] QSG_UR_SATM_v2.0.xlxs – ESA/EC Quantum Space Gravimetry User Requirements Science and Traceability Matrix v2.0 (2022)

[AD8] Quantum Space Gravimetry for monitoring Earth's Mass Transport Processes (QSG4EMT). Project Proposal, Proposal No. TUM/2022-QSG4EMT, Technical University of Munich

36.2. REFERENCE DOCUMENTS

[RD-1] Pail R (2005) A parametric study on the impact of satellite attitude errors on GOCE gravity field recovery. J Geod 79(4–5):231–241. doi:10.1007/s00190-005-0464-z

[RD-2] Romans L (2003) Optimal combination of quaternions from multiple star cameras. JPL Internal Memorandum, Jet Propulsion Laboratory. https://archive.podaac.earthdata.nasa.gov/podaac-ops-cumulus-docs/grace/open/docs/quaternion_memo.pdf

[RD-3] Siemes, Christian. 2018. "GOCE Level 1B Gravity Gradient Processing Algorithms." Noordwijk, The Netherlands. https://earth.esa.int/documents/10174/85857/GOCE-Level-1-Gravity-Gradient-Processing-Algorithms.pdf.

[RD-4] Stummer C, Fecher T, Pail R (2011) Alternative method for angular rate determination within the GOCE gradiometer processing. J Geod 85(9):585–596. doi:10.1007/s00190-011-0461-3

[RD-5] Goswami, Sujata, Beate Klinger, Matthias Weigelt, and Torsten Mayer-Gurr. 2018. "Analysis of Attitude Errors in GRACE Range-Rate Residuals—A Comparison Between SCA1B and the Fused Attitude Product (SCA1B + ACC1B)." IEEE Sensors Letters 2 (2): 1–4. doi:10.1109/LSENS.2018.2825439.

[RD-6] Inácio, Pedro, Pavel Ditmar, Hassan H Farahani, and Roland Klees. 2014. "Analysis of Star-Camera Noise in GRACE Data and Its Impact on Monthly Gravity Field Models." Journal of Geodesy 16. doi:10.1007/s00190-015-0797-1.

[RD-7] Goswami, Sujata, Samuel P. Francis, Tamara Bandikova, and Robert E. Spero. 2021. "Analysis of GRACE Follow-On Laser Ranging Interferometer Derived Inter-Satellite Pointing Angles." IEEE Sensors Journal 21 (17): 19209–21. doi:10.1109/JSEN.2021.3090790.

[RD-8] Abich, Klaus, Alexander Abramovici, Bengie Amparan, Andreas Baatzsch, Brian Bachman Okihiro, David C. Barr, Maxime P. Bize, et al. 2019. "In-Orbit Performance of the GRACE Follow-on Laser Ranging Interferometer." Physical Review Letters 123 (3). doi:10.1103/PhysRevLett.123.031101.

[RD-9] Müller, Vitali, Markus Hauk, Malte Misfeldt, Laura Müller, Henry Wegener, Yihao Yan, and Gerhard Heinzel. 2022. "Comparing GRACE-FO KBR and LRI Ranging Data with Focus on Carrier Frequency Variations." Remote Sensing 14 (17): 4335. doi:10.3390/rs14174335.

[RD-10] Wegener, Henry, Vitali Müller, Gerhard Heinzel, and Malte Misfeldt. 2020. "Tilt-to-Length Coupling in the GRACE Follow-On Laser Ranging Interferometer." Journal of Spacecraft and Rockets 57 (6): 1362–72. doi:10.2514/1.A34790.

[RD-11] Teixeira da Encarnação, João, Himanshu Save, Byron Tapley, and Hyung-jin Rim. 2020. "Accelerometer Parameterization and the Quality of Gravity Recovery and Climate Experiment Solutions." Journal of Spacecraft and Rockets 57 (4): 740–52. doi:10.2514/1.A34639.

[RD-12] Bezděk, Aleš, Josef Sebera, and Jaroslav Klokočník. 2017. "Validation of Swarm Accelerometer Data by Modelled Nongravitational Forces." Advances in Space Research 59 (10): 2512–21. doi:10.1016/j.asr.2017.02.037

[RD-13] Siemes, Christian, João Teixeira da Encarnação, Eelco Doornbos, Jose van den IJssel, Jiří Kraus, Radek Pereštý, Ludwig Grunwaldt, Guy Apelbaum, Jakob Flury, and Poul Erik Holmdahl Olsen. 2016. "Swarm Accelerometer Data Processing from Raw Accelerations to Thermospheric Neutral Densities." Earth, Planets and Space 68 (1): 92. doi:10.1186/s40623-016-0474-5

[RD-14] Iorfida, Elisabetta, Ilias Daras, Roger Haagmans, and Anja Strømme. 2023. "Swarm A and C Accelerometers: Data Validation and Scientific Interpretation." Earth and Space Science 10 (2): 1–18. doi:10.1029/2022EA002458

[RD-15] Tapley, Byron D., John C. Ries, Srinivas Bettadpur, and Minkang Cheng. 2006. "Neutral Density Measurements from the GRACE Accelerometers." Collection of Technical Papers - AIAA/AAS Astrodynamics Specialist Conference, 2006 1 (August): 484–94. doi:10.2514/6.2006-6171

[RD-16] Bruinsma, S., D. Tamagnan, and R. Biancale. 2004. "Atmospheric Densities Derived from CHAMP/STAR Accelerometer Observations." Planetary and Space Science 52 (4): 297–312. doi:10.1016/j.pss.2003.11.004

[RD-17] Siemes, Christian, Roger Haagmans, Michael Kern, Gernot Plank, and Rune Floberghagen. 2012. "Monitoring GOCE Gradiometer Calibration Parameters Using Accelerometer and Star Sensor Data: Methodology and First Results." Journal of Geodesy 86 (8): 629–45. doi:10.1007/s00190-012-0545-8

[RD-18] Siemes, Christian, Moritz Rexer, Anja Schlicht, and Roger Haagmans. 2019. "GOCE Gradiometer Data Calibration." Journal of Geodesy 93 (9): 1603–30. doi:10.1007/s00190-019-01271-9

[RD-19] Zhang, Jiahui, Wei You, Biao Yu, and Dongming Fan. 2023. "GRACE-FO Accelerometer Performance Analysis and Calibration." GPS Solutions, 1–19. doi:10.1007/s10291-023-01487-5

[RD-20] Visser, P. N. A. M. M., J. A. A. van den IJssel, and J. A A van den IJssel. 2016. "Calibration and Validation of Individual GOCE Accelerometers by Precise Orbit Determination." Journal of Geodesy 90 (1): 1–13. doi:10.1007/s00190-015-0850-0

[RD-21] Doornbos, Eelco, Jose Van Den Ijssel, Hermann Luehr, Matthias Foerster, and Georg Koppenwallner. 2010. "Neutral Density and Crosswind Determination from Arbitrarily Oriented Multiaxis Accelerometers on Satellites." Journal of Spacecraft and Rockets 47 (4): 580–89. doi:10.2514/1.48114

[RD-22] Bezděk, Aleš, Josef Sebera, and Jaroslav Klokočník. 2018. "Calibration of Swarm Accelerometer Data by GPS Positioning and Linear Temperature Correction." Advances in Space Research 62 (2): 317–25. doi:10.1016/j.asr.2018.04.041

[RD-23] Klinger, Beate, and Torsten Mayer-Gürr. 2016. "The Role of Accelerometer Data Calibration within GRACE Gravity Field Recovery: Results from ITSG-Grace2016." Advances in Space Research 58 (9): 1597–1609. doi:10.1016/j.asr.2016.08.007

[RD-24] Peterseim, Nadja. 2014. "TWANGS – High-Frequency Disturbing Signals in 10 Hz Accelerometer Data of the GRACE Satellites." Technischen Universität München.

[RD-25] Yu, Kegen, Chris Rizos, Derek Burrage, Andrew G Dempster, Kefei Zhang, and Markus Markgraf. 2014. "An Overview of GNSS Remote Sensing." EURASIP Journal on Advances in Signal Processing 2014 (1): 134. doi:10.1186/1687-6180-2014-134

[RD-26] Pitoňák, M., Šprlák, M., Ophaug, V., Omang, O.C.D., Novák, P., 2023. Validation of Space-Wise GOCE Gravitational Gradient Grids Using the Spectral Combination Method and GNSS/Levelling Data. Surveys in Geophysics 44, 739–782. https://doi.org/10.1007/s10712-022-09762-9

[RD-27] Gruber, T., Visser, P.N.A.M., Ackermann, C., Hosse, M., 2011. Validation of GOCE gravity field models by means of orbit residuals and geoid comparisons. Journal of Geodesy 85, 845–860. https://doi.org/10.1007/s00190-011-0486-7

PART 7:

APPLICATIONS OF QSG MISSION ARCHITECTURES AND RELATED OPERATIONAL SERVICES

37. INTRODUCTION

The purpose of this part is to describe the applications of QSG mission architectures and related operational services. It refers to Task 7-10 of the SoW and WPs 700 to 1000 of the WBS.

38. WP 700: OPTIMIZED REGIONAL SOLUTIONS AND THEIR GEOPHYSICAL PRODUCTS

Interaction with WP's 800, 900 and 1000 allowed to specify relevant regions/catchments and functionals for performing optimized regional solutions. Besides, time resolution of regional solutions to address geophysical and climate-related requirements have been discussed.

Regarding **Solid Earth applications of QSG mission architectures** (WP 800), we selected the following parameters.

- Relevant functionals: gridded values of geoid undulations, gravity anomaly, potential field.
- Relevant regions:
  - For earthquakes, one region at low latitudes, and one at high (negative) latitudes, at 5-10 km grid resolution. The analyses are focused on the 2007 Bengkulu Earthquake;
  - For volcanos, area of radius 8° centered on the Mayotte volcano (Lat 12.83°S, Lon 45.17°E), resulting in Lat min: 4.83° S, Lat Max: 20.83° S, Lon min: 37.00° E, Lon Max=53.00° E;
- Requested time resolution: weekly or monthly depending on the considered phenomenon.

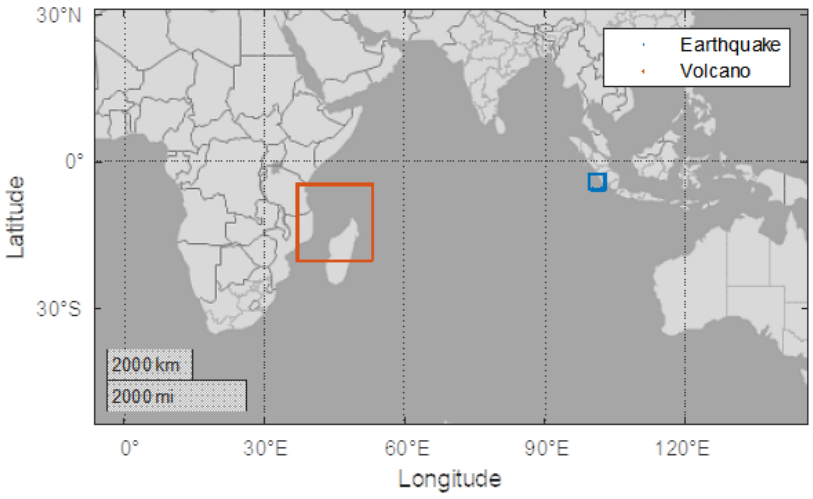

Figure 38-1 Areas of interest for the regional solutions for Solid Earth applications

Regarding **Hydrological (short-term) and ocean applications** (WP 900) and **Hydrological (medium to long-term) and climate applications** (WP 1000), we selected the following parameters.

- Relevant functionals: gridded TWSA (total water storage anomaly) maps in terms of EWH with the corresponding VCMs. Time series will also be important (starting with one year of monthly/weekly data).
- Relevant regions/catchments: regional solutions are focused on the Amazon, Ganges-Brahmaputra, maybe smaller regions as well to showcase gain in resolution. As for the Europe basins focus on Danube, Oder, Rhine. For the oceans, focus on East China Sea. Figure 38-2 shows the polygons of the areas in which HCU and UNB are interested in.
- Requested time resolution: the priority would be on weekly resolution to show improvement in spatial resolution and/or accuracy; second priority would be monthly resolution.

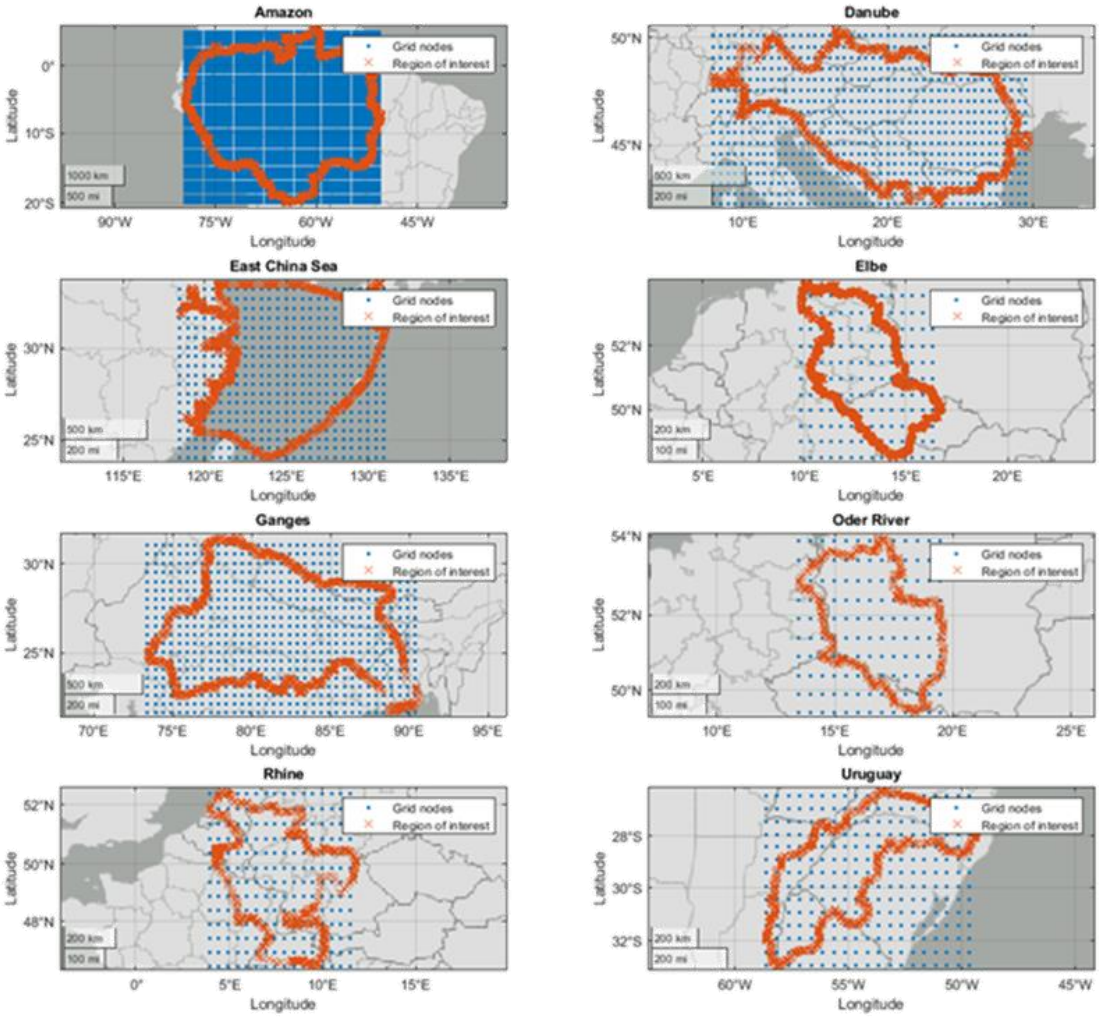

Figure 38-2 Areas (Amazon, Danube, East China Sea, Elbe, Ganges, Oder, Rhine, Uruguay) of interest for the regional solutions for Hydrological, Ocean and Climate applications

38.1. OBSERVATION SELECTION

To have an idea what to expect from hydrological signal at observation level, first the hydrological signal at ground level was taken into consideration. The hydrological signal component of ESA Earth System Model is rather small; the variability of the signal is dominated by the mass variations in the large river basins. Thence, we first considered the larger basins from the selected areas (shown in Figure 38-3) as an example for the study: Amazon, Danube, and Ganges. By considering a grid resolution of 0.2°×0.2°, the expected mean variation of the hydrological signal at ground level is synthesised for 30 days of January 2002 (see Figure 38-4). More dominant and visible signals are seen in Amazon Basin and Ganges River Basin.

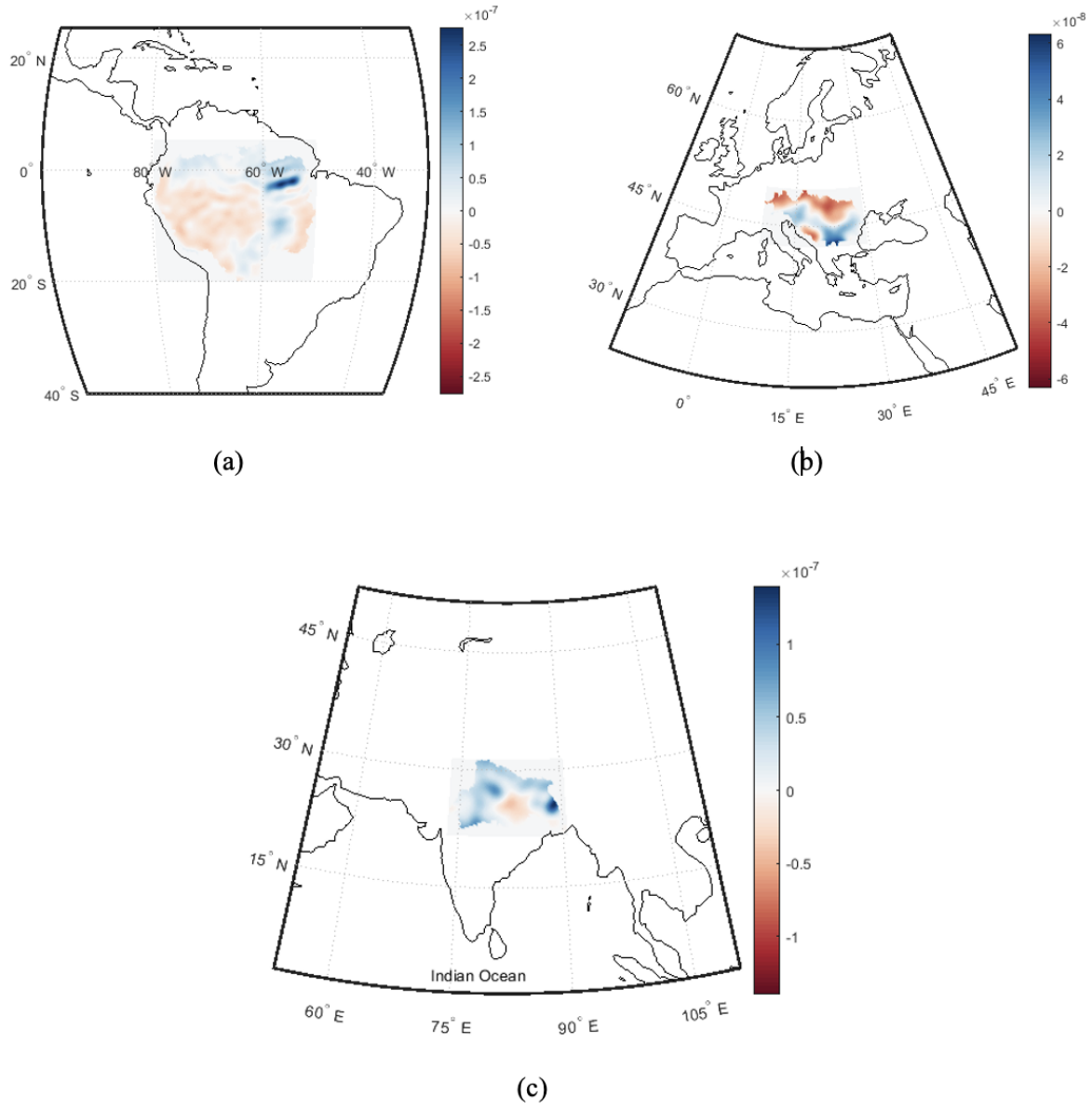

Figure 38-3 Hydrological signal (T_r) from ESA ESM model at ground level ($h = 0$) for (a) Amazon , (b) Danube, and (c) Ganges basin. Units: m/s^2

For all of the areas this procedure was completed and followed by the upward continuation of the ground level signal; this is done by considering just the signal inside the chosen areas, and then preforming a spherical harmonic analysis by a discretization of the quadrature formula. In order to investigate the visibility of the signal at the observation level, the difference between gravitational accelerations projected onto the line-of-sight were calculated for all the observation points of the polar orbit of the 3D_H scenario. This is the expected quantity to be observed after pre-processing the range acceleration. The resulting hydrological signal at satellite altitude in terms of this quantity can be seen in Figure 38-4.

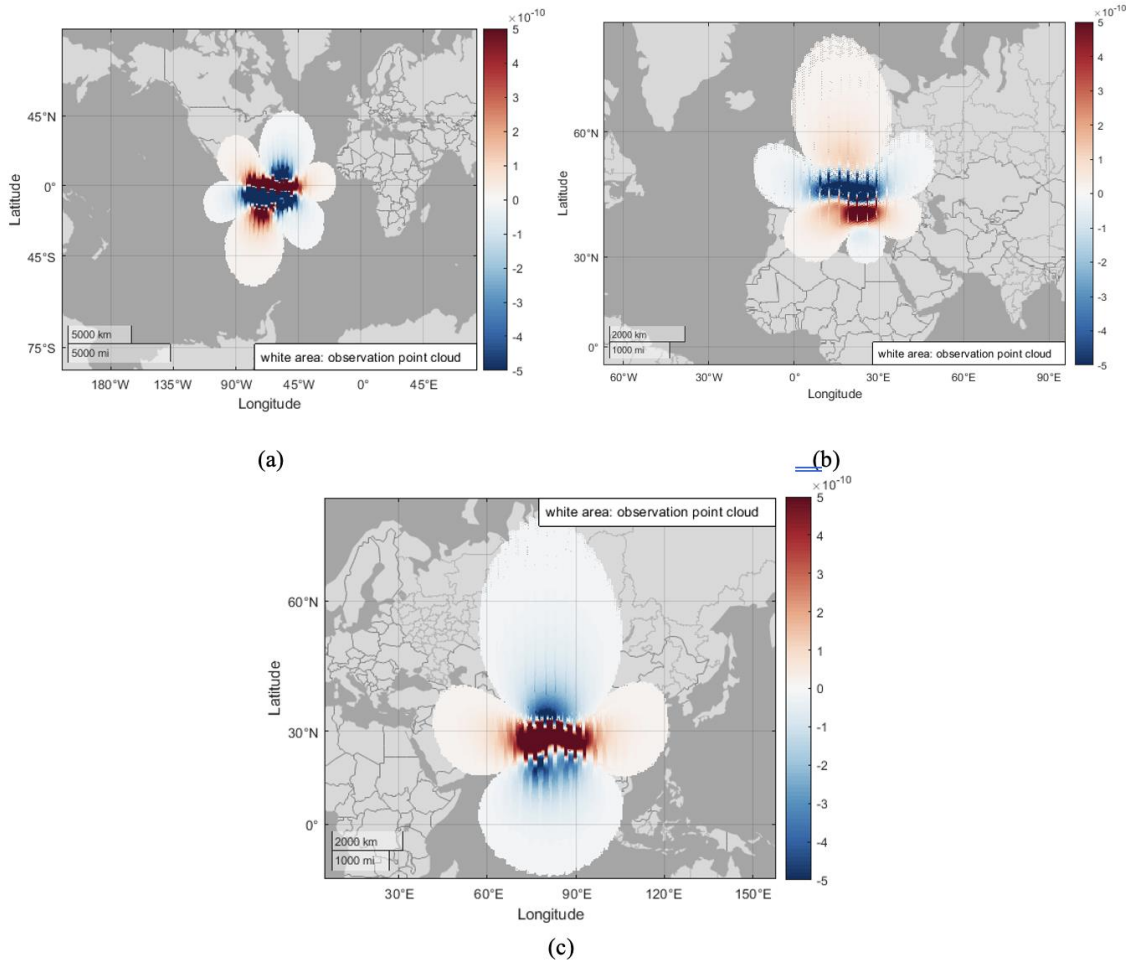

Figure 38-4: Hydrological signal as Line of Sight (LoS) acceleration difference at satellite altitude over (a) Amazon, (b) Danube, and (c) Ganges basin, showing only observation points for which the signal is larger than 10^{-11} m/s^2, chosen as a threshold given by the X1 noise realization. Units: m/s^2

To understand the extension of the area including observations influenced by the considered phenomenon at satellite altitude, we filtered the observations by using a threshold of 10^{-11} m/s^2, corresponding to the order of magnitude of an average instrumental accuracy (when considering the X1 noise realization for quantum accelerometers or electrostatic accelerometers). Therefore, Figure 38-4 shows only observations above this accuracy level, that, in principle, are the ones for which the signal-to-noise ratio is greater than one and, therefore, have to be used for investigating the local signal. The number of points falling into the cloud of observations for

each area over a month is the following: Amazon = 95,252, Danube = 26,626, Ganges = 65,965 points.

A similar job was also done for the provided solid Earth signal, i.e. the Mayotte volcano. The number of points falling into the cloud of observations for this area of interest and this signal is 15,480.

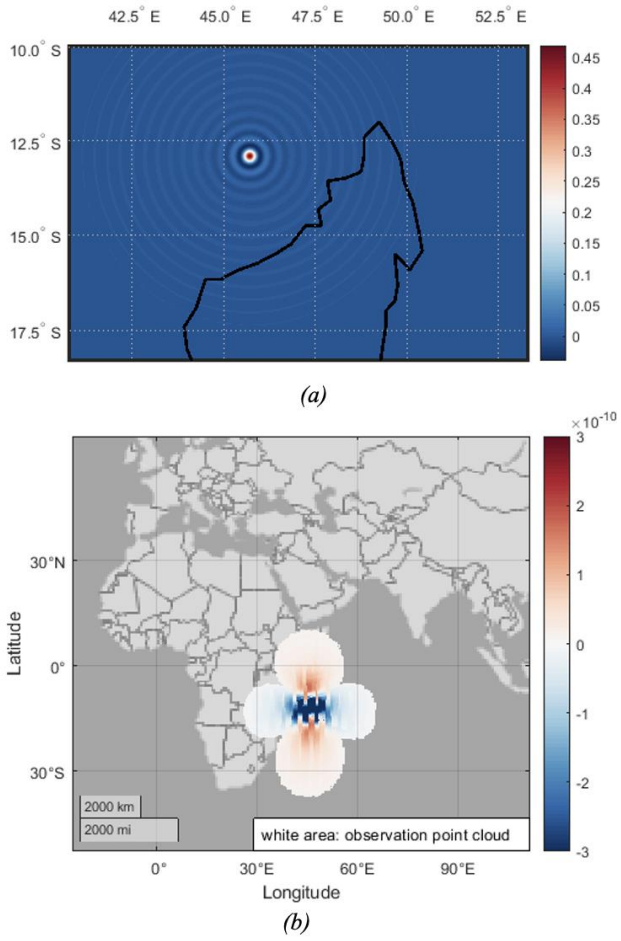

Figure 38-5: Volcano signal (a) at ground level (as T_r) and (b) at satellite altitude (as LoS acceleration differences). Units: m/s^2. In panel (b) only observation points for which the signal is larger than 10^{-11} m/s^2, chosen as a threshold given the X1 noise realization, are shown.

The above-proposed method of selecting the observations for local gridding solutions leads to a very large number of points for each region. Moreover, this number could also increase, by adding more satellite pairs and by considering the X2.1 noise scenario, for which the threshold to have signal-to-noise ratio close to 1 must be further reduced. Given these considerations, a different way of selecting observations to be used for the local gridding procedure must be introduced.

The proposed alternative is to use only the observations falling into the considered region plus the ones falling into a buffer around the perimeter of the region. To choose the size of this buffer, some tests has been performed. In particular, considering either weekly or monthly solutions, local solutions are computed (for the first week or month of the one-year time series) and the overall empirical RMS of the signal retrieval error is computed. Based on this number,

the optimal buffer size is empirically chosen. As an example, Table 38-1 presents the complete results of this test for Ganges and Danube basins evaluated for either 7-days or 30-days solution and considering the IIC2v1 orbit scenario. Both regions show the optimal buffer size to be 1°. Although this value could vary from region to region, also depending on both the chosen orbit configuration and the retrieval period, an acceptable level of the estimation error is generally found around 1° that is then chosen as a standard value for all the following simulations. In particular, a one-year time series is computed for the 2, 3, and 6 pairs of in-line orbit constellations (IIC2v1, IIC3v1, IIC6v1, respectively) and for the 6 pairs mixed in-line and cross-track constellation (PIAC6v1). Solutions are mainly computed over a 7-day time span, but for the 2-pair case also 30-day solutions have been computed.

Table 38-1: Evaluation of the buffer size based on the overall estimation RMSE considering 7-day and 30-day solutions. Example is given for Ganges and Danube.

7-day solution			30-day solution		
Buffer [°]	Ganges RMSE [cm]	Danube RMSE [cm]	Buffer [°]	Ganges RMSE [cm]	Danube RMSE [cm]
1	3.0	1.6	1	3.0	3.6
2	3.1	2.3	2	2.8	2.1
3	3.3	2.2	3	2.7	2.1
6	3.6	3.2	4	2.9	2.1
			5	2.9	2.7
			6	2.9	2.1

38.2. TIME SERIES COMPUTATION (HYDROLOGY)

As for the hydrological studies (WP900 and WP1000), local gridding solutions by collocation approach have been computed according to the procedure explained in Section 6 of document D5. In particular four orbit scenarios, 7-day and 30-day retrieval periods are considered:

- IIC2v1 (7-day and 30-day)
- IIC3v1 (7-day)
- IIC6v1 (7-day)
- PIAC6v2 (7-day).

For all the solutions the noise level of the X2.1 scenario and the FN background model have been considered. As for the latter, the ESA updated ESM model is used for the non-tidal time variable components (AOHIS) and the EOT11a for the tidal components. De-alising is introduced into the simulations through the DEAL+AOerr components of the ESA updated ESM model and removing the GOT4.7 ocean tides model (thus leaving a residual equal to the difference between EOT11and GOT4.1).

The time-series of solutions is computed for an overall time span of one year, considering the time-variable signal of the year 2002. For each solution we computed the local TWSA grids in terms of EWH as well as the covariance matrices of TWSA gridded points. The formal covariance matrix is rescaled based on the empirical RMSE in order to account for the aliasing effect of the time-variable signal in the error.

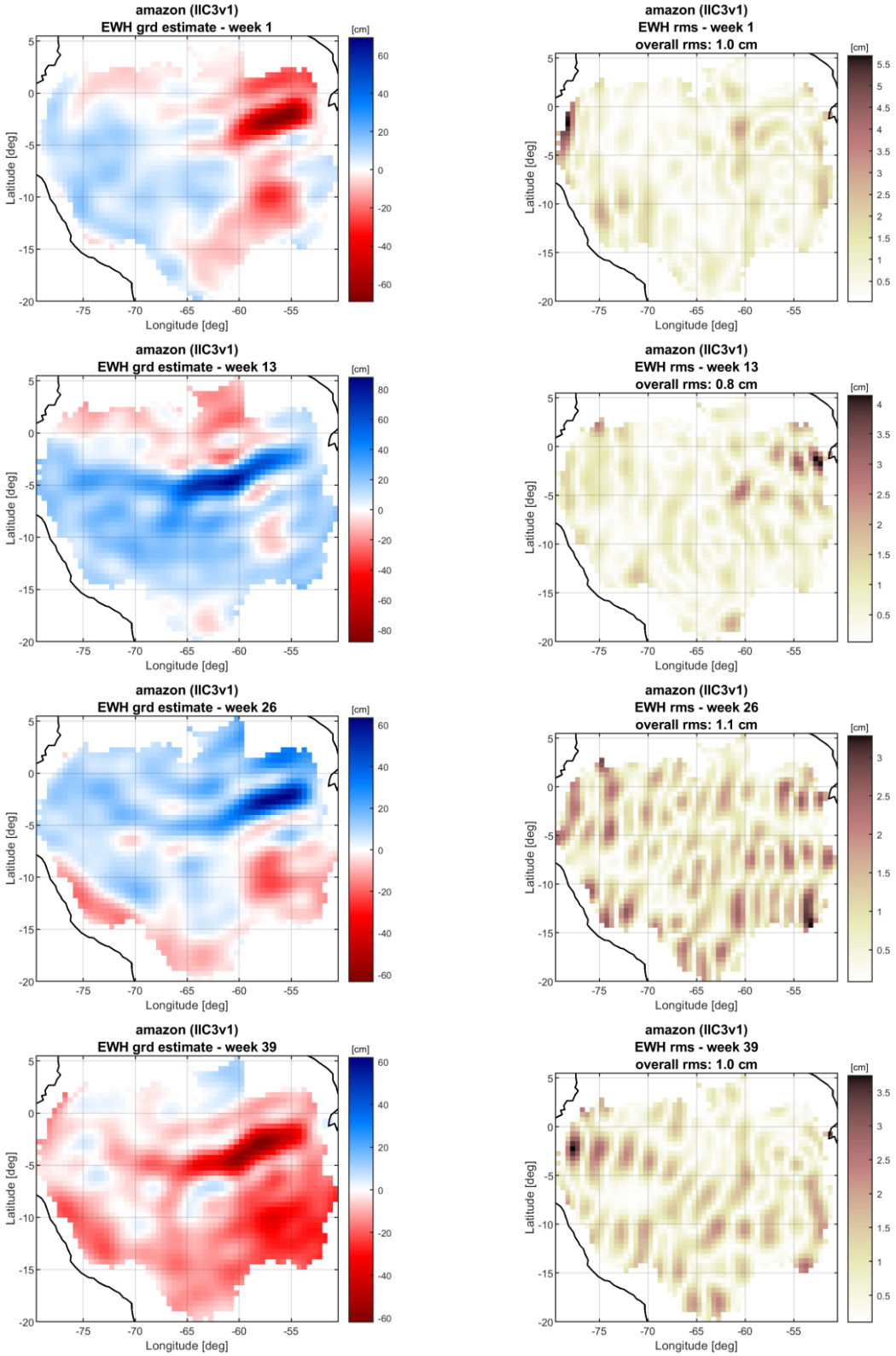

Figure 38-6 Estimated TWSA over the Amazon basin by local collocation gridding considering the IIC3v1 orbit configuration. Week 1, 13, 26, and 39 of the year 2002 are selected for visualization purposes. The estimated signal is shown in the left column, while its empirical RMSE in the right one.

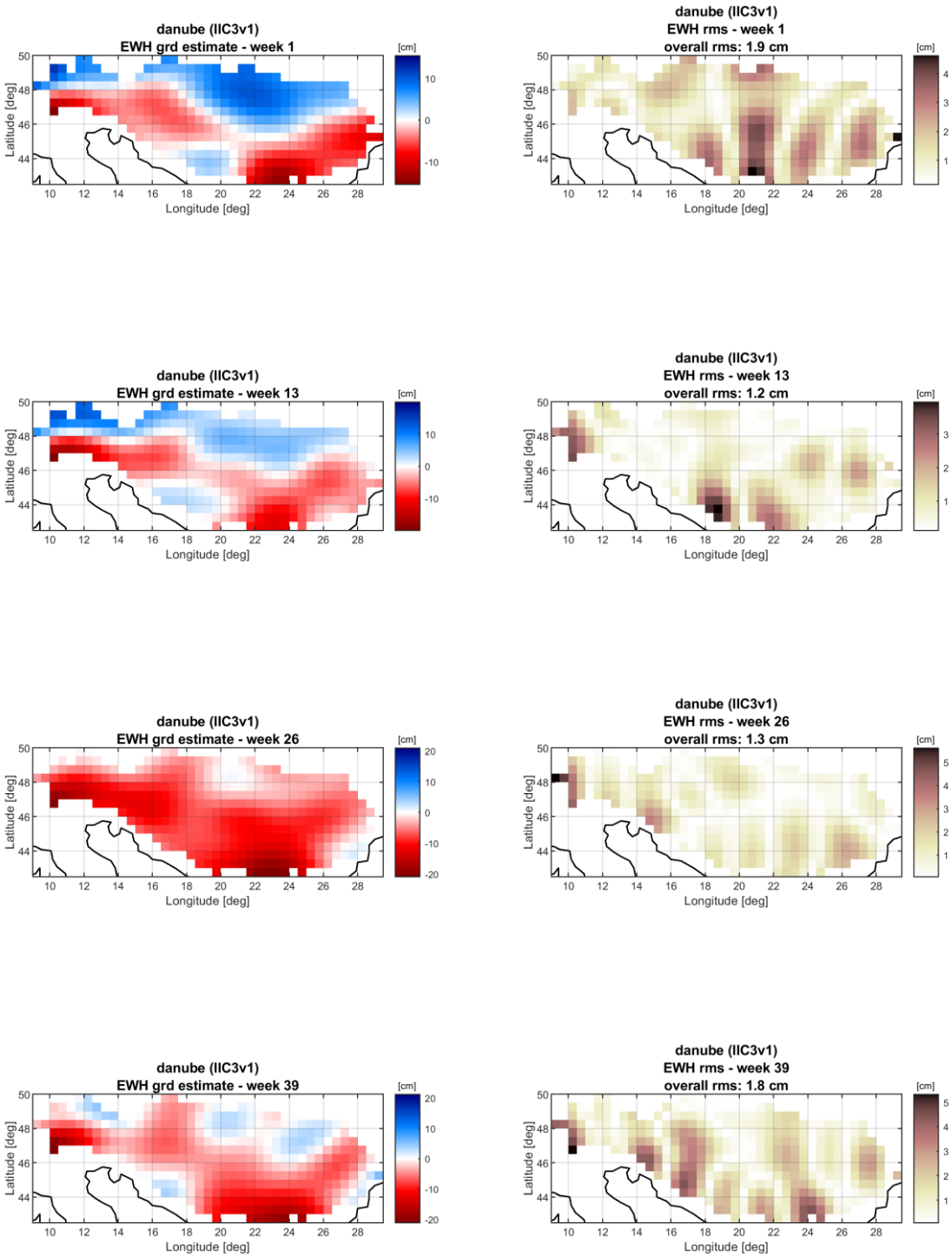

Figure 38-7 Estimated TWSA over the Danube basin by local collocation gridding considering the IIC3v1 orbit configuration. Week 1, 13, 26, and 39 of the year 2002 are selected for visualization purposes. The estimated signal is shown in the left column, while its empirical RMSE in the right one.

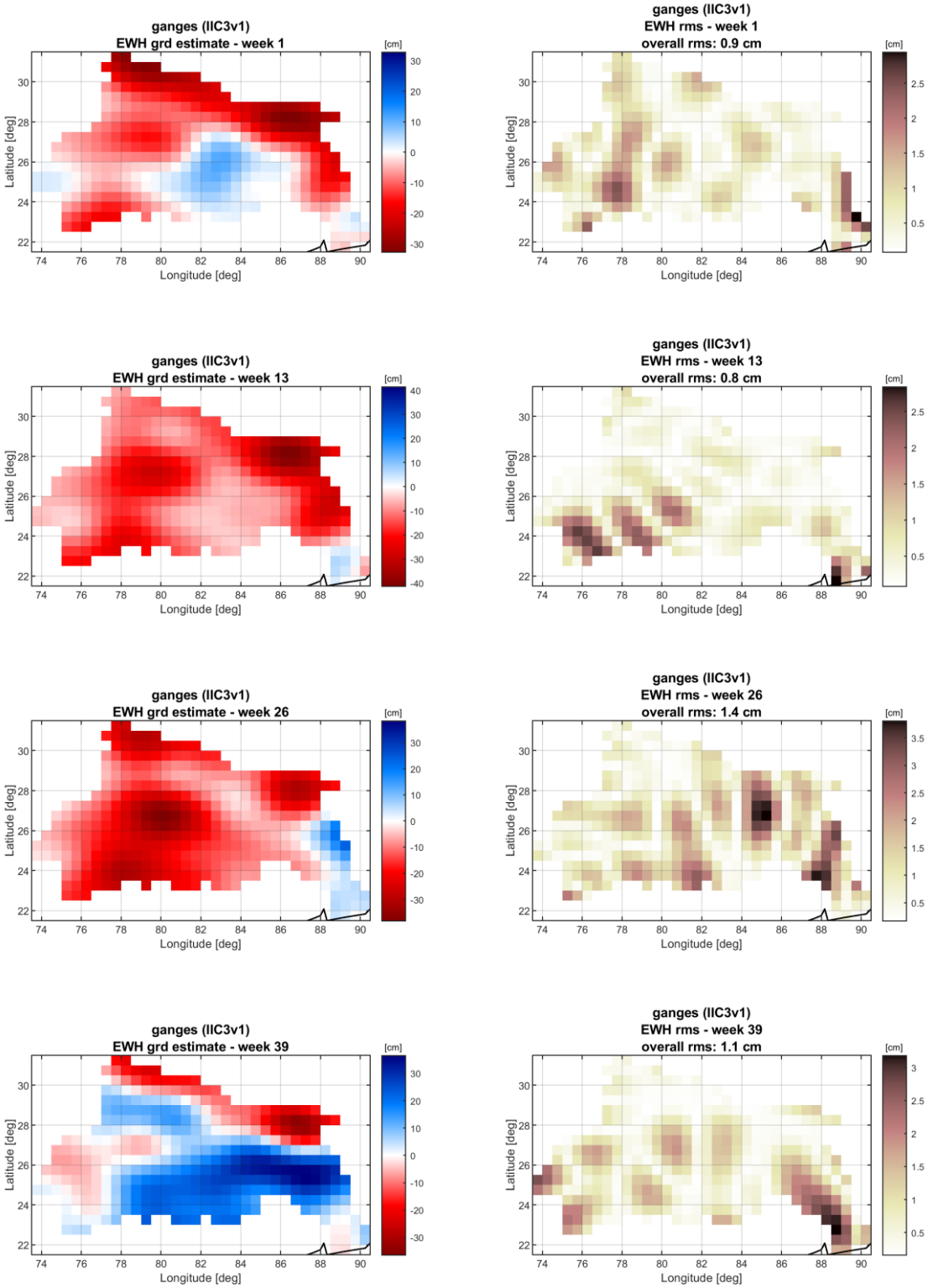

Figure 38-8: Estimated TWSA over the Ganges basin by local collocation gridding considering the IIC3v1 orbit configuration. Week 1, 13, 26, and 39 of the year 2002 are selected for visualization purposes. The estimated signal is shown in the left column, while its empirical RMSE in the right one.

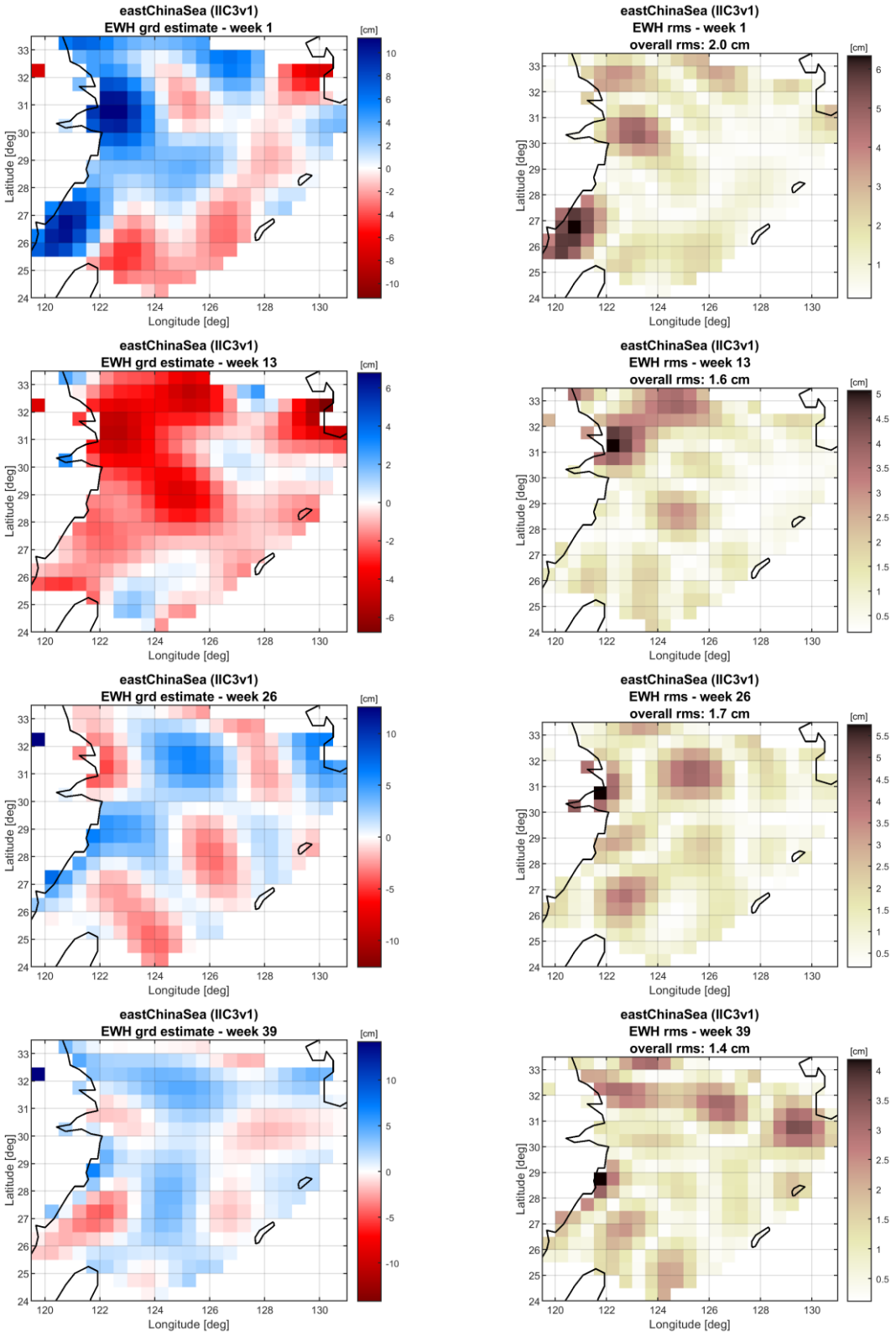

Figure 38-9: Estimated TWSA over the East China Sea by local collocation gridding considering the IIC3v1 orbit configuration. Week 1, 13, 26, and 39 of the year 2002 are selected for visualization purposes. The estimated signal is shown in the left column, while its empirical RMSE in the right one.

In Figure 38-6, Figure 38-7, Figure 38-8, and Figure 38-9 an example of the computed quantities is shown, considering the IIC3v1 orbit configuration over a 7-day retrieval period for the Amazon, Danube, Ganges and East China Sea regions, respectively. Each estimated value is provided with its RMSE (calibrated by exploiting the empirical error in a Monte Carlo scheme) from which an overall average RMS is computed. Thus, for each solution we can use this number as a proxy of the accuracy for the considered solution.

As described in Section 29, a global least squares solution is used to reduce the observations before the local gridding procedure and it is restored after the grid computation, exploiting a remove-restore workflow. In the following Figure 38-10, Figure 38-12, Figure 38-14, Figure 38-16, Figure 38-18, Figure 38-20, Figure 38-22, and Figure 38-24 the overall RMS of the global and local solutions is compared for all the considered regions, considering the four possible orbit configurations and 7-day retrieval period. As it can be noticed from the figures there is a general improvement carried by the local solutions with respect to the achievable accuracy from a global solutions.

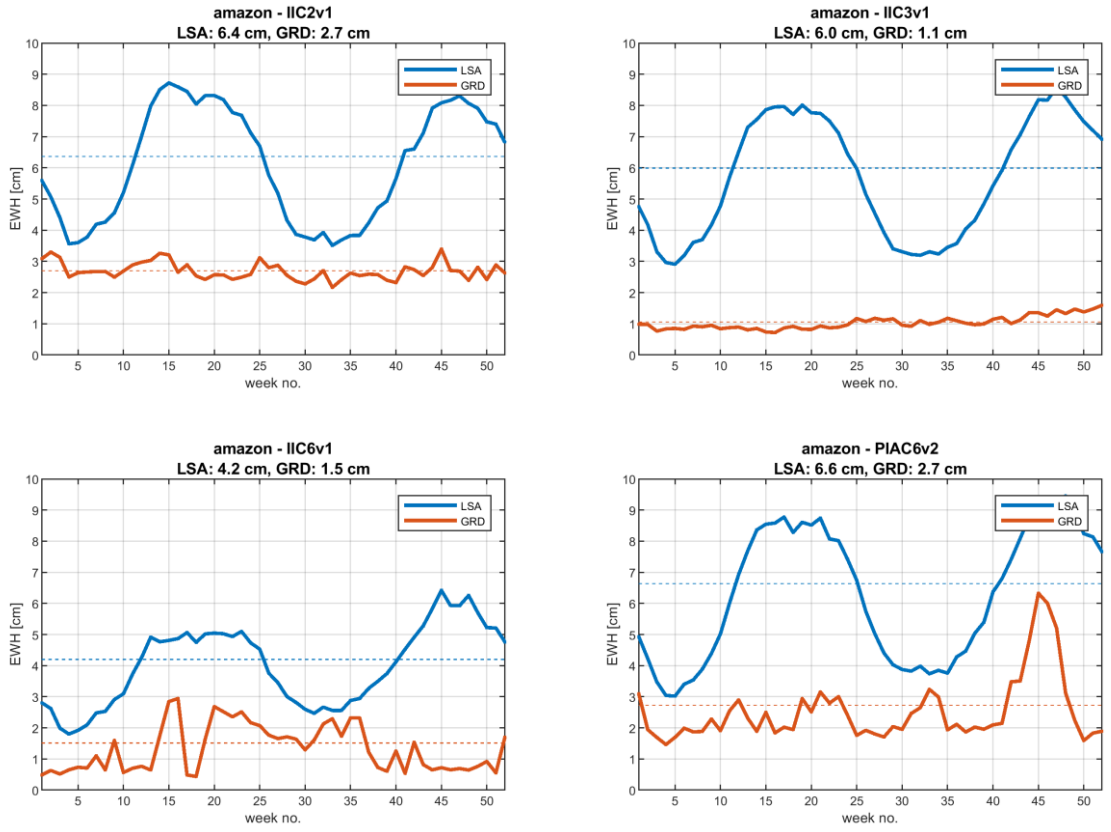

Figure 38-10 Overall empirical error (RMSE) of the estimated TWSA over the Amazon basin considering 7-day retrieval period and different orbit configurations. The error of the global solutions (least squares adjustment) is represented by solid blue lines, while the error of the local gridding solution (collocation) is represented by solid red lines. Dashed lines represent the 1-year average error of global (blue) and local (red) solutions; these average errors are reported in the title of each plot.

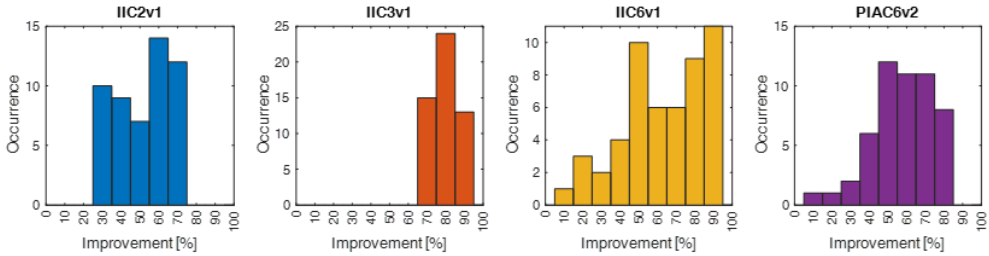

Figure 38-11: Improvement [%] of local solutions with respect to the corresponding global ones in the Amazon basin for one year time series.

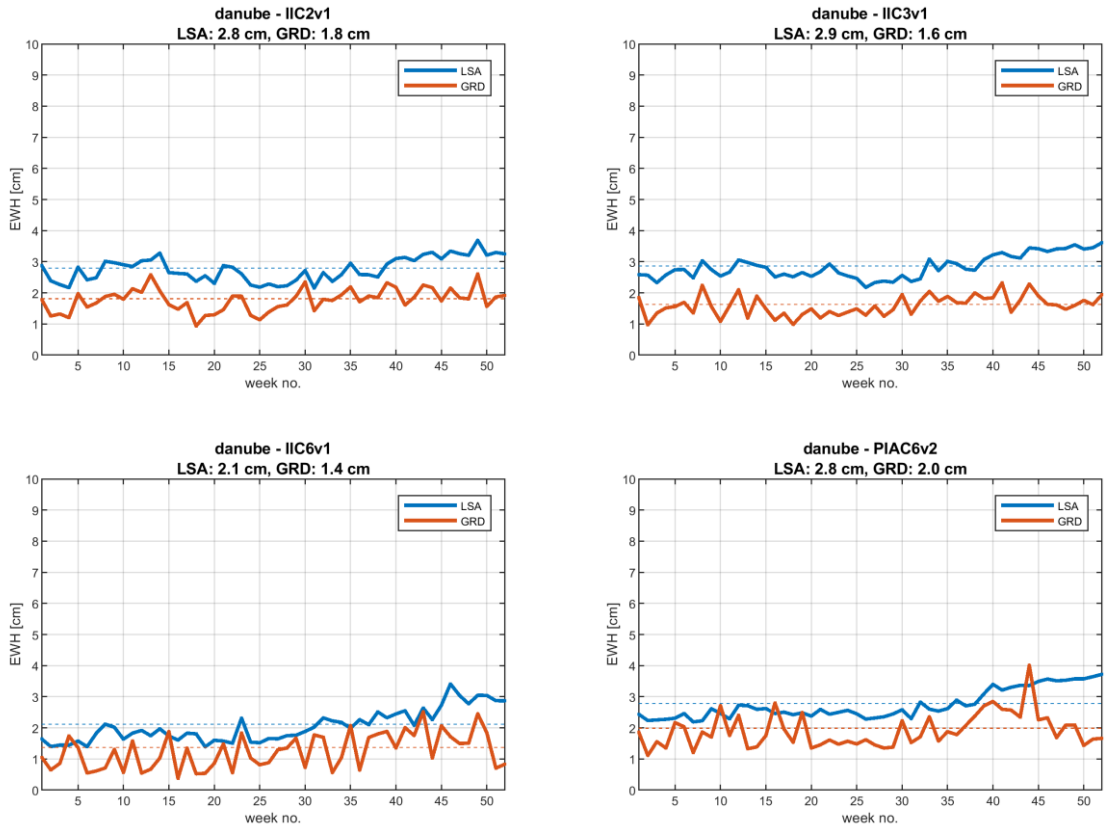

Figure 38-12 Overall empirical error (RMSE) of the estimated TWSA over the Danube basin considering 7-day retrieval period and different orbit configurations. The error of the global solutions (least squares adjustment) is represented by solid blue lines, while the error of the local gridding solution (collocation) is represented by solid red lines. Dashed lines represent the 1-year average error of global (blue) and local (red) solutions; these average errors are reported in the title of each plot.

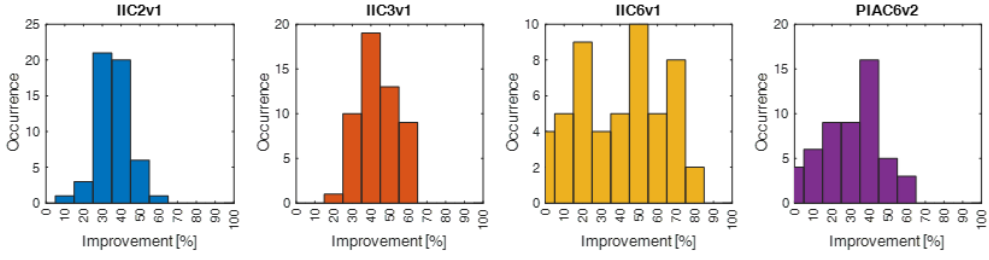

Figure 38-13: Improvement [%] of local solutions with respect to the corresponding global ones in the Danube basin for one year time series.

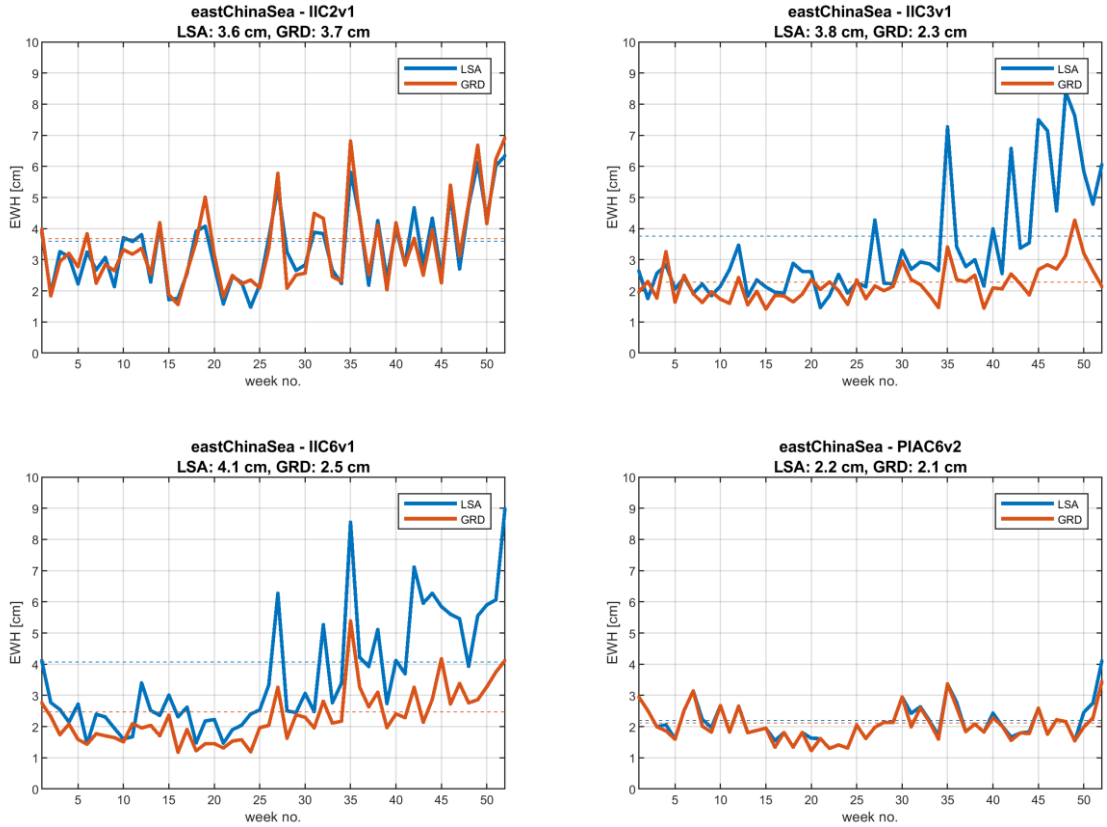

Figure 38-14: Overall empirical error (RMSE) of the estimated TWSA over the East China Sea considering 7-day retrieval period and different orbit configurations. The error of the global solutions (least squares adjustment) is represented by solid blue lines, while the error of the local gridding solution (collocation) is represented by solid red lines. Dashed lines represent the 1-year average error of global (blue) and local (red) solutions; these average errors are reported in the title of each plot.

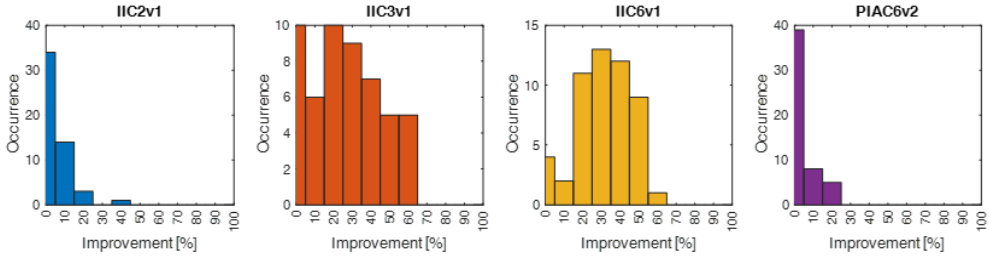

Figure 38-15: Improvement [%] of local solutions with respect to the corresponding global ones in the East China Sea for one year time series.

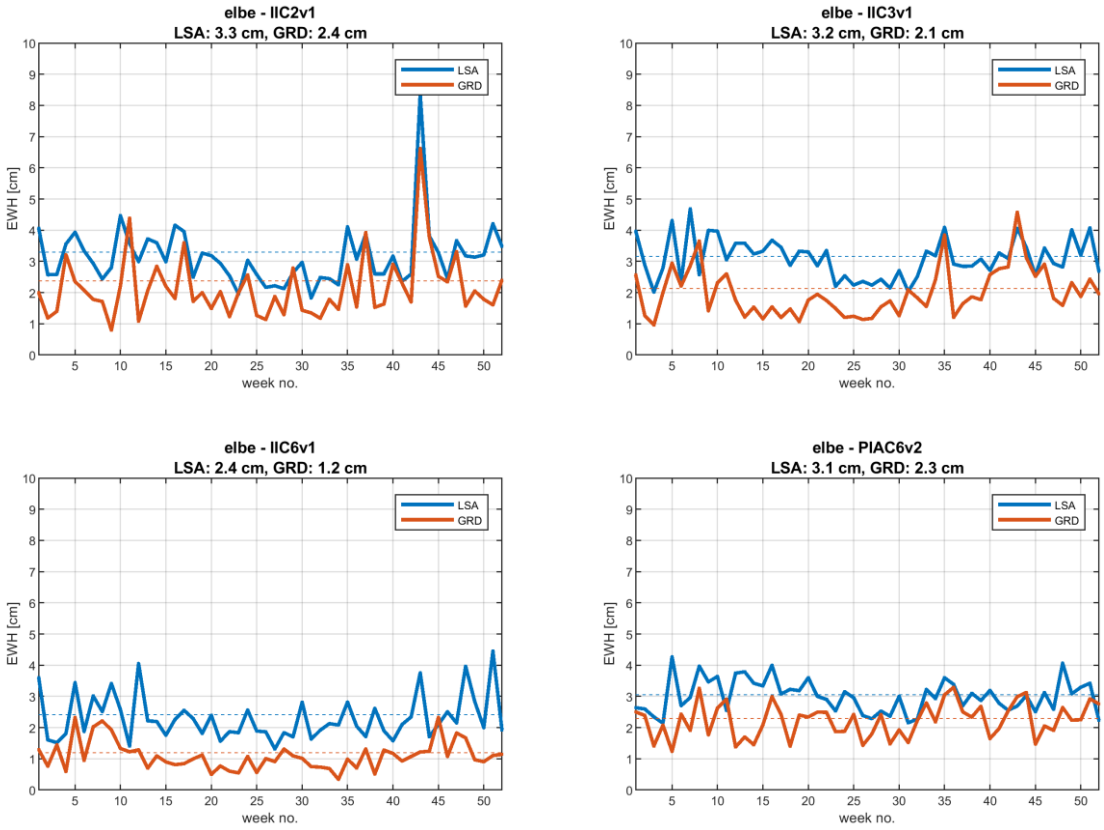

Figure 38-16: Overall empirical error (RMSE) of the estimated TWSA over the Elbe basin considering 7-day retrieval period and different orbit configurations. The error of the global solutions (least squares adjustment) is represented by solid blue lines, while the error of the local gridding solution (collocation) is represented by solid red lines. Dashed lines represent the 1-year average error of global (blue) and local (red) solutions; these average errors are reported in the title of each plot.

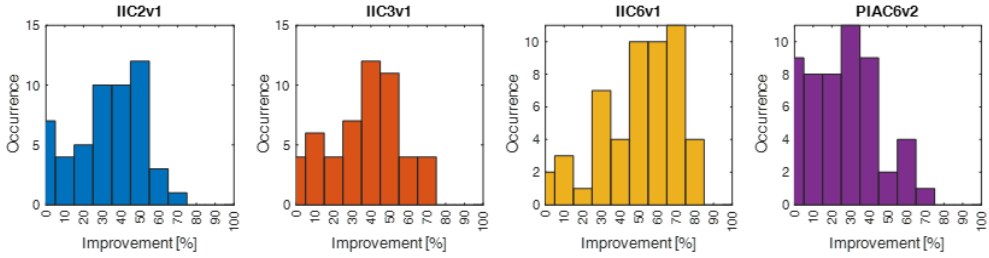

Figure 38-17: Improvement [%] of local solutions with respect to the corresponding global ones in the Elbe basin for one year time series.

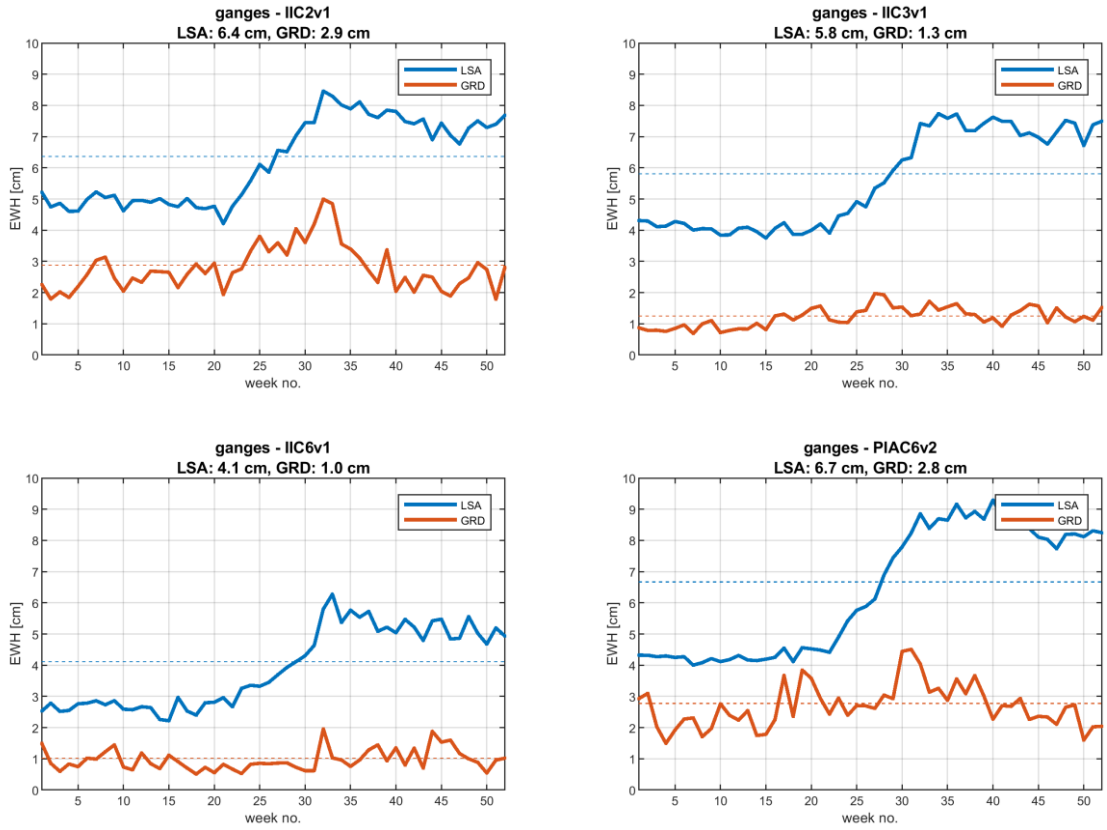

Figure 38-18: Overall empirical error (RMSE) of the estimated TWSA over the Ganges basin considering 7-day retrieval period and different orbit configurations. The error of the global solutions (least squares adjustment) is represented by solid blue lines, while the error of the local gridding solution (collocation) is represented by solid red lines. Dashed lines represent the 1-year average error of global (blue) and local (red) solutions; these average errors are reported in the title of each plot.

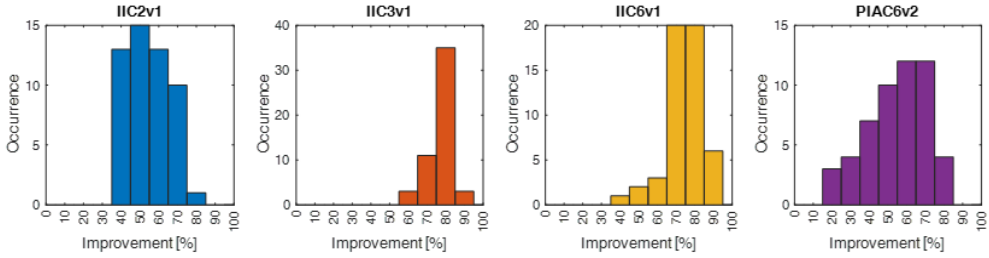

Figure 38-19: Improvement [%] of local solutions with respect to the corresponding global ones in the Ganges basin for one year time series.

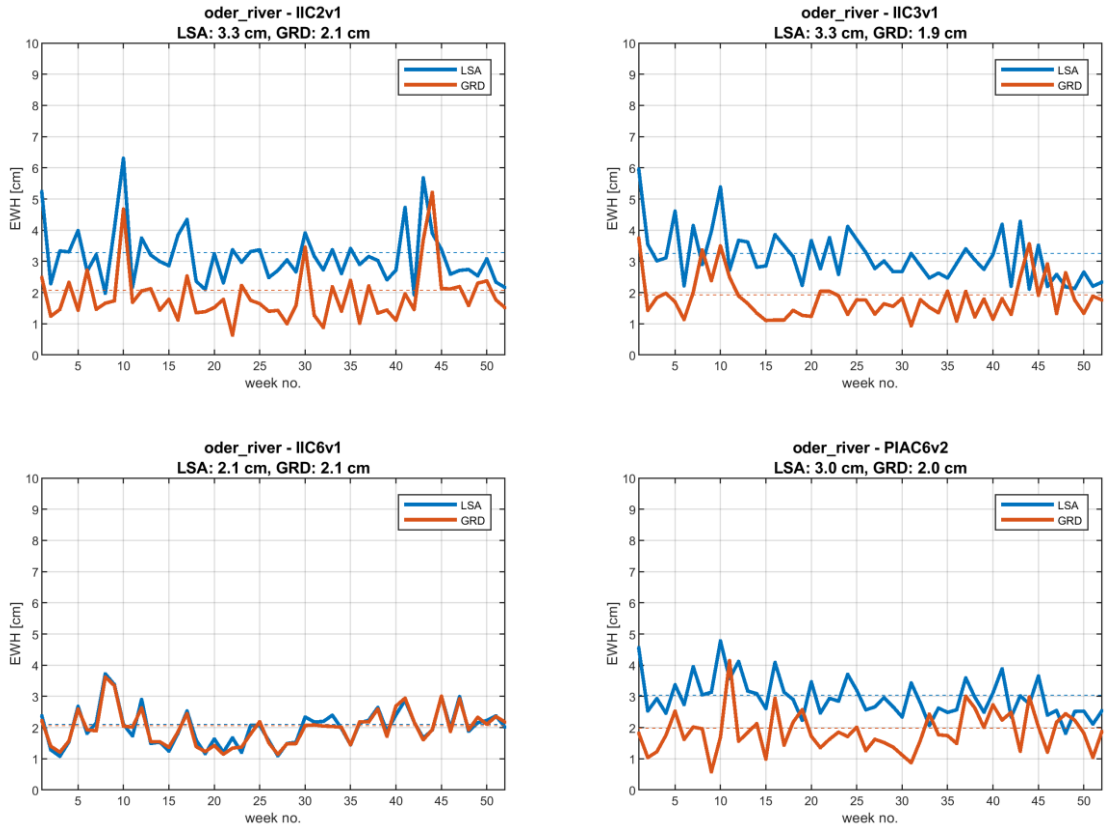

Figure 38-20: Overall empirical error (RMSE) of the estimated TWSA over the Oder basin considering 7-day retrieval period and different orbit configurations. The error of the global solutions (least squares adjustment) is represented by solid blue lines, while the error of the local gridding solution (collocation) is represented by solid red lines. Dashed lines represent the 1-year average error of global (blue) and local (red) solutions; these average errors are reported in the title of each plot.

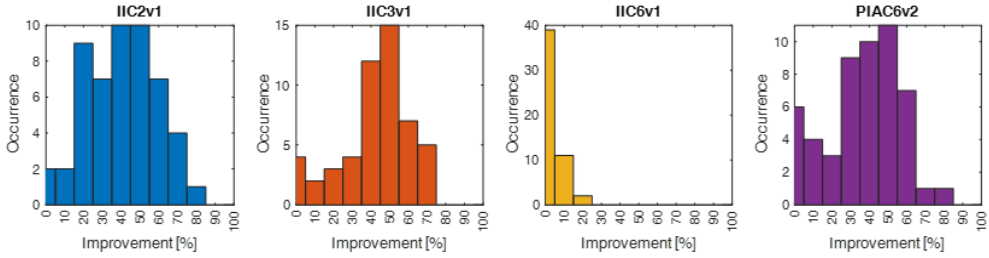

Figure 38-21:Improvement [%] of local solutions with respect to the corresponding global ones in the Oder basin for one year time series.

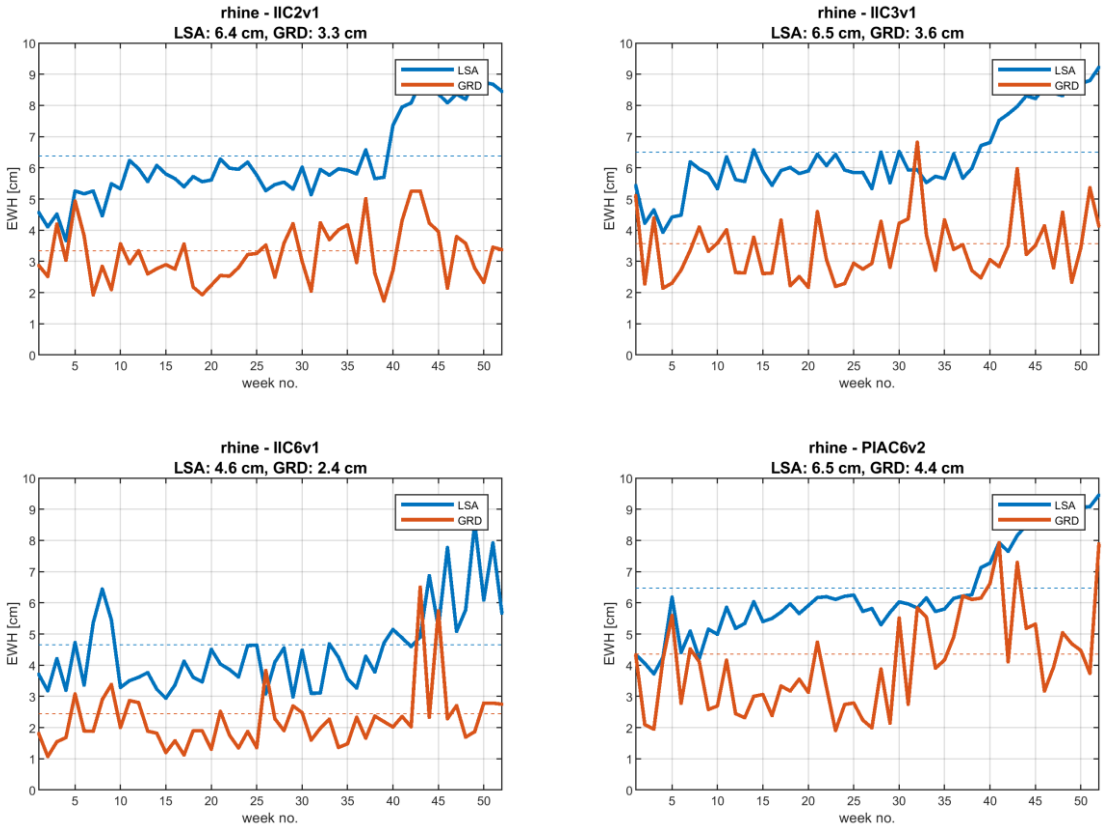

Figure 38-22: Overall empirical error (RMSE) of the estimated TWSA over the Rhine basin considering 7-day retrieval period and different orbit configurations. The error of the global solutions (least squares adjustment) is represented by solid blue lines, while the error of the local gridding solution (collocation) is represented by solid red lines. Dashed lines represent the 1-year average error of global (blue) and local (red) solutions; these average errors are reported in the title of each plot.

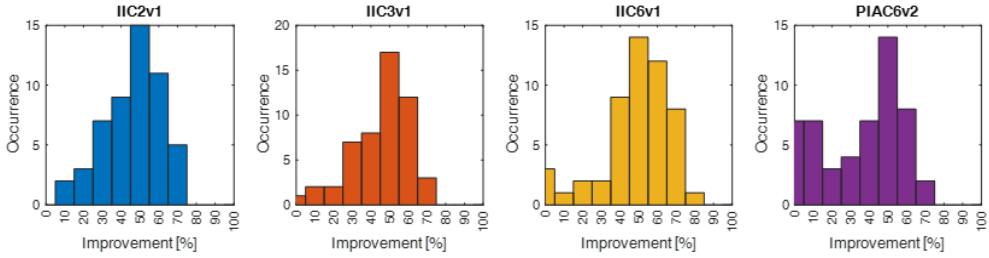

Figure 38-23: Improvement [%] of local solutions with respect to the corresponding global ones in the Rhine basin for one year time series.

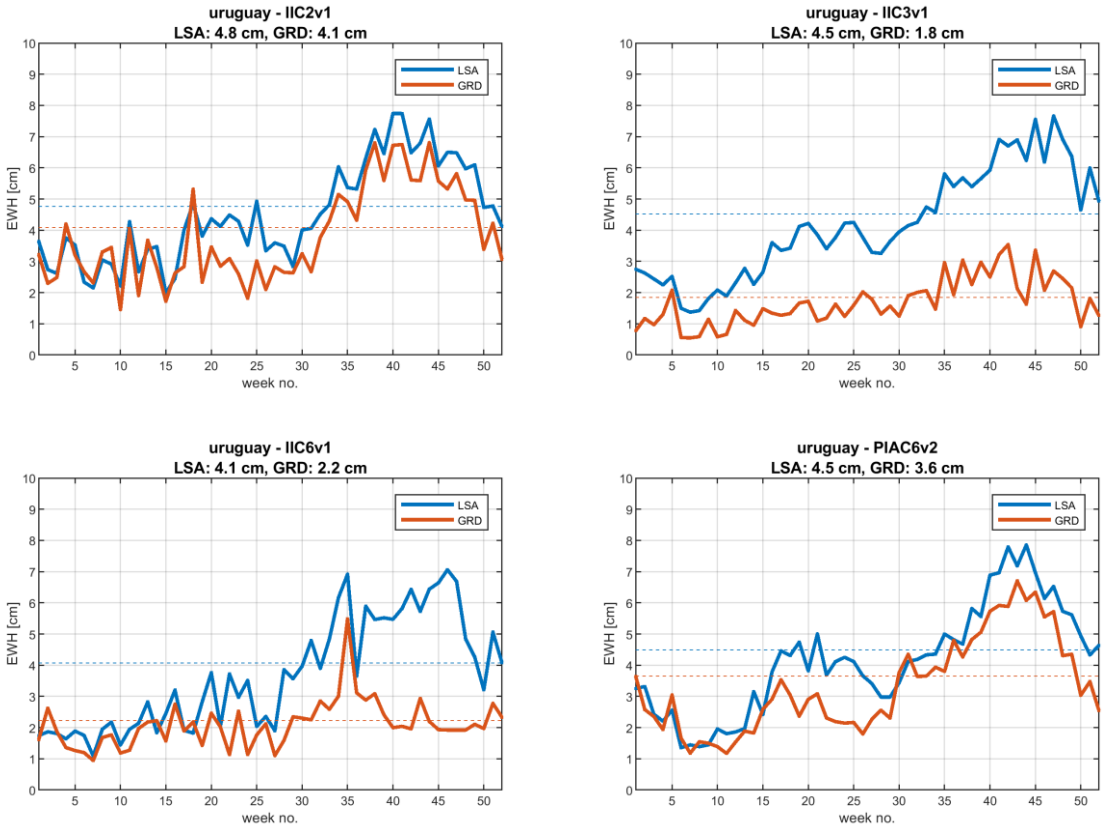

Figure 38-24: Overall empirical error (RMSE) of the estimated TWSA over the Uruguay basin considering 7-day retrieval period and different orbit configurations. The error of the global solutions (least squares adjustment) is represented by solid blue lines, while the error of the local gridding solution (collocation) is represented by solid red lines. Dashed lines represent the 1-year average error of global (blue) and local (red) solutions; these average errors are reported in the title of each plot.

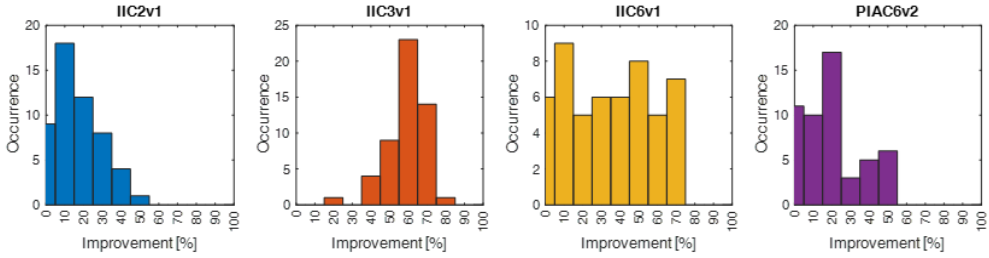

Figure 38-25: Improvement [%] of local solutions with respect to the corresponding global ones in the Uruguay basin for one year time series.

Summarizing, we can state that there is a general improvement carried by the local solutions with respect to the global ones. For instance, considering the Amazon basin, global solutions show a semi-annual trend of the overall error that is not present for the local solutions. This effect is related the power of the medium-high frequency signal of the hydrology that varies during the year (in correlation with the seasons) and that is stronger than the global average. This signal is omitted by the global LSA solution, but can be recovered by local gridding thanks to the local covariance calibration. Table 38-2 shows the average improvement considering the different regions and the different orbit configurations, with an overall average improvement of about 40%. Moreover, as shown in Table 38-3, a general improvement of the quality of the solutions can be obtained by increasing the number of satellites. However, this could be not always true, due to the choice of the orbital planes of the constellations that could also disadvantage some regions even increasing the number of satellite pairs. Considering mixed inline and cross-track pairs of satellites is generally worse than having the same number of inline pairs of satellites.

Table 38-2 Average improvement carried by local collocation solution with respect to global solution considering 7-day retrieval period and the four different orbit configurations.

	Amazon	Danube	East China Sea	Elbe	Ganges	Oder	Rhine	Uruguay	Average
IIC2v1	51.9%	35.8%	-1.7%	32.1%	54.3%	39.4%	46.7%	15.0%	34.2%
IIC3v1	79.7%	43.7%	24.3%	35.2%	77.5%	39.5%	45.1%	58.7%	50.5%
IIC6v1	63.8%	39.0%	30.7%	50.1%	73.8%	1.0%	47.6%	33.7%	42.4%
PIAC6v2	57.3%	29.9%	3.2%	24.3%	54.4%	35.1%	35.1%	18.2%	32.2%
Average	63.2%	37.1%	14.1%	35.4%	65.0%	28.7%	43.6%	31.4%	

Table 38-3: Average overall error (units: cm) of local solutions considering 7-day retrieval period and the four different orbit configurations.

	Amazon	Danube	East China Sea	Elbe	Ganges	Oder	Rhine	Uruguay
IIC2v1	2.7	1.8	3.7	2.4	2.9	2.1	3.3	4.1
IIC3v1	1.1	1.6	2.3	2.1	1.3	1.9	3.6	1.8
IIC6v1	1.5	1.4	2.5	1.2	1.0	2.1	2.5	2.2
PIAC6v2	2.7	2.0	2.1	2.3	2.8	2.0	4.4	3.7

As for the 30-day solutions, these solutions are computed for the 2-pair orbit configuration (IIC2v1) only. Figure 38-26 shows the overall retrieval error (RMS) for the global solutions (evaluated on the considered regions) and for the local solutions. Similarly to the case of weekly solutions, there is a general improvement carried by the local gridding with respect to the global least squares adjustment.

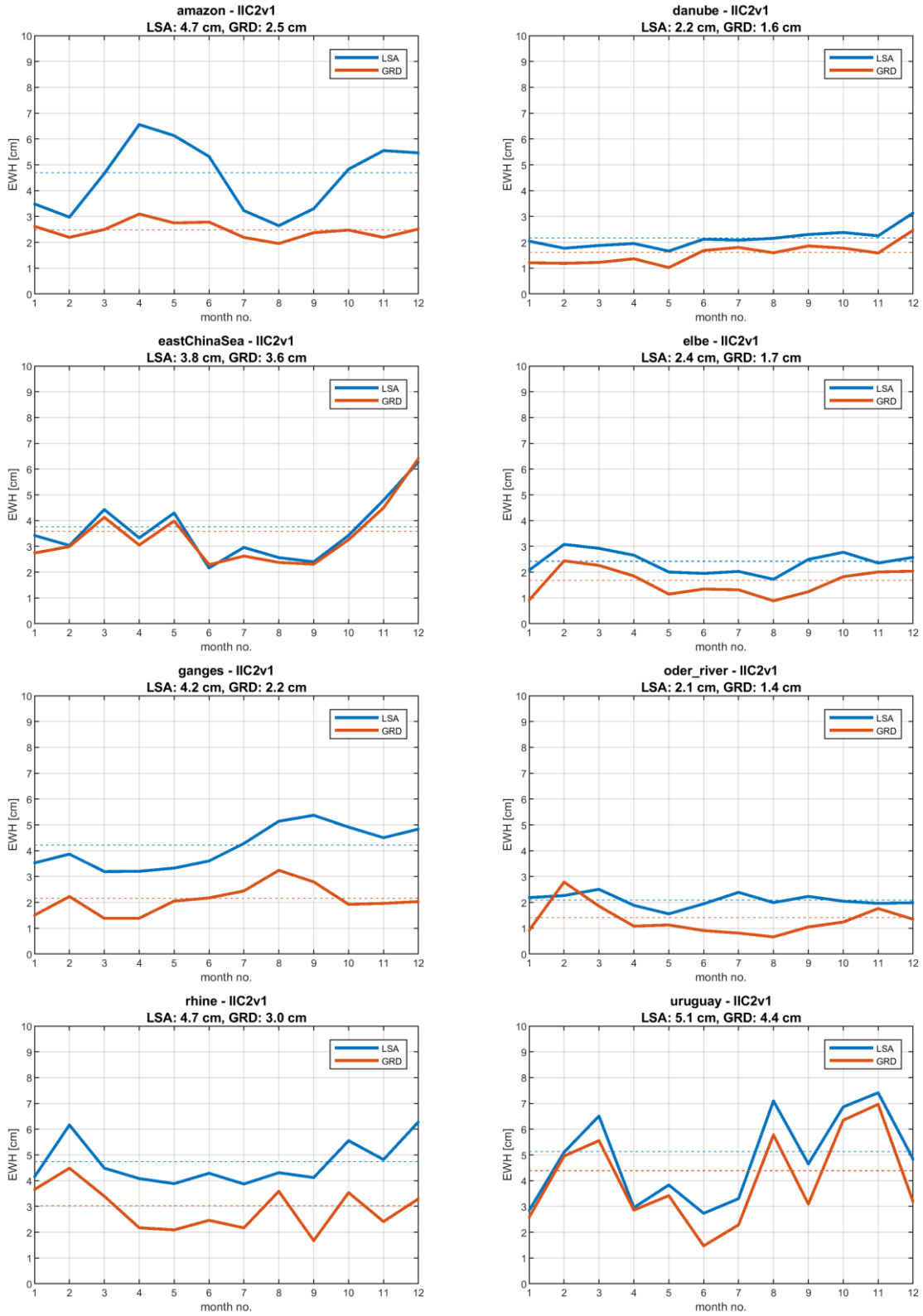

Figure 38-26: Overall empirical error (RMSE) of the estimated TWSA over all the considered basins for 30-day retrieval period and the IIC2v1 orbit configuration. The error of the global solutions (least squares adjustment) is represented by solid blue lines, while the error of the local gridding solution (collocation) is represented by solid red lines. Dashed lines represent the 1-year average error of global (blue) and local (red) solutions; these average errors are reported in the title of each plot.

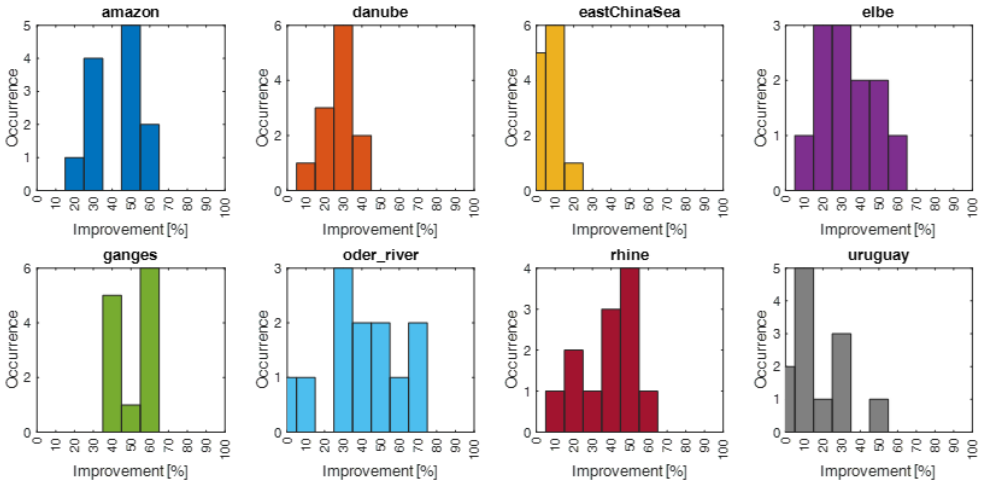

Figure 38-27: Improvement [%] of local solutions with respect to the corresponding global ones for all the considered regions for one year time series computed over 30-day retrieval period.

Similar results are shown also for 30-days solutions. Table 38-4 presents the improvement seen in all the considered regions with a 2-pair constellation, with an average value around 31%. Note that, by comparing the results of Table 38-3 and Table 38-4, we can also state that solutions computed over a 7-day retrieval period have an accuracy almost comparable with the solution over a 30-day retrieval period, even considering the same satellite configuration.

Table 38-4: Average error and average improvement carried by local collocation solution with respect to global solution considering 7-day retrieval period for the 2-pair orbit configuration (IIC2v1).

Region	Local solution RMSE [cm]	Average Improvement
Amazon	2.5	42.0%
Danube	1.6	27.8%
East China Sea	3.6	5.8%
Elbe	1.7	34.0%
Ganges	2.2	49.6%
Oder	1.4	37.7%
Rhine	3.0	37.8%
Uruguay	4.4	18.2%

2.3. Time Series Computation (Solid Earth)

As for the solid Earth studies (WP800), local gridding solutions by collocation approach have been computed according to the procedure explained in Section 6 of document D5, focusing on the earthquake detectability. In particular three orbit scenarios are considered:

- IIC2v1
- IIC3v1

- IIC6v1

For all the solutions the noise level of the X2.1 scenario is considered. As for the background model the signal of the Bengkulu earthquake only is introduced. Ideally, the capability of retrieving this kind of signal rather than isolating it is tested at this level. The considered period is one year after the earthquake and 7-day solutions are computed to see the evolution of the phenomena.

The reference background model has been provided as a time series of coefficients up to spherical harmonic degree and order 1439. To reduce the computational burden, the along-orbit observed signal is simulated up to spherical harmonic degree and order 300, since at ~400 km the omitted signal is smaller than the instrumental accuracy. On the other hand, the estimated local solutions are compared with a reference signal synthetised up to the maximum degree and order (1439).

The local solutions are computed in terms of first radial derivative (T_r) at 10 km altitude, just to be outside from the masses. The resolution is 0.1°×0.1° over an area centred in the epicentre of the earthquake enlarged of about 2°. The overall chosen region ranges in longitude from 99.5° W to 103°.0 W and ranges in latitude from 6.0° S to 2.5° S. An example of the expected signal at ground level (10 km) is reported in Figure 38-28.

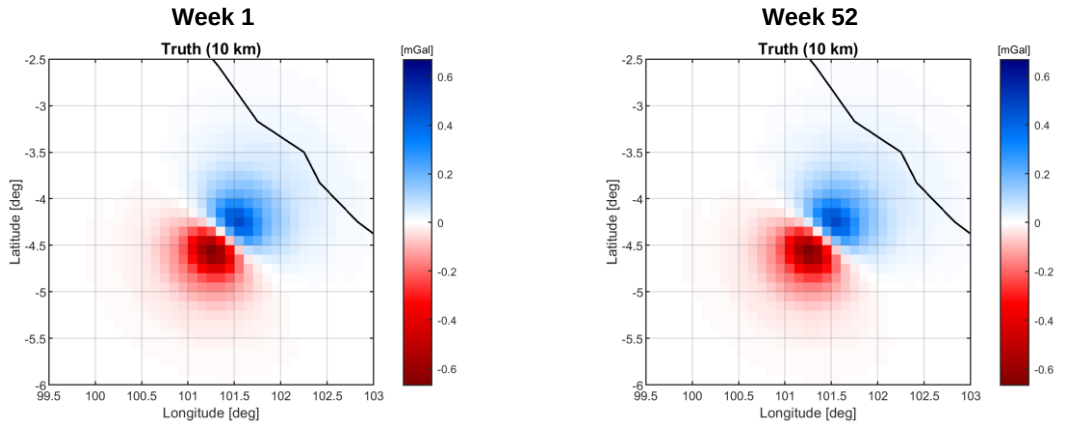

Figure 38-28 Reference signal of Bengkulu earthquake, expressed as first radial derivative computed at 10 km altitude for the week 1 and 52 after the event.

In the following Figure 38-29 the estimated first radial derivative at 10 km altitude is shown for some selected weeks up to one year after the earthquake. It is possible to see that the local gridding solution is able to improve the resolution of the estimate. However, the estimation resolution is far from the actual resolution of the phenomena (compare the estimates of Figure 38-29 with the reference signal in Figure 38-28). Evaluating the empirical error from the direct comparison of the estimate with the true reference signal would lead to a value dominated by the omitted signal. Therefore, a strategy must be devised to empirically evaluate the commission error only. To this aim, the empirical error of the solution is evaluated by comparing the estimated signal with a reference signal computed by limiting the maximum spherical harmonic degree and order. The results, in terms of overall RMSE over the region for the one-year time series, are presented in Figure 38-30, Figure 38-31, and Figure 38-32, for IIC2v1, IIC3v1, and IIC6v1, respectively.

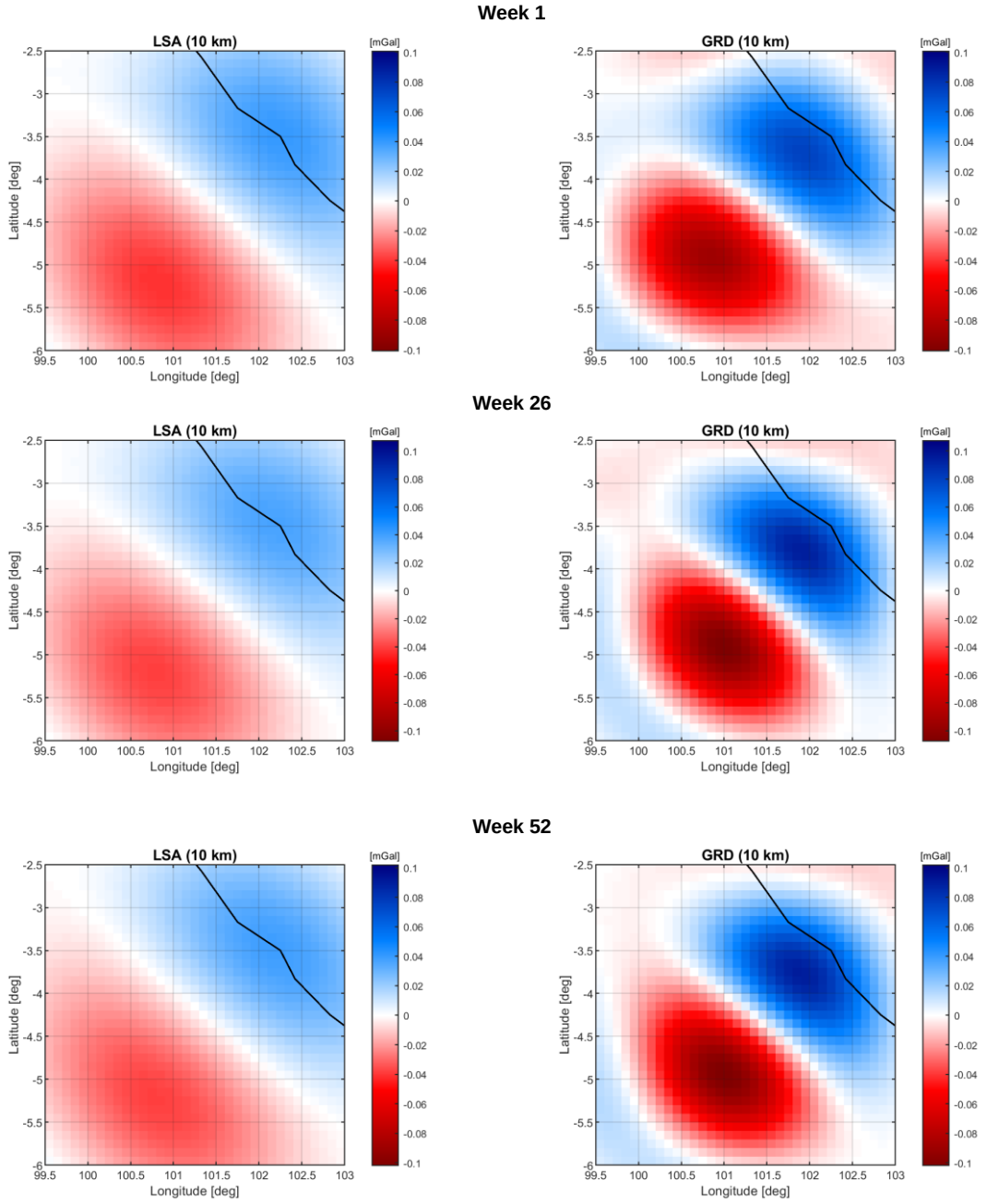

Figure 38-29: Estimated first radial derivative in the region of the Bengkulu earthquake for week 1, 26 and 52 after the event, considering the 3-pair orbit constellation (IIC3v1). In the left column the least squares global solutions are shown, while in right columns the local gridding solutions (collocation) are shown.

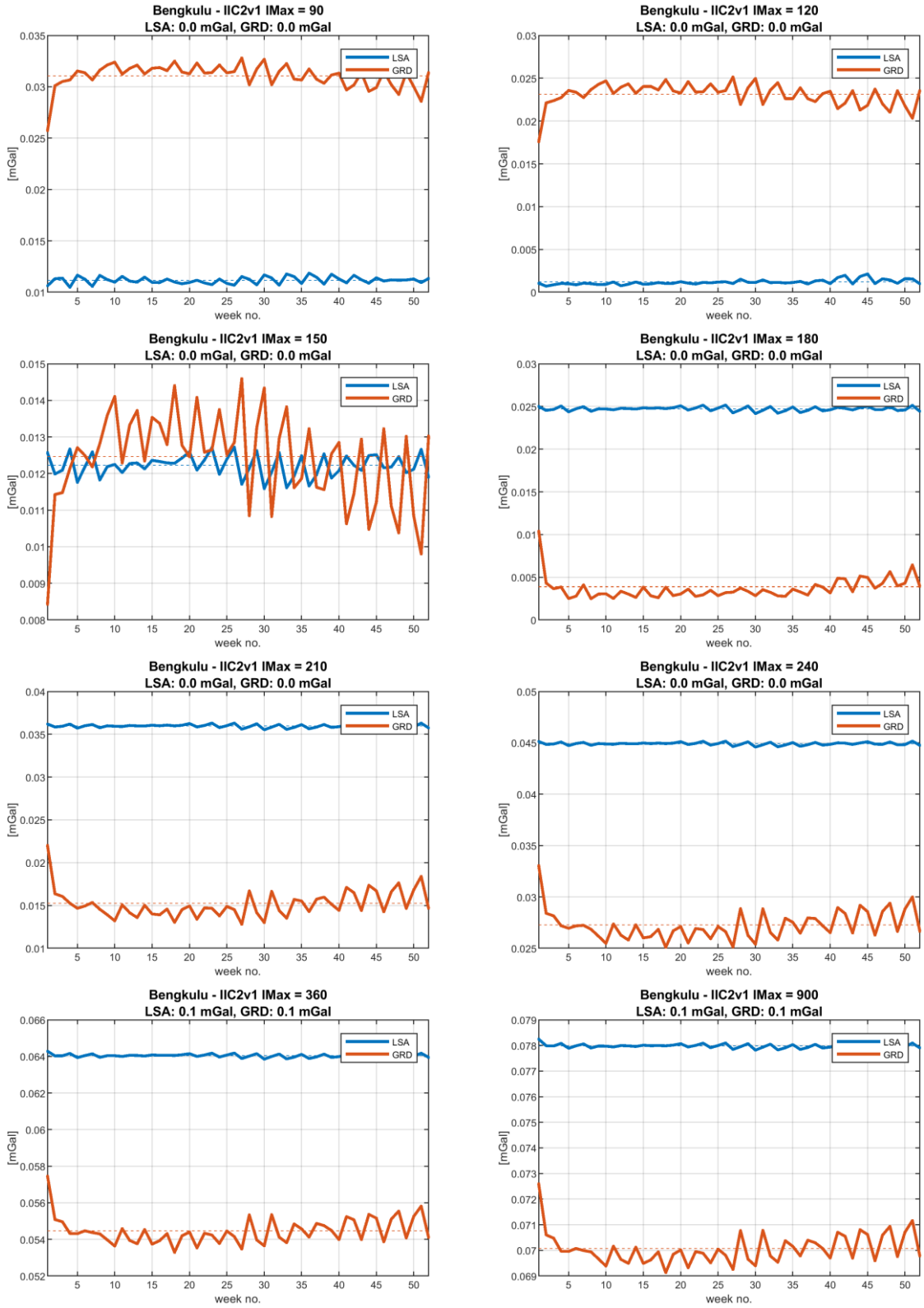

Figure 38-30: Overall empirical error (RMSE) of the estimated first radial derivative for the IIC2v1 orbit configuration. The error of the global solutions (least squares adjustment) is represented by solid blue lines, while the error of the local gridding solution (collocation) is represented by solid red lines. Dashed lines represent the 1-year average error of global (blue) and local (red) solutions; these average errors are reported in the title of each plot. The maximum harmonic d/o used to compute the reference signal to evaluate the empirical error is also reported in the title of each plot.

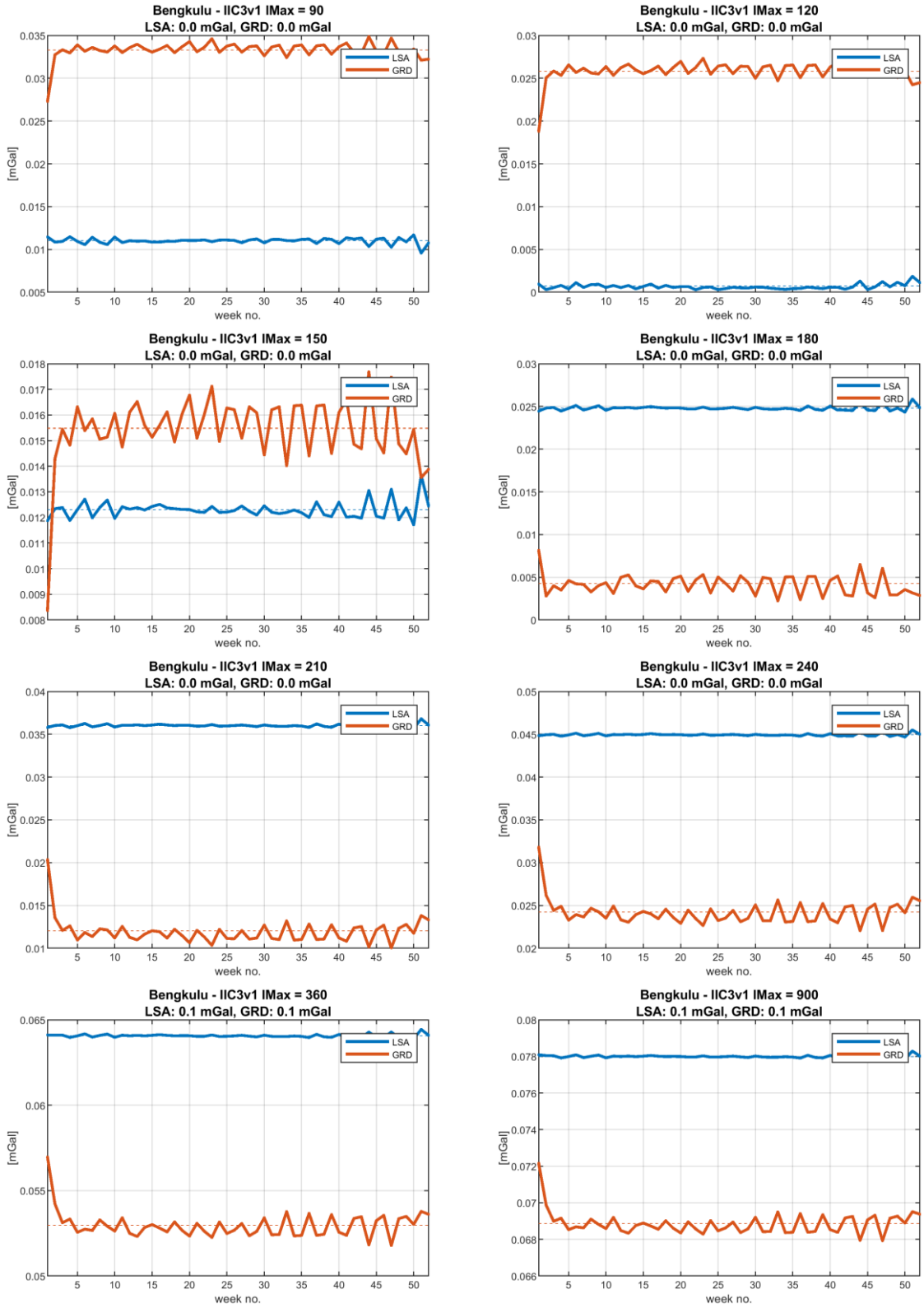

Figure 38-31: Overall empirical error (RMSE) of the estimated first radial derivative for IIC3v1 orbit configuration. The error of the global solutions (least squares adjustment) is represented by solid blue lines, while the error of the local gridding solution (collocation) is represented by solid red lines. Dashed lines represent the 1-year average error of global (blue) and local (red) solutions; these average errors are reported in the title of each plot. The maximum harmonic d/o used to compute the reference signal to evaluate the empirical error is also reported in the title of each plot.

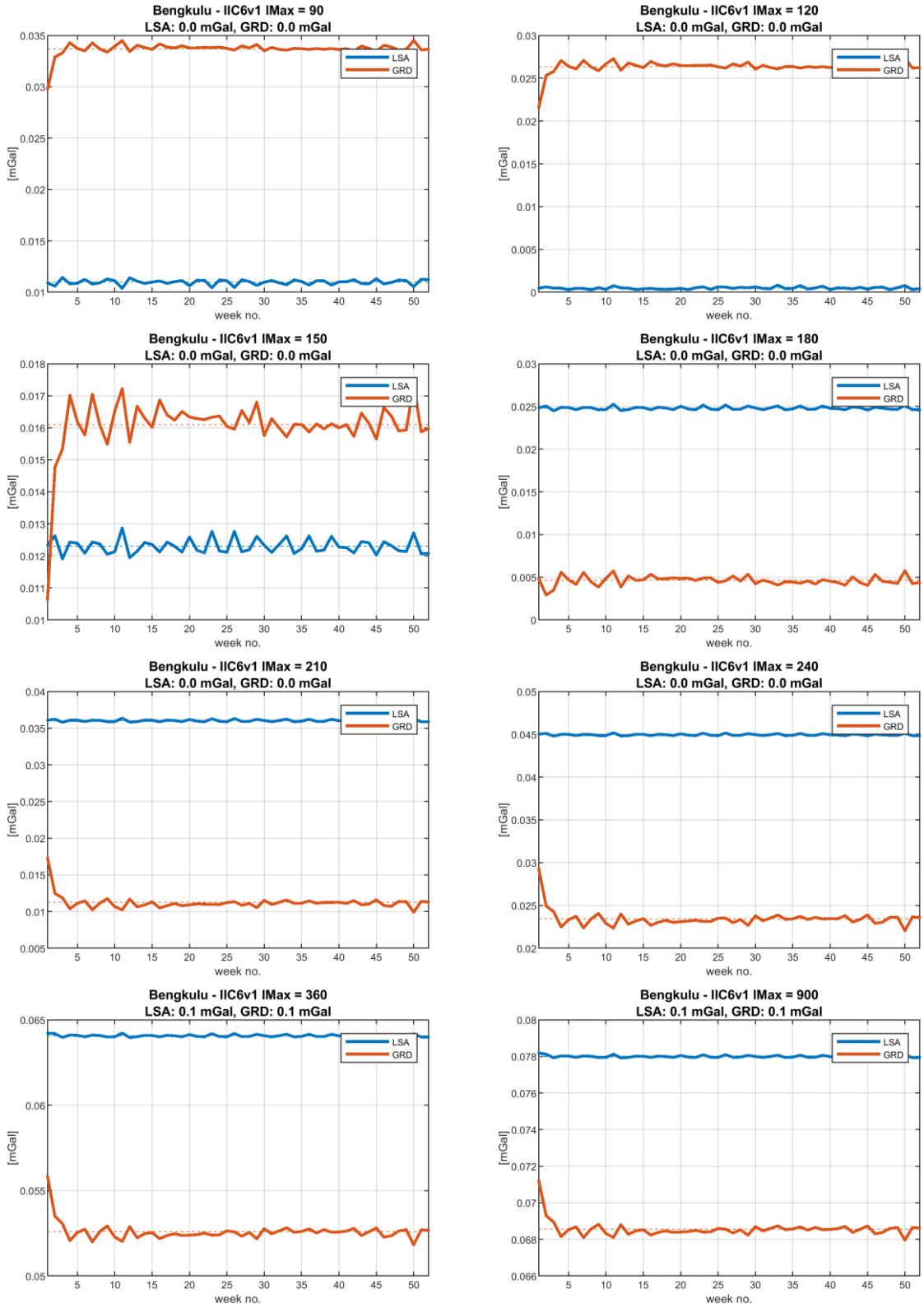

Figure 38-32 Overall empirical error (RMSE) of the estimated first radial derivative for IIC6v1 orbit configuration. The error of the global solutions (least squares adjustment) is represented by solid blue lines, while the error of the local gridding solution (collocation) is represented by solid red lines. Dashed lines represent the 1-year average error of global (blue) and local (red) solutions; these average errors are reported in the title of each plot. The maximum harmonic d/o used to compute the reference signal to evaluate the empirical error is also reported in the title of each plot.

As expected, Figure 38-30, Figure 38-31, and Figure 38-32 show that limiting the harmonic expansion of the reference signal (used for computing the empirical error) at low spherical harmonic degrees (i.e., below 120) results in global solutions to be better than local ones. This could be reasonable, due to the fact that local solutions are weaker in representing long wavelength effects. In fact, they are computed exploiting only observations close to the considered region. On the other hand, increasing the maximum spherical harmonic degree of the reference signal (used for computing the empirical error), it can be noticed that around degree and order 150 global and local solutions are almost equivalent (in terms of estimation error), while, for higher degrees and orders of the reference model, the local solutions show a better behaviour. This is due to fact that local solutions computed by collocation can better model (in terms of covariance function) the power and the correlation length of the local signal than a global least squares adjustment. The minimum error of the local solution is found considering a reference signal up to about degree and order 180, meaning that we are able to estimate the effect of the Bengkulu earthquake with about 1° of spatial resolution. Figure 38-33 shows the empirical error obtained in this case for the three considered constellations for the first week after the earthquake. By considering 6 pairs of satellites the overall error is almost halved with respect to the case with 2 pairs of satellites only.

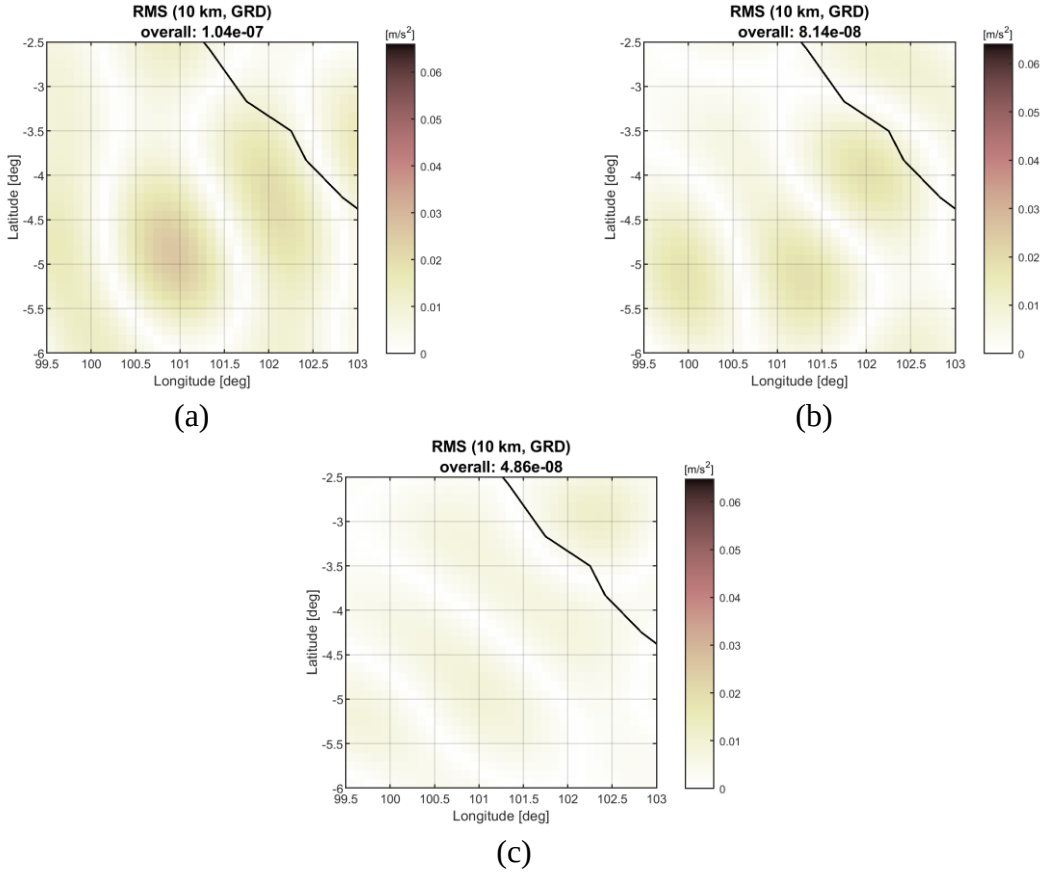

Figure 38-33: Empirical error of the local solution for the first week after the Bengkulu earthquake for (a) IIC2v1, (b) IIC3v1, and (c) IIC6v1 constellations. The reference signal to evaluate the error is synthetised up to harmonic d/o 180.

39. DATA SETS FOR WP800-1000

Experiments and assessments in WPs 800-1000 rely very much (1) on the error scenarios that underly the TUM simulations, and (2) the way how error information from these scenarios is numerically represented and can be used in inversion and data assimilation approaches. Before we describe the data sets which were provided to us, we would like to clarify his with the following table:

Table 39-1: Error scenarios of the TUM simulated SHCs and treatment of error information.

SHC	TWSA grid errors and correlations	Numerics	Realism	Applicability for non expert
Empirical diagonal	Diagonal		Error pattern may be incorrect	No SHC cov required
Empirical full	Diagonal		Good	Needs expert
Empirical full	Full	Rank defect		
Scaled formal diagonal	Diagonal		Error pattern may be incorrect	Needs only standard data
Scaled formal full	Diagonal		Good	No SHC cov required
Scaled formal full	Full	May need localization	Very good	Needs expert
-	constant + isotropic correlation		Good	heuristic

Spherical harmonic coefficient (SHC) errors following from end-to-end simulations can be characterized by scaled (often called calibrated) formal error covariance matrices that follow from normal equations and data residuals, or by empirical errors from a simulation truth. The former may not capture fully the de-aliasing errors (partly only via scaling), while the latter leads to rank-deficient matrices which poses a problem whenever the error correlations are deemed important, such as in collocation or data assimilation.

Furthermore, we can categorize the options into standard approaches, where users have only access to SHC sigmas or they do not want to use full correlations or the analysis system (e.g. operational assimilation framework) does not allow one to consider these, and expert users which have the possibility to work with, and apply full and possibly time-varying error covariances.

The following data sets are available to WPs 800-1000:

Dataset 1 (received on May 11th, 2023)
Different simulation scenarios have been received from TUM for a time period of three months (January 2002 – March 2002)
The data consists of

- Gravity field solutions,
- Normal equation systems.

Three versions with different temporal resolutions are provided:

- 1 day,
- 7 days,
- 30 days.

Simulation scenarios with a different number of satellite pairs and different orbits between 370km and 440km altitude are available (see Figure 39-1). During the selection of mission architectures it has been agreed to use the following scenarios in this study:

- IIC3v1: 3 inclined pairs (89°, 70°, 40°)
  - 1day: max d/o 45
  - 7 days & 30 days: max d/o 120
- IIC6v1: 6 inclined pairs (89°, 80°, 71°, 60°, 48°, 33°)
  - 1day: max d/o 60
  - 7 days & 30 days: max d/o 120

Additionally, the following references are available in the same format:

- Simulations of GRACE-FO
- Simulations of MAGIC
- HIS part of ESA ESM

Input signal:

- HIS + AO - [AO_deal + AO_err]

Constellation types →

Number of pairs ↓

Type / N° pairs	Inclined constellations (inline)		Polar constellations (89°)	
	IICXv0	IICXv1	PACXv1	PIACXv1
2-pair	**IIC2v1** (1x89°,1x70°)		**PAC2v1** (2x ac)	**PIAC2v1** (1x ac, 1x il)
3-pair	**IIC3v0** (1x89°, 2x70°)	**IIC3v1** (89°/70°/40°)	**PAC3v1** (3x ac)	**PIAC3v1** (2x ac, 1x il)
6-pair	**IIC6v0** (1x89°, 2x70°, 3x40°)	**IIC6v1** (89°/80°/71°/ 60°/48°/33°)	**PAC6v1** (6x ac)	**PIAC6v1** (3x ac, 3x il)

Figure 39-1: : Overview of simulation scenarios from TUM (modified from slide 114 of PM2). Scenarios available for WP 800-1000 are marked in red

The (formal) covariance matrices that were received from TUM only contain instrument errors and (so far) no temporal aliasing errors. For WPs 800-1000 realistic covariances are however important. Therefore, a scaling approach of the covariance matrices has been discussed and agreed upon with TUM and implemented. The covariances are scaled degree-wise with factors derived from ratio of empirical and formal degree variances.

Dataset 2 (received on January 29th, 2024)

We received 12 years (1995-2006) of monthly simulated gravity fields for GRACE-FO and MAGIC including spherical harmonic coefficients and the corresponding sigmas. Full NEQs are only available for January and February 1995 and they only contain the instrument noise. Input signal:

- HIS + AO - [AO_deal + AO_err]
- same input signal as in Dataset 1, but different simulator (reduced-scale simulator with 30-day repeat-orbit)

Dataset 3 (Received on February 17th, 2024)

We received 12 years (1995-2006) of weekly gravity fields for the following scenarios:

- IIC1v1 (assuming GFO instrument noise; also referred to as "GRACE-FO")
- IIC2v1 (assuming MAGIC instrument noise; also referred to as "MAGIC")
- IIC3v1 (also referred to as "CAI3")
- IIC6v1 (also referred to as "CAI6")

The data consists of spherical harmonic coefficients and NEQs, which only contain the instrument noise, so far.

Input signal:

- AOHIS_updated-DEALAOerr07 (updated S-component: GIA and simulated earthquakes from WP700)
- Reduced-scale simulator with 30-day repeat-orbit (same as in Dataset 2)

Additionally, we received one representative weekly empirical static VCMs for the whole 12-year period from residuals for each scenario. However, the VCM has a rank defect, such that it cannot be inverted to a NEQ matrix.

In a first step, we have opted therefore to make use only of the diagonal part of these error matrices, i.e. effectively neglecting spatial correlations. This can be considered as an ad-hoc approach, but the problem remains that at the 50km scale large real correlations are present for all scenarios (even smaller for multi-pairs) and disregarding these means that all data are considered as too accurate.

In a second step, we apply degree-wise scaling factors to the full formal covariance matrix. These factors are derived from the main diagonals of the formal and empirical covariance matrices. In this way, the scaled matrix has full rank and is closer to the empirical one.Figure 39-2 shows standard deviations in the spatial domain over South America. They are derived from the full scaled formal covariance matrix and from the diagonal of the empirical matrix. Both maps show the same order of magnitude in the range of several mm.

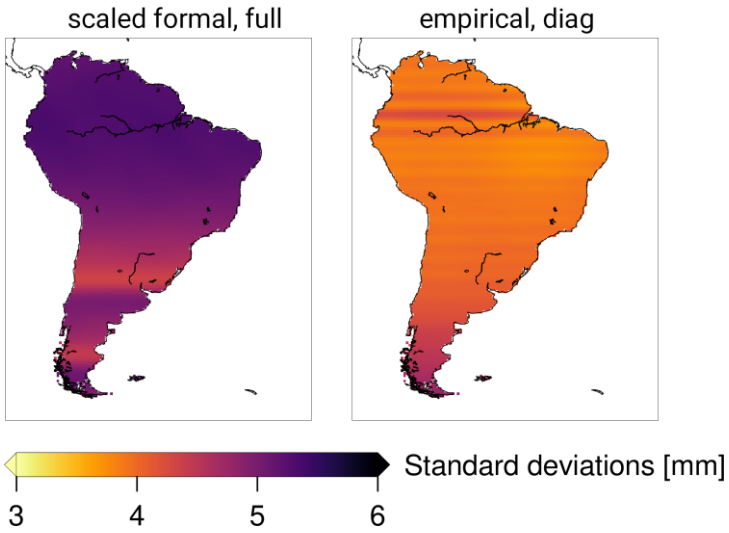

Figure 39-2: Standard deviations shown in the spatial domain for South America. The standard deviations are derived from the scaled formal covariance matrix (left) and from the diagonal of the empirical covariance matrix.

40. WP800: SOLID EARTH APPLICATIONS

In the context of WP 810, interaction with WP 700 was carried out, to provide preliminary regions and signal examples aiding their optimized regional solutions definitions. The following areas were provided:

- South America, rectangle of longitude: [82° W, 64° W], latitude: [45° S, 27° S]. Example signal: Maule (2010) earthquake.
- Mayotte (western Indian Ocean): circle centred on longitude 45.17° E, latitude 12.83° S, with an 8° radius. Example signal: Fani Maoré submarine volcano.
- Eurasia – Arabia plate boundary: rectangle of longitude: [24° E, 64° E], latitude [24° N, 46° N]. Example signal: static gravity field and isolated intra-crustal bodies / sedimentary basins.
- As agreed, these areas were defined with their maximum reasonable extents for the applications of interest, with the option of reducing the extents if beneficial to the optimized regional solutions. Example signals were provided as global equiangular grids and SH expansions.

These areas are plotted in Figure 40-1.

Regarding the signal repository involved in the Solid Earth applications (WPs 820, 830, 840, and 850), the activities involved the computation or collection of the geophysical signals to be used as targets in the detectability analyses:

- **Earthquake Signal Repository:** definition and computation of the co- and post-seismic signal from synthetic models of real events. The repository allows to isolate the gravity change due to the earthquake rupture and the subsequent viscoelastic relaxation, between any given time-frame from the source time to the subsequent years.
- **Seamounts:** computation of the mass change due to sudden submarine eruptions, for a set of documented events, including the Fani Maoré submarine volcano sudden growth (2014-2015) and the Hunga Tonga-Hunga Ha'apai sudden explosion (2022). Onsite

surveys and/or remote sensing, in addition to petrologic analogies to other seamount systems, support the mass change estimates.

- **Vertical movements:** collection of GNSS time series, isolation of the long-term trends in vertical movement, to construct a time-varying surface change model and its gravity effect
- **Lithospheric Structure:** using a model of crustal structure in the test area of the Eurasia – Arabia collision (encompassing the Caucasus and Zagros Mountains and the surroundings basins), the spatial distribution of intra-crustal bodies (e.g. different geologic units, volcanic complexes) and sedimentary basins was isolated. It respectively serves as a target signal for the retrieval of large-scale static structures and to analyse mass changing with different porosity scenarios.
- **Deep Earth Structure:** Dr. Bernhard Steinberger (GFZ) provided a model of long-term mantle dynamics and their gravity effect. In this case, the signal to be detected consists in the difference between two model snapshots, 1 Myr apart, re-scaled according to the timeframe of the observation (e.g. the 1-year change in gravity is represented by 1 ppm of the snapshot difference).

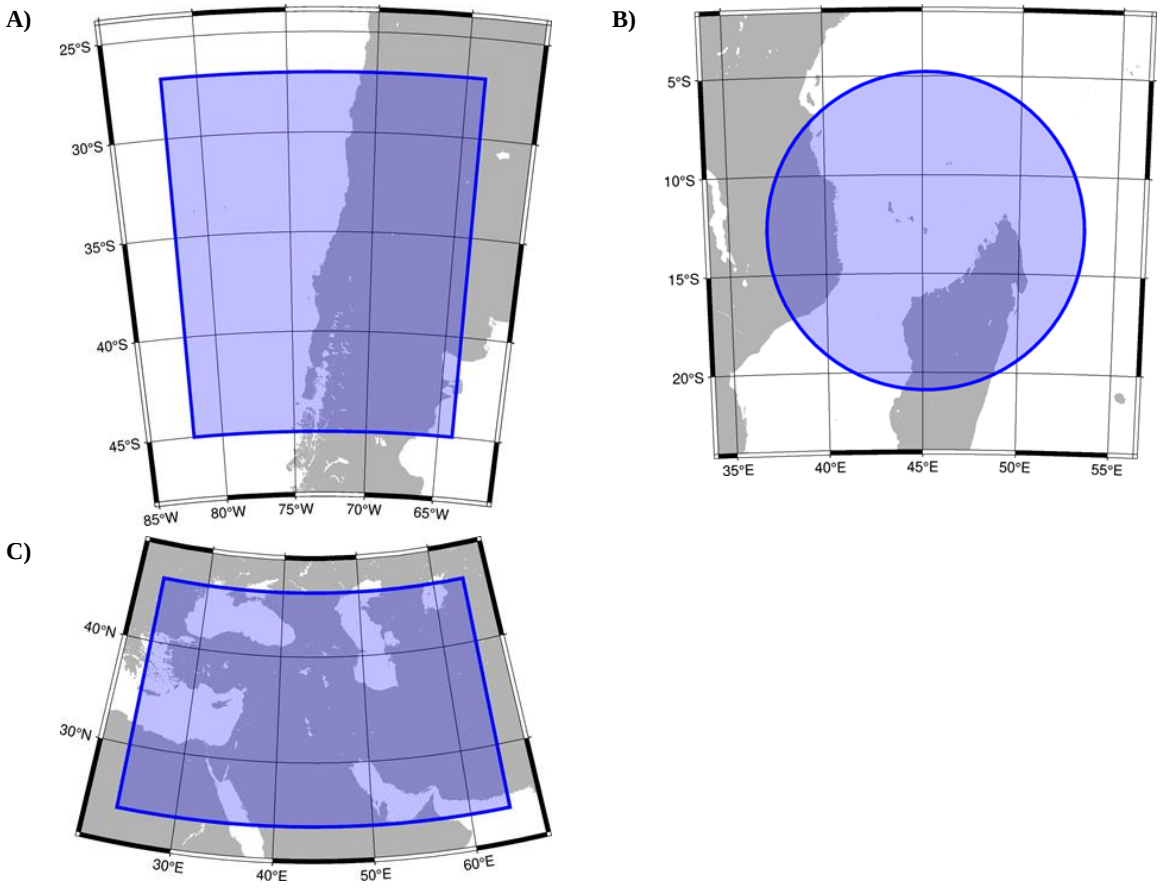

Figure 40-1: Regions provided in the context of interaction with WP700 / POLIMI. **A)** South America; **B)** Mayotte; **C)** Eurasia-Arabia plate boundary

Examples of these signals, synthesized in space on a regular grid, are plotted in Figure 40-2.

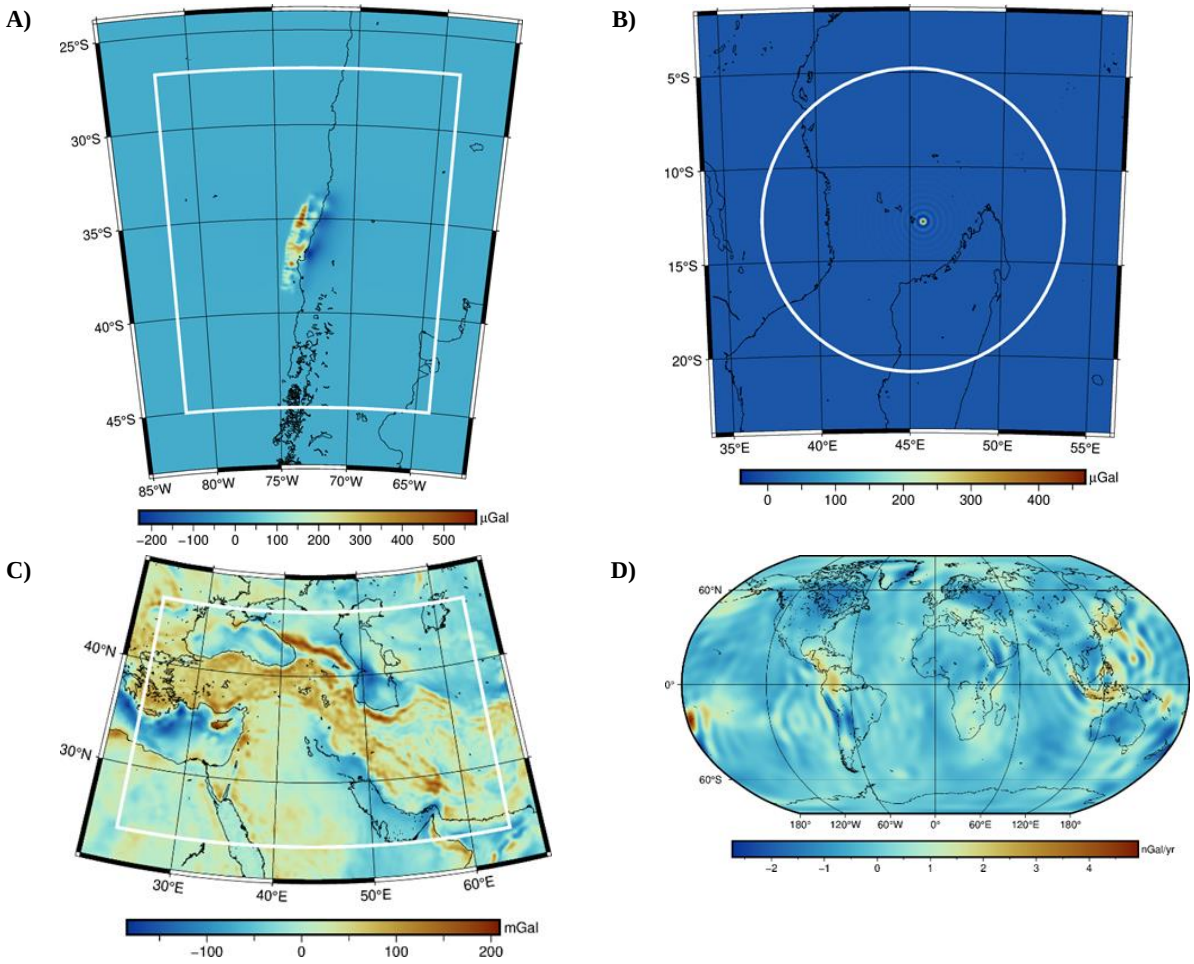

Figure 40-2: Examples of the gravity change from geophysical phenomena part of the repository. **A**) Maule (2010) earthquake, co-seismic signal for a finite-fault solution (units: 1 μGal = 10-8 m s-2); **B**) gravity change due to the 2014-2015 eruption of Fani Maoré submarine volcano, using a synthetic cone source fitted to the surveyed change in bathymetry (units: 1 μGal = 10-8 m s-2); **C**) observed gravity field in the Eurasia-Arabia collision zone (units: 1 mGal = 10-5 m s-2); **D**) 1-year signal of the secular trend due to mantle dynamics (units: 1 nGal yr-1 = 10-11 m s-2 yr-1). All the signals are represented as change in the first radial derivative of the disturbing potential (T_r), at ground level.

In the first stages of the work, the error curves of three different mission architectures: IIC6v1 (6 pair), IIC3v1 (3 pair) and PlAC3v2 (3 pair) were compared with a benchmark signal – a synthetic pure-thrust 30-km deep earthquake, which we scaled to different magnitudes (i.e. for a constant unitary moment tensor $\boldsymbol{M}$, describing the body forces involved in the dislocation, the seismic moment M_0 is changed). The comparison has been carried out for both the 'filtered' and 'unfiltered' solutions. An example with the 'filtered' case is shown in Figure 40-3. The IIC6v1 (6 pair) and IIC3v1(3 pair) are the most favourable and the former has been chosen as baseline scenario. For the solid earth signals we conclude that the non-filtered solutions should be used because the filtered solutions choose the HIS signal as a reference above which the signal is considered noise. The solid earth signals being of greater amplitude than the HIS, the gravity solutions can be used to greater degree and order and the filtering will take away potentially useful signals.

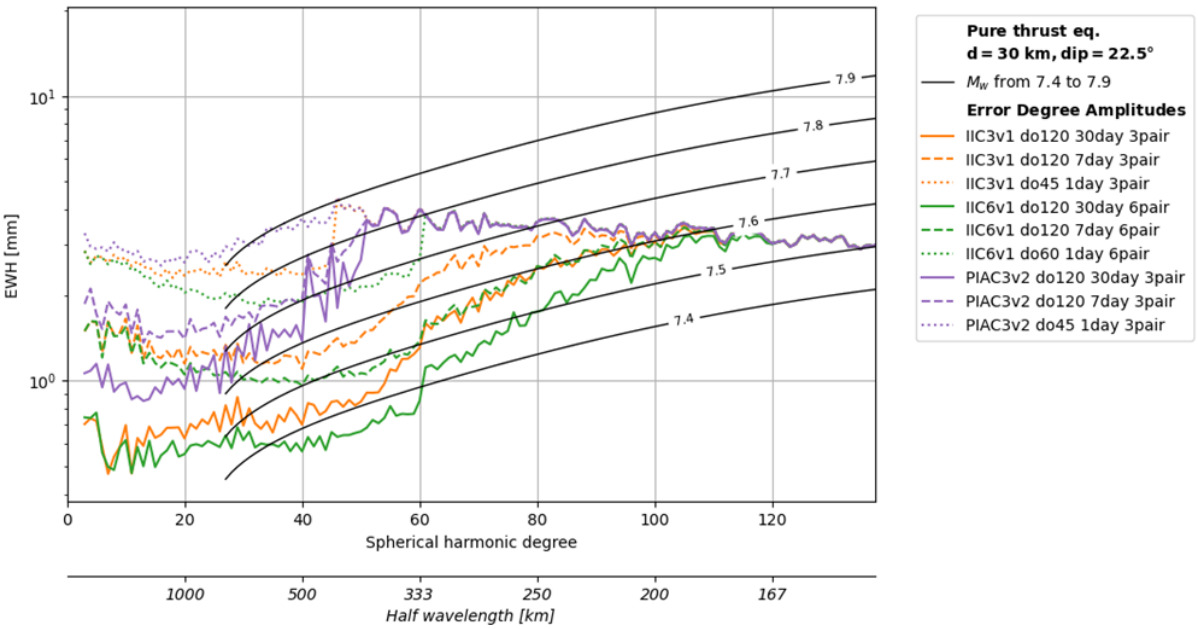

Figure 40-3: Comparison of a benchmark signal (a pure thrust earthquake at 30 km depth, scaled at different magnitudes) with the curves in three provided scenarios (6-pair IIC6v1, 3-pair IIC3v1and 3-pair PlAC3v2), using the filtered version of the solutions. All spectra expressed in Equivalent Water Height (EWH) degree amplitudes, non cumulative. The error degree amplitudes shown refer to the retrieval error with respect to HIS. The earthquake spectra are localized in a 8-degree spherical cap window.

The earthquake detectability segment involved setting up the models output in a format suitable to update the HIS model used in simulators. The activities thus involved a close cooperation with the units involved in the tasks of WP400, which have been responsible for the actual implementation of our models into HIS.

The format we opted to use for the model outputs (global solutions of the geopotential change for the co- and post-seismic deformation) conforming with the format of Earth System Models are provided in files with the spherical harmonics coefficients of the model signal at provided timestamps. The actual file format is the well-documented GFC from ICGEM, with an added header on earthquake specific metadata (including the time since the earthquake source ruptured). The earthquake models - a separate one for each event - were provided as series of GFC files sampled at different time intervals, finer close to the event, when the viscoelastic relaxation shows a faster rate of change in time, and coarsening out through time, up to 4 years since the source time. The files are meant to be interpolated at the required interval in the mission simulation phase.

A time-staggering strategy was agreed on with the TUM unit / WP 400, in order to fit the modelled events and a sufficient coverage of the post-seismic gravity change. The time pattern, which is described in the relevant WP, models the earthquake source time in the simulation in two clusters: 1) events geographically close to the Sumatra 2004 event, where the time distance between events is conserved (to allow modelling a realistic overlap of large earthquakes in the earthquake cycle involving the area) 2) events in other areas of the globe, where it was opted to avoid the overlap between the post-seismic change of the events as much as possible, distancing the events at least 3 months between source times.

We received the simulation results from the TUM unit / WP400 as a series of weekly solutions

covering the 12 years of simulations, for the 4 simulated scenarios (1, 2, 3, 6-pair), accompanied by the 6-hourly reference signal (HIS updated with our earthquakes). The detectability analyses that we set up involve two different strategies:

1) comparing the signals (as localized spectra) with the retrieval errors, which are computed as residuals between the observed (simulated) signal and the average reference signal in the same time interval. In this strategy, which conforms to the type of detectability analysis involved in the other solid Earth signals, the criterion for positive detectability is a SNR > 1 at each spherical harmonic degree at which both the localized signal spectrum and the error degree spectrum are available;

   The significant improvement in detection of the earthquake is found starting from 2 satellite couples. The next figure shows the cumulated spectrum of the coseismic signal and the post-seismic signal accumulated in one week. This signal is compared to the retrieval error for a 7 day solution. In the figure furthermore the isolated postseismic relaxation signal is shown for 30 days with the aim to estimate detectability of the post-seismic signal (co-seismic signal removed) in 30-day solutions. The error degree RMS spectra shown here were obtained by averaging of four 7-day solutions (28 days) and scaling to 30 days.

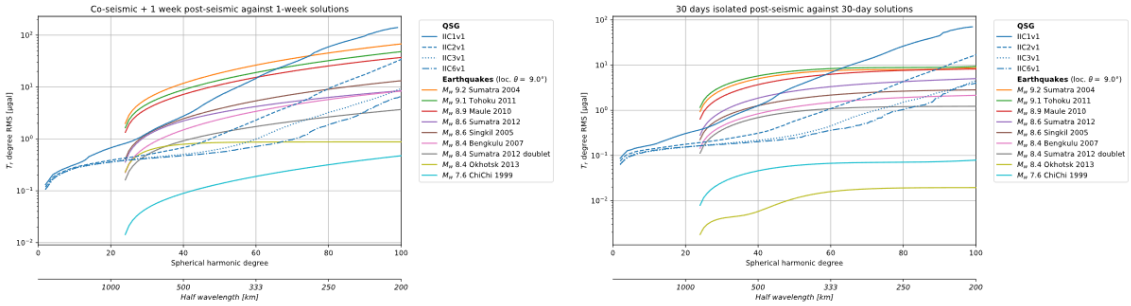

Figure 40-4 Retrieval error spectra of QSG compared to the localized spectra of the collection of earthquake signals. Short-term detectability of co-seismic and post-seismic change in the first 7 days and 30 days, respectively after an earthquake, compared with the average retrieval errors. Fields calculated at zero height, cumulative spectrum.

A means to illustrate the time-spectral degree dependence of the detectability of the postseismic signal in the next figure, the signal-to-noise intersection (SNR=1) is plotted, with contours, and ticks indicating direction towards SNR > 1.

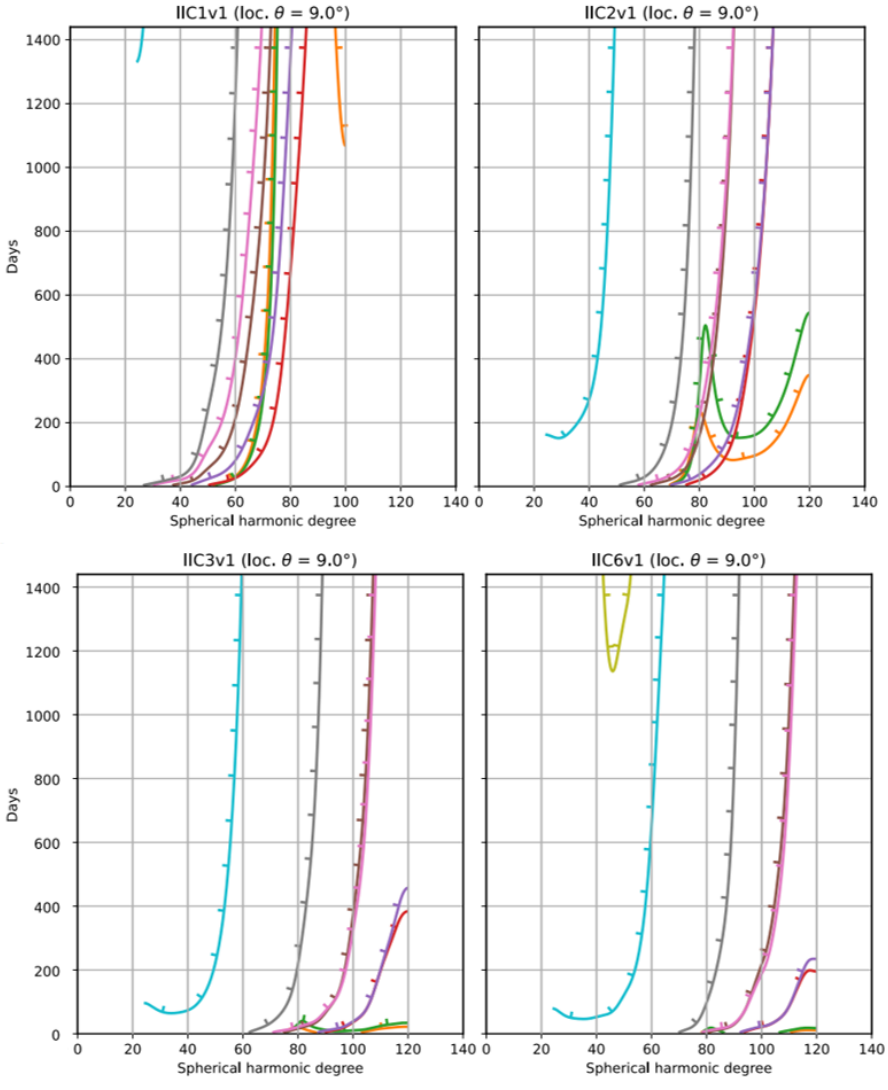

Figure 40-5: Detectability of the post-seismic signal (co-seismic signal removed) for a varying length of observation time. For each observation time, the signal-to-noise intersection (SNR=1) of the non-cumulative spectrum is plotted, with contours. Ticks indicate the direction towards SNR > 1. Color key: same as in the previous earthquake figures. For a longer observation period both the post-seismic signal and the errors are varying – the post-seismic signal decreases at a smaller rate than improvement in errors.

2) performing a realistic signal-retrieval analysis of the simulated gravity products, conforming with a workflow that resembles the signal analysis of any real gravity product (e.g. level-2 global gravity models as available from GRACE). In this strategy two methods have been tested:

A) difference between products (either as 7-days solutions or averages of more solutions), to isolate the change of all time-varying signals (earthquake co- and post-seismic change plus all the rest of HIS signals and their retrieval errors). These are then compared to the known earthquake signals (the aforementioned "reference signals") that are part of the simulations, the updated HIS model.

B) time series analysis in the space domain, where a time-dependent model function is fitted on the time series of signals of each grid node in an area of interest - i.e. the signal in time in each pixel of the grid obtained by synthesising the SH coefficients (up to a chosen maximum SH degree) for all the simulated solutions.

The detectability analysis using strategy 1 (SH-domain, average retrieval error based) has been fulfilled for both the cumulated co- and post-seismic signals and for retrieval of a purely post-seismic signal (isolated through removal of the co-seismic signal). It is shown in Figure 40-4 Retrieval error spectra of QSG compared to the localized spectra of the collection of earthquake signals. Short-term detectability of co-seismic and post-seismic change in the first 7 days and 30 days, respectively after an earthquake, compared with the average retrieval errors. Fields calculated at zero height, cumulative spectrum.Figure 40-4. Analysis using strategy 2 is a means to verify the spectral analysis in spatial domain. The results show that if in strategy 1 an earthquake is not visible because the signal spectrum is never above the noise spectrum, in spatial domain the earthquake signal is not above the retrieval error. In the next figure the signal of the Maule 2010 earthquake is shown, in relation to the amplitude of the retrieval error of a single to six couples scenario. As noticed also in the spectral curves, there is a definitive improvement with the double couple, as the earthquake signal is clearly seen.

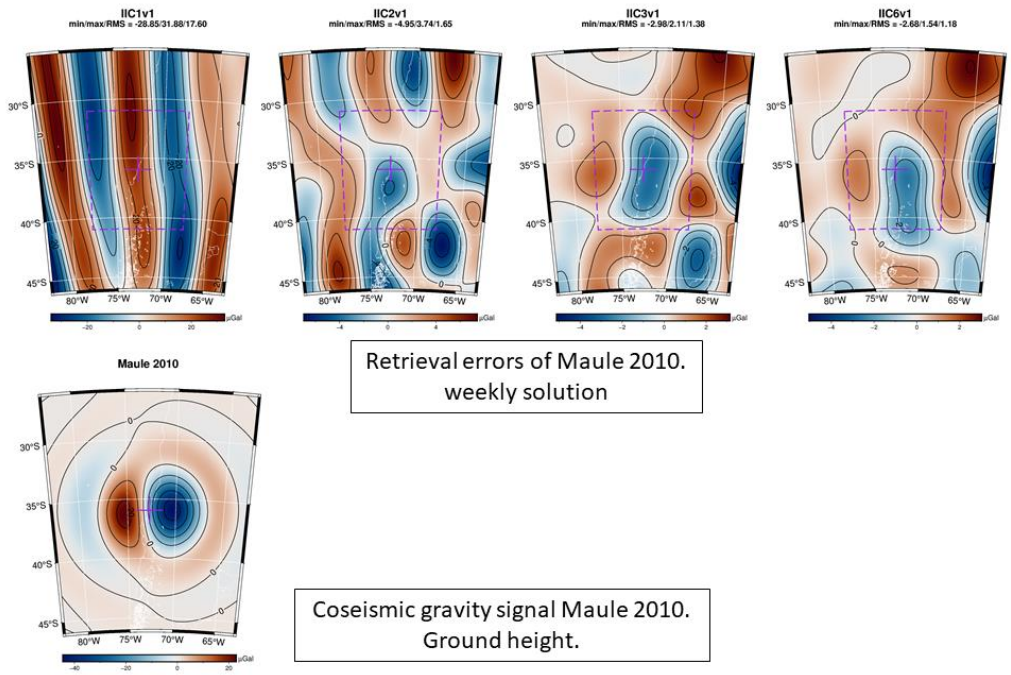

Figure 40-6: Retrieval error for the Maule 2010 earthquake. In this example, the week that includes the seismic event is skipped, not being included in the difference. This example shows the improvement in retrieval (with no signal separation of HIS performed) between the 1- and 2-couple scenario.

The next step is to proceed to strategy 3), that aims at the signal separation of the coseismic earthquake signal from the hydrologic signal present in the observations. The time-series analysis aims to remove the seasonal signal, and isolate the seismic gravity change. The model function includes bias, slope, annual and semi-annual components, and a Heaviside step-function for the coseismic earthquake gravity change. We select one station point (see cross in

Figure 40-6) to create the time series of the retrieved gravity field for illustration. The figure shows the observed field for the four constellations, the fitted field, and the residual, defined as observed minus fitted field. The map of the amplitude of the heaviside function represents the retrieved earthquake amplitude. The spectral analysis had shown that the Maule 2010 event would be seen with a single couple for a restricted bandwidth, whereas the coseismic field is retrieved over a bandwidth up to degree N=100 for the six couples. The outcome is seen in the next two figures.

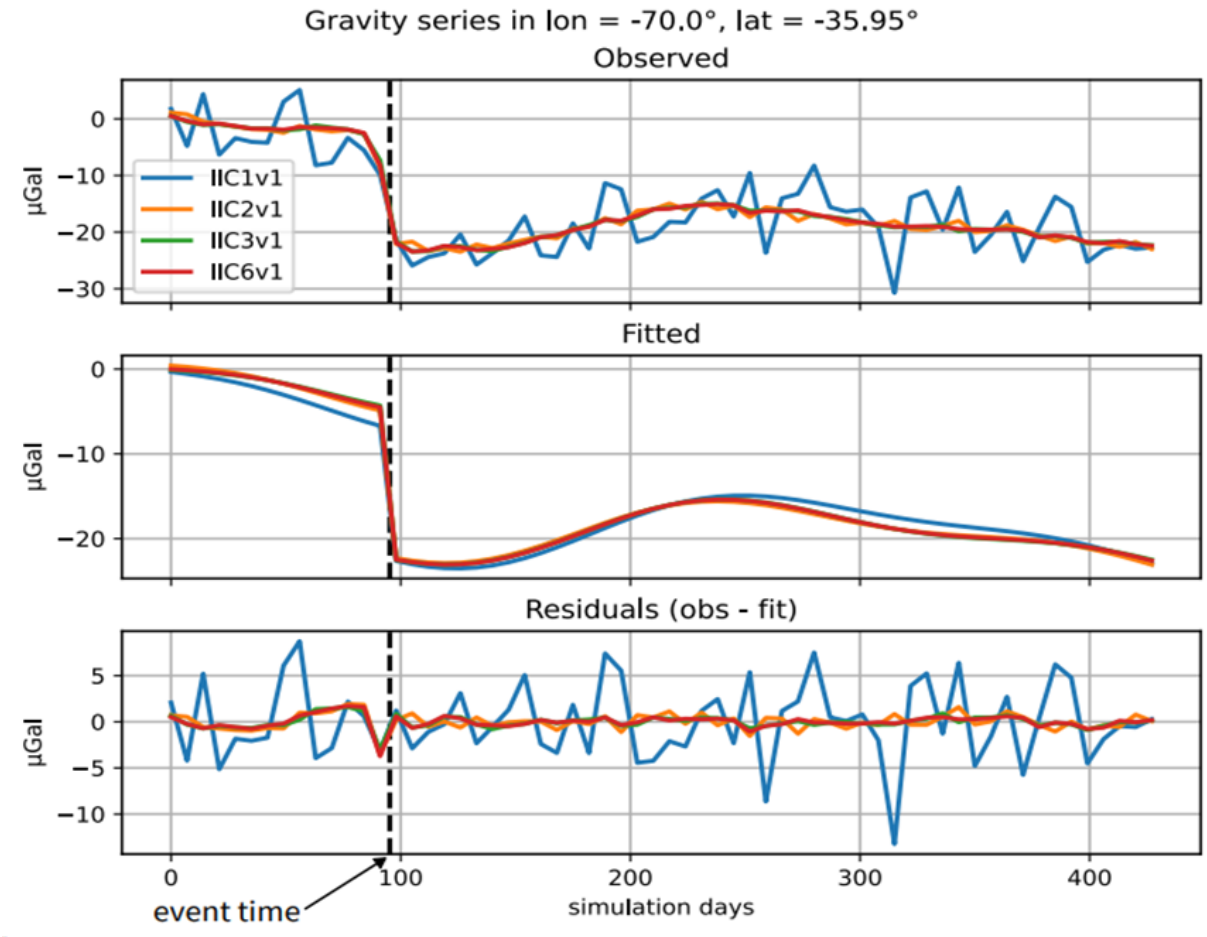

Figure 40-7: Time-series fitting on a selected point (corresponding to the minimum peak, east of Maule 2010 source, as shown in the previous figure). The model function in this example includes a slope, an annual and a semi-annual component, and a step function, corresponding to the earthquake.

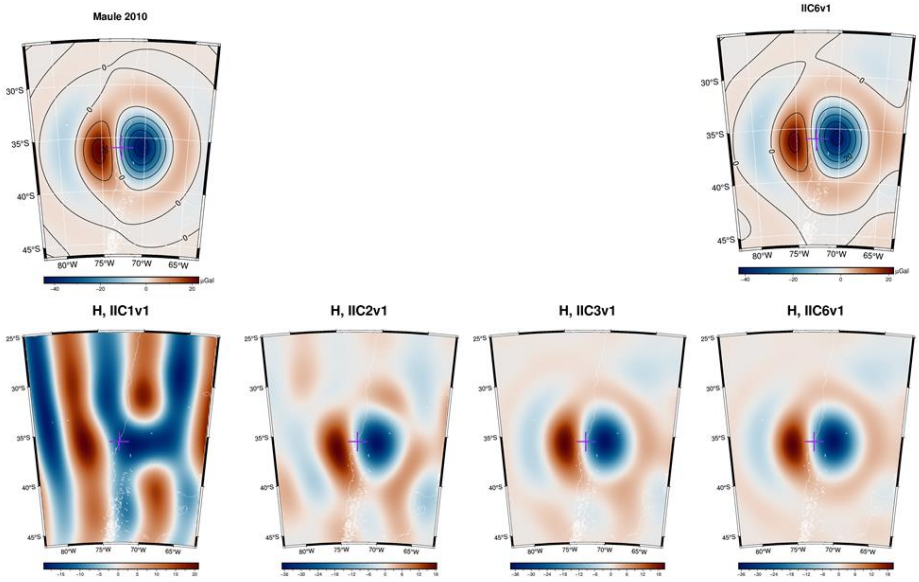

Figure 40-8: Separation of the coseismic gravity change for the Maule 2010 earthquake. The maps show the amplitude of the best-fit Heaviside amplitude for different satellite constellations. In the upper row: the synthetic Maule coseismic signal and the observed signal, including the HIS variation.

The seamount volume and mass change estimates that we collected are summarised in Table 40-1. They serve as input for the gravity modelling, with which we obtained the target signals for the seamount segment of WP 830. The mass change is mostly positive, due to a magma eruption which places mass at the top of the seamount. Only for the HTHH 2022 explosion the mass change is negative (Braitenberg and Pastorutti, 2024, [RD-5]).

Table 40-1: Volume and mass change data used in computing the gravity effect of the seamounts eruptions. The equivalent area is the area of an equivalent cylinder approximating the change in bathymetry and topography, volume and thickness being kept constant. Note

Seamount	Volume [km^3]	Equivalent Area [km^2]	Thickness [m]	Density contrast [kg/m^3]	Mass change [10^{12} kg = 1 Gt]
Axial	0.148	29.6	5	1800	0.27
Loihi	0.03	6	5	1800	0.05
HTHH 2015	0.05 subaerial	1.8	28	2420 (assumed tephra) [4]	0.12
	0.45 submarine	2.8	155	1800 (assumed basalt)	0.81
HTHH 2022	6.5 submarine	8.12	800	1800 (assumed basalt)	−11.7[1]
Kick'Em Jenny	$1.26 \cdot 10^{-6}$	$2.5 \cdot 10^{-3}$	0.5	1800	$2.3\ 10^{-6}$
Surtsey	0.24 subaerial	1.41	170	70% Porous tephra at 50% porosity 30% basalt Average density = 1820	0.44
	1.16 submarine	7.48	155	70% Water filled tephra, 30% basalt Average density contrast : 1170	1.36
Fani Maoré	6.55 submarine	7.99	820	2172	7.68

This mass is modelled with a truncated cone, the spherical harmonic expansion is determined, and the localized spectrum is calculated. The signal spectral amplitude is then compared with the noise spectrum for the different satellite constellations from 1 to 6 pairs. We find a considerable jump in the detectability when passing from 1 couple to more couples (Figure 40-9.

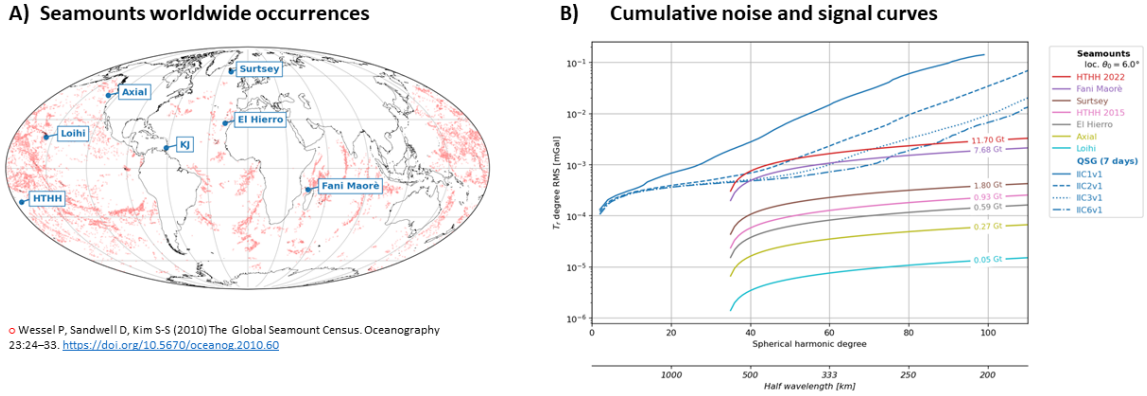

Figure 40-9 Seamounts sensitivity for the different satellite constellations. A) Worldwide occurrence of seamounts (red dots) and seamounts for which mass changes have been estimated (Blue dots). HTHH: Hunga Tonga-Hunga Ha'Apai; KJ: Kick Em Jenny. B) Seamounts mass change signal compared to the noise curves at 7 day sampling. Calculation at gound height.

The seamount signals not being present in the ESM model, the error calculation of the signal recovery cannot be fulfilled in the manner it done for the earthquakes. Nonetheless as a general rule, the size of the ESM retrieval error over the location of the seamount must be lower than the amplitude of the signal to allow its observation. The spectral analysis predicts that the HTHH 2022 mass change, at weekly sampling starts to be visible from the double pair constellation upwards. This is confirmed in the space domain, where the retrieval error for a single pair is about ±140 μGal, reducing to a few units of μGal for the six pairs, which compares to the signal reaching values just above 5 μGal. Therefore in space domain the signal starts to be visible from 2 couples upwards, as predicted from the spectrum.

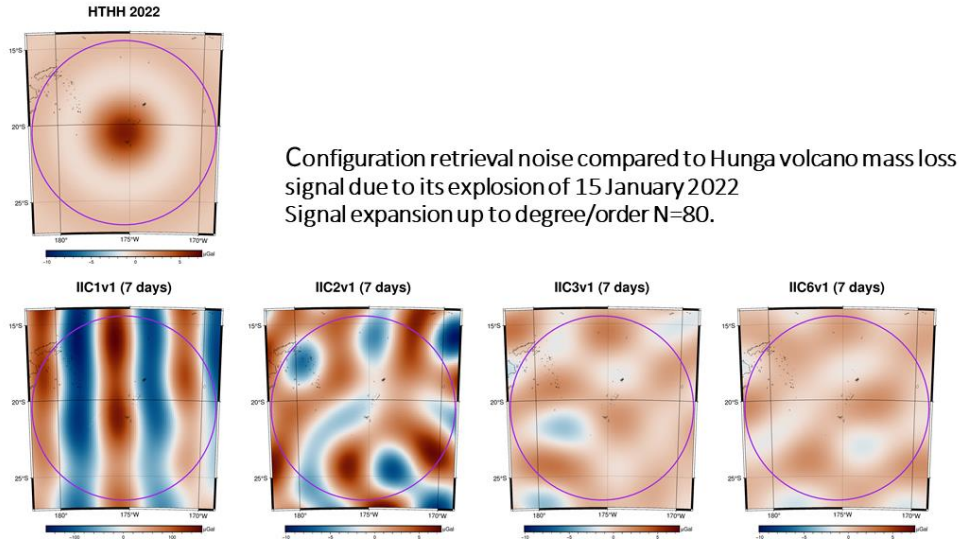

Figure 40-10 Retrieval error form constellations from one to six satellite couples at weekly sampling, compared to the signal of the HTHH 2022 mass change signal.

The Alpine arc is uplifting, as documented by GNSS observations, which implies an expected gravity change through the mass change at the surface, because air is replaced by the uplifting topography. Future fine-tuning of the calculation could also include the surface density across the orogen, presently we use an average homogeneous rock density of granite, as used for the standard calculation of the Bouguer calculation. The residual between the expected gravity and observed gravity gives information on the geodynamic processes generating the vertical movement, that is pure uplift of the crust versus crustal thickening. In the subsiding lowlands and basins, sediment compaction does not lead to mass change, whereas compaction due to fluid extraction does. Our goal is therefore to define the uplift signal compared to the noise level of the satellite constellation.

The area of study extends across the entire Alpine arc, including the northern part of the Apennines, covering a rectangular area from 41° N to 50° N of latitude and from 4.5° E to 18° E of longitude.

The 397 daily stations data were collected from the database of the Nevada Geodetic Laboratory (NGL) (http://geodesy.unr.edu/) and a few from the AGNES database for Switzerland, following a selection based on two main criteria: time series with minimum 6 years of data and data gap length inferior of 6 months.

Post processing procedure was required to remove outliers and steps, some of which are signalized in the documentation, but some are unknown and must be detected and removed. The outliers removal process was based on the 3-sigma criterion. The steps removal process required a few phases; firstly, the collection of the information reported by the NGL related to the presence of abrupt jumps in GNSS time series for each single station. Secondly, the detection of unreported steps, based on the 6-sigma criterion and, lastly, the correction of all the steps.

The results indicate that the Alpine arch is characterized by a positive vertical annual trend, with a mean of about 1 mm/year, and picks up to 2.5 mm/year. In contrast, the Po basin is subsiding, specifically, Po estuary and the area around the city of Bologna, with maximum rate

of – 5.5 mm/year. The Paris basin and the Northern Tyrrhenian zone are characterized by a prevailing subsidence trend around -1.5 mm/year. In the Apennines, the mean trend shows an uplifting rate around 0.7 mm/year, even though some stations are subsiding (Figure 40-11).

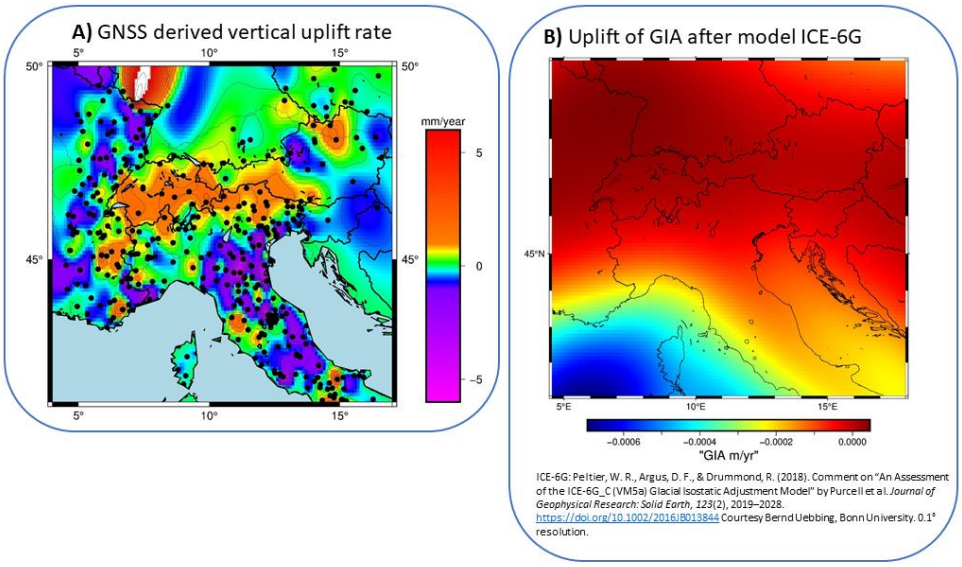

Figure 40-11: Vertical movement rates for Alpine arc. A) Calculated from GNSS in the frame of the project. B) Predicted from the Glacial Isostatic Adjustment (GIA) model, courtesy Bernd Uebbing, Bonn University.

The measured uplift has a greatly articulate pattern which changes sign over distances 100 km and smaller, as for instance across a profile crossing the Alps and continuing along the Apennines. The uplift due to Glacial Isostatic Adjustment (GIA) after the model ICE-6G has much greater wavelength and very different pattern: the subsidence is determined by the increase in sea level in the Mediterranean, and the small uplift of the European plate does not reflect the Alps topography. The GIA rates are one order of magnitude smaller than the GNSS observed rates. We proceed to compare the localized spectrum of the gravity change in one year, with the noise curves for 1 year, and the same for 4 years. The signal of one year is too small to be detected, it must be accumulated over four years, then it is seen starting with the double couple and more satellites constellation.

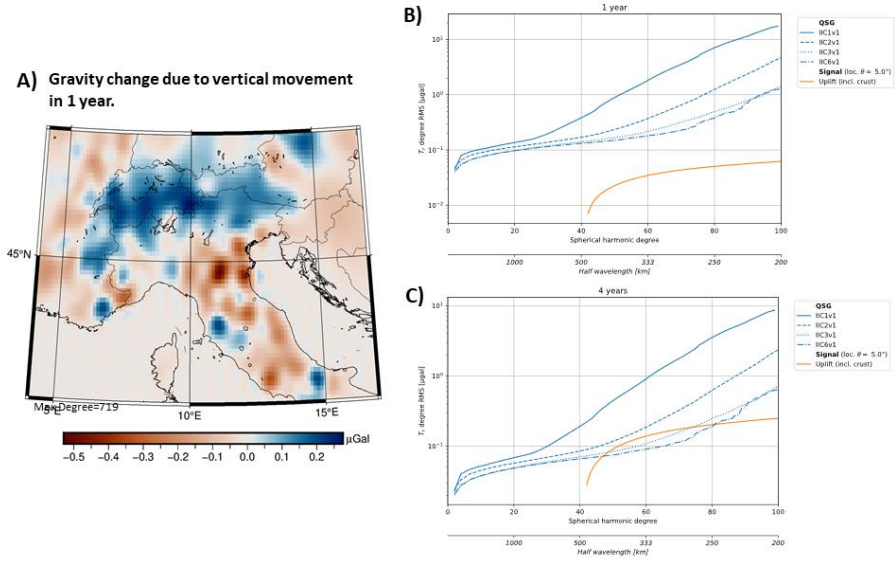

Figure 40-12 Detection of vertical ground movement. A) Gravity change rate of uplift B) spectral noise curves compared to the signal curve. One year signal accumulation and sampling. C) Four year signal accumulation and sampling. The noise and signal must be accumulated by 4 years to achieve sufficient detectability.

We addressed the sensitivity to relevant geologic bodies, starting from a 3D density model we have developed for the entire Iran and surrounding region. 3D density data cube in Iran as a starting point for the sensitivity analysis. The cube comprises crust and lithosphere and has been obtained from joint inversion of the gravity and magnetic field (Maurizio et al., 2024, [RD-4]). The cube allows to forward calculate selected parts of the model for the sensitivity analysis, as the sediment base depth and geometry, magmatic bodies, density lineaments tracing geologic discontinuities, and useful for minerals exploration. We have made a search on connected voxels that have a density contrast above a given threshold (for instance 90 kg/m^3) respect to the average of the crust at each given depth slices. As example the body is shown in Figure 40-13.

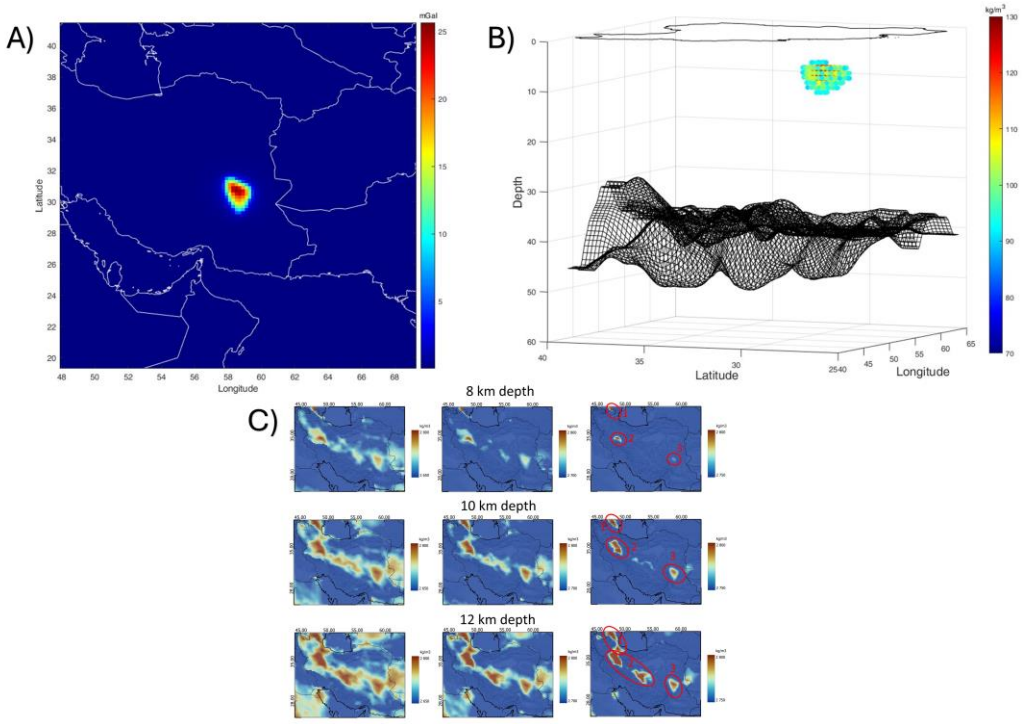

Figure 40-13: Isolated geologic body and corresponding gravity field. A) Map of gravity field of the Lut block. B) 3D view of the Lut block and Moho (Iran). C) Three depth slices from which three geologic bodies are isolated.

The next figure (Figure 40-14) shows the signal spectra of the three isolated geologic bodies of interest, which we then compare with the spectral noise curves.

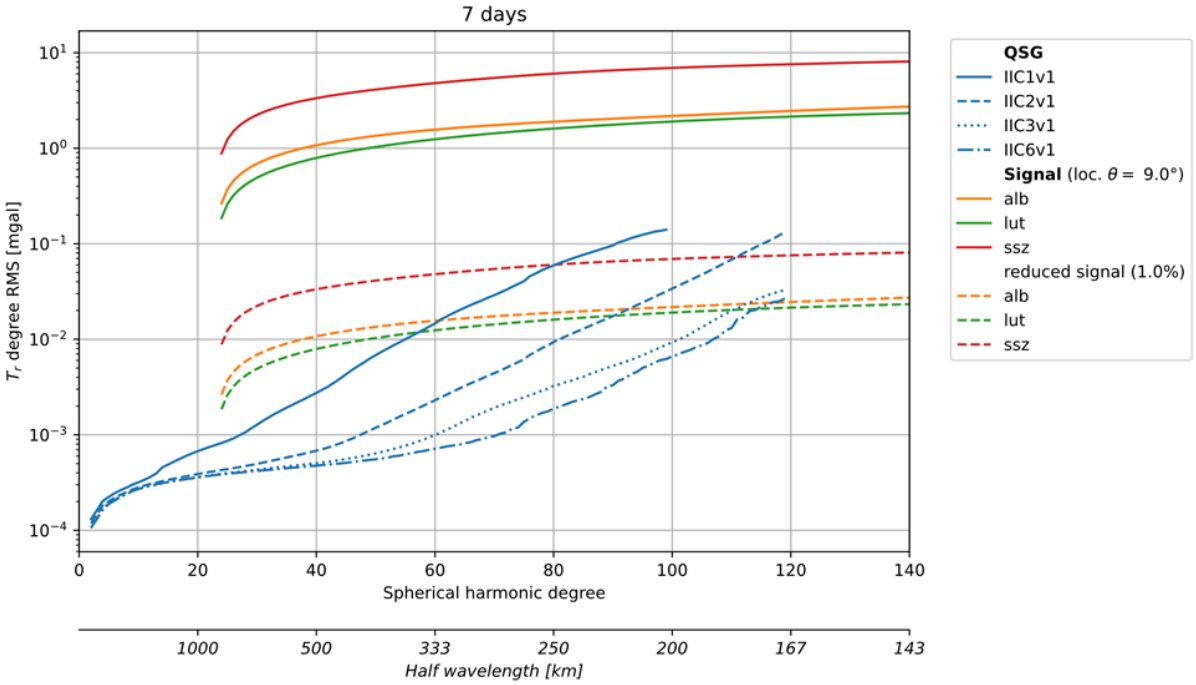

Figure 40-14: Localized signal spectra of the three isolated geologic bodies of interest, and spectral noise curve. Cumulated spectra. Seven days gravity data sampling. Fields at ground height.

We find that the signals generated by such bodies are very large compared to the other signals we have considered, and thus their detection and the possible variation in time for instance by fluid alteration through magmatic processes could be a possible target of observations from satellite. For instance the body of Lut block, of magmatic origin, and in the upper 10 km of the crust, gives a signal two orders of magnitude greater than the error curves up to the full range of available degrees. An alteration process changing the mass by 1% is at the detection limit of the mission. Given the great size of these geologic signals, there is potential to detect bodies which are smaller and nonetheless relevant, in order to be closer to the limit of detection and to pursue the bodies for which a mass change in time is expected.

We applied the same approach to isolate a sedimentary basin. Starting from the inverted volume, we calculate the total mass of a small sedimentary body of the Amu Darya basin (Figure 40-15), to conduct the sensitivity analysis considering mass variation due to changing porosity and fluid migration.

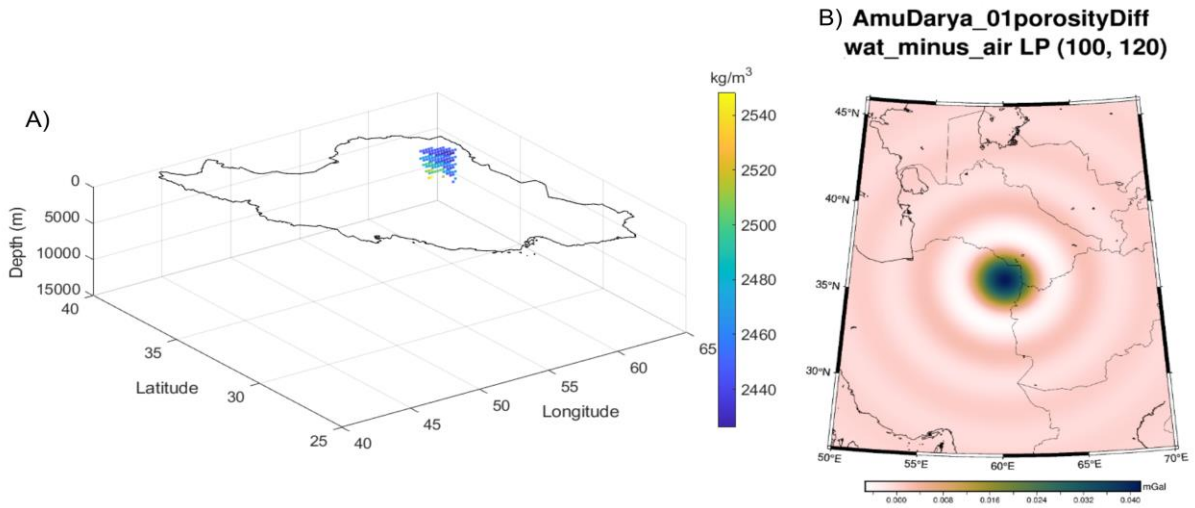

Figure 40-15: Amu Darya basin isolated from the density model. A) 3D density representation of the sedimentary body. B) Gravity field resulted from the subtraction between the signal of the sedimentary body with a 0.1% porosity filled with water and the signal of the sedimentary body with a 0.1% of porosity filled with air. The resulting field is gently cut from 100 to 120 degree/order.

We calculate the signal of the basin considering different stages of material filling the porosity: the pores can be void or filled with water, and the changes are evaluated for the mass difference of consolidated rock without porosity, and the difference between the air filled and fluid filled pores. The latter is representative of an aquifer extraction/replenishment or a fluid injection/extraction experiment. Porosity values are assumed to be equal to 0.1% or 1%. As example, we show the gravity field variation between the sedimentary body with 0.1% porosity filled with water and willed with air (Figure 40-15). In the figure below, we show the signal spectra for the different cases explained in the caption (Figure 40-16).

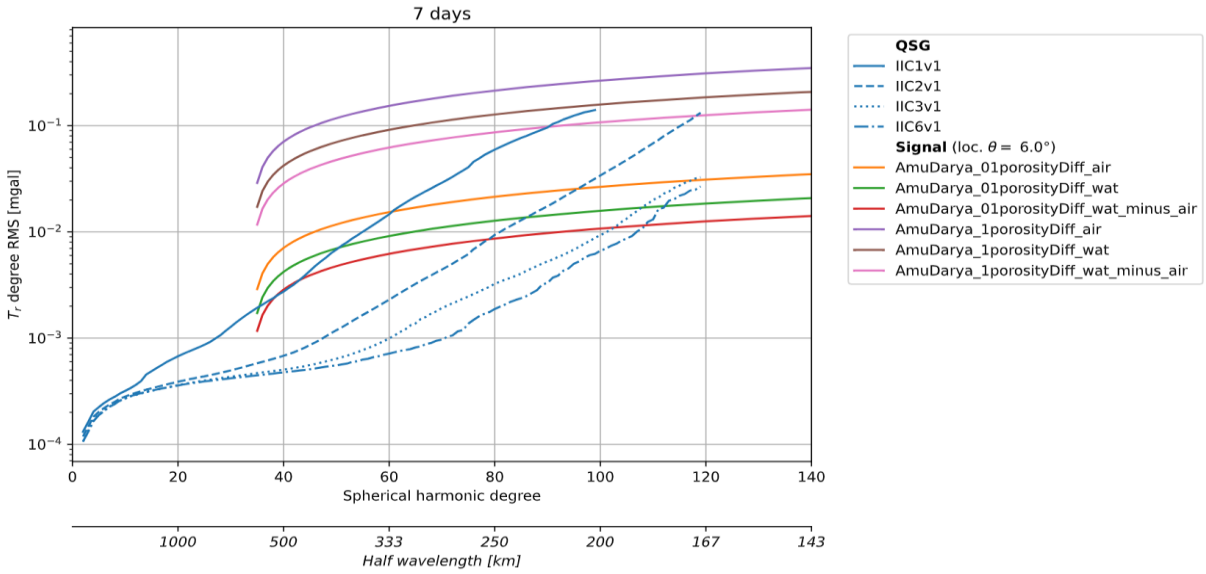

Figure 40-16 Porosity increase detection with the example of the sedimentary body in Amu Darya, Iran. Signal: Change of gravity field of the basin respect different scenarios with 0.1% and 1% porosity. Diff_air: air filled porous rock against solid rock; Diff_wat: water filled porous rock against solid rock; Diff_wat_minus_air: air filled against water filled porous rock. Seven days gravity data sampling. Fields at ground height. Cumulative spectra.

As is intuitive, the signal is proportional to the porosity value, so the signal is 10 fold for the 1% porosity respect to the 0.1% porosity. To our view of great interest is the possibility to detect the fluid incursion/extraction in the basin, be it natural or anthropogenic, which is represented by the curves of air filled against water filled porous rock. The uppermost levels of an aquifer are monitored by wells, but lower depth levels, beyond the reach of direct observation, remain concealed, and the mass changes detected from the satellite are of interest in monitoring these deep levels. Anthropogenic fluid injection in basins is relevant for CO2 sequestration, which is typically stored in exploited hydrocarbon reservoirs. The mass changes we have studied reflect fluid replacing void porosity for a large sediment basin. The present model must be explored further to match the amount of mass change we have obtained to those of industrially used and feasible mass changes in industrial storage plants, in order to assess whether the MAGIC is useful in this context. In the volcanic context, naturally occurring fluid injection is present when volatiles of magma uprise fill the magmatic system, taking the place of the porosity. Also in this context, further study must be done to estimate realistic mass changes due to the volatiles injection. For the size of the chosen sediment block (5 km deep, 15 000 km^2 area), with 0.1% /1% porosity, the water mass is 57 Gt/570 Gt. The single couple with weekly sampling could not detect the fluid filling of the 0.1% porosity, whereas the double couple could.

The final topic we approached is concerned with the possibility to detect deep earth movements, as the mantle flows induced by the history of slab subduction acting on a inhomogeneous mantle, both in terms of density and viscosity. The gravity change signals have been received in the form of SH expansions up to degree and order N=63 of the gravity potential field at present day and at 1 Ma by Bernhard Steinberger, GFZ Potsdam. In his model the mantle density variation is deduced from 3D seismic tomography models, considering pressure, temperature and petrology for the conversion. The mantle movement is constrained by plate velocities of the last 1 Ma. Viscosity is defined for the Lithosphere, Asthenosphere and Lower mantle, with varying values dependent on depth (Straume et al., 2024, [RD-6]). The change rate is obtained by the difference between two snapshots 1 million years apart, divided by 10^6 years. We then calculate the radial derivative of the gravity potential rate of change, which is very small, at the level of several nGal/year (Figure 40-17).

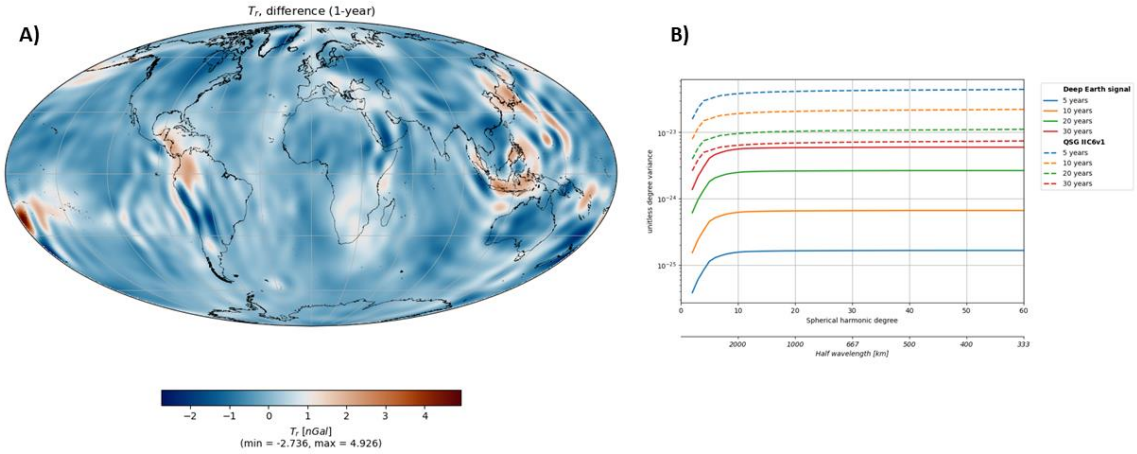

Figure 40-17: Mantle flow signals detectability. A) Gravity field change for 1 year. The ringing results from the sharp cutoff of the spherical harmonic expansion at degree and order 63. B) Cumulative signal degree spectrum for mantle signal accumulated for 5 to 30 years compared to the noise curves of different satellite constellation.

We then compute the degree variance spectrum of the time lapse differences extrapolated to 5 to 30 years, which we display together with the noise curves for analogous time intervals of data acquisitions. The degree variances of the noise curves are scaled linearly with the time interval of data acquisition (Figure 40-17). The detection of these small signals is challenging, and would be approached with a several decade long time of acquisition (30 years). Locally the signals are stronger, as at the subduction arc of Indonesia, or over the subduction arcs of the Pacific plate, or of the Nazca plate in the Caribbean. In future these areas could be investigated in more detail applying a localized spectrum analysis, which could presumably deliver an amplified spectrum detectable over a shorter time period.

41. WP900: HYDROLOGICAL (SHORT-TERM) AND OCEAN APPLICATIONS

41.1. OCEAN

For ocean applications, several components of the ESA Earth System model (AOHIS) are needed: O, AO_deal and AO_err. These components have been averaged according to the respective time periods of the simulation studies (1day, 7 days, 30 days).

Global Fingerprint Inversion I (Dataset 1)

The global fingerprint inversion [RD-7] allows for consistent estimation of global and regional sea level budgets by separating the total sea level change into mass and steric (volumetric) contributions. This is done by fitting time-invariant spatial patterns, i.e. fingerprints, to observations from satellite gravity and altimetry; mass and steric related fingerprints are computed in a pre-processing step based on prior information from models and other sources. The estimates represent time-varying scaling factors for each individual fingerprint, where the sea level or individual contributors can then be reconstructed by linear combination. With the approach it is also possible to further partition the steric changes based on predefined depth levels and the mass contribution regarding individual contributions from the melting of the Greenland and Antarctic ice sheets, melting of land glaciers or terrestrial hydrology down to basin scale.

Running the inversion requires altimetry observations which are taken from the Radar Altimetry Database System (RADS) and time-variable gravity changes, e.g. from GRACE(-FO), SLR or Swarm. Here, the idea is to replace the GRACE(-FO) data with simulated QSG mission scenarios in order to assess the impact on future sea level budgets. For now, the altimetry observations are kept the same. In a first step we read and rescaled the simulation normal equation systems provided by TUM, including restoring the AO_deal component while ensuring a zero basin average over the ocean. Afterwards, the corrected simulation data are converted to the inversion input format, followed by transforming the normal equation systems into the fingerprint space. After minor adjustments, these QSG normal equations can then be utilized within the in inversion framework as time-variable gravity observations.

In a first experiment, the QSG normal equations have been combined with altimetry data from January, February and March in 2006, where the year has been selected more or less arbitrarily. As expected, the resulting estimated mass scaling factors from the simulated scenarios data lead to non-meaningful sea level estimates. Instead it makes sense to investigate the propagated error information from each individual mission scenario.

For the first preliminary experiment, Figure 41-1 shows the diagonal error component from the final covariance matrix for the 111 mass component fingerprints associated to mass change from melting of land glaciers as well as the Greenland and Antarctic ice sheets. Other components, such as hydrology, internal ocean mass change or steric sea level, have not been evaluated, yet. While the simulated GRACE-FO scenario and to a certain extent also the MAGIC scenario shows larger errors compared to a solution using real (ITSG2018) GRACE data, it is possible to observe a significant improvement of the individual error levels, especially

for the IIC6v1 scenario. The next steps will be further analysis of the errors in terms of global and regional sea level change by rigorous error propagation. The possibilities for investigating sea level budget (i.e. trend) errors are limited at the moment since simulated data is only available for a time span of three month.

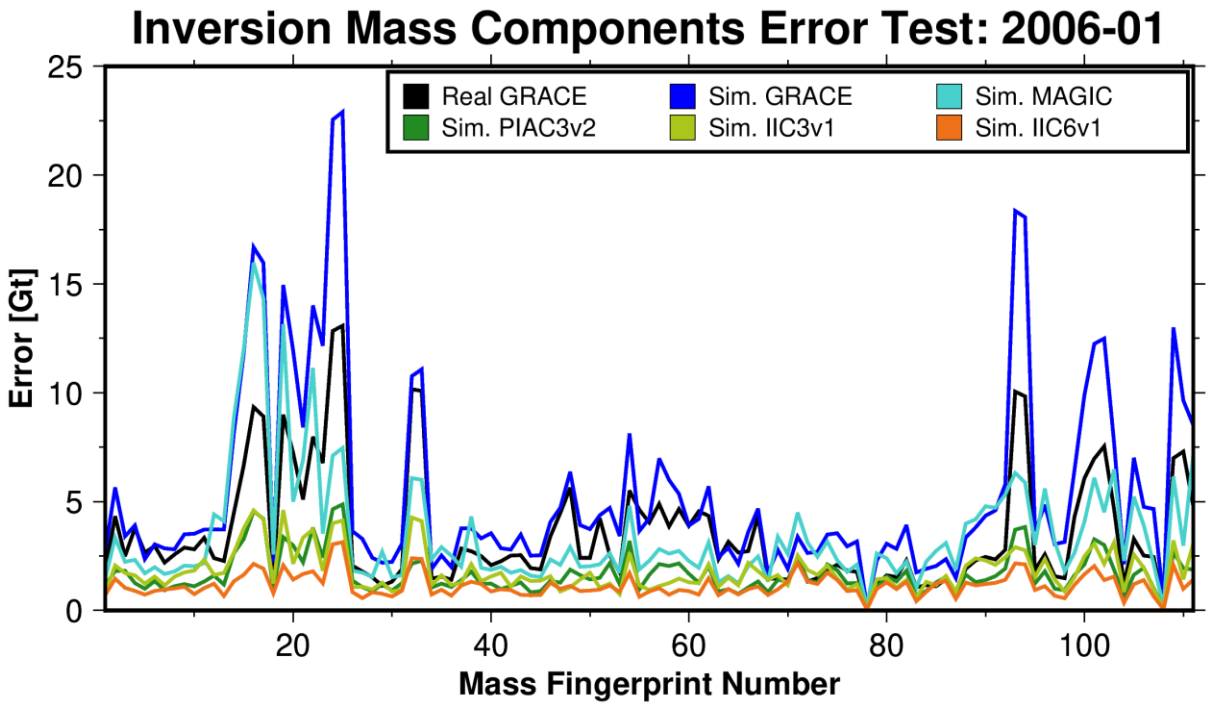

Figure 41-1 Diagonal error for the major mass components (melting of glaciers and the Greenland and Antarctic ice sheets) extracted from the inversion solution error covariance matrix. Errors are provided in gigatons reflecting mass change in the associated fingerprint basins. Preliminary results for the QSG4EMT simulation experiments, which may be subject to change in the future.

Global Fingerprint Inversion II (Experiments regarding ad-hoc request: Dataset 3, Diagonal of static "covariance matrix" as errors)

The diagonal error information contained in the static VCMs for scenarios IIC1/2/3/6 has been extracted and utilized to construct monthly GRACE-like normal equation (NEQ) systems by also prescribing the spherical harmonic coefficients based on real monthly GRACE solutions. These NEQs are then introduced into the global fingerprint inversion together with real monthly altimetry data from the Jason-1 and Jason-2 missions from 2003-01 till 2015-12 in order to cover the whole simulation period of 12 years.

Combining the monthly estimated scaling factors with their corresponding fingerprints allows to reconstruct total sea level change as well as individual contributors from melting of the ice sheets in Antarctica and Greenland, melting of land glaciers, contributions from terrestrial hydrology, internal ocean mass variations (IMV), and steric sea level change. From this, trends over 10 years (2005-2015) are estimated (a) from global mean time series and (b) at grid scale. Here we only consider relative improvements with respect to scenario IIC1 due to only utilizing the diagonal of the static VCMs.

a) Table 41-1 shows that there is actually an increase in error level based on the static IIC2-VCM diagonal errors in contrast to IIC1 with respect to the global mean mass sea level components, especially for Greenland and Antarctica, indicating a potential mismodeling of the IIC2 errors. For scenarios IIC3 we find a moderate improvement of the error level for the global mean ocean mass change for Greenland, Antarctica and internal ocean mass variations (IMV) of 15%, 35% and 26%, respectively. Major error improvements are found for the land glacier (50%) and terrestrial hydrology (70%) components. Adding additional satellite pairs (IIC6) leads to significant improvements for the Greenland and Antarctic components relative to IIC1 of 67% and 66%, respectively, while the error level for the glacier and hydrology components are improved by 80%. However, we only find a 23% improvement for the IMV component even slightly smaller than for scenario IIC3.

The IMV component is also the most dominant contributor to the overall ocean mass change error. Consequently, the overall ocean mass improvement for the individual scenarios is also quite limited.

Table 41-1: Error improvement in global mean sea level trends for individual sea level contributors in % of scenarios IIC2, IIC3 and IIC6 relative to IIC1. Note: Results are based on utilizing only the diagonal error information from a static VCM provided for each scenario.

Basin	IIC2	IIC3	IIC6
Antarctica	-162.6	35.0	66.0
Greenland	-216.3	15.2	67.0
Glaciers	-94.9	50.3	79.7
Hydrology	-29.8	70.6	80.1
IMV	7.9	26.4	23.6
Mass Sum	7.9	26.4	23.6
Steric	0.7	2.2	1.7
Total Sum	3.4	11.3	9.9

b) We investigate the overall ocean mass change component trend error improvement on spatial scales (Figure 41-2), by computing the same metric as in (a) but for every grid point individually. For IIC2 most regions show an improvement of about 20%, which is in line with the value reported in (a). However, around the equator, we find regions where the improvement is significantly larger (30-50%), but also regions where the error of IIC2 is actually worse. For IIC3 and IIC6 we find a generally good error improvement, while also identifying equatorial regions where the error improvement level is smaller.

These equatorial effects result from the IMV component, clearly being the dominant error source. The IMV component is computed based on spatial patterns derived from RL06 AOD1B GAB background models. However, these will not correspond well to the O-component of the ESA-ESM AOHIS and AO_deal simulations utilized as truth during the orbit simulations. For future comparisons it would be very helpful to also provide corresponding fields of AOHIS but especially AO_deal for a more consistent dealiasing for the simulated input data pre-processing.

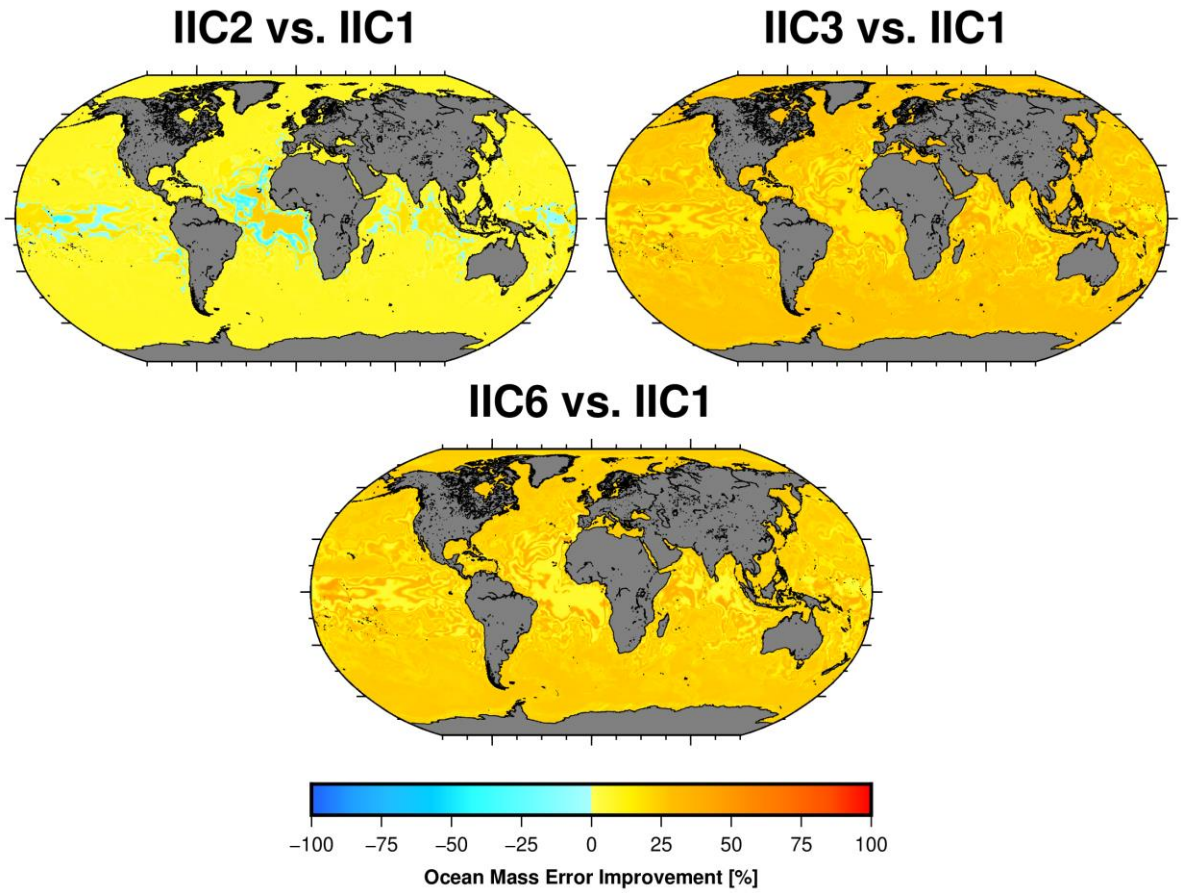

Figure 41-2: Spatial map of ocean mass trend error (over 10yr period) improvement in % for scenarios IIC2, IIC3 and IIC6 relative to IIC1. Note: Results are based on utilizing only the diagonal error information from a static VCM provided for each scenario.

Global Fingerprint Inversion III (Dataset 3, Full scaled formal covariance matrix)

In this section, the scaled formal covariance matrices of the IIC scenarios are used. These are full matrices, which are closer to the respective empirical covariance matrices (which could not be used, as they do not have full rank, see Table 39-1).

We found the results shown in section II to be generally worse compared to the initial test data we used in section I. It turned out that this was related to some issues with the GRACE-like (IIC1) scenario, which affected the empirical variances and, thus, also the scaled formal covariance matrix. We hypothesize this is tied to non-realistic error covariance modeling utilizing an empirical diagonal in combination with only formal error covariances, i.e. neglecting the real error covariance including aliasing errors etc. In other words, employing only a diagonal (or almost diagonal) VCM for weighting the satellite gravity information prohibits the meaningful separation of all individual sea level budget components, especially for the GRACE-like scenario (IIC1); i.e. one would need to reduce the amount of fingerprints for this simulation compared to a run utilizing real GRACE(-FO) data. Consequently, we will focus our results on comparing to the MAGIC-like (IIC2) scenario. Figure 41-3 shows the improvement in error level for the ocean mass change (OMC) component relative to the

MAGIC-like scenario IIC2. For the IIC2, or MAGIC-like, scenario we find slightly larger error levels compared to IIC1. For each of the sub-components of the mass budget (Table 41-2) we find a general improvement for the quantum scenarios relative to the MAGIC scenario (IIC2). The patterns around the equator result from the internal ocean mass variations (IMV) component, which is the most dominant error source in the mass budget (Table 8). The IMV component is the most spatially variable error source as it is closely related to the dealiasing signal, which is removed during gravity L2 processing. However, the dealiasing error is not comprehensively modeled in the individual IICx simulations.

For scenarios IIC3 and IIC6 we find general improvement in OMC error levels relative to IIC2 (Figure 41-3) as well as individual sub-components reaching up to 60% for IIC6 relative to IIC2 (Table 41-2).

The improvements for the steric level and total sea level are close to zero. This is expected as both are dominated by the altimetry errors, where the input data has been kept the same for all individual experiments.

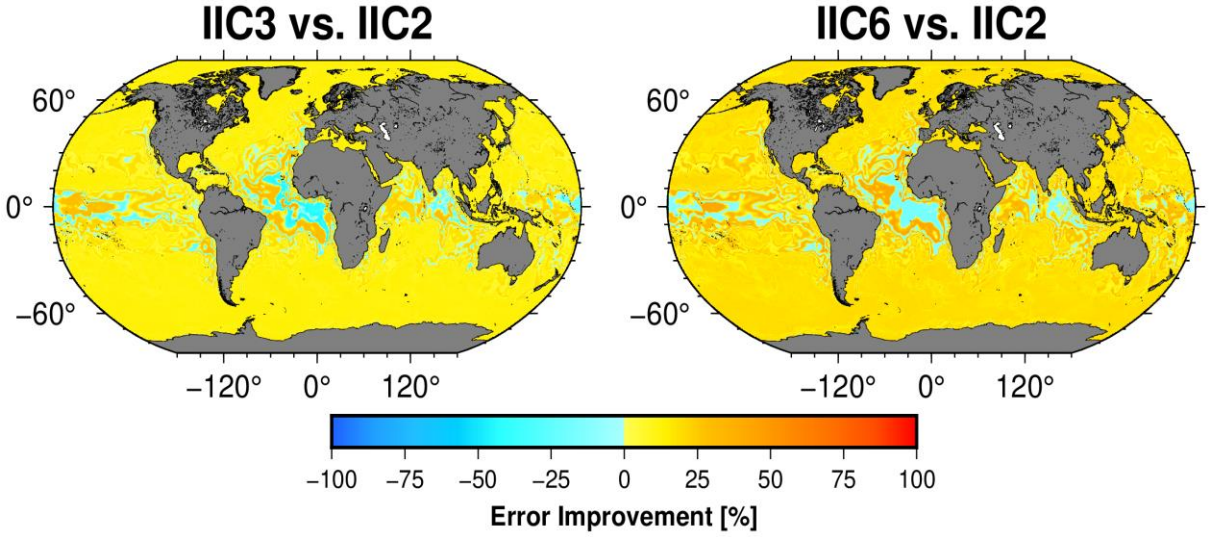

Figure 41-3: Map of error level improvement of the ocean mass change component based on individual IIC simulation scenarios; results are relative to the MAGIC-like scenario IIC2.

Table 41-2: Percentage of error level improvement for individual sea level budget components based on the individual IIC simulation scenarios. All results are relative to the MAGIC-like scenario IIC2. Contributions of each mass sub-component to the overall ocean mass error are provided in the third column.

Basin	IIC3 vs. IIC2	IIC6 vs. IIC2	Contribution to Mass Error
Antarctica	38.4	46.1	1.5
Greenland	38.0	53.3	1.5
Glaciers	42.7	59.9	5.0
Hydrology	46.4	57.6	5.0
IMV	6.5	9.8	87.0
Mass Sum	6.5	9.8	100.0
Steric	0.5	0.7	
Total Sum	2.5	3.8	

Figure 41-4 shows that the correlation between individual fingerprints is reduced (i.e. the separability of individual SLB contributors is improved), when comparing scenarios IIC2 and IIC6 for an arbitrary month. Despite the sub-optimal error covariance modeling of the simulated gravity data, we find an improvement in signal separability for individual basins and groups of mass sea level contributors which can likely be attributed to the better spatial coverage by the increased number of satellite pairs. We find a reduction in inter-basin correlations, especially for the Arctic Canada North and South glaciers (red and cyan). Similarly, inter-basin correlations in for the Greenland and Antarctic ice sheets are also reduced. Furthermore, a slight decrease in correlation between individual EOFs from the terrestrial hydrology component is observed. Correlations between contributions from melting glaciers in Arctic Canada, on Iceland or Svalbard and the neighbouring Greenland ice sheet is found to be reduced, especially for scenario IIC6 (Figure 41-4). The results show that signal separability will improve significantly with future gravity mission concepts, but also require a thorough and realistic error covariance modeling to maximize the resolution and quality of the results.

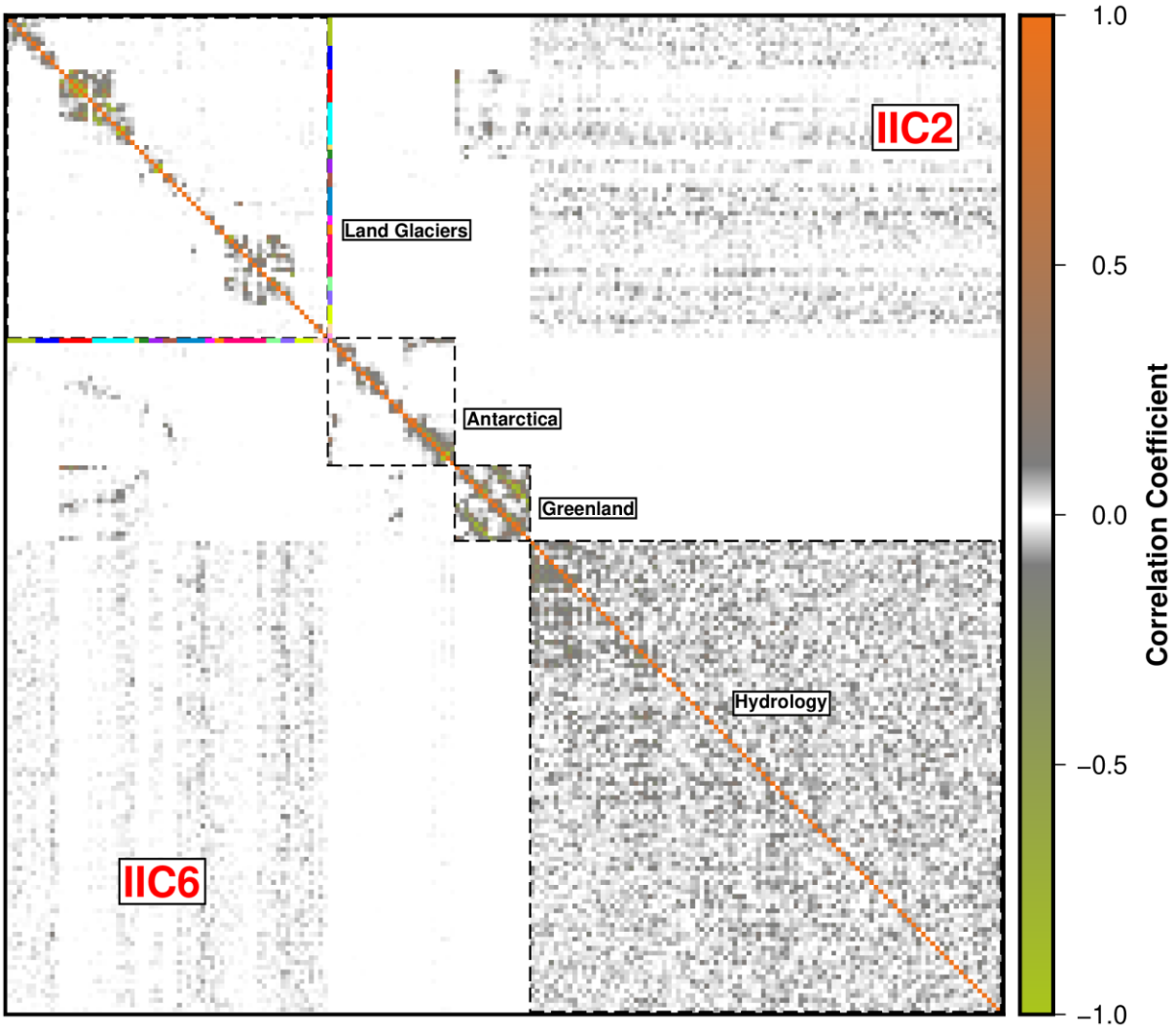

Figure 41-4: Improvement in signal separability from reduced correlations between individual sea level components exemplarily shown for the month 2006-06. We compare the correlations of IIC2 (upper triangle) to those of IIC6 (lower triangle). The figure only shows the major mass components for melting of the land glaciers and ice sheets in Greenland and Antarctica and variations in terrestrial hydrology.

Regional ocean mass change in the East China Sea (Dataset 3)

In this experiment, we compute regional ocean mass change (OMC) in the East China Sea (ECS). Here we consider the common "direct" method as this enables to study the impact of spatial resolution for challenging regions in a more straightforward way. In order to derive regional OMC from the simulated (i.e. ESA ESM) gravity fields, we add a GIA correction to the spherical harmonic coefficients, apply DDK3 filtering and restore the AO_{deal} dealiasing product (see below for a discussion of AO_{deal} and O_{deal}). After converting to water heights and computing the basin average, we apply a leakage correction derived from DDK3-filtering the LSDM hydrology component of the ESA ESM.

Basin averages are derived below for the ECS, a Western Pacific marginal sea with an area of 770 000 km^2. What makes this region unique and challenging for budget studies is its complex current system, the mostly shallow bathymetry and a large amount of sediments that is

transported by rivers or results from coastal erosion. In-situ observations, as e.g. tide gauge data, for external validation are relatively sparse. Simulation results are thus compared to the "truth" from the ocean component of the ESA-ESM.

Figure 41-5 a) shows time series of basin averages for the different simulation scenarios. Additionally, the ocean component (O) of the ESA-ESM is shown as reference. All scenarios follow the harmonic signal of the reference well with GRACE-FO having the largest noise and the CAI simulations being less noisy. In order to better assess the performance of the individual scenarios, we subtract the ESA-ESM ocean reference from the individual scenarios, as shown in Figure 41-5 b). The smaller the residuals are, the closer the simulations are to the reference. The RMS of the residuals is 1.8 cm for GRACE-FO, 1.5 cm for MAGIC and 1.3 cm for both CAI3 and CAI6 (Table 41-3). There is an obvious annual signal of up to 4 cm, which could partly be attributed to the treatment of the dealiasing signal. To derive ocean mass from the simulated gravity fields, O_{deal} should be restored. However, this product is only available together with the atmospheric dealiasing component as AO_{deal}. Even though the atmospheric part should be small, it could lead to larger residuals. Thus, in Figure 41-5 c) the weekly average of 'atm' coefficients is subtracted, which reduces the residuals further and results in RMS of 1.5 cm (GRACE-FO), 1.1 cm (MAGIC) and 0.7 cm (CAI3 and CAI6) (Table 41-3). The RMS is comparable to that of error propagation of the scaled formal covariance matrices, which is 2.3 cm, 0.9 cm, 0.6 cm and 0.7 cm, respectively. A comparison of TUM simulations to POLIMI solutions for the year 2002 is shown in Figure 41-5 d). The difference between the two solutions is smaller than the difference with respect to the ESA-ESM reference.

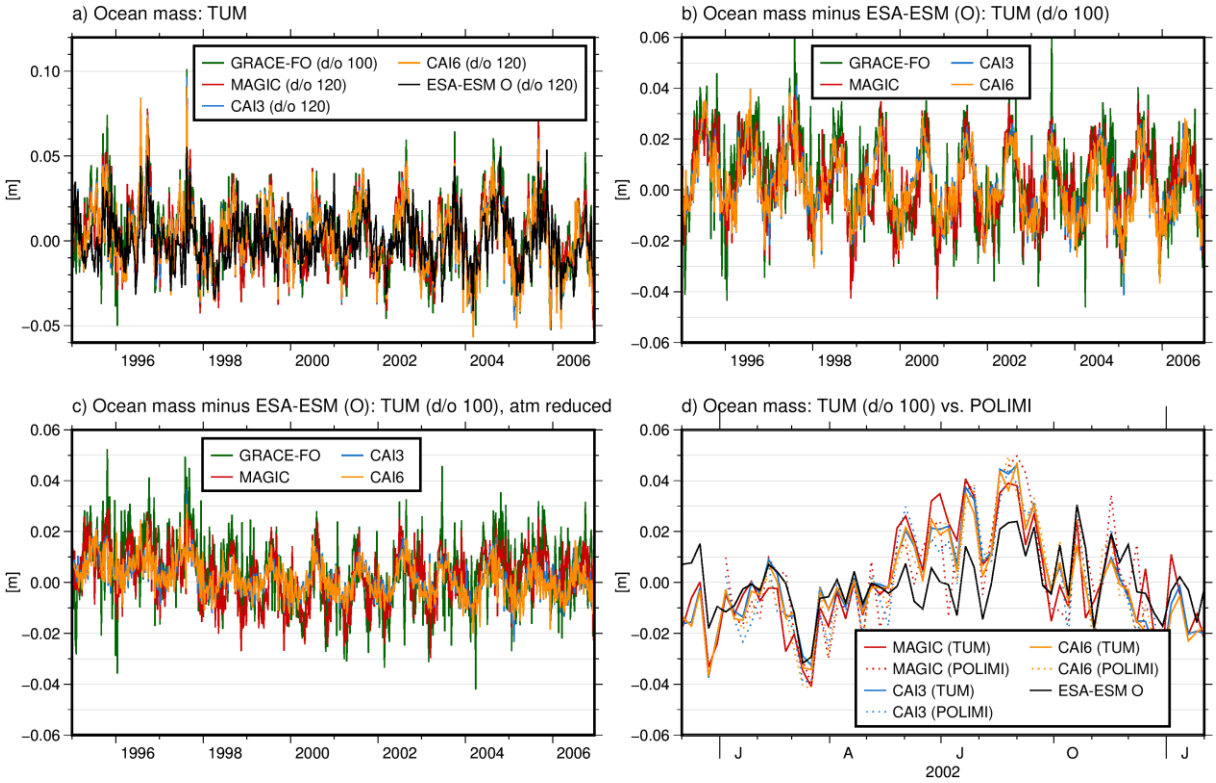

Figure 41-5: Time series of ocean mass change in the East China sea for different simulation scenarios/retrievals and for the ESA-ESM (O) reference. All time series (except POLIMI) are DDK3-filtered. a) Ocean mass change in the ECS from TUM simulations and ESA-ESM; b) Ocean mass change in the ECS from TUM w.r.t. ESA-ESM; c) same as b), but the weekly-averaged 'atm' coefficients are additionally reduced; d) Ocean mass change in the ECS from TUM, POLIMI and ESA-ESM

Table 41-3: Errors of ocean mass change in the ECS [cm]

Scenario	GRACE-FO	MAGIC	CAI3	CAI6
RMS TUM	1.8	1.5	1.3	1.3
RMS TUM (atm reduced)	1.5	1.1	0.7	0.7
error propagation TUM	2.3	0.9	0.6	0.7

5.2 Hydrology

Global data assimilation

Effect of spatial resolution of the input TWSA into the global assimilation

Dataset 1 formal VCM IIC3v1 30 days

In a first preliminary study, we set up a data assimilation (DA) framework for the IIC3 30 days simulations. The framework assimilates WaterGAP total water storage (TWS) anomalies together with QSG error information into the WaterGAP model by using the Ensemble Kalman Filter. This procedure enables us to analyze the effect of different spatial resolutions on the assimilation output. Here, the WaterGAP TWS anomalies on the native 0.5° model resolution serve as "truth", thus, the closer the DA output to the "truth", the better the result.

To run a DA, it is required to produce initial start values, which are typically derived via an initialization and a follow-up spin-up phase. Since an existing spin-up phases can be used in this case, which currently runs to 12/2002, we start assimilating in 01/2003. In future, one could adapt the initialization and spin-up phases so that a start in 01/2002 could be made feasible. In preparation, WaterGAP simulations for 01/2003 to 03/2003 are processed on the required grid, whereas QSG error information is transplanted from 2002 to 2003 for all study regions. A temporal mean derived from open loop simulations (small param. range) from 2003 to 2008 removed from WaterGAP simulations before the assimilation to refer to anomalies of TWS.

In an initial attempt, the QSG error information was pre-process as a full variance-covariance matrix (VCM) onto the TWSA spatial grids. As the Ensemble Kalman Filter (EnKF) requires perturbation of the input observations, the input WaterGAP model simulations are perturbed by using the full VCM. However, the filter also directly integrates the VCM but due to the matrix' properties (not positive definite for all continents on 0.5°) it led to instabilities during the DA and could not be used in this way. Thus, we decided to instead reduce the error information for the direct integration into the assimilation framework for the moment to a diagonal VCM. This means that error correlations between the input simulations are neglected, which is a simplification that most global assimilation systems currently work with In subsequent experiments, we try using a full VCM together with localization techniques to include more error information into the framework.

Figure 41-6 shows the original model simulations on an 0.5° grid (top left) and aggregated to a 4° grid (top right). The study area is due to time limitations shown for South America, but the

conclusions can be transferred to other continents as well. As logical consequence of the aggregation, we notice that the 4° simulations show less spatial variability and important features as, for example, river routing schemes are missing in contrast to the 0.5° simulation. This missing detail is also found when running the assimilation with the two variants. For example, we find that the assimilation is more close to the "truth" in the South-East of the La Plata basin when assimilating WaterGAP on an 0.5° grid than using a 4° grid.

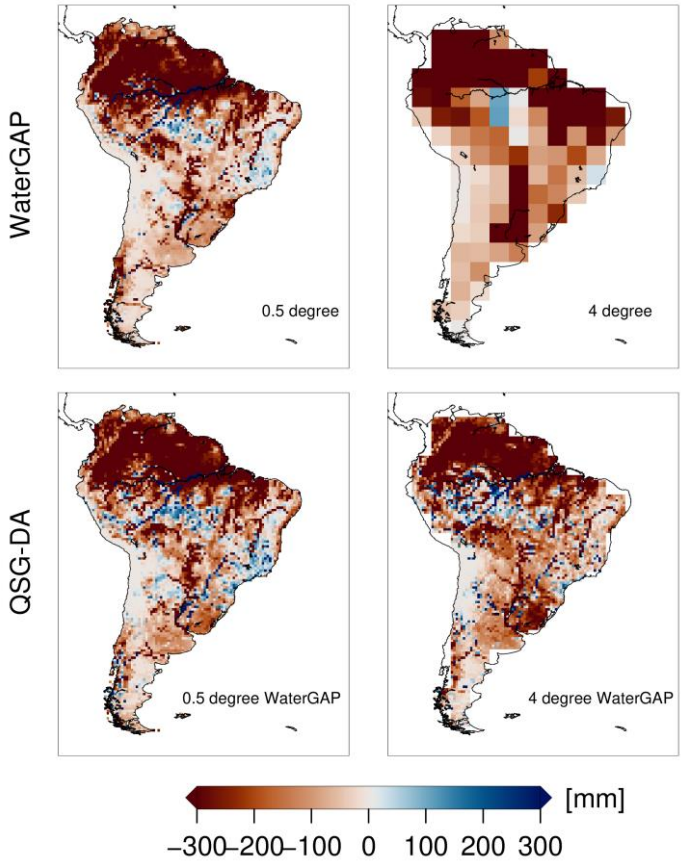

Figure 41-6: TWSA simulation in 01/2003 for a standard WaterGAP run on 0.5° (top left), a standard WaterGAP run aggregated to 4° (top right), an assimilation run that assimilates 0.5° WaterGAP data inclusive QSG IIC3-30 days uncertainties into WaterGAP (bottom left), and an assimilation run that assimilates 4° WaterGAP data inclusive QSG IIC3-30 days uncertainties into WaterGAP (bottom right).

As next, we have set up an assimilation framework for a long time period. In order to derive long time series, WaterGAP simulations were produced on an 0.5° in for South America from 2003 to 2019 and equipped with QSG uncertainties of the IIC3 30 days solution, also on 0.5° spatial resolution. The error information is similarly constructed as before, which means the full formal SHC VCM is transformed to the full VCM on the spatial TWSA grid. Then, the full TWSA VCM is used to generate an ensemble of TWSA that is required for the assimilation. For the direct integration of the VCM into the assimilation framework, the correlations are again neglected to stabilize the DA framework. Since only three months of QSG uncertainties exist from January 2002 to March 2002, these three fields are randomly distributed to 2003 to 2019. The WaterGAP and QSG uncertainties are then assimilated into the WaterGAP model (EnKF) and linear trends computed from the assimilation-derived TWSA results. The aim of this study is to get closer to

the truth, i.e. the WaterGAP model simulation of TWSA on an 0.5° grid, by assimilating a higher spatial resolution than typically used for GRACE/-FO. A comparison of the trends from assimilating 0.5° WaterGAP + uncertainties is made towards assimilating 4° WaterGAP + QSG uncertainties in Figure 41-7. By using a finer spatial degree for the TWSA and the uncertainties for assimilation, we get closer to the truth.The RMS difference towards WaterGAP model simulations reduces significantly when considering the 0.5° input fields and error information to the assimilation (RMSE = 12.44mm/a) instead of the 4° input and error information (RMSE=30.06mm/a).

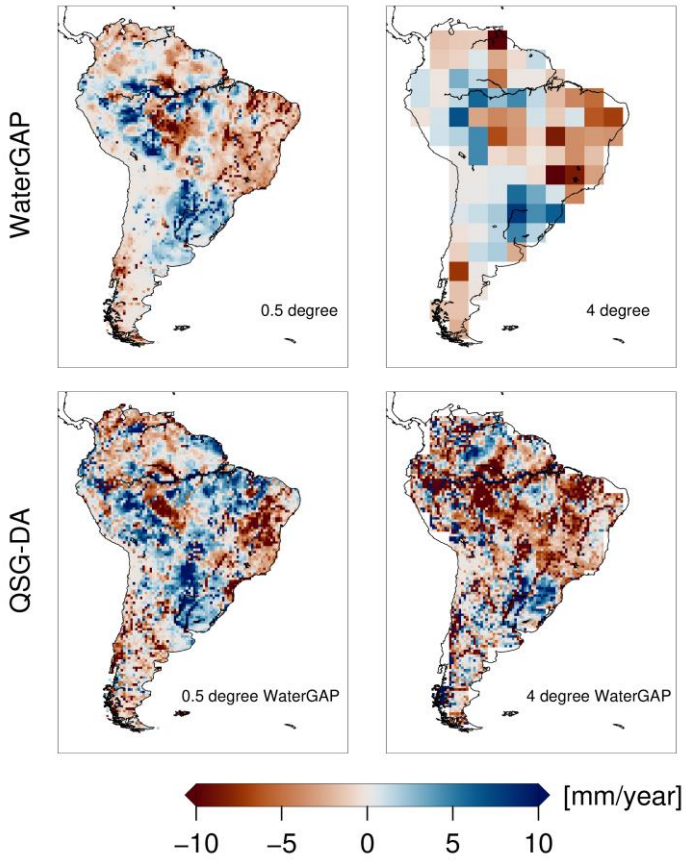

Figure 41-7: Linear trends of TWSA (2003-2019) from 0.5° WaterGAP model simulations (top left), WaterGAP aggregated to a 4° grid (top right), and from assimilation by either assimilating the 0.5° (bottom left) or 4 ° WaterGAP simulations (bottom left) together with error information from the QSG-IIC3 scenario.

Since new datasets became available after performing the previous analyses, the dataset 1 will not further be considered for the global data assimilation in the following but dataset 3.

Dataset 3 IIC1 scaled formal weekly VCM of Jan 1995

To verify if the found improvement in spatial resolution could also be achieved with current assimilation systems, we now perform and compare two assimilations with the simulated one-pair error information. This analysis (and also further analyses) will be applied to an updated version of dataset 1. In fact, dataset 3 is used, which provides a full formal VCM for SHC that is scaled to mimic the magnitude of an empirical VCM. Again, the full VCM is used for

perturbing the simulated input TWSA but reduced to a diagonal VCM for the direct integration to the assimilation.We either use the 0.5° WaterGAP TWSA + uncertainties of the scenarios or the 4° WaterGAP TWSA + uncertainties of the scenarios as input for the assimilation. Figure 41-8 shows linear TWSA trends for the input simulation either on 0.5° degree (top left) or aggregated to 4°(top right). In addition, the figure shows the linear TWSA trends from the assimilation output when either assimilating the 0.5° (bottom left) or the 4° (bottom right) TWSA simulations + IIC1 uncertainties. By using a coarser spatial degree of (4° grid size) the TWSA and the uncertainties for assimilation, we get closer to the truth as compared to when we use the 0.5° input grid size. The RMS difference towards WaterGAP model simulations reduces significantly when considering the 4° input fields and error information to the assimilation (RMSE = 34.32mm/a) instead of the 0.5° input and error information (RMSE=44.67mm/a).

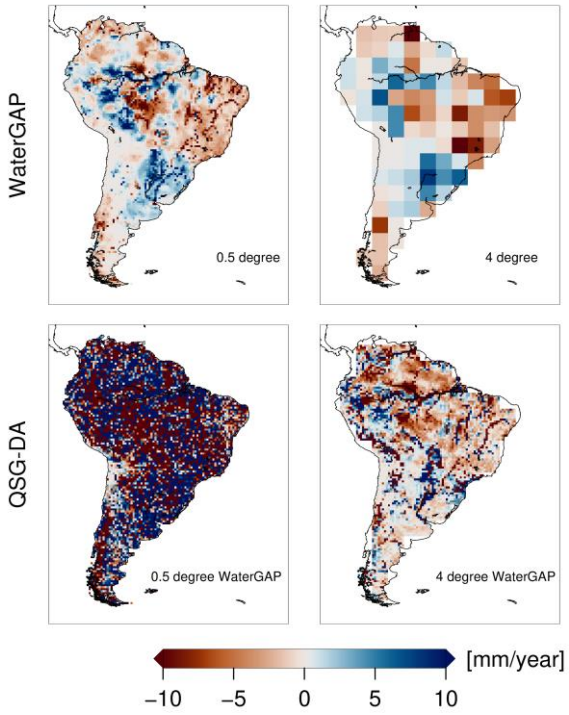

Figure 41-8: Linear trends of TWSA (2003-2019) from 0.5° WaterGAP model simulations (top left), WaterGAP aggregated to a 4° grid (top right), and from assimilation by either assimilating the 0.5° (bottom left) or 4 ° WaterGAP simulations (bottom left) together with error information from the QSG-IIC1 scenario.

All in all, we found that the assimilating simulations with a one-pair uncertainty as in GRACE/-FO only works when aggregating the simulations to a coarse grid, e.g. 4° prior to the assimilation because the mission constellation does not provide enough precision to assimilate on finer scales such as 0.5°. In contrast, with the uncertainties of 3- or 6-pair scenarios of QSG we are able to assimilate finer scale input data of 0.5° into the model and get closer to the truth as compared to when using a 4° coarser input grid.

Effect of scenario uncertainty on the global assimilation

Dataset 3 IIC1, IIC2, IIC3, IIC6 empirical weekly VCM

In order to compare the QSG scenarios with GRACE/-FO and MAGIC scenarios and to analyze the differences with respect to linear trends and seasonality, another long-term study is set up. Upon a specific ad-hoc request by ESA, this study utilizes the diagonal weekly empirical variance-covariance matrix provided by TUM on the level of spherical harmonic coefficients for the scenarios IIC1, IIC2, IIC3 and IIC6. Thus, additional processing steps for the VCM are required for the transformation to a monthly VCM where correlations are removed in the spectral domain of spherical harmonic coefficient but also in the spatial domain of TWSA on the 0.5° grid (native resolution of WaterGAP model) as it was found that the original VCM have a rank deficiency. By assuming that the errors do not change significantly from month to month, the gridded VCM is then multiplied for each month for the 2003 to 2019 study period. This decision was jointly discussed and decided in the team after viewing the temporal changes in the VCMs. The 0.5° WaterGAP simulations of TWSA are assimilated together with the uncertainty for each scenario separately. Ideally, the better the uncertainties of the respective scenario, the closer the TWSA from assimilation will be to the WaterGAP model simulation.

Figure 41-9 shows the differences of linear TWSA trends [mm/year] for South America derived from the assimilation of WaterGAP TWSA with empirical uncertainties of the IIC1, IIC2, IIC3 and IIC6 scenarios towards the WaterGAP model simulations. For the first scenario IIC1, the results show very large trend differences between the simulation and the assimilation. As this scenario represents the uncertainties from GRACE/-FO resolution and the mission does not provide spatial information below about 300km, assimilation on an 0.5° grid leads to outliers and instabilities. In contrast, the IIC2, IIC3 and IIC6 scenarios lead to successful results but with slight differences between each other. For example, strong negative differences between the trends from WaterGAP simulation and assimilation for IIC2 are found in South Brazil, whereas the comparison to IIC6 shows mainly negative differences.

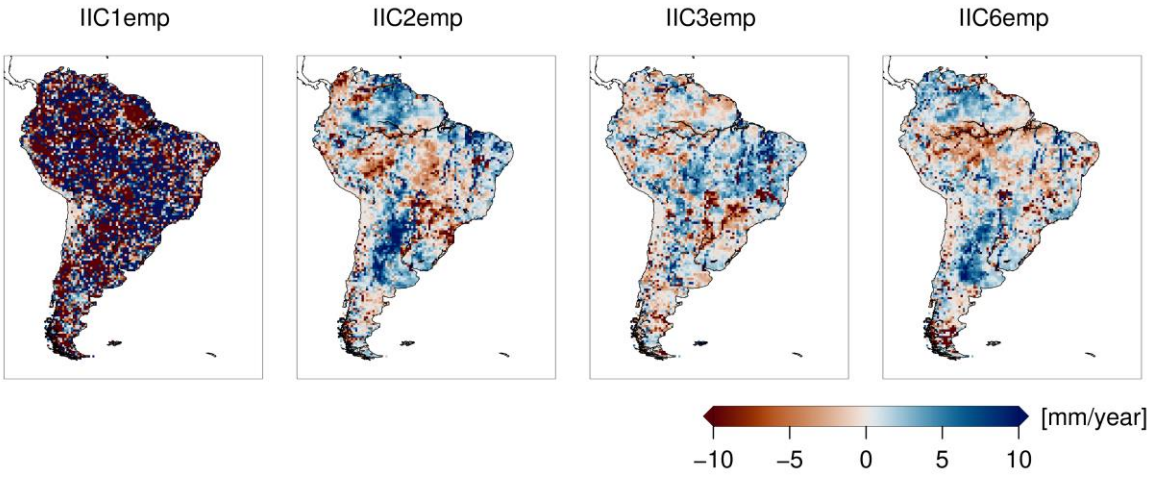

Figure 41-9: Differences of linear TWSA trends [mm/year] for South America derived from the assimilation of WaterGAP TWSA with empirical uncertainties of the IIC1, IIC2, IIC3 and IIC6 scenarios towards the WaterGAP model simulations.

To provide a quantitative comparison, Table 41-4 summarizes the spatial mean root mean square error between WaterGAP and the four scenarios for different signatures (linear trends, annual amplitudes, annual phases) and storages (TWSA, groundwater, surface water, soil moisture). The lowest and highest RMSE values per storage and signature are marked in green and red colors respectively.

As the observation correlations needed to be neglected for this study for the direct integration of the VCM into the assimilation framework, the results might change with full VCM applications. It is expected that with including more correlations or formal VCM for the observations into the assimilation leads to stronger improvements of QSG and MAGIC scenarios (IIC2, IIC3 and IIC6) compared to GRACE/-FO scenarios (IIC1). When considering TWSA and groundwater, the largest RMSE values are only found for the IIC1 scenarios for all signatures, while the lowest RMSE values and thus the best performance is found either found for the IIC3 scenarios or the IIC6 scenario (except for annual groundwater amplitudes). This means that the assimilation-derived TWSA and groundwater is closest to the truth (WaterGAP) for the QSG-scenarios. Similar findings are given for the surface water when analyzing annual amplitudes and phases. Surprisingly, the lowest RMSE for surface water and soil moisture trends and soil moisture amplitudes is found for the IIC1 scenario. Thus, the assimilation with the IIC3 and IIC6 uncertainties strongly improves TWSA, groundwater trends but (slightly) deteriorates surface water and soil moisture trends. We hypothesize that this can be explained by the fact that groundwater is the in most grid cells the storage with the largest variability and thus contributes to TWSA stronger than surface water and soil moisture. Further, the missing spatial correlations could improve the results, because they can indirectly change weighting of, for example, surface body locations.

Table 41-4: RMSE between for South America spatially averaged storage information (either TWSA, groundwater, surface water or soil moisture) from WaterGAP model simulations versus assimilation for the scenarious IIC1, IIC2, IIC3 or IIC6 (WaterGAP TWSA + scenario empirical uncertainty assimilated into WaterGAP). The lowest and highest RMSE values per storage and signature are marked in green and red colors respectively.

	Signature	Scenario	TWSA	Groundwater	Surface water	Soil moisture
RMSE	Linear trend [mm/yr]	IIC1	38.76	35.48	9.83	1.17
		IIC2	10.78	6.97	14.17	3.27
		IIC3	9.26	6.71	13.11	3.17
		IIC6	8.85	5.86	10.95	3.15
	Annual amplitude [mm]	IIC1	122.02	44.85	117.20	30.59
		IIC2	57.23	19.30	80.93	51.74
		IIC3	60.41	21.01	94.96	40.83
		IIC6	61.58	25.39	87.00	48.60
	Annual phase [month]	IIC1	3.04	3.20	3.39	3.77
		IIC2	2.51	2.79	3.18	4.34
		IIC3	2.51	2.58	2.94	3.40
		IIC6	2.45	2.67	3.15	4.49

From the same assimilation outputs for the four scenarios, insights into variations in time series can be further analyzed, for example, for extreme events like droughts. Thus, Figure 41-10 shows the spatially averaged TWSA for the La Plata river basin for the assimilation for the WaterGAP TWSA with empirical uncertainties of the IIC1, IIC2, IIC3 and IIC6 scenarios and from WaterGAP model simulations. As shown before, the IIC1 scenario shows strong differences compared to WaterGAP and the other assimilation scenarios because of instabilities during the assimilation. Generally, the scenarios IIC2, IIC3 and IIC6 are relatively close to WaterGAP.

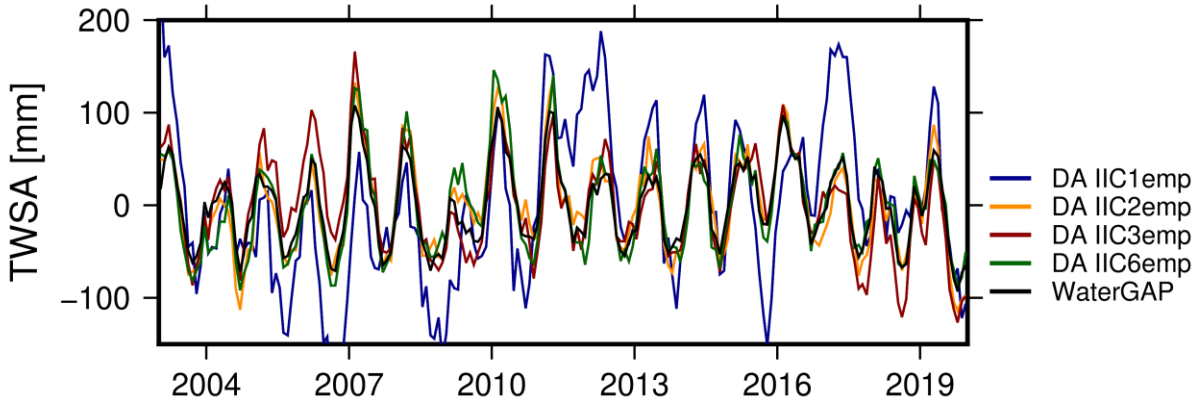

Figure 41-10: TWSA [mm] spatially averaged for the La Plata river basin derived from the assimilation of WaterGAP TWSA with empirical uncertainties of the IIC1, IIC2, IIC3 and IIC6 scenarios and from WaterGAP model simulations.

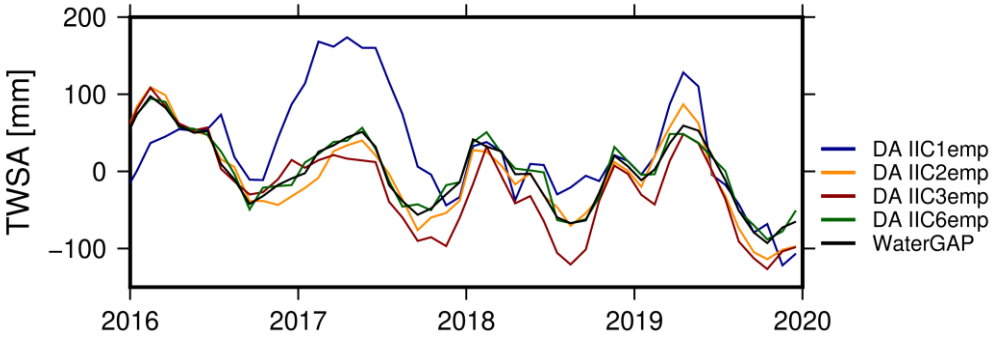

Figure 41-11: Same as Figure 41-10: TWSA [mm] spatially averaged for the La Plata river basin derived from the assimilation of WaterGAP TWSA with empirical uncertainties of the IIC1, IIC2, IIC3 and IIC6 scenarios and from WaterGAP model simulations.

Dataset 3 IIC1, IIC2, IIC3, IIC6 scaled formal weekly VCM of Jan 1995

In the following, we will repeat the analyses of the ad-hoc request with the most recently derived data set (dataset 3) that provides the scaled formal full weekly full VCM of January 1995 provided by TUM for the scenarios IIC1, IIC2, IIC3 and IIC6. The scaled formal full VCMs are derived and preprocessed to enable their use in the data assimilation framework. This means that first the formal full VCM is degree-wise scaled by using the empirical VCM.

Then, the weekly formal full VCM is transformed to a monthly formal full VCM and propagated to the 0.5° spatial grid of TWSA. With this full formal scaled VCM, we again develop an ensemble of TWSA simulation required for the assimilation filter algorithms. However, as in the previous section, correlations in the input VCM that is directly used in the assimilation are removed in the spatial domain of TWSA on the 0.5° grid to stabilize the data assimilation (native resolution of WaterGAP model). By assuming that the errors do not change significantly from month to month, the gridded formal VCM of January 1995 is then multiplied for each month for the 2003 to 2019 study period. The 0.5° WaterGAP simulations of TWSA are assimilated together with the uncertainty for each scenario separately . Ideally, the better the uncertainties of the respective scenario, the closer the TWSA from assimilation will be to the WaterGAP model simulation.

Figure 41-12 shows the differences between linear TWSA trends from model simulations and the output from the assimilation for the four scenarios with formal errors. The smallest difference between simulated trends and trends from assimilation is found for the IIC3 scenario. The largest difference in trends is found when comparing the assimilation with IIC1 errors to the model simulations. This results from the fact that the input TWSA and the corresponding uncertainties for the assimilation are provided on an 0.5° grid. This scenario simulates the spatial error information of GRACE/-FO because GRACE/-FO cannot sense geophysically meaningful signatures below approximately 300 km. In addition, Figure 41-13 shows the difference between annual TWSA amplitudes from model simulations and the output from the assimilation for the four scenarios with formal errors. As with the linear trends, the lowest difference between the annual TWSA amplitude of the model simulation and the assimilation with one of the four scenarios is found for IIC3 whereas the highest difference is found when comparing to IIC1 (cmp. Table 41-5).

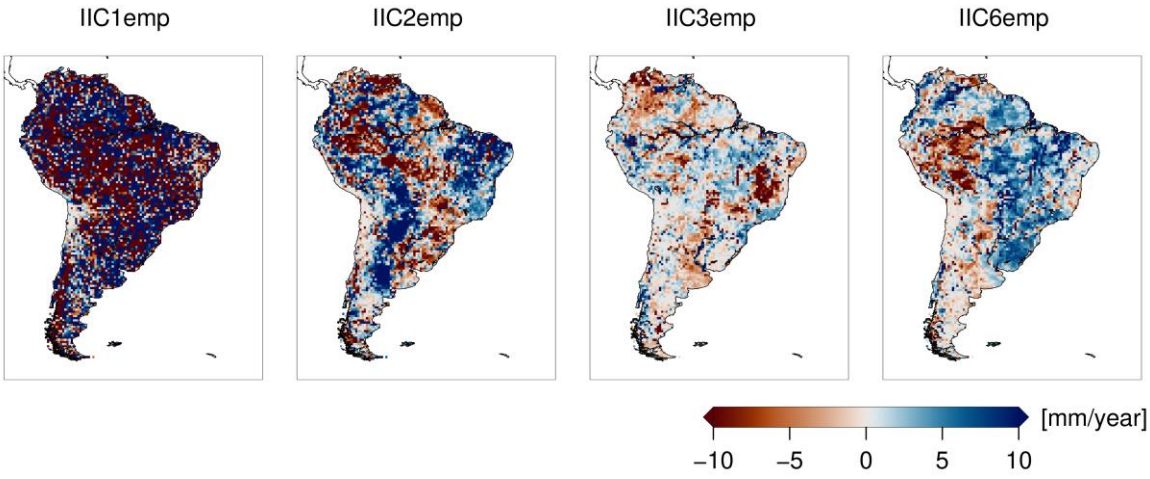

Figure 41-12: Differences of linear TWSA trends [mm/year] for South America derived from the assimilation of WaterGAP TWSA with formal uncertainties of the IIC1, IIC2, IIC3 and IIC6 scenarios towards the WaterGAP model simulations.

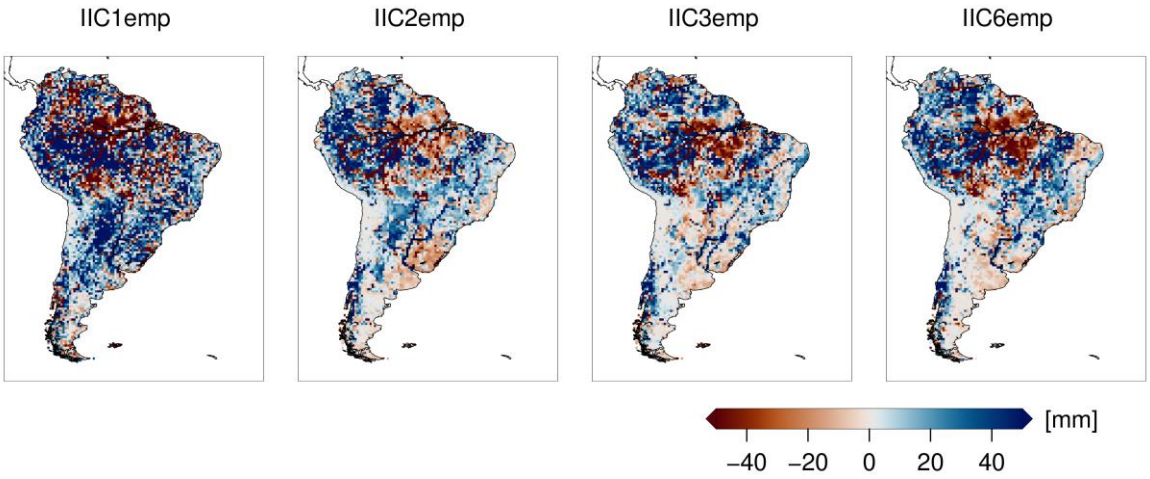

Figure 41-13: Differences of annual TWSA amplitudes [mm] for South America derived from the assimilation of WaterGAP TWSA with formal uncertainties of the IIC1, IIC2, IIC3 and IIC6 scenarios towards the WaterGAP model simulations.

To compare the different water storages TWSA, groundwater, surface water and soil moisture, the spatially average RMSE (South America) between simulated signatures and signatures from the assimilation for the four scenarios is shown per storage in Table 41-5. As with empirical VCM in the ad-hoc request, the RMSE drops dramatically from IIC1 to IIC2 especially for TWSA and groundwater when using the formal VCM. This means a clear improvement of TWSA and groundwater can be observed from IIC1 to the IIC2 scenario but this is not always the case for surface water and soil moisture. Mixed results are found for IIC3 and IIC6, often we find that scenario 3 performs best for TWSA and groundwater but in rare cases it can also perform worse than the other scenarios, for example, for linear trends in the soil moisture storage. However, the IIC2 to IIC6 scenarios generally show similar magnitudes of the RMSE and an improvement compared to the IIC1. As next, we aggregate the water storages to a spatial resolution of 1° (approx. 100 km, Table 41-6) or 3° (approx. 300km, Table 41-7) before computing the spatial average RMSE between the assimilation outputs and the simulation per storage, scenario and signature. The 100 km or 300 km represent typical grid sizes used for GRACE/-FO. We find that at 100 km, the RMSE is generally much smaller as compared to the RMSE values when using the 50 km grid size (Table 41-5). The TWSA linear trend RMSE for the scenarios IIC2, IIC3 and IIC6 at 50 km corresponds approximately to the TWSA trends RMSE for IIC1 at the 300 km scale. The same can also be observed when considering groundwater linear trends. In addition, the TWSA annual and semi-annual amplitude RMSE for the scenarios IIC2, IIC3 and IIC6 at 100 km are smaller than the TWSA amplitude RMSE for IIC1 at the 300 km spatial scale.

Table 41-5: RMSE between for South America spatially averaged storage information (either TWSA, groundwater, surface water or soil moisture) from WaterGAP model simulations versus assimilation for the scenarios IIC1, IIC2, IIC3 or IIC6 (WaterGAP TWSA + scenario formal uncertainty assimilated into WaterGAP). The lowest and highest RMSE values per storage and signature are marked in green and red colors respectively.

	Signature	Scenario	TWSA	Groundwater	Surface water	Soil moisture
RMSE	Linear trend [mm/yr]	IIC1	44.46	40.39	14.48	1.83
		IIC2	16.18	14.29	10.36	2.16
		IIC3	12.69	11.51	11.92	3.25
		IIC6	13.83	13.08	22.20	2.64
	Annual amplitude [mm]	IIC1	122.13	46.94	114.37	32.25
		IIC2	65.55	18.75	88.98	41.00
		IIC3	53.84	23.67	81.85	55.60
		IIC6	54.47	25.08	156.64	49.11
	Annual phase [month]	IIC1	3.39	3.67	4.45	3.76
		IIC2	2.47	2.54	3.51	3.48
		IIC3	2.57	2.65	3.40	3.93
		IIC6	2.57	2.47	3.22	4.18

Table 41-6: Same as Table 41-5 but this time the assimilation and simulation outputs were aggregated to a spatial resolution of 1° before computing spatially averaged RMSE. The lowest and highest RMSE values per storage and signature are marked in green and red colors respectively.

	Signature	Scenario	TWSA	Groundwater	Surface water	Soil moisture
RMSE	Linear trend [mm/yr]	IIC1	27.39	25.19	7.94	1.58
		IIC2	10.58	9.76	5.70	1.98
		IIC3	8.89	8.29	4.22	2.87
		IIC6	8.86	8.80	12.82	2.24
	Annual amplitude [mm]	IIC1	79.15	37.50	75.64	29.77
		IIC2	42.13	16.70	54.53	40.33
		IIC3	35.03	21.21	44.76	51.90
		IIC6	36.17	23.38	90.88	45.53
	Annual phase [month]	IIC1	2.52	2.69	3.22	3.11
		IIC2	1.67	2.07	2.52	2.86
		IIC3	1.71	2.16	2.39	3.28
		IIC6	1.72	2.02	2.21	3.54

Table 41-7: Same as Table 41-5 but this time the assimilation and simulation outputs were aggregated to a spatial resolution of 3° before computing spatially averaged RMSE. The lowest and highest RMSE values per storage and signature are marked in green and red colors respectively.

	Signature	Scenario	TWSA	Groundwater	Surface water	Soil moisture
RMSE	Linear trend [mm/yr]	IIC1	13.28	12.60	3.87	1.30
		IIC2	7.14	6.74	3.27	1.62
		IIC3	4.26	3.77	2.07	2.02
		IIC6	4.81	5.39	3.25	1.31
	Annual amplitude [mm]	IIC1	45.49	29.91	49.29	25.73
		IIC2	23.20	14.07	29.24	40.68
		IIC3	20.95	18.68	19.52	37.83
		IIC6	20.67	20.69	19.09	34.26
	Annual phase [month]	IIC1	1.90	2.03	2.42	2.40
		IIC2	0.87	1.56	2.15	2.43
		IIC3	0.98	1.68	2.41	3.17
		IIC6	1.02	1.53	1.26	2.93

In summary, updating the assimilation framework to use formal scaled VCM instead of empirical VCM did not lead to major conclusion changes. Unrealistic results were found for the IIC1 scenario when assimilating input data on 0.5°, which is due to the GRACE specific spatial resolution, which does not contain hydrological meaningful signatures below approximately 300 km. We found improvements of the assimilation outputs when using the IIC2 to IIC6 error scenarios compared to IIC1 error scenario. The improvements were most dominant for the TWSA and groundwater storages, whereas mixed results were found for surface water and soil moisture. We would like to note that this experiment was performed by neglecting correlations between spatial grids for the input VCM directly used in the assimilation. Using the full VCM instead of the main diagonal for the assimilation was not successful and lead to unrealistic results although localization techniques, which usually stabilize the outputs, were implemented. Nonetheless, by neglecting spatial correlations in the assimilation is typically done for global assimilation systems, thus, our procedure presents a common approach.

Regional Assimilation Experiments over Europe

(Observation covariance matrices based on Dataset 3 IIC1, IIC2, IIC3, IIC6 scaled formal weekly VCM of Jan 1995)

Over Europe, we investigated the impact of different gravity mission simulation scenarios in the context of data assimilation by assimilating TWSA into a high-resolution regional hydrological model. The Community Land Model version 3.5 (CLM3.5) was set up over Europe with 12.5 km spatial resolution and hourly model steps. Synthetic TWSA observations with QSG error information were introduced into the model via an Ensemble Kalman Filter (EnKF) approach.

In the following experiments, we used the scaled formal weekly VCM of January 1995 provided by TUM for the scenarios IIC1, IIC2, IIC3 and IIC6. For DA purposes (i) the formal VCM was scaled degree-wise based on the empirical VCM, then (ii) the weekly formal VCM was transformed to a monthly VCM and (iii) the monthly VCM was propagated to the observation grid, i.e., 2° or 4°. In the spectral domain correlations between spherical harmonic coefficients were considered. By assuming that the errors do not change significantly from month to month, the gridded formal VCM of January 1995 was then applied for each month of the 2003 to 2018 study period.

We performed Observing System Simulation Experiments (OSSEs) by generating a synthetic truth from the updated CLM5 version, which was then gridded to the 2° and 4° observation grids and perturbed with QGS error covariance matrices for different mission scenarios using the fully populated matrices. Subsequently, we assimilated the synthetic observations of the four QGS error scenarios into CLM3.5 using only the main diagonal of the observation covariance matrix in the assimilation framework, which is common standard in many current GRACE DA frameworks. Finally, we evaluated the individual DA experiments on catchment scale.

One major insight from experiments with previously provided IIC scenarios (Dataset 1 and Dataset 2) was that when applying the CLM3.5 - DA scheme — originally tuned for real-world GRACE/-FO data — the model ensemble tends to diverge, often causing the DA runs to crash. To solve this issue we adapted the forgetting factor, which helps to control the ensemble spread of the model. The forgetting factor was obtained from previous tuning of the DA framework with respect to real world GRACE data, which lead to a value of 0.7 (values below 1 means that the ensemble spread is increased before each assimilation step). For the updated experiments we set the forgetting factor to 1, which accounts for the higher accuracy of the IIC scenarios. However, when applying a filter algorithm with domain localization, e.g. the Local Error Subspace Transform Kalman Filter (LESTKF) the assimilation process is still unstable and further tuning with adapting forgetting factors would be necessary to take into account different properties of the model ensemble in Eastern and Western Europe. Therefore, we focus in the following on results obtained with the global EnKF. All results refer to the 2° observation grid — results with the 4° grid are similar.

Data Assimilation Increments

Figure 41-14 illustrates the assimilation increments for the first assimilation step (January 2003) for both TWSA and snow. It is evident that the increments of the IIC6 scenario are almost twice as large as those of the IIC1 scenario. This difference arises from the higher accuracy of the observations in the IIC6 scenario, which leads the model to adjust more significantly to these precise observations. Moreover, we can observe that during winter, the snow component plays a substantial role in the overall TWSA over North-Eastern Europe. As a result, the snow compartment undergoes significant updates in the assimilation process, reflecting its importance in maintaining the accuracy of the TWS estimates.

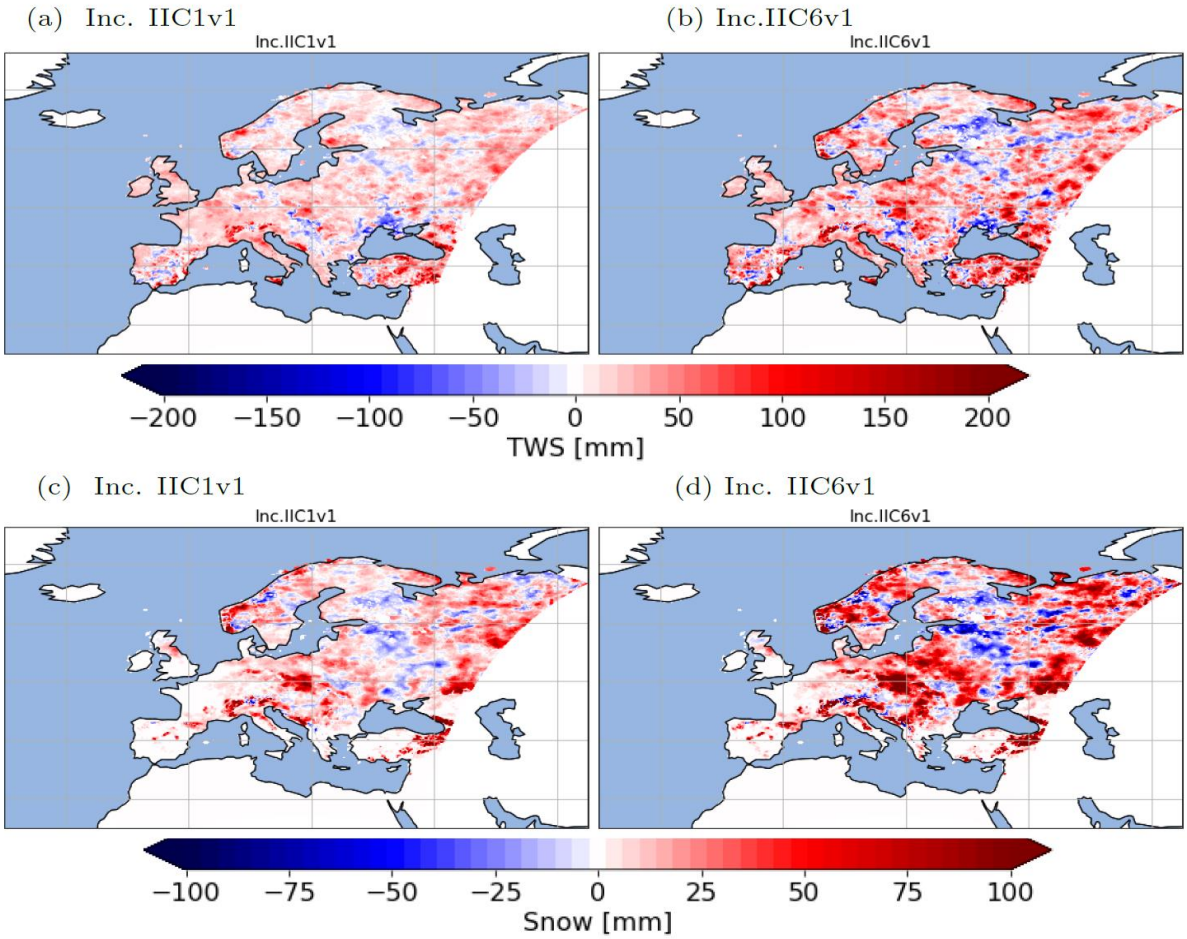

Figure 41-14: Assimilation increments for TWSA simulated by CLM3.5 in 01/2003 for (a) TWS in the IIC1 scenario, (b) TWS in the IIC6 scenario, (c) snow water in the IIC1 scenario, (d) snow water in the IIC6 scenario.

Catchment Averages

Figure 41-15 shows exemplarily catchment averaged terrestrial water storage anomalies in the Danube and in the Narva catchment for the synthetic truth (CLM5, black), the open-loop run (OL, blue) and model output after assimilating the different IIC scenarios. In the Danube catchment in particular the the seasonal signal improves with respect to the open-loop run. In the Narva catchments extremes are better represented after data assimilation. In particular the RMSD improves for both catchments significantly (Table 41-8), In the Narva-Jogi catchment correlation with respect to CLM5 increases from 0.740 for the open-loop run to 0.931 for scenario IIC6. Indeed, overall the IIC6 scenario performs best for both catchments closely followed by the IIC3 scenario.

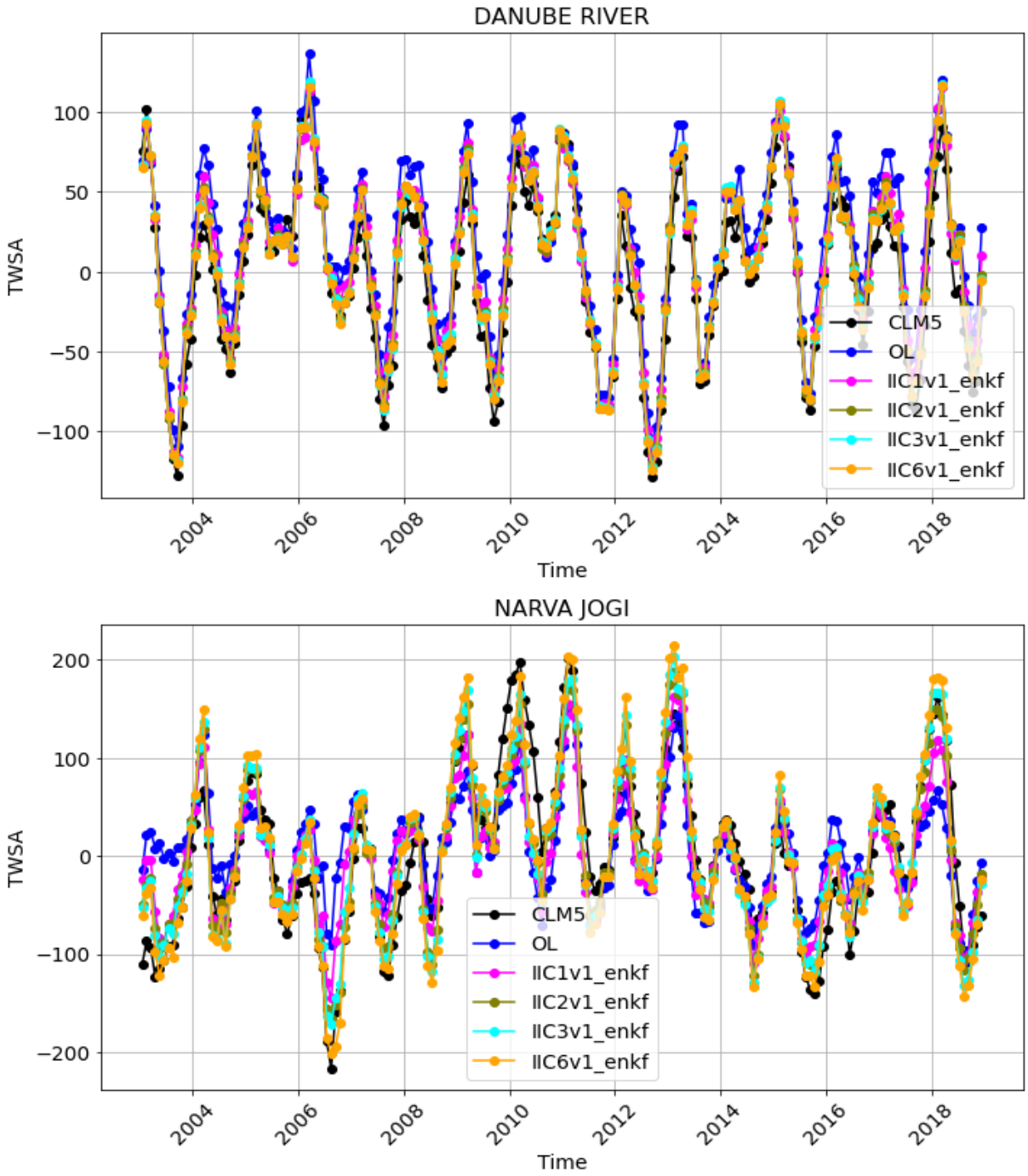

Figure 41-15: Terrestrial water storage anomalies (TWSA) in the Danube catchment and the Narva-Jogi catchment for the synthetic truth (CLM5, black), the open-loop run (OL, blue), and model output after assimilating the different IIC scenarios.

Table 41-8: Performance of DA scenarios in the Danube and Narva-Jogi catchment in terms of RMSD and correlation. CLM5 denotes the synthetic truth.

	Danube		Narva - Jogi	
Scenario	RMSD w.r. to CLM5 [mm]	Correlation with respect to CLM5	RMSD w.r. to CLM5 [mm]	Correlation with respect to CLM5
OL-CLM3.5	25.5	0.972	55.3	0.740
IIC1	15.7	0.979	39.7	0.880
IIC2	12.5	0.985	30.8	0.924
IIC3	11.7	0.988	32.6	0.917
IIC6	11.4	0.988	32.5	0.931

Performance of the IIC scenarios in terms of RMSD and correlation

In comparison to other European catchments, in the Danube catchment the CLM3.5 model output matches already quite well the reference truth before data assimilation (Figure 41-16Figure 41-16 (a) and (c)). In contrast, in the most North-Eastern European catchments correlation is lower and RMSD higher for the open-loop run, and here we see most of the improvement due to data assimilation (Figure 41-16 Figure 41-16 (b) and (d)).

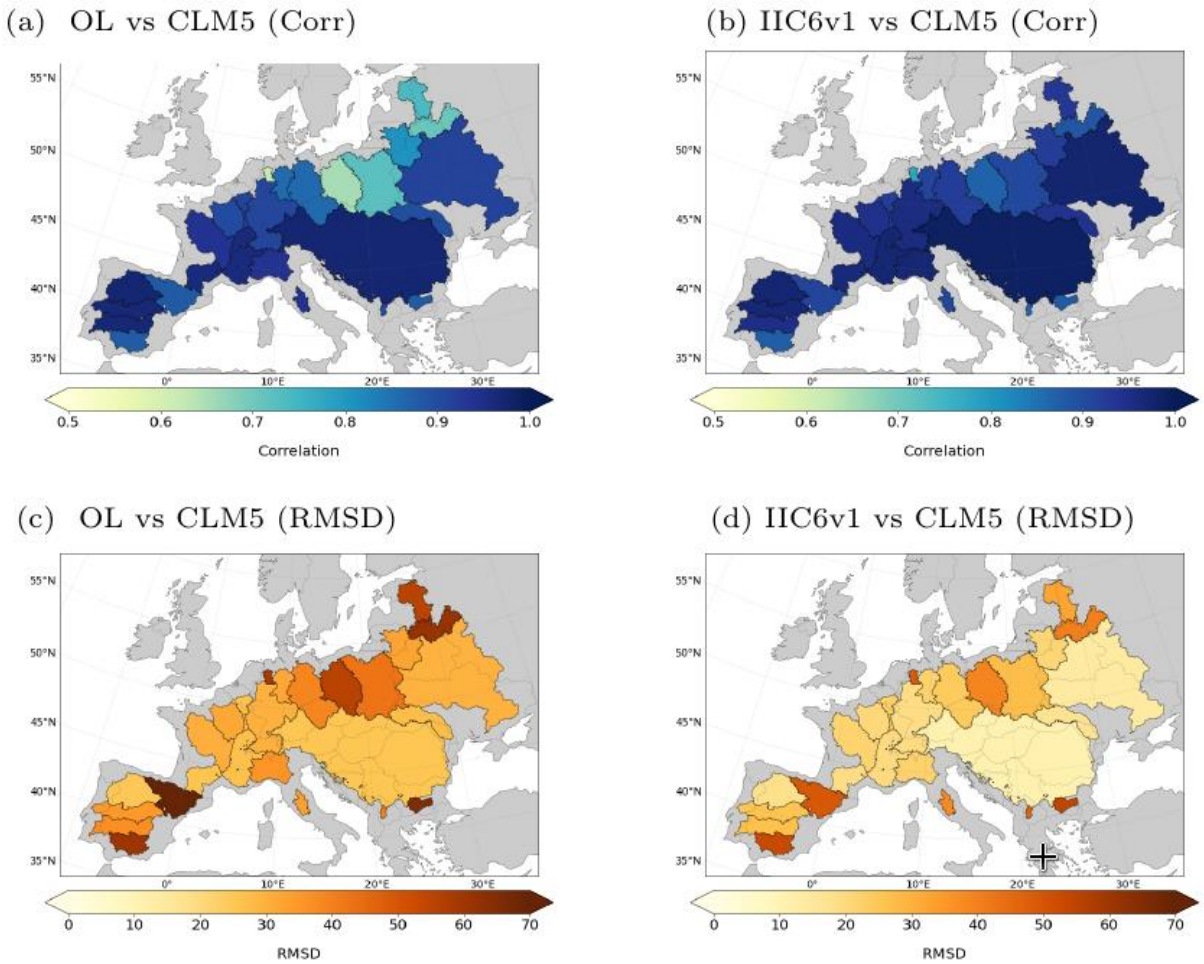

Figure 41-16: Correlation of TWSA (a) from the open-loop run (OL) with respect to the reference truth CLM5 and (b) from the data assimilation scenario IIC6 with respect to the reference truth CLM5. (c) and (d) show corresponding RMSD values.

Indeed, correlation improves by more than 0.2 for some of the North-Eastern catchments and also the RMSD is reduced by up to 20%. Figure 41-17 shows the different performance of IIC1, IIC3 and IIC6 in terms of RMSD reduction and correlation changes. Scenario IIC2 performs very similar to scenario IIC3 and is not shown here. Most catchments show a better performance for IIC3 and IIC6 than for IIC1 in terms of correlation and RMSD. This is also confirmed by Table 41-9, which shows RMSD and correlation of each individual IIC DA scenarios with respect to the synthetic truth averaged over all catchments.

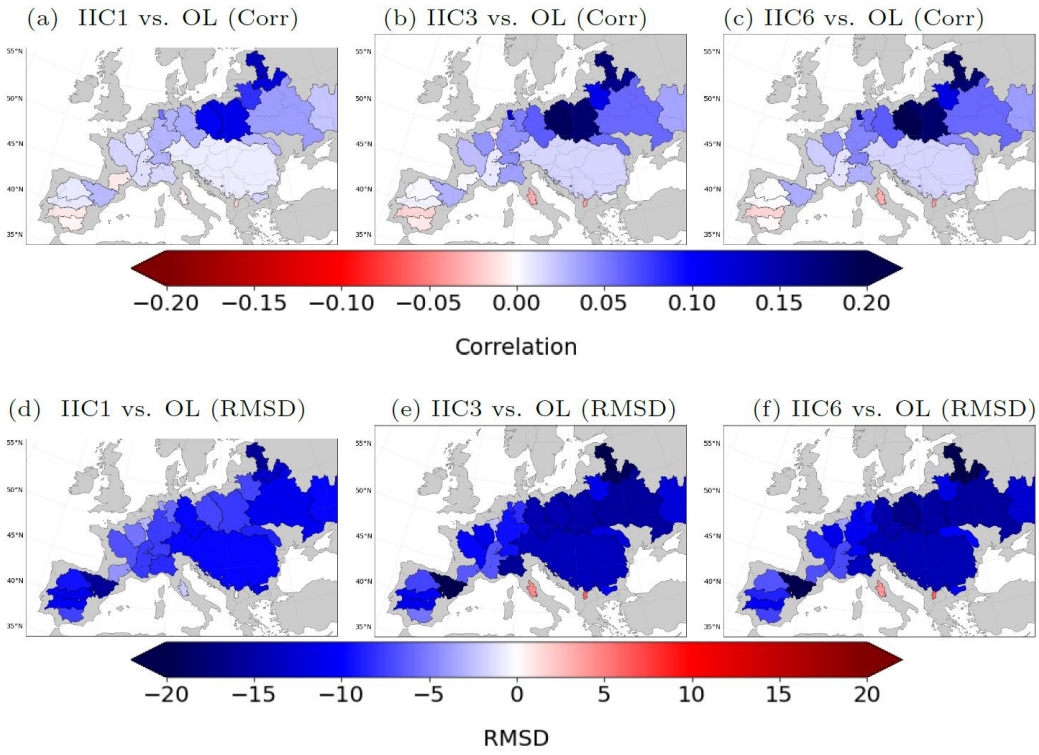

Figure 41-17: First row - Improvement of correlation due to data assimilation for individual IIC scenarios with respect to open-loop. Second row - Improvement of RMSD (in mm) due to data assimilation for individual IIC scenarios with respect to open-loop.

Table 41-9: Linear trends of TWSA (2003-2018) and RMSD as well as correlation coefficients between open-loop and DA versions of CLM3.5 with respect to CLM5 averaged over all river catchments.

Scenario	Linear Trend [mm/year]	RMSD w.r. to CLM5 [mm]	Correlation with respect to CLM5
CLM5	-038		
OL-CLM3.5	1.02	39.5	0.87
IIC1	0.68	31.3	0.91
IIC2	0.69	29.7	0.92
IIC3	0.66	28.9	0.92
IIC6	0.66	28.7	0.93

The assimilation results could be further improved by applying localization. In this scope, we tested the LESTKF, where domain localization is applied, which means that the analysis step

is not applied to the whole state vector, but to specified model subdomains using only observations within a certain localization radius. This enables us to avoid unwanted effects from long range correlations in the observation data – but so far the assimilation runs become unstable over the Eastern European catchments. This will require further tuning with respect to the forgetting factor, the set up of the model ensemble and the ensemble size.

Terrestrial Water Storage Trends

While the open-loop model shows a clear positive TWS trend in Central and Western Europe, the TWS trend based on CLM5 shows a negative direction in most European catchments with few exceptions mostly located in Eastern Europe (Figure 41-18). During data assimilation, the prevalent negative trend of the OL model is reduced and in some catchments a change in sign can be observed.

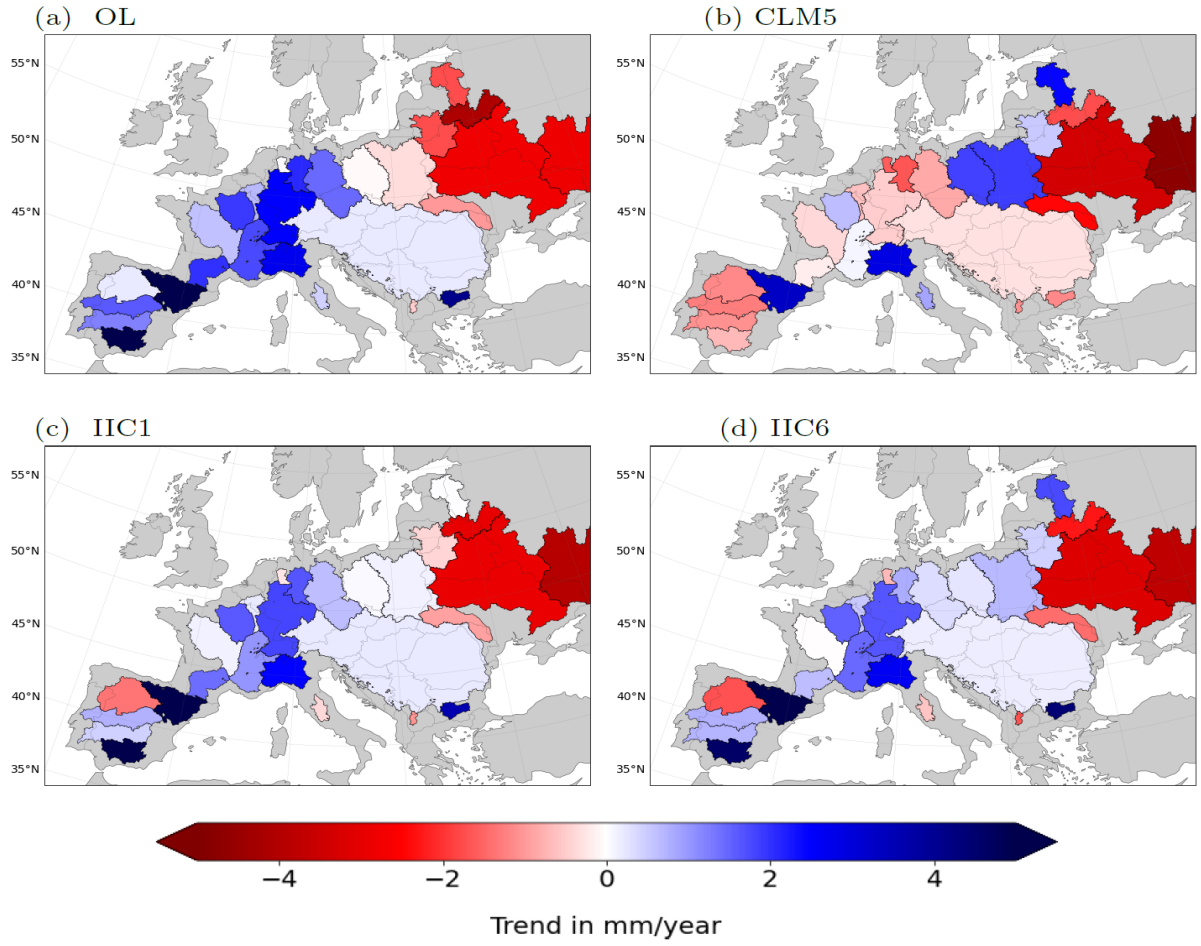

Figure 41-18: Trend in TWSA based on (a) the open-loop run (OL) (b) the reference truth CLM5 and (c), (d) the data assimilation scenarios IIC1 and IIC6.

5.2.1 Impact analysis on coupled atmosphere/hydrology models

Coupled atmosphere/hydrology models are used to simulate not only parts of the Earth System individually but also exchanging processes between them. Exchanged variables are for example surface temperatures and evapotranspiration from land surface to atmosphere and precipitation and 2m temperature from atmosphere to land surface. In contrast to offline modelling where these information are provided by predefined products like reanalysis, including this coupling leads to more realistic simulation of feedbacks between different parts of the Earth System.
Experiments showed that either using GRACE data assimilation or GRACE calibration in land surface models leads to changes in storage compartments, TWS and water and energy fluxes. In coupled systems, this leads to changes in exchanged variables, subsequently changing simulation results.

As coupled surface-atmosphere models are often part of large Earth System Models which are used e.g. for CMIP projections or feedback simulations, more realistic patterns in water storages and fluxes obtained via GRACE data assimilation or GRACE calibration are of major importance. Improving this through a future gravity mission has the ability to provide much more realistic representation of Earth's water cycle.

In a first step, we conducted an extensive literature review of studies in which GRACE data assimilation or calibration was conducted using a land surface model that is also used in a coupled system. The overview of this review is given in Figure 41-19.

It can be seen that a variety of land surface models that are used in coupled systems exist. On some of them, GRACE data assimilation has been used. The most used model here is CLM. This is also the only model where GRACE calibration has been used. GRACE assimilation studies have shown little impact of the assimilation on land-atmosphere interactions. The only variable that is investigated in this context is evapotranspiration where no real impacted can be seen. For GRACE calibration, a larger impact can be seen. For some frequently used models like CABLE, no assimilation framework has yet been implemented. As shown in WP 100, user desire for a sub-weekly latency, a spatial resolution of below 100 km, a daily temporal resolution and an accuracy that is below 1 cm. Especially the data assimilation of gravity data would greatly benefit from this.

5.2.2 Impact analysis on short-term operational/NRT service applications

Near real time systems that use GRACE (-FO) data are sparse as GRACE solutions are not provided in real time. As weekly solutions are used more frequent, near real time applications are more feasible. However, the skill of those solutions is not as good as the monthly ones as only a part of the Earth is covered in this time frame. A new mission will introduce new application possibilities as the spatial resolution will be much higher using more satellites.
In a first step, we conducted an extensive literature review of systems that use GRACE data are GRACE-like data for near real time applications. The overview of this review is given in Figure 41-20. As shown in WP 100, user desire for a sub-weekly latency which would make the application of NRT systems that use real time gravity data much more feasible.

ID	Land Surface Model	Coupled System(s)	Operational?	Atmopshere model	Paper on using GRACE calibration/ DA in LSM	Title	DA/Calibration	Description	Impact analysis on land-atmosphere interactions
1	**Community Land Model (CLM)**	Terrestrial System Modeling Platform (TSMP)	No	Cosmo/ICON	Swenson and Lawence (2014)	Assessign a dry surface layer-based soil resistance parametrization for the Community Land Model using GRACE and FLUXNET-MTE data	Calibration	-new soil resistance parametrization -calibrated using GRACE data	-new parametrization reduces evaporation when soils are moist but increases evaporation later in the season due to higher soil moisture storage -old parametrization may underestimate the effect of soil moisture memory on land-atmosphere fluxes
		Community Earth System Model	CMIP	Community Atmopshere Model (CAM)	Swenson and Lawence (2015)	A GRACE-based assessement of interannual groundwater dynamics in the Community Land Model	Calibration	-Existing bulk aquifer layer is removed and Richards equations is solved using a zero-flux boundary condition at the bottom of the soil column - needs a global soil depth data set having the necessary vertical resolution to constrain the CLM soil thickness parameter --> GRACE used for deriving data set	-effects on evapotranspiration of changing groundwater parametrization are relatively small, with a small reduction in annual mean ET bias seen in the modified model
		Community Integrated Earth System Model	CMIP	CAM	Su et al. (2010)	Multisensor snow data assimilation at the continental scale: The value of Gravity Recovery and Climate Experiment terrestrial water storage information	DA	- assimilate both GRACE TWS and MODIS snow cover fraction into CLM3.5	-
		CMCC-ESM2	CMIP	CAM	Zhao and Yang (2018)	Multi-sensor land data assimilation: Toward a robust global soil moisture and snow estimation	DA	- assimilation of AMSR-E, GRACE and MODIS observations into CLM4	-
		E3SM	CMIP	EAM (modified CAM)	Springer (2019)	A water storage reanalysis over the European continent: assimilation of GRACE data into a high-resolution hydrological model and validation	DA	- assimilate GRACE TWS into CLM3.5	-evapotranspiration only slightly impacted by data assimilation with no positive effect comparing to observation based data.
		FGOALS	CMIP	FAMIL2.2	Springer et al. (2019)	Evidence of daily hydrological loading in GPS time series over Europe	DA	- hydrological loading assessement in GPS time series at daily time scale through a high-resolution GRACE-assimilating hydrological model	-
		FIO-ESM	CMIP	CAM	Klos et al. (2021)	Quantifying Noise in Daily GPS Height Time Series: Harmonic Function Versus GRACE-Assimilating Modeling Approaches	DA		
		KIOST-ESM	CMIP	GFDL-AM2.0	Wu et al. (2022)	The impact of multi-sensor land data assimilation on river discharge estimation	DA	- multi sensor DA from AMSR-E, GRACE and MODIS observations for discharge	-
		NORESM	CMIP	CAM					
		SAMO	CMIP	CAM					
		TAIESM1	CMIP	TAIAM1					
2	**NOAH**	WRF-Hydro	no	WRF	Nie et al.(2019)	Assimilating GRACE Into a Land Surface Model in the Presence of an Irrigation-Induced Groundwater Trend	DA	- 4 experiments: with/without DA, with/without irrigation - does NOAH capture trends without irrigation - can DA overcome deficits?	- without irrigation captures the variation of evapotranspiration quite well, with less agreement in representing inter-annual variability - the impact on the area-averaged ET is small (for irrigation acitivated as well as DA)
		Climate Forecast System	CMIP	NCEP Global Forecast System					
3	**HTESSEL**	IFS-HTESSEL	CMIP	IFS					
		EC-Earth3	CMIP	IFS					
4	**JSBACH**	MPI-ESM	CMIP	ECHAM6.3					
		AWI-ESM	CMIP	ECHAM6.3					
		ICON-ESM	CMIP	ICON					
		NESM3	CMIP	ECHAM6.3					
5	**CABLE**	ACCESS-ESM1	CMIP	HadGAM2	Tangdamrongsub et al. (2020)	Multivariate data assimilation of GRACE, SMOS, SMAP measurements for improved regional soil moisture and groundwater storage estimates	DA	- assimilate SMOS, SMAP and GRACE into CABLE	-
					Yin et al. (2020)	Improved water storage estimates within the North China Plain by assimilating GRACE data into the CABLE model	DA	-correct estimates of groundwater storage over the North China Plain	- near-surface and root zone soil moisture receives only a small update, the change in other fluxes such as evapotranspiration is insignificant
					Tangdamrongsub et al. (2020)	Development and evaluation of 0.05° terrestrial water storage estimates using Community Atmosphere Biosphere Land Exchange (CABLE) land surface model and assimilation of GRACE data	DA	- change the resolution from 0.5° to 0.05° - GRACE TWS observations are assimilated to improve accuracy	- the impact on the surface components and flux estimates (SSM and ET) is trivial with a slight improvement using GRACE DA
6	**JULES**	HadGEM3	CMIP	MetUM-GA7.1					
		UKESM1	CMIP	MetUM-GA7.1					
7	**ORCHIDEE**	IPSL-CM5A2	CMIP	LMDZ					
8	**MATSIRO6**	MIROC-ES2L	CMIP	CCSR AGCM					

Figure 41-19: GRACE calibration and data assimilation studies for coupled hydrological models

ID	Project / Paper	Group / Author	Description/Objectives	Operational?	Forecast possibility?
1	US drought monitor	NDMC, NOAA and USDA	- droughts inidcators in the US - based on terrestrial water storage observations derived from GRACE-FO satellite data and integrated with other observations And land surface models in a data assimilation system (Houborg et al, 2012)	yes, weekly outputs	no
2	Improved the Characterization of Flood Monitoring Based on Reconstructed Daily GRACE Solutions over the Haihe River Basin	Nie et al. (2023)	- use daily GRACE like data (reconstructed from near real-time precipitation and temperature data) and derive three daily flood monitoring indexes	no	maybe (GRACE data could Be reconstructed for Future)
3	EGSIEM (European Gravity Service for Improved Emergency Management)	University of Bern, University of Luxembourg, German Research Centre for Geosciences, Graz University of Technology, Leibniz University Hannover, German Aerospace Center	- reduce the time delay of necessary input data and derived output gravity models to less than 5 days - increase time resolution of gravity models to just one day - improve their quality by transferring the accuracy level of the monthly fields to the daily ones	no (research project ended in 2018)	no
4	Grace-Enhanced Flood Monitoring and Forecasting Tool Using a Five-Day Grace Product and Physics-Based Data Analytics	Global Council for Scienceand the Environment	- new 5-day, mascon-based, near real-time GRACE satellite product for enhancing flood early warning and monitoring	not yet, ongoing research group	no
5	Monitoring the Catastrophic Flood With GRACE-FO and Near-Real-Time Precipitation Data in Northern Henan Province of China in July 2021	Xiao et al. (2023)	- rainstorm process based on near-real-time precipitation data from the China Meteorological Administration Land Data Assimilation System (CLDAS-V2.0) - reconstructed daily terrestrial water storage anomalies (TWSAs) based on GRACE and GRACE-FO data and CLDAS-V2.0 datasets - wetness index based on the reconstructed daily TWSA for flood warnings	no	maybe (GRACE data could Be reconstructed for Future)

Figure 41-20: NRT systems using GRACE or GRACE-like data

42. WP1000: HYDROLOGICAL (MEDIUM TO LONG-TERM) AND CLIMATE APPLICATIONS

42.1. MEDIUM TO LONG-TERM HYDROLOGY

ACCURACY ASSESSMENT FOR TIME SERIES IN HYDROLOGICAL UNITS

One of the most common applications of satellite gravimetry is the analysis of time series of water storage variations in hydrological units such as river basins or aquifers. The following data sets have been used (dataset 1) to assess the benefit of quantum mission for this purpose:

- spherical harmonic coefficients of three monthly (30 days) simulation solutions for the different mission scenarios
- spherical harmonic coefficients of 12 weekly (7-days) simulation solutions (GRACE N=90, MAGIC N=120, IIC3v1 N=120, IIC6v1 N=120)
- spherical harmonic coefficients of 90 daily (one day) solutions for each of the four missions simulations
- spherical harmonics coefficients of the corresponding input signal (reference signal) from ESA ESM HIS fields

While for the assessment of medium to long-term hydrological variations monthly solutions would be the natural choice, the only three monthly solutions available so far hamper a reasonable quantitative analysis of empirical uncertainty estimates. Therefore, the 7-days solutions were used for the first assessment presented in the following.

Time series of equivalent water heights were derived for basin averages of 405 individual river basins defined by the Global Runoff Data Center (GRDC), representing the largest river basins worldwide. Figure 42-1 shows an exemplary time series for the Amazon (left) and Danube basin (right, both N=50 and unfiltered). The temporal root-mean-square difference (RMSD) between the reference and the simulation time series was computed for each river basin to assess the accuracy of the simulation results.

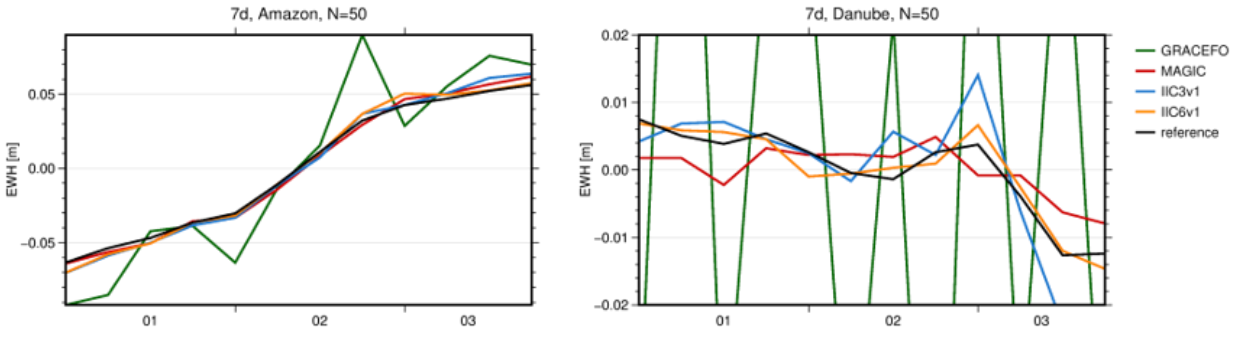

Figure 42-1: Time series for Amazon (left) and Danube river basin (right)

UNFILTERED SOLUTIONS

To stay consistent with mission performance assessments previously carried out for the MAGIC mission, for which the MRD numbers were explicitly based on unfiltered solutions, here a first look is again taken at unfiltered simulation output. Figure 42-2 (left) shows the degree amplitudes of an exemplary 7-days solution for the four different simulation scenarios with the solid lines denoting the signal of each solution and the dashed lines representing the difference degree amplitudes of the simulation w.r.t the reference. The smaller errors in the quantum scenarios (blue and orange) compared to the GRACE-FO and MAGIC case can clearly be identified. For GRACE-FO the error curve intersects with the signal below n=10, for MAGIC around n=35, for IIC3v1 around n=45 and for IIC6v1 between n=55-60. Thus it can be concluded that above these degrees the unfiltered solution is strongly dominated by noise. The right part of Figure 42-2 additionally shows degree amplitudes of DDK filtered solutions that will be discussed in the next section.

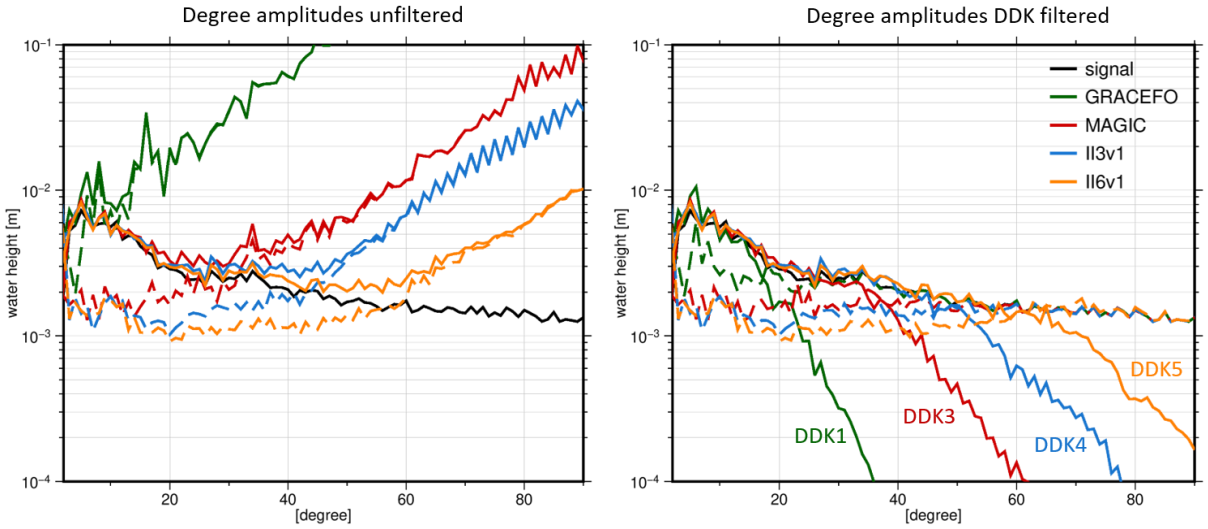

Figure 42-2: Degree amplitudes for exemplary 7-days solution (2002/01/01-07) for unfiltered simulation output (left) and simulation output filtered with differently strong DDK filters (right).

Figure 42-3 shows the RMSD between the simulation output and the reference solution, here truncated at degree N=50, which corresponds to a 400km spatial resolution that was also used in assessing the MAGIC mission performance for weekly models. While it is not possible to derive reasonable results from unfiltered GRACE solutions (mean RMSD of ~10cm), the MAGIC mission (mean RMSD 0.8cm) allows the assessment of time series in large river basins, due to the averaging effect filtering out the noise, which is already dominant at n=50 in case of MAGIC. The three-pair QSG scenario (IIC3v1, mean RMSD 0.6cm) shows on average small errors compared to MAGIC, but there are also a few basins, e.g. in central Africa and northern Canada, for which the MAGIC RMSD is smaller. The 6-pairs QSG scenario (IIC6v1, mean RMSD 0.4cm) reveals the added benefit of the additional pairs with generally smaller RMSD values.

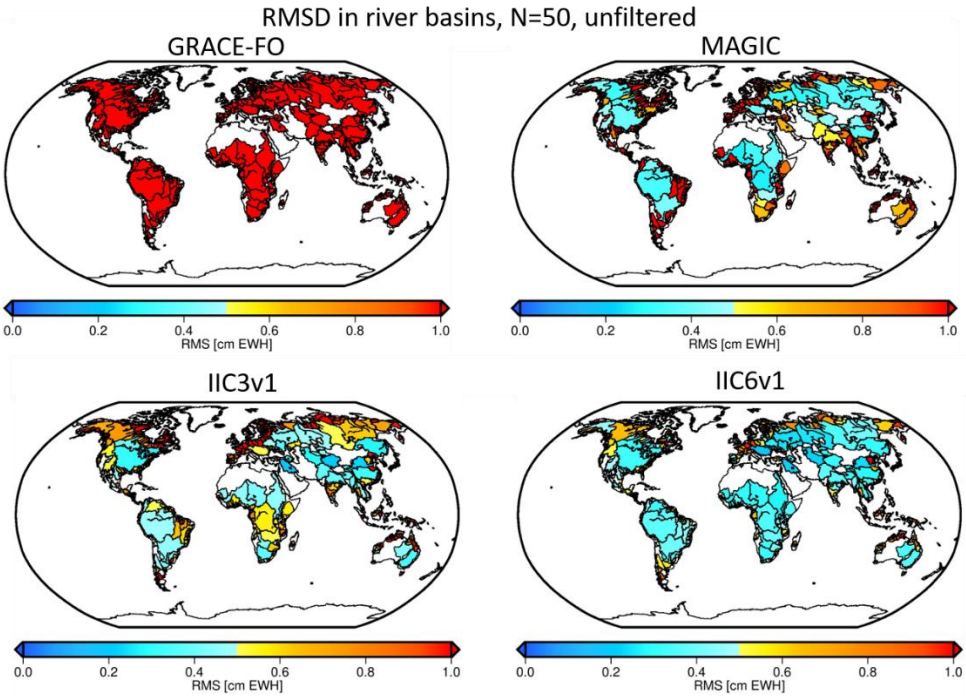

Figure 42-3: Temporal RMSD of 7-days simulation output (four different scenarios, N=50, unfiltered) and reference solution for basin averaged time series of 405 river basins defined by the Global Runoff Data Center (GRDC).

For a better overview of the RMSD values computed for the individual basins, scatter plots were created in addition to the maps. Figure 42-4 displays the RMSD value for each river basin and each mission scenario w.r.t the size of the river basin for N=50 and additionally for N=90, which is the maximum degree available for all simulation outputs. Again the dominating noise in the GRACE scenario is evident with the RMSD being about one order of magnitude larger than for MAGIC and even more for the quantum missions. The improvement of the IIC3v1 scenario over MAGIC and of the IIC6v1 scenario over its 6-satellites counterpart can also be seen. For N=50, the thresholds that 70% of the river basins fall below are 32.4cm, 2.18cm, 1.0cm, and 0.7cm for GRACE-FO, MAGIC, IIC3v1, and IIC6v1, respectively. The differences become more prominent for higher degrees (here: N=90), as the noise reduction caused by the additional satellite pairs becomes more relevant for smaller spatial scales (70% threshold of 442cm vs. 16.5cm vs 5.1cm vs. 2.7cm). However, as the unfiltered solutions are of only limited relevance from a user perspective, post-processed models will be assessed in the following paragraph.

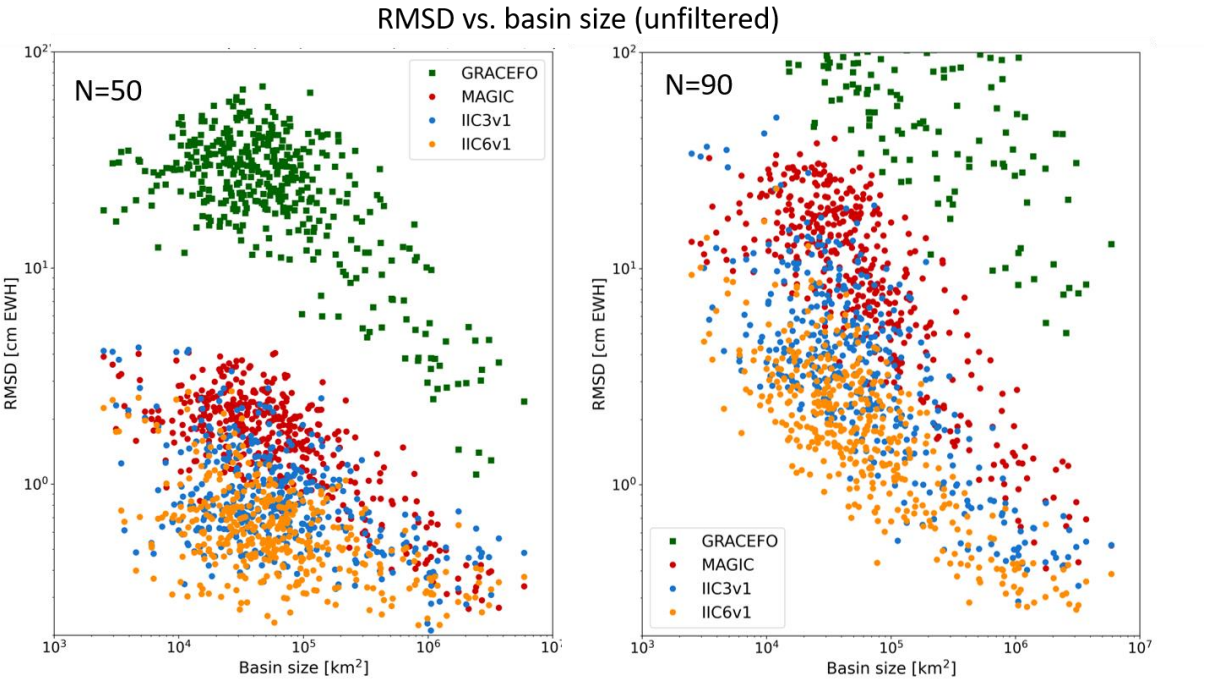

Figure 42-4: Scatter plot of RMSD of basin average time series vs. size of the river basin for different mission scenarios for unfiltered solutions truncated at N=50 (left) and N=90 (right).

POST-PROCESSED (FILTERED) SOLUTIONS

TAILORED FILTERING FOR EACH MISSION SCENARIO

While the unfiltered solutions assessed in the previous paragraph are helpful to define mission performance numbers that should not be biased towards any kind of post-processing, from a user perspective the potential of a mission after post-processing is certainly more relevant. Therefore, the following paragraph is dedicated to deriving accuracy estimates for filtered solutions, again for the hydrological units defined by GRDC. The first question that arises is the choice of the appropriate post-processing filter. Here DDK filter family was chosen due to well-established filter performance, easy implementation, and a wide acceptance/use in the hydrological community. For each mission scenario the optimal filter strength was defined as the smallest filter possible, i.e. sustaining as much signal as possible, while filtering out enough noise that it does not dominate the signal. This was identified by the degree amplitude curves (Figure 42-2) as the error curve just not intersecting with the signal curve. The degree amplitudes in Figure 42-2 (right) shows the resulting filtered solutions. For GRACE-FO, e.g., the strong DDK1 filter was necessary, while for MAGIC DDK3 and for the quantum missions even smaller filters (DDK4 for IICv3 and DDK5 for IIC6v1) were sufficient. For each of these choices the next smaller filter leads to an intersection of the error and signal curves, while a stronger filter causes unnecessary smoothing. Figure 42-5 displays global maps of EWH for an exemplary 7-days solution for the "optimally" filtered mission scenarios. While the noise level appears to be quite similar for each of them, the gain in spatial resolution from GRACE-FO over MAGIC to IIC3v1 and IIC6v1 due to the less strong filtering needs becomes evident.

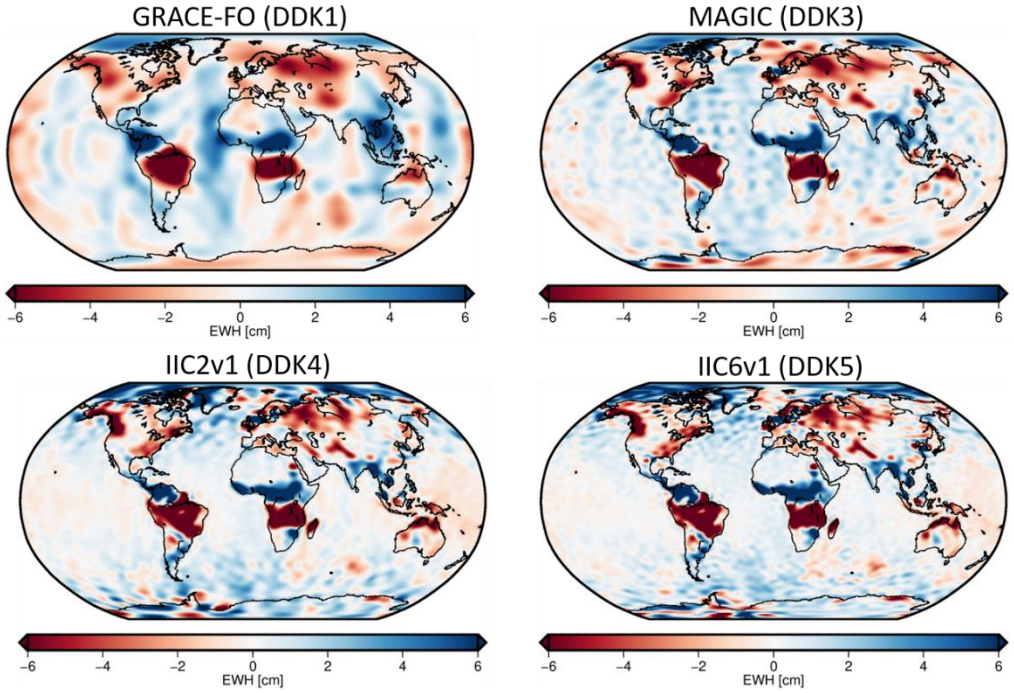

Figure 42-5: Maps of equivalent water heights for an exemplary 7-days time span, each scenario filtered using a tailored DDK filter

To assess the accuracy of post-processed solutions up to a certain spatial resolution, not only the processing errors (which strongly get smoothed out by filtering) but also the filter commission error (i.e. the loss in resolution caused by filtering) needs to be considered. Therefore, in the following the filtered solutions are compared to the unfiltered reference solution up to degree N=90 corresponding to a spatial resolution of approximately 222km. The analysis for the 405 GRDC river basins was repeated for the filtered solutions, using the "optimal" filters for each mission as indicated above. Figure 42-6 shows the corresponding maps of RMSD values for each basin. Again, the GRACE-FO scenario is clearly inferior (mean RMSD 1.1 cm) to the other missions, as most of the signal is being missed when filtering with DDK1. Between MAGIC and IIC3vs (mean RMSD of both 0.6) the picture is less clear as there are basins performing better for each of the two missions compared to the other one. The 6-pairs IICv1 scenario (mean RMSD 0.5) shows a general improvement over the other missions.

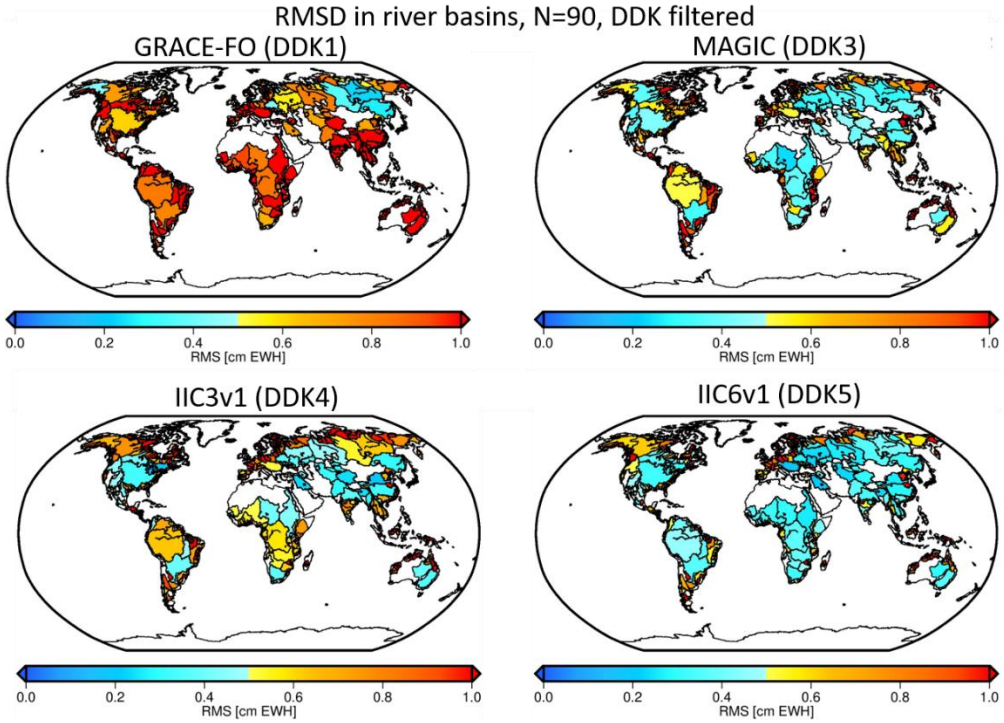

Figure 42-6: Temporal RMSD of 7-days simulation output (four different scenarios, N=50, filtered using tailored DDK filters) and reference solution for basin averaged time series of 405 river basins defined by the Global Runoff Data Center (GRDC).

The corresponding scatter plot of the RMSD values w.r.t the basis sized is shown in Figure 42-7 and it largely confirms the statements made above. The GRACE-FO RMSD values are largely above the other missions (70% threshold at 1.93cm), while MAGIC and IIC3v1 perform rather similar (70% threshold at 1.37 and 1.36 cm) and the IIC6v1 scenario presents smaller RMSD values (70% threshold at 1.05cm).

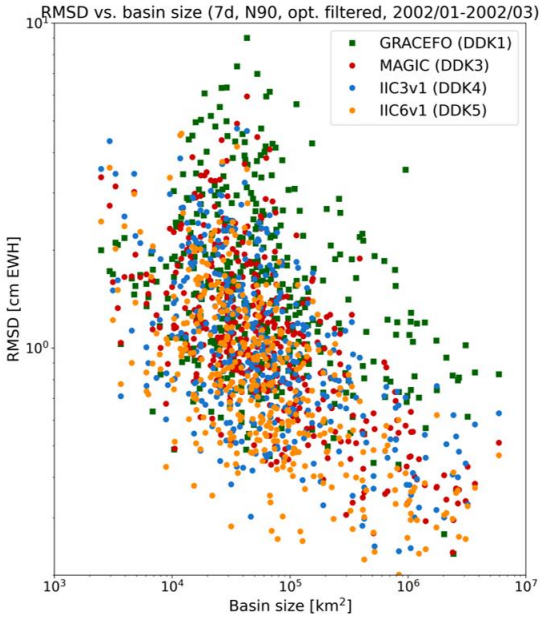

Figure 42-7: Scatter plot of RMSD of basin average time series vs. size of the river basin for different mission scenarios for DDK filtered solutions truncated at N=50

Summarizing it can be concluded that the gain in accuracy and the reduced noise of the quantum mission scenarios compared to GRACE-FO and MAGIC for hydrological applications can clearly be identified. For the filtered solutions the gain of the 3-pairs scenario over MAGIC is not as clear, thus adding a third low-inclination pair does not strongly improve the RMSD for basin-averaged time series. However, it should be noted that this is not a general statement on the potential of the mission design, as an improvement w.r.t .noise level and spatial resolution is generally also visible for IIC3v1 compared to MAGIC (see

Figure 42-2 and Figure 42-5) Only for the specific application shown here (basin average time series that inherently provide an additional smoothing) these improvements are less visible. The 6-pairs simulation then again shows a clear improvement of all other mission scenarios.

EQUAL POST-PROCESSING APPLIED FOR EACH MISSION SCENARIO

In the paragraphs above, the strength of the post-processing filter was determined for each mission scenario individually based on the signal to noise characteristics, resulting in different filters (DDK1 to DDK5) for the different missions. This procedure particularly reveals the difference in the spatial resolution achievable by the different satellite constellations, see Figure 42-5. Equally valid, however, is the question how the relative accuracies of the different missions behave when the same post-processing is applied to all simulation outputs, i.e. when the same spatial resolution is targeted by all mission scenarios. Applying no post-processing at all (as shown in Figure 42-4), does not appear to be realistic, as even for the quantum constellations the noise dominates the signal when trying to achieve high spatial resolutions, as shown in Figure 42-4 (right) for degree N=90. Users will certainly apply some kind of post-processing. Therefore, in the following, the DDK5 filter is chosen, which has shown to be appropriate for the IIC6v1 7-days solutions, and it will be applied to each of the four mission scenarios. Figure 42-8 shows global maps of equivalent water heights for an exemplary 7-day solution and strongly reveals the difference in signal-to noise ratio. While with GRACE-FO it is not possible to see any signal, also the MAGIC solution is also still very noisy. The three-pairs quantum mission already shows strong improvement, while adding additional pairs in the IIC6v1 constellation can further reduce the noise.

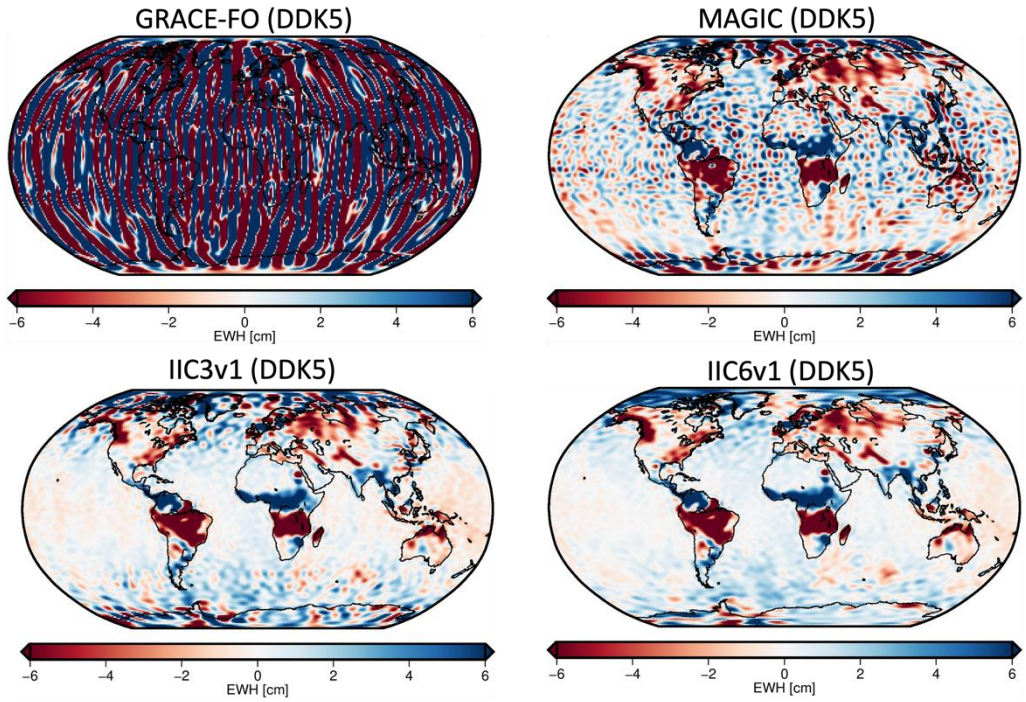

Figure 42-8: Maps of equivalent water heights for an exemplary 7-days time span, each scenario filtered with a DDK5 filter.

The corresponding scatter plot for RMSD values of the basin average time series of the 405 river basins is shown in Figure 42-9 again including the filter omission error, i.e. comparing the filtered solution to the unfiltered ESA-ESM reference time series. In general, the indication

already seen in the exemplary snapshot in Figure 42-8 is confirmed by the river basin analysis. Especially the strong improvement of the future constellations over the current GRACE-FO mission becomes evident by the green dots being always higher than the other colors. Also the RMSD values of the MAGIC mission can be observed to be on average larger than those of the two quantum missions. While the difference between the IIC3v1 and the IIC6v1 scenario is less obvious, there is still an improvement visible from the blue to the orange dots in Figure 42-9.

In addition to the basin-scale analysis the RMSD values are also plotted for each individual grid cell in Figure 42-10. The improvements from GRACE-FO over MAGIC towards ICC3v1 and IIC6v1 are again clearly visible. These empirically determined accuracies for the 7-days solution grid cell values serve as the basis for the error propagation approaches described in Section 42.2.

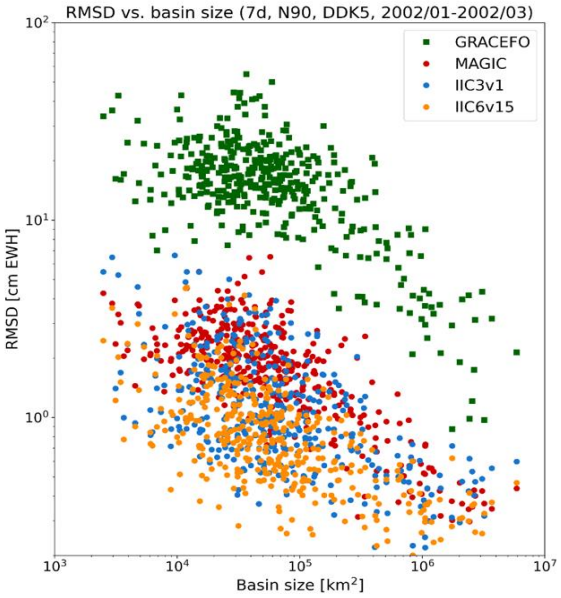

Figure 42-9: Scatter plot of RMSD of basin average time series vs. size of the river basin for different mission scenarios for DDK5 filtered solutions truncated at N=90, including filter omission error

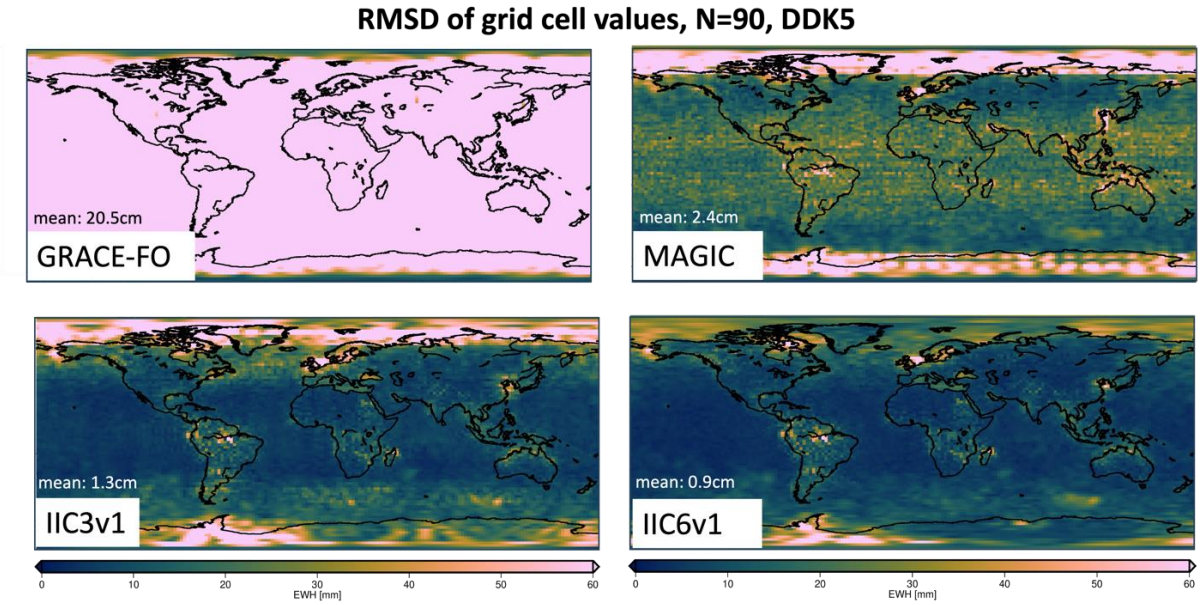

Figure 42-10: RMSD of grid cell time series w.r.t reference solution for different mission scenarios for DDK5 filtered solutions truncated at N=90, including filter omission error.

COMPARISON OF REGIONAL AND GLOBAL SOLUTIONS

The global spherical harmonic solutions by TUM discussed so far (dataset 1 in Chapter 3) were additionally compared to the regional simulation output provided by POLIMI (see Chapter 2). The regional solutions were available as gridded values for seven river basins of different sizes (Amazon, Ganges, Danube, Uruguay, Rhine, Elbe, Oder) for the year 2002. Here the 7-days solutions in the overlap period with dataset 1 (2002-01 to 2002-03) were analyzed. From the gridded regional solutions basin averages were computed and the time series of basin averages was analyzed in the same way as the time series of the 405 river basins described above. Figure 42-11 shows a comparison of the RMSD values between the simulation output and the reference for both the global models (dots) and the regional models (crosses). It can be seen that in case of the MAGIC (IIC2v1) mission, the regional time series exhibits a smaller RMSD than the global counterpart in 4 out of 7 river basins. This number is even larger for the quantum missions (IIC3v1: 6/7, IIC6v1: 5/7). Thus it can be concluded that the regional solutions generally fit slightly better to the reference than the global solutions. However, it should be noted that the specific conclusions are only valid for the specific comparison, i.e. the comparison with DDK5-filtered global spherical harmonic models up to degree N=90. Other post-processing choices might lead to different results.

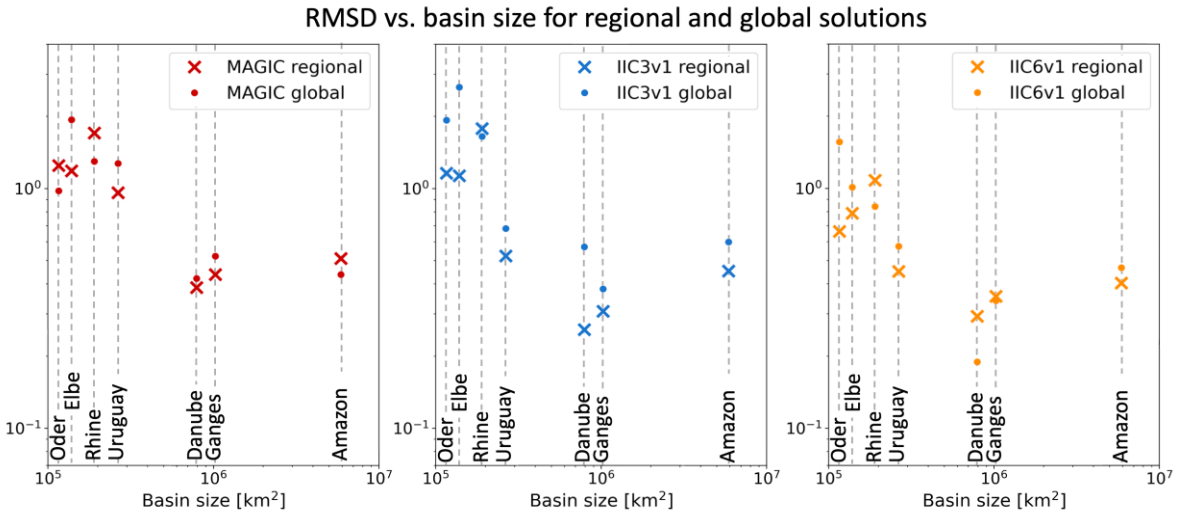

Figure 42-11: Comparison of basin-averaged RMSD values (i.e. simulation vs. reference) for different mission scenarios (left: MAGIC, middle: IIC3v1, right: IIC6v1) and for the global (dots) vs. the regional models (crosses).

Figure 42-12 summarizes the results for the regional solutions for the different mission scenarios. It can be seen that generally the IIC3v1 constellation performs better than MAGIC (i.e. in 6/7 river basins the RMSD is smaller) and the IIC6v1 scenario is superior to IIC3v1 (i.e. in 5/7 basins the RMSD is smaller). This confirms the improvement of the quantum mission scenarios over existing concepts also for the regional analyses scheme.

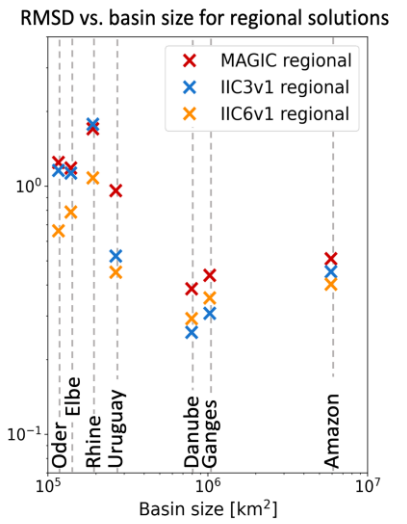

Figure 42-12: Comparison of RMSD of regional solution w.r.t. the reference for different mission constellations.

42.2. CLIMATE APPLICATIONS

For the investigation of climate signals, we used the 12-years simulation output provided by TU Munich (dataset 3) and error propagation based on empirical error estimates derived for the full-scale simulations (dataset 1, see Figure 42-10). From dataset 3 the one-pair scenario (IIC1v1) was used for a GRACE-FO-like mission and the two-pair scenario (IIC2v1) was used for MAGIC.

EVALUATING TWS-RELATED COMPONENTS OF CLIMATE MODELS

If intending to use satellite gravimetry for the evaluation of coupled climate models, such as those models taking part in the sixth phase of the Climate Model Intercomparison Project (CMIP6), the observed and modelled time series cannot be compared on a point-by-point basis due to the stochastic nature of the model output. Therefore, only higher order metrics can be compared, such as trends, amplitudes, or (inter-annual) signal variability. Following Jensen et al. (2020) [RD-1], a signal decomposition of the CMIP6 model ensemble (years 1850-2100) was carried out according to the following parameter model:

$$TWS(t) = a + b \cdot t + c \cdot \cos(\omega t) + d \cdot \sin(\omega t), \qquad (1)$$

to determine the linear trend (b), and the seasonal signal (c,d). The residuals of this parameter estimation (i.e. the full signal minus the estimated model) contain long-term (inter-annual) as well as short-term (sub-seasonal) variations. To isolate the inter-annual part of the variations, low-pass filtering using a 3rd order Butterworth filter with cut-off frequency of 12 months was applied. The multi-model median (MMMed) of the results of the decomposition computed for 105 model runs from 17 different CMIP6 models (see [RD-1] for details on the model selection) are shown in Figure 42-13.

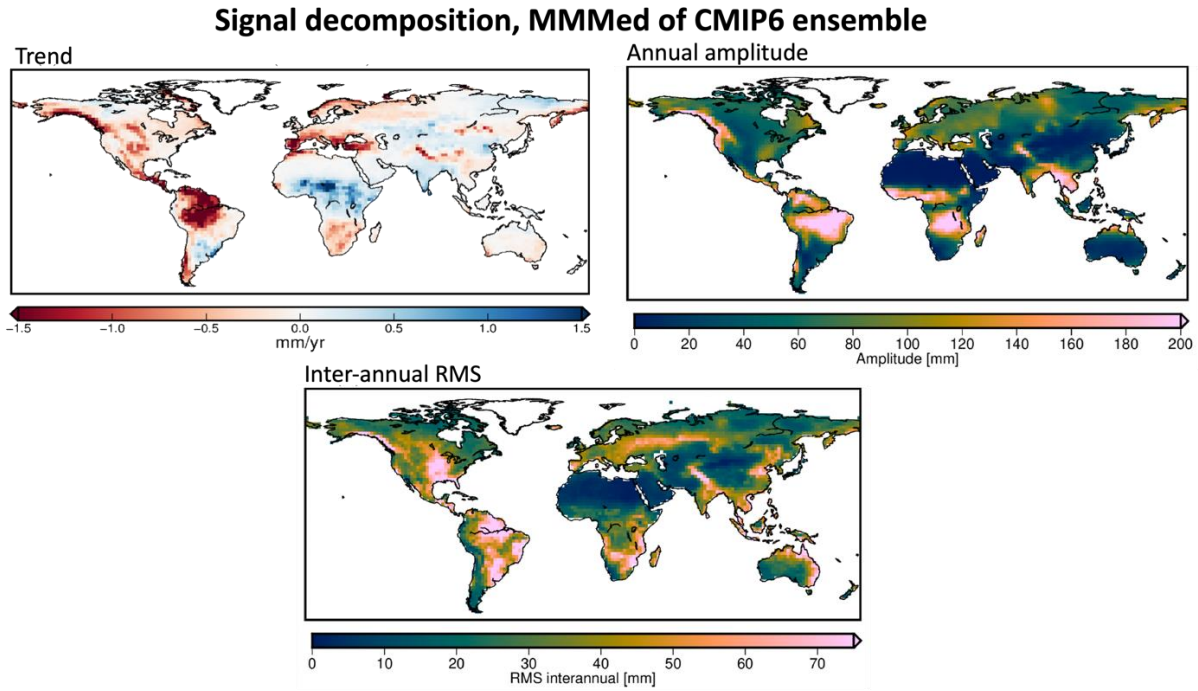

Figure 42-13: Multi model median (MMMed) of the signal decomposition of the CMIP6 model ensemble for the linear trend (top left), the annual amplitude (top right), and the inter-annual RMS (bottom), derived from model simulation from 1850-2100.

The same parameter model was fitted to the 12-years of 7-days simulation output time series (years 1995-2006, dataset 3) and the results were compared among the different satellite mission scenarios and to the CMIP6 model output. We use again weekly post-processed (DDK5 filtered) solutions truncated at N=90 and show the results in Figure 42-14.

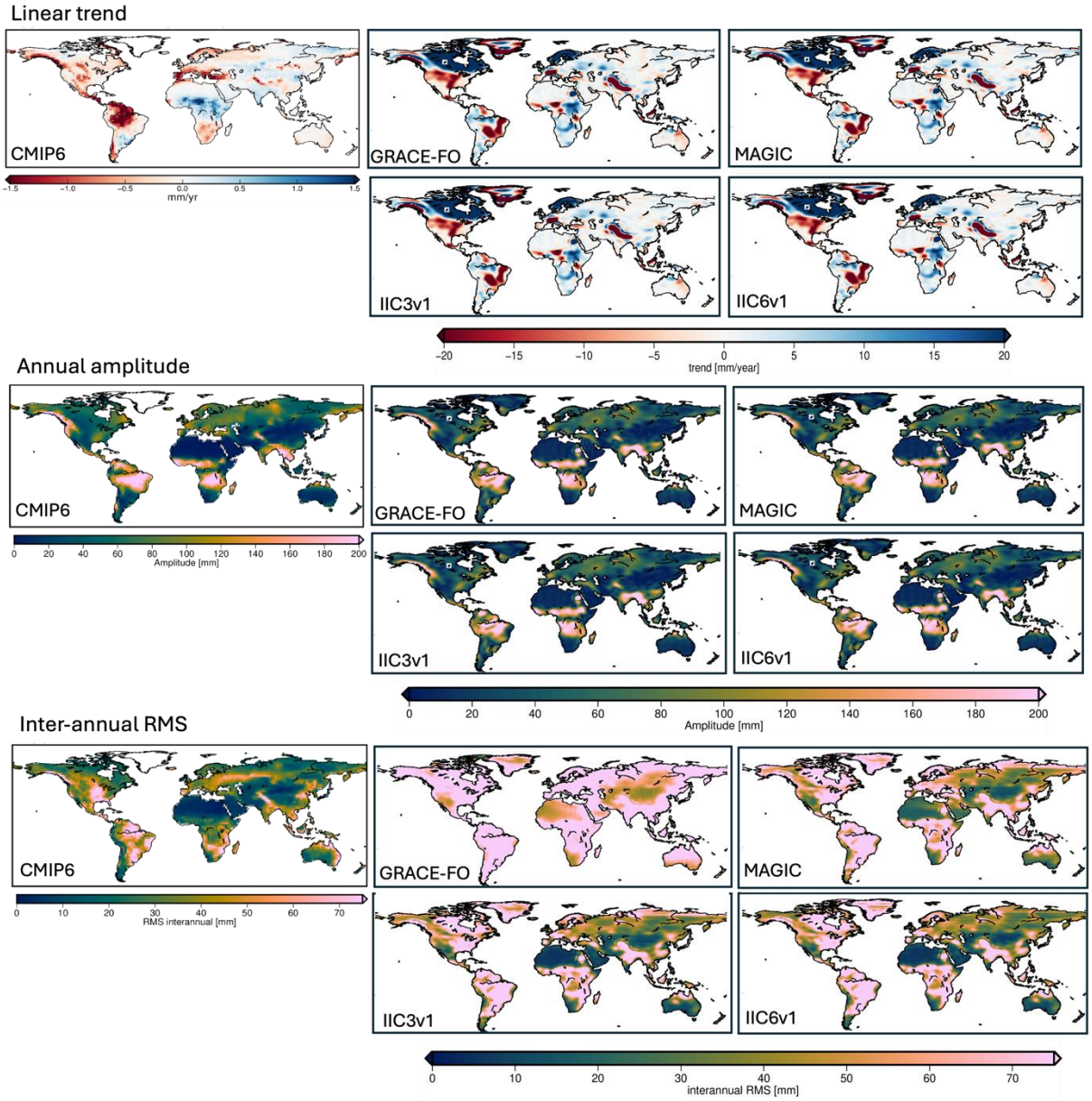

Figure 42-14: Comparison between CMIP6 models (1950-20100, ensemble median) and different 12-years simulation output for the linear trend (top), the annual amplitude (middle), and the inter-annual RMS (bottom). Simulation output filtered with DDK5 and truncated at N=90.

First, it can be noted that in case of the trend and of the annual amplitude (top and middle part of Figure 42-14) there is hardly any qualitative difference visible between the maps of the different mission scenarios. Neither of the maps show any sign of spatial noise or error stripes. Even though the errors of the individual 7-days solution for the same post-processing (see Figure 42-8) is quite different, the stabilizing effect of the amplitude and trend estimation from altogether 624 data points (almost to 12 years of 7-days estimates) largely mitigates the uncertainties even for only one polar satellite pair. However, as will be shown in the next section, the accuracies of the trend estimates are different, but the signal-to-noise ratio for all mission scenarios is large enough that these differences are not visible in the shown plots. Only if unfiltered solutions are used until high (e.g. N=90) resolution, error stripe patterns become visible particularly for the GRACE-FO case (not shown). For the interannual variations Figure

42-14 (bottom part) does reveal visible differences between the mission scenarios. While the two quantum missions show very similar results, the signal variation is slightly larger for the MAGIC mission, visible, e.g., in the Sahara Desert region. As there is no major inter-annual signal expected in this area, this is most likely a sign of larger noise in the time series leading to spurious inter-annual variations that remain even after the temporal lowpass filtering. This is even more pronounced in the GRACE-FO case with generally larger inter-annual variations that can most likely again be related to increased noise levels. A comparison to the CMIP6 model output shows quite a reasonable agreement of CMIP6 with the ESA-ESM simulations for the inter-annual RMS (at least for the MAGIC and quantum missions) and a good correspondence between satellite simulations and climate models for the annual amplitude, that was also noted by [RD-1] for the comparison between CMIP and real GRACE observations. This hints at a good skill of the models to simulate the seasonal cycle. The linear trend, however, cannot be directly compared between climate models and simulations due to the very different time spans (250 years vs. 12 years) and the inter-annual variations masking the long-term trend in the shorter times span (see also discussion on trend stability in the next section). Therefore, previous studies in [RD-2] only compared the direction (i.e. the sign) of the trends to identify "hot-spots" in which current (short-term) trends might already be hinting towards long-term wetting or drying. All mission scenarios are in principle suitable for carrying out similar studies and the longer mission duration will increase the accuracy of the trend estimates (see section below).

TREND STABILITY VS. INTER-ANNUAL VARIATIONS

To assess the accuracy and stability of linear trends, in a first step approximate errors were derived for trend estimates from differently long time spans by error propagation starting from the empirical gridded accuracies of 7-days solutions shown in Figure 42-10. Assuming the estimation of the linear trend parameters in a least squares sense from the time series of each grid cell, the resulting formal standard deviations of the trend parameters are shown in Figure 42-15 for different mission scenarios and an assumed 12-years time span (i.e. the one provided by the simulations).

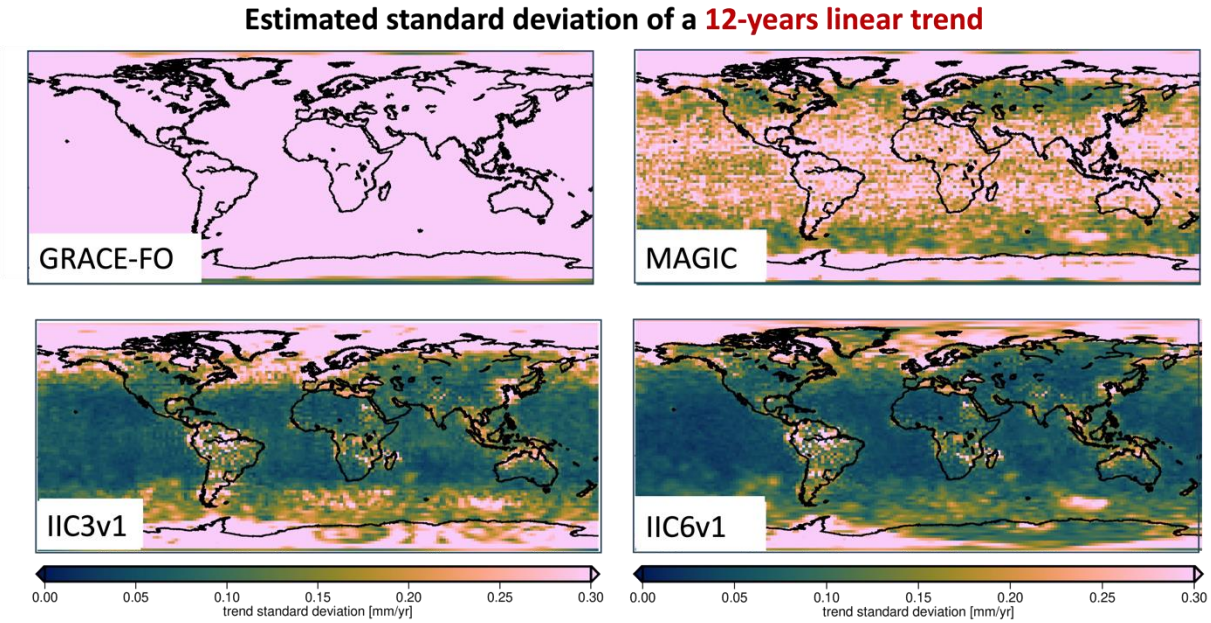

Figure 42-15: Standard deviation of a 12-years linear trend estimate derived by error propagation from the empirical accuracies of 7-days solution time series (DDK5 filtered, truncated at N=90)

While trend maps in Figure 42-14 looked very similar for the different missions, the error estimates show a more diverse picture. Here the GRACE-FO scenario has considerable larger standard deviations with strong improvements already achieved by MAGIC and even smaller propagated errors for the two quantum missions. The error propagation was repeated for differently long time spans and the mean grid cell value for each time span and each mission constellation is summarized in Figure 42-16. Here it can be seen that with increasing time span the standard deviations of the trends decrease (as it is expected) and the differences between MAGIC and the two quantum missions become smaller. After around 30 years of data, all three scenarios show mean trend accuracies of smaller than 0.1mm/year and after 40-50 years the numbers are in the range of 0.05mm/year or even below for the quantum missions. Only for the GRACE-FO-like mission, the trend accuracy is still much higher with a propagated uncertainty of around 0.6mm/year. However, this is already as very small number that might be sufficient in many regions with rather large trend signals. Nevertheless, and increase in the trend accuracy achieved by the new mission scenarios will become relevant in regions with small trends or overall small TWS signals, in which trends below 1mm/year shall robustly be quantified.

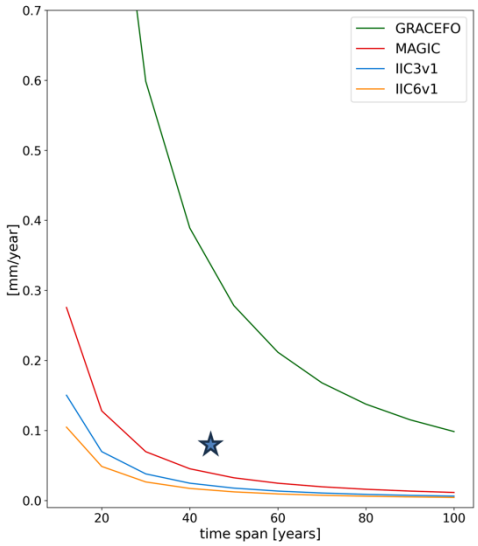

Figure 42-16: Mean trend accuracies for different time spans. Blue star: propagated trend accuracy assuming 25 years of GRACE-FO, 10 years of MAGIC, and 10 years of IIC6v1 accuracies.

It should be noted that of course 40-50 years of quantum constellation data will not be available any time soon. Therefore, an additional error propagation was performed assuming a more

realistic case of 25 years of GRACE(-FO) data, followed by 10 years of MAGIC, and another 10 years of IIC6v1 observations and the result is indicated by the blue star in Figure 42-16. Here it should be kept in mind that such an error propagation assumes lower observation standard deviations (and consequently much higher weights) for the last 20 years of the data set compared to the first 25 years, which will distort the trend estimate particularly in the presence of inter-annual variations non-linear accelerations. The trend estimation must, therefore, be handled with caution. While it can be summarized that the new mission constellations starting from MAGIC will most likely be sufficient to deliver trend estimates with high enough accuracies for most applications based on pure error propagation of the measurement uncertainties, an important challenge of the upcoming decades will be the combination of differently accurate satellite missions to derive robust trend estimates over long time spans.

The second challenge, very likely dominating trend uncertainties beyond the pure measurement accuracy, is the stability of linear trends compared to overlaying inter-annual variations. To investigate this issue, a model study was performed based on the methodology described in Jensen et al. 2019 [RD-2] using the 250-years time series provided by the CMIP6 model ensemble. For each of the 105 model runs of the ensemble, short-term trends (=”tendencies”) were derived for differently long time spans from 5 to 100 years. The time span to compute the short-term tendencies was shifted over the whole 250-years time span in 5-years steps and for each of these time slices the short-term tendency was compared to the long-term 250-years trend of the same model run. Subsequently, the fraction of the continental grid cells, for which the short-term tendency agrees with the long-term trend was averaged over all model runs. The resulting fractions for agreement (blue) and disagreement are plotted in Figure 42-17 with the shaded areas indicating the ensemble spread. It can be seen, that for time spans up to a little over around 10 years the difference between agreement/disagreement of short-term trends with the long-term trends is almost only by chance with the difference between the blue and red line not exceeding the model uncertainty (shaded area). With the ~20 years of data available today, it is clearly possible to differentiate between agreement (56%) and disagreement (44%). With about 50 years of data, e.g. after 10 years of a quantum mission to be launched in the 2040s, the two lines considerably spread from each other (63% agreement vs. 37% disagreement), showing the added benefit of the longer time series. The difference between the absolute numbers for 20 vs. 50 years might appear small, but here it needs to be kept in mind that the y-axis cannot be expected to reach 100%, as can be seen even for 100 years of time series for which the agreement is only 72%. The reasons for this are probably manifold: The continental grid cells include large areas (e.g. deserts) with trend signal around zero (both for the short-term tendencies and for the long-term trend) leaving the agreement completely up to chance. Furthermore, part of the CMIP6 models might include unrealistic multi-decadal oscillations and

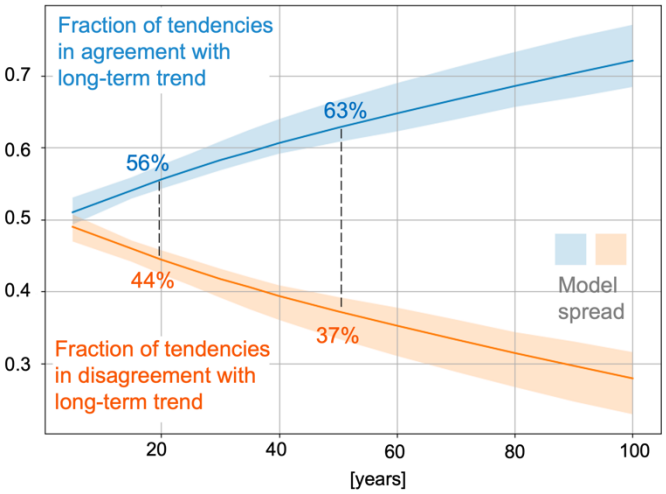

Figure 42-17: Proportion of continental grid cells of short-term trend maps for different time spans in agreement and disagreement with the direction of the bicentennial long-term trend in CMIP6 models. Methodology based on [RD-2], figure created with the support of L. Jensen.

some of them show rather peculiar long-term behavior in various areas due to, e.g., a saturation of water storage in the too shallow soil layers. Despite these inherent limitations of the model study and the resulting limited meaning of the absolute numbers of agreement/disagreement, the relative added benefit of future satellite missions and the resulting longer observation time spans are obvious.

DETECTABILITY OF CHANGES IN THE SEASONAL CYLCE

Following theories about climate change possibly leading to an "intensification" of the global water cycle resulting in, e.g. an increase in the annual amplitude of water storage change, and/or that climate-induced changes in atmospheric circulation patterns changing the phase of the annual peak, Jensen et al. 2020 [RD-1] investigated the detectability of such changes in the annual water cycle using satellite gravimetry. A satellite mission that is able to observe and quantify these changes would be beneficial in two ways: (i) Satellite gravity could be used as tool to proof (or falsify) the postulate of an intensification of the water cycle in different regions of the world, and (2) the data could serve to validate whether climate models correctly simulate such changes. Projected changes in amplitude were derived from an ensemble of global climate models taking part in the CMIP6 model inter-comparison project following [RD-1].

To analyze the detectability of these projected changes of the annual cycle by current or future satellite gravimetry missions, they were compared to the achievable accuracies of these quantities from the end-to-end simulations provided within this project. To this end the grid-wise RMSD values of the simulated 7-days temporal residuals (full-scale simulations for months 2002-01/-2002-03) were error propagated to derive standard deviations of amplitude/phase change after 30 years. For the amplitude change these standard deviations are shown in Figure 42-18 (top) for the GRACE-like mission (left) and for the MAGIC mission (right) and in Figure 42-18 (bottom) for the two quantum constellations IIC3v1 and IIC6v1. Here we use equally DDK5 filtered solutions for all scenarios with a truncation degree of N=90, as the resulting 220 km spatial resolution resembles the resolution of the climate models. DDK5 has been shown to be sufficient for the quantum missions and the experiment should compare how the different missions perform for the same spatial resolution.

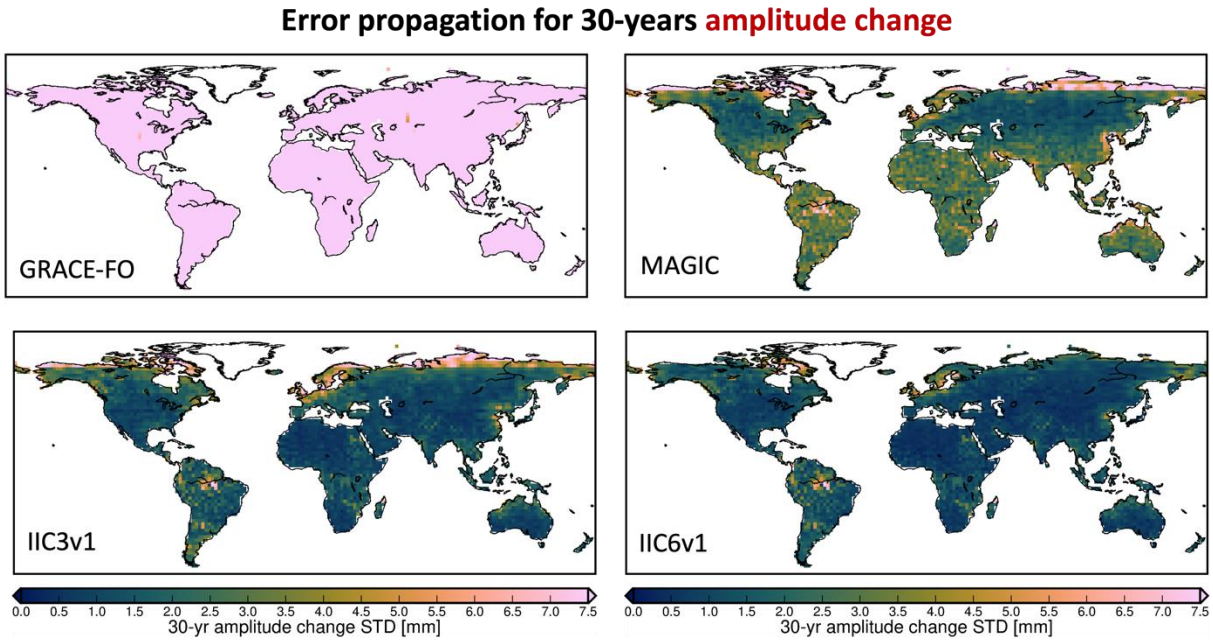

Figure 42-18: Standard deviation of 30-year amplitude change for the GRACE-FO (top left) and MAGIC (top right) missions and for the two quantum constellations (bottom)

The projected amplitude changes from the ensemble of CMIP6 models are now challenged against these accuracies and colored pixels in Figure 42-19 denote regions where the projected amplitude change exceeds the magnitude of the accuracy. In this case we assume the amplitude change to be "detectable". It can be seen, that a GRACE-like mission with the chosen weak DDK5 filtering cannot detect the anticipated amplitude changes apart from some very few grid cells. The MAGIC mission, however, already performs much stronger, with amplitude changes being detectable in 57% of the land area after 30 years of observations for the given setting. The quantum constellations show a considerable added benefit with a detectability in 72% (IIC3v1) and 77% (IIC6v1) of the continental area. Particularly the latter leaves only a few desert areas for which the anticipated amplitude changes are not detectable.

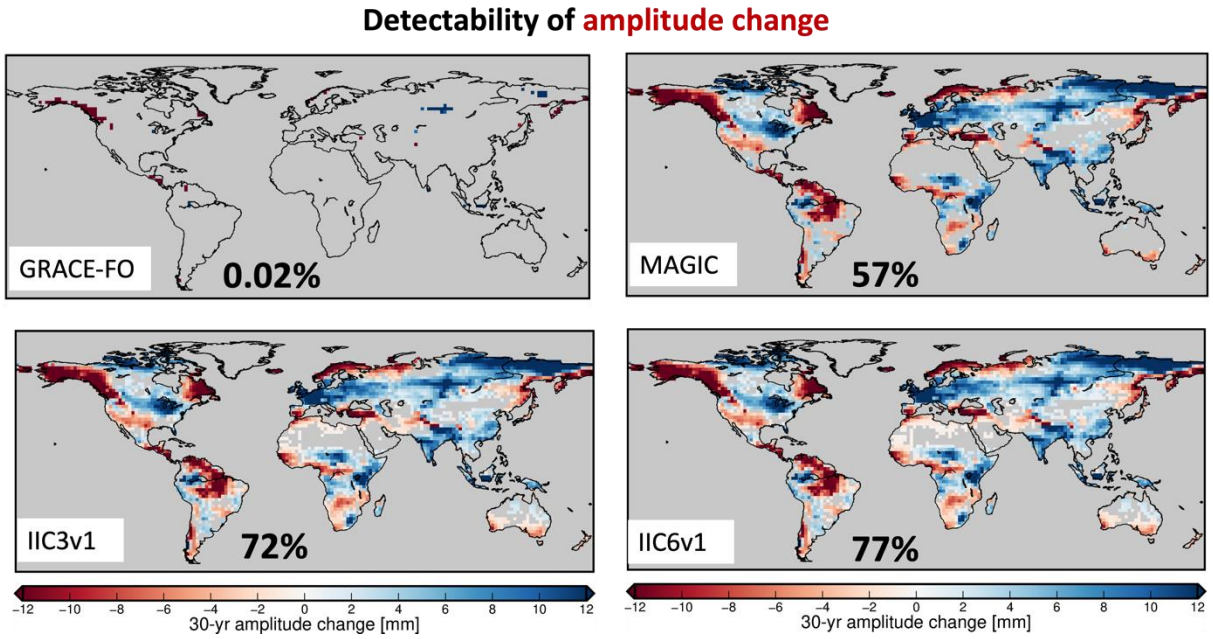

Figure 42-19: Detectability of amplitude change after 30 years. Colored pixel: amplitude change is regarded as detectable.

The same analysis was repeated for the change in the phase of the annual cycle. The results look qualitatively very similar to the results for the amplitude change. The maps are, therefore, not plotted in detail. However, the table in Figure 42-20 summarizes the results for both the detectability of amplitude and phase changes and the improvement achievable with additional satellite pairs (and improved sensors) can strongly also be seen for the phase change, for which MAGIC allows a detectability in 48%, IIC3v1 for 60% and IIC6v1 for 66% of the global land area compared to hardly any detectability for GRACE-FO.

Mission	Amplitude	Phase
GRACE-FO	0.02%	0.04%
MAGIC	57%	48%
IIC3v1	72%	60%
IIC6v1	77%	66%

Figure 42-20: Table of percent of land area for which 30-years amplitude and phase changes are detectable.

DIRECT USE OF LONG-TERM PARAMETERS VS. MONTHLY SOLUTIONS

The global maps of trend estimates shown in Figure 42-14 was derived from 12 years of 7 days solutions (dataset 3) to which a bias, trend and seasonal signal was fitted according to the parameter model shown in Eq. (1). A promising alternative is the direct estimation of the trend, sine and cosine parameters (b, c, and d in Eq. 1) from the 12 years of inter-satellite observations. The direct estimates ("long-term parameterization") have been provided by TUM in addition to the 7-days solutions. Figure 42-21 shows the difference of the trend estimate derived from the 7d solutions to the reference trend estimated from the ESA ESAM. Here the unfiltered solutions are used, as the trend estimation introduces an inherit stabilization that allows a very high spatial resolution. While for the GRACE-FO and also the MAGIC case, the unfiltered trends still show large differences to the reference, the quantum missions actually allow a reasonable trend estimation without additional post-processing.

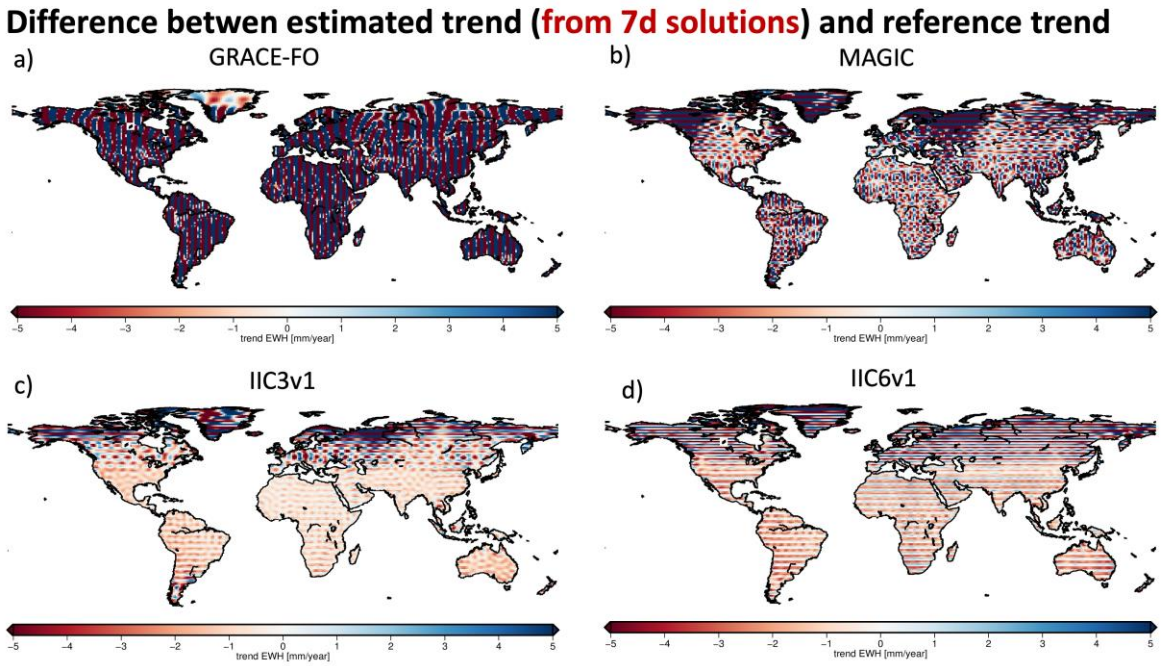

Figure 42-21: Difference between the reference trend (form ESA ESM) and the trend estimate derived from 12 years of 7 days solutions (N=90, unfiltered).

Figure 42-22 shows the equivalent maps of trend estimates that were derived by direct long-term parameterization from the 12 years of satellite data. Comparing the respective results for GRACE-FO (a) and MAGIC (b) in Figure 42-21 and Figure 42-22 reveals a slight increase in the differences w.r.t to the reference trend. This is counter-intuitive and was attributed to the fact that the long-term estimations are more sensitive to the applied noise models than the weekly estimations. The current noise models are not yet ideal for describing the system as they consider instrument noise, whereas the errors introduced through temporal aliasing are not statistically described in these models. The estimations of IIC3v1 and IIC6v1 are less sensitive to this issue because of the higher intrinsic de-aliasing capabilities through the constellation configuration.. For the two quantum missions IIC3v1 (c) and IIC6v1 (d), however, the direct trend estimation reveals its potential. The large east-west striping visible especially for IIC6v1 in Figure 42-21d has vanished to a large extend in Figure 42-22d. Very similar conclusions can be drawn for the estimation of the annual amplitude (not shown): Large errors persist in the estimation of the annual amplitude for GRACE-FO and (to a much lesser extent) for MAGIC and substantially smaller differences can be found for the quantum missions. The latter again improve slightly further by the direct long-term parameterization of the annual signal.

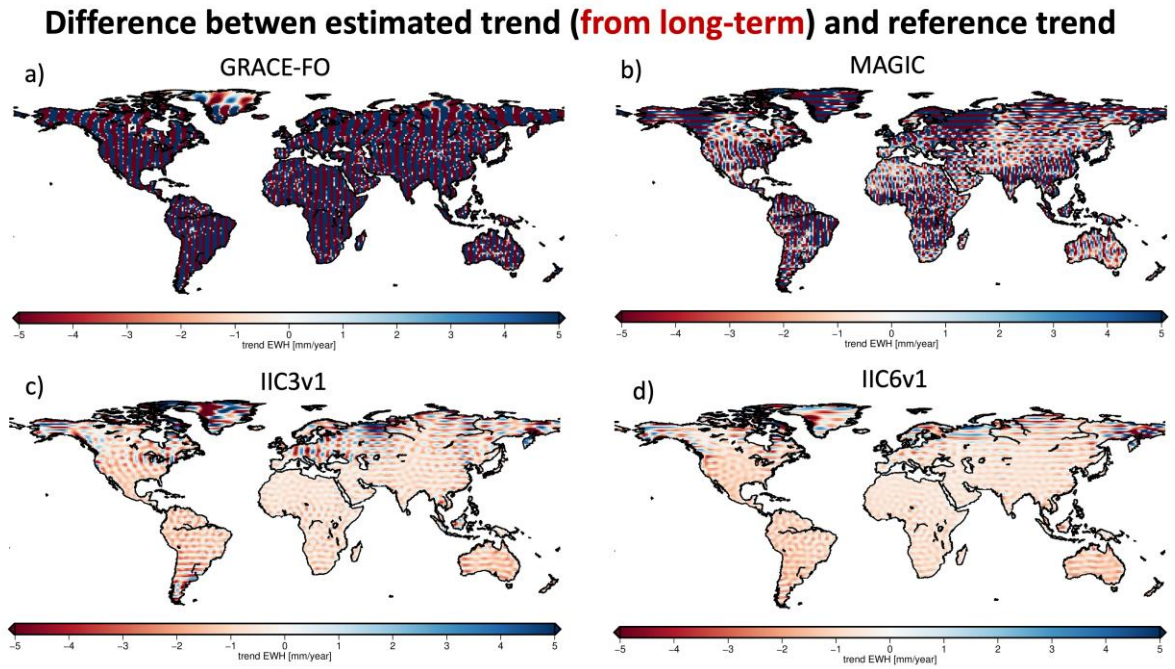

Figure 42-22: Difference between the reference trend (from ESA ESM) and the long-term trend estimate derived directly from 12 years of satellite data (unfiltered, N=90).

43. APPLICABLE DOCUMENTS, REFERENCE DOCUMENTS, AND PUBLICATIONS TO PART 7

43.1. APPLICABLE DOCUMENTS

[AD-1] Mission Requirements Document, Next Generation Gravity Mission as a Mass-change And Geosciences International Constellation (MAGIC) - A joint ESA/NASA double-pair mission based on NASA's MCDO and ESA's NGGM studies (2020). ESA-EOPSM-FMCC-MRD-3785

[AD2] Scientific Readiness Levels (SRL) Handbook, Issue 1, Revision 0, 05-08-2015

[AD3] Study of Cold Atom Interferometry (CAI) Gravity Gradiometer Sensor and Mission Concepts - ESA Contract 4000112677, Summary Report "Concept study and preliminary design of a cold atom interferometer for space gravity gradiometry"

[AD4] Cold Atom Inertial Sensors: Mission Applications – ESA Contract 4000117930, Final Report TASI-SD-CAI-FR

[AD5] Hybrid Atom Electrostatic System for Satellite Geodesy – ESA Contract 4000113573, Final Report RF_7-24721_DMPH

[AD6] Hybrid Atom Electrostatic System for Satellite Geodesy Follow-On – ESA Contract 4000112290, Final Report RT 6/27346 DPHY

[AD7] QSG_UR_SATM_v2.0.xlxs – ESA/EC Quantum Space Gravimetry User Requirements Science and Traceability Matrix v2.0 (2022)

[AD8] Quantum Space Gravimetry for monitoring Earth's Mass Transport Processes (QSG4EMT). Project Proposal, Proposal No. TUM/2022-QSG4EMT, Technical University of Munich

43.2. REFERENCE DOCUMENTS

[RD-1] Jensen, L., Eicker, A., Dobslaw, H., & Pail, R. (2020): Emerging Changes in Terrestrial Water Storage Variability as a Target for Future Satellite Gravity Missions. Remote Sensing, 12(23), 3898.

[RD-2] Jensen, L., Eicker, A., Dobslaw, H., Stacke, T., & Humphrey, V. (2019). Long-term wetting and drying trends in land water storage derived from GRACE and CMIP5 models. Journal of Geophysical Research: Atmospheres, 124(17-18)

[RD-3] Besnier, J., Getirana, A., Beaudoing, H., & Lakshmi, V. (2024). Characterizing the 2019-2021 drought in La Plata River Basin with GLDAS and SMAP. Journal of Hydrology: Regional Studies, 52, 101679.

[RD-4] Maurizio, G., Braitenberg, C., Sampietro, D., & Capponi, M. (2023). A new lithospheric density and magnetic susceptibility model of Iran, starting from high-resolution seismic tomography. Journal of Geophysical Research: Solid Earth, 128, e2023JB027383.

[RD-5] Braitenberg, C., & Pastorutti, A. (2024). Detectability of seamount eruptions through a Quantum Technology Gravity Mission MOCAST+: Hunga Tonga, Fani Maoré and other smaller eruptions. Surveys in Geophysics, 45, 1331-1361.

[RD-6] Straume, E.O., Steinberger, B., Becker, T.W., Faccenna, C., 2024. Impact of mantle convection and dynamic topography on the Cenozoic paleogeography of Central Eurasia and the West Siberian Seaway. Earth Planet. Sci. Lett. 630, 118615.

[RD-7] Uebbing, B., J. Kusche, R. Rietbroek, and F. W. Landerer. "Processing Choices Affect Ocean Mass Estimates From GRACE", Journal of Geophysical Research: Oceans 124.2 (2019), pp. 1029–1044. doi: 10.1029/2018JC014341.

PART 8:

OUTREACH

44. SCIENTIFIC PAPERS

This purpose of this part is to describe the 3 scientific papers (deliverables D8 to D10), which summarize the main scientific results of this project QSG4EMT. They are either already published or are going to be submitted soon (status: Oct. 2024):

- Encarnação J., Siemes C., Daras I., Carraz O., Strangfeld A., Zingerle P., Pail R. (202x): Towards a realistic noise modelling of quantum sensors for future satellite gravity missions. In preparation for re-submission to Advances of Space Research.
- Zingerle P., Gruber T., Pail R., Daras I. (2024): Constellation design and performance of future quantum satellite gravity missions. Earth Planets Space 76, 101. https://doi.org/10.1186/s40623-024-02034-3
- Kusche J. et al. (202x): Benefit of multi-pair quantum satellite gravity missions in Earth science applications. In preparation for submission to Nature Reviews Physics.

Additionally, further scientific papers on the results of the user survey, the regional solutions and spline parametrization schemes are planned to be written as an offspring of this study.